CRANFIELD UNIVERSITY

SCHOOL OF INDUSTRIAL AND
MANUFACTURING SCIENCE

Ph.D. THESIS

Academic Year 1996-1997

Y.B.P. KWAN

Processing and Fluid Flow Characteristics of Hot Isostatically Pressed Porous Alumina for Aerostatic Bearing Applications

Supervisors: D.J. Stephenson
J. Corbett

December 1996

This thesis is submitted in complete fulfilment of the requirements
for the degree of Doctor of Philosophy

La magnifique et pitoyable famille
des hypersensibles est le sel de la terre.
Ce sont eux et non les autres qui ont fondé
des religions et produit des chefs-d'œuvre.

Proust

Cette famille-là est ma seconde famille; et
tout ce que j'ai pu réaliser qui approche
du chef-d'œuvre, c'est à cette affiliation que je le dois...
Du temps de mes premières souffrances,
je ne percevais pas la souffrance mentale comme un don...
Mais maintenant, je sais que c'en est un.

Y. Saint Laurent

ABSTRACT

Despite their well known superior load and stiffness characteristics, the wide-spread use of porous aerostatic bearings in preference to other bearing types has been hampered by difficulties in controlling the permeability of the porous material during manufacture and machining, in addition to instability problems caused by the additional volume of air trapped amongst the pores. Recent development in porous aerostatic bearings centres around the use of a thin dense surface layer to overcome the stability problem.

The production of single and two-layered porous ceramic structures for aerostatic bearing applications have been investigated using the free-capsule hot isostatic pressing process, and in conjunction with slip and tape castings. The influence of various process parameters on open porosity, and the empirical relationships between porosity, particle size and the resulting fluid flow and structural properties were determined from experimental data. The measurement accuracy and uniformity of temperature within the furnace are identified as the most important factors affecting consistency and predictability of the permeability of the porous substrate.

Prototype bearings were produced and tested, based on the above materials. The single-layer bearing was, not unexpectedly, found to be unstable over a wide operating range. The use of a two-layered bearing material eliminated the stability problem.

Initial measurements of the slip coefficient of the porous material in air and at small gaps indicated significant deviation from the Beavers' theory. The effect of velocity slip was found to be significant in both test bearings, and was allowed for by the addition of an equivalent clearance to the bearing gap. The value of the equivalent clearance was deduced from experimental data. The static load characteristics and the pressure profile of both test bearings agreed well with published theories, once the above-mentioned correction for slip was applied.

ACKNOWLEDGEMENT

The author would like to take this opportunity to express his gratitude to the Committee of Vice-Chancellors and Principals for providing part of the finance under the Overseas Research Award Scheme, without which his stay at Cranfield would not have been possible.

His most special thanks are due to Mr. A. Baldwin at the Central Workshop of the School of Industrial and Manufacturing Science (SIMS). His strong and consistent support on the machining work was crucial to the timely completion of the present project. Of equal importance was the outstanding service provided by the staff of the Cranfield Library, and in particular the continuous support of the Enquiry and Inter-library Loans sections throughout, for which the author is truly grateful. Thanks are also due to Dr.-Ing. T. Kneisel at the Technische Hochschule Darmstadt, Germany, and Mr. M. Osawa of NEC Corp., Japan, for helping to locate some of the literature at their respective countries.

Particular thanks also go to Dr. G. Oddie at the School of Mechanical Engineering (SME), and Dr. J.R. Alcock of SIMS for the numerous inspiring discussions on fluid flow measurements and ceramic processing respectively, and for their constant encouragement. Equally, the author is obliged to Messrs. J. Hedge, K. Lawson, P. Logan, A. Dyer, M. Collins, and M. Faulkner of SIMS for their assistance during the equipment commissioning and the experimentation stages of the project. He is also most grateful to Dr. J.W.P. Ho of the British United Shoe Machinery Ltd., Leicester, for his advises on CAD related matters, and to Dr. I.M. Thompson of Alcan Chemicals Europe Ltd. for his generous offer of a range of free ceramic powders used in the present work.

Finally, the author would like to thank his supervisors, Prof. D.J. Stephenson and Prof. J. Corbett, for the provision of excellent research facilities at Cranfield, and the very significant part they played in ensuring that the project was completed on time. He owes much to his family for their moral support during his stay in Cranfield.

Y.B.P. Kwan
Dec. 1996.

CONTENTS

LIST OF FIGURES

NOTATIONS

Symbol	Description	Units (SI)
A_m	mutual collision cross section	m^2
A_p	cross sectional area of the porous specimen	m^3
E	Young's modulus	Pa
E_o	Young's modulus of the fully dense material	Pa
E_r	Error function	
F_1	correction factor for fundamental flexural mode to allow for the finite thickness of bar, Poisson's ratio, etc.	
I_0	zero order modified Bessel function	
K_b	dimensionless bearing stiffness	
L_b	length of journal bearing	m
L_e	distance of slot restrictor to end of bearing	m
L_s	length of a rectangular specimen	m
L_{sl}	length of a rectangular specimen	m
$\dot{M}$	mass flow rate	$kg\ s^{-1}$
$\dot{M}_p$	mass flow rate between a porous and a solid surface	$kg\ s^{-1}$
$\dot{M}_s$	mass flow rate between two solid surfaces	$kg\ s^{-1}$
P_{go}	gauge pressure ratio	
P_o	corrected pressure difference to allow for compressibility	Pa
Q	volume flowrate at flow sensor local pressure	$m^3\ s^{-1}$
Q_{mean}	volume flowrate at mean pressure across specimen	$m^3\ s^{-1}$
Q_p	volume flowrate between a solid and a porous boundary	$m^3\ s^{-1}$
Q_s	volume flowrate between two solid boundaries	$m^3\ s^{-1}$
ΔQ	relative increase in flow due to the presence of a porous surface	
R	universal gas constant	$N\ m\ K^{-1}$

R_a	arithmetic mean deviation of the profile	m
R_p	maximum profile peak height	m
R_z	ten point height of irregularities	m
T	temperature	K or °C
T_s	sintering or hipping temperature	K or °C
V_{pore}	total volume of open pores within a specimen	m^3
V_{res}	volume of trapped air after repressurisation	m^3
V_s	total volume of the porous specimen	m^3
W	load carrying capacity	N
W_0	theoretical maximum load capacity ($= \pi r_p^2 [p_o - p_a]$)	N
$\overline{W}$	dimensionless load carrying capacity ($= W / W_0$)	N
W_f	Load at failure for the fracture test	N
X_o	elastic constants at full density	
a	empirical constant	
a*	slot factor	
b	empirical constant	
b_l	centre distance between supporting and loading rollers	m
c	empirical constant	
d	empirical constant	
d_{10}	value at 10% cumulative distribution	
d_{50}	value at 50% cumulative distribution	
d_{90}	value at 90% cumulative distribution	
d_b	diameter of journal bearing	m
d_{pk}	pore diameter corresponding to the peak of distribution	m
d_{pore}	circular-capillary-equivalent pore diameter	m
$d_{pore\ ave}$	average circular-capillary-equivalent pore diameter	m
$d_{pore\ max}$	maximum circular-capillary-equivalent pore diameter	m
d_w	mean particle size	m
f	friction factor	

f_1	correction factor to the bearing number	
f_r	fundamental resonance frequency	Hz
g	gravitational acceleration	$m\ s^{-2}$
h	physical clearance of the flow channel	m
h_e	equivalent clearance correction for velocity slip	m
h_o	equivalent clearance due to surface roughness of the porous bounding surface	m
h_s	equivalent clearance due to surface roughness of the solid bounding surface	m
h_w	height of water column above the test specimen	m
k	proportionality constant	
k_1	proportionality constant	
k_b	bearing stiffness	$N\ m^{-1}$
k_n	Knudsen number	
m	mass of the porous specimen	kg
$\dot{m}$	mass flow rate per unit area	$kg\ m^{-2}\ s^{-1}$
m_1	dry mass of the porous specimen	kg
m_2	fully impregnated mass of the porous specimen	kg
m_3	mass of the weighing pan in air	kg
m_4	mass of the weighing pan in water	kg
m_5	mass of the porous specimen and pan in water	kg
n	number of gas molecules per unit volume	m^{-3}
n_{meas}	number of measurements	
n_{re}	Reynold's number	
n_s	number of restrictor slots	
p	pressure	Pa
$\bar{p}$	dimensionless pressure ($= p / p_o$)	
p_a	atmospheric pressure	Pa
$\bar{p}_a$	dimensionless ambient pressure ($= p_a / p_o$)	
p_e	gas pressure at restrictor exit (absolute)	Pa
p_{mean}	mean absolute gas pressure across the specimen	Pa

p_{ref}	absolute pressure to which the measured flowrate refers	Pa
p_o	gas supply pressure (absolute)	Pa
p_{og}	gas supply pressure (gauge)	Pa
p_{pore}	absolute pressure within pores	Pa
p_s	hipping pressure (gauge)	Bar
p_{vac}	absolute pressure in desiccator during evacuation	Pa
p_1	absolute gas pressure upstream of the specimen	Pa
p_2	absolute gas pressure downstream of the specimen	Pa
p_3	absolute gas pressure at exit	Pa
p_3'	absolute exit pressure in the porous flow stream	Pa
Δp	pressure difference across the specimen	Pa
r	radius	
$\bar{r}$	dimensionless radius ($= r / r_p$)	
r_l	pitch radius of the ring fracture loading balls	m
r_p	radius of the porous pad	m
r_s	pitch radius of the ring fracture supporting balls	m
s_v	specific surface area	m^{-1}
t	time	s
u	fluid velocity in the radial direction	$m\ s^{-1}$
v	fluid velocity in the axial direction	$m\ s^{-1}$
v_s	sensor output voltage	V
w	width	m
w_b	width of bar specimen	m
w_s	slot width	m
x	distance between pressure tappings	m
x_{ij}	distance between pressure tappings i and j	m
z_b	thickness of bar specimen	m
z_g	bearing gap	m
z_{go}	bearing gap at zero eccentricity	m
z_p	thickness of the porous pad or specimen	m
z_{pf}	effective thickness of fine-pored layer of the porous pad	m

z_s	slot restrictor thickness	m
Φ_e	equivalent permeability coefficient	m^2
Φ_i	inertial permeability coefficient	m
Φ_{i2}	modified inertial permeability coefficient	$kg\ m^{-1}\ s^{-1}$
Φ_v	viscous permeability coefficient	m^2
Φ_z	viscous permeability coefficient in the axial direction	m^2
Φ_{zc}	permeability coefficient of the coarse substrate	m^2 or m
Φ_{zf}	permeability coefficient of the fine-pored layer	m^2 or m
Φ_{zt}	permeability coefficient of the combined layers	m^2 or m
ϑ	shrinkage of ceramic specimen after sintering / hipping	
ϑ_d	diametrical shrinkage	
ϑ_a	axial shrinkage	
ϑ_v	densification (increase in density)	
Λ	bearing number	
α_s	slip coefficient	
α_t	linear thermal expansion coefficient	K^{-1}
δ_c	deflection at the centre of the porous pad	m
γ	surface tension	$N\ m^{-1}$
γ_w	surface tension of water in air	$N\ m^{-1}$
η	viscosity of air	Pa s
λ	molecular mean free path	m
ν	Poisson's ratio	
ρ	density of air at atmospheric pressure	$kg\ m^{-3}$
ρ_g	green density of the powder compact (before sintering) as a fraction of the true density ρ_p	
ρ_{mean}	density of air at atmospheric pressure	$kg\ m^{-3}$
ρ_p	true density of ceramic powder	$kg\ m^{-3}$
ρ_s	density of the porous specimen (after sintering)	$kg\ m^{-3}$
ρ_w	density of deionised water	$kg\ m^{-3}$

σ	stress	Pa
σ_f	flexural strength	Pa
σ_o	flexural strength at full density	Pa
σ_r	stress in the radial direction	Pa
σ_t	stress in the tangential direction	Pa
σ_s	non-dimensional slip flow passage height	
τ	tortuosity factor	
ζ	porosity	
ζ_c	closed porosity	
ζ_{cr}	critical porosity at which the elastic modulii approach zero	
ζ_o	open porosity	
ζ_t	total porosity	

1. INTRODUCTION

As we approach the next century, the knowledge of mankind has developed at such a tremendous pace that, as an example, the shaping of material atom by atom, known as atom bit processing, is no longer science fiction but reality [1]. In particular, advances in microelectronics [2] have not only taken nanoengineering away from laboratories to high volume production lines, but also made it an essential, indispensable part of everyday life (Fig. 1.1).

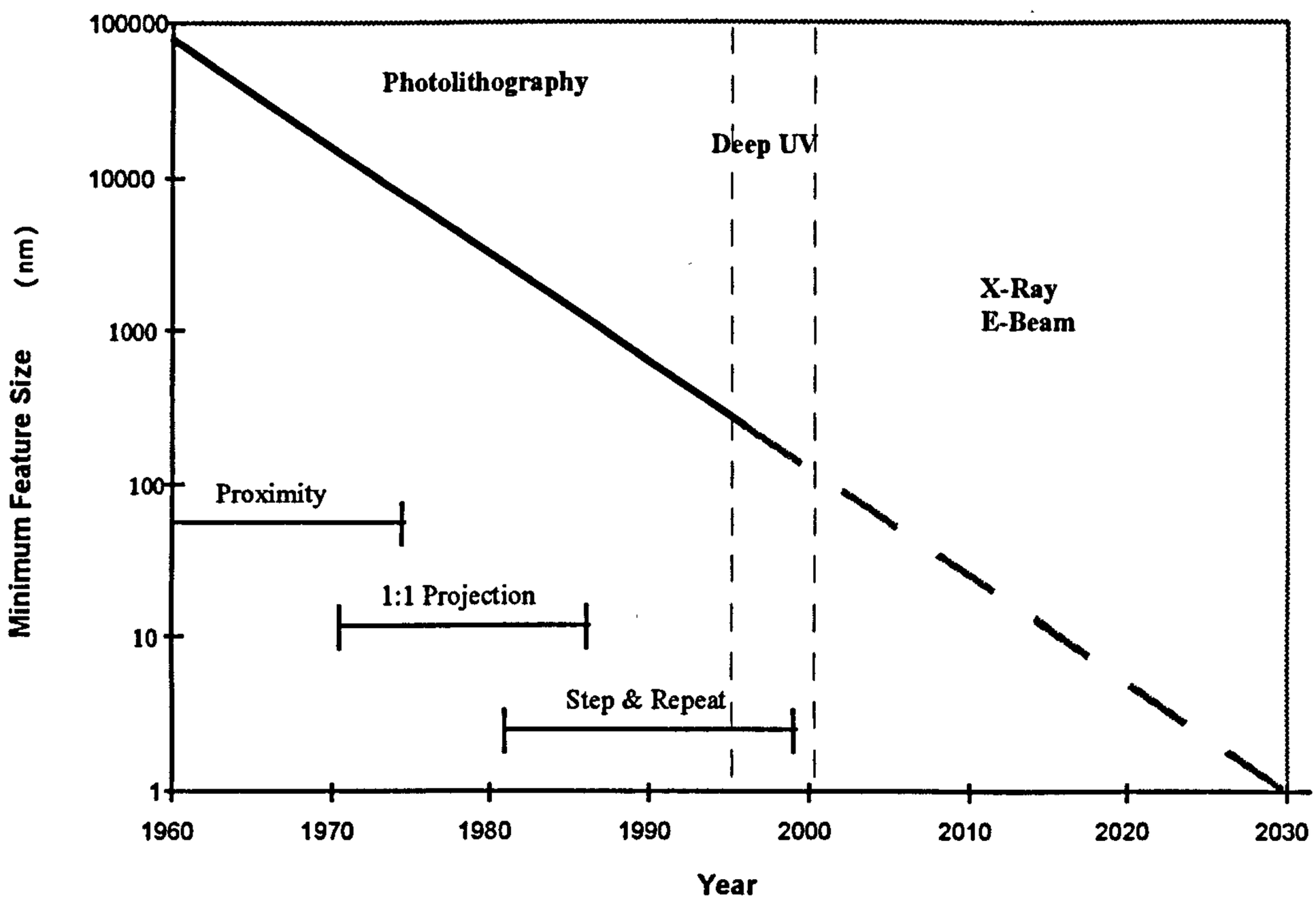

Fig. 1.1 Evolution of MOS Memory Device Feature Size (Data from [2])

As a recent study in Germany into high precision machining [3] has shown, conventional rolling element bearings and guideways used in most modern day production equipment are fast reaching their limits. Even with specially hand-lapped and matched sets,

geometrical accuracies attainable are typically above the 2 μm level, while in the state of the art lithography, production equipment for feature sizes down to 0.15 μm has already been reported [4], with a corresponding demand for equipment with accuracy better than 30nm [1].

The ever increasing demand on accuracy and frictionless running of bearings (linear and rotary) means that the use of externally pressurised fluid film bearings has become the norm rather than the exception. In particular, aerostatic bearings are widely used in the manufacture of semiconductors because of their cleanroom compatibility, not only in 'front-end' lithography [5, 6, 7, 8, 9], but increasingly in 'back-end' assembly equipment as well [10]. Typically, aerostatic air bearings provide improved accuracy of up to two orders of magnitude better than that of conventional rolling element bearings [3].

1.1 AEROSTATIC BEARINGS -- BACKGROUND AND OPERATING PRINCIPLE

The use of pressurised air as a lubricant was first recorded around 1920 [11]. Most of the intensive research, however, was done in the 1950's, when the need arose, mainly from the nuclear and the defence industries, for high accuracy machining [12, 13, 14, 15]. Surveys of earlier work on the subject have been published by Gross and others [16, 17, 18, 19, 20]. There are also numerous publications thereafter, some notable examples being those by Bartz [21], Constantinescu [22], Powell [23], and Stout [24].

Although aerostatic bearings come in different types and forms, the basic operating principle is the same. A fluid (in this case air) film is forced under pressure into a gap by an external source between two machine components, the relative motion between which being guided by the bearing. The two components are thus physically separated from each other at all times, i.e., even when stationary, by the fluid film. When a low viscosity fluid, such as compressed air, is used as the lubricating medium, the bearing can be

considered to be virtually friction free except at extremely high pressures or running speeds.

To increase the stiffness of the bearing, i.e., its resistance to variation in bearing gap as a result of load variation, a flow restrictor is placed between the pressurised air supply and the inlet to the bearing gap. This, in the case of air bearings, is very often placed conveniently at the air inlet to the bearing surface. The restrictor usually takes the form of a fine orifice or a capillary [24], but could also be a microgroove machined on the bearing surface [25, 26, 27, 28, 29] or even inherently the bearing gap itself [24, 30]. It serves to reduce the pressure supplied to the bearing gap as flow increases with an increase in air gap, and vice versa. This change in pressure within the bearing gap returns the bearing to its static, stable equilibrium position after any slight disturbances.

Between the air inlet point and the rim of the bearing, the air pressure drops continuously until it reaches ambient at the bearing edge. The exact pressure profile depends very much on the particular bearing (or more precisely bearing gap) geometry. Aerostatic bearings often operate off compressed air line pressure, which in most cases is limited to not more than 6 bar. Their load capacity is therefore size-to-size comparatively limited (to e.g. hydrostatic bearings). Attempts to operate aerostatic bearings at much higher pressure have been reported [31, 32], but the higher pressure not only leads to much higher air consumption but also turbulent flow in the bearing gap and thus increases the chances of instability.

1.2 COMPARISON OF BEARING TYPES

One method that has been widely used in hydrostatic bearings to create a more uniform fluid pressure within the bearing gap is to incorporate a shallow pocket of optimum size around the fluid inlet, thus providing a large area at inlet fluid pressure. The pocket could be of uniform depth, which is typically not more than a few tenths of a millimetre.

This practice has not been popular with aerostatic bearings, however, because the extra dead volume of air, added to its compressibility, delays the response of the bearing pressure to any sudden changes in its operating gap and is believed to be the major cause of an instability phenomenon known as pneumatic hammering. Although recent reports [33, 34, 35, 36, 37] have indicated that more complex pocket geometries might be employed to overcome this problem, the stringent machining requirements and the difficulties in incorporating them in any bearing geometry other than simple circular thrust pads have so far prevented their widespread application.

A more practical approach to generate a more uniform pressure profile within the bearing gap would be to increase the number of inlet points, provided the bearing surface is sufficiently large to make this possible [38, 39]. The argument can be carried further that an infinite number of minute restrictors uniformly distributed over the entire bearing surface would provide the best pressure distribution and thus the highest load capacity and stiffness. The simplest way to achieve this is, of course, to use a porous material as the bearing surface.

2. PRESENT STATE OF DEVELOPMENT OF AEROSTATIC POROUS THRUST BEARINGS

As already discussed in the previous chapter, the use of a porous material at the bearing surface to provide a large number of minute restrictors, uniformly distributed over the entire bearing surface, would potentially create the most uniform pressure distribution, and thus the highest load capacity and stiffness [40]. Given a porous material with uniform and predictable fluid flow properties, porous aerostatic bearings are among the simplest to design and manufacture, as the restrictors are practically already built in. Even complicated bearing geometries, such as spherical bearings or aerostatic leadscrews, can be achieved without difficulties [41]. Such bearing geometries, on the other hand, require very complex constructions when using other restrictor types.

2.1 LITERATURE SURVEY

Works on the theory of porous aerostatic bearings have been widely published, for both journal and thrust bearings of various geometries. Amongst the many publications are two bibliographic reviews, the first of which by Sneck in 1968 [42]. This was later updated in 1976 by Majumdar [43]. Published literature up to then had already laid down the fundamentals of externally pressurised porous bearings, despite the inclusion of certain simplifications such as one-dimensional and incompressible flow. Two dimensional analyses for axisymmetric systems have also been performed numerically. Other work included corrections for compressible and slip flows. Dynamic and stability characteristics have also been studied, both theoretically and experimentally. Most of these publications assumed that flow through the porous medium obeys Darcy's law.

Work on thrust bearings after 1976 can be subdivided into two main streams. A number of theoretical studies have been the main interest of a group of researchers in India.

Their publications, entirely theoretical, include three dimensional, numerical analyses on rectangular thrust bearings, and incorporate additional conditions such as permeability anisotropy, tilt, slip flow, offset load, etc., both for rectangular and circular pads. Also included are a number of papers on instability and dynamic analyses. However, no experimental data have been attached.

The second stream, based largely on the research work in Germany and Japan, attempts to deal with pneumatic stability problems with the development of a so-called surface loaded porous material. This is essentially a porous material made up of a relatively coarse substrate and a thin dense layer, achieved either by deliberate smearing (or pore warping) of a ductile substrate, or by coating or surface impregnation techniques. This new approach appears to have solved the stability problems associated with the additional void volume within the pores at the bearing surface, and provokes a renewed interest in porous aerostatic bearings which have not seen widespread application in practice so far despite their tremendous potential.

2.1.1 Aerostatic Porous Thrust Bearings

The present literature survey concentrates on aerostatic circular thrust bearings of the porous type. This is by far the simplest geometry, both in terms of manufacture and theoretical analysis. It therefore provides the ideal background for the testing of new porous materials developed specifically for aerostatic bearing applications. For the sake of completeness, literature on rectangular porous bearings are also included.

2.1.1.1 Static Characteristics

One of the first reports of the theory of porous aerostatic thrust bearings was by Sheinburg & Shuster [44], in which the thrust bearing of a grinding spindle using a porous graphite restrictor was described. Theoretical analyses of the pressure distribution under

the bearing surface, load capacity and gas consumption were carried out, assuming laminar and incompressible flow, and treating the porous material as a uniaxial array of uniformly distributed fine capillaries across which fluid flow was assumed to obey Darcy's law. The concept of a bearing parameter χ, which was renamed by later authors [45] with minor modifications as the bearing number Λ, was introduced.

A different approach was adopted by Mori and co-workers [46] by treating the porous medium as equivalent to an additional fluid film to account for two dimensional flow, and hence the introduction of the method of equivalent clearance. Incompressibility and Darcy's law remained amongst the assumptions. A further 3 dimensional analysis of the same bearing geometry [47] showed close agreement with the simplified analysis.

One of the most complete analyses on porous aerostatic circular thrust bearings was performed by Gargiulo & Gilmour [45] , using finite difference method to solve the two dimensional problem numerically. The compressible, isothermal, laminar flow of the lubricating medium was assumed to obey Darcy's law. Analytical results for load and mass flow rate were compared with those obtained experimentally. This pointed to a need to compensate for the 'surface roughness', which as a result of the presence of the pores were much higher than a solid surface. The effect of anisotropy of permeability in the axial and radial directions were also analysed, the result revealing very little difference in load carrying capacity, but a reduction in gas consumption (by 10%) as transverse permeability reduces (by a factor of ten).

Supplementary to Gargiulo, Andrisano and Maggiore [48] carried out an additional numerical analysis using a lumped parameter model, and included in the results the effects of bearing tilt. Their analysis was accompanied by experimental results on load capacity and gas consumption. Correction to the bearing gap was also applied to compensate for the effect of surface roughness, with theoretical values lying between corrections using R_a and R_p respectively.

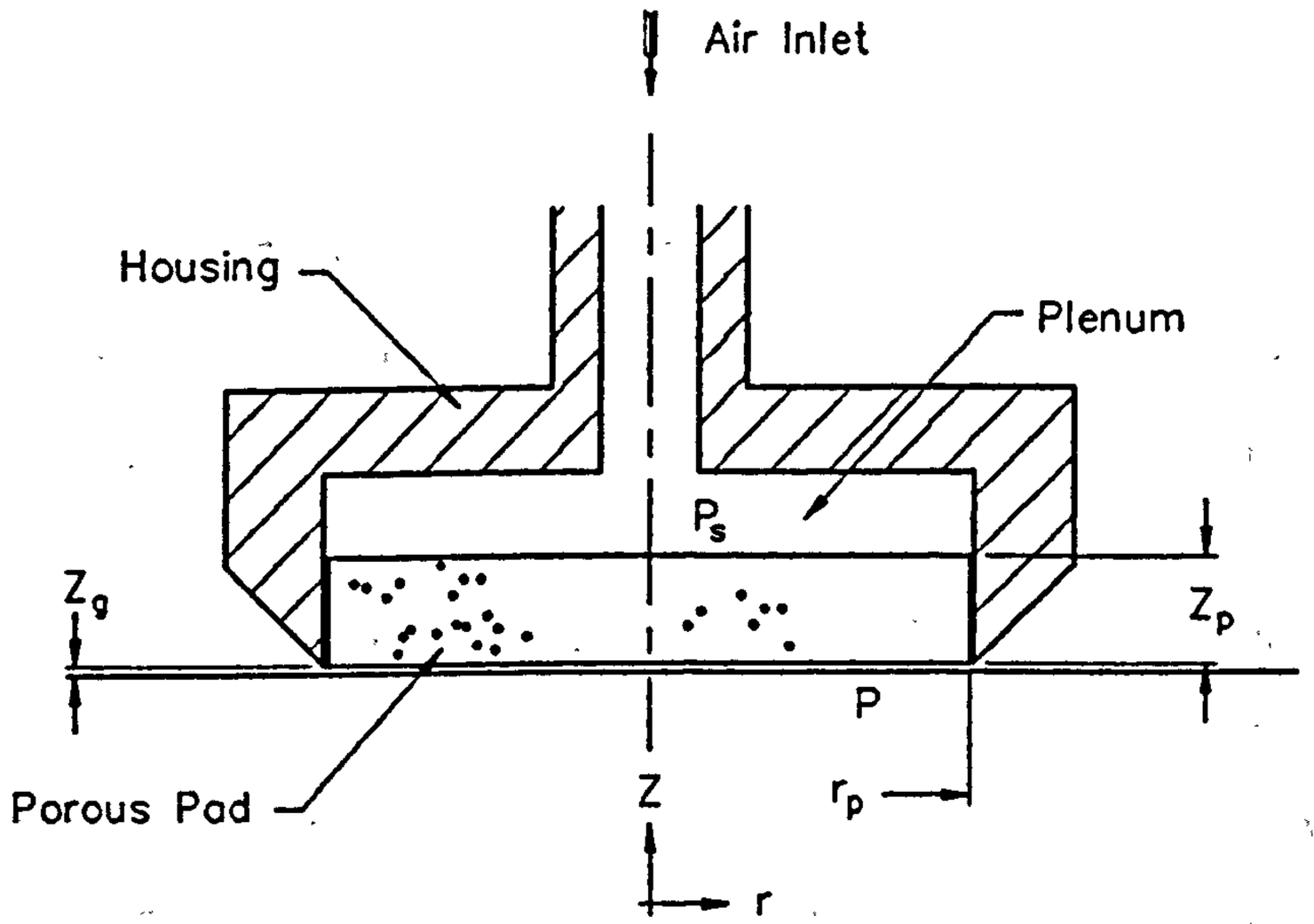

Fig 2.1 Schematic of a Porous Aerostatic Circular Thrust Bearing

The above analyses ignored the effect of velocity slip at the porous bearing surface, treating it as if it were solid (i.e. zero velocity) and attempting to compensate for its effect by adding a roughness value to the bearing gap instead. This assumption was first questioned by Ishizawa and Hori [49]. A number of authors also suggested that this slip component was not insignificant, and corrections to the original definition of the bearing number were proposed to incorporate the effects of slip flow at the surface boundary. Murti published two papers in succession, the first one suggesting a correction for compressibility of the gas medium but with no slip flow [50], and the second [51] with slip flow based on the Beavers and Joseph model [52] but assuming incompressible flow. Both corrections appeared to give better agreement with the experimental data from Gargiulo & Gilmour [45]. Jones and co-workers [53] assumed that the slip velocity at the bearing surface obeyed Darcy's law, and proposed a slightly different correction for slip flow, using perturbation methods to account for both compressibility and velocity slip. Agreement with Gargiulo [45] on load capacity was good, but not on the theoretical values of gas consumption. Further updates on the topic include that by Verma [54], and by

Singh [55] which was based on the full slip criterion as opposed to the simplified model used by Murti [51].

Investigations into the effects of fluid inertia have also been reported. Numerical analysis carried out by Hsing [56], for example, indicated that, for the range of bearing clearance commonly used in aerostatic bearings, inertia effects are confined to a narrow region near the bearing perimeter, with little effects on load capacity and stiffness. McCrea and Donaldson [57] developed further corrections to the bearing number to include both slip and inertia, and proposed the concept of an inertia criterion to assess its significance in specific applications. Generally, inertia effects are significant for materials with fine pore structures, large supply pressure and bearing clearance. The consequences are reduction in flow rate (blocking effect) and thus increase in load capacity.

The limitations of the Reynolds equation were looked into by Wang [58] and Bhatt [59]. Revised equations for pressure profile and load capacity using an approximated solution of the Navier-Stokes equation were presented. A quick calculation for a typical bearing geometry under normal working conditions indicated that the Reynolds number is well below 0.01, and the improvement of the correction therefore not significant.

Change in bearing-gap geometry due to elastic deformation of the porous pad under working pressure was the subject of investigation by Taylor and Lewis [60]. They assumed a perfectly flat pad under no load, resulting in a diverging gap when pressure was applied and leading to a reduction in pressure. A possible remedy was suggested by Polome and Gorez [61]. This approach involved subjecting the porous pad to the working differential pressure during machining. The porous pad would therefore resume a concave shape in the natural state, but flat at the design working clearance. At a bearing clearance below the design point, the pressure difference across the pad would be smaller, and the pad would therefore be concave. The reverse would be true for larger than design clearances. As indicated by Rehsteiner [62] for the case of orifice-regulated bearings, a slightly converging gap geometry produces more favourable load and stiffness characteristics.

Literature on the theory of rectangular aerostatic porous thrust bearings only began to appear at the late seventies. Notable examples are publications from Majumdar [63], Rao [64], and Singh [65]. They are again pure theoretical studies without experimental data to validate them. Work in Japan on rectangular bearings, both theoretical and experimental, has been reported by Aoyama and Inasaki [66, 67], using a porous block of large thickness but with a high permeability and unsealed on the perimeter. Further work including additional conditions such as offset loads [68, 69], bearing tilt, permeability anisotropy [70], velocity slip [71, 72] and sliding effects [73, 74] have also been reported. Theory for opposed-pad thrust bearings, both circular and rectangular, has been reported by Wu [75].

The change in permeability of the porous pad after machining, due to partial closure of pores by ductile 'smearing', is widely recognised [76]. Mori, for example, published a modification [77] to traditional bearing theory to allow for this 'surface loading effect' for journal bearings. Kawashima [78], on the other hand, treated the surface layer as an additional porous shell with a lower permeability instead. Modified theory and experimental results were also published by Okano [79] for thrust bearings using surface loaded, ductile porous materials, incorporating velocity slip and inertia effects in his analysis. Amongst the first reports of actually utilising this 'pore warping' is that by Polome and Gorez [61]. The pore warping was achieved in this case by 'over-grinding', and required constant monitoring of the effective permeability during machining. The unpredictability of this process prevented its widespread use despite obvious advantages in terms of pneumatic stability. In recent years, however, there is a revival of interest in the topic due to the emergence of different approaches to the production of such materials.

A substantial amount of work has been done in recent years by Heinzl [80] and co-workers in Germany. Using an electrical analogy and finite element methods, Köhler [81] compared the static and dynamic performances of a surface-loaded porous thrust bearing with those of orifice-restricted and conical-gap bearings of comparable size and geometry. Fundamental theory and simplified design equations for circular thrust bearings were the

main subject of the dissertation by Gerke [82]. The machining of such materials was described in detail by Hopfner [83]. The stability criteria of such bearings were described in more detail by Schroter [84]. Most recently, a change in approach has been reported [85] for establishing the dense surface layer. Laser drilling after surface densification by mechanical rolling seemed to have gained favour over pore warping by grinding, possibly due to better control of the process.

2.1.1.2 Dynamic Characteristics and Stability

One of the important advantages of aerostatic porous bearings in comparison to other restrictor designs is believed to be its better stability and damping characteristics [44, 81]. The performance of aerostatic porous circular thrust bearings under dynamic loads of varying frequencies was analysed theoretically by Taylor [86, 87] and by Sun [88], and complemented by experimental results from Andrisano [89].

Sun has published a number of reports on the question of stability. His initial theoretical analyses [90, 91] were further refined by a later study [88] including the effect of the moving mass which was believed to enhance the tendency of instability. His experimental work with Chang and Wang [92] later not only provided verifications to his earlier theories, but also revealed oscillations of gas pressure in the bearing plenum during instability, and pointed to the significance of the plenum volume as a factor affecting stability. The modified theory to include this factor successfully predicted the presence of a second zone of stability at large bearing clearances, which was not evident in earlier work.

Work on the dynamic characteristics of porous rectangular thrust bearings is by comparison very limited [93, 94].

2.1.1.3 Flow through Porous Media

But for a few exceptions [56, 57], all published theoretical analyses have been based on Darcy's law. This states that in the case of incompressible flow, the volume flow rate bears a linear relationship to the pressure difference across the porous material:

$$Q = \Phi_v . \frac{A_p}{z_p . \eta} . \Delta p \qquad (2.1)$$

For compressible flow, the equation becomes

$$Q = \Phi_v . \frac{A_p}{z_p . \eta} . \frac{p_1^2 - p_2^2}{2 . p_{ref}} \qquad (2.2)$$

or by referring the volume flow rate to the mean pressure across the porous body

$$Q_{mean} = \Phi_v . \frac{A_p}{z_p . \eta} . \Delta p \qquad (2.3)$$

In recent years, a number of reports based on numerical analyses [82, 84] has attempted to address the effect of inertia. Although their results do not appear to be significantly different to those neglecting inertia effect, this could be misleading in itself, for the effect of inertia is largely dependent on Reynolds number [95] of the flow within the pores, and hence on the microstructure of the porous material employed. If a thin piece of porous material with very fine pores is employed as the flow restrictor in an aerostatic bearing, fluid velocity within the pores may be high enough for inertia effects to be of significance.

Inertia flow largely results from the loss in momentum as the fluid continues to expand and contract, twist and turn within the complex matrices of inter-connected pores of constantly varying sectional area [96]. The losses increase with local fluid velocity, and result in a decrease in flow rate (blockage effect). The most widely accepted model to describe the effect of inertia flow is the Forchheimer equation [97] which, for compressible flow, takes the form :

$$\frac{p_1^2 - p_2^2}{2.p_{ref}} = \frac{z_p.\eta.(Q/A_p)}{\Phi_v} + \frac{z_p.\rho.(Q/A_p)^2}{\Phi_i} \qquad (2.4)$$

Several authors [98, 99] produced experimental evidence to indicate that there exists a regime at lower flow rate in which Forchheimer appeared to be no longer valid, and that Darcy's law would provide a much better fit to the experimental data. Taylor [60] further suggested that this low-flow regime would normally apply to aerostatic bearing applications, thereby justifying the use of Darcy's law in his theories. Experimental results obtained by Greenberg [100] also showed similar trends. The concept of a modified Reynolds number :

$$n_{re} = \frac{\Phi_v}{\Phi_i}.\frac{\dot{m}}{\eta} \qquad (2.5)$$

and that of a friction factor :

$$f = \frac{2}{n_{re}} + 2 \qquad (2.6)$$

were introduced.

Auriault [101] recently carried out extensive numerical analysis on the flow through the microstructure of porous media, and suggested that a 3rd order equation be used to describe both the Darcy's and the Forchheimer's regime in a generalised form. His modified theory, which applies to a Reynolds number of 150 and below, represents a parabola on the standard permeability plot [102] (as opposed to a straight line for Forchheimer) :

$$-\frac{\partial p}{\partial x} = \frac{\eta}{\Phi_v}.v + \frac{\rho^2}{\Phi_{i2}}.v^3 \qquad (2.7)$$

Many attempts have been made by research workers on porous materials to correlate permeability coefficients with parameters characterising the pore structure. Robinson [103] was amongst the first to look into the empirical dependence of permeability on porosity and particle size, using porous specimens of partially sintered tungsten powders of 12 - 420 μm and a range of porosity between 0.095 to 0.36. Cliffel [104] used the same power law model :

$$\Phi = k.\zeta^{a}.d_w^{\ b} \qquad (2.8)$$

and obtained different exponentials to that of Robinson, using sintered nickel samples of particles ranging from 5 - 30 μm, and porosity from 0.15 to 0.85. The same study was repeated by German [105] for water atomised 316L stainless steel particles of 59 - 715 μm, and porosity values of 0.25 -0.56. A different approach was used by Smith [106], using the specific surface area of the porous structure instead of the particle size. His experimental results were also obtained from water atomised 316 stainless steel specimens sintered to a porosity between 0.12 to 0.44 from 38 - 417 μm particles. His experimental data were also used by German [105] in his mathematical model, resulting in quite different exponential constants.

The empirical results from the above mentioned authors are summarised in the following:

Table 2.1 Comparison of Theories - Porosity Dependence of Permeability

Reference	Equation	k	a	b
Robinson [103]	$\Phi = k.\zeta^{a}.d_w^{\ b}$	--	4.38	2.18
Cliffel [104]	$\Phi = k.\zeta^{a}.d_w^{\ b}$	--	1.871	1.871
German [105]	$\Phi = k.\zeta^{a}.d_w^{\ b}$	4.6×10^{-11}	6.8	0.73
German [105] (Data from [106])	$\Phi = k.\zeta^{a}.d_w^{\ b}$	4.8×10^{-13}	4.8	1.3
Smith [106]	$\Phi = k.\zeta^{a}.s_v^{\ b}$	190	2.42	-2.42

2.1.1.4 Slip Flow at Porous Boundaries

As mentioned earlier, many authors working on the theory of aerostatic porous bearings have pointed out the necessity to make corrections to the geometrical bearing clearance, due to the additional gas flow through extra void volume at the porous bearing surface. While some [45, 48] added a roughness value (which is highly dependent on the method of measurement and definition) to the physical bearing gap, others [49, 51, 53, 54, 55] used the slip flow theory to allow for this effect.

Slip is considered to occur between a solid boundary and a gas flowing next to it, when there exists a discontinuity in velocity at the gas - solid interface.

There are two circumstances under which this discontinuity of velocity could occur. The first occurs when the gas is flowing within a narrow passage which is of comparable dimension to the molecular mean free path of the gas medium [107, 96] . In such cases, the gas medium can no longer be considered as a continuum. The phenomenon is known as molecular velocity slip [108] .

The molecular mean free path of a gas medium is given by :

$$\lambda = \frac{1}{\sqrt{2}.n.A_m} \qquad (2.9)$$

The occurrence of molecular velocity slip can be characterised by a dimensionless term known as the Knudsen number :

$$k_n = \lambda / z_g \qquad (2.10)$$

For $k_n > 0.01$, the gas velocity immediately next to a solid surface may no longer be zero relative to the surface, i.e., slip between the gas and the wall takes place. Discontinuities

also exist in temperature between the solid boundary and gas. For gas bearings working at high Knudsen numbers, the result is usually a decrease in load capacity.

The mean free path of air at atmospheric pressure is approximately 0.064 μm [108], but becomes shorter at higher pressure, as the number of molecules per unit volume increases. For example, λ = 0.026 μm at 2.5 bar above atmospheric. For an aerostatic thrust bearing working at a gap pressure of around 2 to 3 bar, and with a bearing gap of 5 to 10 μm, the Knudsen number would be no more than 0.005. The effect of molecular slip would be insignificant in such cases.

The second phenomenon of velocity slip exists only in a porous medium. A porous medium does not have a solid boundary surface as such, but rather exposed surfaces of the particles joined together at some point below the outermost apexes. If the surface boundary is defined to be a fictitious plane that envelopes all the outermost particles of the porous material, it would not be a solid, continuous one, but would be interrupted by a large number of voids filled with gas. Within the porous medium, tangential flow (Darcy's flow) could exist immediately below the surface, as long as there was a pressure differential in the same direction. Immediately outside a pore opening, the air velocity in the bearing gap at the fictitious 'surface boundary' has to match that immediately inside the pore, as the gas behaves as one continuum with no discontinuity in velocity. The existence of this tangential velocity component implies that the gas could be considered to slip relative to the surface, when the latter is treated as equivalent to a solid surface. The phenomenon is known as tangential velocity slip [52].

According to Beavers and Joseph [52], tangential slip at the surface of a porous medium could be characterised by the slip coefficient, defined as

$$\frac{\partial u}{\partial z} = -\frac{\alpha_s}{\sqrt{\Phi_v}}.u \qquad (2.11)$$

at the porous surface.

The value of the coefficient depends on the porous structure, and is considered independent of the flow velocity or Reynolds number. Pore size seems to have a direct effect on α_s [52]. Typical figures quoted [52, 109, 110] varied from 0.01 to 4.

This slip flow theory proposed by Beavers has gained widespread acceptance, with much additional theoretical work by a number of authors [111, 112, 113, 114] supporting its validity.

A detailed account of the measurement method used by Beavers and co-workers can be found in [115]. This also forms the basis of the measurement technique used in the present work, which will be described in greater detail in chapter 6.

Theories of aerostatic porous bearings including slip flow corrections published so far commonly assume a slip coefficient of 0.1 as published by Beavers [52]. This is unfortunately by no means universally applicable to all porous materials. As pointed out by Beavers himself, just a remachining of the porous surface itself is sufficient to cause significant changes in its value. Theoretical analyses by Larson [116, 117] and Sahraoui [118] also suggested that the slip coefficient may not be a constant, but a function of many variables, including the clearance itself. Also of significance is the extreme sensitivity of the slip coefficient to the definition of the nominal porous boundary interface, as highlighted by Larson [116]. Published experimental data on the slip coefficient of porous materials, and in particular its dependence on pore structure, have been very limited indeed.

The presence of velocity slip generally leads to a lower resistance to fluid flow within the bearing clearance, with a resulting increase in flow rate. The fluid mechanics of the bearing behaves as if the bearing clearnace is larger than its physical dimensions. The need to compensate for this increase in flow with a roughness correction was mentioned in a number of references earlier.

2.1.2 Aerostatic Porous Journal Bearings

The present literature survey also includes publications on aerostatic porous journal bearings.

The first, and to date still one of the most complete, report on the theory and application of aerostatic porous journal bearing was published by Robinson and Sterry [103] in 1958. They reported the successful implementation of a journal bearing using a porous graphite lining. Theory was developed based on a non-rotating, infinitely long bearing in which flow through the porous sleeve was one dimensional. Deviations from Darcy's law due to inertia effects at high Reynolds numbers were also investigated experimentally.

This work was complemented by that of Constantinescu [119], who carried out an analysis based on a short bearing. A series of papers was also published by Sneck, in which perturbation solutions were developed for journal bearings with [120] or without [121] rotation. There were no restrictions regarding length of the journal in both analyses. The theoretical work was also supported by experimental investigations [122]. As in the case of thrust bearings, experimental results pointed to the need of correction for the bearing clearance values used in calculations due to the 'surface roughness' of the porous bearing surface. Similar theoretical [123] and experimental [124] work was published by Mori and Yabe, using their equivalent clearance technique instead.

A summary of similar development work in Germany has been published [125, 126]. Further refinements of the theoretical analyses [127, 128] were performed by Majumdar using 3-dimensional analyses based on the finite-difference method. His results were summarised in a design guideline [129]. Gargiulo also complemented his work on thrust bearings by theoretical and experimental results [130, 131]. Further work on aerostatic porous bearings with journal rotation was reported by Castelli [132] and Rao [133].

The effect of slip flow was included in the investigation by Rao [134]. Theories were also developed to allow for the change in permeability coefficients due to surface loading after machining [79, 80].

The dynamic performances of porous journal bearings have been looked into by Mori [135], Rao [136], Malik [137, 138], Majumdar [139, 140]. Majumdar [141, 142] and Rao [143] also attempted to deal with the subject of instability from pure theoretical perspectives.

Porous bearings of other geometries have also been reported, a notable example being an aerostatic porous graphite spherical bearing [144] which formed the backbone of the work spindle in an earlier design of an ultra-precision turning centre developed at Cranfield.

2.1.3 Partially Porous Bearings

A number of authors [92, 145, 146] argued that instead of using the porous restrictor over the entire bearing surface, even better characteristics, and especially that of stability, could be achieved if the porous material were to be applied as inserts (single or multiple) in an otherwise solid bearing surface. The void volume between pores would be greatly reduced as a result, thus making the machining of the porous material much less critical. Chang [92] pointed out, as an example, that the porous insert could be offset inward of the solid surface by as much as 0.1mm without adversely affecting load capacity and stability.

The first article on partially porous circular thrust bearing was published by Loch [147]. Mori also included a similar bearing type in [148]. The same configuration was much favoured by researchers at Leuven, Belgium, with a number of publications [149, 150] on different bearing configurations. A similar bearing of the circular type and working at high supply pressure was reported by Donaldson [151]. Bearings of this geometry, but with an annular (as opposed to solid cylindrical) porous plug are currently available as off the shelf items [152].

Interestingly, literature on partially porous bearings of other geometries, such as journal or spherical, does not appear to exist.

2.2 PROBLEM IDENTIFICATION

The literature review on aerostatic porous bearings to date highlighted two main problems that could contribute to the lack of widespread applications for this type of aerostatic bearing, namely, the availability of porous material with predictable fluid flow properties before and after machining, and pneumatic instability due to additional dead air volume entrapped amongst the pores at the bearing surface.

2.2.1 Permeability Predictability

The first problem originates from the production and processing of the porous material. As indicated by previous empirical equations, permeability of a porous material is extremely sensitive to its porosity as well as particle size. The control of both parameters, especially the former, is notoriously difficult.

Currently remedial action in the form of an additional adjustment process, in which the pores are partially sealed with successive layers of a blocking agent such as shellac solution [153, 154] or electroless nickel plating [41] is required, until the permeability of the material reaches the desired value. The measurement of permeability after every application of pore-sealing agent adds greatly to the cost of manufacture; in addition to destroying the whole purpose of using the porous media as the flow restrictor, i.e., its simplicity and enhanced performance characteristics. Further complications come from the smearing of the material during machining in cases where a ductile material is used.

This results in complete or partial pore closure at the surface, with drastic influence on the flow restriction behaviour of the porous media [61].

2.2.2 Pneumatic Instability

The second problem occurs when bearing materials with relatively coarse particle size (approaching the nominal working clearance of the bearing) are used. This is especially true when brittle materials such as ceramics are used which could not be ductile machined by conventional means. The extra dead volume of air between the peaks of the porous surface and the narrowest 'throat' of the porous passage, approximately half the particle size below the surface, is sufficient to cause pneumatic instability [76, 84].

Recent research in Japan [79], and in particular at the Technical University of Munich in Germany [80], suggested the use of a two layered porous medium as a solution to the problem, using a core of coarse grain, highly permeable substrate as structural support, which was topped by a thin surface layer with high restriction to fluid flow, believed to be crucial for enhancing pneumatic stability.

The economical production of this structured material in batch production volumes has, however, yet to be achieved. Researchers in Munich, for example [85], have resorted to laser drilling to create the fine pores of the required size and distribution density on the surface of a porous bronze core material, with the surface pores closed up by mechanical rolling or 'over-grinding' prior to drilling. The bearing surface is then finished machined by single-point diamond turning. This method is still relatively simple for thrust flat bearing pads, but is almost impractical for journal bearings due to access restrictions for the laser inside the bore. Also the repeatability of the pore warping process appears doubtful.

2.3 MATERIAL SELECTION

Recent years have seen an increase in interest in the use of advanced structural ceramics in ultra-precision machines and their components [155, 156, 157]. Advanced ceramics are known for their superior mechanical properties as well as dimensional stability. Their high specific flexural modulus and specific strength, for example, can be of significance in highly dynamic positioning systems where weight saving has a direct positive influence on the system performance. They also have a low coefficient of thermal expansion compared with most materials. Coupled with low thermal conductivity and high specific heat values, they process a large thermal inertia which contributes to low thermal distortions when subjected to temperature fluctuations. In addition, ceramics are generally very corrosion and wear resistant, and have a high strength retention at high working temperatures. These properties make them the ideal choice of material for harsh environments (Table 2.2).

Table 2.2 Comparison of Material Properties

Material	Steel	Bronze	Graphite	Alumina
E-modulus (GPa)	200	110	20	410
flexural strength (MPa)	620	515	50	600
rel. density	7.8	8.8	1.7	3.8
α (c.t.e.) (10^{-6} K^{-1})	11.6	17.8	1	5.4
thermal conductivity ($W\,m^{-1}\,K^{-1}$)	52	84	5-90	30
specific heat capacity ($J\,kg^{-1}\,K^{-1}$)	486	380	800	775
dimensional stability	poor	poor	moderate	good
wear resistance	moderate	moderate	poor	good
corrosion resistance	good (if stainless)	good	good	excellent

Most examples of porous aerostatic bearings published so far were based on metallic or graphite materials, because of their lower cost and also ease of machining. The use of porous ceramics in such applications would, on the other hand, eliminate the problems of pore smearing, which is one of the main causes of poor permeability control associated with other ductile materials.

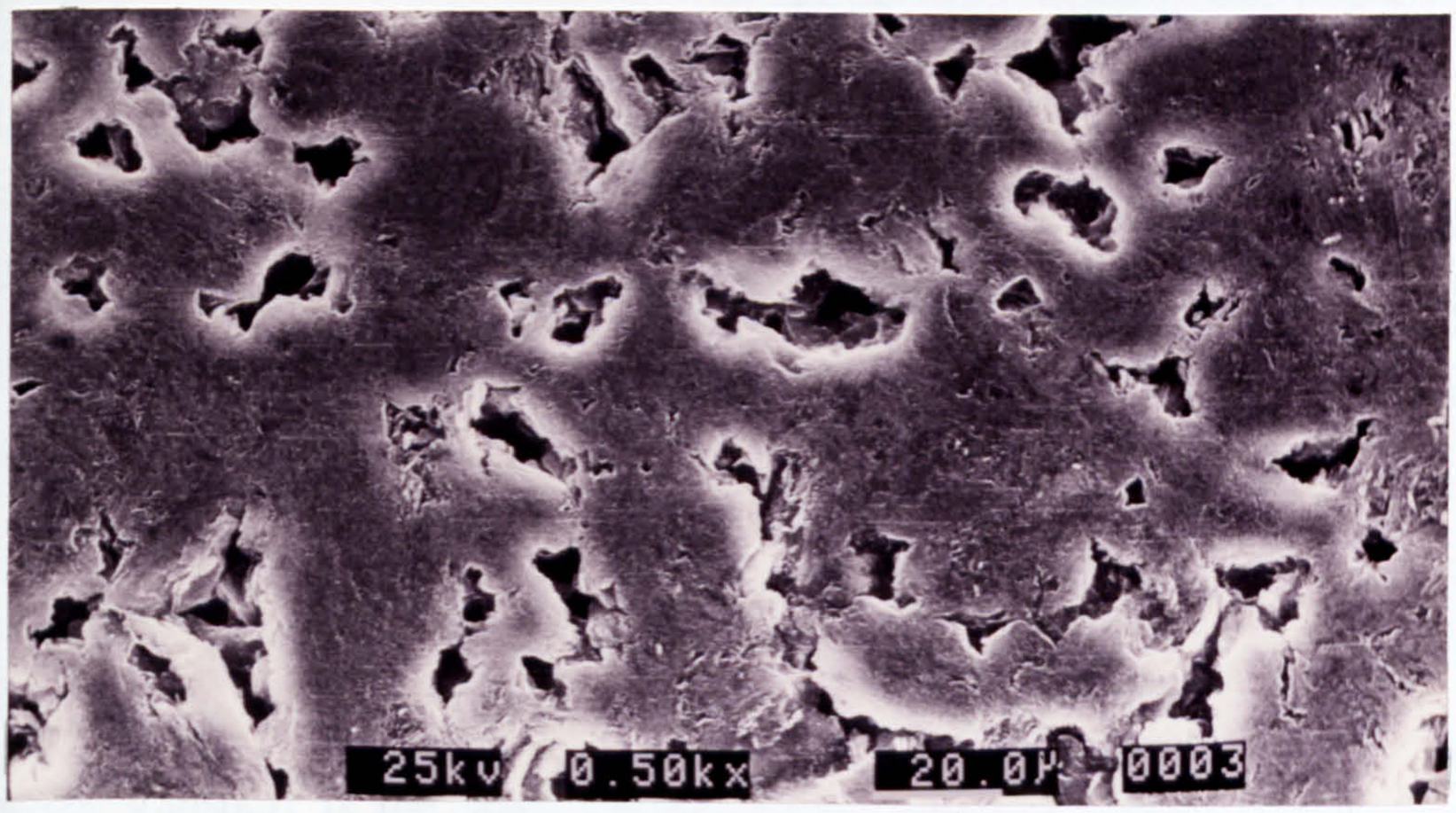

Fig 2.2 Scanning Electron Micrograph of a Diamond Turned Porous Graphite (pore smearing noticeable)

2.4 TECHNIQUES FOR PRODUCING POROUS CERAMICS

2.4.1 Survey of Methods

Powder sintering is one of the most common methods for the production of porous materials. Sintering can be considered as coalescence of solid particles at elevated temperature below the melting point of the material. There are generally three stages of sintering. The initial stage, commonly known as stage zero, includes small neck

formation between particles and some particle rearrangement to a higher packing density. During stage one, further neck growth occurs at inter-particle contact points. The neck growth is in this stage, still discrete, and the pores are open and interconnected. Further neck growth and densification in the second stage seals off the pores into isolated closed voids within the material. Stage two is sometimes divided into a further third stage. According to this latter definition, the pores are much reduced in size in the second stage, but still open, and approximately cylindrical in shape. They become isolated in the third stage.

The mechanism behind the particle rearrangement in stage zero is not fully understood, especially in the case of normal sintering at atmospheric pressure. The application of a high isostatic pressure is believed to be a contributing factor in hot isostatic pressing (HIPing).

Sintering can take place without densification. This occurs via surface transport of material to the neck region, without any changes in particle spacing. The driving force for surface transport is the difference in vapour pressure due to surface curvature. Regions of positive curvature have a higher vapour pressure than those of negative curvature, resulting in material transfer by evaporation and condensation.

The transition from stage zero to stage one of sintering is not a discrete one, but densification or shrinkage are usually associated with the latter. Bulk transport of material occurs at this stage, from the particle interior to the neck region, resulting in a reduction in particle spacing. A number of diffusion controlled processes are believed to be responsible of this bulk material movement, including volume diffusion, grain boundary diffusion, plastic and viscous flow. The latter two are believed to be insignificant in most crystalline engineering ceramics. Grain boundary diffusion is believed to be the most important mechanism for alumina.

Diffusion is a thermally activated process, requiring a minimum activating energy before ionic transport can occur. The driving force behind solid-state diffusion is free surface

energy. Loose powders have a tendency to reduce their total surface energy by sintering together and reducing the total surface area in the process. Smaller particles have higher surface energy per unit volume, which explains their higher sintering rate at the same temperature.

Compared with conventional sintering to achieve full densification, sintering of porous materials is usually carried out at lower temperatures and for shorter durations. Pore-forming agents such as carbon black can also be used, which are subsequently burned off or leached out to reveal the pores [158]. Reactive sintering has also been mentioned as a possible method [159]. In recent years, a foam impregnation method for ceramic porous materials has also received much attention [160, 161]. In this technique, an open cell polymer foam materials of the required microstructure is fully impregnated with a ceramic slurry of fine, highly reactive powders. After the slurry is allowed to set upon drying, the polymer foam is burned off, and the ceramic powders are fired to the required strength. The pore structure of the finished product is determined by that of the polymer foam.

In addition, the sol-gel method is also gaining in popularity [162, 163]. The ceramic material is usually formed by chemical precipitation, and held together in its green state by the gelling agent. Subsequent firing produces a fine porous structure of micrometre-sized precipitates.

Many of the above mentioned methods, however, do not offer sufficient control of the pore size and distribution of the finished material. The resulting porosity is often relatively high, resulting in poor strength and low elastic modulus. The range of pore size available with each method is also limited.

2.4.2 Free-Capsule Hot Isostatic Pressing of Ceramics

One of the most interesting developments in recent years on the processing of porous materials is the pioneering work carried out by Ishizaki and colleagues [164, 165, 166]. Their

newly developed method, known as free-capsule hot isostatic pressing (HIPing), is believed to be capable of producing a whole range of porous materials with improved porosity, mechanical strength, and consistency. An overview of their work can be found in [167].

Conventional HIPing [168] involves the packing of loose powders in a metal or, in cases of high sintering temperatures, glass container designed to match the finished size and shape of the component. The can is then evacuated and sealed, before being placed in the HIPing furnace. The HIPing furnace is essentially a furnace sitting inside a high pressure vessel, which is to be pressurised by a gaseous fluid (usually an inert gas) during sintering. Both the temperature and pressure profiles can be controlled separately. By applying an external pressure on the sealed can, which is designed to soften but not melt at sintering temperature, extra compacting forces are being exerted on the green compact isostatically during the entire sintering phase, resulting in higher densification than otherwise achievable, and more uniform shrinkage in all directions.

The free-capsule HIPing technique developed by Ishizaki differs from the conventional in that the green compact is not held in a sealed container, but rather a porous one or none at all (provided that the packing of powders give the green compact sufficient strength to allow handling and shape retention during sintering). This allows the pressurising gas to penetrate the pores throughout the process. The high pressure gas within the pores serves two purposes. Firstly, the powders are sitting in an isostatic environment, and as such the points of contacts between particles are subjected to the same isostatic pressure. As this pressure is normally much higher than atmospheric (up to 2000 bar), the increase in contact pressure enhances surface diffusion during sintering, resulting in improved neck growth between particles and hence mechanical strength [169, 170]. As sintering progresses, however, the presence of high pressure gas within the pores helps to prevent their complete closure. This helps to bring about the reduction in closed porosity and improved consistency in open porosity.

Results published to date include both metals [171] and ceramic substrates [172, 173, 174, 175, 176]. However, no permeability data were published.

2.5 OBJECTIVES OF THE PRESENT WORK

The importance of the ability to produce porous media with uniform, predictable permeability has already been argued in the previous sections. The advantages, especially in terms of pneumatic stability, of using a two-layered porous structure, in which the flow restriction is performed by a thin porous layer of low permeability supported structurally by a coarse substrate, have also been highlighted. The use of ceramic as the core material has been proposed, not only to overcome the smearing (pore warping) problem during final machining of the bearing surface, but also to provide superior dimensional stability as well as structural properties.

Pioneering work in Japan has identified free-capsule hot isostatic pressing as a promising method of producing porous ceramics economically, with superior strength and improved consistency in pore structures. Hot isostatic pressing (HIPing) of porous alumina thus forms the backbone of the current work as proposed by Corbett [177, 178].

In light of the problem areas identified in the literature survey, the immediate concern has to be a more in-depth understanding of the effect of all process parameters (e.g., particle size and distribution, packing method, HIPing parameters such as pressure and temperature profiles, etc.) on the fluid flow properties of the resulting porous ceramic material. Only then would one be able to ascertain the sensitivity of the process and identify the importance of individual variables, which would enable the repeatable reproduction of porous ceramic bearing materials with specific flow restriction properties.

The main objectives of the present work are, therefore :

a) to identify the influence of individual process parameters on the fluid flow as well as mechanical properties of the porous substrate;

b) to correlate fluid flow properties of the porous material, in particular permeability and slip coefficient for a variety of samples to their microstructure porosity, and pore size distribution.

c) to establish mathematical models, based on experimental results in (a) and (b), and hence to obtain an idea of the precision to which processing parameters would have to be controlled, in order to achieve the required tolerances on the fluid flow and structural properties of porous material as required for aerostatic bearing applications;

d) to look into methods of producing two layered porous structures as mentioned in Section 2.2.2 for improved pneumatic stability.

e) to manufacture samples of flat circular thrust bearings of both the single and two-layered type, as a means of verifying the process model, and to compare performance results with published bearing theories.

3. MATERIAL REQUIREMENTS

How can an ideal porous material for aerostatic bearing applications be described ? The subject has been dealt with in certain aspects by a number of authors [61, 76]. Amongst the most important characteristics, the substrate should have a uniform open pore structure, with permeability coefficients which are consistent and repeatable from batch to batch. The coefficients should be predictable at the production stages, so that the processing parameters could be controlled and customised to suit the particular application. The bearing should be light in weight, especially for highly dynamic applications with high accelerations. It should have a high flexural modulus to minimise deflection, and be strong enough to sustain the working pressure. It should be chemically and dimensionally stable, and should have a low coefficient of thermal expansion. Although the guiding surfaces of externally pressurised bearings are not supposed to be in physical contact during operation, the possibility of sudden loss of fluid pressure demands a certain degree of wear and impact resistance. In these respects, alumina appears to be an ideal choice as the bearing material.

To help to quantify the range of values of material properties that would be relevant to typical aerostatic bearing applications, parameters based upon an example of a circular thrust test bearing need to be defined.

3.1 CHOICE OF BEARING PARAMETERS

3.1.1 Outer Diameter

In the present work, the size of the hot isostatic pressing (HIPing) furnace put a limit on the diameter of the finished sample. Further allowances had to be made for subsequent

machining. Taking shrinkage into account, the maximum size of the thrust pad could not be more than 42mm in diameter. For the test bearing, the diameter at the bearing surface was chosen to be 40mm.

3.1.2 Thickness

Although the advantages of using a thin porous substrate of low permeability had been mentioned by various authors [51], considerations of the deflection of the porous substrate under working pressure would favour a maximum thickness to maximise bending stiffness. In the case of a single layered porous material, the thickness should be chosen such that the plate deflection of the porous pad under working pressure would not exceed 10% of the working gap [179, 180]. This deflection is a function of the diameter of the pad, the flexure modulus, and the thickness.

Assuming a porosity level for the porous pad of around 20-35%, mathematical models by Wagh [181] were used to estimate the likely range of flexure modulus of the HIPed samples:

$$E = E_o . (1 - \zeta_t)^{2.14} \qquad (3.1)$$

for most sintered porous materials.

If one assumes that the material used is α-alumina, then for $\zeta_t = 0.35$ and $E_o = 410$ GPa [182],

$$E = 163 \text{ GPa}$$

The minimum thickness required to limit the elastic deflection of the porous pad, simply supported at its perimeter, to 10% of the nominal bearing working gap, or 1.0 μm, is given by [183] :

$$\delta_c = - 0.070 . \frac{\Delta p . r_p^4}{E . z_p^3} . 12 (1 - \nu^2) \qquad (3.2)$$

$$= -1.0\ \mu m$$

For alumina with open pores, $\nu = 0.15$ [182] and $r_p = 20$ mm,

$$\Delta p = p_{og}/3 = 0.17\ MPa$$

as the pressure drop across the restrictor amounts to approximately one third of the supply pressure for optimum bearing stiffness [82].

This gives

$$z_p = \left[0.070 \cdot \frac{p_{og} \cdot r_p^4}{3.E.\delta_c} \cdot 12(1 - \nu^2) \right]^{1/3} \qquad (3.3)$$

$$= 3.91\ mm$$

The total porous pad thickness was chosen to be 6mm to give sufficient room for holding the workpiece during machining (e.g., diamond grinding).

3.1.3 Working Gap

Having determined the diameter and thickness of the porous pad, the choice of a nominal working gap of the bearing would complete the definition of bearing geometry to enable the calculation of permeability and other material properties of the test bearing porous pad.

For most precision engineering applications, the nominal bearing gap varies between 5μm and 25 μm. For a given bearing number (e.g. optimised for maximum stiffness), a smaller gap would not only reduce gas consumption, but would also give increased stiffness. There is therefore a drive towards using a smaller bearing gap. In fact, porous aerostatic bearings working at submicron gaps have been reported [184].

The limitation in bearing gap reduction is to date still the cost of manufacture. As mentioned in previous sections, the bearing surfaces should have geometrical accuracies of better than 10% of the nominal bearing gap in order that bearing performances would not be significantly affected. Finishing thrust bearing pads and mating surfaces to better than 0.5 μm in flatness is, while technically possible, expensive and time consuming. At such levels of geometrical accuracies, the long-term stability of the material, in addition to the thermal distortion of the bearing under working conditions, also comes into question. To date, 5 μm is still considered the practical limit of bearing gaps for the majority of aerostatic bearing applications, including ultraprecision engineering, although more often than not, 10 μm is a figure favoured by most bearing designers.

At the opposite end of the scale, aerostatic bearings are rarely designed to work at gaps greater than 20 μm, at which the gas consumption would increase significantly, making the operation of the bearing considerably more uneconomical.

The working gap of the test bearings was therefore chosen to be 5 to 15 μm, based on the bearing number Λ optimised for maximum stiffness.

3.1.4 Bearing Number

The bearing number Λ was used by most porous bearing researchers in determining the bearing performance [44, 45, 50, 51]. Mathematical models have been developed to predict load capacity, stiffness and gas consumption as a function of Λ. For most precision engineering applications, especially in the electronic industry where the load involved is usually small, stiffness, which determines the guiding accuracy of the bearing, is of more significance.

For a simple, singe-layer porous pad, the bearing number at maximum stiffness lies between 5 and 100, depending on the mathematical model used [44, 45, 50, 51]. As a starting point, the bearing number was chosen to be 20 for the test bearings. This was only a

target figure which enabled the desired permeability coefficients to be determined. In the actual experiments, the bearing could be set to work at different bearing numbers by simply varying the bearing gap. As the bearing number is inversely proportional to the cube of the bearing gap, the gap only needs to be changed by a factor of 1.7 for a change of bearing number from 20 to 5 or to 100. For a 10 μm nominal gap, this would mean a change to 5.9 μm for $\Lambda = 5$, and 17 μm for $\Lambda = 20$ respectively.

3.1.5 Permeability Coefficient

The permeability coefficient was determined from the bearing number, using the definition by Gargiulo & Gilmour [45]. Although the definition of Λ is different depending on the mathematical model used, it can be considered as being based on [45] with an added-on correction factor to account for slip flow and compressibility.

According to Gargiulo,

$$\Lambda = \frac{12.\Phi_z.r_p^2}{z_p.z_g^3} \qquad (3.4)$$

For $\Lambda = 20$, bearing diameter = 40mm, thickness = 6mm,

$\Phi_z = 3.13 \times 10^{-15}\ m^2$ for bearing gap = 5 μm

$= 8.44 \times 10^{-14}\ m^2$ for bearing gap = 15 μm

3.1.6 Two-Layered Porous Structure

The use of a two-layered structure would, among its most important advantages, give the designer the freedom to separate the structural and flow restriction requirements almost entirely. One could optimise the geometry of the coarse substrate to satisfy the

structural requirements, and simultaneously design the fluid flow properties of the thin surface layer with low permeability to suit the desired flow restriction performance, provided that the pressure drop across the coarse substrate is insignificant (say 5% or less) compared with that across the thin restricting layer.

It is generally accepted that the permeability of a porous material is proportional to powder size to the power **a**, where **a** lies between 1.3 and 2.3 (Section 2.1.1.3). However, both the proportional constant k and the exponent **a** vary significantly between different published theories, and seem to depend as much on the pore microstructure as on open porosity and powder size. Nevertheless, by choosing a sufficiently large particle size ratio between the coarse substrate and the thin surface layer, it is possible to control the fluid flow through the two-layered structure such that over 95% of the pressure drop occurs across the thin, fine-pored layer, even when its thickness is only a fraction (e.g., 5 - 10%) of that of the coarse substrate.

As the shrinkage through the specimen thickness during sintering is not entirely uniform, and some additional distortion is normally unavoidable [185], it is highly unlikely that subsequent machining of the substrate on the fine-pored surface can be avoided. In this case, a reasonable thickness of the fine-pored layer would prevent spatial variations of the pressure restricting characteristics due to any uneven thickness of the fine-pored layer after machining. Initially, a nominal value of 0.5mm would be used. This is, however, only a physical value (i.e., total pad thickness after machining - coarse substrate thickness). The effective thickness in flow restricting terms would be slightly different due to penetration of the fine-pored layer into the much larger pores of the coarse substrate, an essential feature to ensure good inter-lamination bond strength.

Using the same set of equations for the single-layered structure, the permeability of the fine-pored layer should be

$$\Phi_{zf} = \frac{\Lambda z_{pf} . z_g^3}{12 . r_p^3} \qquad (3.5)$$

For $\Lambda = 20$, bearing diameter = 40mm, thickness = 0.5mm,

$$\Phi_{zf} = 2.60 \times 10^{-16}\ m^2 \qquad \text{for bearing gap} = 5\ \mu m$$

$$= 7.03 \times 10^{-15}\ m^2 \qquad \text{for bearing gap} = 15\ \mu m$$

The thickness ratio between the coarse- and the fine-pored layers will be approximately 11:1. Assuming the pressure drop across the coarse layer to be less than 5% of that across the fine layer, the permeability coefficients of the coarse layer should therefore be

$$\Phi_{zc} = 5.73 \times 10^{-14}\ m^2 \qquad \text{for bearing gap} = 5\ \mu m$$

$$= 1.55 \times 10^{-12}\ m^2 \qquad \text{for bearing gap} = 15\ \mu m$$

3.2 STRUCTURAL REQUIREMENTS

As mentioned earlier, the porous material should have a sufficiently large flexural modulus such that its deflection under working pressure would not be excessive (less than 10% of the design bearing gap).

Equation 3.2 can be used to calculate the minimum flexural modulus of the porous material, given the thickness of the thrust pad

$$E = 0.070 \cdot \frac{\Delta p . r_p^4}{\delta_c . z_p^3} \cdot 12 (1 - \nu^2) \qquad (3.6)$$

$$= 102\ GPa$$

A lower figure for the flexural modulus would, however, be acceptable if the deflection of the porous pad under working pressure could be compensated for. This can be achieved, for example, by pressurising the porous pad from the substrate side, to a value

equivalent to the design differential pressure across the pad. The resulting bearing surface would therefore be concave in its free, unpressurised state; but would resume its flatness once in operation.

The material would have to possess sufficient strength to sustain the working pressure. The maximum stress on the circular pad is given by [183]

$$\sigma = \frac{3.p.r_p^2.(3+\nu)}{8.z_p^2} \qquad (3.7)$$

$$= 6.56 \text{ MPa}$$

when subjected to full supply pressure (0.5 MPa).

A target value of around 35 MPa for the flexural strength of the porous substrate would therefore ensure sufficient strength under normal circumstances. This figure also compares well with that quoted by Morrell [182].

The structural requirements for the porous substrate are essentially the same for both the single- and double-layered designs. This is particularly the case, when strength and flexural modulus of a porous substrate are believed to be independent of the pore size, and solely a function of the porosity [181].

3.3 STABILITY CONSIDERATIONS

As already discussed in Chapter 2, the dead volume between the pores on the bearing surface layer is believed to be a major cause of pneumatic instability in porous aerostatic bearings. This dead volume can only be minimised by using a finer pore structure as in the case of the two-layered bearing. For the case of a single layer bearing, the void volume can be minimised if the particles are bonded to each other with sufficient strength

to resist grain pullout during machining. A lower porosity, on the other hand, implies larger particle size and therefore greater depth of void, given the same permeability coefficient. A compromise would have to be reached.

3.4 SUMMARY

For porous aerostatic circular thrust bearings working at 5 μm to 15 μm design gaps, the permeability coefficient ranges from 3.1×10^{-15} to 8.4×10^{-14} m^2 for a simple single-layered porous pad. For a two-layered design, the fine-pored layer has a typical permeability coefficient ranging from 2.6×10^{-16} to 7.0×10^{-15} m^2. The coarse structural substrate should have a permeability coefficient at least 200 times that of the fine layer, so that the bulk of the pressure drop would occur across the latter.

The porous material should have a bulk flexural modulus of not less than 102 GPa, and a flexural strength of no less than 35 MPa. Porosity level should lie between 20 and 35%, and should be predominantly open. Pores should be uniform, both in terms of size and spatial distribution.

For the case of the test thrust bearing, the outer diameter of the porous pad at the bearing surface is set at 40mm. Total thickness is nominally 6mm. In the case of the two-layered design, the nominal thickness of the fine-pored layer is 0.5mm.

4. MATERIAL PROCESSING

4.1 POWDER CHARACTERISATION

Alumina powders used in the present work for producing porous materials range from 0.5 to 400 μm. These could be divided into three main groups. Powders with a mean particle size of 7 μm and below were reactive grades of calcined alumina from Alcan Chemicals [186], with a 99.8% purity. The 13 μm powder from Universal Abrasives was a white fused alumina which was 99.7% pure [187]. Above 13 μm, the powders were obtained from Washington Mills, and were also white fused alumina with a purity of 99.6%. The latter also had a closed porosity of 5.5% as supplied [188].

Particle size distribution for all powders below 100 μm was measured using a Micromeritics 5100 Sedigraph. A sample of each powder was taken at random from the bulk container, 4 grams of which was added to 100 ml of deionised water with a 0.1 wt% Darvan C dispersant. Powders below 13 μm were then ball milled for 24 hours to break down any agglomerations. For 13 μm and above, the powders were dispersed by placing in an ultrasonic bath for a minimum of 15 minutes. Records of the Sedigraph measurements can be found in Appendix E. The results are summarised in Table 4.1.

Powders larger than grit 120 were beyond the range of the sedigraph. As very few experiments were performed using such powders, mean particle sizes quoted by the manufacturers were used. Experience from smaller powders showed that the manufacturers' figures agreed well with sedigraph results.

Table 4.1 Powder Size Distribution by Sedigraph Measurement

Nominal Size (μm)	Median (μm)	Modal (μm)
0.5	0.44	0.41
7	6.25	6.71
13	12.2	12.5
23	22.6	24.2
Grid 220	42	38.3
Grid 120	71.2	69.4

4.2 POWDER PACKING AND MIXING

Loose powders had to be first compacted into a shape close to the finished article, with as high and uniform a green density as possible, before firing to create inter-particle bonding.

The most commonly used method of packing loose powers into a disc shape is uniaxial pressing in a set of hardened steel tool and die. Though simple to use, this method has the drawback that packing density is not uniform, especially through the thickness, due to friction between particles and the die wall. Density is higher near the surface of the moving die(s), but lower towards the centre of the green compact. Addition of surface active agents such as stearic acid gives improved results, but does not cure the problem entirely.

More uniform packing can be achieved using methods in which all particles are subjected to the same packing action, irrespective of their position in the green compact. Examples for such methods are vibratory based packing and those based on powder deposition by removing the liquid from a slurry, such as slip casting.

4.2.1 Vibratory Packing

Powder packing can be effected through reorganising the stacking arrangement of particles as they are subjected to vibration. The agitation, coupled with gravitation, encourages the particles to organise themselves into an arrangement with minimum potential energy, i.e., downward packing. Vibratory packing is known to be particularly effective for larger particles, and can result in packing density uniform to 0.05% [189].

Vibratory packing was performed in the present study using a Vibratechniques K16 / FFT300 pneumatic ball vibrator. Only the frequency of the vibration could be adjusted with this simple set-up, by varying the supply air pressure. The amplitude of vibration was determined by the centrifugal force of the vibrator ball, and the total moving mass. The frequency was measured by a Thurlby Thander PFM 1300 frequency counter, which was a.c. coupled to a reflective sensor (RS 307 - 913). This reflective sensor was set to operate in its linear regime to detect the movement of a reflective target attached to the vibrating table (Appendix H, drawing no. MG291 A600 0A).

A series of initial tests were carried out to determine the optimum vibration frequency for individual powder size, the green density achievable, and its repeatability. A 54mm diameter perspex sleeve, with a matching base and piston, simulated the actual graphite packing tooling used in the HIPing process (Fig. 4.1). The transparent sleeve allowed visual observation of the powder movements during the packing process. A known amount of powders was placed into the sleeve, then closed by the piston but leaving a space of 2 mm minimum between piston and powders to allow movement. The piston was gently pressed down when vibration was applied, 'encouraging' the powders to settle to a parallel sided disc shape. The height of the ball-ended piston top was measured first with no powders, and again after packing was complete. Knowing the cross-sectional area of the piston, the volume of the green body after packing could be determined, from which the packing density was calculated.

Experience showed that an intermittently applied pressure on the piston was the most effective, as it allowed some degree of rearrangement to occur, as well as helping the downward movement of the powders as a whole. A continuously applied load would, on the other hand, restrict particle movement once the piston came into contact with the powders, due to the added friction between particles in the presence of the applied load. An axial load of around 0.2 MPa was applied on and off at 2 second intervals.

At least five tests were performed for each particle size from 3 to 400 μm. The results are summarised in Fig 4.2. It could be seen that the method was very effective and consistent for powders larger than 23 μm. The average green density of approximately 0.54 was almost independent on particle size, with a standard deviation of less than 0.01. Below 23 μm, the effectiveness of the method rapidly deteriorated, as the influence of short-range, weak forces such as electrostatic charges, surface adsorption and agglomeration began to dominate in smaller particles.

The vibrating frequency did not appear to have a significant effect on the green density achieved, as long as it was above 150 - 200 Hz. Below that value, particle rearrangement still occurred, but at an unacceptably low rate. A higher frequency was more favourable for smaller particle sizes. These findings are similar to observations by German [189].

As a result of this initial investigation, specimens with powders of 13 μm and above were vibration packed at 200 Hz in graphite tooling (Appendix H, drawings MD291 A101, A102) for HIPing. The dimensions of the green bodies were deduced from external and internal measurements of the individual tooling before and after packing. Combined with weight information, an estimate of the packing density could be obtained.

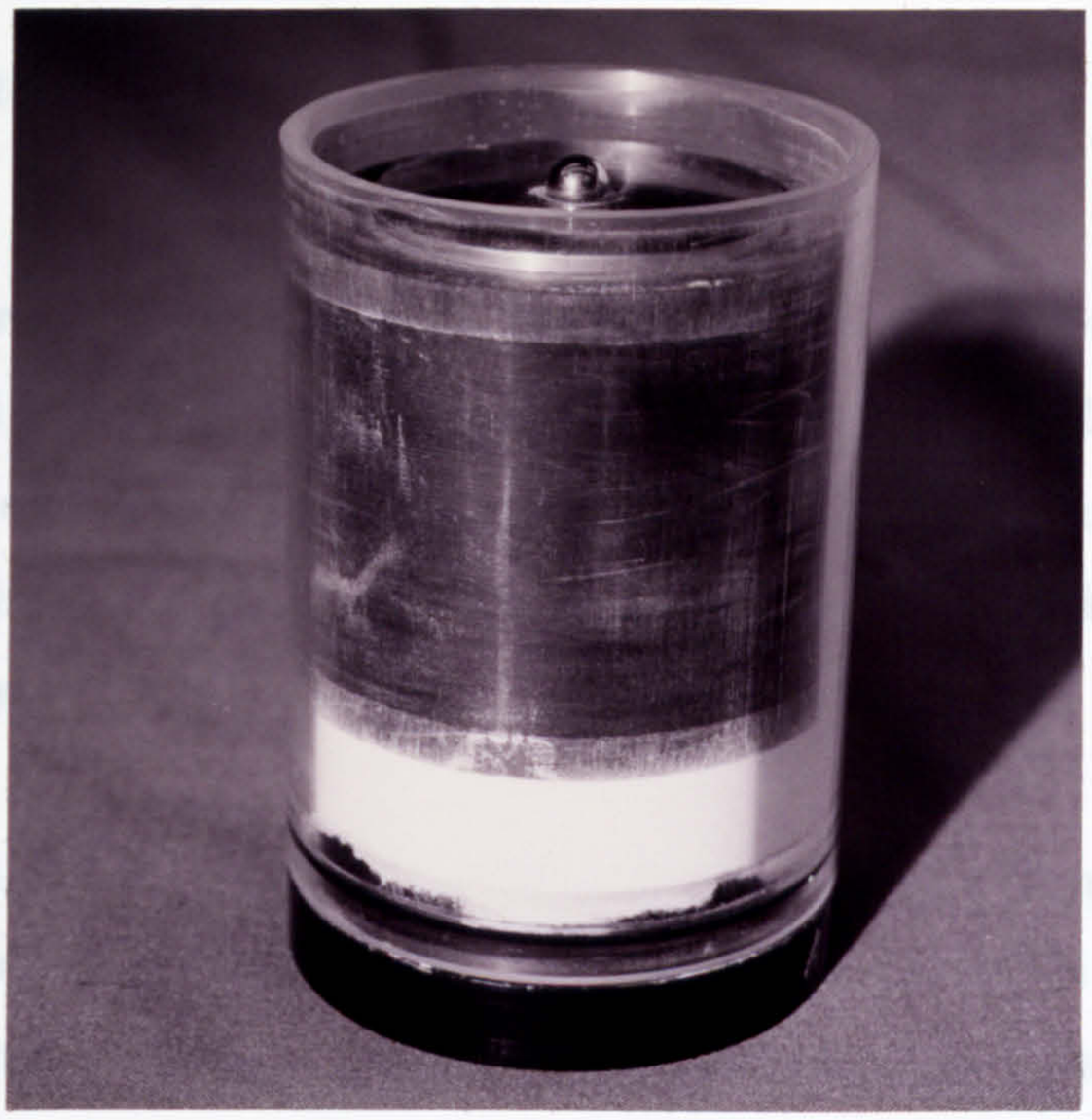

Fig 4.1 Dummy Vibratory Packing Tool for Green Density Measurement

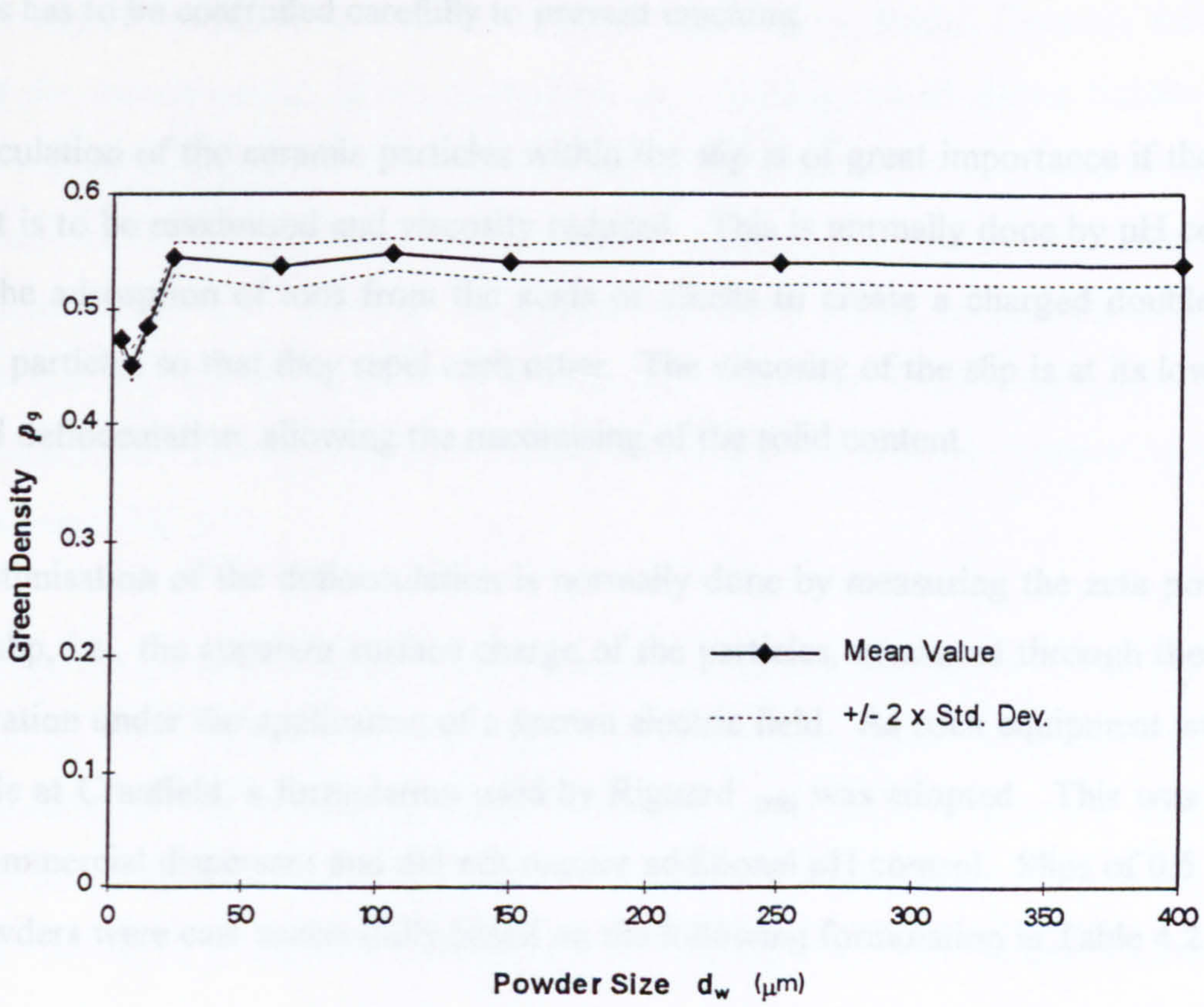

Fig 4.2 Vibration Packing Density and Consistency for different Powder Sizes

4.2.2 Slip Casting

Attempts to sinter vibration-packed specimens of 7 μm alumina powders by HIPing invariably resulted in internal and surface defects in the form of cracks and inclusions. The poor packing density and uniformity of the vibratory process for such powders were believed to be the main causes. An alternative, more reliable packing method was therefore necessary.

A commonly used packing method for ceramic powders is slip casting. This involves suspending the ceramic powder in water to form a slurry, which is then cast into a porous plaster mould. Pores in the plaster extract the water from the slurry by capillary action, resulting in a shell type green body resembling the internal shape of the plaster mould. Components produced from slip casting are usually thin walled, and the drying process has to be controlled carefully to prevent cracking.

Deflocculation of the ceramic particles within the slip is of great importance if the solid content is to be maximised and viscosity reduced. This is normally done by pH control, using the adsorption of ions from the acids or alkalis to create a charged double-layer around particles so that they repel each other. The viscosity of the slip is at its lowest at optimal deflocculation, allowing the maximising of the solid content.

The optimisation of the deflocculation is normally done by measuring the zeta potential of the slip, i.e., the apparent surface charge of the particles, measured through their rate of migration under the application of a known electric field. As such equipment was not available at Cranfield, a formulation used by Riguard [190] was adopted. This was based on a commercial dispersant and did not require additional pH control. Slips of 0.5 and 7 μm powders were cast successfully based on the following formulation in Table 4.2 :

Table 4.2 Formulation of Alumina Casting Slip

Contents		wt %
ceramic	α - alumina	74.3
dispersant	polyacrylic ammonium (Darvan C)	0.94
deionised water		24.76

The mixture was mixed thoroughly by wet ball milling for 24 hours, using a Pascall 9VS mill with a 150mm porcelain jar and alumina balls. Milling speed was at 46 rpm, determined from the critical speed at which the balls began to centrifuge inside the jar [191, 192, 193].

Porous plaster moulds were cast from Pottery Plaster from British Gypsum, following closely the recommended mixing procedures [194]. Initially, an all-plaster female-cavity mould with internal diameter of 53 mm was used. This resulted in a concave top surface after removal of water, as the alumina powders close to the plaster wall clung to the latter immediately after pouring, while particles in the centre compacted themselves further as water was drawn away. Particles on the top also settled much slower than those immediately next to the plaster mould, resulting in different microstructures across the thickness (Fig. 4.3).

The mould design was modified, using a plaster plug as the base with a PTFE ring fitted on top (Fig. 4.4). The non-absorbing side wall of the cavity reduced the water removal to essentially one dimensional (axially downwards), and removed the above mentioned problem altogether. Discs cast with the new tooling had a top surface flat to better than 0.5mm. Drying took place for a minimum of 72 hours, in a sealed container filled with silica gel. Attempts to shorten the drying time invariably led to cracking. Very little shrinkage could be observed in the radial direction (around 0.56%).

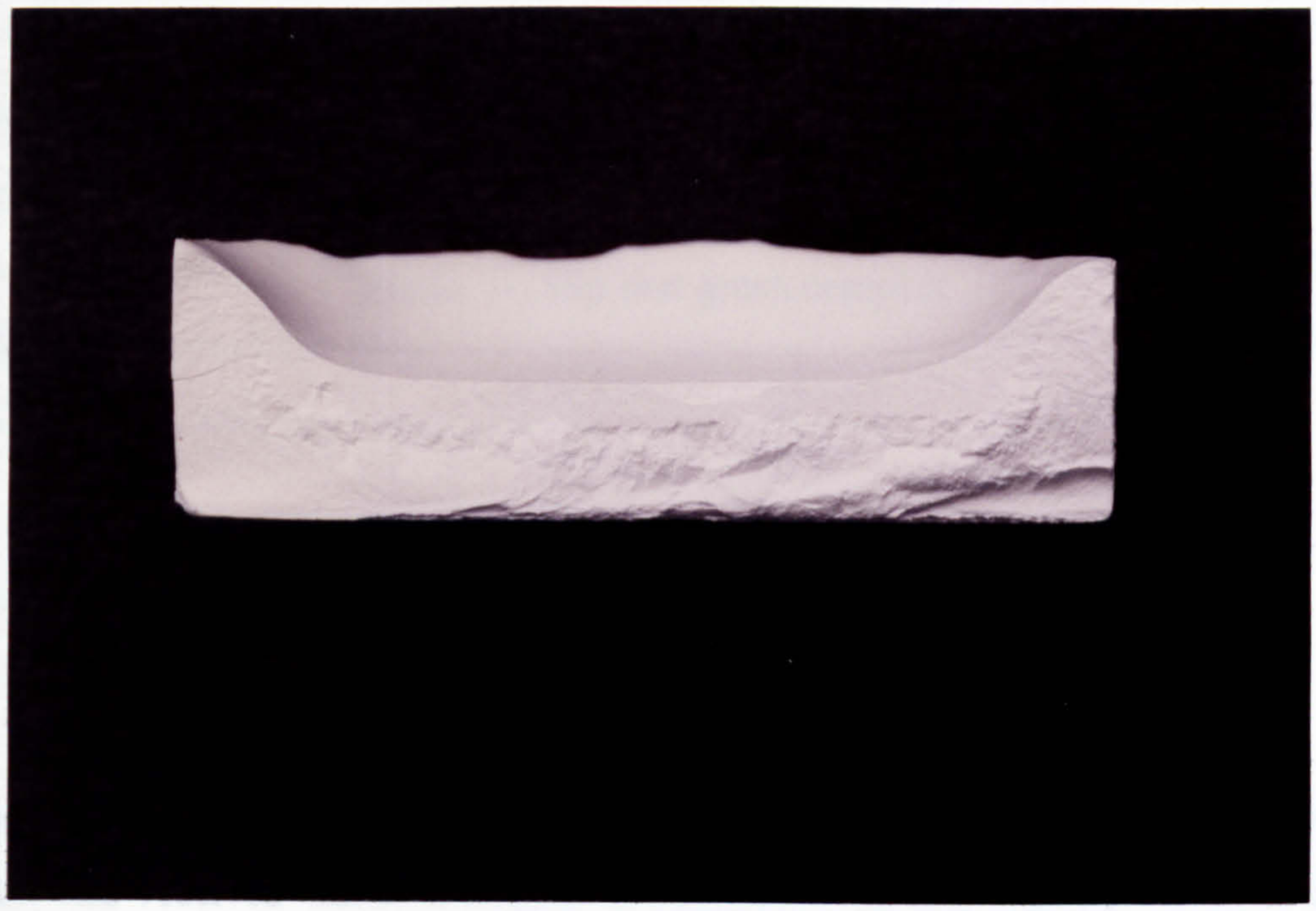

Fig 4.3 4μm Alumina Slip Cast from an All-Plaster Tooling

Fig 4.4 Modified Slip Casting Tool with PTFE Wall

Packing density achieved was on average 0.59 to 0.60, close to the theoretical limit for random packing of monosize particles. Thickness was however somewhat limited (to about 10% of the lateral dimension), as thicker casts had a great tendency to crack. This might be due to local variations in packing density, as a result of the different water removal rate between the centre portion of the cast to that close to the plaster mould, the water being removed much quicker there.

4.2.3 Injection Moulding

In recent years, the injection moulding of metal and ceramics, as a packing and forming method, has received much attention, due to the versatility of the process and its capability in producing components of complex geometry in large quantities and to tight tolerances, despite the relatively high tooling costs. The process is suitable for very small powder sizes, and achieves highly uniform green densities. Packing density achievable is comparable, if not superior, to other packing methods such as slip casting.

In this process, metal or ceramic powders are added to a thermoplastic as a filler, and the resulting mixture injection moulded to the required shape in standard moulding machinery, very similar to the case of reinforced thermoplastics. The thermoplastic binder is then removed from the moulded component by thermal debinding, leaving behind the filler powders only. The latter are then sintered to the required density. To facilitate the removal of the thermoplastic binder without blistering, different waxes are added, which are removed first in a solvent debinding stage at much lower temperature, leaving minute cavities within the moulded body to allow easier removal of the thermoplastic binder, and to relieve any pressure build-up during thermal debinding.

Following the success in injection moulding carbonyl iron at Cranfield, attempts were made to adapt the process to alumina powders to study its feasibility in the production of porous bearing material. The original formulation for injection moulding carbonyl iron was based on the binder system developed by Lin and German [195, 196], and used two

waxes in addition to polypropylene as binders. Two sizes of alumina powders (4 and 7 μm) were tried, the modified composition of the binder system used being listed as below:

Table 4.3 Formulation for Injection Moulding of Alumina

Material	Supplier / Cat. no.	Wt%
Alumina		87.62
Polypropylene	Montell VS6100K	7.39
Paraffin Wax	BDH 29841	3.94
Carnuba Wax	BDH 33129	0.86
Stearic Acid	BDH 30267	0.19

The components were first ground into a powder form, and premixed for three hours in a figure-of-eight shaker. They were then compounded into granules for injection moulding in an APV MPF19 twin screw extruder. The key settings of the extruder are listed as follows :

Table 4.4 Extruder Settings for Compounding of Alumina Powders

Parameter	Setting
Material pressure (bar)	220
Material temperature (°C)	240
Screw speed (rpm)	300
Torque	20 %

After compounding and thorough drying at 50 °C for 12 hours, the granules were injection moulded into a disc shaped mould of 70 mm diameter and 4 mm in thickness. The settings of the Dassett D30 injection moulding machine are summarised in Table 4.5.

Table 4.5 Settings for Injection Moulding of Alumina Powders

Parameter	Setting
Packing pressure (bar)	20
Injection speed	90 %
Front zone temperature (°C)	200
Middle zone temperature (°C)	200
Rear zone temperature (°C)	200
Nozzle temperature (°C)	200
Shot size (mm)	75
Injection high pressure (bar)	200
Injection high time (s)	10
Transfer pressure (bar)	150
Injection low time (s)	20
Screw speed (rpm)	200

The injection moulded ceramic discs were then solvent and thermal debound to remove the binders. Solvent debinding took place in a heptane vapour bath at 80 °C for 30 hours, with the moulded component sitting on top of a porous plaster block. Pores in the latter helped to remove the waxes from the moulded disc through capillary action. The polypropylene was then removed in a thermal debinding cycle, involving two two-hour dwells at 250 °C, 600 °C, followed by a pre-sintering stage at 1200 °C for an hour to give the green body some strength for handling. Temperature rise between stages was controlled at 2 °C per minute. Subsequent cooling to room temperature was natural.

The resulting ceramic discs had an average green density of 0.60, comparable to that of slip casting. Some blistering was observable on occasions, suggesting that the thermal debinding might be problematic if the thickness was to be further increased. Heavy wear on the extruder barrels were also observed when powders larger than 13 μm were used,

due to the abrasive nature of alumina. Even if such wear on the equipment could be tolerated, the significant level of iron contamination in the extruded granules rendered them practically useless. At the other extreme, reduction in particle size to below 4 μm increased the viscosity of the molten mixture drastically, requiring the reduction of the filler content to less than 50 volume percent (from 62%). The packing density of the ceramic powders suffered as a result, although this might improve with further optimisation of the binder system.

4.2.4 Use of Bimodal Systems and Sintering Aids

Sintering of alumina particles larger than 50 μm is not feasible, as the temperature required approaches the melting point of alumina. Densification of such powders can be achieved at reduced temperature by the addition of a sintering aid such as LiF or much finer alumina powders to form a bimodal mixture. The former enhances sintering as it liquefies at a lower temperature (around 950 °C). This liquid phase provides a medium for solution-precipitation of alumina to take place.

Finer alumina particles, on the other hand, sinter at much lower temperature due to their higher surface energy. These fine powders, when thoroughly mixed with coarser powders, act like a solder of the same material, attaching the coarser powders to each other. Densification is consequently limited.

The mixing of the sintering aid or fine powders with the coarse powders has to be uniform and homogenous in order to minimise density (and hence permeability) variations within the sintered body.

Mixing of alumina powders with LiF (1 - 4 %) was done by 24-hour dry ball milling. The set-up was essentially the same as in the case of slip casting. Sedigraph measurements revealed no measurable breakdown of the alumina powders up to and including 43 μm. The breakdown of larger particles, especially those above 100 μm,

was however very significant, resulting a very broad-band powder size distribution. No alternative method of mixing was however available in Cranfield, bearing in mind the very minute amount of LiF in the mixture and the importance of even mixing.

The bimodal mixture was to a certain extent easier to handle, as the amount of fine powders was significantly more. Fine alumina powders of 0.5 μm were used as the secondary particles in the bimodal mixtures, as they sintered at lower temperatures, and provided a thin uniform 'coating' around the primary particles. The secondary powders, between 13 and 33 % by weight, were first mixed into a slurry in isopropanol with a ratio of 10:4 by weight. Coarse powders between 105 to 400 μm of varying amount were then added. Mixing was done by hand with a steel spoon in order to minimise the chances of large particle breakdown. The mixture was allowed to dry overnight before regranulation for vibratory packing. Inspection under optical microscope showed an even distribution of fine particles around coarse ones. Further improvements could be made on the evenness of the mixing process should mechanised equipment such as a blade mixer become available.

4.3 HOT ISOSTATIC PRESSING

4.3.1 Single Mode Powders

Single mode alumina powders were packed in porous graphite moulds for hot isostatic pressing. Initial trials showed that retaining the powders in a container during HIPing was necessary, irrespective of packing method, in order that the sintered body would remain a near flat disc shape. To retain the free capsule HIPing concept (Section 2.4.2), the container had to be permeable to gas, so that the HIPing gas could penetrate the pores between powders during pressurisation. A barrier layer of boron nitride was sprayed onto the porous graphite mould cavity before loading with powders.

The HIPing cycle for vibratory packed specimens of 13 - 43 μm began with a pre-purge of the HIPing chamber by three successive evacuations and repressurising to 1.5 bar with argon to remove all oxygen. Heating up to sintering temperature took place at a rate of 5 °C per minute. Pressurisation was synchronised to the temperature ramp-up.

Pressure and temperature were then held level for the pre-programmed sintering duration, before ramping down to ambient levels. The ramp-down was at 15 °C per minute.

Specimens of 7 μm particles and smaller were packed by slip casting. The slip casts already processed sufficient strength to allow handling in the green state. The dried green compacts were placed in porous graphite moulds as before, the latter only providing additional support during HIPing. The HIPing cycle was similar to that of vibration-packed specimens, except for the rate of temperature change. A much slower rate of temperature increase was found to be necessary to prevent premature cracking of the green body before sintering, as a result of excessive temperature differences. The ramp up rate was reduced to 2 °C per minute, and the ramp down rate to 5 °C per minute.

A range of experiments was performed for each particle size to study the relationship between HIPing temperature and densification. These were done at temperatures between 1600 and 1900 °C at a fixed steady state pressure of 500 bar. Work by Ishizaki [167] indicated that this would be a safe pressure setting to prevent formation of closed porosity. The effects of pressure and HIPing time were also investigated at selected temperatures by varying each parameter in turn.

4.3.2 Bi-Modal Mixtures

Due to the low rate of sintering of the coarse particles in a bimodal mixture, even at the maximum HIPing temperature of 1900 °C, a much longer sintering time of 4 hours was

used throughout. HIPing pressure was set at 500 bar. Ramping rates were the same as single-mode, vibration-packed specimens.

4.3.3 Powders with Sintering Aid

HIPing of powders with lithium fluoride (LiF) required special attention. Scanning electron microscopy of specimens with LiF, HIPed using a simple ramp up cycle as in the previous sections, revealed a high concentration of LiF at the centre of the porous specimen, whereas sections closer to the surfaces were essentially all alumina. This appeared to indicate that the LiF, which melted at a lower temperature, was being pushed towards the centre once it turned liquid, as the HIPing pressure kept increasing at that stage.

A two-stage ramp up was therefore tried. The pressure was first brought up to the steady state level, together with a temperature increase to about 250 °C, well below the melting point of LiF. The temperature was then increased while the pressure was kept constant. This action appeared to be effective.

4.4 POST-SINTER PREPARATION

After HIPing, outside dimensions and flatness of each porous alumina specimen were measured before being ground to shape for subsequent testing.

Machining was necessary, not only to reshape the sintered article to a near perfect disc shape, but also to remove the irregular packing of the particles at the immediate vicinity to the walls of the graphite tooling. German [189] mentioned a minimum thickness of four particle layers before this wall effect would become negligible. Machining was performed on conventional toolroom grinders using an epoxy bonded diamond wheel of 175 mm

diameter at 3600 rpm. Grit size for the diamond was 90 μm. Depth of cut was fixed at 10 μm. The grinding was done without coolant to avoid clogging up the pores. To ensure the complete removal of the above mentioned wall effect, a minimum of 0.5 mm was removed after the diameter and the surfaces had been cleaned in the rough grinding. Tolerances achieved were within ± 0.01 mm, with flatness to within 5 μm.

The finished ground specimens were cleaned of all loose debris by immersing in an ultrasonic bath of isopropanol for 15 minutes. Drying was at 80 °C for 12 hours.

5. QUANTIFYING MATERIAL PROPERTIES

5.1 SINTERED BODY MICROSTRUCTURE

An ABT 55 scanning electron microscopy was used to examine the microstructure of the free capsule hot isostatically pressed alumina specimens (Figs 5.1 to 5.6). As can be seen from Fig. 5.4, the microstructure is very uniform on a 'macroscopic' scale. Neck formation can clearly be observed, especially for well densified specimens. Specimens based on bimodal mixtures show a smooth, well-formed neck, due to the presence of the fine powers which act as a 'solder' to hold the large particles together (Figs. 5.5, 5.6). Such well formed necks are also noticeable in specimens sintered to a low porosity (Fig. 5.3). Particle bridging, though present, is generally uniformly distributed and not extensive, despite the relatively crude powder packing methods. As fluid flow properties of the porous specimens are extremely sensitive to pore size and structure, any visual assessment is unlikely to yield useful conclusions. Thus, quantitative measurements are the only meaningful means of assessing the sensitivity of fluid flow properties to each processing parameter.

5.2 DIMENSIONAL CHANGES

5.2.1 Densification and Shrinkage

Dimensional changes after HIPing or sintering offer a quick assessment as to the degree of sintering that has taken place [197, 198]. As the diameter and the height of the green compact can be determined accurately from dimensions of the graphite tooling, the amount of shrinkage can be calculated, from the diameter and the thickness of the

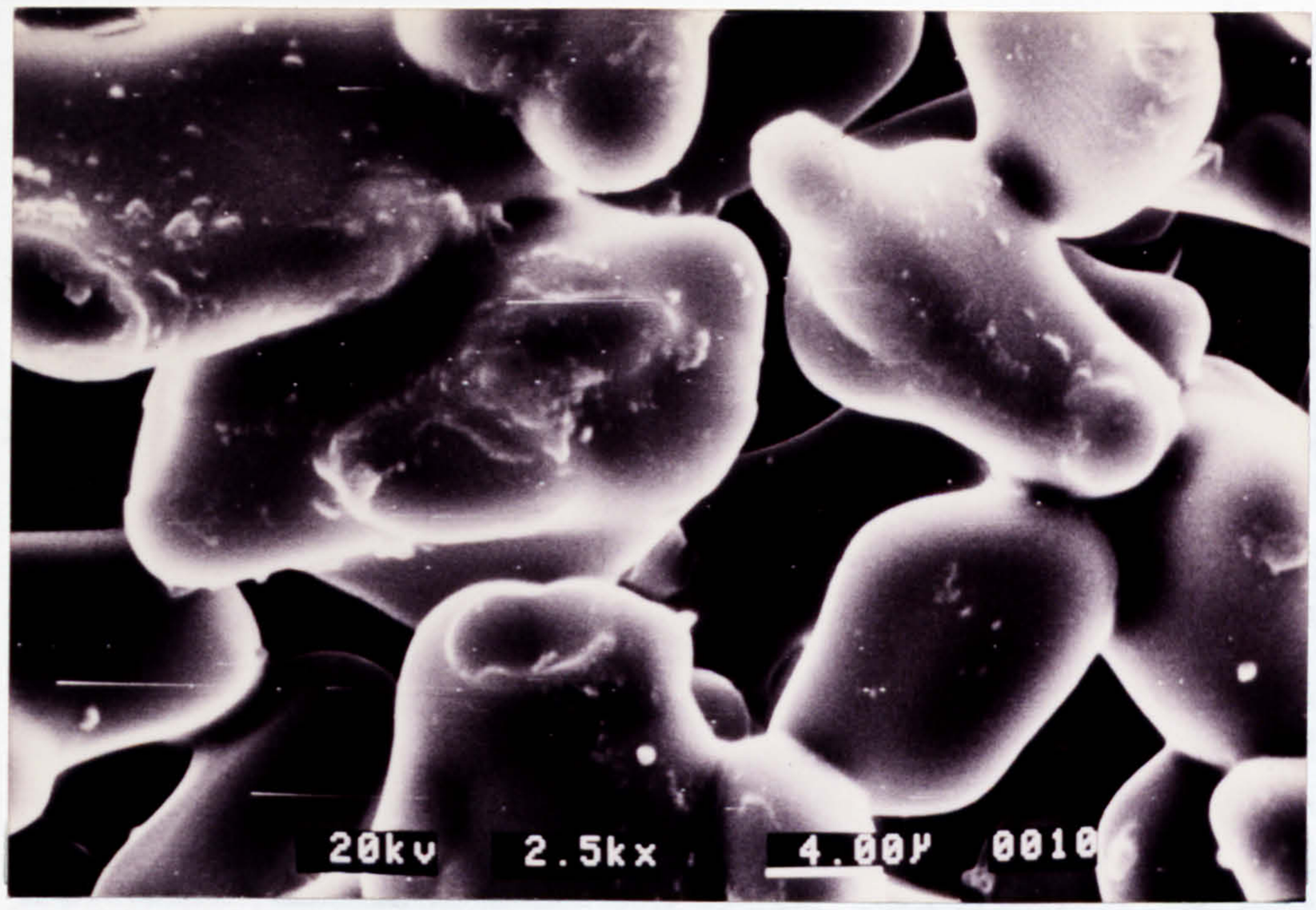

Fig 5.1 SEM Microstructure of a HIPed Porous Alumina
(7 μm Particles, Porosity 0.365)

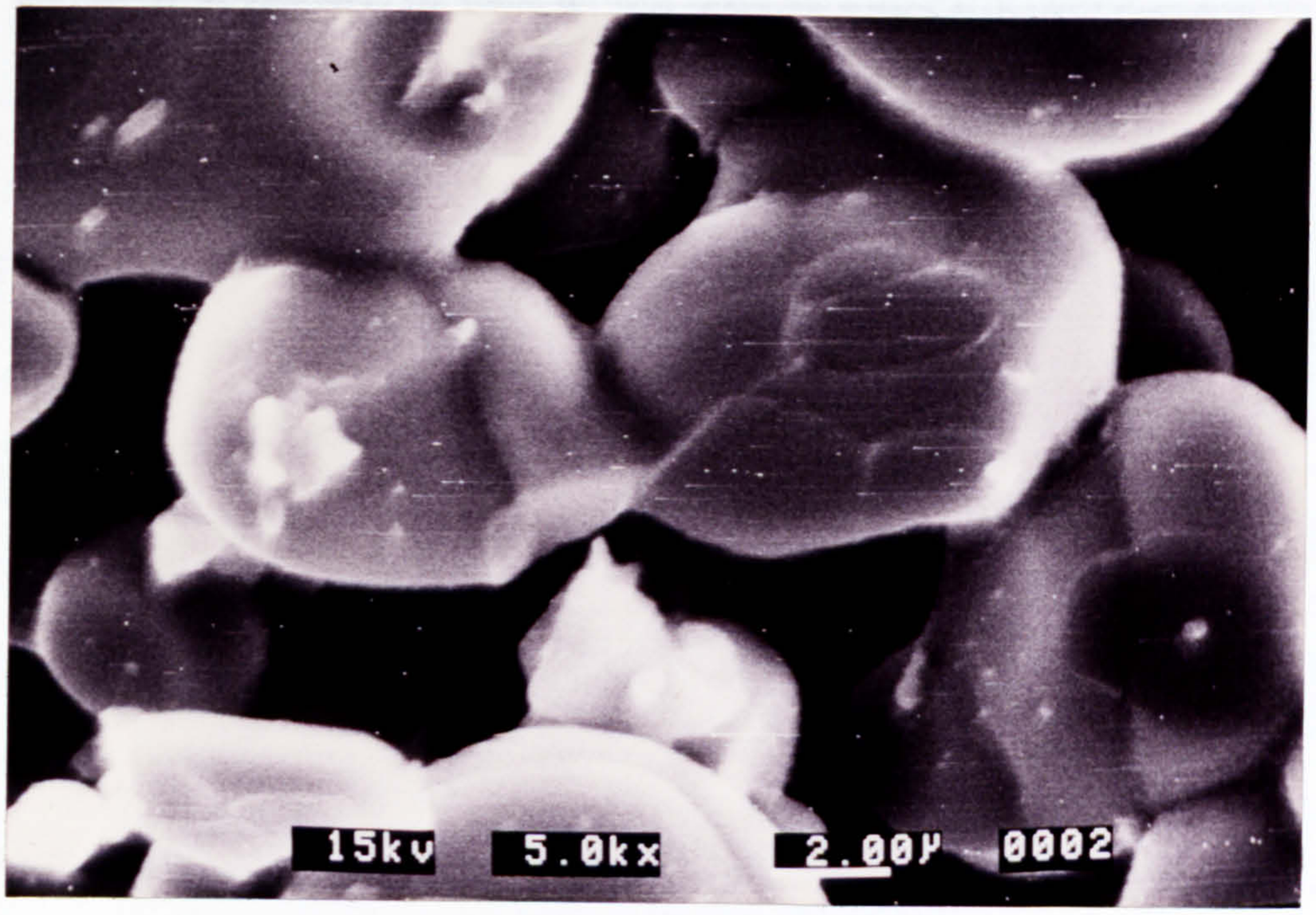

Fig 5.2 SEM Microstructure of a HIPed Porous Alumina
(7 μm Particles, Porosity 0.433)

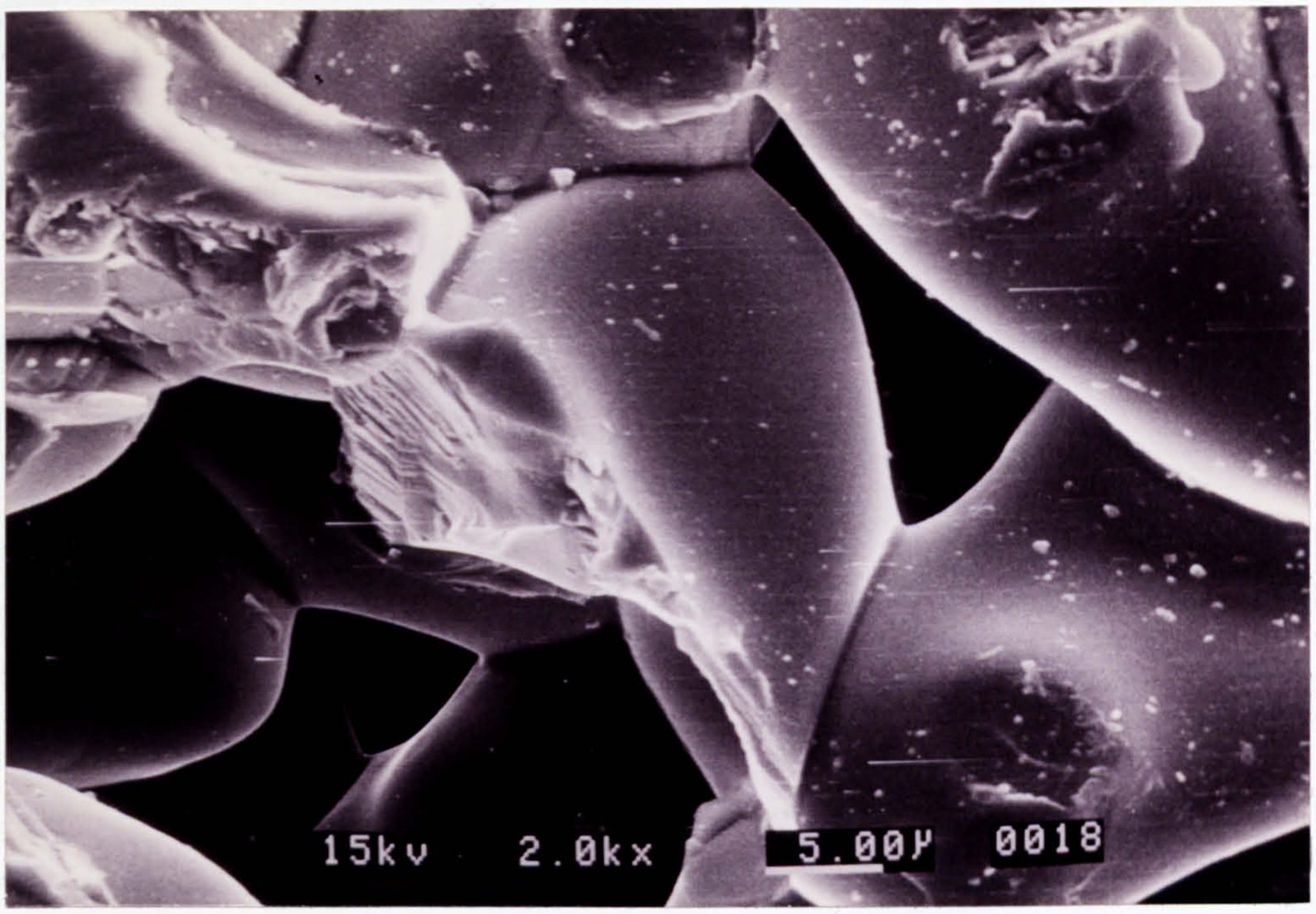

Fig 5.3 SEM Microstructure of a HIPed Porous Alumina
(23 µm Particles, Porosity 0.300)

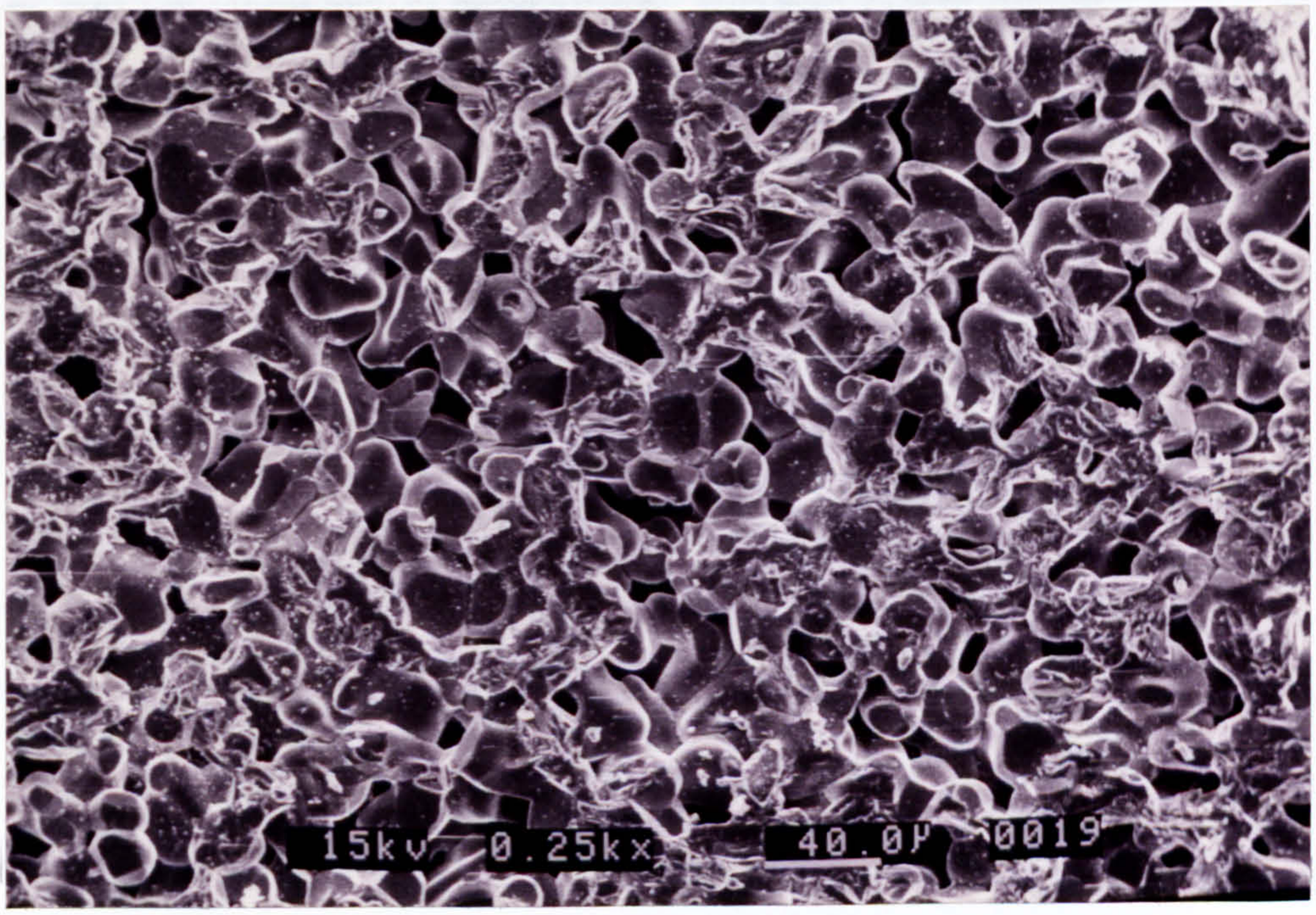

Fig 5.4 SEM Macroscopic View of the Above Specimen
(23 µm Particles, Porosity 0.300)

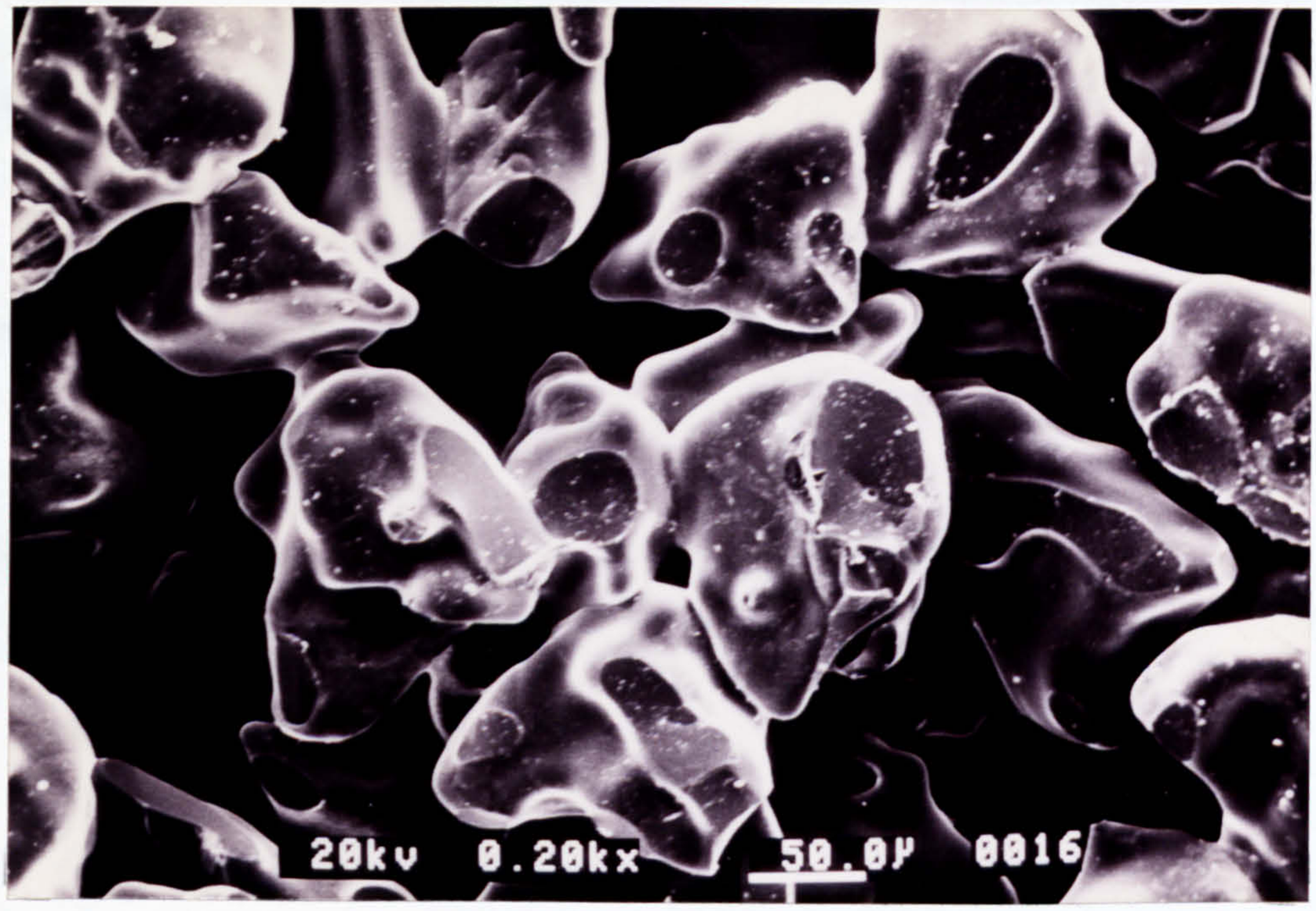

Fig 5.5 SEM Microstructure of a HIPed Bimodal Porous Alumina
(105 / 0.5 µm Particles, 5:1; Porosity 0.434)

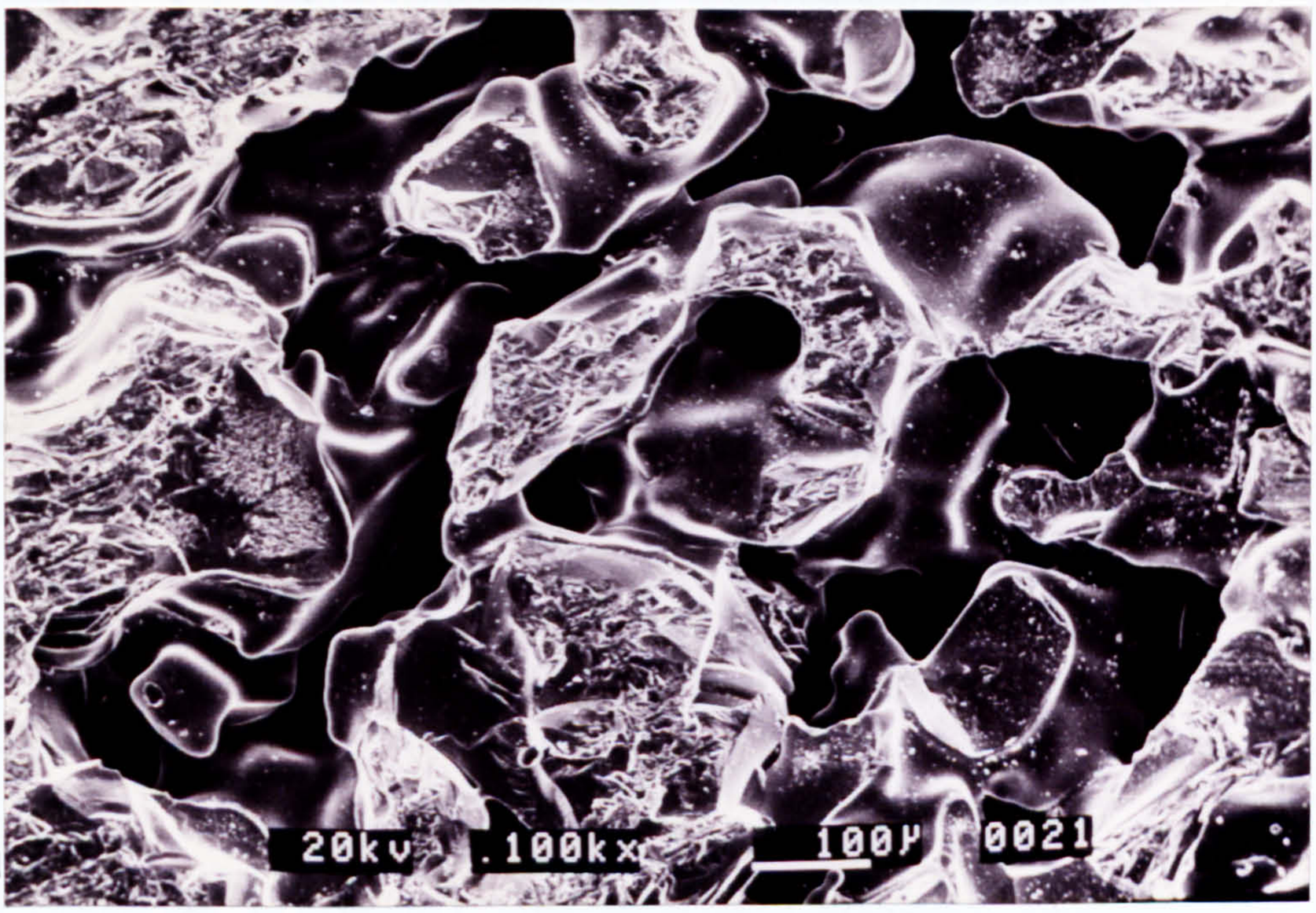

Fig 5.6 SEM Microstructure of a HIPed Bimodal Porous Alumina
(149 / 0.5 µm Particles, 3:1; Porosity 0.446)

HIPed specimen measured with a digital micrometer:

Diametrical shrinkage is defined as

$$\vartheta_d = 1 - (\text{specimen OD after HIPing} / \text{mould ID}) \qquad (5.1)$$

and axial shrinkage as

$$\vartheta_a = 1 - (\text{specimen thickness after HIPing} / \text{green compact thk.}) \qquad (5.2)$$

where

green compact thickness = height of empty mould cavity +
total mould height after powder packing -
total height of empty mould

Densification of the porous specimens can be defined as the increase in density after sintering :

$$\vartheta_v = \left(\frac{\rho_s}{\rho_g \cdot \rho_p}\right) - 1 \qquad (5.3)$$

The densification of specimens with particle size from 7 - 23 μm, HIPed at temperatures between 1600 and 1900 °C, were plotted against a number of HIPing parameters in Figs 5.7 to 5.13. Both the sintered and the green densities were calculated from weight and volume information. As expected, the HIPing temperature T_s had the most dominant effect on densification (Fig. 5.7). The spread of data was wide, especially at higher temperatures. This could largely be due to inaccuracies in the temperature measurement by the tungsten-rhenium thermocouples, which age rapidly at temperatures above 1800 °C, with a resulting change in their thermoelectric properties. There are, however, no alternatives for temperature measurement at such range which gives substantially more reliable results [199]. In addition to that, the process itself might not be as repeatable at a high degree of densification. It was also noticed that specimens placed on the top and bottom of a stack of four in the HIPing chamber densified consistently less than the

middle two. The HIPing furnace is a two-zone furnace with separate control of top and bottom heating elements. Feedback of the control loops comes from two thermocouples located near the top of the bottom graphite tool, and the bottom of the top one respectively. It might well be possible that the temperature outside the middle zone could be considerably lower, resulting in reduced sintering.

The densification appeared to bear a near linear relationship with HIPing temperature. The rate of increase was higher for smaller particles, due to their higher surface energy and therefore greater tendency to sinter at a given temperature. A purely empirical relationship could be established from Fig. 5.7 to express ϑ_v as a function of both temperature and particle size :

$$\vartheta_v = (21.46 - 0.423 \times 10^6 . d_w) . T_s + (3.45 - 7 \times 10^4 . d_w) \qquad (5.4)$$

The effects of the HIPing pressure were far less obvious (Fig. 5.8). At low HIPing temperatures and densification, the HIPing pressure had no noticeable effect on densification. At higher densification (above 0.4), however, the HIPing pressure appeared to increase porosity. As mentioned earlier in Chapter 2, the pressure is believed to resist complete pore closure for a high degree of sintering. The reduced densification at high HIPing pressures appeared to support this hypothesis. As an example, specimens from 7 μm powders HIPed at 1900 °C showed a reduction of some 20% in the degree of densification, when the pressure was increased from 250 to 1000 bar.

The influence of HIPing time was similarly negligible at low densification, but increasingly more significant at higher densification. Specimens of 13 μm powders and HIPed at 1900 °C exhibited a 20% increase in densification as the HIPing time was doubled from 1 to 2 hours (Fig. 5.8). The rate of increase in densification also appeared to be constant with time. The effects of both time and pressure were much less prominent compared with that of HIPing temperature.

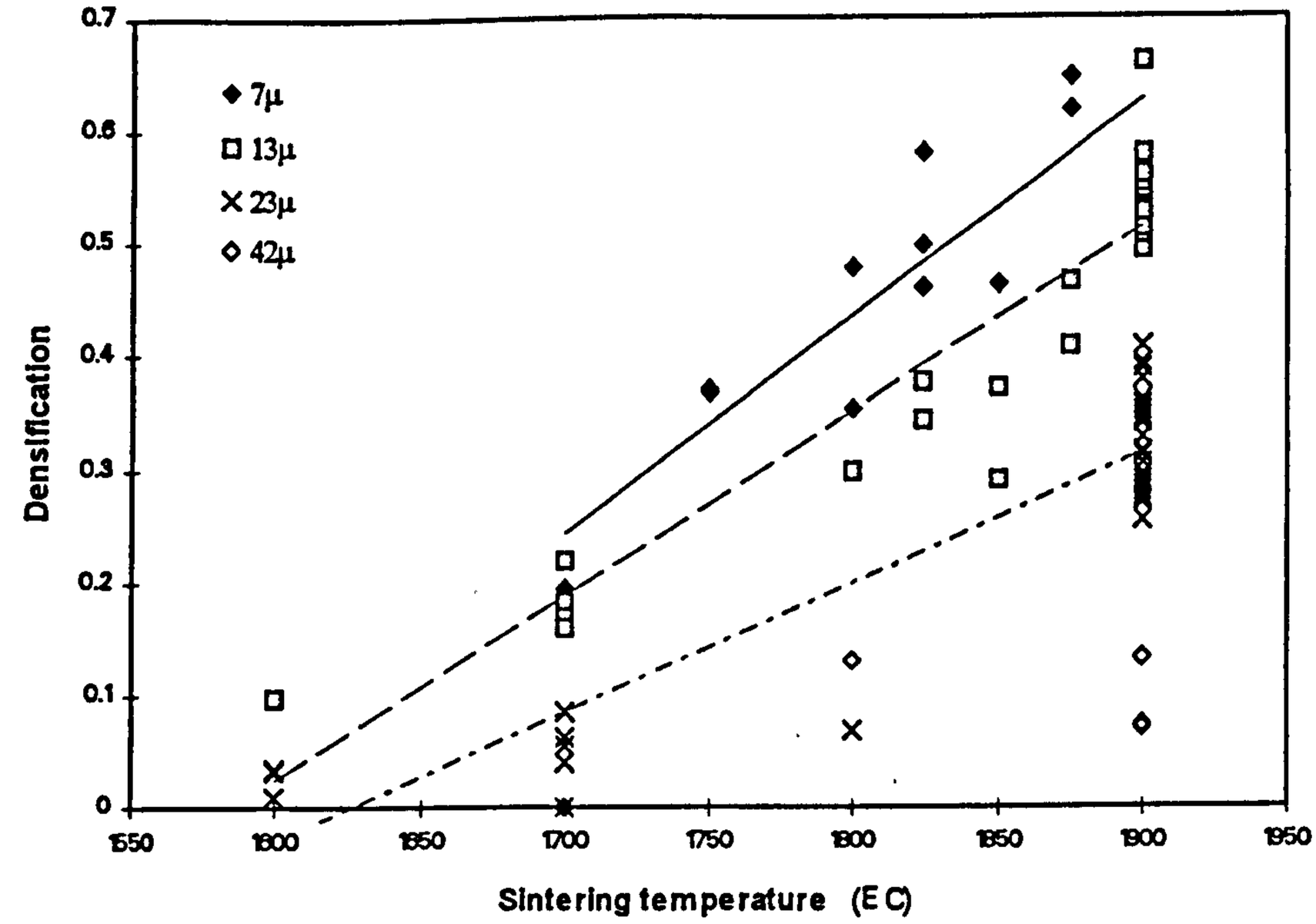

Fig 5.7 Temperature Effects on Densification
(HIPing time = 1 hour ; Pressure = 1000 bar)

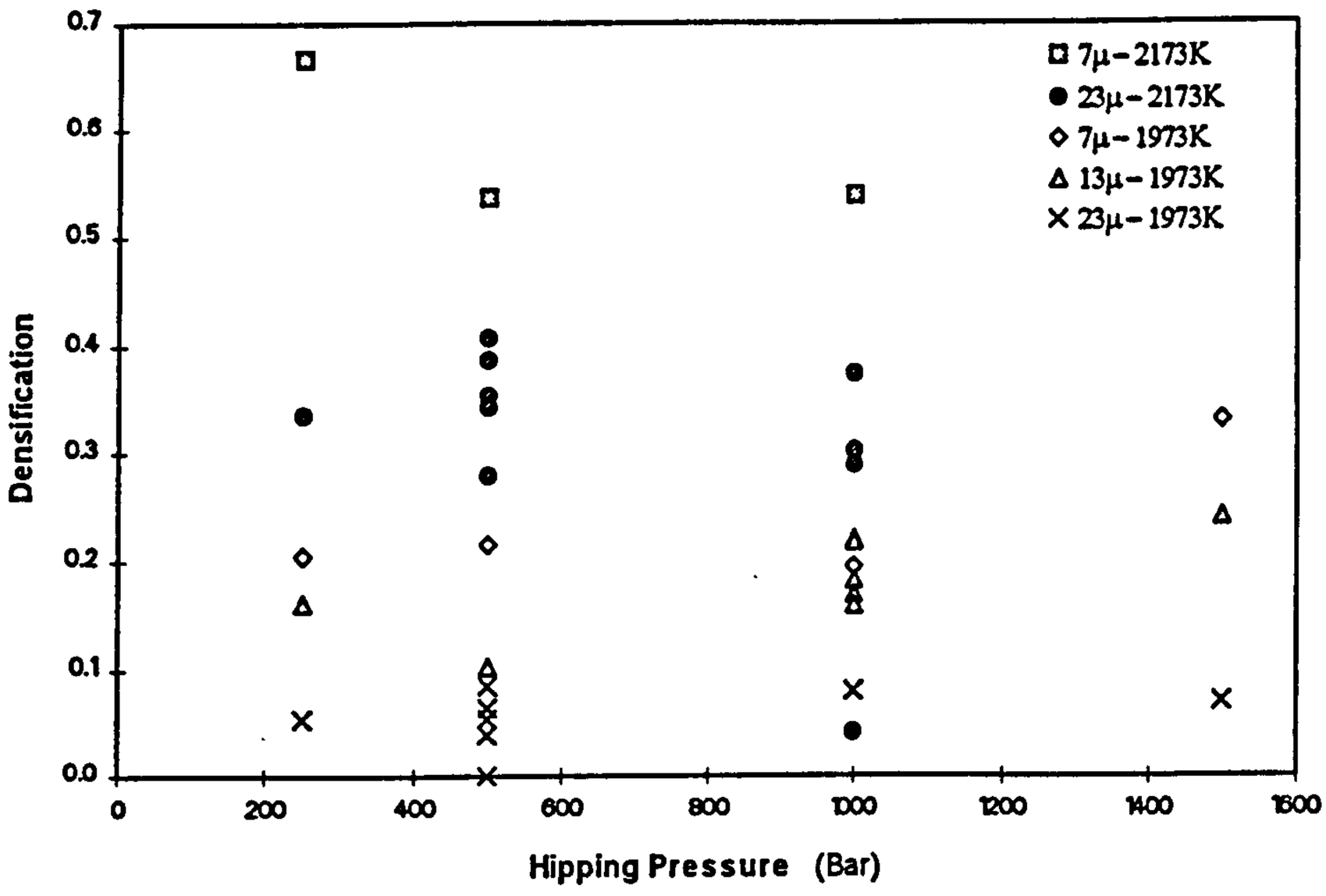

Fig 5.8 Pressure Effects on Densification
(HIPing time = 1 hour)

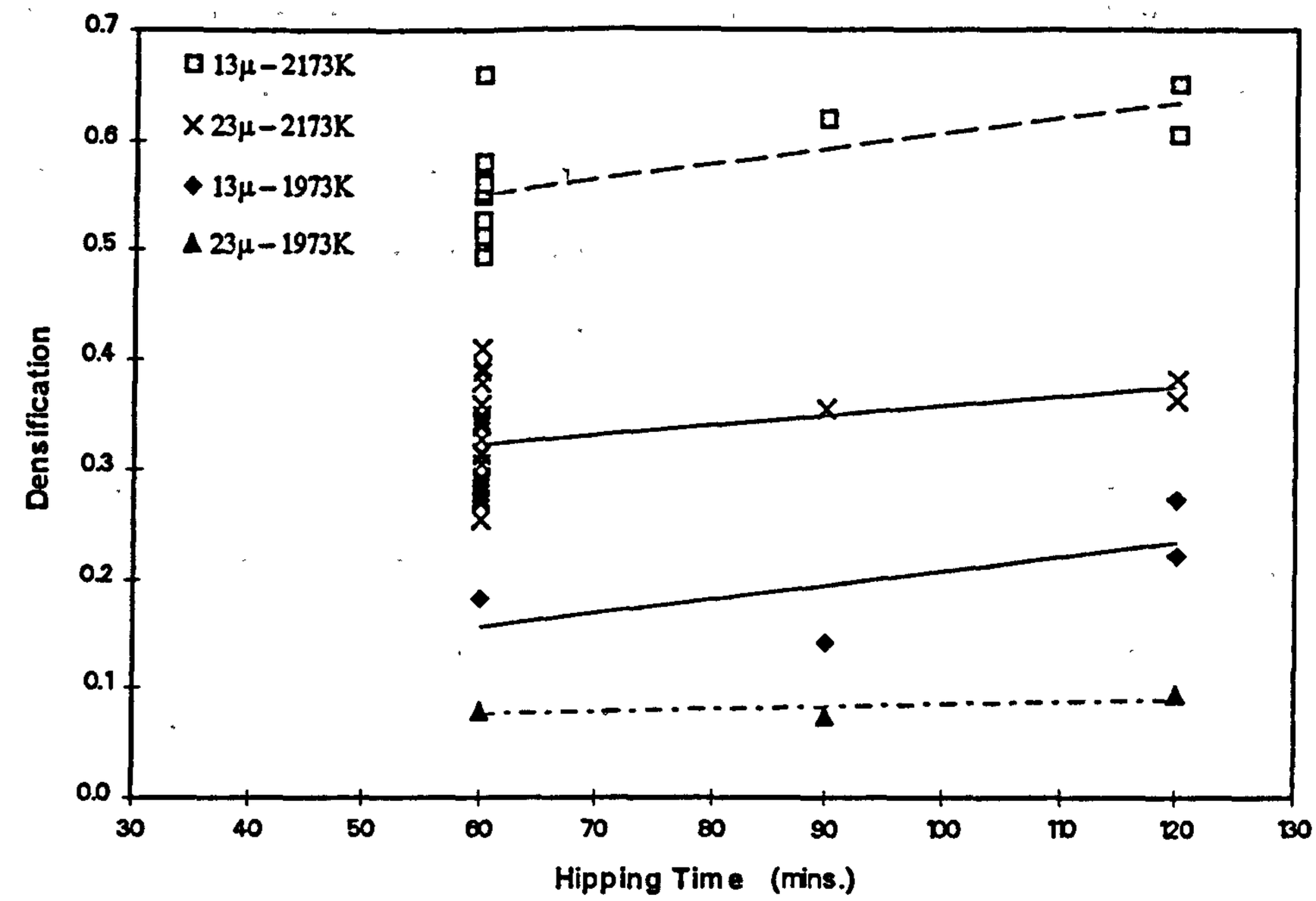

Fig 5.9 Effects of HIPing Time on Densification
(HIPing pressure = 500 bar)

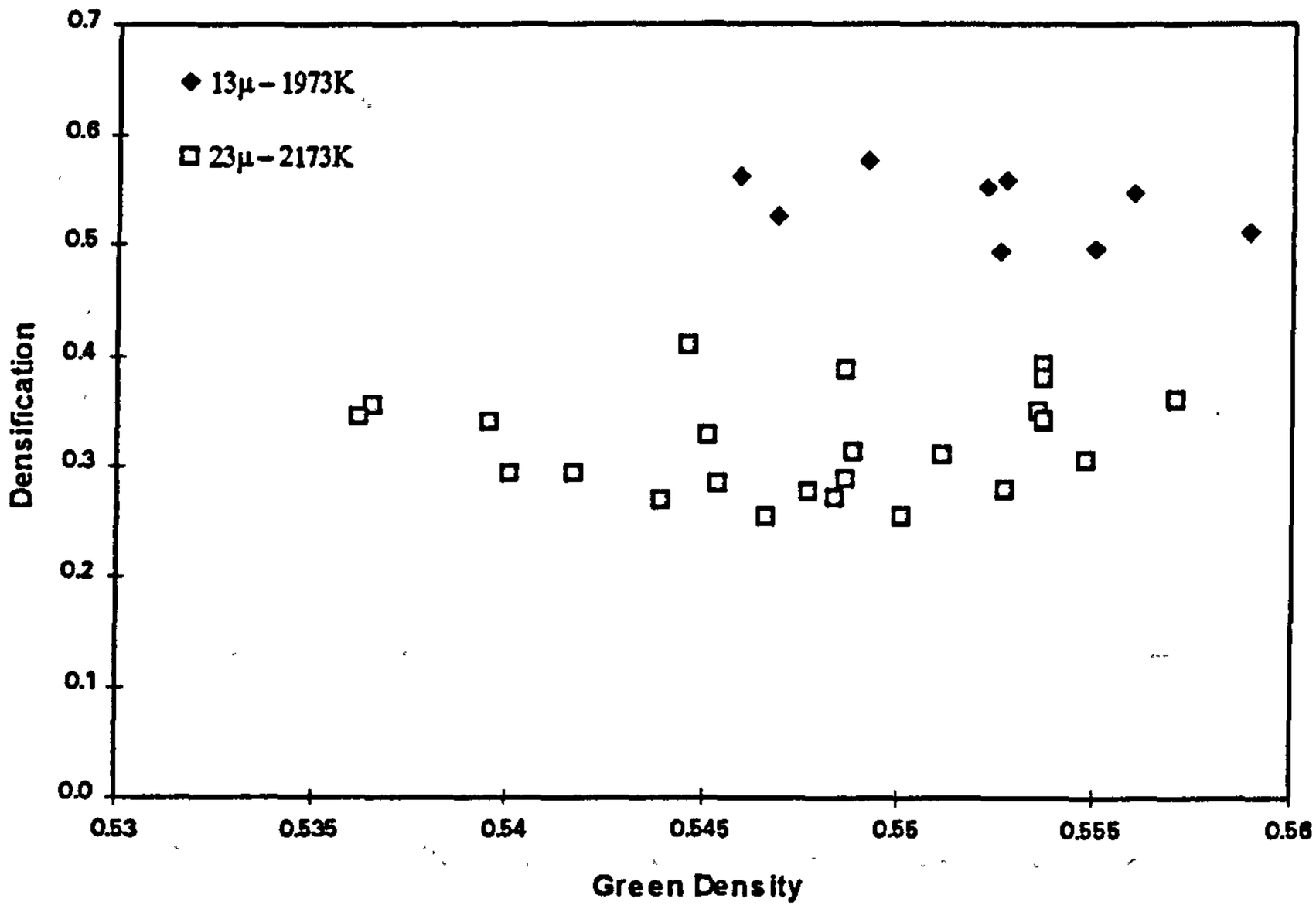

Fig 5.10 Effects of Green Density on Densification
(HIPing pressure = 500 bar)

Dependency on the green density of powder compacts was similar (Fig. 5.10). Only at densification of more than 0.5 could the influence of the green density be noticed. A lower green density implies the presence of more particle bridging in the powder compact, and hence allows more room for particle rearrangement to occur during the stage zero of sintering, resulting in a higher degree of densification.

The presence of lithium fluoride as a sintering aid, however, had a drastic effect on densification (Fig. 5.11). The increase in densification was especially sharp between 0 and 1 wt% LiF. The rate of density increase became less as the LiF content increased to 4 wt%. Such extreme sensitivity to LiF content also means that any uneven mixing would undoubtedly lead to non-uniform shrinkage.

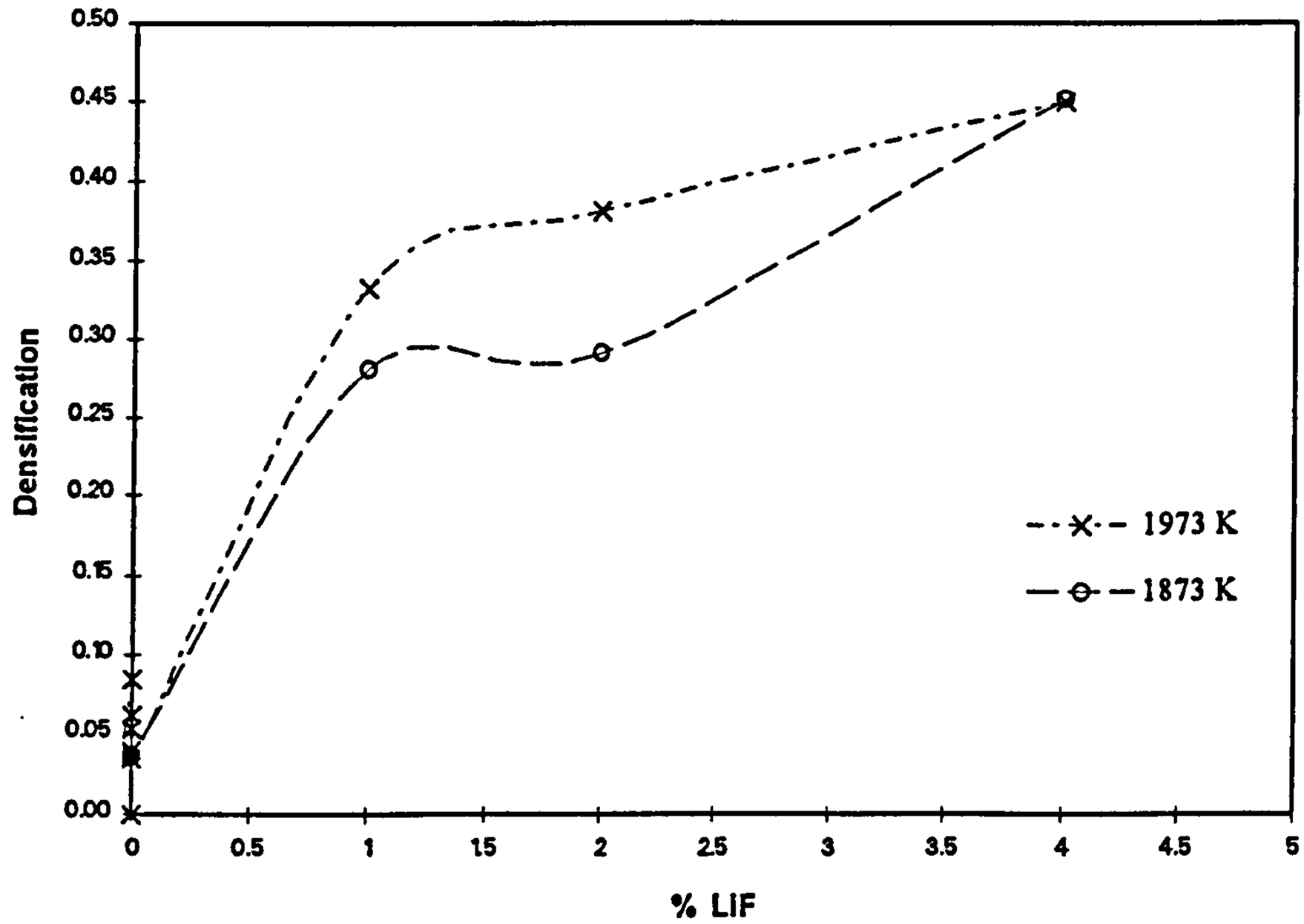

Fig 5.11 Effects of Sintering Aid on Densification
(23 μm Alumina, 500 bar, 1 hour sinter)

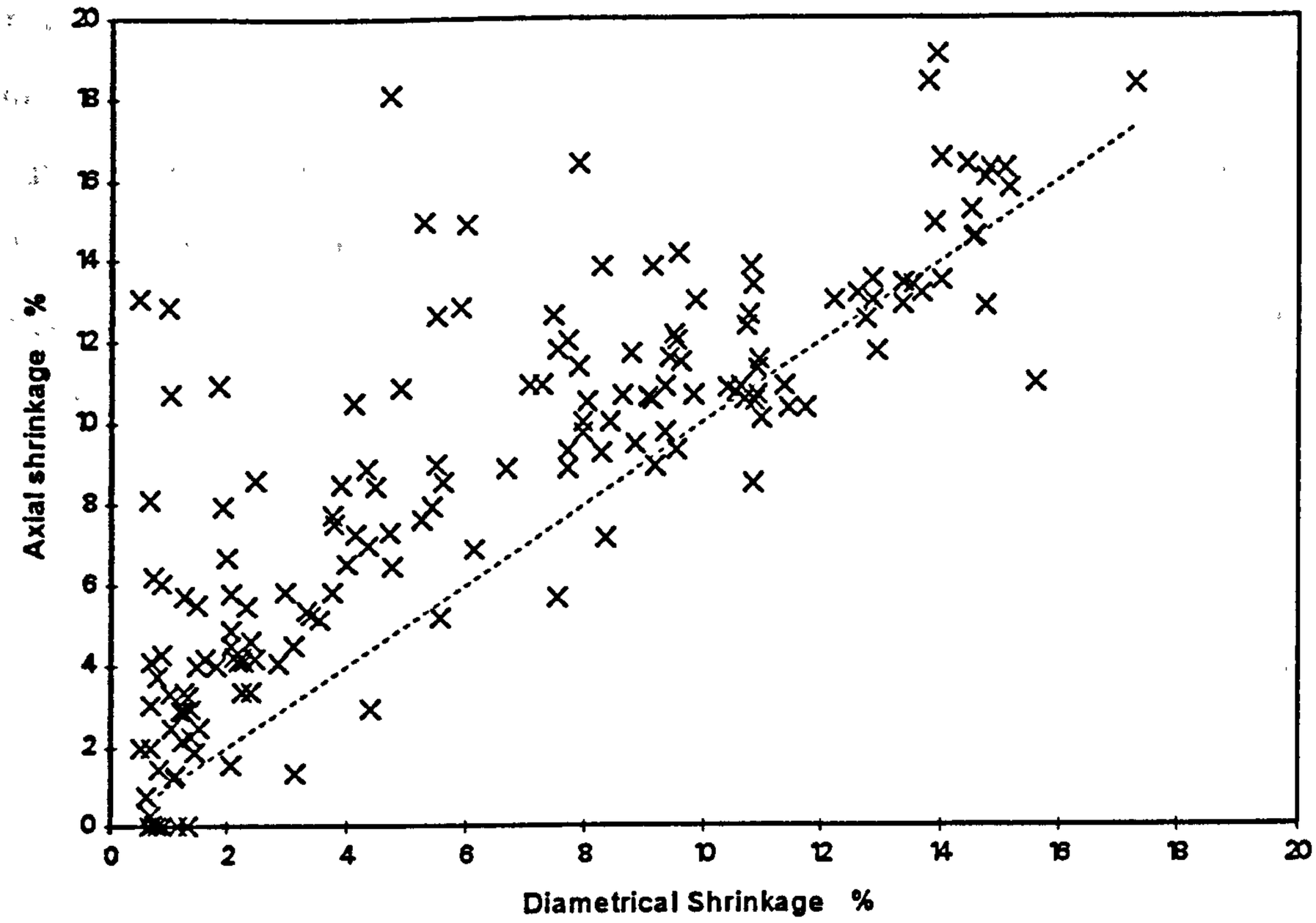

Fig 5.12 Uniformity of Linear Shrinkage

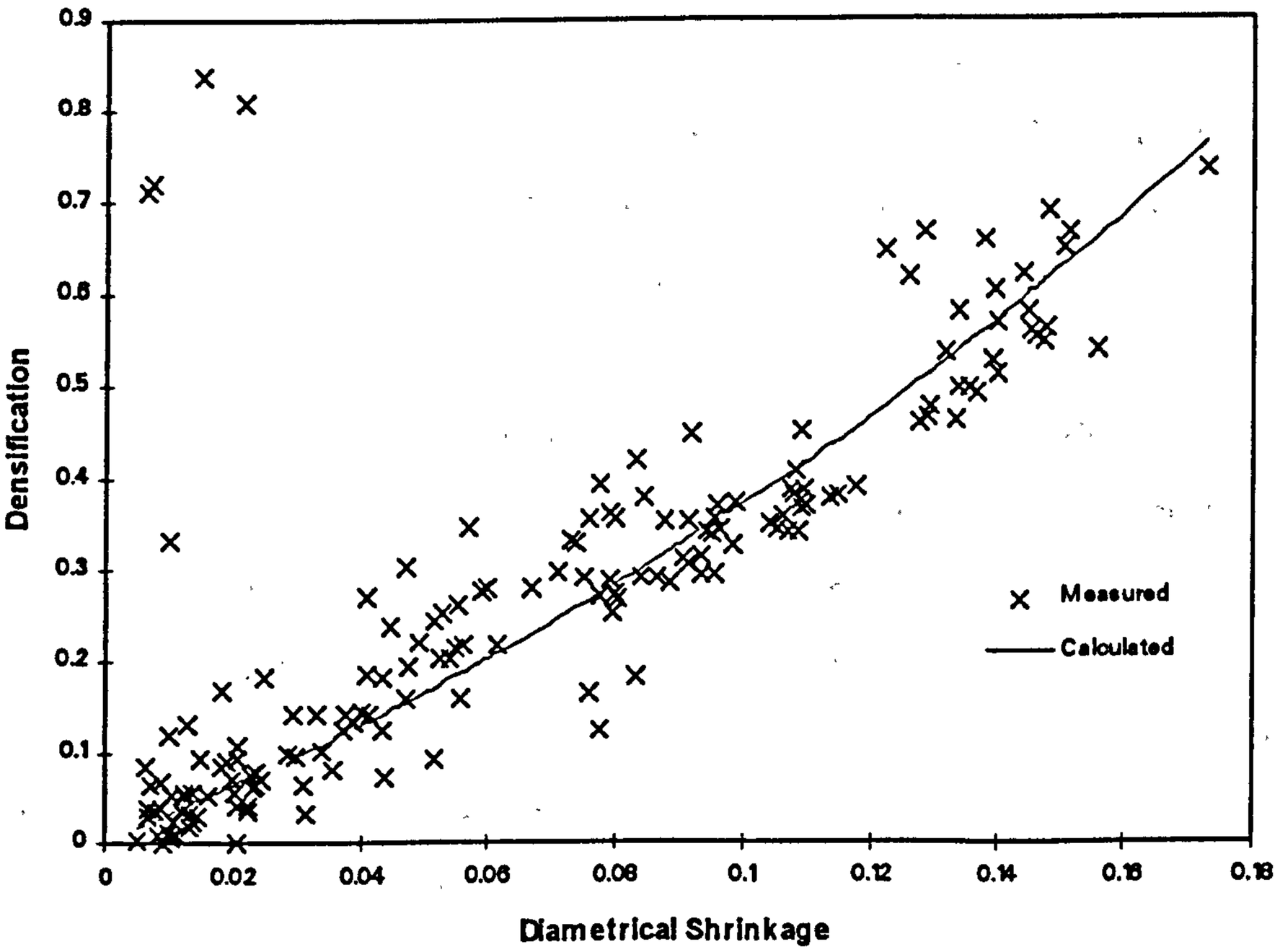

Fig 5.13 Uniformity of Linear Shrinkage II

Linear shrinkages (axial and diametrical) measured from external dimensional changes were mostly uniform and isotropic (Fig. 5.12). Certain specimens, particularly those placed at the bottom of a stack of four specimens in one HIPing batch, showed higher axial shrinkage at the expense of diametrical. The dead weight of the specimens and tooling above is believed to cause preferential densification in the axial direction, similar to the action of hot pressing. Apart from the above mentioned specimens, the relationship between measured diametrical shrinkage and densification generally obeyed the theoretical relationship of :

$$\vartheta_v = (1 - \vartheta_d)^{-3} - 1 \qquad (5.5)$$

assuming isotropic densification (Fig. 5.13).

5.2.2 Distortions

The end surfaces of the graphite tooling were manufactured to a flatness of 0.01mm or better. It would therefore not be unreasonable to assume that the green compacts started off flat to 0.01mm. Flatness errors after HIPing were measured using a simple feeler gauge between the specimen and a reference straight edge. The flatness measurement gives an indication of the amount of additional machining allowance necessary when producing more complex shapes on a commercial scale.

Most specimens exhibited a significant degree of distortion after sintering. The majority had a slight bow upwards, resulting in a concave top surface. The bottom surfaces were mostly convex, but with much larger radii of curvature. The finished thickness was generally less at the centre than at the perimeter, suggesting higher densification there. The side wall was also slightly tapered towards the top. Two explanations could be suggested for this phenomenon - temperature gradient across the specimen causing differential sintering, or lower green density at the centre due to wall effects of the vibratory packing, and subsequent higher densification (c.f. Fig. 5.10). The effect was also present in slip-cast specimens.

The amount of distortion, measured as an out-of flatness value, could be as high as 0.8mm for a green body diameter of 53mm. No relationship could be established between this out-of flatness value and green density, total porosity, or densification, as illustrated in Figs. 5.14 - 5.16. The random manner of this occurrence implied that near net-shape components could be difficult to achieve, and sufficient machining allowance would have to be made.

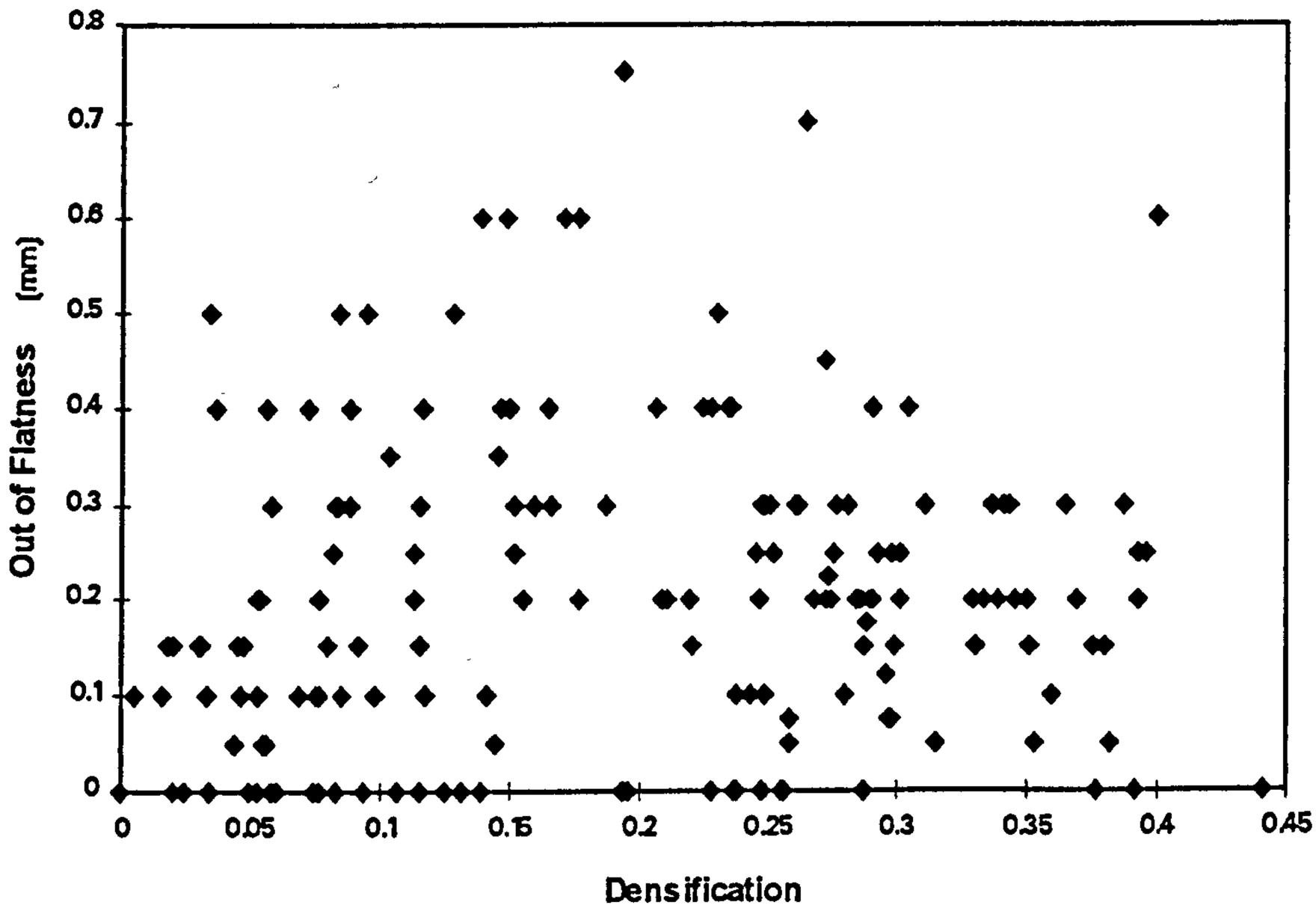

Fig 5.14 Out of Flatness vs Densification

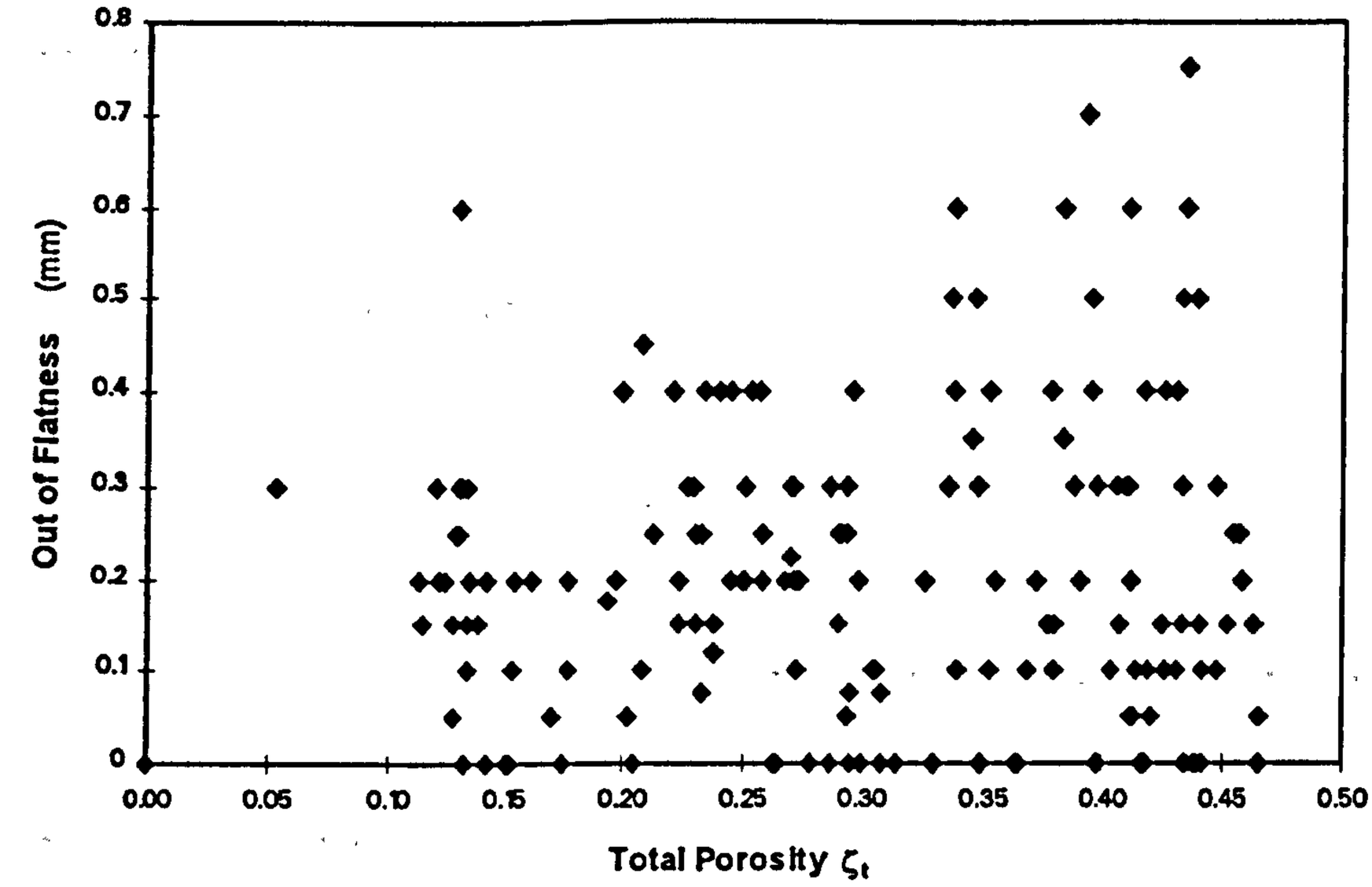

Fig 5.15 Out of Flatness vs Total Porosity

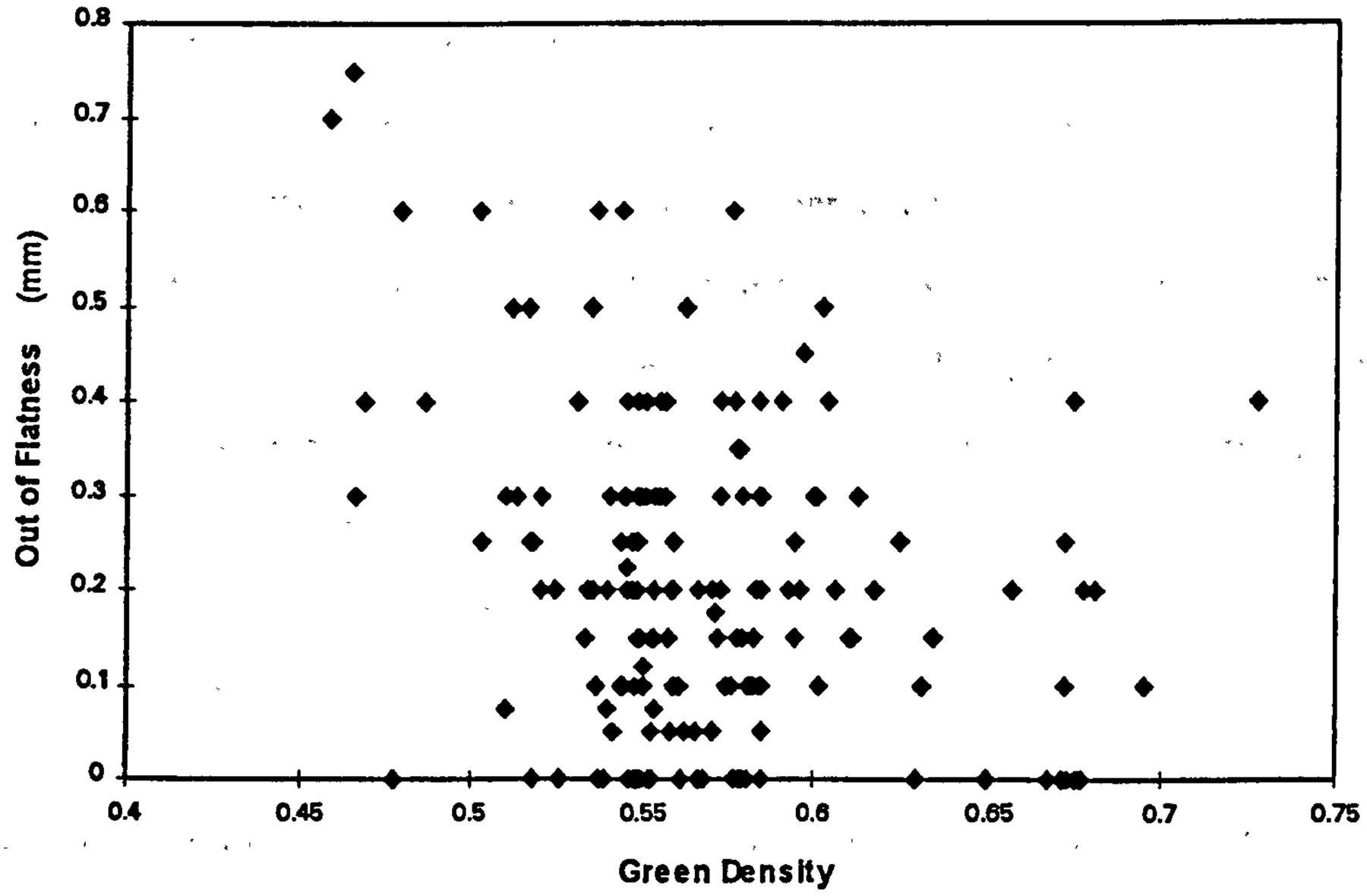

Fig 5.16 Out of Flatness vs Green Density

5.3 POROSITY

5.3.1 Open Porosity Measurement

The measurement of open porosity followed closely the method laid down in ISO 2738:1987 [200] for porous metals, with the exception that deionised water was used for impregnation rather than oil as suggested in the standard. The use of oil to prevent corrosion is not necessary for ceramics. In addition, alumina has good affinity with water, and as such complete wetting could be expected.

After thorough cleaning and complete drying, the dry weight of the specimen m_1 was measured with an electronic balance with a resolution of 1 μg (Sartorius Type 1712). The specimen was then fully impregnated with water, so that the open and closed porosity could be determined using Archimedes principle.

The standard technique for impregnation in ISO 2738 involves submerging the porous specimen in the infiltration liquid, in this case deionised water, and then vacuum degassing in a desiccator until no bubbles can be seen emerging from the specimen. This method was found to be inadequate in the present work. Initial measurements with specimens sintered from fine powders, based on the original impregnation method in ISO 2378, resulted in large closed porosity (up to 10%). This was particularly noticeable for specimens with pores smaller than a couple of micrometers. As the total porosity was around 0.28 for these first samples, little closed porosity was expected. This led to the conclusion that the water impregnation was incomplete.

An improved method was developed in the course of the present work in which the dry specimen was first vacuum degassed above a beaker of deionised water, then dropped and fully submerged in the water, before the desiccator was repressurised to atmospheric pressure. Experimental evidence to demonstrate the effectiveness of this new method, as

well as the proposed theory to describe the phenomenon, will be dealt with in the following section. This revised method was used throughout the present work. Evacuation time was a minimum of 15 minutes.

After complete water impregnation, the excess water was wiped off the surfaces of the specimen before weighing to give m_2 .

The fully wetted specimen was then placed on an X-shaped pan, the weight of which had been pre-determined, both in air and in water (m_3 & m_4 respectively). The pan, together with the specimen, was then weighed again, fully immersed in deionised water, giving m_5 .

The volume of the specimen can then be calculated from

$$V_s = \frac{m_2 + m_4 - m_5}{\rho_w} \qquad (5.6)$$

The open porosity is then given by

$$\zeta_o = \frac{m_3 - m_2}{\rho_w . V_s} . 100 \qquad (5.7)$$

5.3.1.1 Mathematical Model for the Mechanisms of Water Impregnation

As mentioned earlier, water impregnation according to the method laid down in ISO 2738 is believed to be incomplete, resulting in an overestimated percentage of closed porosity.

One common modification to the ISO method is the use of a low surface tension fluid, such as xylene or toluene, to aid penetration [170]. This was also tried for a number of specimens, and did give improved results. The level of closed porosity was, however,

still higher than expected. Also, the vapour of both liquids is extremely flammable as well as a hazard to health. The additional need to infiltrate the pores completely with water in the pore size distribution test led to the current development.

The problem with the ISO method lies in the evacuation of trapped air under water. Assuming perfect vacuum above the water surface, the absolute pressure at the surface of the porous specimen equals to the hydrostatic pressure due to the column of water above. Pressure within the pores is yet higher, as it has to overcome surface tension at the water / air interface before being able to escape. Pressure within the pores is therefore :

$$p_{pore\,1} = \rho_w.g.h_w + \frac{4.\gamma_w}{d_{pore}} + p_{vac} \qquad (5.8)$$

as the contact angle is zero for complete wetting.

Surface tension is lowest at the pore of maximum size, through which the last bubbles would escape. As the pores are interconnected, one can expect the residual pressure in the submerged sample to be limited by the largest surface pore, determined by the reversed bubble point (Section 6.2.1). The hydrostatic pressure could be minimised by reducing the water column to just above the specimen surface, and the absolute vacuum pressure is limited only by the water vapour pressure at room temperature (around 24 mbar). The surface tension component is, however, by far the most dominant. For a maximum surface pore of 20 μm, pressure due to surface tension is as high as 0.15 bar. Only 85% of the mass of trapped air would have managed to escape.

Upon repressurisation, water begins to penetrate the pores under the action of both the external pressure (atmospheric) and surface tension, the latter acting now in favour of penetration. This combined absolute pressure is therefore

$$p_{pore\,2} = \frac{4.\gamma_w}{d_{pore}} + p_a \qquad (5.9)$$

The residual air would then attain a volume determined by

$$V_{res} = \frac{p_{pore1}}{p_{pore2}} \times V_{pore} \qquad (5.10)$$

This amounts to 13% of the total open pore volume when the largest surface pore is 20 μm, but increases to 22.5% for a 10 μm surface pore. This residual volume would show up in the calculations as closed porosity, as if it were not penetrable. Changing the liquid to xylene would improve the results to 5.3% and 2.7% respectively.

The residual volume of trapped air could be largely reduced if the surface tension component of equation 5.8 could be eliminated. This points to evacuation in free space rather than submerged. The new technique developed in the course of the present study involves placing the porous specimen above a beaker of water during evacuation. Not only is the trapped air within the pores free to escape, but the water is also degassed in the process. Furthermore, the continuous evacuation fills the entire volume of the desiccator largely with water vapour evaporated under the high vacuum. After a minimum period of 15 minutes, the steel wires supporting the specimen are disturbed externally with a magnet to drop the specimen into the water (Fig 5.17). Full penetration could then be achieved by repressurising to atmospheric pressure.

To prove the effectiveness of the revised impregnation method, experiments were conducted on a 7 μm porous alumina specimen. Three separate methods were compared -- the ISO method using water, the same using xylene, and the method proposed. The specimen was thoroughly cleaned and dried to remove all traces of penetrating fluid between methods. The results shown in Table 5.1 revealed a 29% and 14% less impregnation from the first two methods compared to the third. The calculated residual volume based on the theory above showed excellent agreement to the measured values. The agreement between the measured and calculated porosity values for a large number of specimens gave further support to the validity of the method. Closed porosity values for most specimens were zero to within $\pm 0.5\%$.

Table 5.1 Comparison of Water Impregnation Methods for Porosity Measurement

Particle Size	7 μm		Vac. pressure	24 mbar
Calculated total porosity	0.131		H_2O Column	30 mm
Maximum surface pore	7 μm	measured		
Bubble point pressure	0.416 bar	in water		
	0.163 bar	in xylene		

Penetration method	Open Porosity	Closed Porosity	V_{res} / V_{pore} measured	V_{res} / V_{pore} calculated
degas in water	0.051	0.079	0.71	0.70
degas in xylene	0.063	0.067	0.86	0.86
degas in air, repressurise in water	0.074	0.057	1 * * assumed	

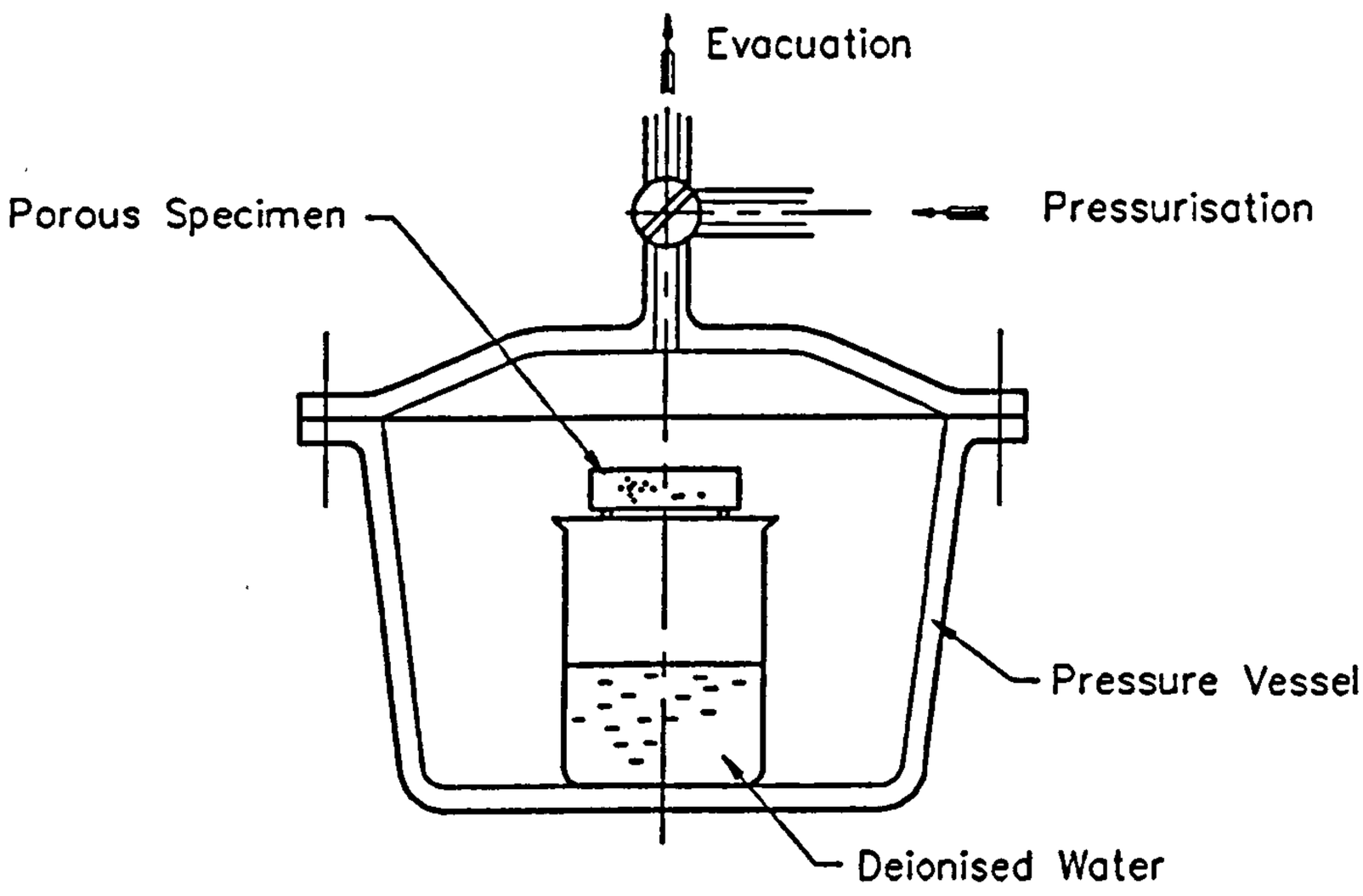

Fig. 5.17 Schematic of the Water Impregnation Equipment

5.3.2 Closed Porosity Measurement

Closed pores are not accessible during the impregnation stage mentioned in the previous section, and could therefore not be quantified directly. However, if the true density of the powder ρ_p with 0% porosity could be determined (e.g. using a pyknometer), the total porosity could then be calculated from

$$\zeta_t = \left(1 - \frac{m_2}{\rho_p . V_s} \right) . 100 \qquad (5.11)$$

The closed porosity is then

$$\zeta_c = \zeta_t - \zeta_o \qquad (5.12)$$

In the present work, the theoretical value of 3950 kgm^{-3} was used for ρ_p [182].

5.3.3 Dependency of Porosity on HIPing Parameters

According to their definitions, the total porosity can be expressed as a linear function of the green density and densification :

$$\zeta_t = 1 - \rho_g . (1 + \vartheta_v) \qquad (5.13)$$

The effects of the most important HIPing parameters on densification have already been discussed in section 5.2.1. Thus, knowing the green density (from direct measurement or powder packing process predictions), the total porosity of the sintered specimen could be predicted.

Most of the specimens prepared in the present investigation had very little closed porosity. Equation 5.13 could therefore be used, in combination with equation 5.4, to predict open porosity without incurring significant error.

As densification increases with increase in HIPing temperature, neck growth between certain particles might approach the third stage of sintering in which closed pores are beginning to form. The percentage of open porosity is therefore expected to fall (Fig. 5.18). Repeatability of data was poor at above 1800 °C, for the same reasons as those mentioned in Section 5.2.1. For specimens with a final open porosity $\zeta_o < 0.4$, a reduction in the open porosity level could be observed with increased HIPing time, and reduced HIPing pressure (Fig. 5.19, 5.20). The increase in HIPing time allows further densification, and hence a higher probability for closed pores to form. The HIPing pressure, on the other hand, is believed to resist closed-pore formation. A lower HIPing pressure therefore leads to increased closed porosity. The effects of both parameters were not as significant as that of temperature. No change in open porosity could be observable at $\zeta_o \geq 0.4$ due to lack of sintering for such specimens.

The effect of the HIPing pressure on closed porosity was more noticeable at high densification, as in the case of 7 μm powders HIPed at 1900 °C. At 250 bar HIPing pressure, the porosity of 12% was almost entirely closed porosity. This reduced to some 2% as the pressure was increased to 1000 bar (Fig. 5.21). The increase in closed porosity with increasing HIPing time and temperature could be observed in Figs. 5.22 and 5.23, but no concrete mathematical relationship could be established. This is partly due to the fact that closed porosity figures are generally not very reliable, as they have to be determined indirectly from the total and open porosities, which in turn are calculated from some five or six different weight measurements. Up to a densification of 0.5, closed porosity was generally not more than 3 % (Fig. 5.24). Only above that value did the proportion of closed pores become more significant, particularly at low HIPing pressures. Open and closed porosities are expressed as a fraction of total porosity in Fig. 5.25. Comparison with published data for pressureless sintering [201] indicated the effectiveness of the free-capsule HIPing process in reducing closed porosity. The latter was effectively zero at a total porosity of 0.15 and above.

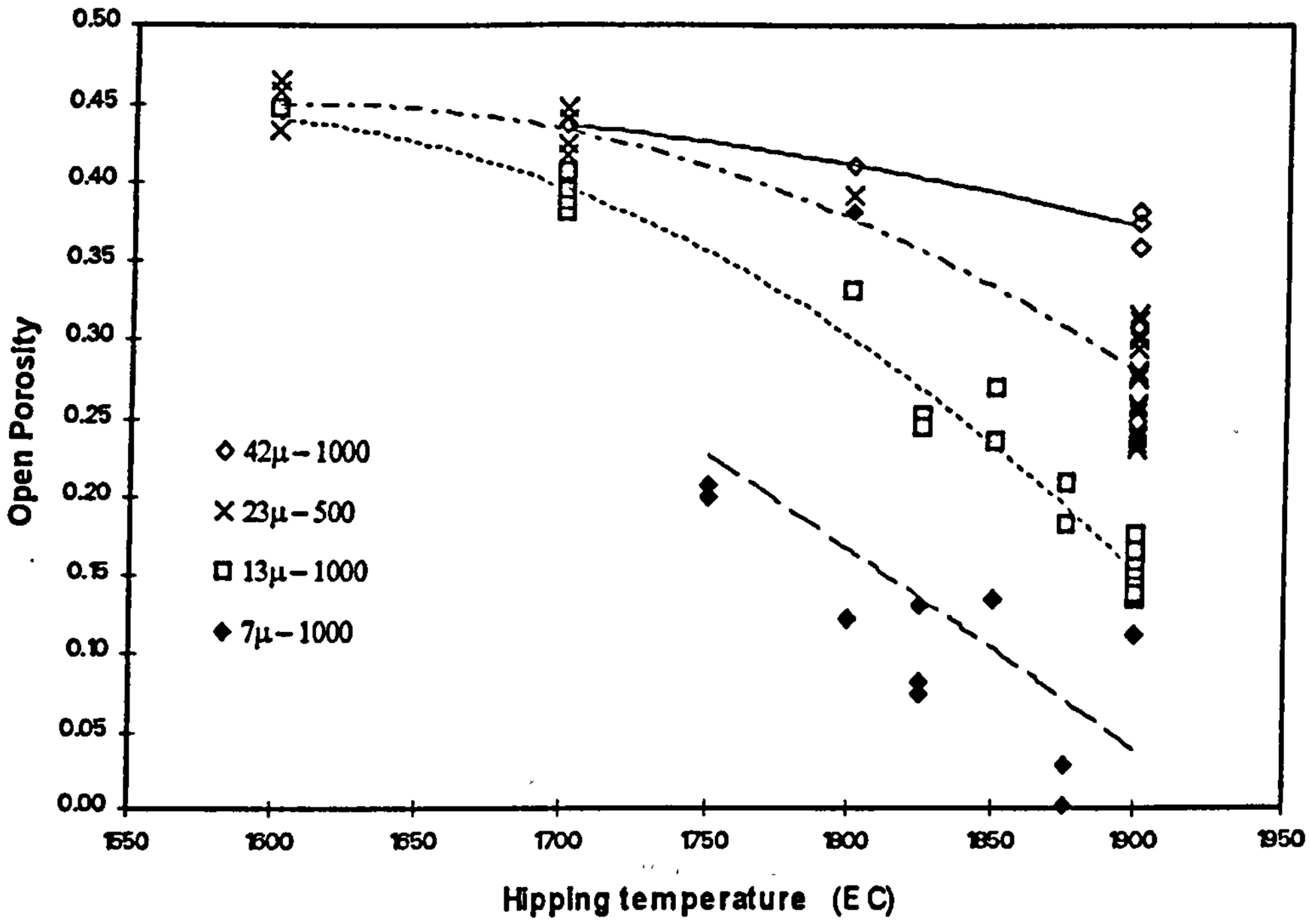

Fig 5.18 Temperature Effects on Open Porosity (100% Alumina)
(HIPing time = 1 hour)

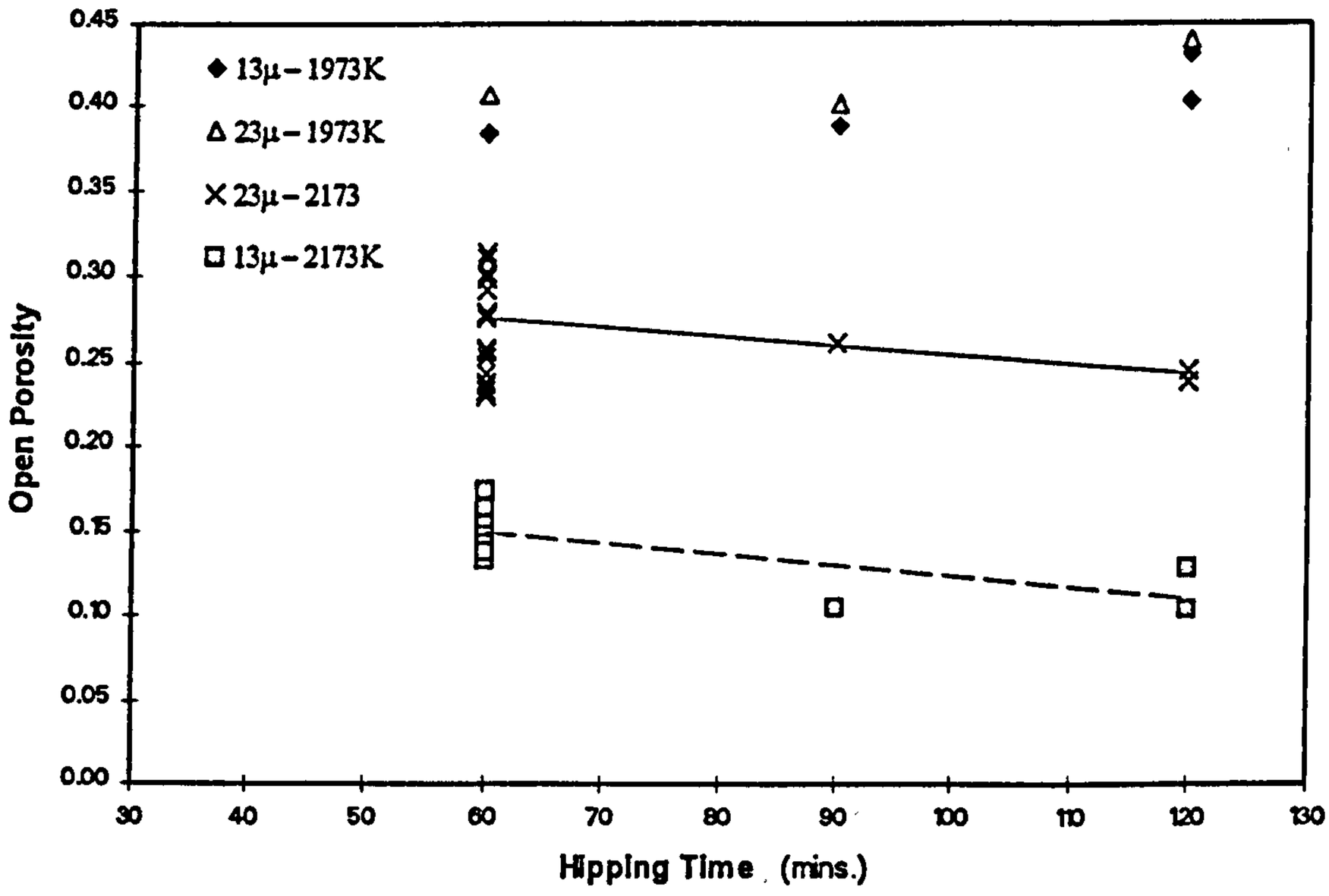

Fig 5.19 Effects of HIPing Time on Open Porosity (100% Alumina)
(HIPing pressure = 500 bar)

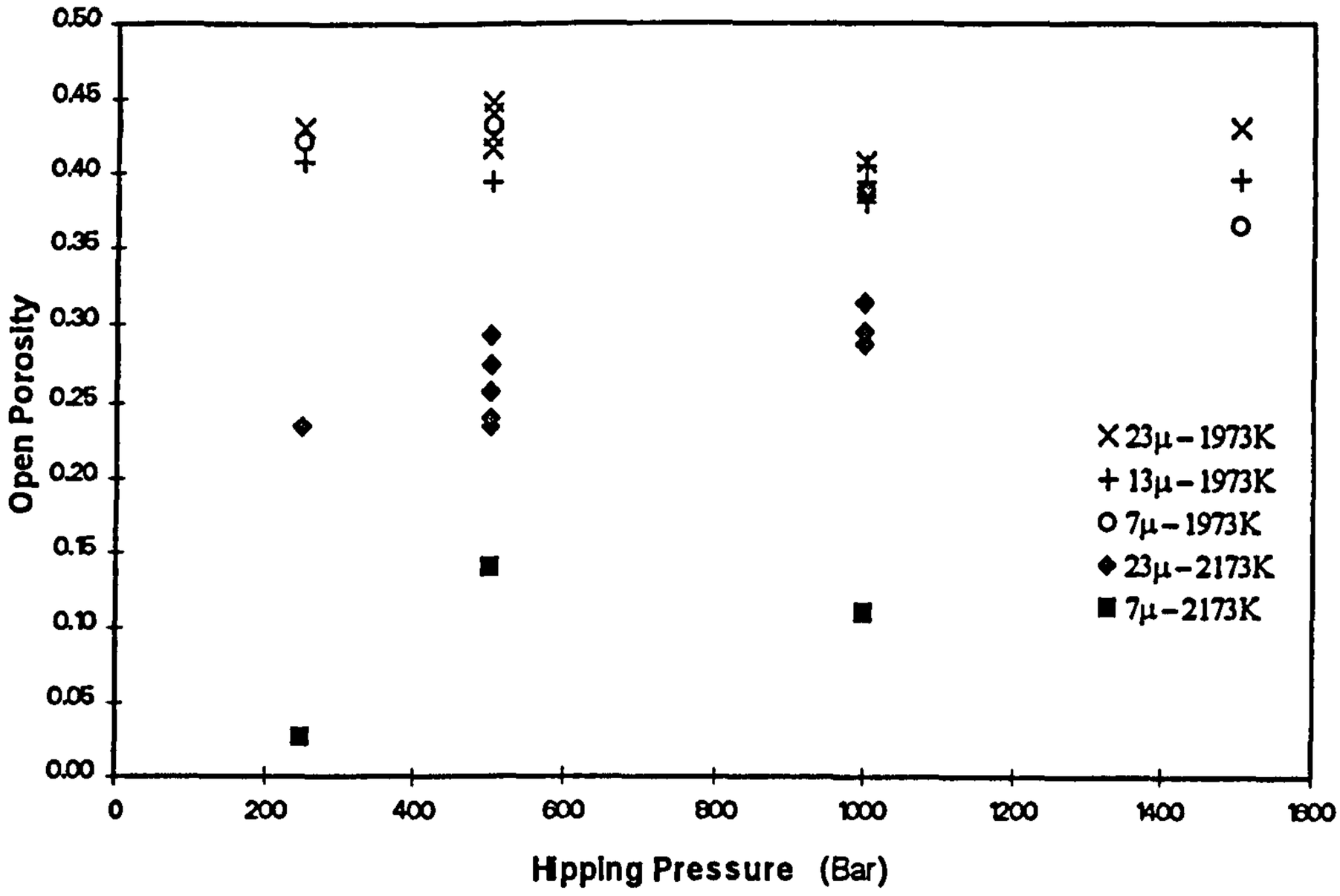

Fig 5.20 Pressure Effects on Open Porosity (100% Alumina)
(HIPing time = 1 hour)

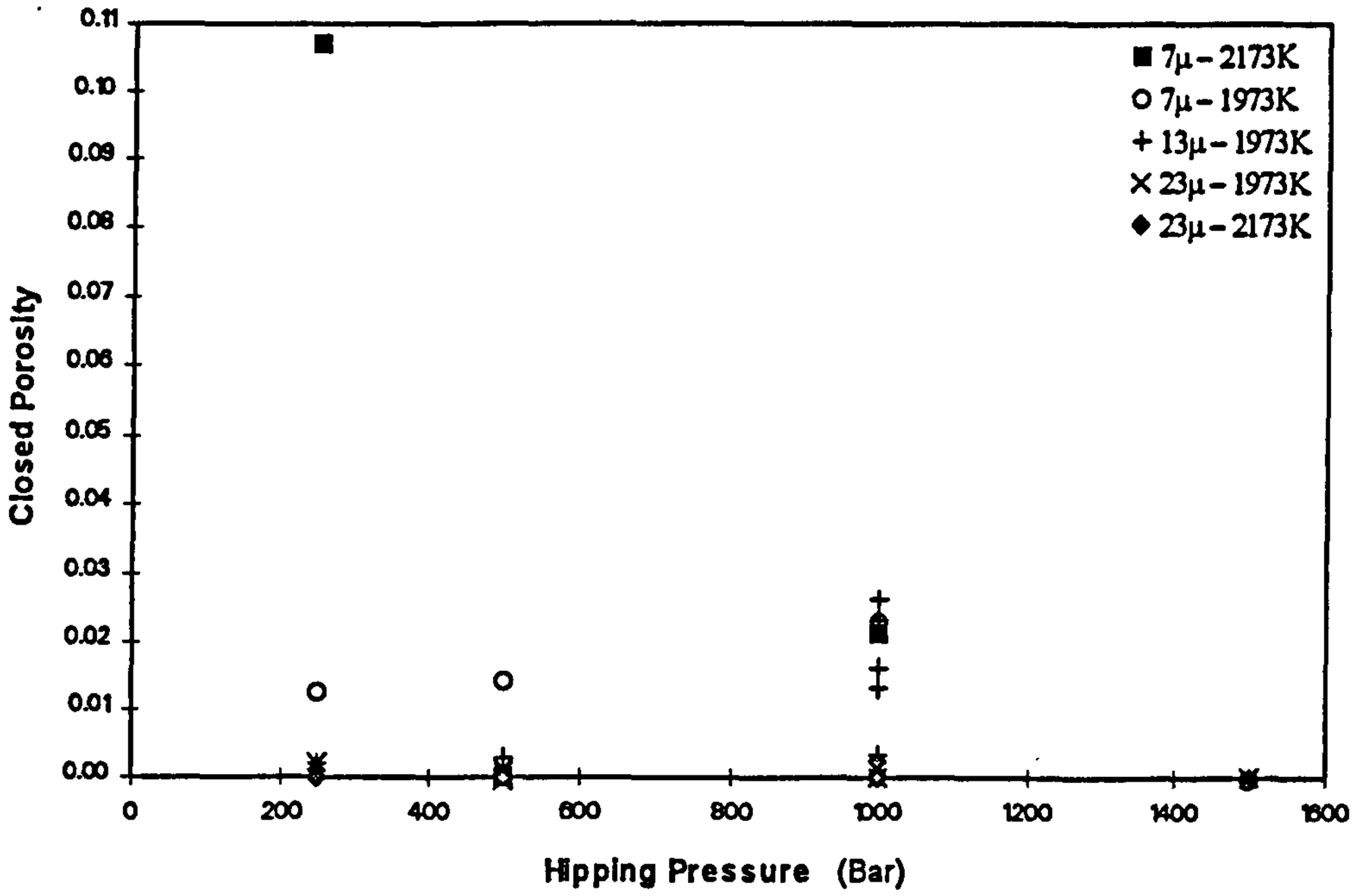

Fig 5.21 Pressure Effects on Closed Porosity (100% Alumina)
(HIPing time = 1 hour)

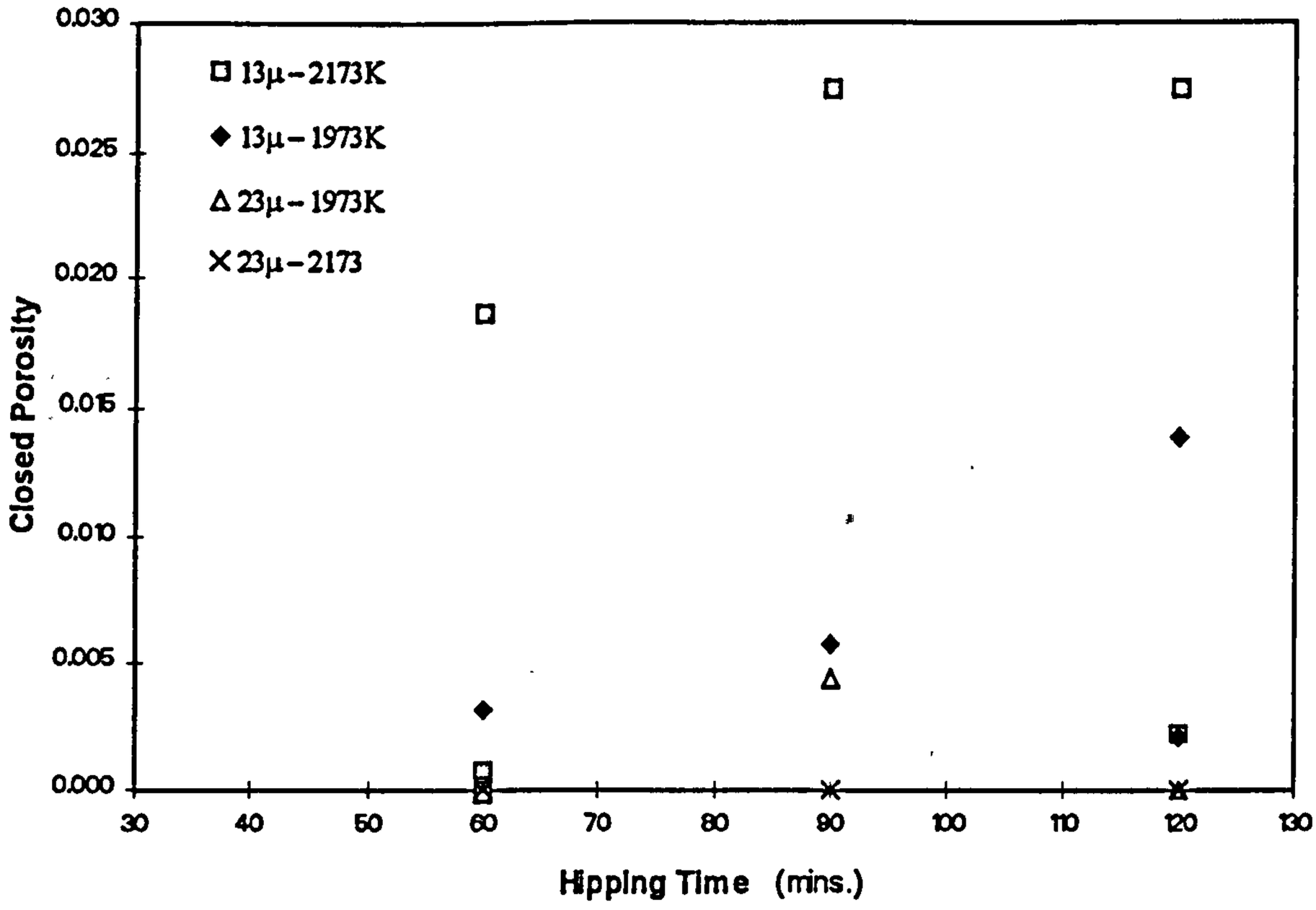

Fig 5.22 Effects of HIPing Time on Closed Porosity (100% Alumina)
(HIPing pressure = 500 bar)

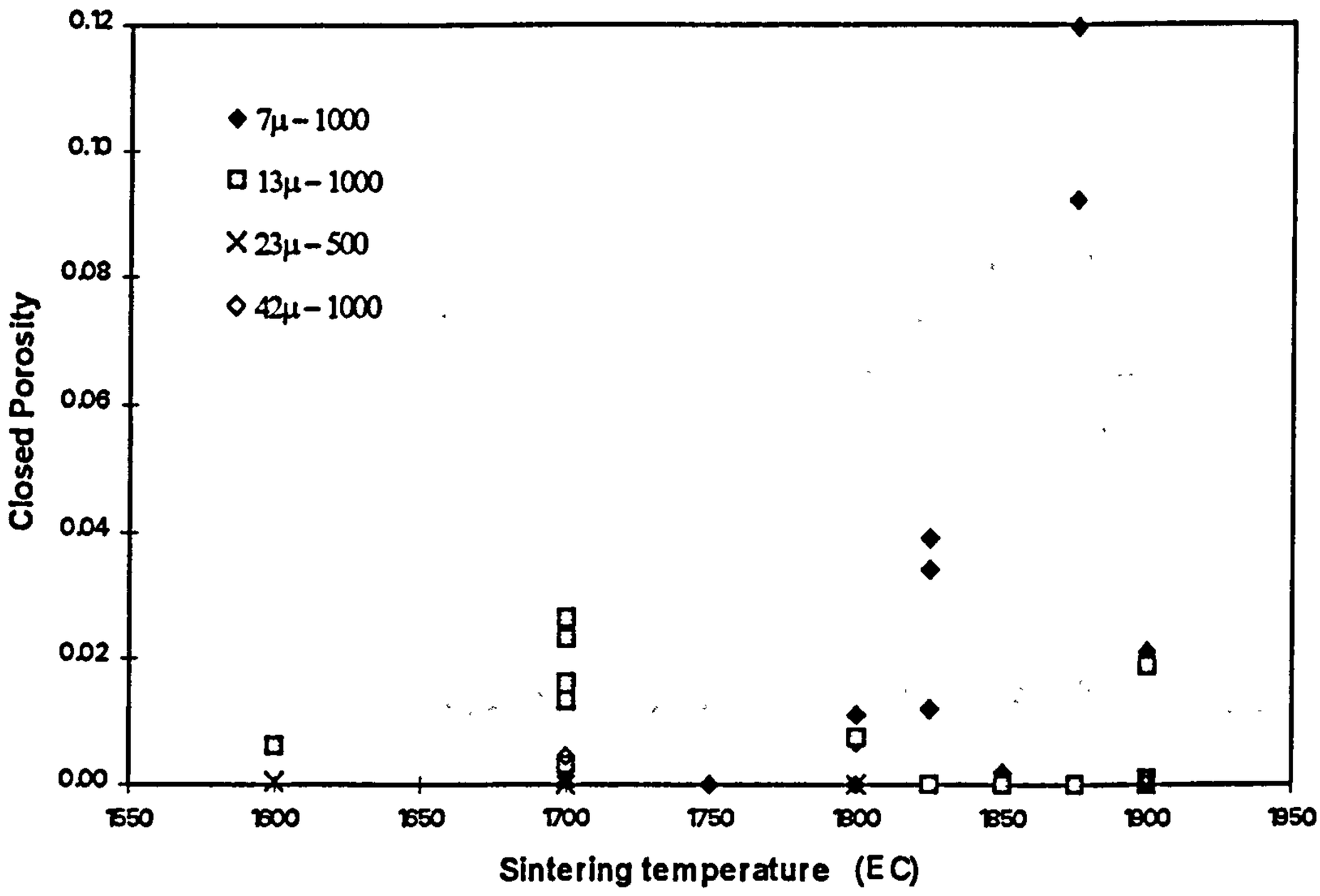

Fig 5.23 Temperature Effects on Closed Porosity (100% Alumina)
(HIPing time = 1 hour)

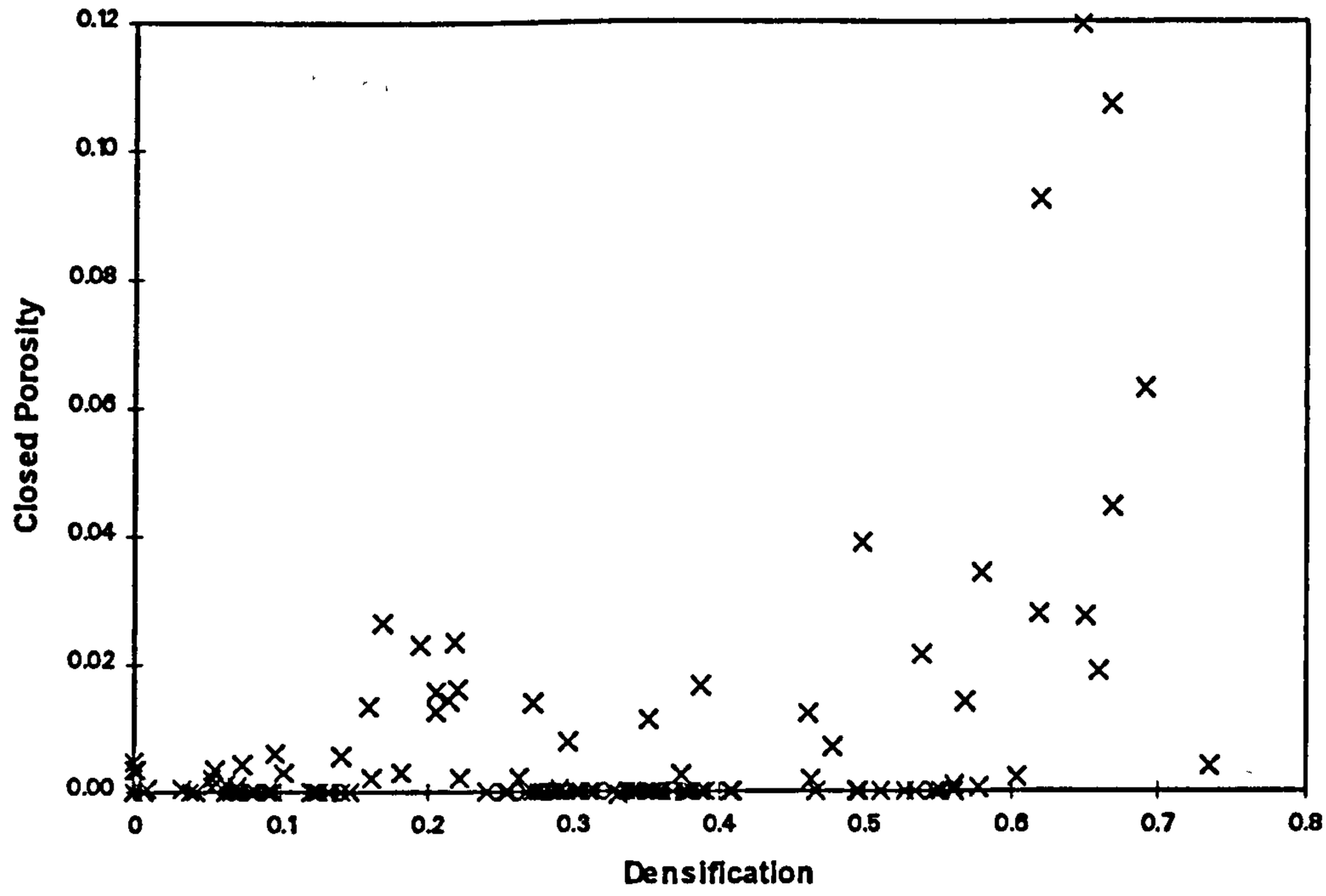

Fig 5.24 Relationship between Densification and Closed Porosity

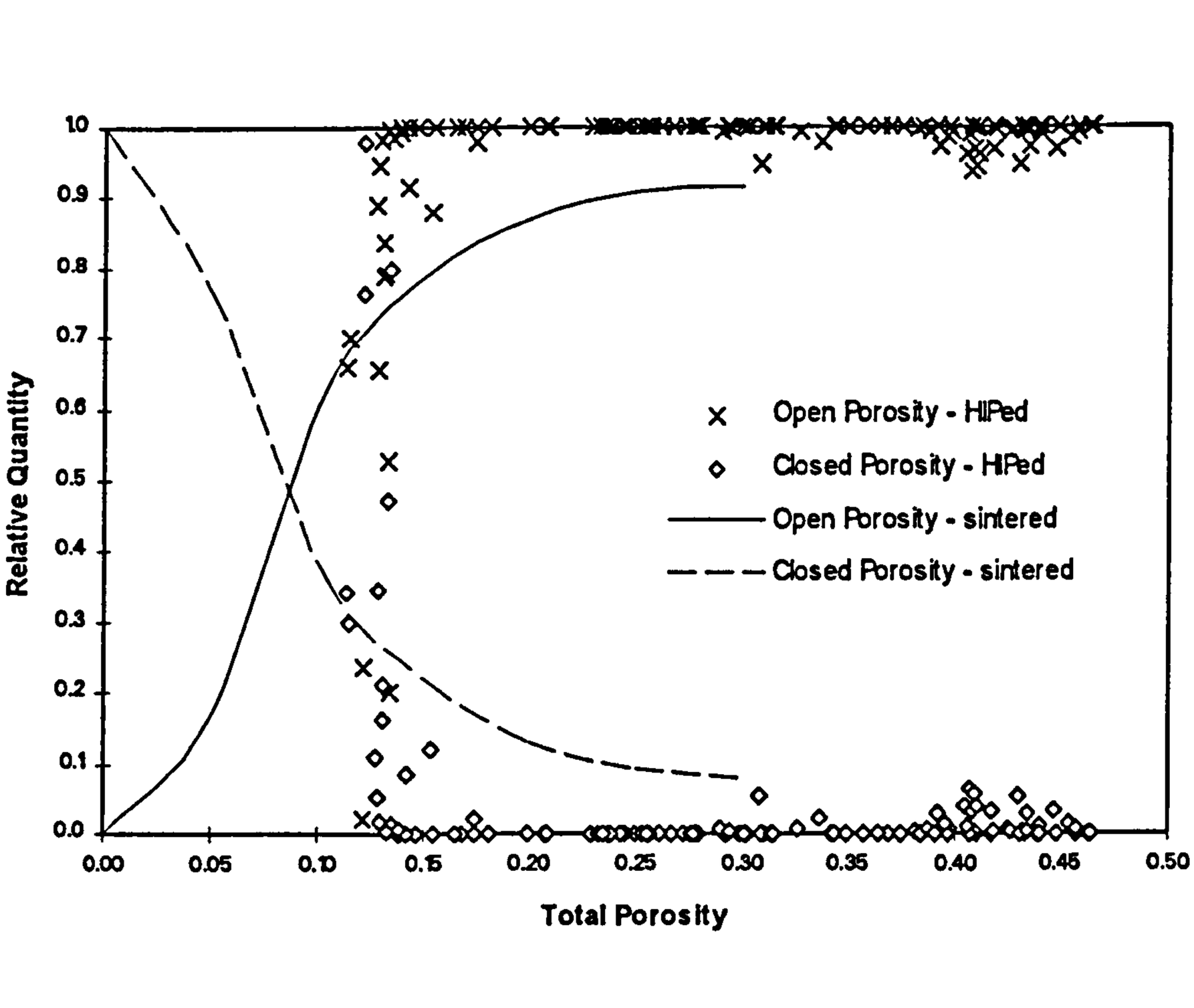

Fig 5.25 Variation of Open and Closed Porosities with Total Porosity

(Values for sintering from [201])

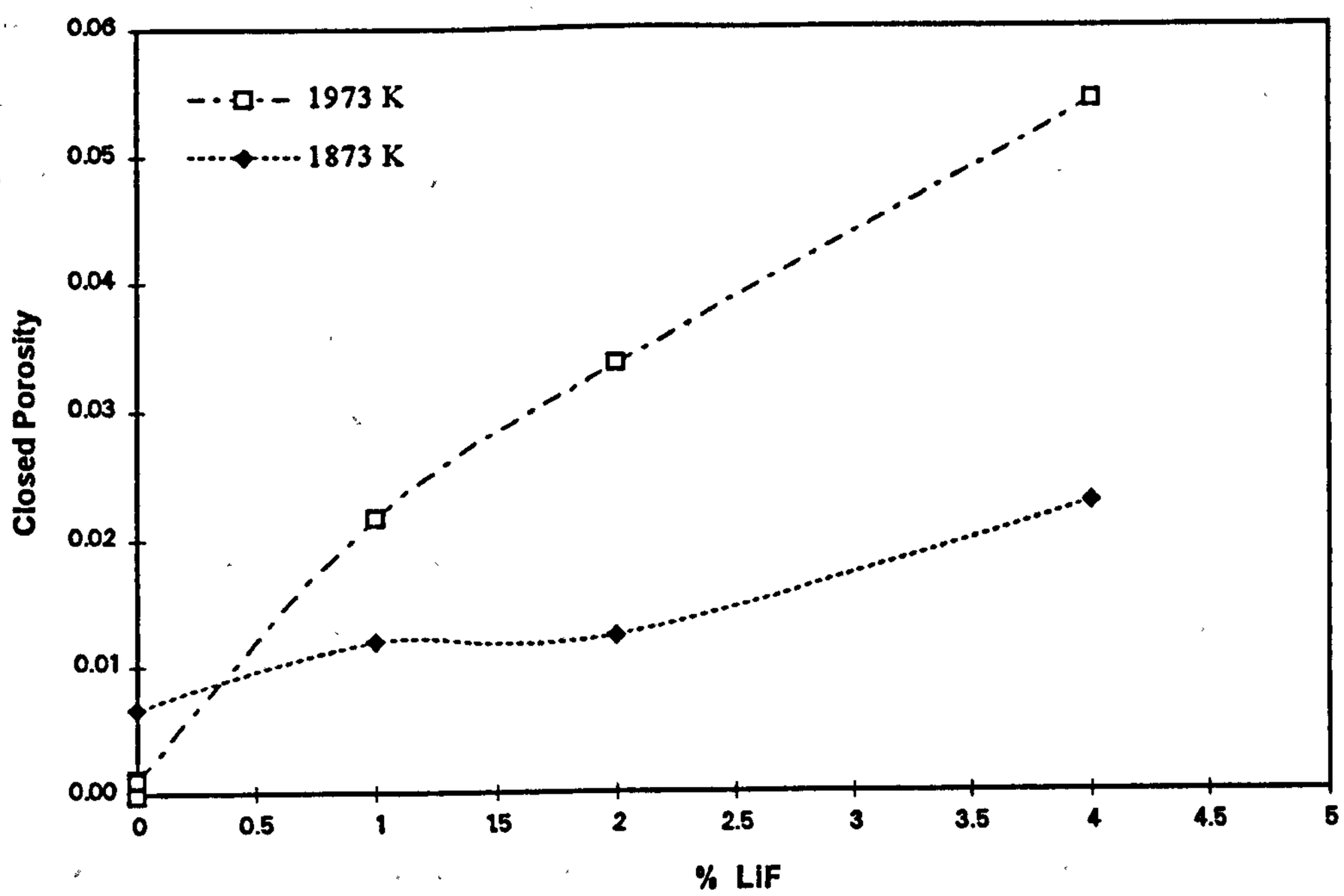

Fig 5.26 Effect of Sintering Aid on Closed Porosity
(23 mm Alumina, 500 bar, 1 hour sinter)

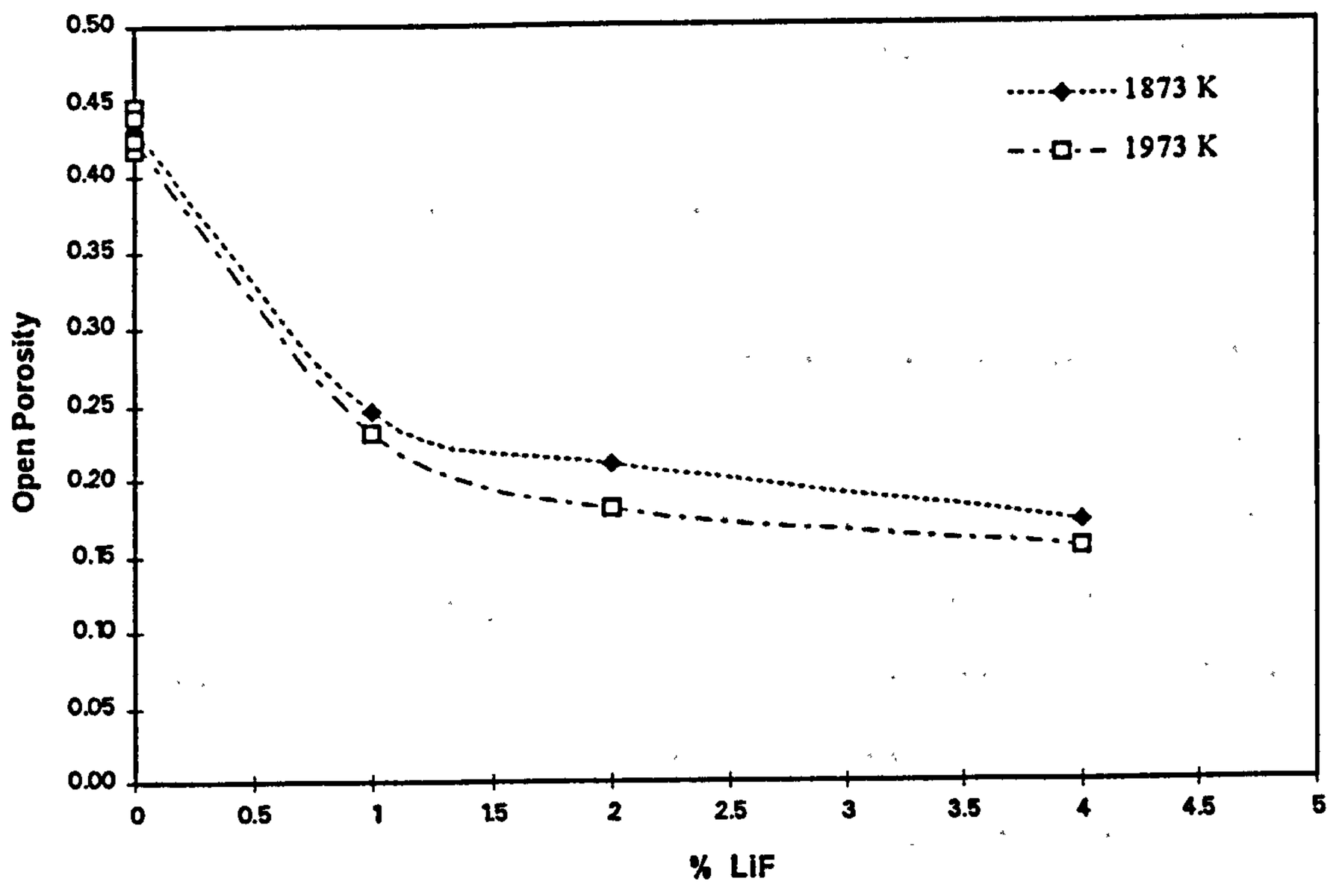

Fig 5.27 Effect of Sintering Aid on Open Porosity
(23 mm Alumina, 500 bar, 1 hr. sinter)

The effect of LiF on both open and closed porosities was equally significant as in the case of densification (Fig. 5.26, 5.27), especially at high temperature and between 0 - 1 wt% concentration. Above 1%, the reduction rate of open porosity began to slow.

The prediction of final porosity after free-capsule HIPing is complicated by the existence of the many different mechanisms of mass transport. Different mechanisms become dominant in different stages of sintering, and follow different mathematical expressions. The transition of one stage to another is also not a discrete one. Conventional sintering theories cannot be applied directly, as they do not account for the effects of pressure.

A computer simulation program has been developed by Ashby [202] for hot isostatic pressing. Correlation with experimental data did not, however, produce useful results. An example of this comparison is shown in Fig. 5.28. The densification of free-capsule HIPed specimens from 7 μm alumina powders was compared with Ashby's sintering diagrams, both for pressureless sintering and conventional HIPing. Whereas the increase in density based on the pressureless sintering model is much lower than that for free-capsule HIPing at higher temperatures, the conventional HIPing model predicts a higher densification at lower temperatures, even at a much lower HIPing pressure of 50 bar. The experimental data for free-capsule HIPing were based on a HIPing pressure of 1000 bar, at which conventioal HIPing would have achieved full densification.

The Ashby model is developed for conventional HIPing of particles in sealed containers. This means that any residual pressure in the sealed container not only increases with temperature during heating up, but also with densification in the dwelling stage of the HIPing cycle. Furthermore, the model assumes that sintering ceases when the pore pressure equals the external HIPing pressure, whereas in free-capsule HIPing, the two pressures are equal throughout. The computer program also requires calibration to improve the accuracy of the default material data in the program. The experimental data used for this calibration purpose has to be accurate, which is not the case as far as the temperature measurements in the present study are concerned.

To obtain a better understanding of the fundamentals of the free-capsule HIPing process requires additional experiments such as dilatometer measurements, in which the densification of the specimen is continuously monitored during the HIPing cycle. Such measurements would provide additional information on the variation of densification rate at different stages of sintering, and would thus help to identify the dominant mechanism at each stage. This fundamental work is, however, beyond the scope of the present study.

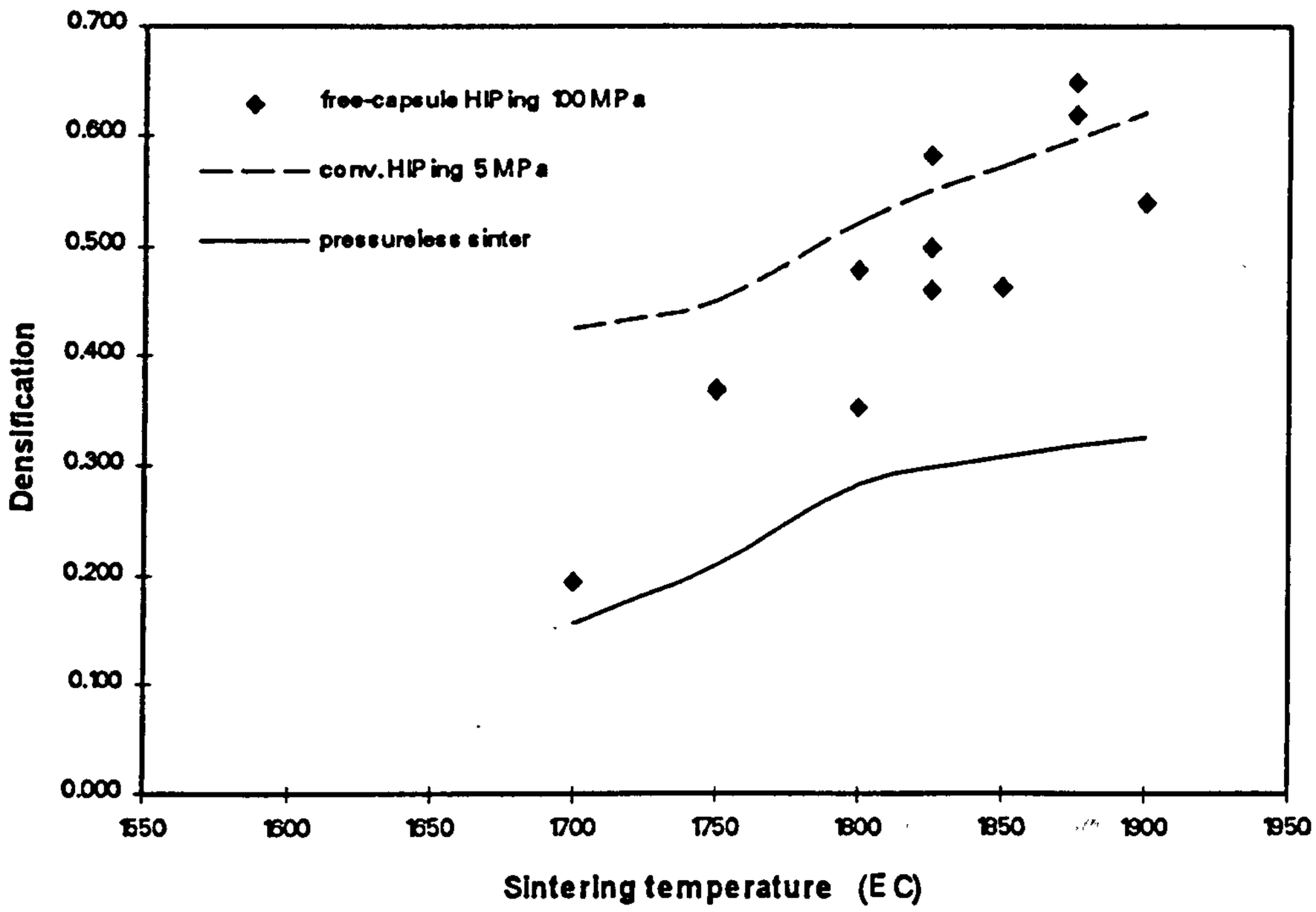

Fig 5.28 Comparison of Free-Capsule HIPing Data with Conventional Sintering and HIPing Theories for 7 μm Alumina

6. MEASUREMENT OF FLUID FLOW PROPERTIES

6.1 PERMEABILITY COEFFICIENTS

The material property that is of most importance to a porous aerostatic bearing designer is its permeability coefficients Φ. For while it would be relatively simple to alter the geometry and the operating conditions (such as supply pressure, operating gap, etc.) of the bearing, the permeability coefficient can only be fine tuned using laborious methods such as partial pore warping through deliberate overgrinding [61], or partial sealing using shellac solution infiltration [153, 154], or controlled thickness electroless nickel plating [41]. The permeability coefficients, together with the geometry of the bearing, determine the bearing number to which all bearing performance characteristics are related. The significance of being able to measure Φ to a high degree of accuracy cannot be overemphasised.

6.1.1 Review of Measurement Methods

A comparison of different methods of measuring permeability coefficients has been published by Cliffel [104]. Amongst methods suitable for plate specimens, the guide ring method is believed to provide the best accuracy despite more elaborate experimental procedures and equipment.

The method used in the present work for measuring the permeability coefficients is essentially based on the guide ring method as described in the ISO 4022 [102] recommendation for disc specimens. Although an alternative dynamic measurement method has been reported by Cieslicki [203], it does not appear to offer any significant advantage over the ISO method.

Permeability measurement, in its simplest form, involves passing a fluid (usually gaseous) of known physical properties through a specimen of known, uniform cross-section and thickness. The outflowing fluid is collected at the outlet end, the flow rate of which is measured by a flowmeter. By varying the inlet pressure, a set of measurement points of pressure difference across the specimen and flow rate could be obtained, from which the permeability coefficients could be calculated. The ISO measurement is essentially based on the Forchheimer model [97], i.e.,

$$\frac{p_1^2 - p_2^2}{2.p_{ref}} = \frac{z_p.\eta.(Q/A_p)}{\Phi_v} + \frac{z_p.\rho.(Q/A_p)^2}{\Phi_i} \qquad (2.4)$$

This is presented in the ISO 4022 in the following form :

$$\frac{\Delta p.A_p}{z_p.Q_{mean}.\eta} = \frac{1}{\Phi_v} + \frac{Q_{mean}.\rho_{mean}}{A_p.\eta}\frac{1}{\Phi_i} \qquad (6.1)$$

The conversion is based on the assumption that $p_{ref}.Q = p_{mean}.Q_{mean}$ (isothermal), and also

$$\rho_{ref}.Q = \dot{M} = \rho_{mean}.Q_{mean} \qquad (6.2)$$

By plotting $\frac{\Delta p.A_p}{z_p.Q_{mean}.\eta}$ against $\frac{Q_{mean}.\rho_{mean}}{A_p.\eta}$, the slope of the least square fitted line gives the reciprocal of the inertia permeability coefficient Φ_i, and the y-intercept the reciprocal of the viscous permeability coefficient Φ_v.

The British version of the ISO 4022 actually specifies $\frac{Q_{mean}.p_{mean}}{A_p.\eta}$ as the y value. This is clearly neither compatible with the Forchheimer equation, nor dimensionally correct. As a result, the air density at mean pressure across specimen ρ_{mean} is used in the present work instead.

The measurement equipment as specified in the ISO standard differs from the simple set-up commonly used [106, 44, 79, 204]. By incorporating an extra annular flow outside the centre core of the specimen, it minimises the effects of any irregular flow pattern at the edge of the specimen. Only the central flow stream is piped to the flowmeter for measurement. The outer stream acts as a dummy to ensure that flow through the porous specimen over the entire measured section is as unidirectional as possible, and is dumped to atmosphere. A throttling valve at the outlet of the outer flow stream ensures that the exit pressure in the two streams is equalised.

6.1.2 Equipment Design

A permeability measurement rig was designed following recommendations laid down in ISO 4022:1987 [102]. (Refer to Appendix H, drawing no. MG291 B101) A schematic of the equipment is also shown in Fig. 6.1. As explained earlier in Chapter 3, the size of the HIPing furnace limited the diameter of the finished specimen to about 44 mm. An inner diameter of 39 mm was therefore chosen for the outer tube. The ISO recommendation also specifies an inner tube mean diameter at least two times the specimen thickness less than the outer tube. As the maximum thickness of the specimens was around 8 mm, an inner diameter 21 mm was specified for the inner tube. Both the inner and outer tubes were from cast Perspex, as they provided a good surface finish on both inner and outer walls as supplied, and any scratches were easily visible and repolished without difficulty. Stress calculations indicated that they would sustain the maximum test pressure of 5 bar with a wide margin.

Dried, filtered air, pre-regulated to 6 bar, was fed to a precision pressure regulator which was controlled electronically. This, in turn, was fitted to a 0.01 μm filter before entering the inlet side of the inner tube, ensuring that no contamination could block up the fine pores in a specimen. Pressure between the inner and outer streams at the inlet

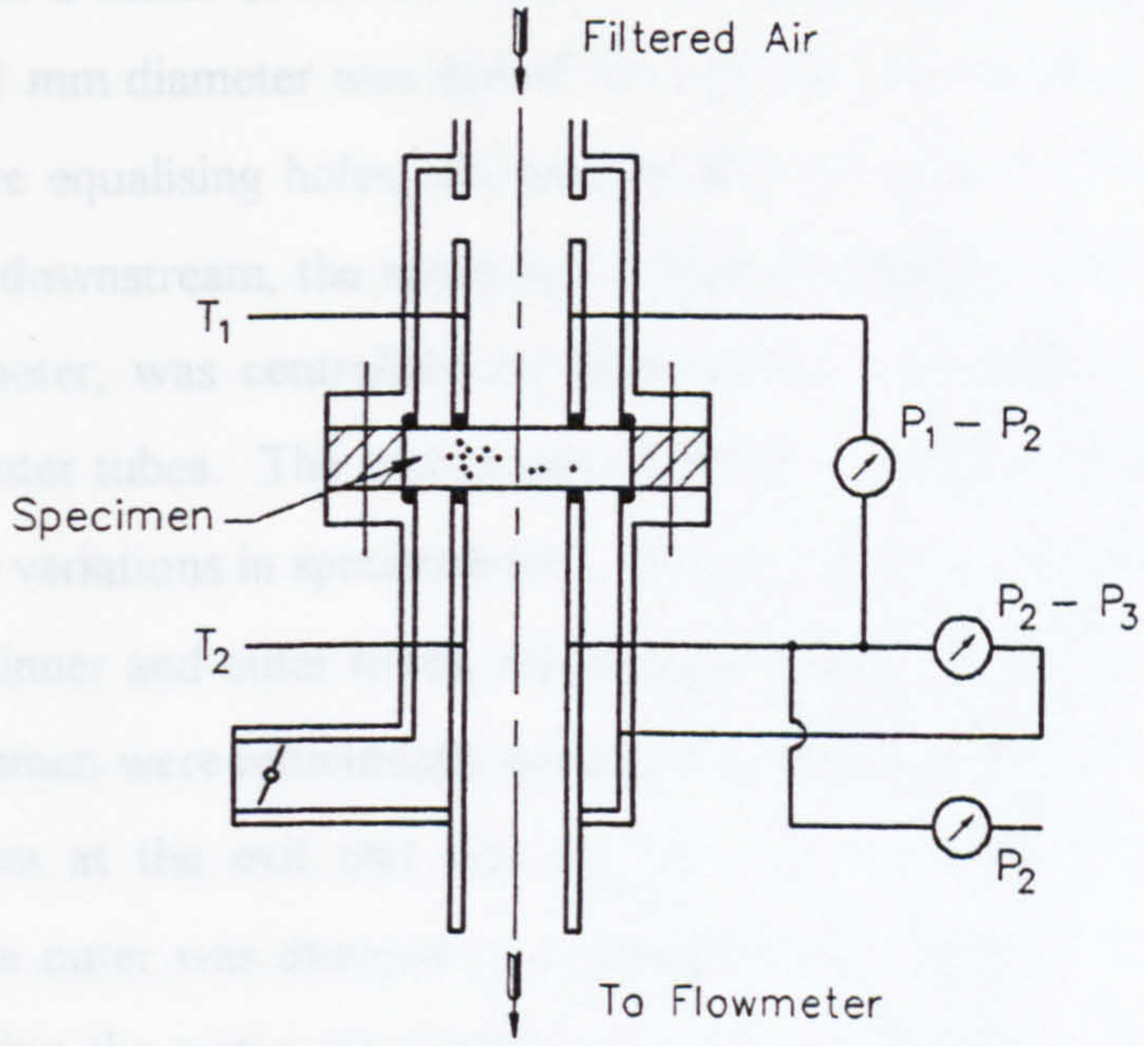

Fig. 6.1 Schematic Diagram of the Permeability Measurement Rig

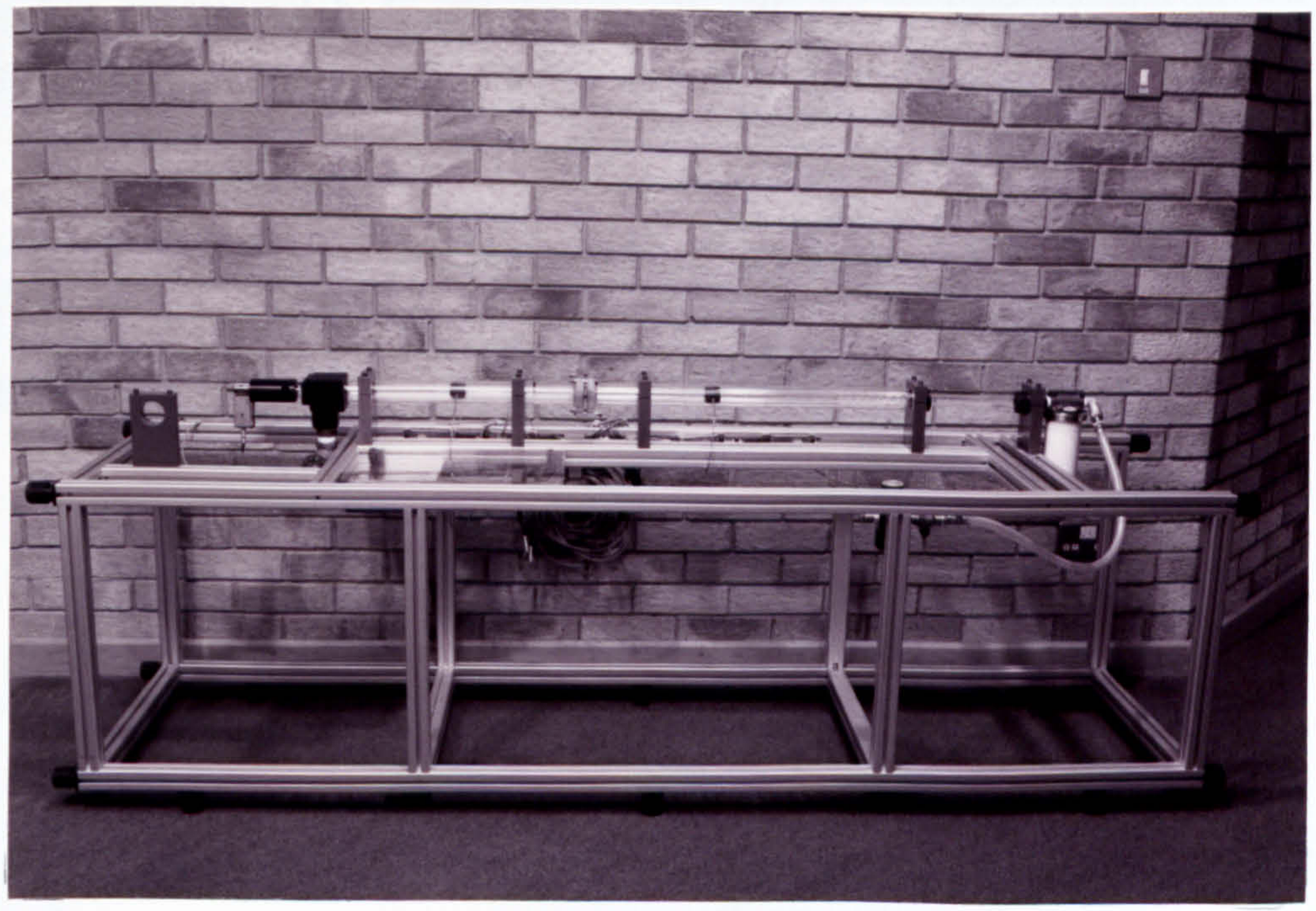

Fig. 6.2 Permeability Measurement Rig

was equalised via a series of holes at the front section of the inner tube. A pressure tapping hole of 1 mm diameter was drilled through the inner tube, 200 mm downstream from the pressure equalising holes, allowing sufficient length for the flow to settle. A further 200 mm downstream, the specimen, which was glued to an aluminium carrier of fixed outer diameter, was centralised by three dowel pins and clamped between two flanges on the outer tubes. The carrier served to provide an outer-edge seal, as well as to accommodate variations in specimen size. O-rings, placed in machined grooves on the end faces of the inner and outer tubes, sealed against the specimen. Inner tubes on both sides of the specimen were individually adjustable axially to ensure positive sealing. The inner flow stream at the exit end was fed to a flow sensor, before exiting to free atmosphere. The outer was dumped to atmosphere via a gate valve, which provided a means of equalising the static exit pressures. All air connections were o-ring or gasket sealed to ensure no leakage.

Static pressure tappings 1 mm in diameter were incorporated 200 mm from the specimen, both on the inner and the outer tubes. Additional tappings were made on the outer tubes, approximately 40 mm downstream of the pressure tappings, for the fixing of thermocouples used to measure static temperatures.

The entire assembly, some 1.6 m in total length, sat on a rectangular frame of bolted aluminium structural profiles. This also served to house all the sensors and the accompanying cabling. Its modular construction enabled ease of modification.

6.1.3 Instrumentation & Calibration

Mass-produced semiconductor sensors were used for all pressure and flow measurements, as they offered reasonable accuracy at relatively low costs. Mechanical transducers such as rotameters were ruled out at the start, as they were incompatible with automatic data acquisition. For temperature measurements, K-type thermocouples were used. As the accuracy of the pressure and flow-rate measurements has a direct

bearing on that of the measured permeability values, all sensors were individually calibrated to ensure maximum accuracy.

All pressure sensors (Sensortechnics 144, 144LP, 103LP series) were of the semiconductor piezoresistive strain gauge bridge type. Accuracy and linearity specified by the manufacturer were both 1% span. A differential pressure sensor with a 5 bar range was used to measure the pressure difference across the specimen. Differential pressure between the downstream inner and outer tubes was measured with a sensor of ± 5 mbar range. For the downstream gauge pressure of the inner stream, a sensor of 5 mbar range was used. Additionally, an absolute pressure sensor with a 2 bar range was used to monitor ambient pressure during measurements.

Four flow sensors of 0.2, 1.0, 5.0 and 20 lit./min. respectively were necessary to cover the range of permeability coefficients. As in the case of the pressure sensors, semiconductor bridge type sensors were used (Honeywell AWM 3000 & 5000 series). These flow sensors [205] operate on a thermal principle [206, 207], and consist essentially of three semiconductor thermistors lined in a series in the direction of flow. The first and the last of the three are used as thermometers, and measure the air stream temperatures before and after the middle element. The latter is used as a heating element to warm up the gas flowing by. The power input to the heater is closed-loop controlled to give a constant temperature difference between the upstream and downstream thermometer, and in turn gives a measure of the mass (not volume) flow rate of the gas. The sensors have a repeatability of 0.5% of the actual reading, and a response time in the order of 60 ms. Additional integrated circuitry preamplifies the signal output from the sensors. The output is however only linear for the two sensors with high flow ranges, but highly nonlinear for the remaining two with low flow ranges.

Air-supply pressure regulation was done by an electronic pressure regulator, which was controlled electronically to a resolution of 1.22 mbar with a 5 bar full range. The regulator was also recalibrated using the calibrated 5 bar pressure sensor as pressure reference. The response time of the regulator was of the order of 50 - 300 ms, but was

not of great significance as most of the measurements were essentially under steady state conditions.

Detail specifications of the pressure regulator, the pressure and flow sensors can be found in [208, 209, 210].

The use of a data acquisition card (National Instruments AT-MIO-16-DL9), in conjunction with a 486 personal computer and the LabWindows software (Version 2.3a), enabled automatic collection of measurement data of up to 16 analogue input channels with 12 bit resolution, as well as real time adjustment of the supply air pressure via the analog output channel. The entire permeability measurement, with the exception of pressure equalisation of the outflowing streams, was software controlled.

All pressure sensors were individually calibrated to their respective data acquisition (DAQ) channels, using a Druck DPI 601 calibrator. An additional inclined water manometer was used for sensors with mbar range. For the absolute pressure sensor, the sensitivity $\Delta v/\Delta p$ was obtained using the Druck calibrator. Zero reference came from a mercury barometer with a resolution of 0.05 mm Hg (0.067 mbar).

Calibration data provided by the flow sensor manufacturer was based on large production batches, to an accuracy of only ± 3% span. In addition, the calibration was done with nitrogen rather than air. Recalibration was therefore considered necessary. This was performed, with air, using a bell prover (Thomas & Glove, London 1928) together with a handheld electronic timer. A measurable volume of air at known pressure and temperature was allowed through the sensor at a constant rate, the output of which was continuously monitored. The time elapsed was measured to determine the mean flow rate, the air volume corrected to standard atmosphere (0 °C, 760 Torr). Calibration time for each reading was a minimum of 15 minutes, so that the error in manual starting and stopping of the timing device became insignificant. Curve fitting using polynomial regression of the 5th order was used to linearise the output of the two

low-range sensors. The degree of fit was better than 1% span over the entire working range. The output of the remaining two was essentially linear, also to within 1% span.

The thermocouples were also calibrated at 0 °C and 100 °C in iced and boiling deionised water respectively.

Calibration curves for individual pressure and flow sensors can be found in Appendix F.

6.1.4 Measurement Procedures

The permeability measurement involved measuring the flow through the porous specimen at a number of pressure differentials, and line fitting the data to obtain the permeability coefficients. But for the few cases in which the permeability was too high for the largest flow sensor, the permeability measurement for each specimen covered a pressure range of up to 4 bar. The minimum pressure was set at 10% of the maximum, and at least 25 measurement points were recorded at fixed pressure increments.

The entire measurement procedure was controlled by the LabWindows software, which checked the supply air pressure, and recorded the ambient temperature and pressure upon initialisation. Datum for key measurements such as flow rate was then reset to minimise zero errors. Air viscosity was calculated based on measured ambient conditions. Pressure settings were adjusted via a sinusoidal ramp-up to reduce overshoot. The pressure across the specimen, that across the two outflowing streams, up- and downstream temperatures and the flow rate were monitored continuously. Downstream pressure in the two flow streams was balanced to better than 0.5 Pa by hand. Stabilised readings were recorded after lowpass filtering before incrementing the pressure to the next value, and then the procedure repeated.

Calculations were performed according to ISO 4022. These included linearisation of the flowmeter readings, conversion of gauge pressures to absolute, correction of flow rate to

mean pressure and temperature. Values of $\frac{\Delta p.A_p}{z_p.Q_{mean}.\eta}$ were plotted against $\frac{Q_{mean}.\rho_{mean}}{A_p.h}$ and a least square fit performed to give values of Φ_v and Φ_i. The ISO permeability plot essentially determines the first and second order coefficients of the flow rate as a function of pressure, and is therefore extremely sensitive to zero errors of the flow measurements, particularly at low flow rates. It was found that the line fitting results could be improved by first fitting Q against Δp with a second order polynomial (Fig. 6.3). The zero error in flow rate Q so obtained was then subtracted from the measured values, before converting to the ISO format for determining the permeability coefficients (Fig. 6.4).

6.1.5 Experimental Results

Over 100 HIPed porous specimens of 100% α-alumina were tested for permeability using the guide ring method described in ISO 4022. The specimens were sintered from powders of average size of 7 to 42 μm, with an open porosity of 0.07 - 0.47. The viscous permeability coefficient as measured ranged from 1.3×10^{-17} to 7.3×10^{-13}. But for a small number of samples which were either of low porosity, or were sintered from very fine powders, the Q vs. Δp curve was largely linear, which indicated that little inertia effect was present for the pressure range measured.

Due to uncertainties in the accuracy of the sintering temperature measurements, it was considered more meaningful to correlate permeability measurements with porosity and particle size, rather than directly to sintering conditions (such as temperature).

Most published theories also expressed permeability as a function of both particle size and porosity. The definition of permeability was, however, based on Darcy's law, with no consideration for the inertia effect. Also, the term particle size was not clearly defined. Most of the previous studies used atomised metal powders which were likely to

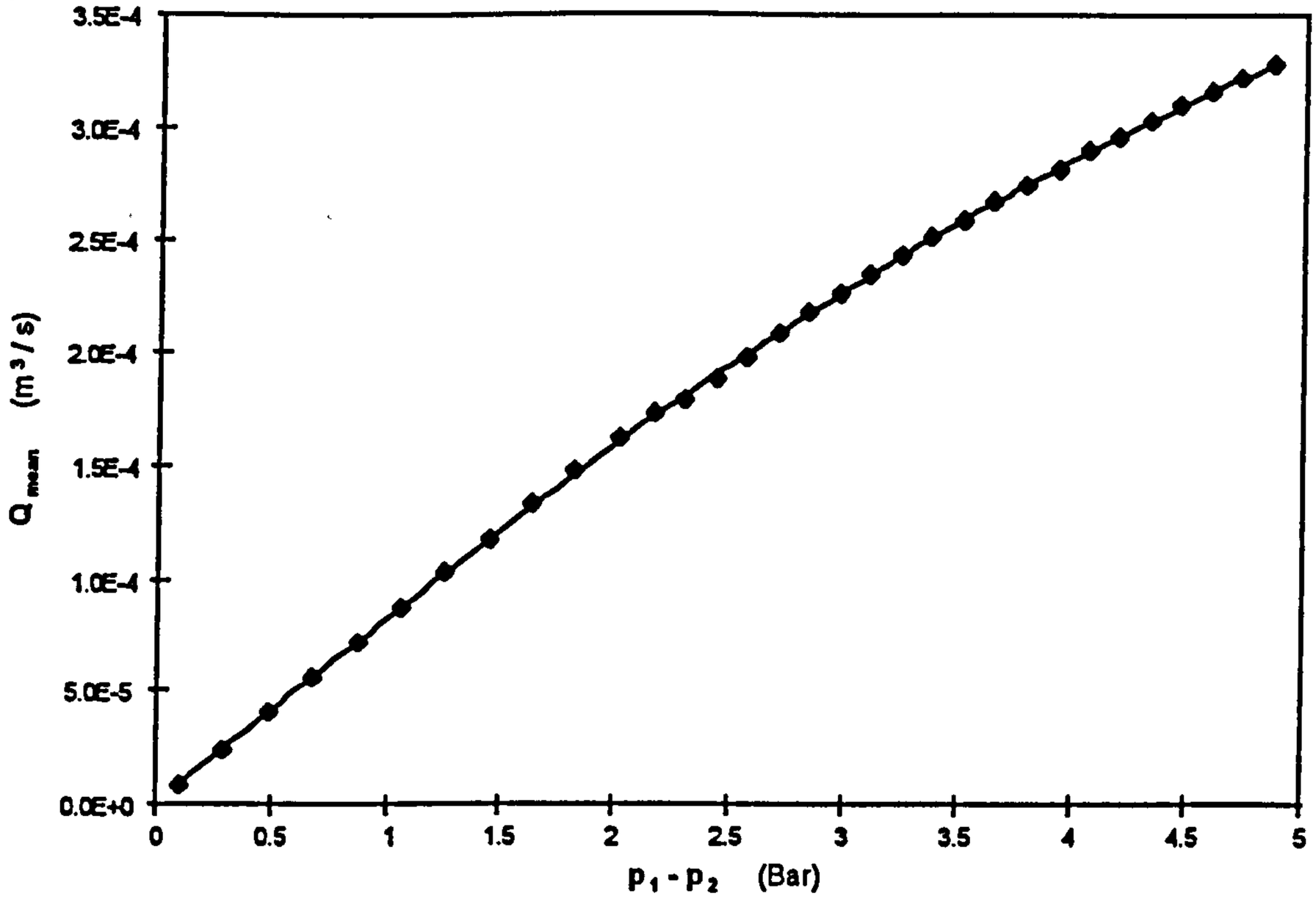

Fig. 6.3 Permeability Measurement -- Flow Rate vs Pressure Difference
($d_w = 23\ \mu m$, $\zeta_o = 0.277$)

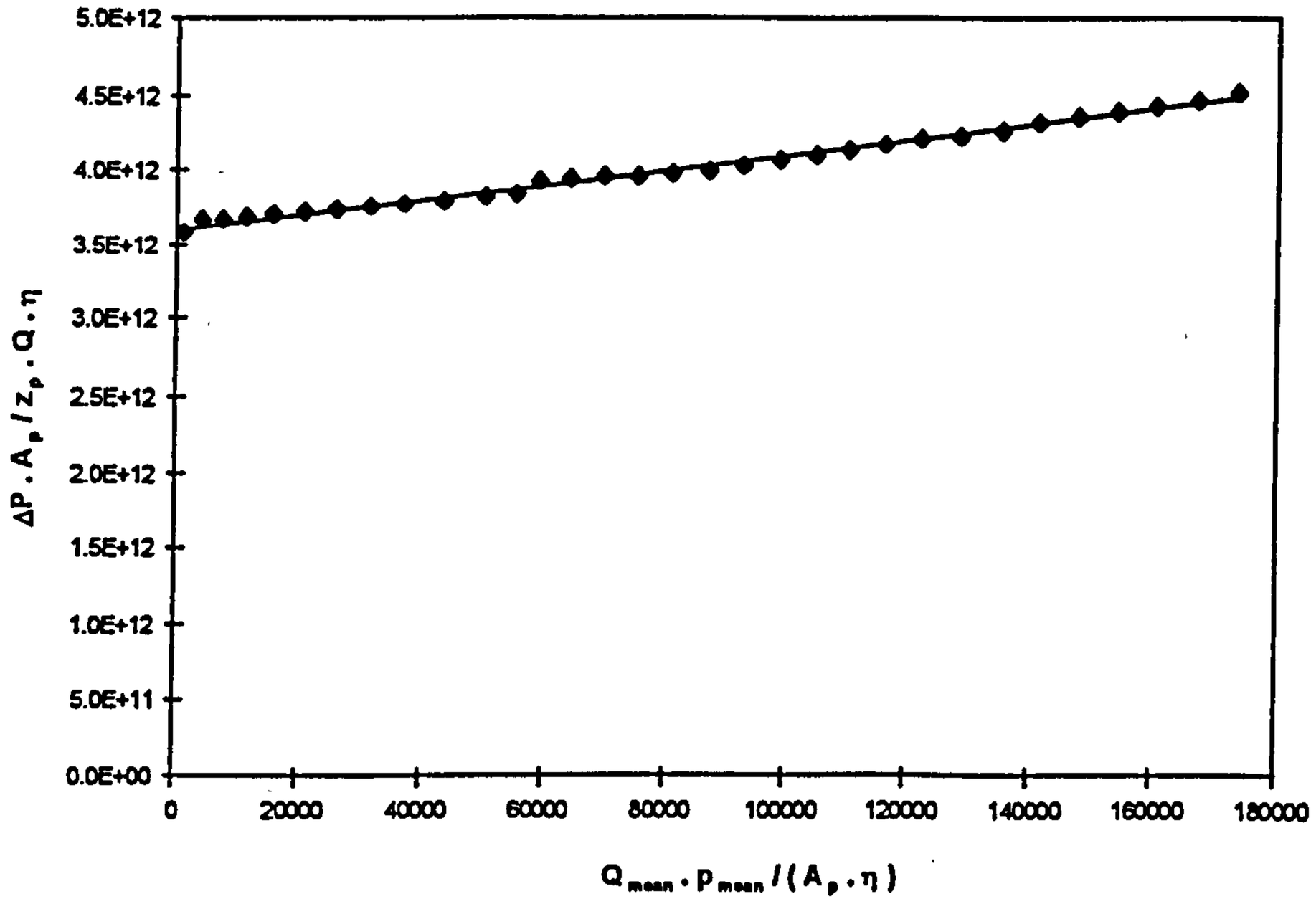

Fig. 6.4 Permeability Measurement Plot per ISO 4022
($d_w = 23\ \mu m$, $\zeta_o = 0.277$)

be near perfect spheres, and it could only be assumed that the mean particle size was used in the calculations.

The situation is much more complex with ceramic powders. The shape of individual particles varies widely from each other, even within the same batch, and has a high aspect ratio. Correlating particle shapes of different powder sizes is equally difficult, as both shape variations and size distribution could be vastly different between different sizes of powders. The term particle size is therefore to be treated with caution. Different particle size measurement methods, such as sedigraph or image analysis, are likely to yield different results.

In view of this, each size of particles was first treated individually when correlating permeability to porosity, leaving the analysis of particle size effects towards the end. The effect of the porosity could thus be evaluated on its own, without being obscured by any likely error or ambiguity in the particle size data, as in the case of a 3-variable correlation being used right at the onset. Open porosity values were used, as closed pores would not play any part in the flow of fluid through the porous medium. Most of the specimens measured had very little (<1%) closed porosity, so the difference, if any, would also be small. For the final analyses involving particle sizes, median values from sedigraph measurements were used.

Both viscous and inertia permeability coefficients were expressed as a power law function of the open porosity for each group of specimens of the same particle size :

$$\Phi_v = k . \zeta_o^{\ a} \qquad (6.3)$$

$$\Phi_i = k_1 . \zeta_o^{\ b} \qquad (6.4)$$

The results of the curve fitting (Figs. 6.5, 6.6) are summarised in Table 6.1.

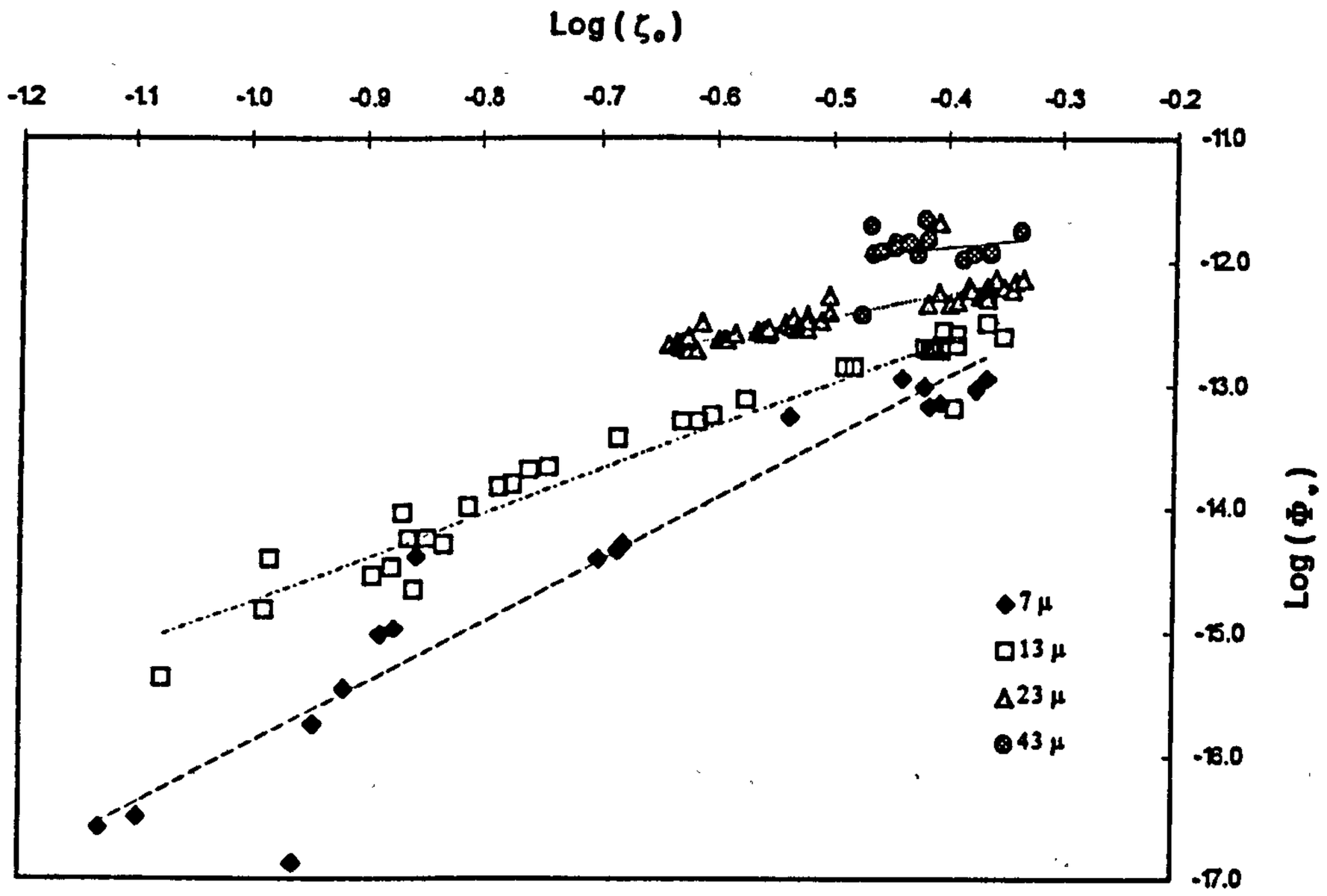

Fig. 6.5 Porosity Dependency of Viscous Permeability Coefficient

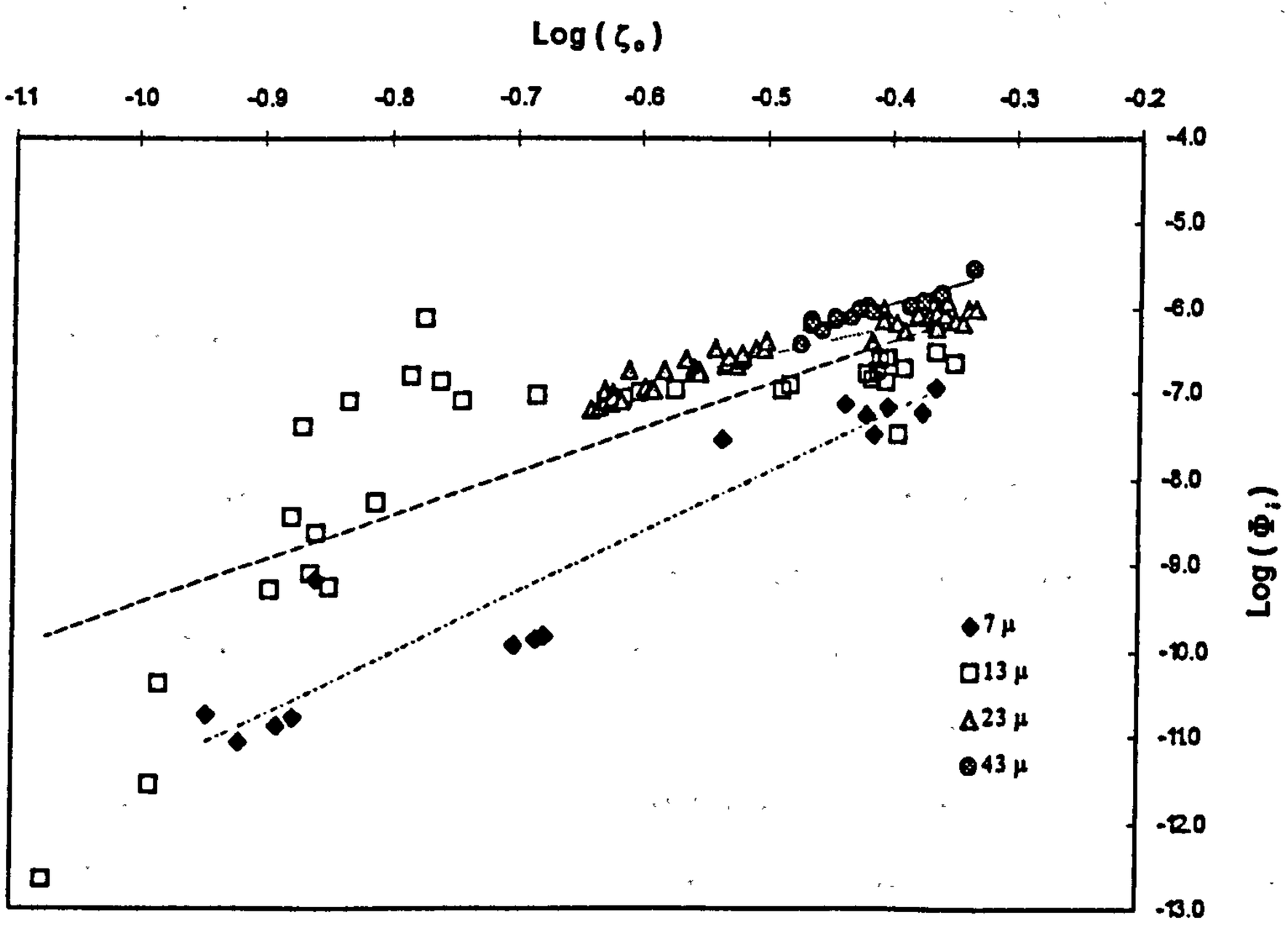

Fig. 6.6 Porosity Dependency of Inertia Permeability Coefficient

Table 6.1 Porosity Dependency of Permeability -- Experimental Results

Particle size (μm)	k	a	k_1	b
6.25	1.09×10^{-11}	4.94	3.71×10^{-5}	6.99
12.2	5.47×10^{-12}	3.46	4.29×10^{-5}	5.06
22.6	3.02×10^{-12}	1.82	1.6×10^{-5}	3.50
42	3.20×10^{-12}	0.948	6.8×10^{-5}	4.44

The range of porosity for both 23 and 42 μm powders were rather limited, due to lack of sinter even at 1900 °C. Thus the empirical constants obtained above should be treated with caution. Both the proportional constants k and k_1, and the exponentials **a** and **b** vary with particle size. Applying the power law to the variation of d_w yields :

$$k = 2.74 \times 10^{-15} . d_w^{-0.68} \qquad (6.5)$$

No single mathematical function provided a perfect fit to the relationship between **a** and d_w, the better amongst them being :

$$a = 7.05 - 3.83 \times 10^{5} . d_w + 7.94 \times 10^{9} . d_w^{2} - 5.41 \times 10^{13} . d_w^{3} \qquad (6.6)$$

with d_w expressed in meters.

Similar to the findings by German (Section 2.1.1.3), the permeability coefficients change rapidly with the level of open porosity. The exponential constants **a** obtained by German [105] lie between 4.5 and 7, which are of comparable magnitude to the present findings for smaller particle sizes. Lower values of **a** were obtained for specimens with larger particle size, but the limited porosity range of these specimens cast some doubts on the reliability of the fitting results. Permeability was, as expected, much less sensitive to particle size. Exponent values of d_w as listed in section 2.1.1.3, for example, range from

0.6 to 1.9. The importance of accurately predicting and controlling open porosity can therefore not be overemphasised.

The observation by Taylor [63] of a separate, Darcy's flow regime at small flow rates, followed by the Forchheimer regime, was not evident in the current results. This could be due to the limited useful range of the flow sensors at the low end, as specimens with noticeable inertia effects invariably had low permeability and required the use of flow sensors with the smallest range.

Data for the inertia permeability coefficient as a function of porosity and particle size were more widely spread. No simple function would provide a meaningful description of the variation of k_1 and **b** with particle size d_w.

A number of specimens with powder size above 42 μm and up to 400 μm, but sintered either with LiF or using the bimodal mixture, were also tested. The number of measurements for each particle size was limited, and the porosity range narrow because of sintering temperature limitations (Figs. 6.7, 6.8). The trend obtained, however, appeared to suggest that the exponential a was similar in value for all particle sizes, with an average value of 6.67. This implies an even higher sensitivity of permeability to open porosity. Mean particle size provided by the manufacturer were quoted here as they were outside the range of the sedigraph measurement. The exponential function gave a better fit on the variation of proportional constant k with particle size d_w. The generalised equation for viscous permeability coefficient for such specimens is therefore:

$$\Phi_v = 9.09 \times 10^{-10} . e^{9730.d_w} . \zeta_o^{6.67} \quad (6.7)$$

A similar function could also be applied to the inertia permeability coefficient :

$$\Phi_i = 7.56 \times 10^{-3} . e^{7974.d_w} . \zeta_o^{9.6} \quad (6.8)$$

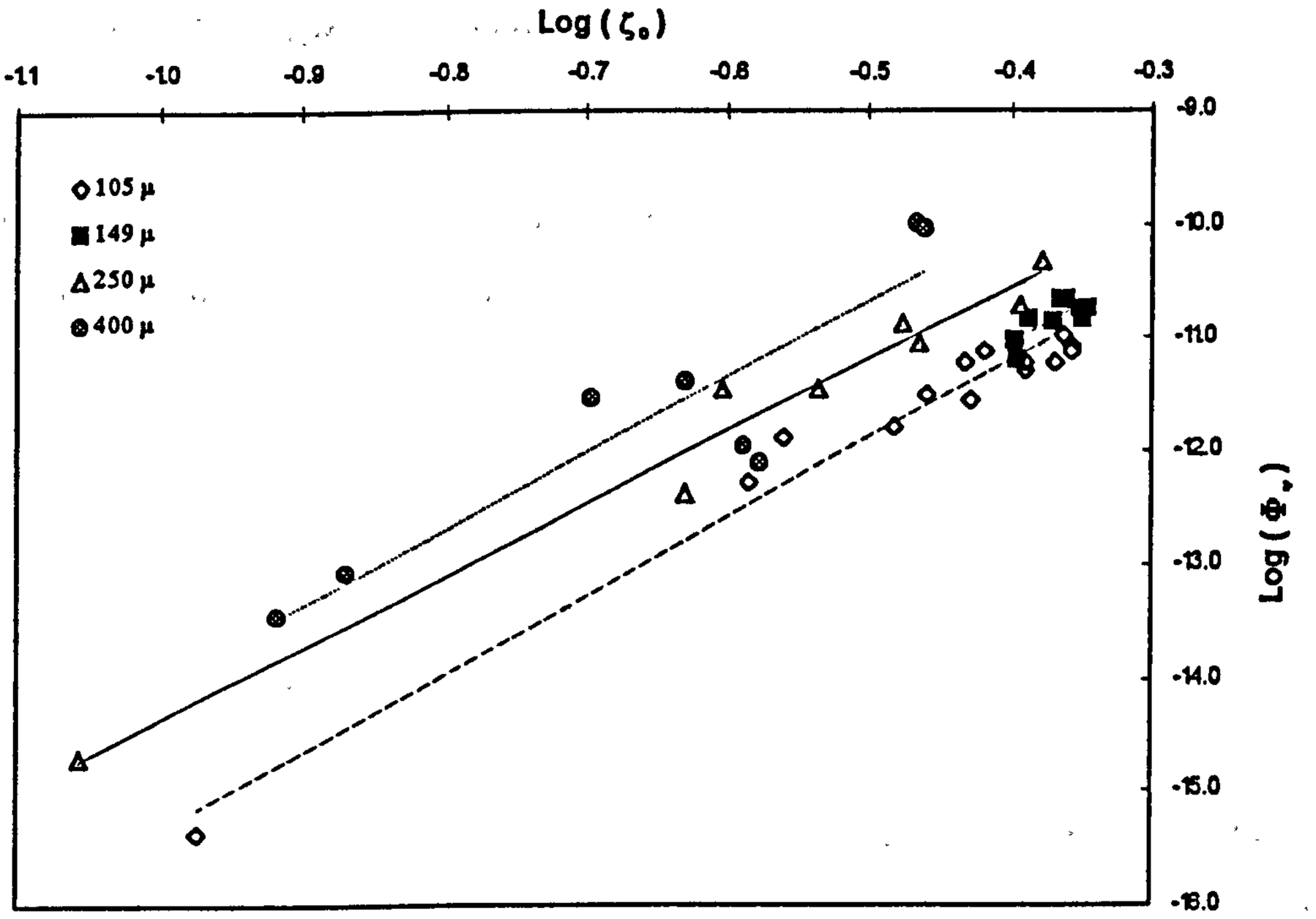

Fig. 6.7 Porosity Dependency of Viscous Permeability Coefficient
(Large particles, bimodal or with LiF)

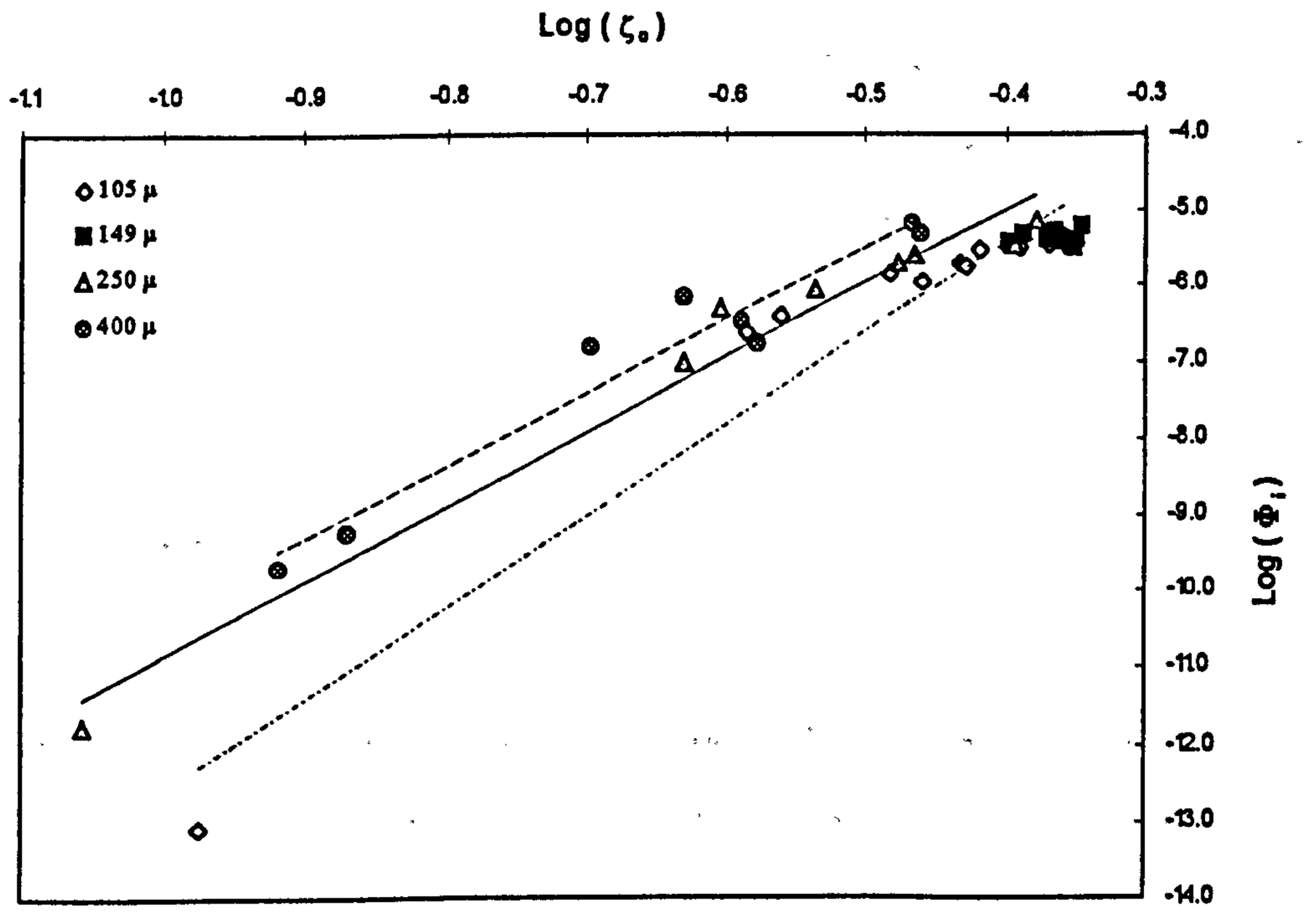

Fig. 6.8 Porosity Dependency of Inertia Permeability Coefficient
(Large particles, bimodal or with LiF)

6.1.6 Spatial Variation of Permeability

It would also be of value to have an assessment, either qualitative or preferably quantitative, of how uniformly permeable the specimen or bearing material is over its entire area. One way of achieving this is to obtain permeability values over a small local area of the porous material, and repeating the measurement at a different location as desired [211]. This could be achieved in the case of a plate specimen quite simply by using the guide ring method, which is originally designed for large plate specimens without sealed edges. While the principal is simple to apply, the flow rate involved would be so small for the size of specimens considered in the present scope of work that no reliable methods of flow measurement can be applied other than using the bubbling technique. In this method, the outflowing gas exits through a capillary of known diameter which is submerged in a fixed depth of water. The bubbles coming out of the capillary are of the same size and its volume can be determined. By counting the rate of appearance of bubbles, and knowing the static head at the submerged capillary exit, a measure of the flow rate at a known pressure can thus be obtained. This method does not, however, lend itself easily to automatic data acquisition. Moreover, considerable work would be required in instrumentation development and a reliable means of calibration was not available. As a result, an indirect assessment of the uniformity of permeability distribution was obtained in the present work through the measurement of pore size distribution by the extended bubble test and the dynamic water expulsion method.

6.2 PORE SIZE DISTRIBUTION

In an ideal porous material for aerostatic bearing applications, not only is one looking for predictable permeability, but equally important, uniformity in pore distribution, both in terms of pore size variations within a specimen and of spatial distribution. A uniform pore size distribution in turn implies homogenous permeability.

6.2.1 The Extended Bubble Test

The only method in the ISO standards relevant to measurement of pore sizes is the bubble test [212]. In this method, the porous specimen is first fully impregnated with deionised water. One surface of the specimen, facing upwards, is further covered entirely with a known depth of water (h_w). Pressurised air is gradually introduced onto the bottom surface, at a fixed rate of pressure increase of 5 - 50 mbar per second. The pressure (p_1) at which the first bubble begins to emerge on the top submerged surface, known as the first bubble point, is used to calculate the maximum equivalent capillary diameter of the pore :

$$d_{pore\ max} = \frac{4.\gamma_w}{p_1 + \rho_w.g.h_w} \qquad (6.9)$$

This method, although relatively simple to carry out, only provides information on the maximum through-pore over one specimen surface. No information on the size and spatial distribution can be obtained.

The bubble test was extended in the present study to provide a qualitative assessment of the uniformity of the spatial distribution of pores. After reaching the first bubble point, the pressure was further increased incrementally to cause general bubbling over the entire surface. Each pressure corresponded to an equivalent capillary diameter, as given by equation 6.9. Holding the pressure at specific values during the measurement allowed a visual inspection of how uniformly the bubbling pores were distributed, and when not uniform, where they were concentrated. Measurements could be made at as many ascending pressure levels as desired until bubbling occurred over the entire test surface.

A further test was also performed in the present work to give an additional assessment of the pore structure at the test surface. After the pressure had been increased to cause

general bubbling as mentioned above, it was then gradually reduced (at 50 mbar per second) until a point was reached when the last bubble just ceased to appear. This is named the reverse bubble point, and corresponds to the largest surface pore on the top of the specimen. Whereas the first bubble point, at which the specimen is still fully impregnated with water, corresponds to the maximum through pore, the reverse bubble point is an entirely surface phenomenon, and generally has a larger value than the first bubble point. This is due to the fact that the specimen has been previously purged with compressed air, and should by now contain little water. As the air pressure at the bottom specimen surface is reduced, bubbling at the top surface starts to reduce until the reverse bubble point is reached when the last bubble collapses at the top test surface under surface tension. Pore-necks from within, which may be of smaller size than those on the surface, no longer play any part here.

Simple reconfiguration of the permeability rig enabled the bubble test to be carried out on porous specimens. The inner tube at the exit end, together with the flow sensor and the gate valve, was removed. The whole assembly was tilted vertically with the air inlet end downwards. Specimens were fully impregnated with deionised water, using the method in Section 5.3.1, before mounting onto the rig. The top outer tube was then filled with deionised water to a measured height of 100 mm nominal, and the inlet air pressure slowly increased until the first bubble appeared (Appendix H, drawing no. MG291 B100 0A).

Generally, the spatial distribution of all tested specimens was very uniform. More often than not, the first bubble points occurred simultaneously at more than one location, which were also randomly spaced. For certain specimens with open porosity below 0.15, however, there appeared to be a higher probability that some degree of bias in the spatial distribution (certain part of the specimen having a higher concentration of larger pores) might occur. This appeared to indicate that while sintering to a lower porosity would improve strength and reduce elastic deformation, a penalty would have to be paid in the form of non-uniform permeability distribution. It would be advisable to avoid values of open porosity of 0.15 and below, in the interest of a more uniform pore structure.

6.2.2 Survey of Other Measurement Techniques

The bubble test, even in its extended form, does not provide any information of the pore size distribution of the test specimen. There are a number of established methods for measuring pore size distribution (Fig. 6.9). The most common of these include mercury porosimetry, water expulsion method, and image analysis. Other methods based on adsorption, capillary condensation, thermoporometry, and x-ray scattering are also used. A comparison of the different methods could be found in [213].

The most popular method to date remains to be mercury porosimetry. This technique is well developed, and is applicable to a wide range of pore sizes. It does, however, suffer from two main drawbacks - hysteresis and incomplete mercury retrieval. The latter is of particular concern as the specimen can only be measured once, and would no longer be useful for other tests.

The use of image analysis, on the other hand, only reveals pore size information over a relatively small area of the specimen. Other problems include the risk of false porosity by improper polishing, and difficulty in locating the exact throat of the pores, the shape of which is by no means cylindrical with a constant diameter through the thickness. It does, however, provide qualitative and quantitative measures of spatial uniformity. The result of any pore size distribution method is not in any way an absolute measure, and is highly dependent on the measurement method. This is fully demonstrated in Fig 6.10, in which two methods gave different results for the same test specimen [214].

In the absence of any equipment based on other methods, the dynamic water expulsion test appeared to be very attractive for the present work, despite its limited range of pore size of 0.5 to 100 μm. The water expulsion method has the added advantage of ease of handling. The test fluid, namely distilled water, is non-toxic, and any residue remaining in the sample could simply be driven out by heating to a high temperature (say 100°C).

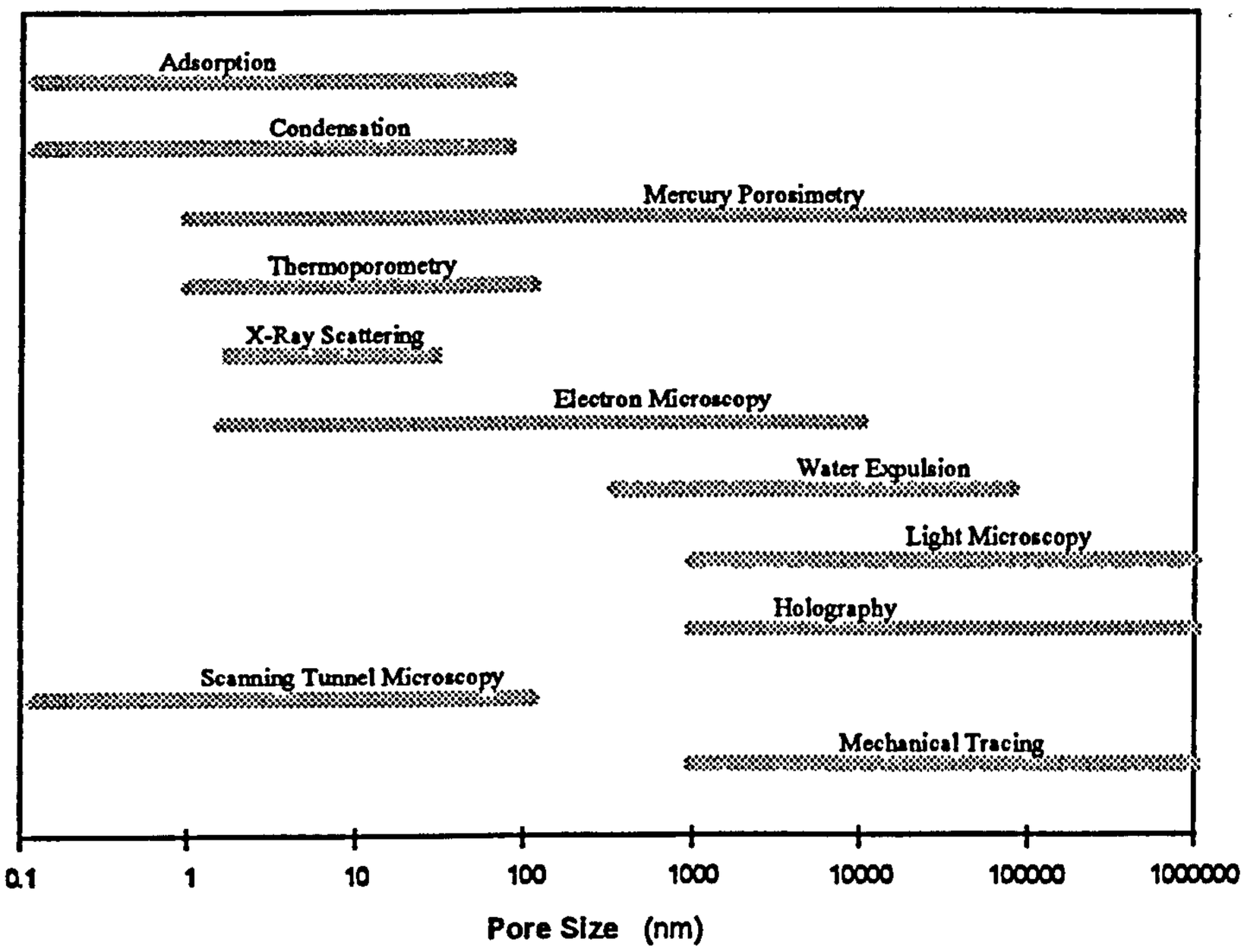

Fig 6.9 Measurement Range of Pore Size Distribution Methods Ref. [215]

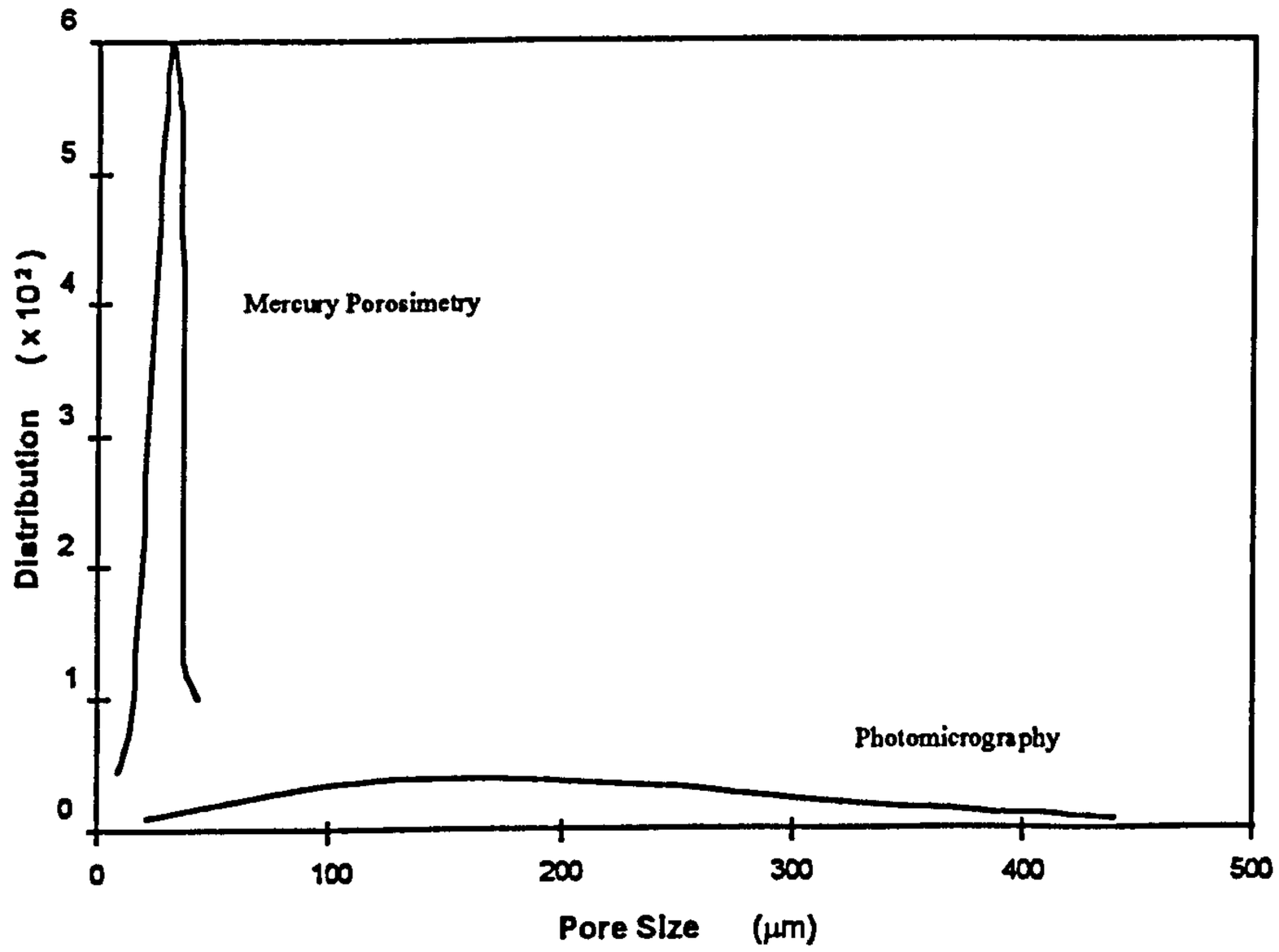

Fig 6.10 Comparison of Results - Mercury Porosimetry & Photomicrography

The test could therefore be repeated as many times as desired, with the specimen still useable subsequently for other tests or purposes.

Work by a number of authors [215, 216, 217] has confirmed that the method gives comparable results to mercury porosimetry within the above-mentioned pore size range.

6.2.3 Theory behind the Water Expulsion Method

The water expulsion method was first developed in the 50's by Zagar [218, 219, 220, 221]. Although not as widely used as mercury porosimetry, due partly to the lack of commercially available equipment and partly to the limited range, a number of successful applications of the method have been reported [215, 222]. The same method was also mentioned by Johnston [223] as the extended bubble-point test. An improved version of the method was published by Gélinas and Angers [204], which forms the basic theory of the pore size distribution measurement of the present work.

The dynamic water expulsion method involves passing compressed air with gradually increasing pressure through a porous specimen impregnated with water, hence the relation to the bubble-point test according to Johnston [223] . As the pressure increases beyond the bubble point, surface tension of the impregnated water in an increasing number of pores of decreasing pore sizes is being overcome, and thus the water expelled. These pores are thereafter free for air to flow through. The supply air pressure is increased in small increments, and the pressure difference across the specimen, as well as the steady state air flow rate monitored. The equivalent capillary (pore) size corresponding to a particular differential pressure, plus the number of pores contributing to the increase in air flow rate, can then be determined. Details of the mathematics for the dynamic water expulsion method could be found in the report by Gélinas [204].

6.2.4 Equipment Adaptation

As no separate equipment was available for the pore distribution measurement, the permeability measurement rig had to be adapted to perform the water expulsion test.

Different from its bubble-test configuration, the rig was tilted upside down, such that the air supply came in from the top. (Refer to Appendix H, drawing no. MG291-B103.) The inner tube and the gate valve downstream of the specimen were removed and replaced by a drain trap with a right-angled exit, to which the flow sensor was fitted. The expelled water was prevented from entering the flow sensor by filling the lower half of the drain trap with silica gel beads.

The sensors used in the dynamic water expulsion test were the same as those in the permeability test. As a result, no additional sensor calibration was necessary.

6.2.5 Measurement Procedures

The test procedure followed that of Gélinas [204]. The specimen, still held in its aluminium carrier, was fully impregnated with deionised water. The test pressure range was pre-determined. The starting, also the minimum, pressure was set at 0.9 of the first bubble point (Section 6.2.1) for each specimen. The maximum pressure corresponded to the capillary pressure for a pore size equal to 0.10 to 0.15 of the mean particle size, the smaller value used for specimens with lower porosity. Thirty intermediate measurement points were taken at equal pressure increments.

The operating sequence of the data acquisition software was similar to that for the permeability test. One significant improvement was that the measurement could be run fully automatically, as it was no longer necessary to balance flow streams manually. Flow was allowed to settle for 40 seconds after every change of pressure, as recommended by Clements [215]. Steady flow was detected in the software by calculating

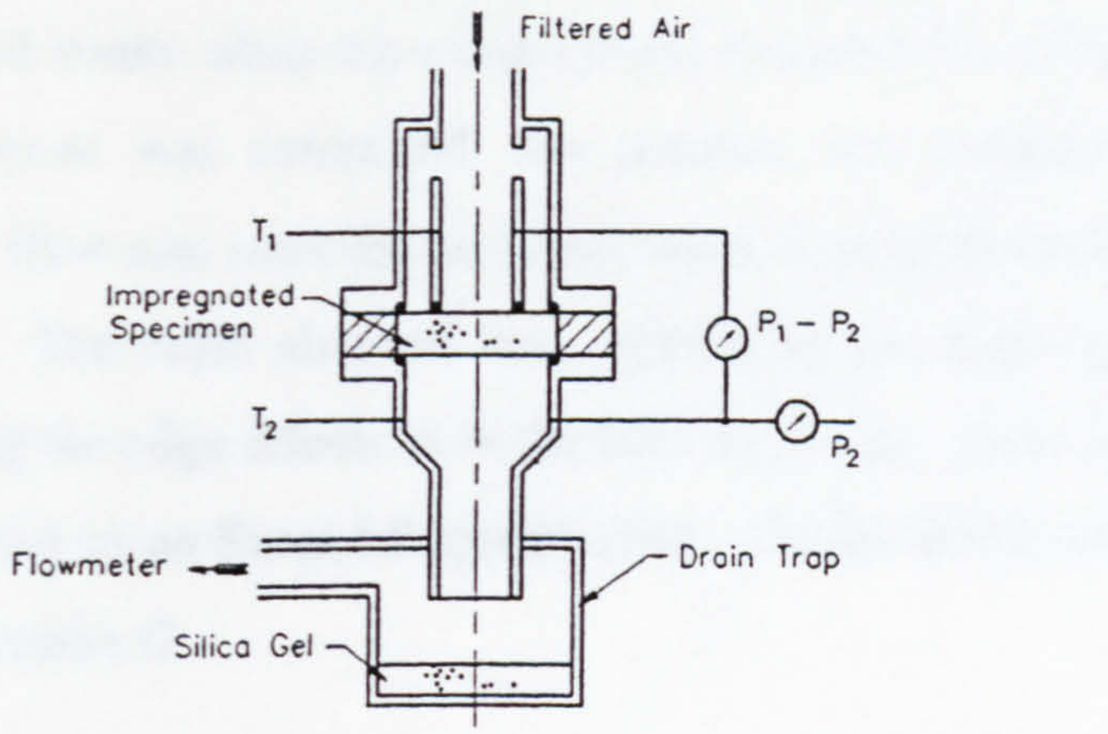

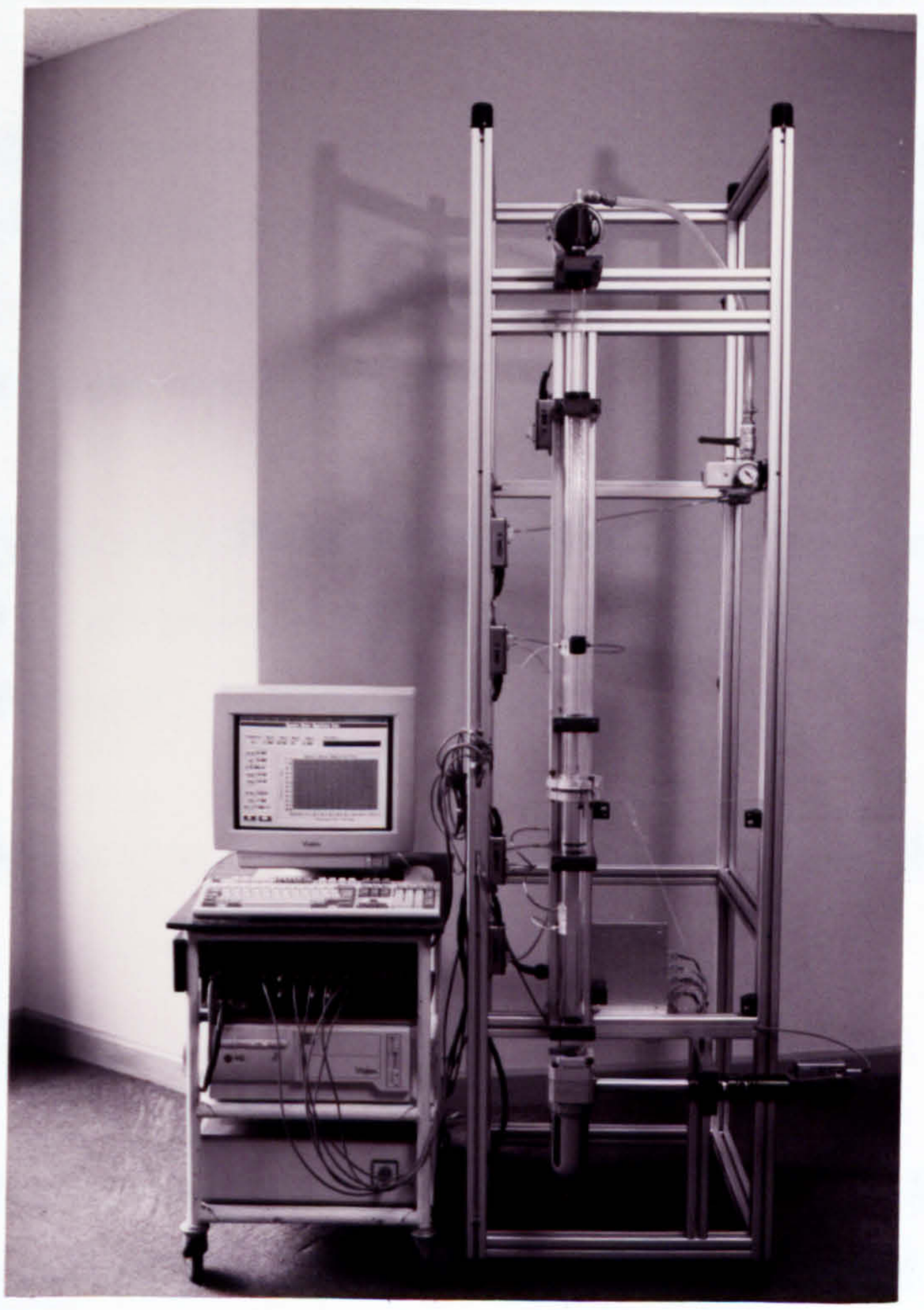

Fig. 6.11 Dynamic Water Expulsion Test Rig

the standard deviation of five successive flow rate measurements, each 0.5 second apart. Flow was considered steady when this value did not exceed 0.5% of the mean flow rate. Once the measurement was completed, the pressure was reduced to zero in five increments and the flow rate recorded at steady state to provide cross checking of the permeability value. The value obtained here referred to the entire specimen, with no means of eliminating the edge effects as in the ISO 4022 test. Data analyses and curve fitting were performed on an Excel 5.0 spread sheet. Details of the controlling software can be found in Appendix G.

6.2.6 Experimental Results

A total of 30 specimens with particle size ranging from 7 - 105 μm, and open porosity between 0.1 and 0.44 were tested for their pore size distribution using the dynamic water expulsion method. Three of these specimens were produced with 1 to 4 wt% of LiF as sintering aid, while the rest were 100% α-alumina.

Test results for a typical specimen of 100% α-alumina sintered from 7 μm powders to an open porosity of 0.207 are shown in Figs. 6.12 to 6.14. The flow rate vs. pressure plot followed very similar trends to that reported in [204].

No flow could be measured until the corrected differential pressure P_o, defined by :

$$P_o = \frac{p_1^2 - p_2^2}{2.p_{ref}} \qquad (6.10)$$

reached a value of 0.246 MPa, when the air pressure began to clear the first through-pores. The flow rate continued to rise at an increasing rate, and reached a maximum at a P_o value of 1.18 MPa. This corresponded to the point where the largest number of pores became cleared of water at an incremental increase in pressure. After this, the rate of increase in flow rate began to slow down, reaching a constant value at P_o = 1.4 MPa and beyond. The constant increase in flow rate against pressure was an indication that

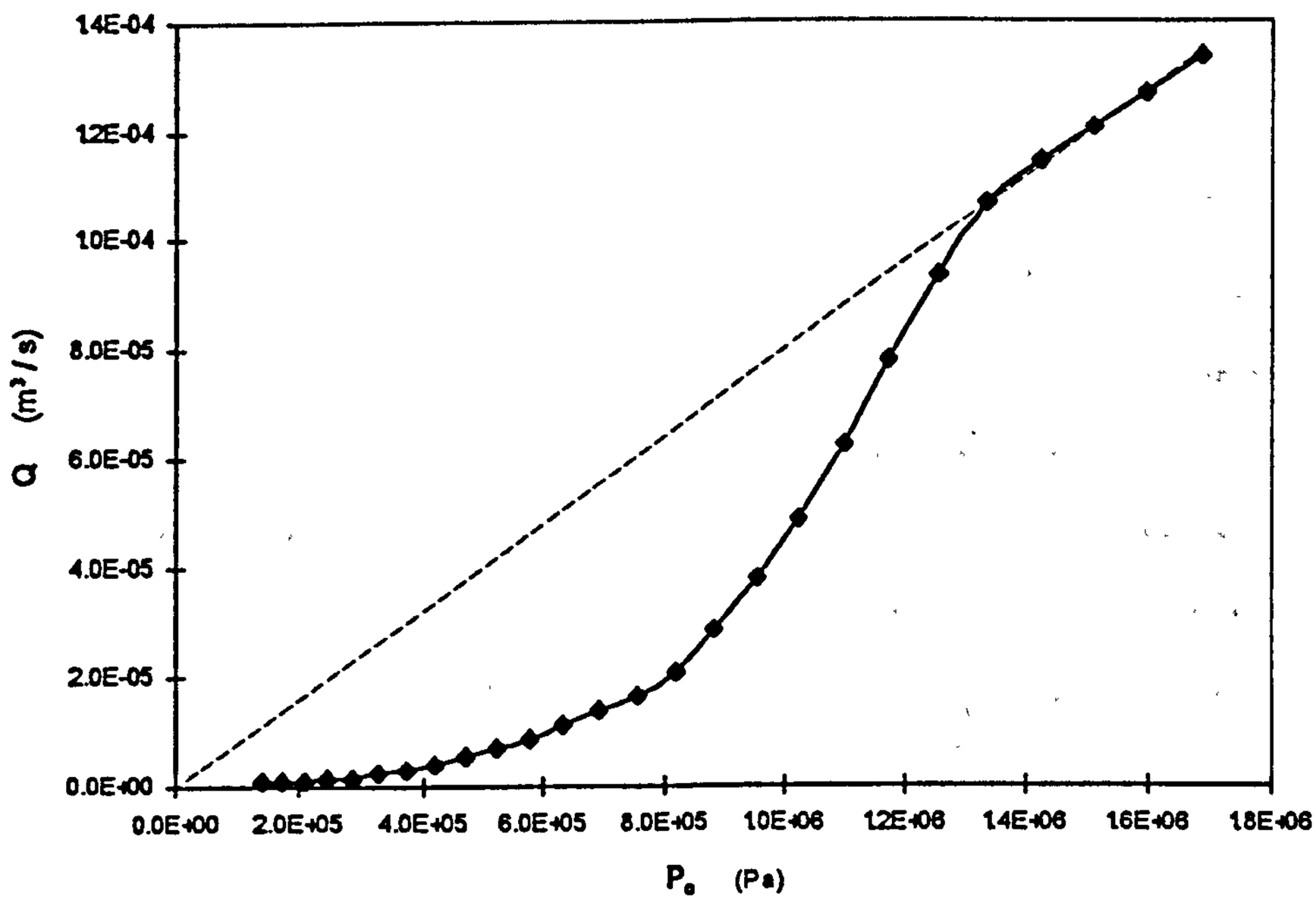

Fig 6.12 Pore Size Distribution -- Dynamic Water Expulsion Method
($d_w = 7\mu m$; $\zeta_o = 0.207$)

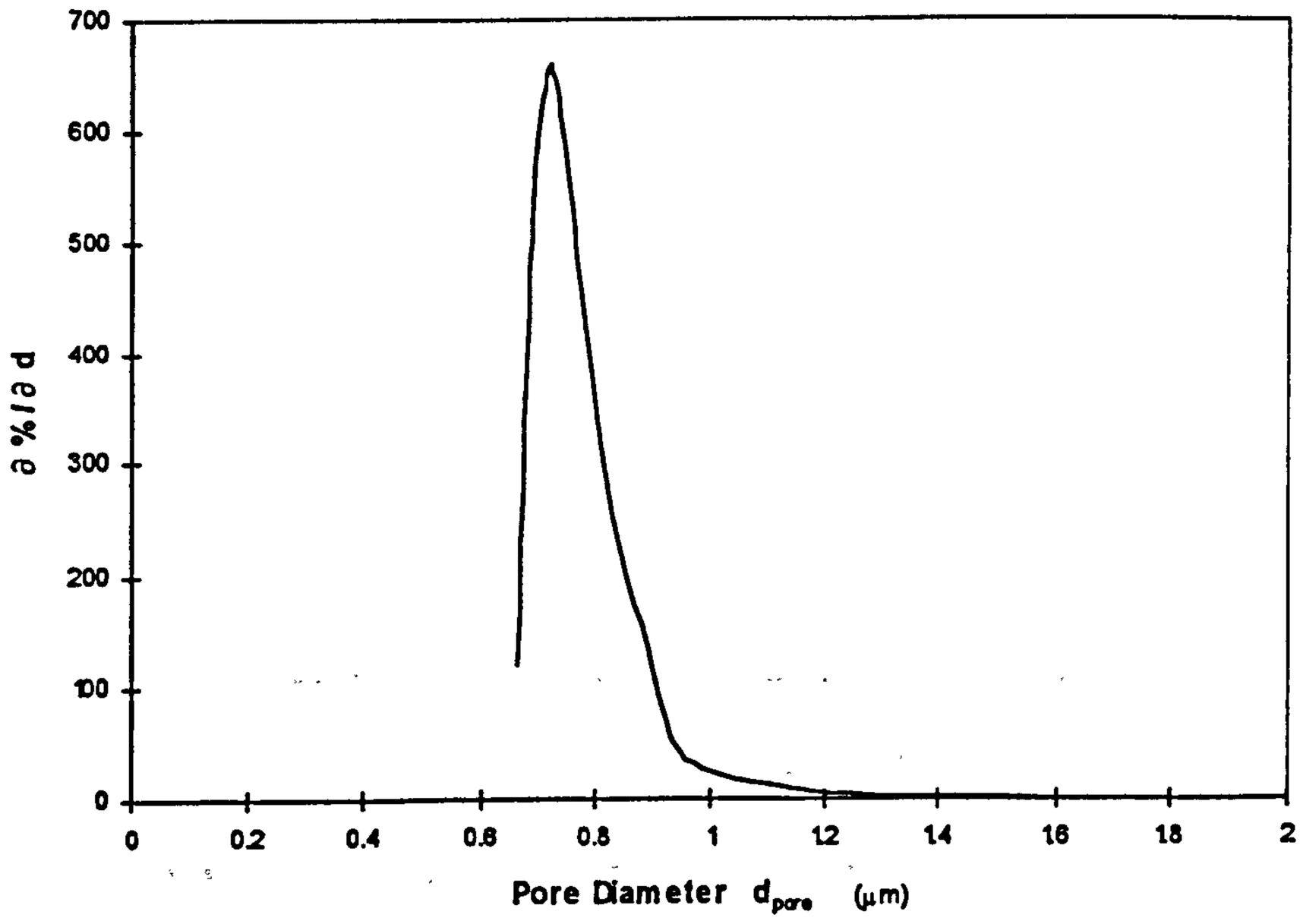

Fig 6.13 Pore Size Distribution Plot ($d_w = 7\mu m$; $\zeta_o = 0.207$)

all pores had been cleared, and the slope of the Q vs. P_o curve at that point could be used to calculate the permeability coefficient corresponding to that pressure.

The permeability coefficient so obtained was calculated as 3.93×10^{-15} m^2. This compares with the viscous permeability coefficient of 4.75×10^{-15} m^2 obtained using the ISO 4022 guide ring method. While the pore distribution test was performed on the entire specimen of 44 mm in diameter, the permeability test only measured an area of 23 mm diameter at the centre. The centre portion of the specimen thus appeared to have a higher permeability than the outer part, a fact consistent with evidence of higher shrinkage across the thickness at the centre, suggesting lower green density and higher degree of particle bridging there during powder packing.

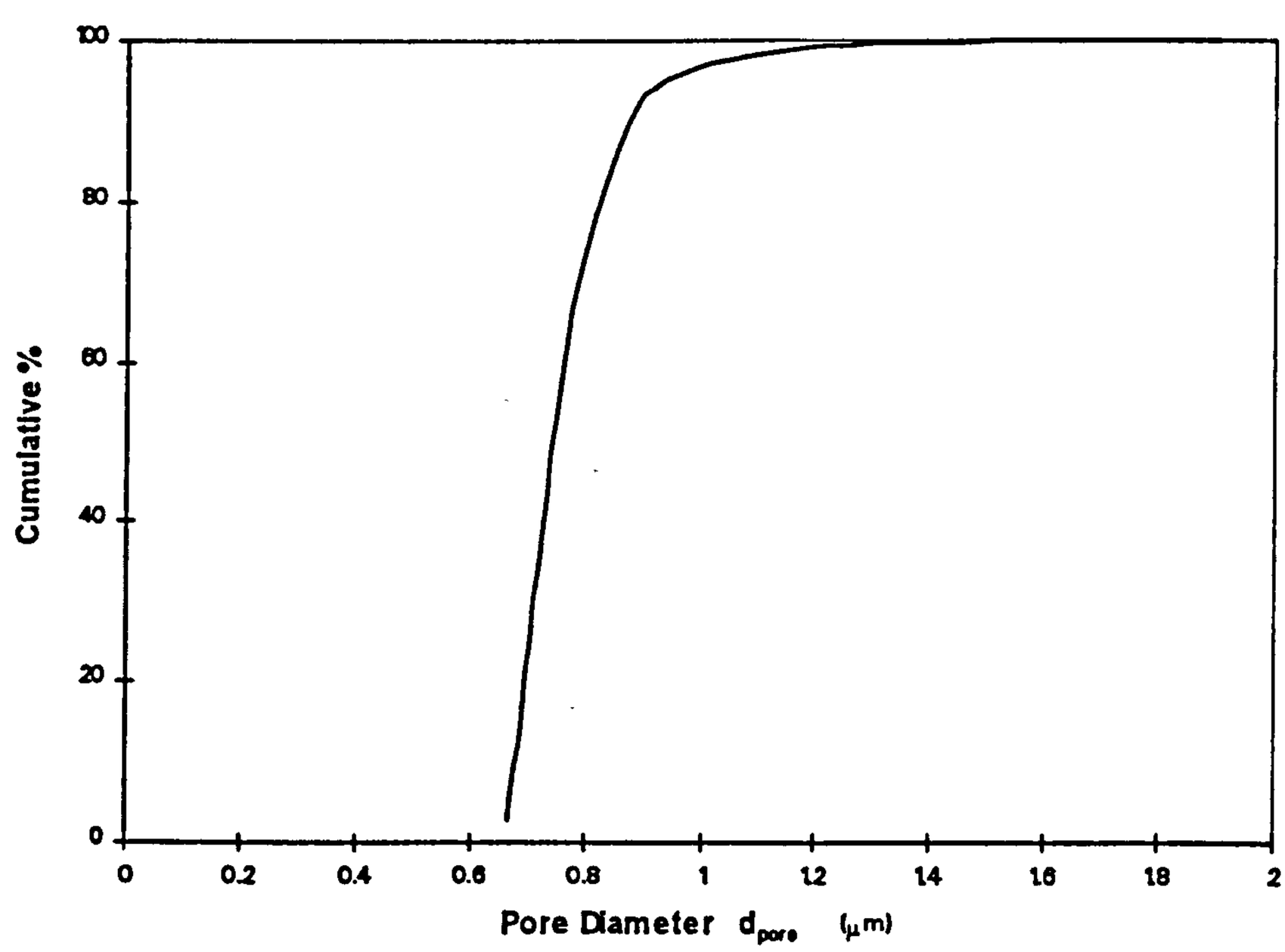

Fig 6.14 Cumulative Pore Size Distribution Plot ($d_w = 7$ μm ; $\zeta_o = 0.207$)

The cumulative pore distribution plot is shown in Fig. 6.14. To describe the distribution quantitatively, four typical values are commonly used :

a) modal equivalent pore diameter (at peak distribution frequency) d_{pk} ;

b) median equivalent pore diameter (at 50% distribution) d_{50} ;

c) equivalent pore diameter at 10% distribution d_{10} ;

d) equivalent pore diameter at 90% distribution d_{90} .

80% of all pores (within the range of the water expulsion test) lay within the d_{10} value of 0.68 μm and 0.87 μm, the d_{90} value. Differentiating the cumulative value with respect to pore size yielded the pore distribution plot, showing a sharp peak at the modal pore diameter of 0.73 μm (Fig. 6.13). The sharpness of this peak was , as in the case of the d_{10} and d_{90} values, also a measure of the uniformity of pores within the specimen. The skew of the distribution towards smaller pore values was typical of all specimens. Pores larger than the peak value resulted from particle bridging during the packing stage, and could not be eliminated completely. Smaller than average pores were possibly created by groups of smaller particles sintering close to each other, or a higher degree of sintering at certain locations due to temperature difference within the HIPing furnace.

The modal pore sizes obtained from all thirty experiments showed a trend of near exponential increase when plotted against open porosity, but seemed to bear a directly proportional relationship with the powder size (Fig. 6.15). Values used for particle sizes were actual data obtained from Sedigraph measurements. Also noticeable were the lower values of equivalent pore sizes obtained from specimens with LiF (Fig. 6.15). When compared with pure alumina specimens of comparable porosity, the modal pore sizes as measured could be more than 50% smaller. A possible explanation could be the partial blockage of the pores by the lithium fluoride.

Neither the power law of the form :

$$d_{pk} = k \,.\, d_w \,.\, \zeta_o^{\,a} \qquad (6.11)$$

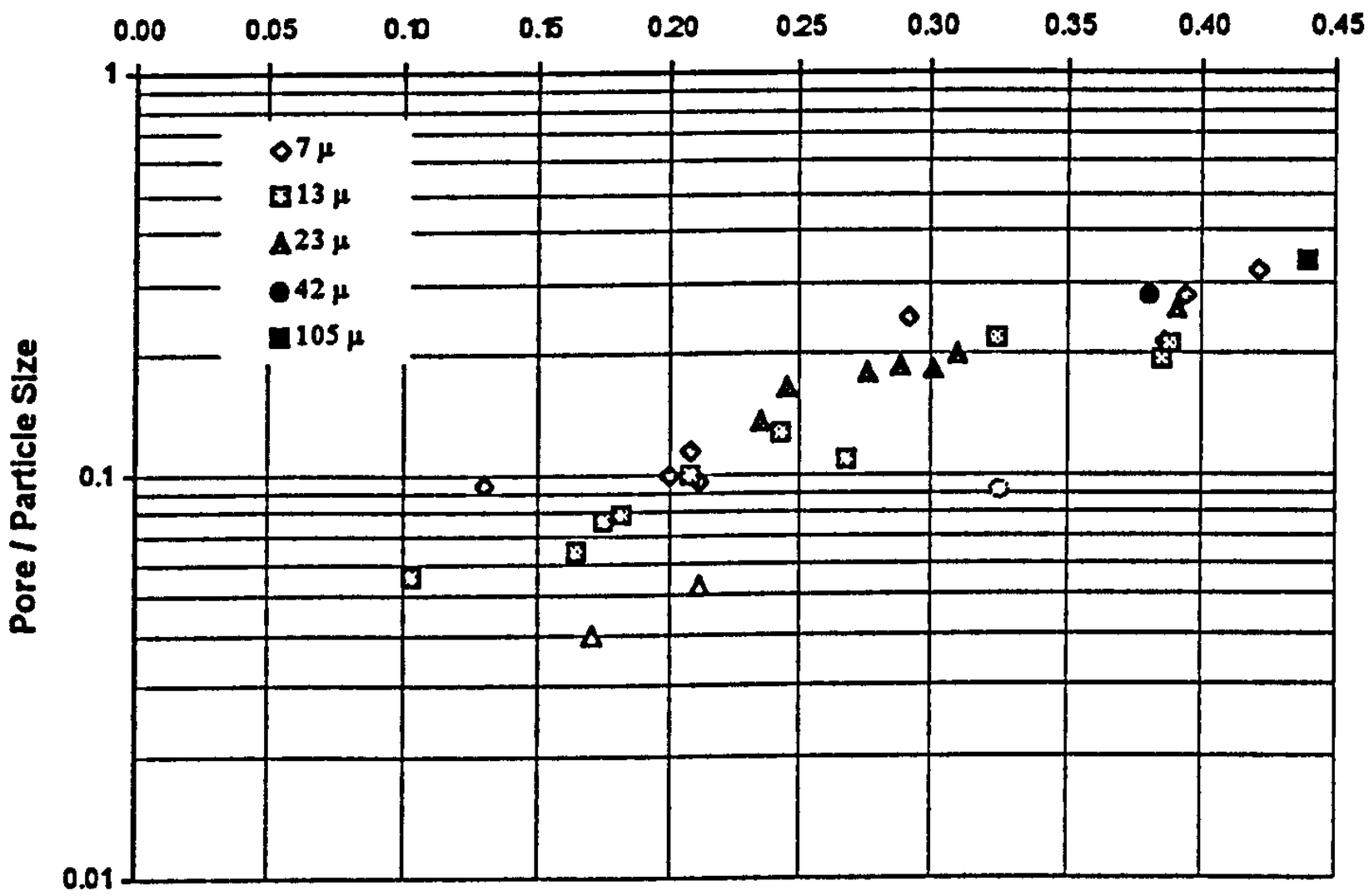

Fig 6.15 Dependency of Peak Pore Size on Open Porosity

(3 hollow legends represent LiF samples)

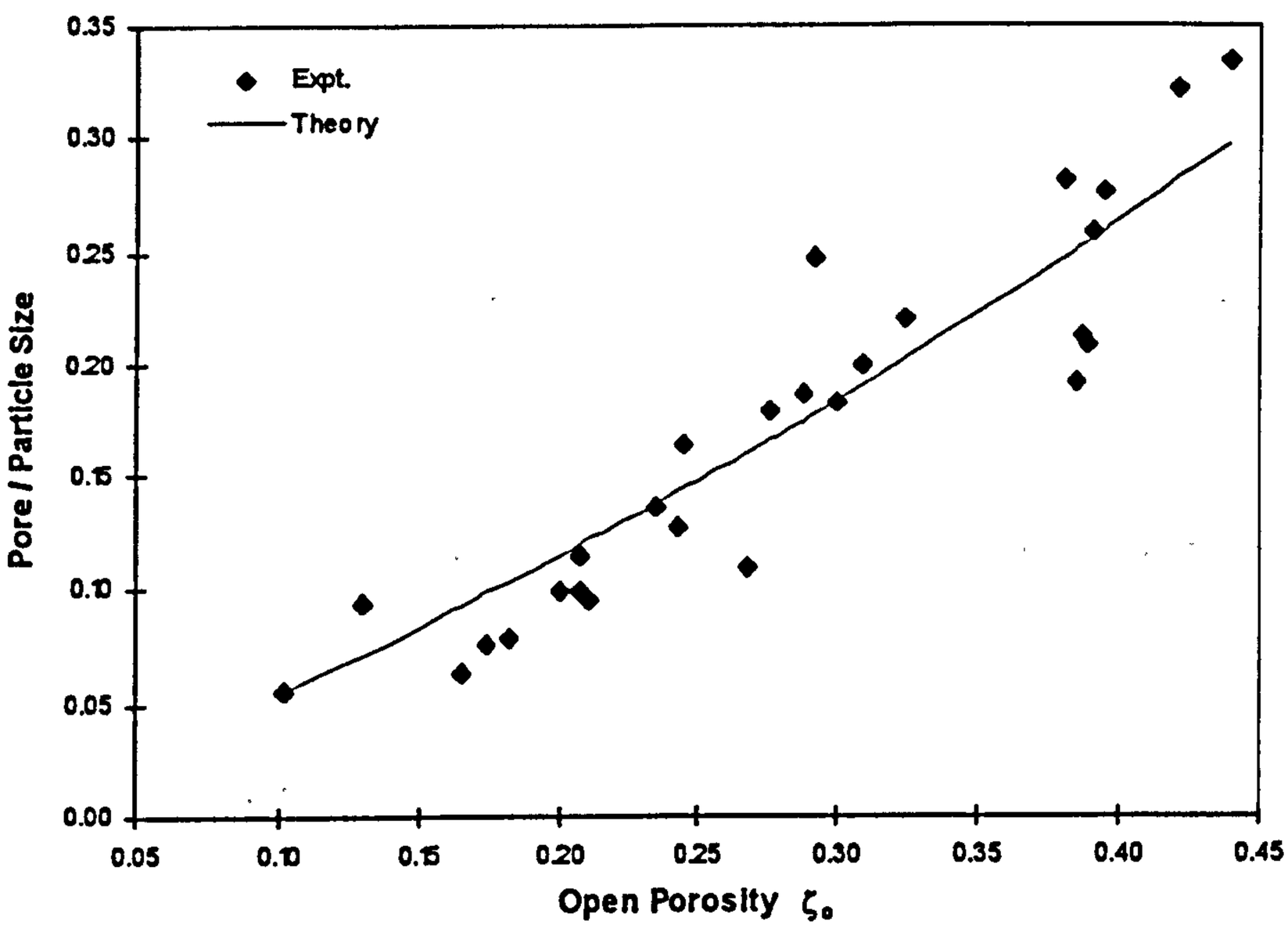

Fig 6.16 Dependency of Relative Pore Size on Open Porosity

$$\zeta_o = 1 - e^{-1.943.d_{pk}/d_w}$$

nor the exponential function :

$$d_{pk} = k_1 . d_w . e^{b.\zeta_o} \qquad (6.12)$$

was thought to describe the relationship between open porosity and pore size adequately. One would expect that as porosity approaches zero, so would the pore size. The exponential function still has a non-zero value in this case. In this respect alone, the power law provides a more accurate prediction.

On the other hand, as porosity approaches one, implying that the separation between solid particle should be infinitely large, the pore size should also approach infinity. The value predicted by the power law is, however, limited to $k.d_w$. The exponential function also returns a finite value of $k_1.d_w .e^b$.

To satisfy both of the above boundary conditions, the following function is proposed :

$$\zeta_o = 1 - e^{-c\left(d_{pk}/d_w\right)} \qquad (6.13)$$

or

$$\frac{d_{pk}}{d_w} = - \frac{1}{c} . \ln (1 - \zeta_o) \qquad (6.14)$$

At $\zeta_o = 0$, $d_{pk} = 0$. As ζ_o approaches 1, d_{pk} tends to an infinitely large value. Thus both conditions are satisfied.

Excluding specimens with sintering aid, least square fitting of the experimental data gives the following empirical values :

$$\frac{d_{pk}}{d_w} = - 0.4564 . \ln (1 - \zeta_o) \qquad (6.15)$$

Hence, $c = 2.19$ (Fig. 6.16).

The relationships between the d_{10}, d_{50} and d_{90} values and the modal pore size were also investigated (Fig. 6.17). As can be seen from Fig 6.18, the d_{50} (median) values are practically identical to the modal values, an indication of a distribution with a narrow bandwidth. At larger values of porosity, both the d_{10} and d_{90} values follow an almost linear relationship with open porosity, with a tendency to a wider spread as porosity decreases. This spread of distribution becomes more significant as porosity drops below 0.3, with both values deviating further from the modal value in a near quadratic manner. As an approximation, the following equations could be used :

$$d_{10} = d_{pk} . (0.78 + 0.67 \zeta_o - 0.69 \zeta_o^2) \quad (6.16)$$

$$d_{50} = d_{pk} \quad (6.17)$$

$$d_{90} = d_{pk} . (1.42 + 1.35 \zeta_o + 1.86 \zeta_o^2) \quad (6.18)$$

As ζ_o approaches zero, $d_{10} \cong 0.78\ d_{pk}$, $d_{90} \cong 1.42\ d_{pk}$, giving further indication to the skew of the distribution towards smaller pore values.

As far as aerostatic bearing applications are concerned, the pore distribution tests do not provide any direct information on the fluid flow properties of the porous specimens on its own, but would give a measure of the uniformity of the pore structure, which in turn is related to the permeability of the material. In a production environment, it would also provide a means of assessing batch to batch variations.

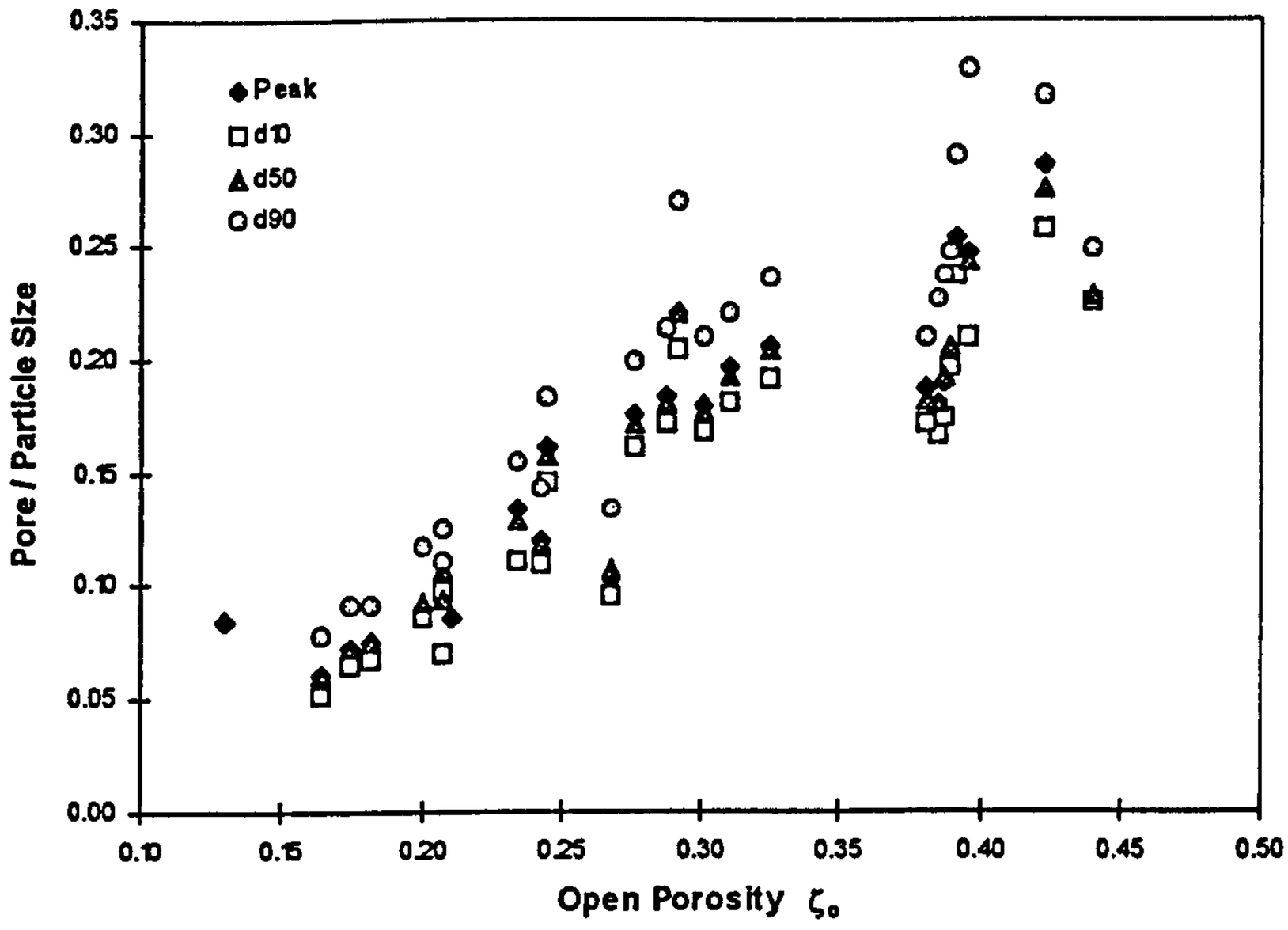

Fig 6.17 Dependency of Relative Pore Size on Open Porosity

(100% Alumina ; d_{10}, d_{50}, d_{90} values)

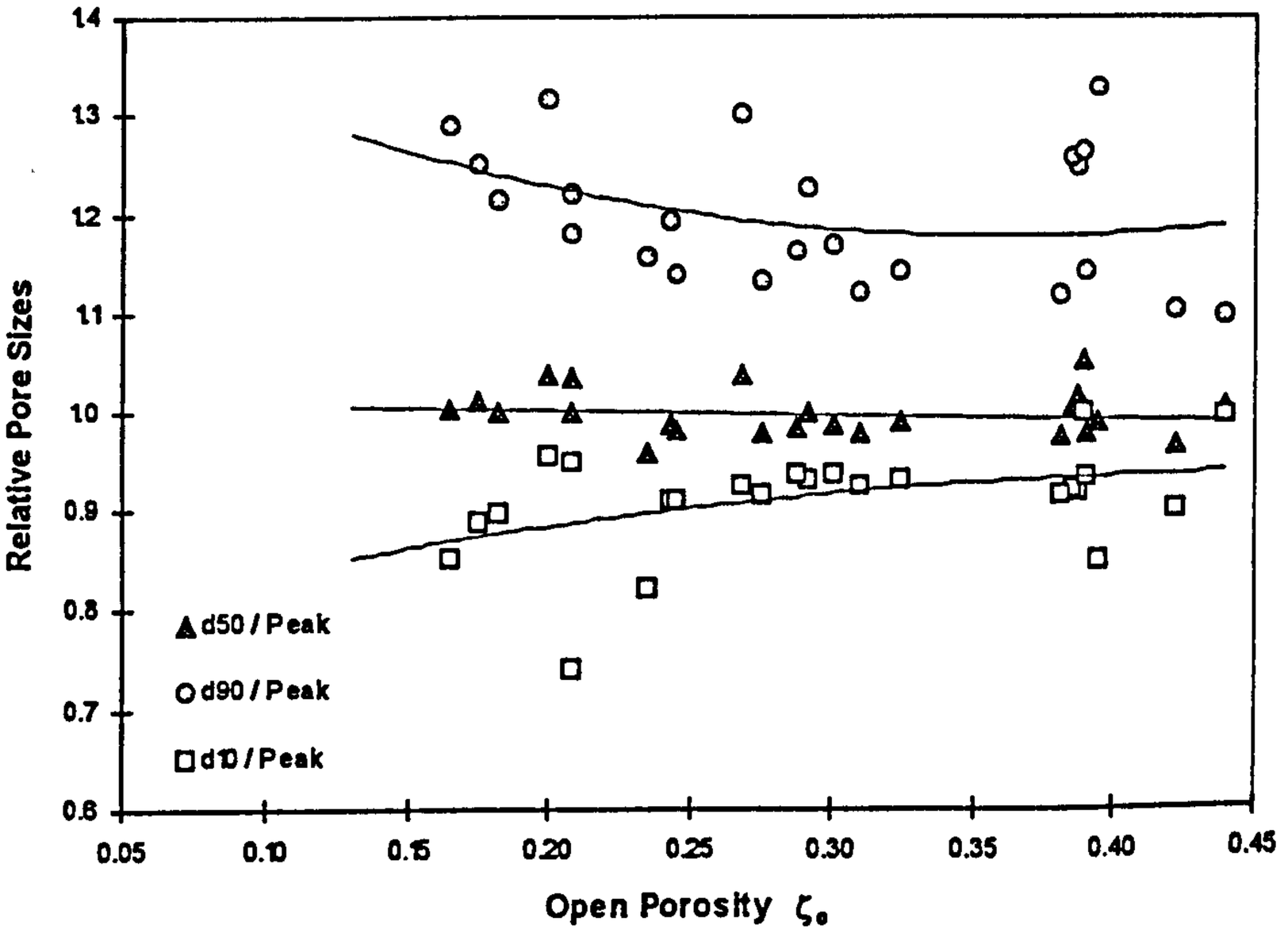

Fig 6.18 Variation of d_{10}, d_{50} and d_{90} Values with Open Porosity

6.3 SLIP COEFFICIENT

As already mentioned in chapter 2, very little data have been published on the measured value of slip coefficients α_s of porous materials. In order to assess the significance of the tangential velocity slip, it was felt that additional experiments to measure α_s were necessary.

6.3.1 Measurement Method

The measurement method for α_s in the present work was based on that developed by Beavers and co-workers [115]. This initial work by Beavers, using water as the test fluid, was supplemented by a later publication on tests based on compressed air, with comparable results [224]. It was concluded then that the slip coefficient was a function of the structure of the porous surface alone, and was independent on the test fluid.

The experiments in the present study were conducted with air as the test medium. Not only was this because air was the actual medium for aerostatic bearings, but also because the specimens in the present work were limited in size, thus dictating a narrow flow passage if the same gap to width ratio was to be maintained. A fluid of much lower viscosity to water had to be used to give a reasonable flow rate without resorting to a high pressure differential.

The measurement method essentially involved forcing compressed air of a known pressure through a narrow passage, bounded by a porous substrate on one side, and a solid one on the other. Flow between the porous and the solid surface was channelled off for flow rate measurement. The pressure gradient along the porous medium had to be maintained to be identical to that across the flow passage, ensuring that no pressure difference could exist across the porous surface, so that flow would essentially be axial (along the length of the porous substrate). In the experiments performed by Beavers, the

flow through the porous medium was also collected to provide a measurement of the permeability coefficient, which in the present work had already been measured in accordance with ISO 4022. This flow was therefore simply dumped to atmosphere.

The same procedure was repeated for a number of passage gaps, and also for flow between two solid surfaces (the porous substrate replaced by a solid one with identical dimensions). The slip coefficient could then be determined by comparing the two resulting flow rates :

$$\frac{\dot{M}_p}{\dot{M}_s} = 1 + \frac{3.(\sigma_s + 2\alpha_s)}{\sigma_s.(1+\alpha_s.\sigma_s)} \qquad (6.19)$$

where

$$\sigma_s = \frac{h}{\sqrt{\Phi_e}} \qquad (6.20)$$

6.3.2 Equipment Design

The maximum useful length of the HIPed specimens was about 40 mm. The width of the substrate was to be a minimum of 60 times that of the gap, so that any edge effects of the side walls could be neglected. The length of the passage was five times that of the width, as recommended in [52]. The flow passage width was therefore set at 8 mm. The flow gap ranged from 12 μm to 100 μm, of the same order of actual working clearances for porous aerostatic bearings. Although it would have been desirable to reduce the gap even further to, say, 5 μm, practical problems such as flatness of the boundary surfaces as well as sealing problems prevented this from being realised in the current work.

Sufficient thickness of the porous substrate was necessary to minimise any boundary effects at its blind side (opposite to the flow channel surface), where the air velocity

should be zero. The same nominal thickness of 6 mm for the test thrust bearing pads was used for the slip coefficient measurements. (Figs. 6.19 to 6.21, also Appendix H, drawing no. MU291-B200)

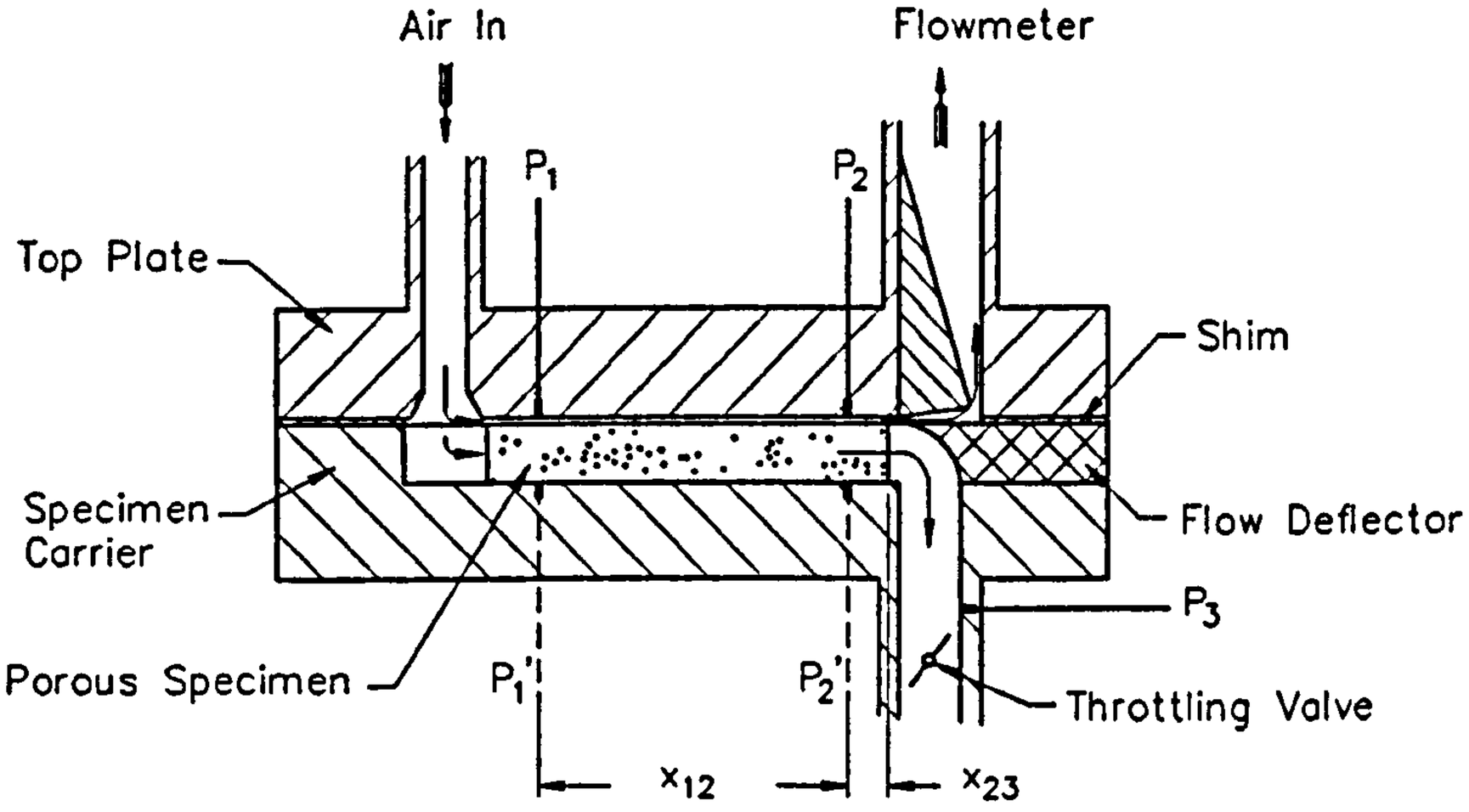

Fig 6.19 Schematic Diagram of the Slip Coefficient Measurement Fixture

The gap between the porous specimen and the upper solid surface of hardened 440C stainless steel was controlled by precision stainless steel shims of thickness uniform to within 1 μm. Each shim had a round-ended, parallel-sided slot 8 mm wide which formed the flow passage. The slot ended beyond both ends of the specimen, so that the length of the flow passage was controlled only by that of the specimen itself. The slots were produced by electro-chemical machining (etching), and the widths were measured individually by a Mitutoyo PJ - 300 profile projector with a digital readout of 0.1 μm resolution. An exit flow deflector, pushed tight against the bottom surface of the shim, which in turn sat directly above the specimen, served as a partition for the two flow streams. A vertical opening on the top plate across the full width of the passage led the outflowing air to the flow sensor. Flow emerging from the exit end of the porous specimen was dumped to atmosphere via a throttling valve. The latter was used to

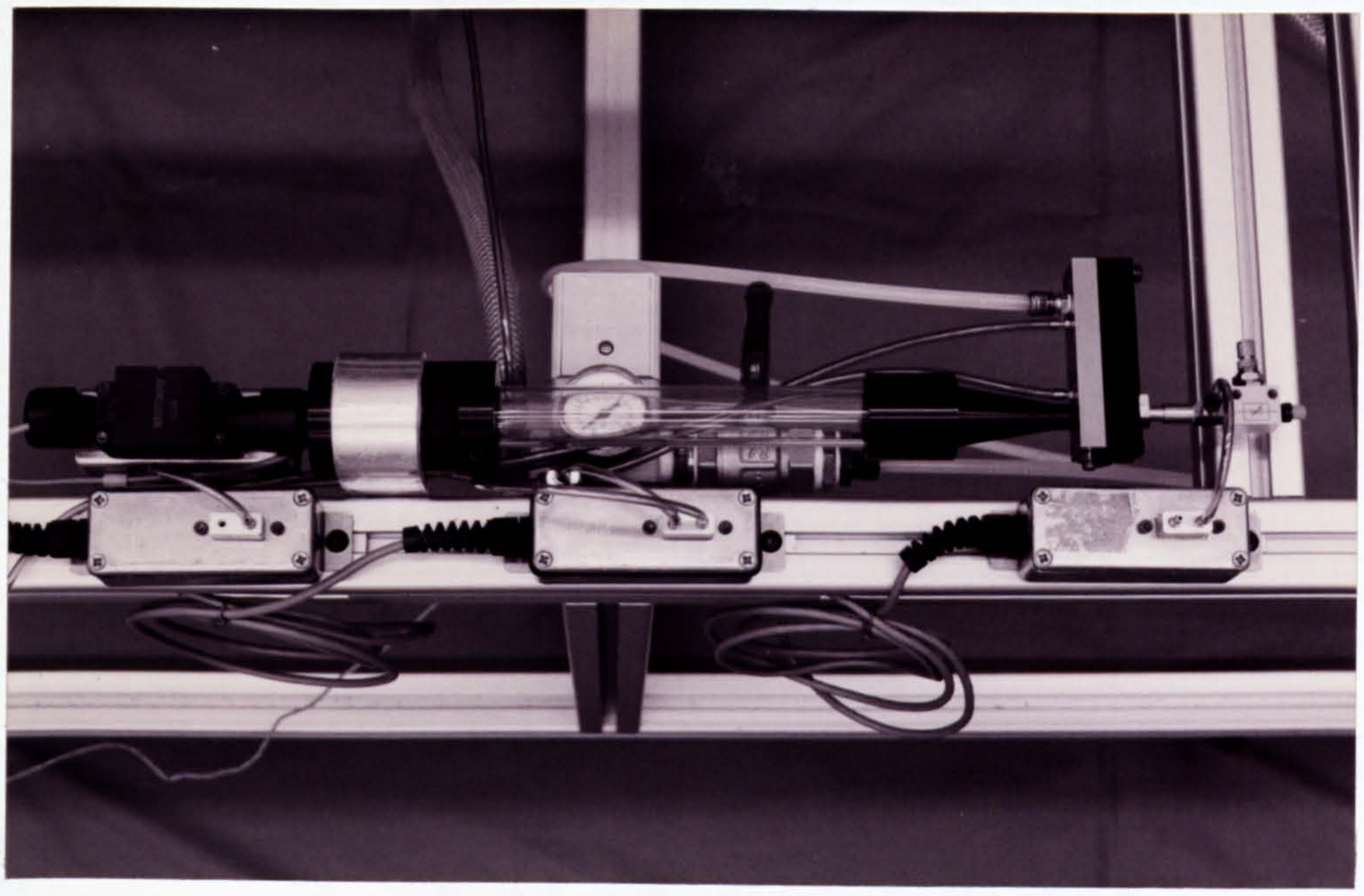

Fig. 6.20 Experimental Set-up for the Slip Coefficient Measurement

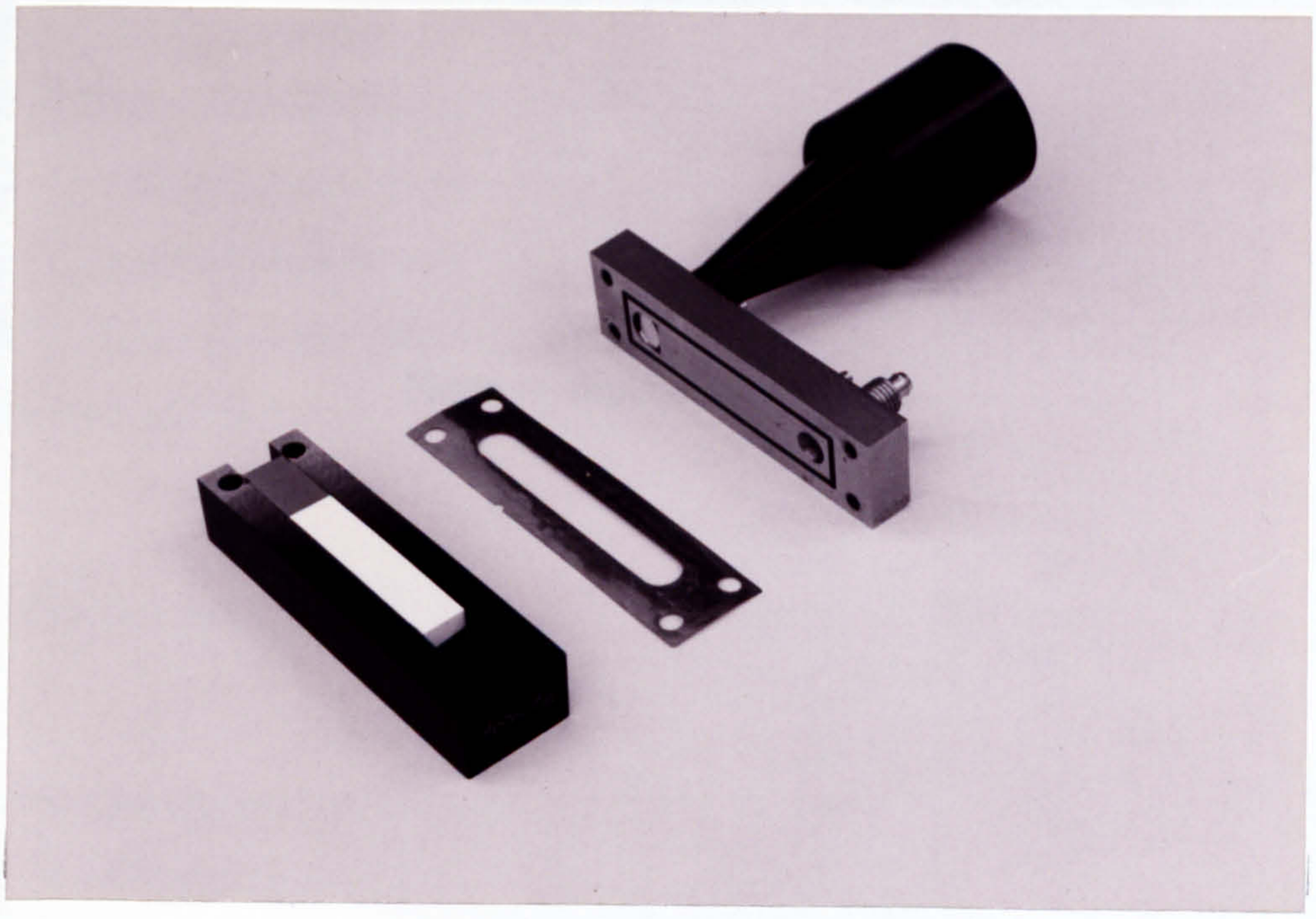

Fig. 6.21 Exploded View of the Slip Coefficient Testing Fixture

equalise the pressure differences between the two flow streams at the exit, in order to maintain equal pressure across the porous surface, and to minimise any leakage flow across the flow deflector at the exit end. The in- and out-flow from the passage had to go through a 90° bend, which was not ideal from the fluid flow's point of view. Such an arrangement was however adopted for its mechanical simplicity. Pressure tappings of 0.5 mm diameter were placed precisely 30 mm apart and 5 mm from the entrance and exit to measure the pressure gradients along the two flow streams.

A solid dummy specimen of 440C stainless steel was used in place of the porous specimen for flow calibration between two solid surfaces. This was found to be necessary due to the surface roughness of the solid boundary surfaces, which was not negligible when compared to the smallest shim thickness.

Pressure and flow sensors were the same as used in permeability measurements, and had already been calibrated. Data acquisition was software controlled as in the permeability measurement, with operator interface due to the need to manually balance the exit pressure in the two streams. Post-measurement processing included the curve fitting of Q vs Δp plot to eliminate flow sensor zero error as before, and the calculation of the slip coefficient for each measurement. Substantial data processing was, however, found to be necessary afterwards in order to eliminate the effect of the poor finishes of the boundary surfaces. This would be dealt with in the following section. Details of the LabWindows software could be found in Appendix G.

6.3.3 Measurement Procedures

Twelve porous alumina specimens of various particle sizes and porosity were chosen for the slip coefficients measurement. The testpieces of dimensions 40 mm x 9 mm x 6.5 mm were sliced from the HIPed, disc-shaped specimens. This was done in such a way that the surface forming the porous boundary of the flow channel was identical to that should the same specimen be used as a thrust bearing. The testpieces were diamond ground to

size before being glued onto channel shaped aluminium carriers with metal loaded epoxy. The top face was then finished ground. Grinding parameters and set-up were the same as those described in Section 4.4.

Each specimen was tested ten times, using the complete set of shims in 10 μm increments. For each shim size, ten measurement points were recorded at fixed supply pressure increments, with the maximum flow rate limited to a Reynolds number of 250 in the flow passage [224]. The Reynolds number was calculated in real time by the measurement software based on the gap dimensions and flow rate as measured.

The readings for each shim, representing a straight line on the Q_{mean} vs Δp plot, were least-square fitted to eliminate any zero error of the flow sensor. The slope so obtained was used to calculate the increase in flow due to the presence of the porous surface (equation 6.19).

Values of Qp / Qs obtained from the ten shim thicknesses were then used in the data analysis to obtain the slip coefficient. The process was complicated by the poor finishes of the boundary surfaces (more details later).

In the experimental set-up used by Beavers and Joseph [52], the exit pressure in both flow streams were balanced through pressure tappings both at the solid surface and the porous body. A similar arrangement was initially planned. The difficulty lay in establishing pressure tappings during the attachment of the porous alumina to the carrier with metal loaded epoxy. Too much epoxy around the pre-drilled pressure tappings on the carrier would seal the 0.5 mm holes, and subsequent re-drilling on the ceramic was not possible. Leaving too large a cleared area around the hole would affect the accuracy of the tapped pressure value, especially when the pressure gradient could be as high as 0.0167 MPa mm^{-1}.

A compromise pressure balancing method was used, in view of the practicality of establishing meaningful pressure tappings at the porous body. Assuming laminar flow,

the downstream pressure at the exit edge of the porous specimen, p_3, could be extrapolated from the readings of the two pressure tappings on the solid surface, applying Poiseuille equation for compressible laminar flow through a uniform gap **h** between p_2 and p_3 (Fig. 6.19) :

$$Q = \frac{h^3}{12.\eta} \cdot \frac{p_2^{\,2} - p_3^{\,2}}{2.p_{ref}} \cdot \frac{1}{x_{23}} w_c \qquad (6.21)$$

Similarly for p_1 and p_2,

$$Q = \frac{h^3}{12.\eta} \cdot \frac{p_1^{\,2} - p_2^{\,2}}{2.p_{ref}} \cdot \frac{1}{x_{12}} w_c \qquad (6.22)$$

Combining the two equations,

$$p_3^{\,2} = p_2^{\,2} \cdot \left(1 + \frac{x_{23}}{x_{12}}\right) - p_1^{\,2} \cdot \frac{x_{23}}{x_{12}} \qquad (6.23)$$

knowing x_{12} and x_{23} from profile projection measurement, p_3 could be calculated for all values of p_1 and p_2.

This calculation was incorporated in the Labwindows software, using the instantaneous measured values of p_1 and p_2. For more effective adjustment, a needle valve was installed at the exit of the porous flow stream, in place of the original shuttle valve. An additional pressure tapping was incorporated to measure the exit pressure p_3' of the porous flow stream. Balance was achieved when the measured p_3' equalled the calculated p_3.

While this pressure balancing method was not ideal, the good linearity obtained in the Q_{mean} vs Δp plot for all measurements at Reynolds number below 250 provided evidence of its effectiveness (Fig. 6.22).

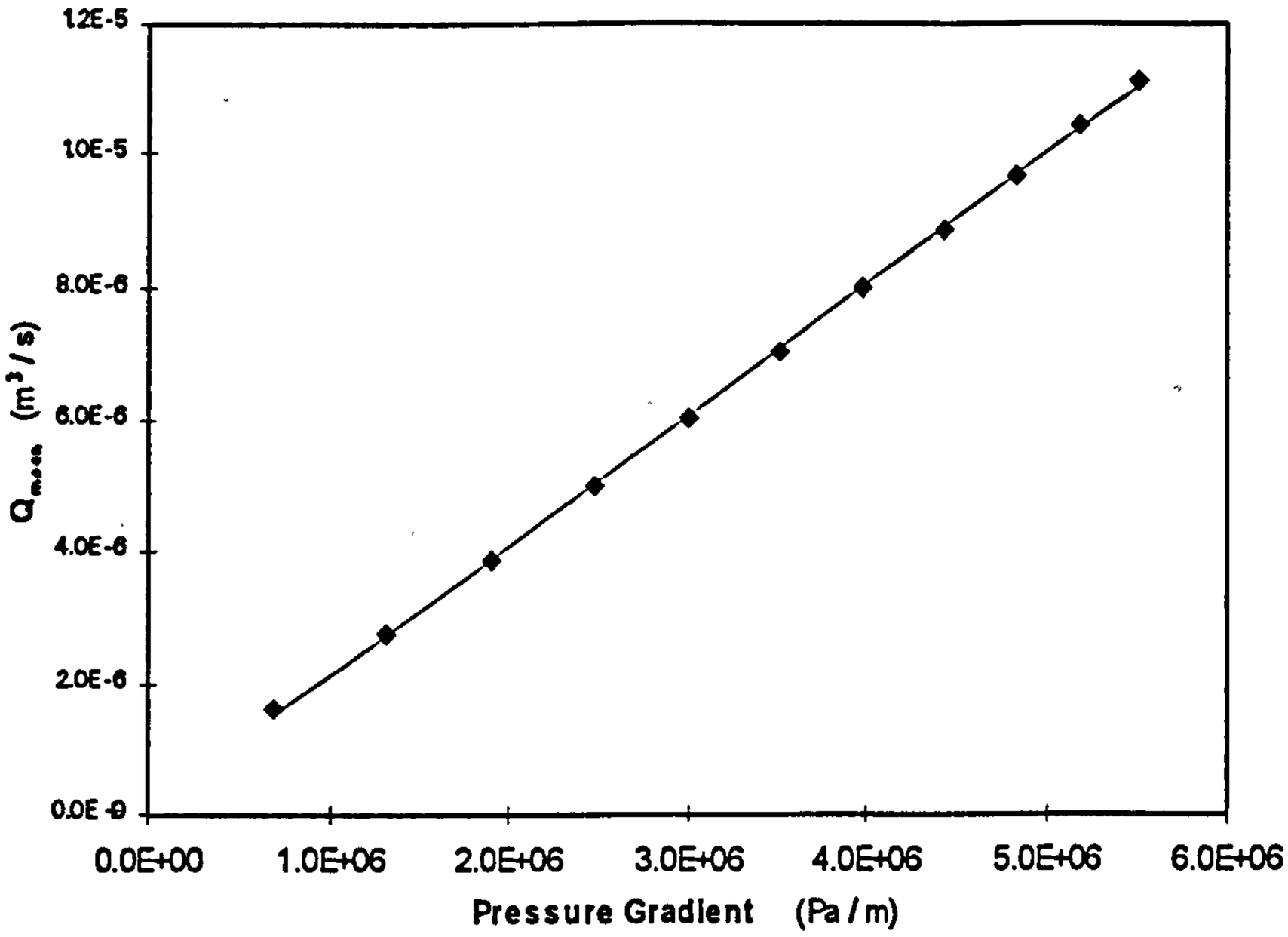

Fig. 6.22 Flow vs Pressure Gradient Plot for Specimen SC2 (7 μm ; $\zeta_o = 0.114$)

Roughness and flatness values of both the solid surface in 440C stainless steel and those of the porous testpieces, measured using a Rank Taylor-Hobson Form Talysurf 120L with a stylus radius 2 μm and 0.5 mm respectively, was far from ideal. The R_t value for the solid surface, for example, was close to 6.4 μm in the transverse direction. Longitudinal flatness was also no better than 3 μm.

Values for the porous surfaces were generally worse, and are summarised in the following section. Scanning electron microscopy also revealed that the mode of material removal was by grain pullout, instead of flattening of peaks of individual grains protruding above the plane test surface. The effect on the accuracy of the slip coefficient measurement would be significant due to the small flow gaps involved.

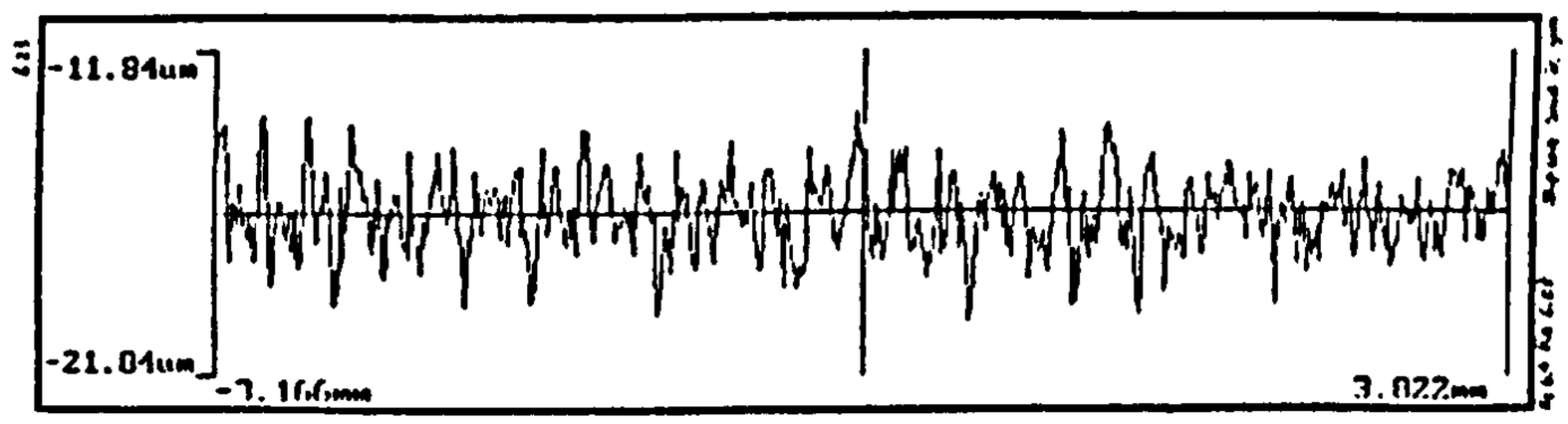

Fig. 6.23 Talysurf Measurement of the Solid Boundary Surface
(Transverse ; Probe radius 2 μm)

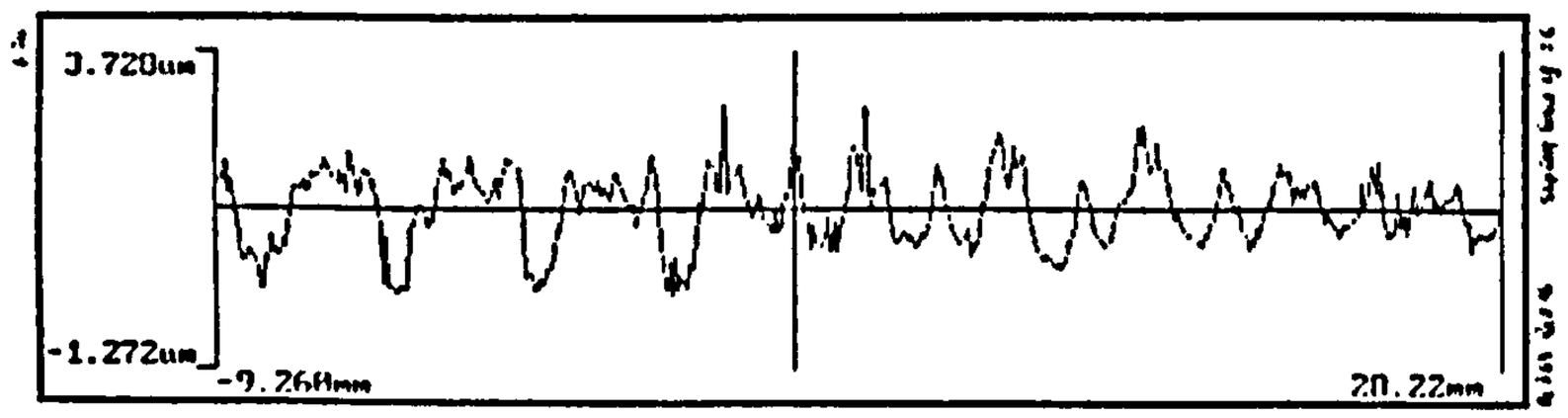

Fig. 6.24 Talysurf Measurement of the Solid Boundary Surface
(Longitudinal ; Probe radius 0.5 mm)

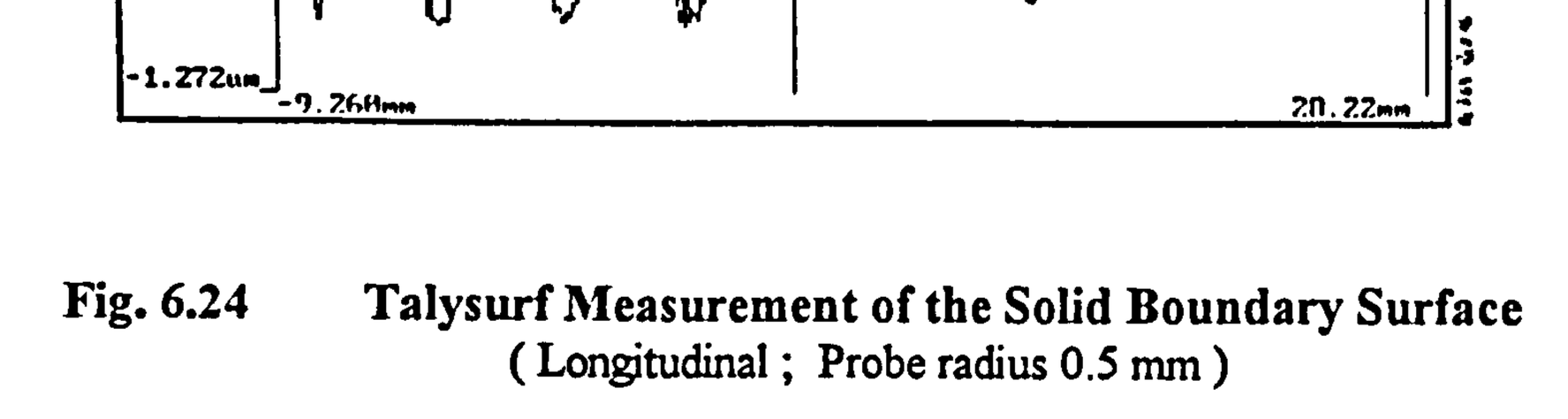

Fig. 6.25 Talysurf Measurement of Specimen SC4 (7 μm, $\zeta_o = 0.139$)
(Longitudinal ; Probe radius 0.5 mm)

In an attempt to quantify the increase in flow due to the roughness of the solid boundary surface, a dummy specimen was prepared from a solid piece of 440C stainless steel,. Flow measurements between the two solid surfaces were repeated as per the procedures above.

Rewriting equation 6.22 by referring the flow rate to the mean absolute pressure

$$Q_{mean} = \frac{h^3}{12.\eta} \cdot \frac{p_1 - p_2}{x_{12}} \cdot w_c \qquad (6.24)$$

Reorganising

$$Q_{mean} / \frac{p_1 - p_2}{x_{12}} / w_c = \frac{h^3}{12.\eta} \qquad (6.25)$$

or

$$\left(Q_{mean} / \frac{p_1 - p_2}{x_{12}} / w_c \right)^{1/3} = \frac{1}{(12.\eta)^{1/3}} \cdot h \qquad (6.25a)$$

The flow rate per unit pressure gradient per unit width, on the left hand side of equation 6.25, was determined from the slope of the Q_{mean} vs Δp plot as mentioned previously. The cube root of this left hand term was then taken, and plotted against the shim thickness as measured by a digital micrometer and averaged over ten points around the perimeter of the shim. As can be seen from Fig 6.26, equation 6.25a represents a straight line passing through zero, with a slope equal to $(1 / 12\eta)^{1/3}$, or 1.66×10^{-5}. The least square fitted line from the experimental data with solid boundaries, on the other hand, has a slope of 1.65×10^{-5}, but passes through an x-intercept of 6.5 μm.

This x - intercept represented an equivalent clearance to be added to the measured shim thickness, which accounted for the increase in flow rate through the channel due to surface roughness. As both top and bottom surfaces had similar surface finishes, the equivalent roughness clearance for each surface would be 3.25 μm, a value corresponding to halve the R_t value of the surfaces. As only one solid surface was

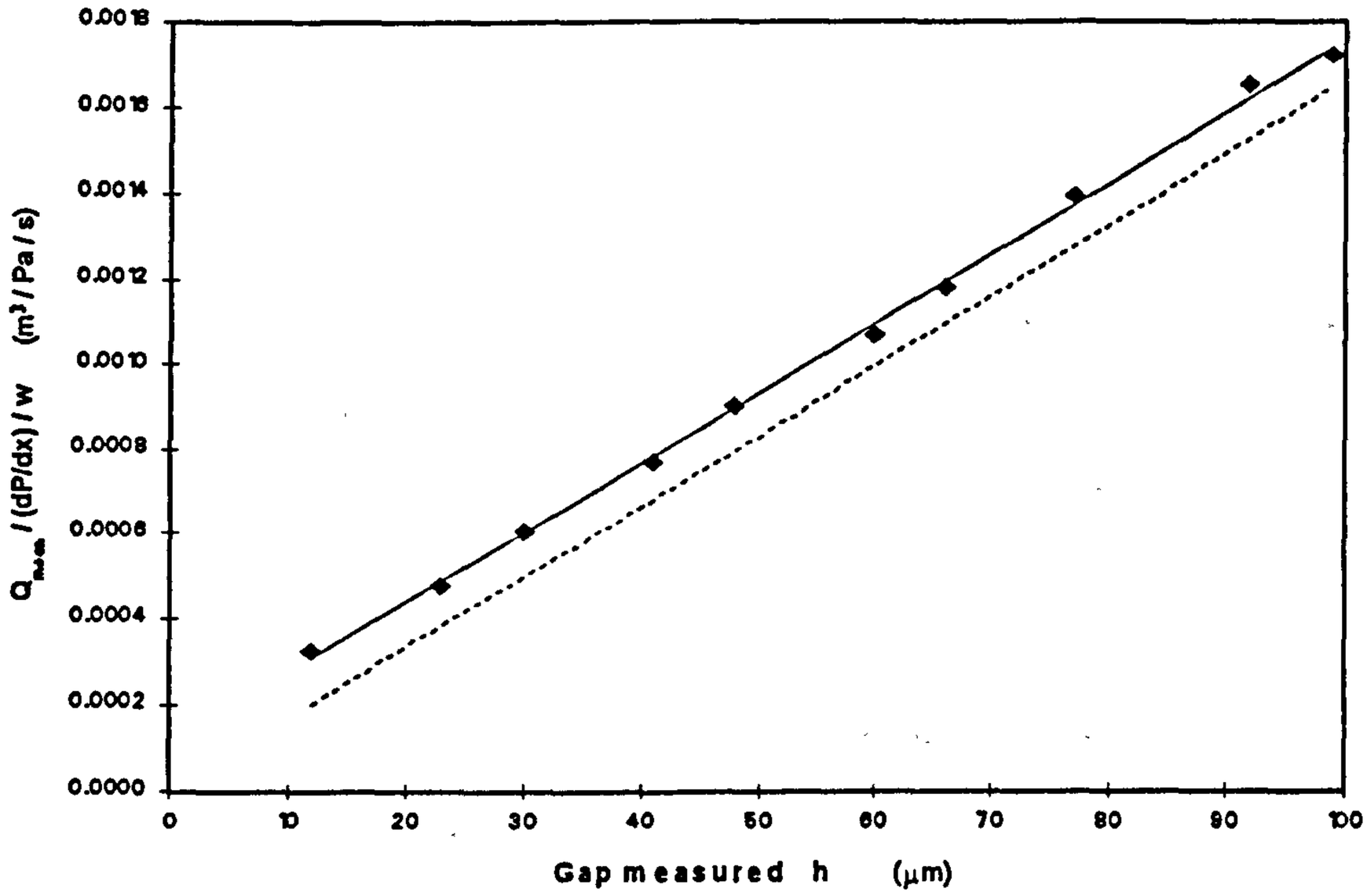

Fig. 6.26 Calibration of Slip Coefficient Measurement Fixture

(Flow between 2 solid surfaces)

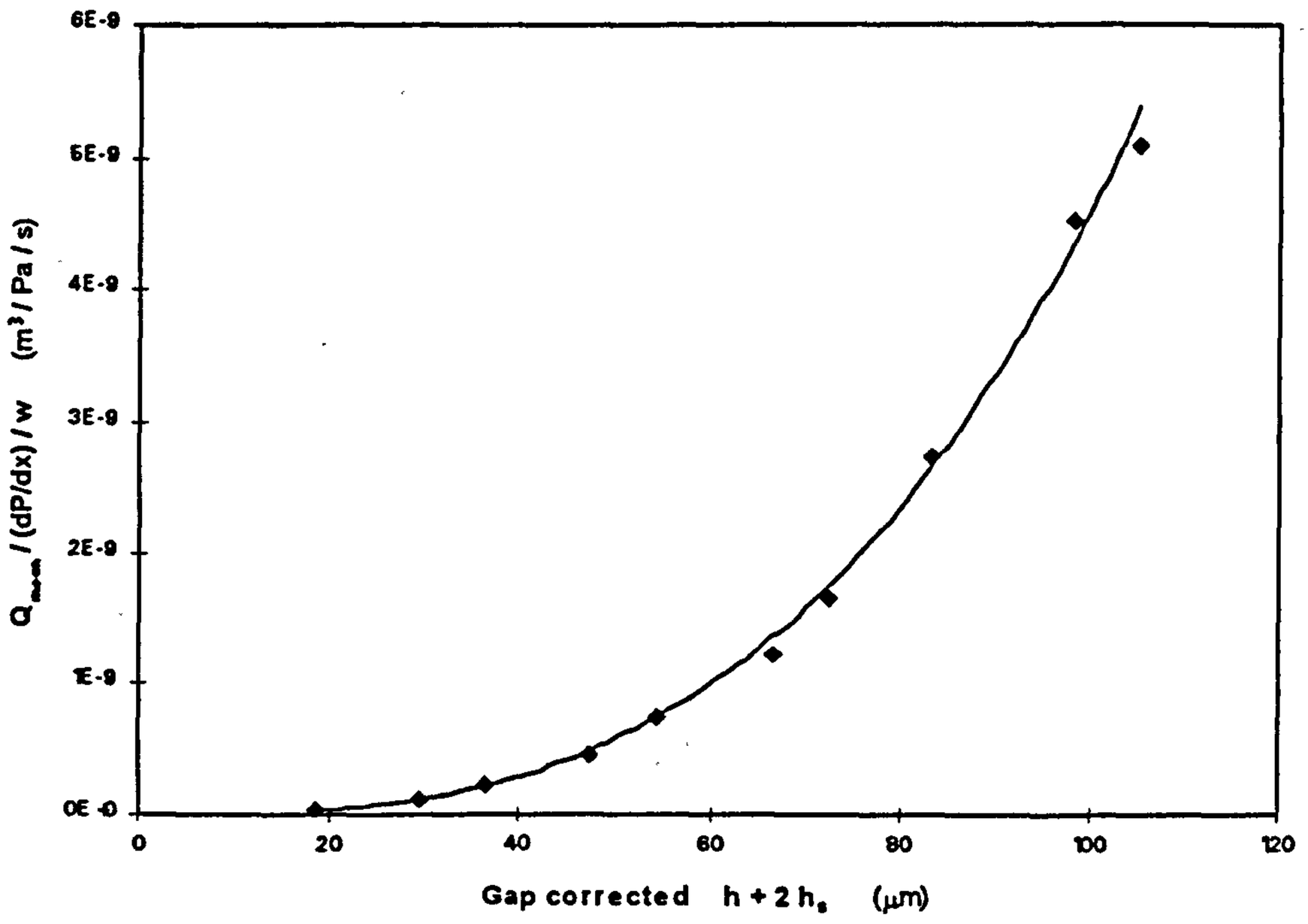

Fig. 6.27 Calibration of Slip Coefficient Measurement Fixture II

(Roughness correction for solid surfaces)

present during the slip coefficient measurement of porous specimens, the corrected flow channel clearance h_{cor} was then used in the calculations :

$$h_{cor} = h + h_s \tag{6.26}$$

where h_s equals 3.25 μm as determined from above. The roughness effect of the porous surface, however, could not be corrected in the same manner, as the R_t values were not a true measure of the surface finish in the presence of the pores. An indirect mathematical correction was used instead.

Assuming first the increase in flow due to the unevenness of the porous surface alone could be accounted for by an equivalent additional clearance h_o, as in the case for the solid surface, the total clearance would be $h + h_o + h_s$. The value for h_s had already been determined from solid surface pre-calibration. By obtaining a series of values for Q_p / Q_s at different values of h, a least square fitting routine could be applied to determine the slip coefficient α_s and the clearance correction h_o , using the definition

$$\Delta Q_{cal} = \frac{3.(\sigma_s + 2\alpha_s)}{\sigma_s.(1+\alpha_s.\sigma_s)} \tag{6.27}$$

where σ_s was determined from

$$\sigma_s = \frac{h + h_s + h_o}{\sqrt{\Phi_e}} \tag{6.28}$$

and an error function defined by

$$E_r = \frac{1}{n_{meas}}. \sum \left[(\Delta Q_{meas} / \Delta Q_{cal}) - 1\right]^2 \tag{6.29}$$

Values for α_s and h_o corresponding to the minimum mean square error was determined iteratively on an Excel 5.0 spreadsheet. The range of h used in the fitting was limited to

$2.d_w$ and above. Below that value, the measured values deviated significantly from the theoretical prediction, as the flow was no longer believed to be rectilinear.

The inertia effect of some of the test samples was quite significant in the permeability tests. This would in turn affect the value of σ_s. Rather than using just the viscous coefficient, an equivalent permeability coefficient Φ_e was introduced to combine the inertia effect with the viscous term, and was determined from the two measured coefficients and the upstream and downstream pressure according to the Appendix D. The correction was incorporated in the LabWindows software.

6.3.4 Experimental Results

The slip coefficient of thirteen porous alumina specimens was measured. The specimens were HIPed from particles of 0.5 - 23 μm, and had a porosity between 0.1 and 0.4. Properties of the test samples, as well as results for the slip coefficient α_s and the flow channel height correction h_o, are listed in Table 6.2.

As already pointed out by Beavers [52], measurements of α_s deviates significantly from the theoretical predictions for flow channel clearances approaching individual particle size of the porous substrate. This is because at such small clearances, the assumption of rectilinear flow of fluid at the porous boundary is no longer valid.

Measurement results obtained in the present investigation appeared to support this argument. At gaps below $2 \times d_w$, the measured increase in flow rate in the presence of the porous boundary, given by $(Q_p / Q_s) - 1$, was in most cases much higher than that predicted by the average value of α_s from measurement points with larger gaps. Slip coefficient values calculated on a point to point basis were much smaller at small gaps, increasing asymptotically to a steady value at larger clearances. This deviation from the Beavers' model was more significant for samples with higher porosity. Data obtained from samples with porosity below 0.15, for example, showed much better agreement

with the Beavers and Joseph model (Fig. 6.28, 6.29). It is believed that the smaller void volume in low porosity samples reduces the interaction between the flow in the flow channel and that at the immediate vicinity of the porous surface, thus resulting in a more rectilinear flow than otherwise. The values listed from the above table were obtained by the analysis procedures as described in the previous section, but excluding clearances below $2 \times d_w$.

Table 6.2 Summary of Slip Coefficient Test Sample Properties

ID	d_w (μm)	ζ_o	Φ_v (m^2)	Φ_i (m)	α_s	Flat's (μm)	R_a (μm)	R_t (μm)	h_o fitted
SC1	0.5	0.285	2.52E-16	5.61E-14	0.003	0.3	0.1	0.92	0.2
SC2	7	0.114	1.87E-16	2.01E-11	0.0036	4	2.6	18.5	1.2
SC3	7	0.134	1.11E-15	1.76E-11	0.0064	3	1.96	14.8	0.8
SC4	7	0.139	4.28E-15	6.86E-10	0.008	2	2.4	15.5	1.2
SC5	7	0.395	7.16E-14	7.05E-08	0.025	4	2.1	15.7	-2.5
SC6	13	0.268	7.43E-14	1.11E-07	0.039	4	2.8	19.4	0.2
SC7	13	0.388	1.98E-13	1.85E-07	0.037	5	3.1	23.4	-0.8
SC8	13	0.389	1.92E-13	2.38E-07	0.052	5	3.4	24.9	2.2
SC9	23	0.211	1.86E-14	9.87E-10	0.022	5	3.4	23.8	1
S10	23	0.245	7.73E-14	2.92E-08	0.028	5	3.9	25.4	1
SC11	23	0.288	3.33E-13	3.26E-07	0.043	5	4.5	25.9	0
SC12	23	0.391	5.80E-13	7.41E-07	0.06	4	5.8	42	2.5

Correlation of the slip coefficient with open porosity suggested a possible linear relationship (Fig. 6.30), given by :

$$\alpha_s = 0.14 \times (\zeta_o - 0.09) \qquad (6.30)$$

The wide spread of data implies that the equation should be treated with caution. Further experimental results, and in particular, with much improved surface finishing, would make a more reliable correlation possible.

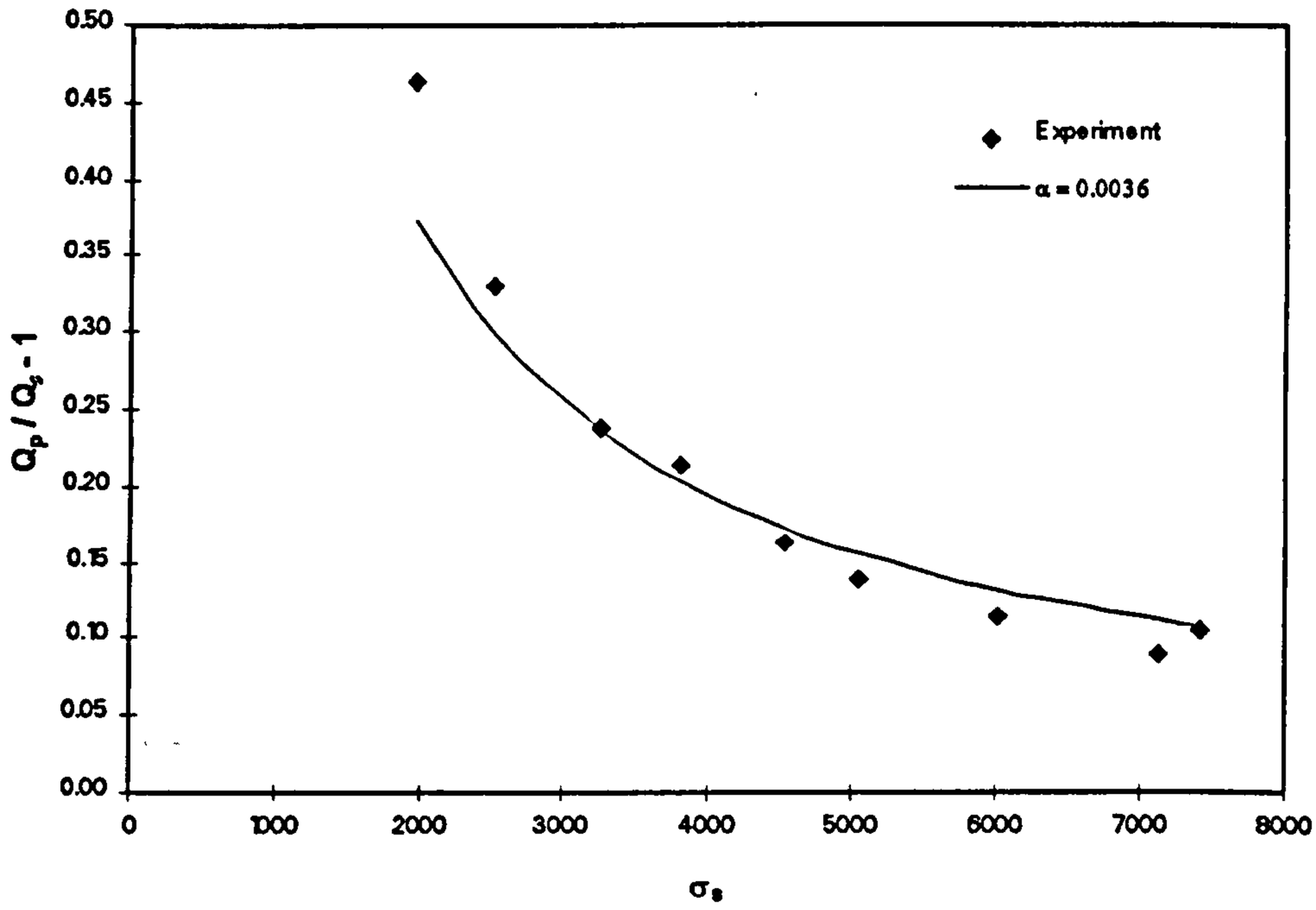

Fig. 6.28 Slip Coefficient Plot for Specimen SC2 (7 μm, $\zeta_o = 0.114$)

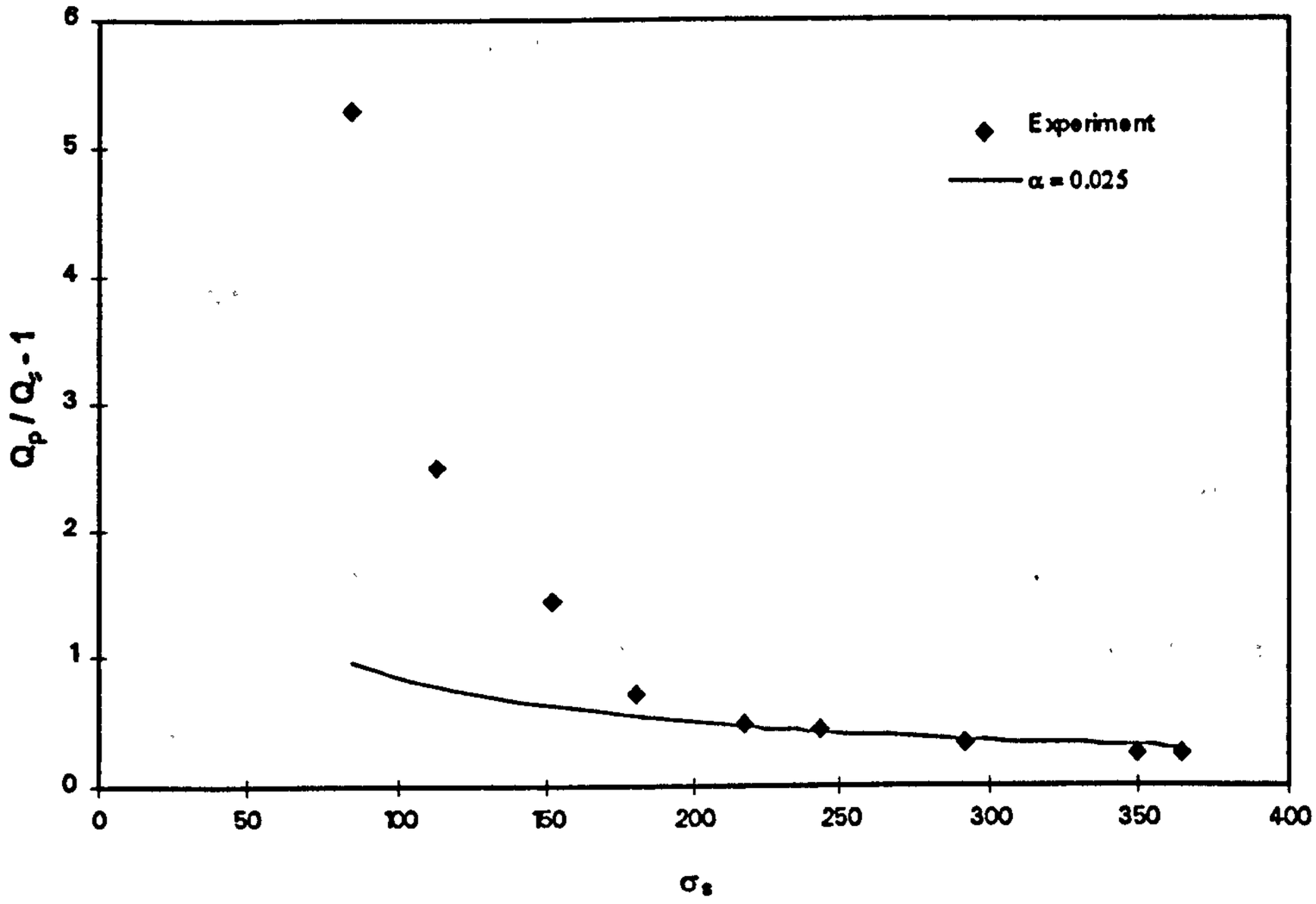

Fig. 6.29 Slip Coefficient Plot for Specimen SC5 (7 μm, $\zeta_o = 0.395$)

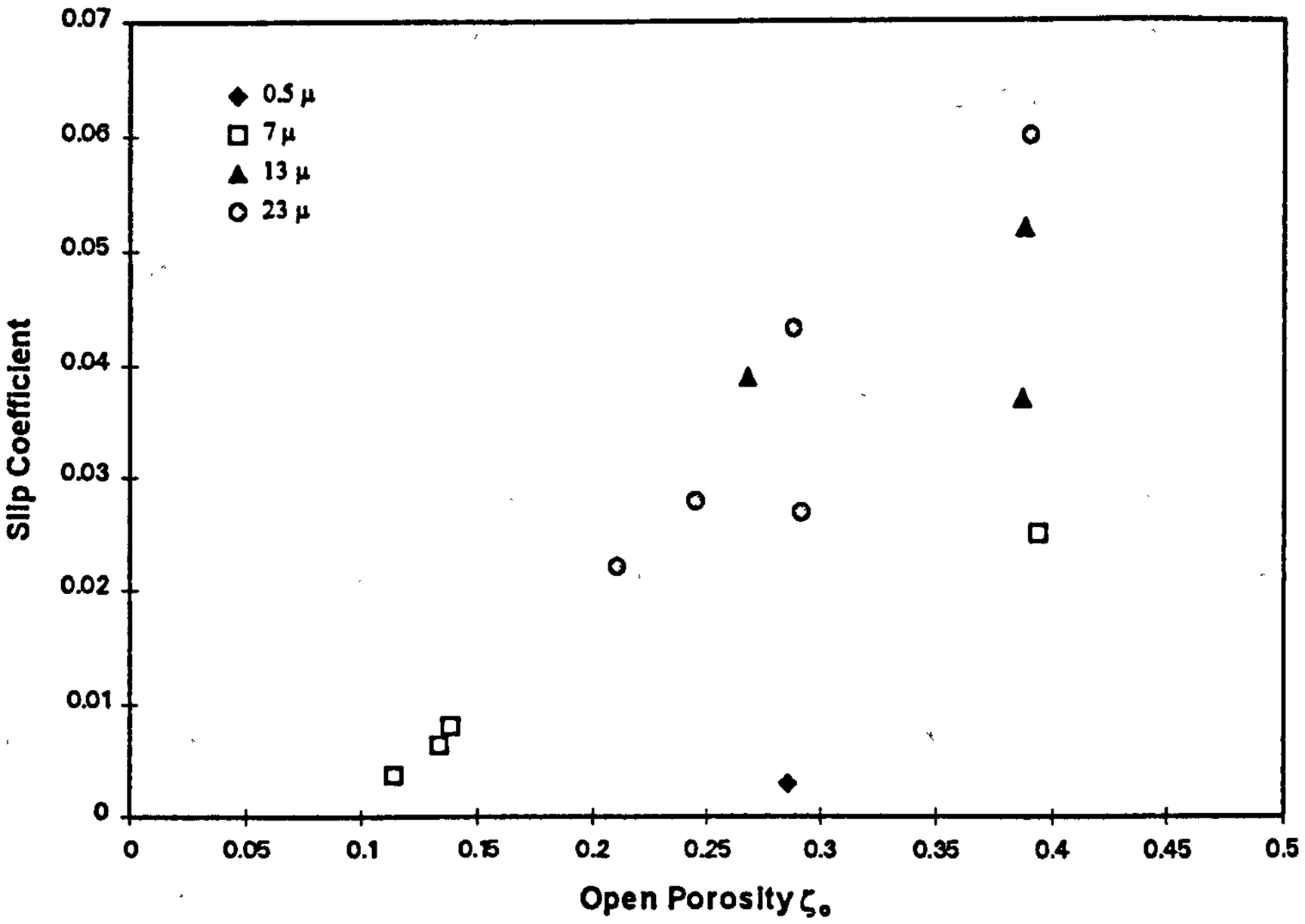

Fig. 6.30 Porosity Dependency of Slip Coefficient

7. MEASUREMENT OF STRUCTURAL PROPERTIES

7.1 FLEXURAL MODULUS

As already mentioned in chapter 3, the flexural modulus of the porous material is of interest to the bearing designer, as excessive deviations from the ideal bearing geometry due to bearing pad deflection under pressure could have negative effects on the actual bearing performance [60].

7.1.1 Measurement Method

Compared with metals, most ceramics have a relatively low strain to fracture. As a result, most standard methods of testing their flexural modulus are based on resonance frequency [225, 226, 227] of rectangular beam type specimens, also known as the free-free beam resonance technique. Other measurement methods such as those based on sonic velocity [228], ultrasonic pulse spectroscopy, and ultrasonic composite oscillator technique [229] have also been used, with good agreement between results obtained by different methods. Successful application of these methods to the testing of porous materials has also been reported [230].

As the specimens produced in the present work were of a circular disk shape, it would be more logical to use a test method based on the resonance of disks, rather than machining every specimen to a rectangular beam. Despite the readily available information on the vibration of circular plates [231, 232], methods based on resonance by continuous excitation do not appear to be widely used. The literature survey revealed only one report of using a centrally clamped disk specimen in the measurement of elastic modulus [233], but the agreement between such measurement and data obtained from other established test methods was not satisfactory. The limitation appeared to be the determination of the

exact boundary conditions (e.g. the rigidity of the clamp interface at either the centre or perimeter). As the numerical results in [234, 235] indicated, the resonance frequency could vary significantly with the rigidity of the clamping.

A technique recently developed in Belgium [236, 237], and based on impulse excitation, was also considered to be suitable for disk-shaped specimens. A number of published reports [229, 238, 239] indicated that the technique produced results consistent with the above mentioned established methods for beam type specimens. Successful applications for disk specimens have also been published [240].

The initial plan was to use the free-free beam resonance method to determine the flexural modulus of the porous specimens, using the measurement equipment developed at Cranfield [241]. The working principle behind this equipment is essentially identical to the ASTM method [226], except for the exciting and measuring transducer configurations. Simple modifications to the existing rig were necessary to accommodate the much smaller specimen size of 40 mm x 4 mm x 2 mm, as documented under drawing no. MU291-A400.

Despite the success of the mechanical modifications, the electronic systems of the equipment unfortunately ceased to function in the course of the present work. There were additional difficulties in grinding the specimens to such a small thickness. As a result, the impulse excitation method was used instead. Measurements were carried out on disc specimens courtesy of J.W. Lemmens-Elektronika N.V., using their GrindoSonic measuring system (Fig. 7.1).

7.1.2 Porosity Dependency

Values for flexural and shear moduli, as well as the Poisson's ratio, for a range of porous disc specimens were measured with the impulse excitation technique. The specimens were hot isostatically pressed from 100% α-alumina powders of 0.5 - 63 μm,

with a porosity range between 0.12 and 0.45. Diameters of the specimens ranged from 40 to 50 mm, thickness from 4 to 8 mm. The results showed an almost exponential increase in elastic moduli as total porosity approaches zero. The Poisson's ratio also tended to increase at lower porosity, the trend resembling more that of a linear relationship (Figs. 7.2 to 7.4).

The empirical relationship between flexural modulus and porosity of various materials has been extensively investigated, both theoretically and experimentally. Up-to-date reviews have been published by Wagh [181] and Rice [242]. There are two main schools of thought. The first, represented by Duckworth [243] and Spriggs [244], attempted to describe the relationship with an exponential function :

$$E = E_o.e^{-b\zeta} \qquad (7.1)$$

Others, amongst them Wagh [181], used a power law function :

$$E = E_o.(1 - \zeta)^a \qquad (7.2)$$

where the constant **a** could be shown to be equal to **b** in the exponential function for low porosity values.

The power law model was actually first proposed by Phani and Niyogi [245] in a slightly different form, based on theory of elasticity of a continuum with the pores as a second phase :

$$E = E_o.(1 - \zeta / \zeta_{cr})^a \qquad (7.3)$$

where ζ_{cr} is known as the critical porosity, at which the elastic modulus becomes zero. Wagh [181] argued that fitting of experimental data yielded $\zeta_{cr} = 1$, hence the above simplified form.

More complicated functions have also been proposed, e.g. that by MacKenzie [246] :

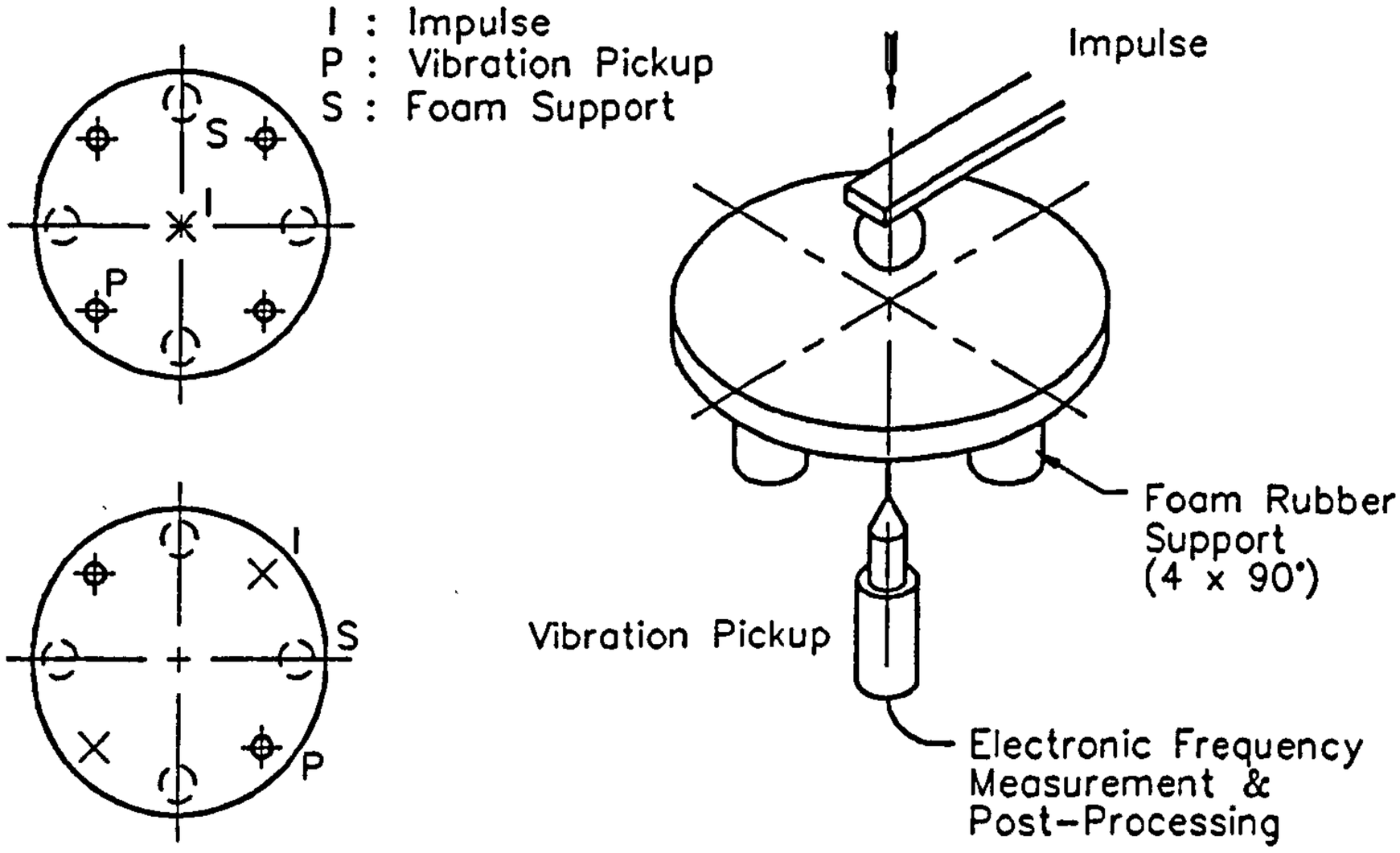

Fig. 7.1 Flexural Modulus Measurement of Discs by Impulse Excitation

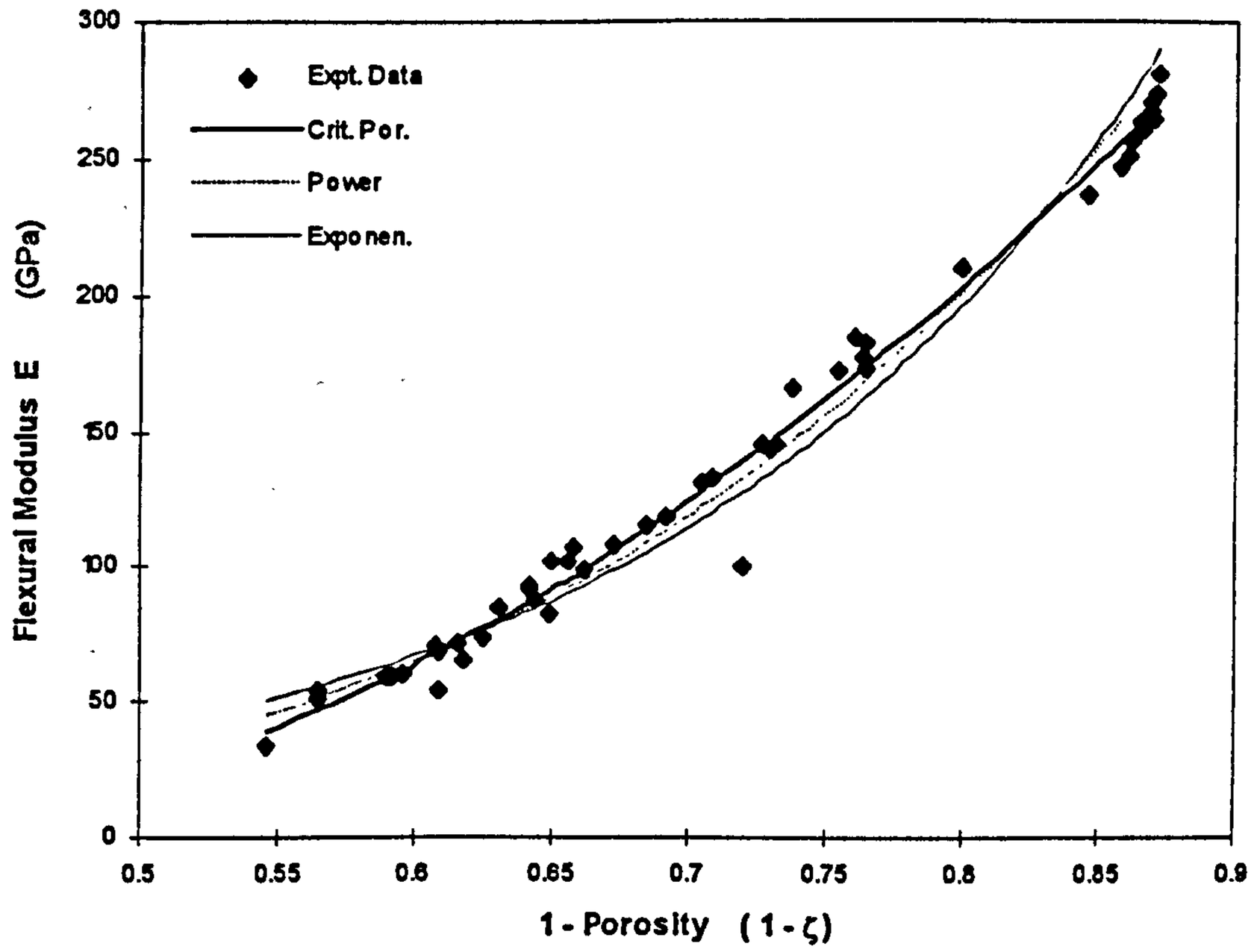

Fig. 7.2 Porosity Dependency of Flexural Modulus

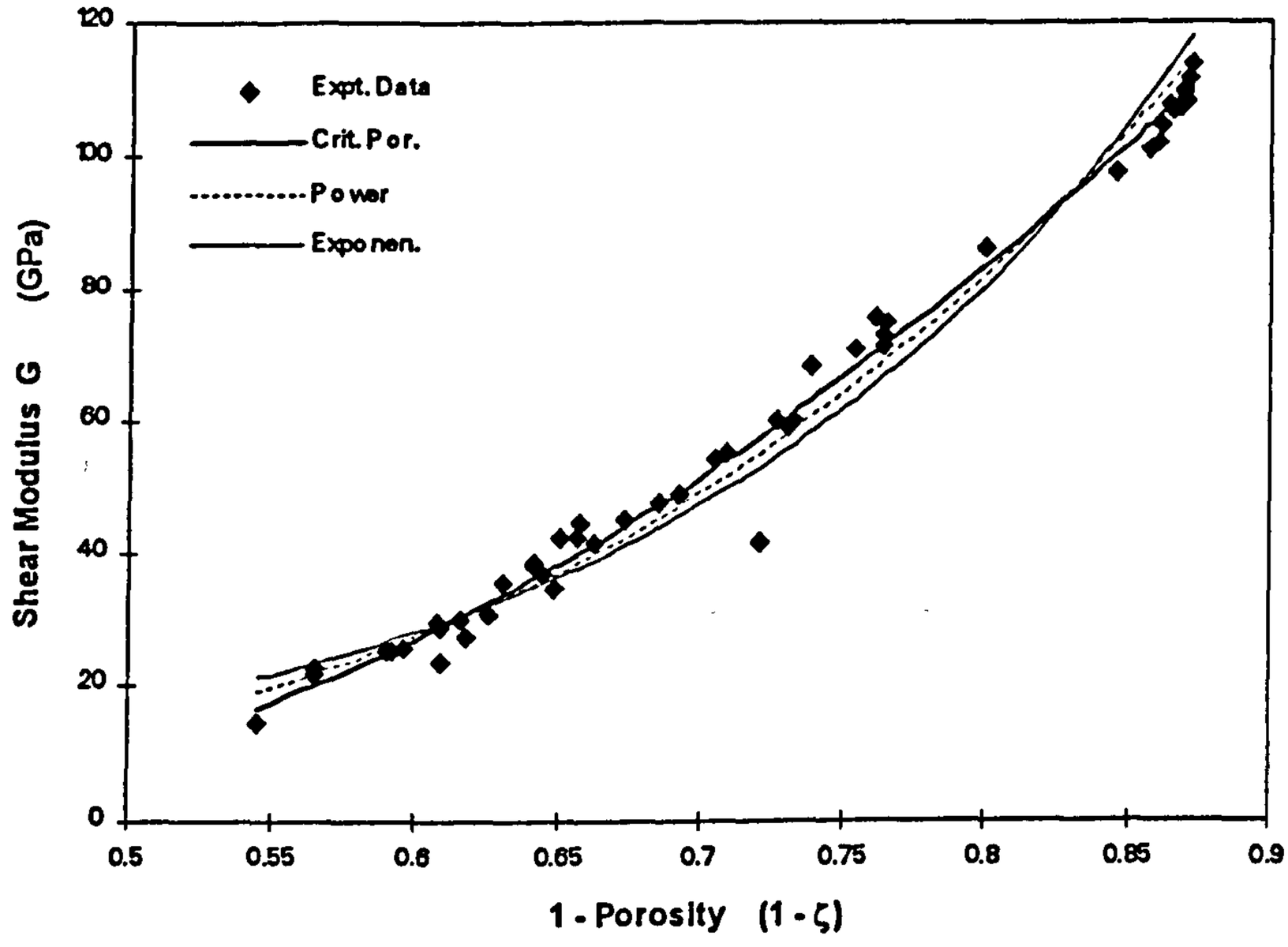

Fig. 7.3 Porosity Dependency of Shear Modulus

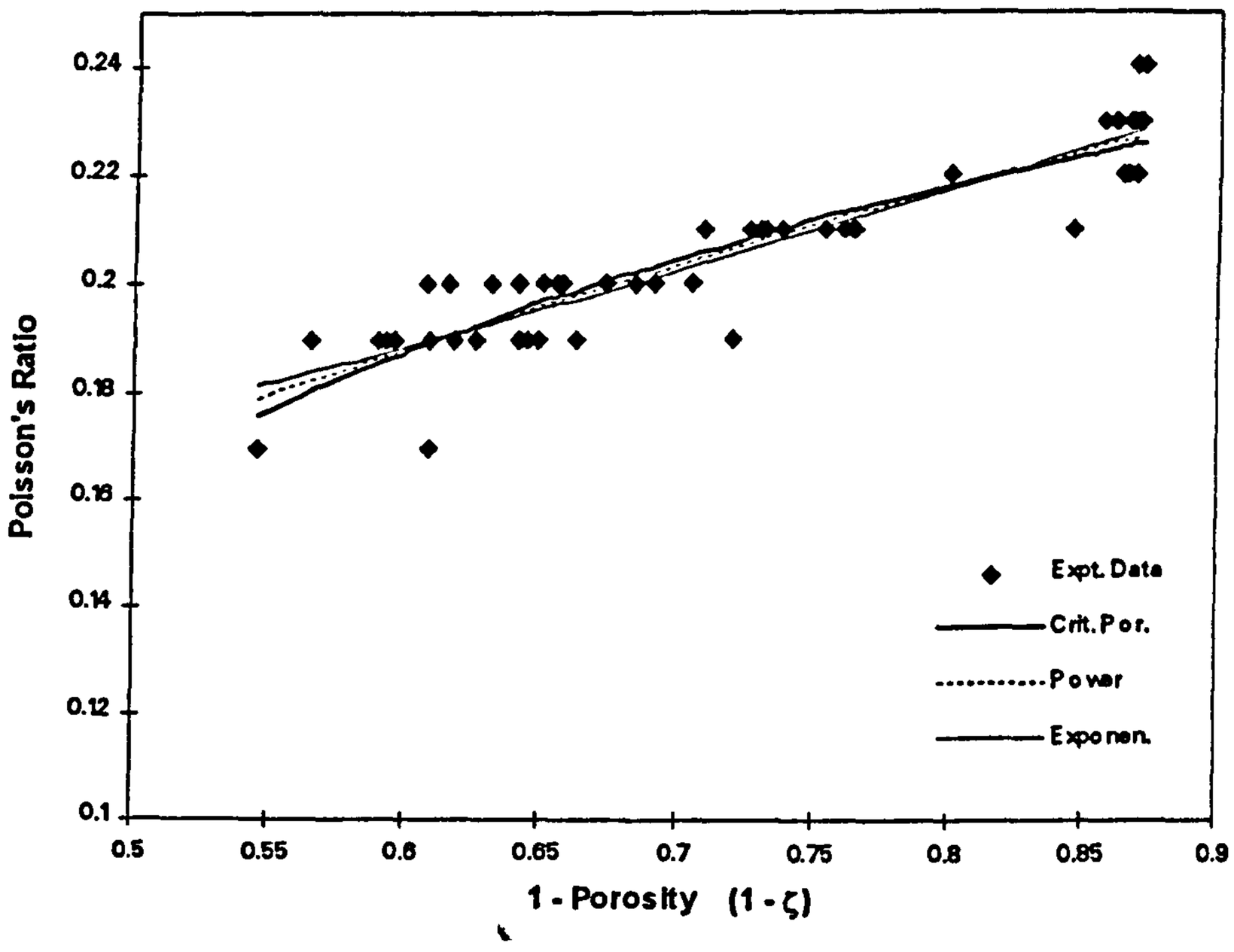

Fig. 7.4 Porosity Dependency of Poisson's Ratio

$$\frac{1}{E} = \frac{1}{E_o\zeta} + 3.\frac{1-\zeta}{4.G_o.\zeta} + O\left[(1-\zeta)^3\right] \qquad (7.4)$$

though they do not appear to be in widespread use. Also, no data for the porosity dependency of Poisson's ratio appear to exist.

Experimental results obtained in the course of the current work were least-squares fitted to all of the first three functions listed above. All three functions gave a reasonably good fit to the measured data, with very little difference in their mean square errors of fit. The results are summarised in Table 7.1.

Table 7.1 Porosity Dependency of Elastic Constants

Elastic Constant	$X = X_o.(1-\zeta)^a$ [181]		$X = X_o.e^{-b\zeta}$ [243]		$X = X_o.(1-\zeta/\zeta_{cr})^a$ [245] $\zeta_{cr} = 0.625$	
Empirical Constants	X_o	a	X_o	b	X_o	a
Flex-modulus E (GPa)	479.7	3.91	576.1	5.38	409.5	1.82
Shear-modulus G (GPa)	193	3.82	230.8	5.26	165.4	1.78
Poisson's Ratio ν	0.244	0.508	0.25	0.71	0.239	0.234

The empirical function based on the theory of Phani [245] appeared to provide a slightly better fit. The critical porosity value ζ_{cr} of 0.625 was obtained numerically as one that gave the least error of fit to measured data. Also worth noting are the fitted values for the elastic constants at full density X_o. The flexural modulus E_o of α-alumina, for example, has been quoted as 410 GPa [182]. Both mathematical models based on power laws appeared to give X_o values in better agreement with published data.

Data listed in [181] from a number of different sources gave a value for the exponential **a** in equation 7.2 between 2 and 5. According to the theory proposed by Wagh, this value is

an indirect measure of the tortuosity, with a higher value of a implying a wider distribution of pore cross-sectional area. Wagh obtained a value close to 2 for the constant a, first theoretically and then experimentally for a large collection of specimens of various ceramics sintered under normal pressure, but a value close to 4 for hot-pressed specimens and those with sintering aids. The fitted value obtained from the present work is 3.91, indicating a resemblance to hot pressing, suggest a higher tortuosity. Also worth noting is the slightly higher value of the constant b obtained from the exponential fit, which is expected to be equal to a in the simple power law model.

7.2 Flexural Strength

7.2.1 Measurement Method

Fracture testing of the disk-shaped specimens was carried out using the concentric ring loading method developed by Godfrey [247], which has been successfully employed at Cranfield [248] and elsewhere [249]. One particular advantage of this method is that the edges of the specimen are not subjected to any loading, and as such do not require a high degree of finish. The method was a natural choice for the present work as the specimens were of a circular disc shape. It also resembled the actual loading conditions of the thrust bearing pad more closely.

The test involved axially loading the specimen to fracture in a compression testing machine (Instron 6025 with a 5 kN load cell of 0.5% accuracy) between two concentric rings of ball bearings. As the outer diameters of the specimens ranged between 46 mm and 50 mm, a simple fixture was designed to hold the specimen centre to a supporting ring of 69 bearing balls, the latter located accurately (to within 0.02 mm diametrical) on a 44 mm pitch circle, and seated on a hardened reference surface. (Refer to drawing no. MU291-A200 in Appendix H.) The load ring of 25 bearing balls, also of 2 mm in

diameter, was held concentric to the lower supporting ring at the outer diameter of the top plate which carried the loading balls in an annular groove. The pitch diameter of the loading balls was 16 mm. A ground conical centre, screwed onto the compression tester, engaged onto a centre hole on the top plate to ensure concentric loading and to minimise the effect of any angular misalignment between the compression tester and the specimen holder.

The biaxial flexural failure stress was then calculated using the following equation:

$$\sigma_r = \sigma_t = \frac{3.W_f}{2\pi.z_p^2}\left[(1+\nu).\ln(r_s/r_l)+\frac{(1-\nu).(r_s^2-r_l^2)}{2.r_p^2}\right] \qquad (7.5)$$

For certain specimens experiencing higher than expected shrinkage, or those actually used as test bearings, the outer diameter was too small to fit into the ring fracture tester. As a result, these specimens were sliced into small rectangular bars of approximately 40 mm x 6 mm x 4 mm, and fracture tested using a 4-point bend test fixture. The point loading was applied through hardened needle rollers of 2 mm diameter, which were located in ground V-grooves to ± 0.01 mm. The supporting rollers had a separation of 20 mm, the loading rollers 10 mm.

The flexural failure stress is given by:

$$\sigma_f = \frac{6.W_f.b_1}{w_b.z_b^2} \qquad (7.6)$$

The actual width and thickness of the bar specimens were measured with a digital micrometer. Locating pins embedded in the support roller block ensured the proper alignment of both the specimen and the loading block, thus guaranteeing b_1 to be exactly 5 mm.

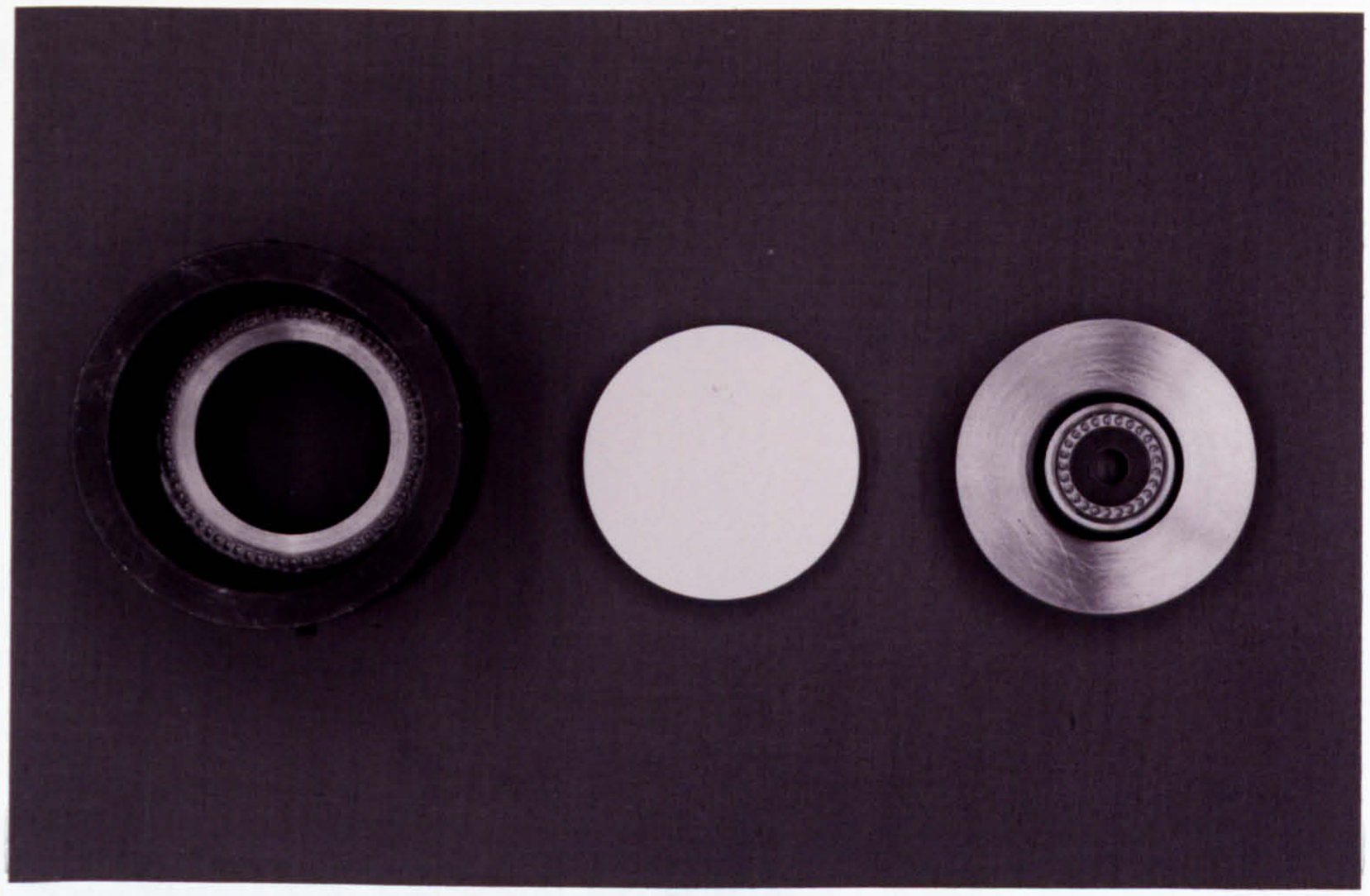

Fig. 7.5 Fixture for Concentric Ring Fracture of Disc Specimens

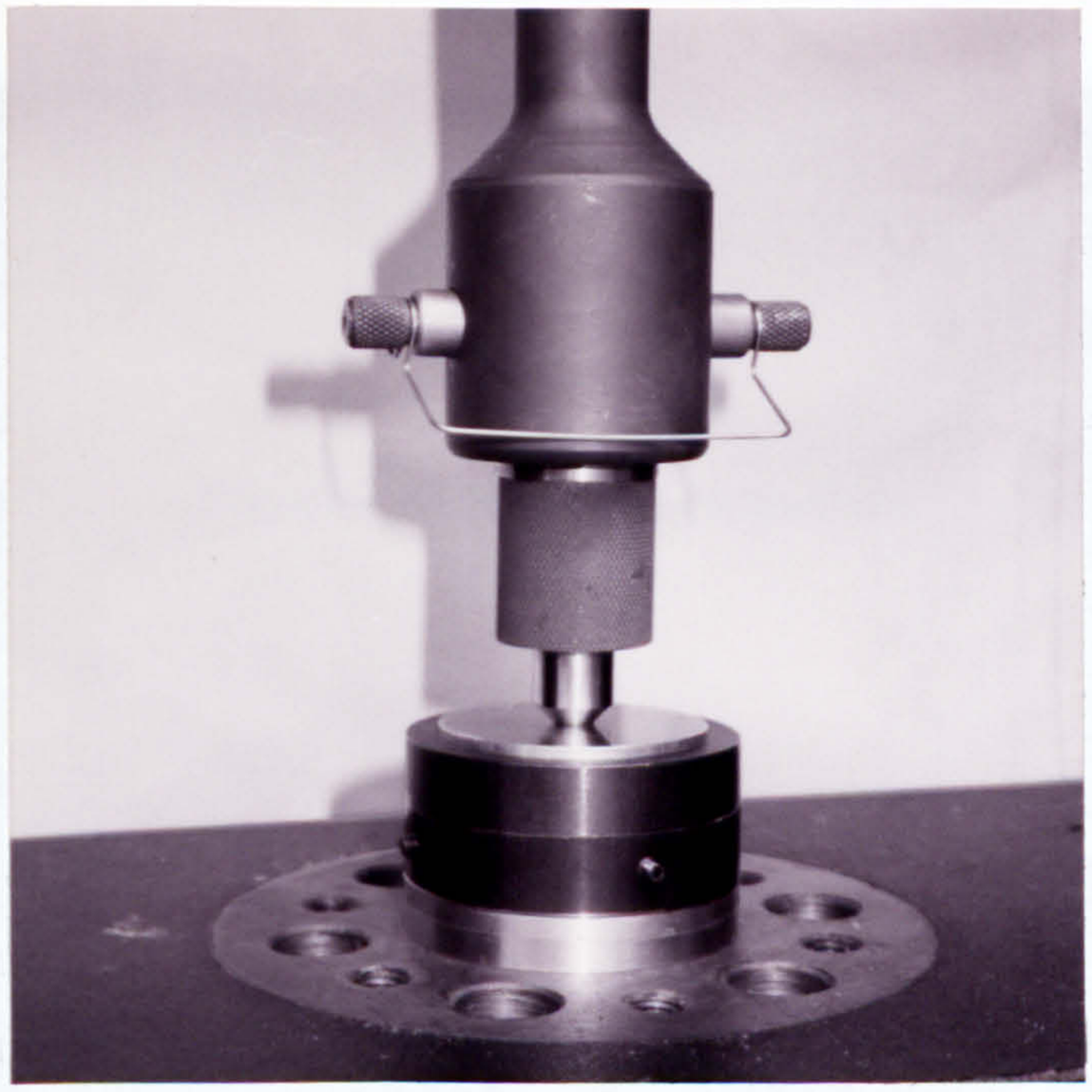

Fig. 7.6 Set-up for Concentric Ring Fracture of Disc Specimens

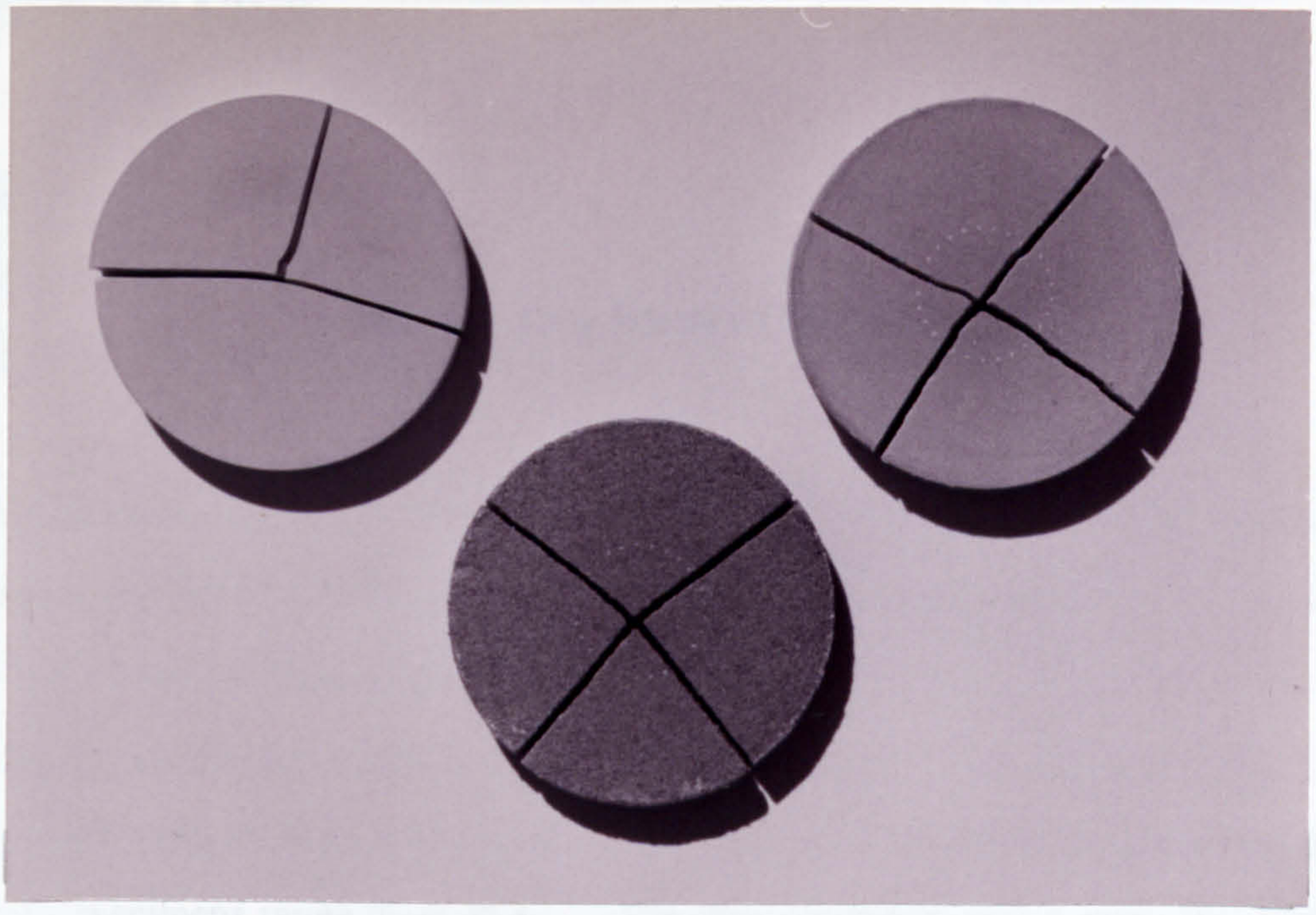

Fig. 7.7 Examples of Fractured Specimens
(Note radial fracture lines through the centre)

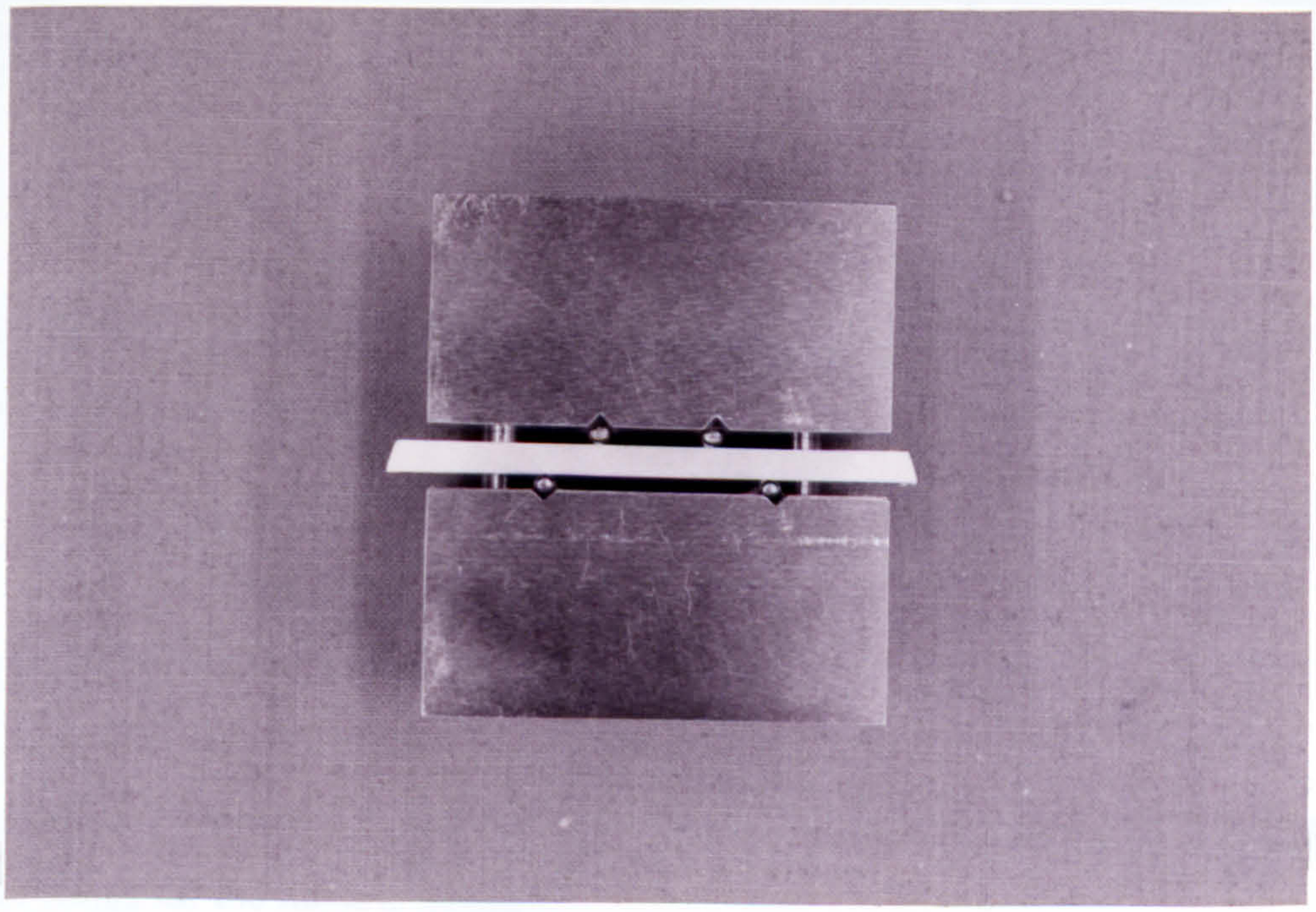

Fig. 7.8 Four - Point Bend Test for Bar Specimens

7.2.2 Porosity Effects

Specimens used in flexural strength testing in the current work can be subdivided into three main categories -- concentric ring-fractured discs, 4-point bend test of bars, and ring fracture of specimens with lithium fluoride as sintering aid.

All specimens except those with sintering aid were hot isostatically pressed from 100% α-alumina powders of 0.5 - 400 μm, with a porosity range between 0.11 and 0.46. Specimens from powders larger than 42 μm were based on a bi-modal mixture to aid sintering , with 0.5 μm powders of 13 - 33% by weight as the second mode. Lithium fluoride of 1 - 4% by weight was used as sintering aid for the rest. Diameters of the disc fractured specimens range from 45 to 50 mm, thickness from 4 to 8 mm. Bar specimens were cut and ground to give a cross section of approximately 6 x 4 mm.

The dependency of fracture properties on porosity has also been studied extensively. Wagh [250] extended his work on elastic constants to include flexural strength. Using the same power law model :

$$\sigma_f = \sigma_o.(1 - \zeta)^c \qquad (7.7)$$

he conducted theoretical analysis to deduce that the exponent **c** should be related to **a** for the case of elastic modulus by :

$$c = a + 0.5 \qquad (7.8)$$

This was backed up in his study by experimental evidence.

An exponential function similar to that of the elastic constants was also used by Duckworth [243] for the flexural strength :

$$\sigma_f = \sigma_o.e^{-d\zeta} \qquad (7.9)$$

Experimental results obtained in the course of the current work were least square fitted to both of the above listed functions. As in the case of the elastic constants, the results show a similar trend of increase with decreasing porosity. Both functions fit the measured data well. The empirical constant **c** has a value around five for both bar and disc specimens, but a slightly lower value of 4.5 for specimens with LiF. As expected, flexural strength is highest for bar specimens, followed by disc specimens and those with LiF. The lower values obtained in the concentric ring-fracture test was attributed to the bi-directional stresses in an axisymmetric loading system. The use of sintering aids has been known to result in lower strength. Again the Duckworth model consistently gives higher values of σ_o.

The empirical constants **c** and **d** also differ from **a** and **b** (corresponding to the elastic constants) by more than 0.5 as suggested by Wagh [250]. Such larger than theoretically predicted differences also appeared in actual experimental data in his report [250], although Wagh attributed the discrepancy to a possible glassy phase in that particular set of specimens. Bearing in mind that the constants are an indirect measure of the tortuosity, and that the constants **a** and **b** assumed higher than expected values as deduced from elastic constants measurements, such deviation might also be attributed to the difference in pore structure between the specimens from the present work and those used by Wagh.

A summary of the results is given in Table 7.2 and Figs. 7.9, 7.10. The spread of data was not unexpected, as each point only represents one single fracture test result. The fracture of ceramics is known to be statistical by nature. More reliable data could only be obtained by repeating the fracture test at least 20 times on specimens of the same porosity and particle size, and using the results to calculate the characteristic strength and the Weibull modulus [251].

Table 7.2 Porosity Dependency of Fractural Properties

Flexural Strength (MPa)	$\sigma = \sigma_o.(1-\zeta)^c$ [250]		$\sigma = \sigma_o.e^{-d\zeta}$ [243]	
Empirical Constants	σ_o	c	σ_o	d
Disc specimens	352	5.03	580	7.7
Bar specimens	745	5.16	893	6.9
Disc specimens with LiF	94.9	4.54	116	6.11

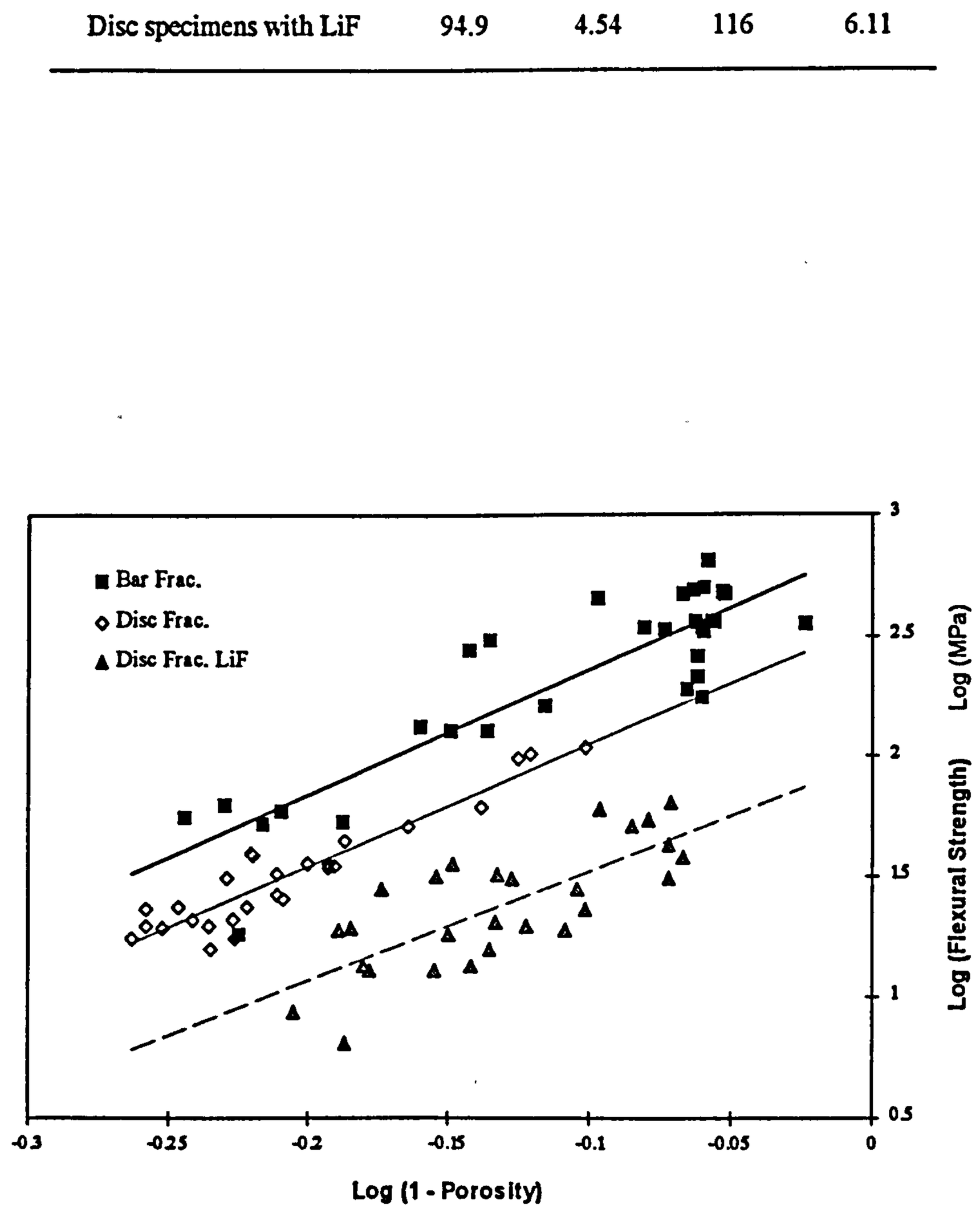

Fig. 7.9 Porosity Dependency of Flexural Strength (Power law)

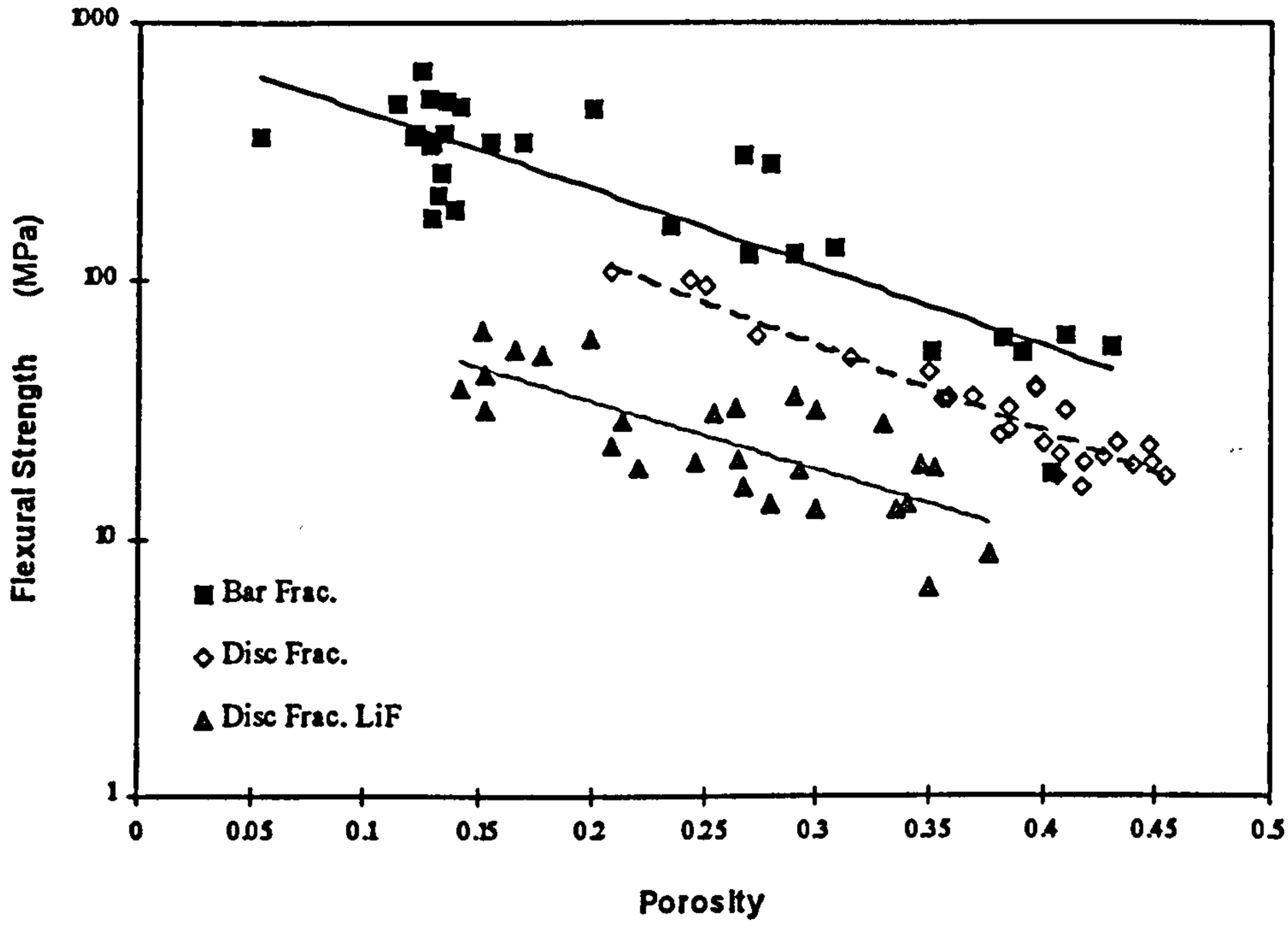

Fig. 7.10 Porosity Dependency of Flexural Strength (Exponential)

8. TWO-LAYERED POROUS STRUCTURES

The performance advantages, particularly in terms of pneumatic stability, of aerostatic bearings with a two-layered porous structure have already been discussed in Chapter 2. The processing and mechanical properties of hot isostatically pressed porous alumina substrates have also been investigated. Such a substrate with the correct permeability and porosity could also be used to form the backbone of the two-layered structure.

A fine pored layer has to be deposited onto the coarse substrate to provide the flow restricting function. Some form of surface coating technique could be the answer to this fine layer deposition [252]. A number of techniques for creating this surface layer were studied for their feasibility in the present work. Coarse substrates based on 23 μm alumina powders and HIPed to a porosity of around 0.28 were used throughout. This was chosen in preference to a 13 μm substrate with 0.38 porosity due to higher strength and elastic modulus of the former. The required permeability was the same in both cases.

8.1 FLAME SPRAYING

Flame spraying is normally used to apply a layer of metal or ceramic onto a substrate of a different material, in order to modify the surface properties of the latter (e.g. for better wear resistance). The coating material, in a powder form, is conveyed into an oxy-acetylene flame by a carrier gas, and sprayed onto the substrate. Sintering occurs simultaneously as the powders come into contact with the flame, usually well above 1500 °C in temperature. A high final density (15 - 20 % porosity) is achievable.

Flame spraying of alumina has been applied largely on metal substrates for improved wear resistance. The recommended powder size for this purpose is around 23 μm.

Unfortunately, this would be too coarse for the target range of permeability, even assuming the lowest porosity practically achievable.

To attain the permeability required for the fine pored layer of a two-layered material, the particle size is estimated to be around 0.5 - 1 μm. Such powders are usually heavily agglomerated, and require breaking-down of the agglomeration by ball milling or otherwise.

Trials using 23 μm particles on a 23 μm HIPed substrate were successful, the coated layer attached to the substrate without peeling off. Flame temperature, and hence the degree of sintering, was difficult to control, as was uniformity of the coating. Trials with smaller powders, such as 4 μm, were unsuccessful. Continued presence of agglomeration, even after dry ball milling, rendered the conveying action of the carrier gas ineffective. In addition, the comparatively low flame temperature required for the powder size, estimated to be around 1200 °C, could not be attained using the present equipment.

8.2 PHYSICAL VAPOUR DEPOSITION

One of the surface coating methods considered to be more promising is physical vapour deposition (PVD) by ion plating. This process involves the evaporation through an argon plasma of rods of the coating material using a tungsten-arc electron beam, and depositing the vapour onto the exposed surface of the target material, in this case the alumina substrate. For the present work, coatings of ytrium stabilised zirconia were deposited.

Two trial runs were carried out in the surface coatings laboratory at the university. The processing conditions, as well as the resulting coating thickness and measured permeability, are listed in the following table. Specimen A was coated to a thickness of 506 μm, close to the target value, but the permeability as measured was too high. The

permeability of specimen B was closer to the target value of 5×10^{-16} m^2, although the thickness was insufficient, despite the much longer coating time.

Table 8.1 Summary of Physical Vapour Deposition Trial Runs

Specimen	A	B
Coating duration (mins)	90	140
Upper chamber pressure (Torr)	9×10^{-3}	8×10^{-3}
High tension (kV)	8.3	8.7
Current (A)	0.56	0.45
Temperature (°C)	1020	980
Lower chamber pressure (Torr)	3.5×10^{-4}	6.4×10^{-4}
Coating thickness (μm)	506	236
Viscous permeability (m^2)	1.39×10^{-15}	8.49×10^{-16}
Inertia permeability (m)	6.50×10^{-11}	5.52×10^{-11}

Uniformity of the microstructure was not ideal, especially in the case of specimen A. Splats of zirconia, rather than deposition by vapour, was noticeable with the naked eye. Scanning electron microscopy also provided further evidence (Fig. 8.1). The surface structure of specimen B was much improved (Figs. 8.2 to 8.6), but still not sufficiently smooth for direct use as a bearing surface without machining. Lack of access to coating and machining equipment prevented further progress with this process.

8.3 TAPE CASTING

Tape casting was also identified as a viable method for producing the two-layered structure. Traditionally, tape casting has been used to produce thin sheets of ceramics for applications such as multilayer capacitors or integrated circuit packaging. The

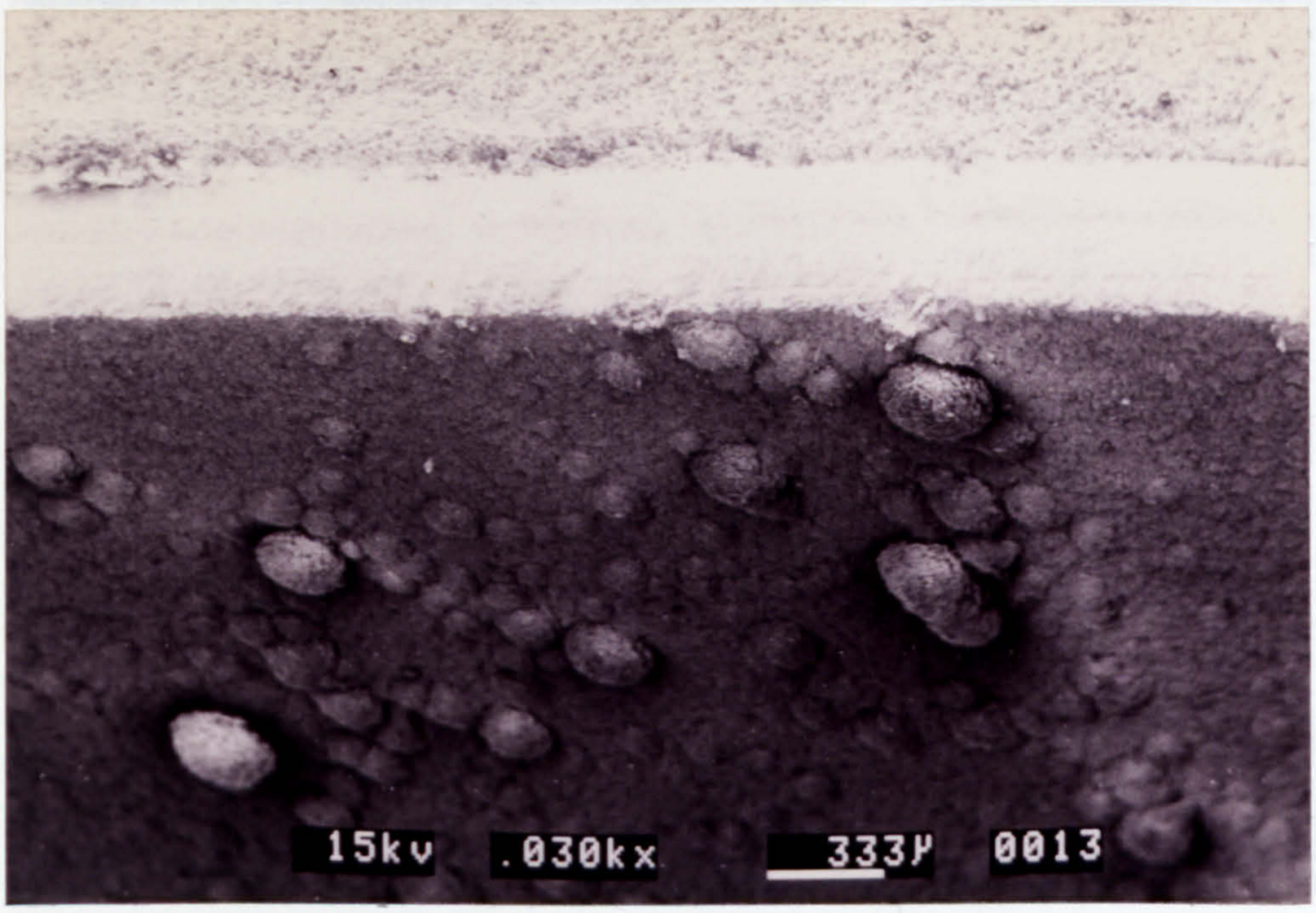

Fig. 8.1 Spattering of Zirconia on PVD Specimen A
(Dynamic angle = 60° ; coating facing downwards)

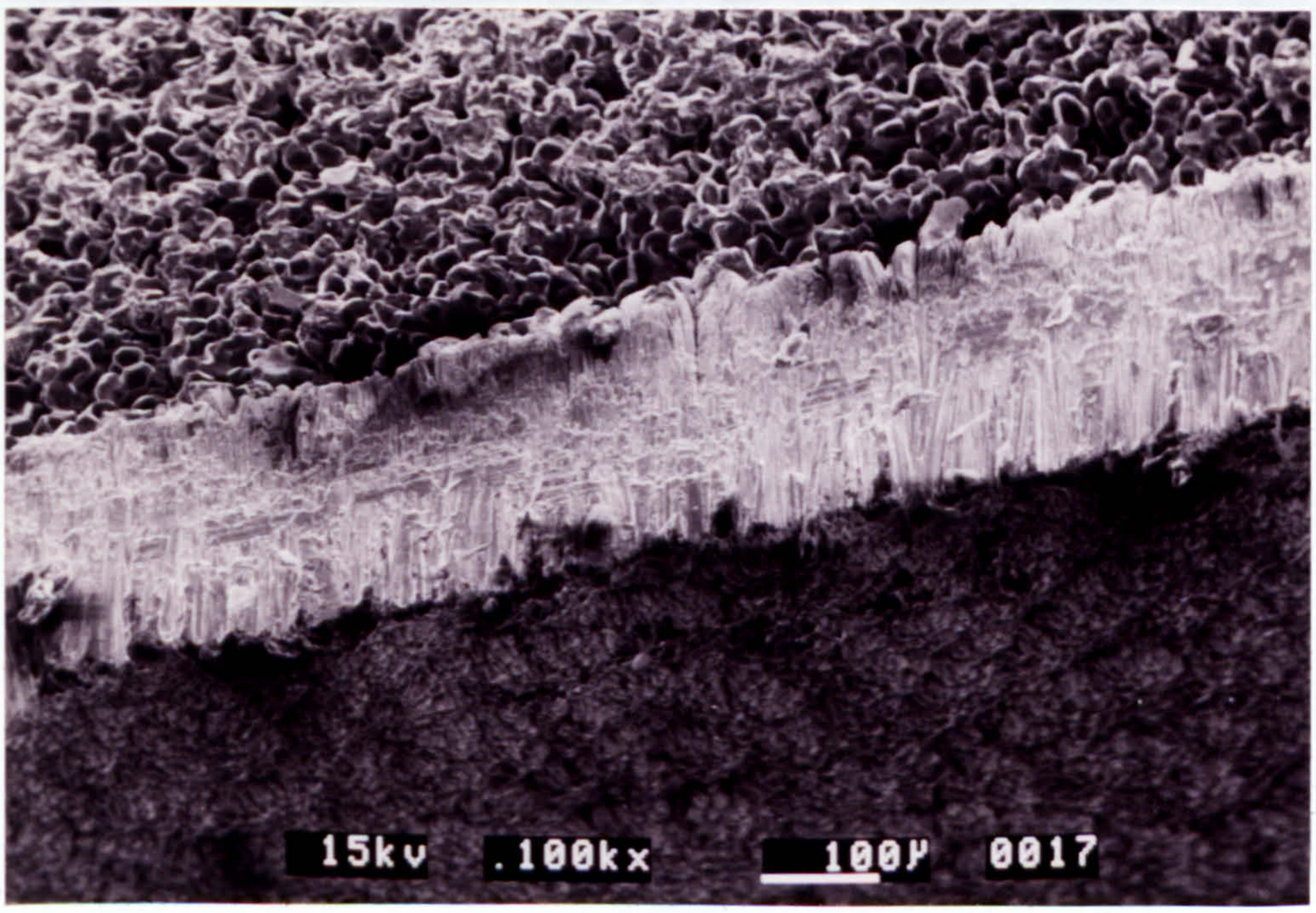

Fig. 8.2 Improved Surface Texture on PVD Specimen B
(Dynamic angle = 60° ; coating facing downwards)

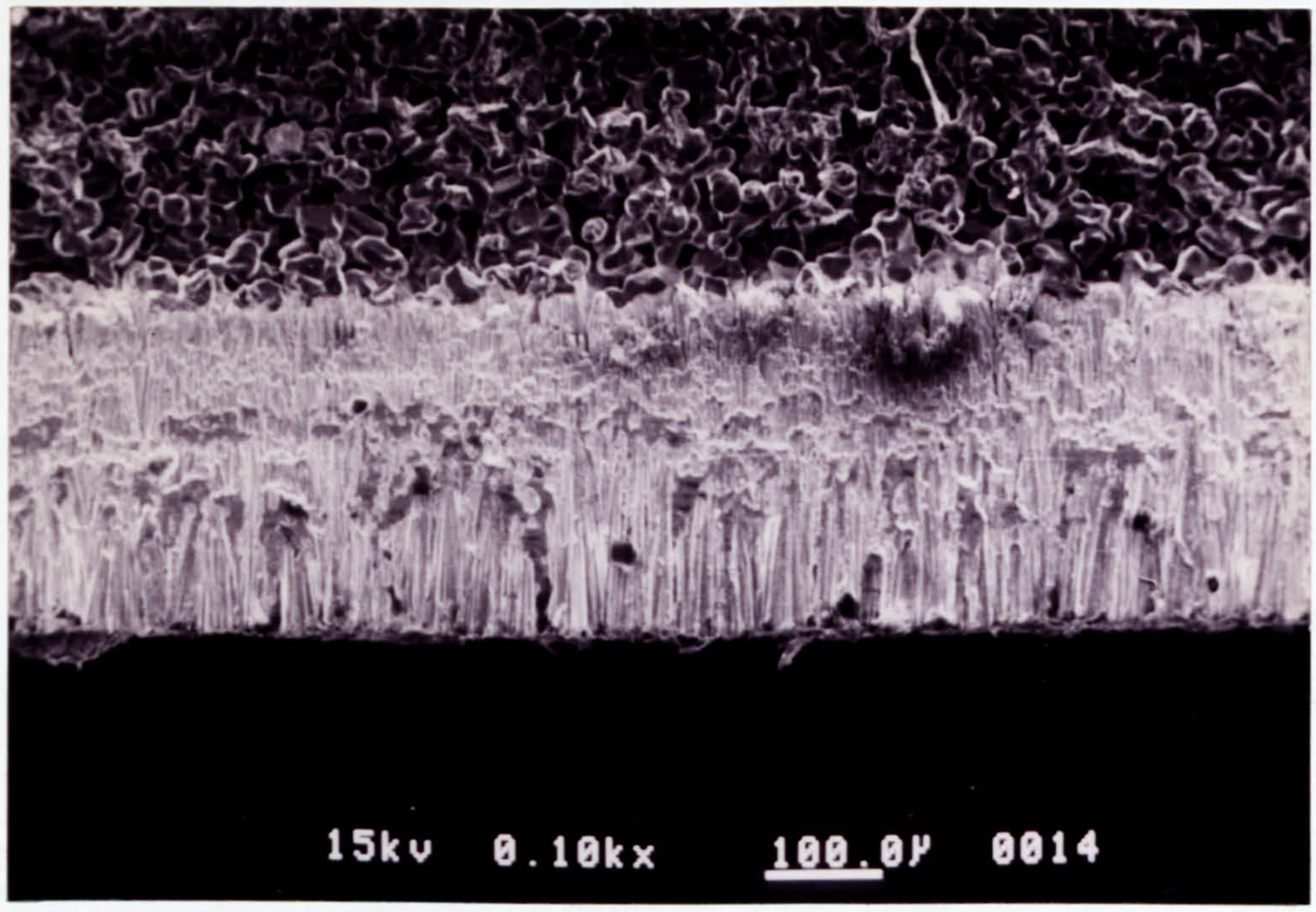

Fig. 8.3 Sectional View of the PVD Layer in Specimen B
(Coating facing downwards)

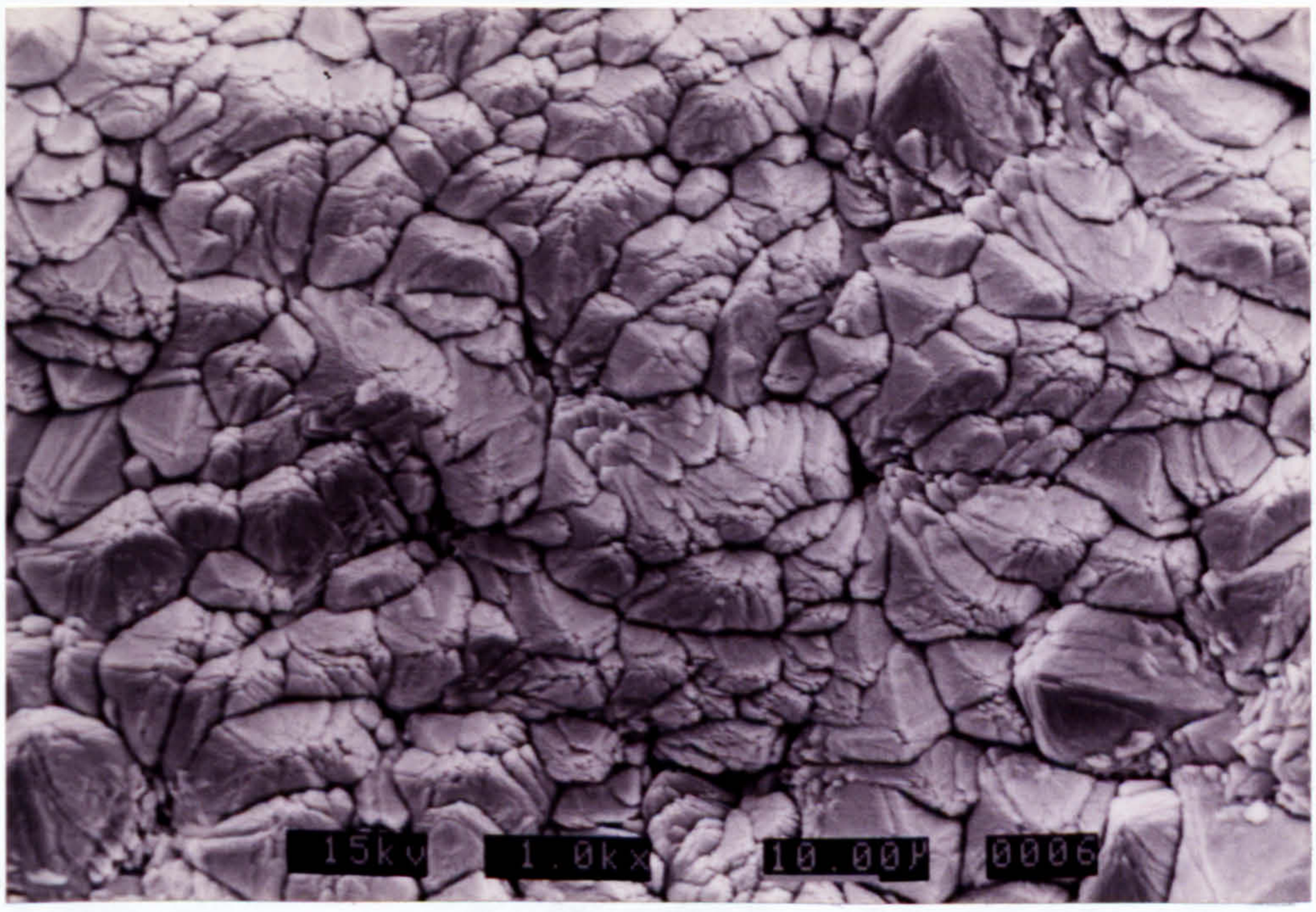

Fig. 8.4 Topology of the PVD Layer Top Surface in Specimen B

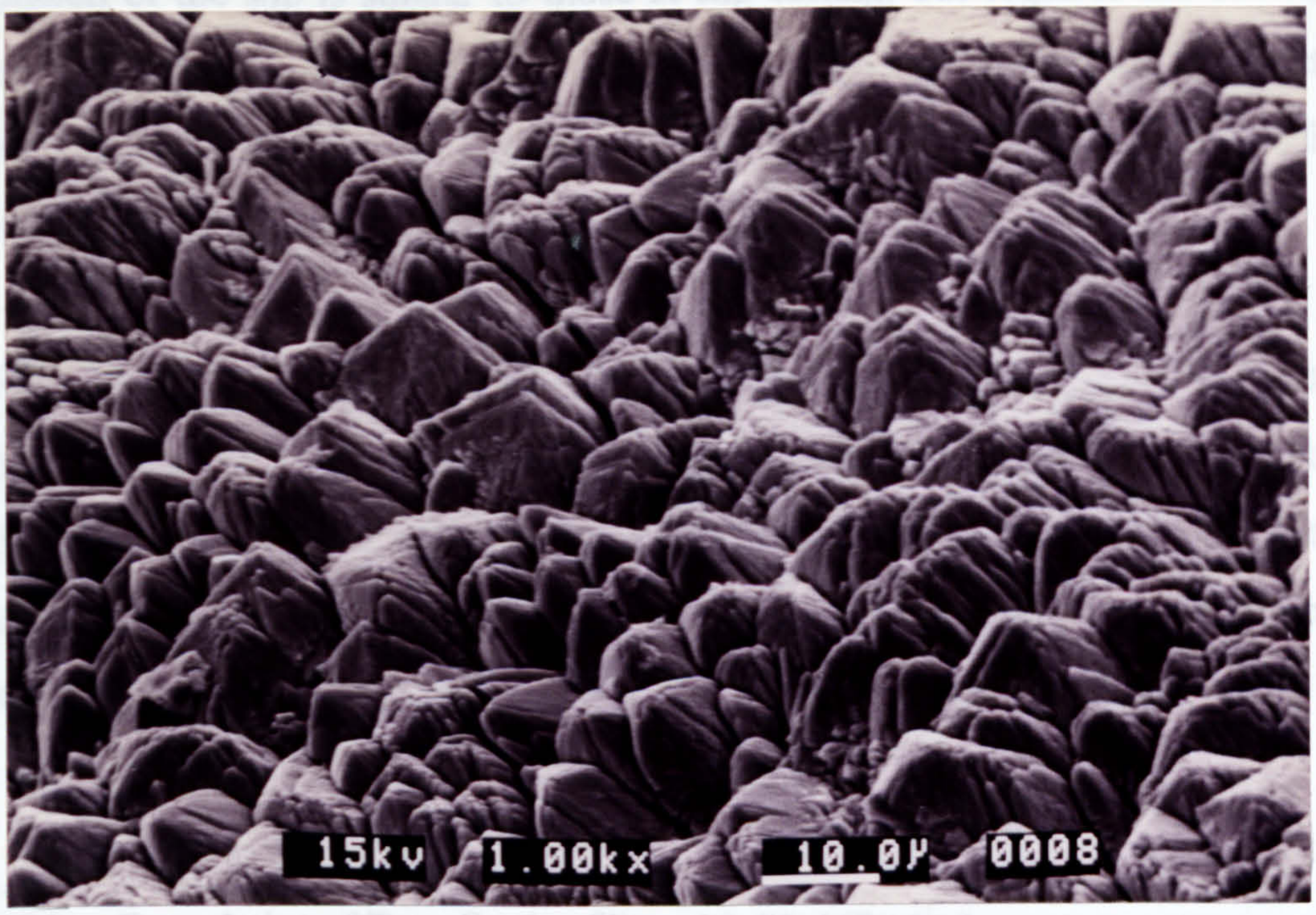

Fig. 8.5 Topology of the PVD Layer Top Surface in Specimen B
(Dynamic angle = 60°)

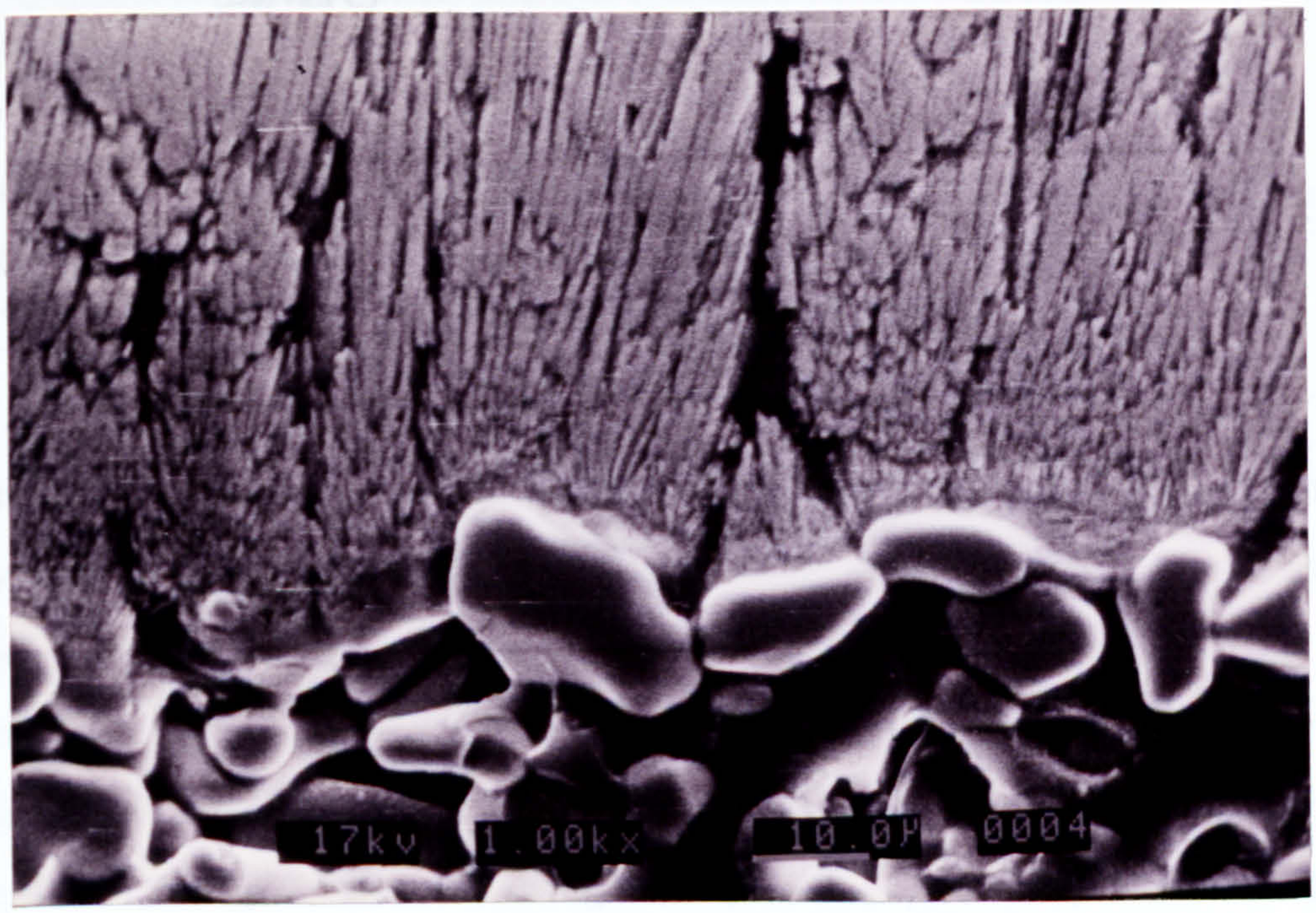

Fig. 8.6 PVD Zirconia / HIPed Alumina Substrate Interface

formulation of the slip is similar to those in slip casting, but requires the addition of binders and plasticisers to give the tape some flexibility after drying. Structured ceramic materials have also been produced by stacking tapes of different compositions and subsequently sintering [253, 254].

The formulation of the tape casting slip used in the present study was based on that by Chartier [255], chosen from a review of different formulations by Hotza [256] for its superior flexibility. Modifications were necessary as the viscosity of the slip based on the original formula was too high. The binder content was reduced to 67% of that of the original, resulting in the following mixture :

Table 8.2 Formulation of Tape Casting Slip (Modified Chartier)

Contents		wt %
ceramic	α - alumina	41.93
dispersant	polyacrylic ammonium (Darvan C)	0.38
deionised water		50.70
binder	Methocel	1.70
plasticiser	polypropylene glycol	1.84
release agent	glycerol	3.46

The alumina powders were first ball milled with the deionised water and dispersant for 3 hours for effective deflocculation. The mixture was then heated to 70 °C, before the Methocel, premixed in a 10 wt% solution in 95 °C deionised water, was added. This was then further ball milled for an hour, after which the binder and plasticiser were added. A further 11 hours of ball milling were required before the slip was ready for casting. Degassing in vacuum, though thought to be desirable, was not entirely successful due to the high viscosity of the slip and its tendency to foam. Further handling such as pouring into the doctor blade was also prone to trapping air. Addition of 0.1 wt% of an anti-foaming agent, though not optimised, appeared to show some improvement in reducing trapped air in the slip.

When mixed, the slip was poured into a doctor blade designed for manual casting (Figs. 8.7, 8.8). The doctor blade essentially consisted of a slurry reservoir, with two steel blades at the rear end (Appendix H, drawing no. MU291 D101 2A). Both blades were adjustable in height, leaving a gap between their ground, downward facing edges and the surface on which the tape was being cast. The front blade was set at a gap twice that of the rear blade, the latter being 1 mm for most of the present work, resulting in a dried tape thickness of 0.24 mm. This represented the upper limit on the thickness of the cast. Further increases in the blade gap resulted in curled upper surface of the tape upon drying. The two blades were separated by a distance of 4 mm by a stacker plate to allow venting of any trapped air.

The blade was dragged along a flat glass surface at a speed of approximately 30 cm per minute to produce the tape. The cast slip was then allowed to dry in open air overnight before peeling. The finished tape possessed good strength, was highly flexible, easy to handle, and could be cut to shape using ordinary scissors or punching tools. Thickness of the finished tape was uniform to better than 0.01 mm in any single tape.

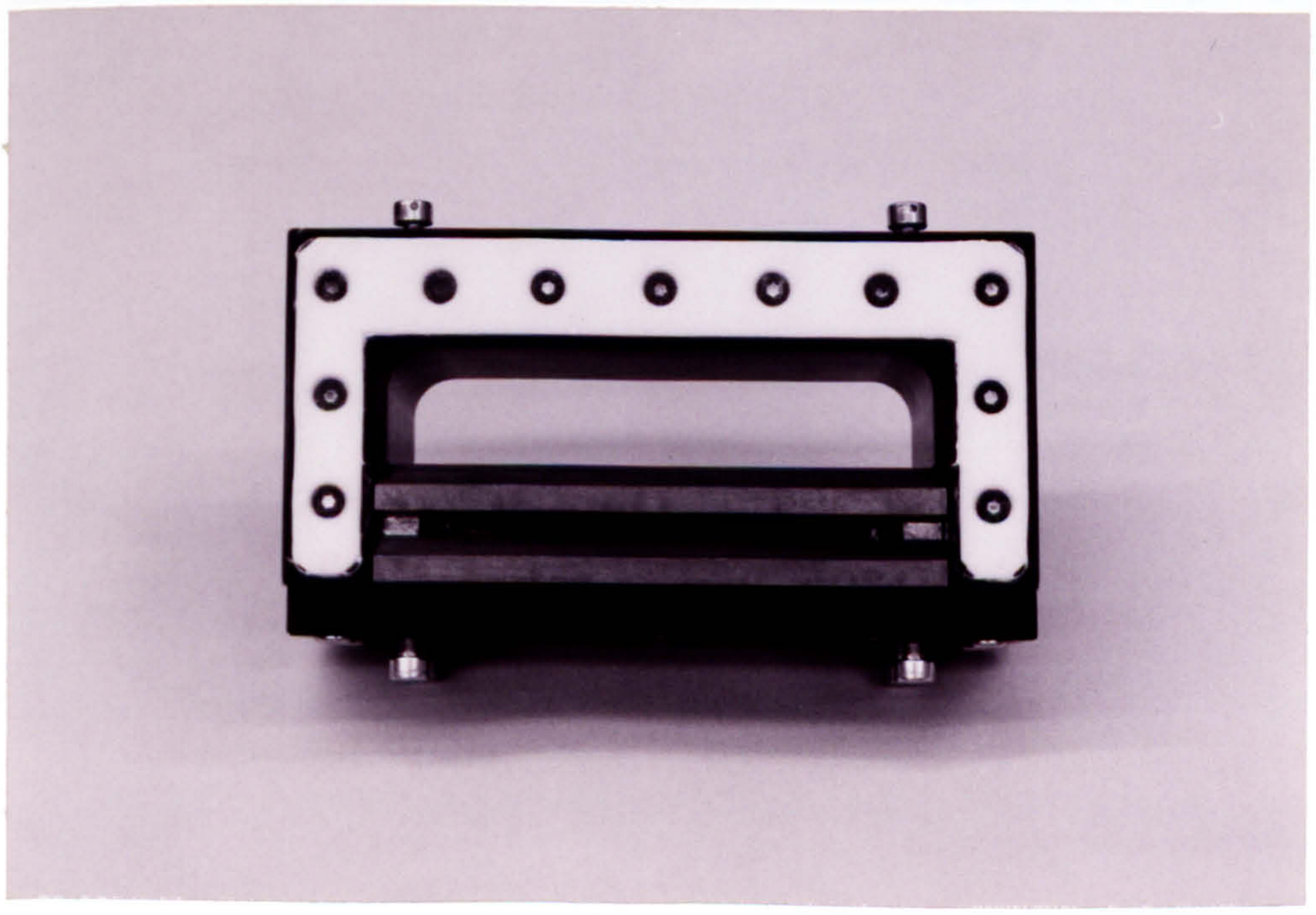

Fig. 8.7 Bottom View of the Doctor Blade for Tape Casting

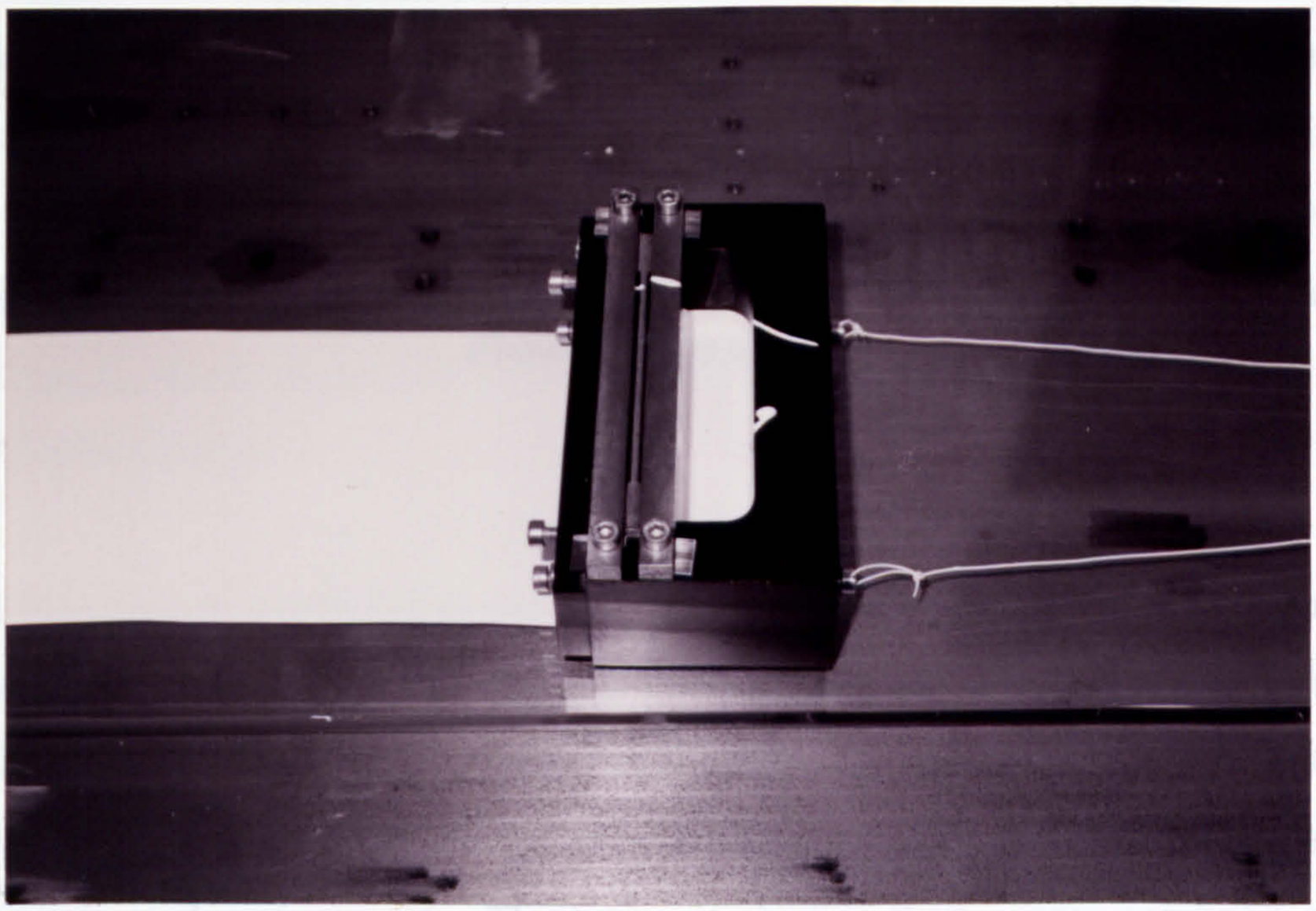

Fig. 8.8 Aqueous Tape Casting of Alumina using the Doctor Blade

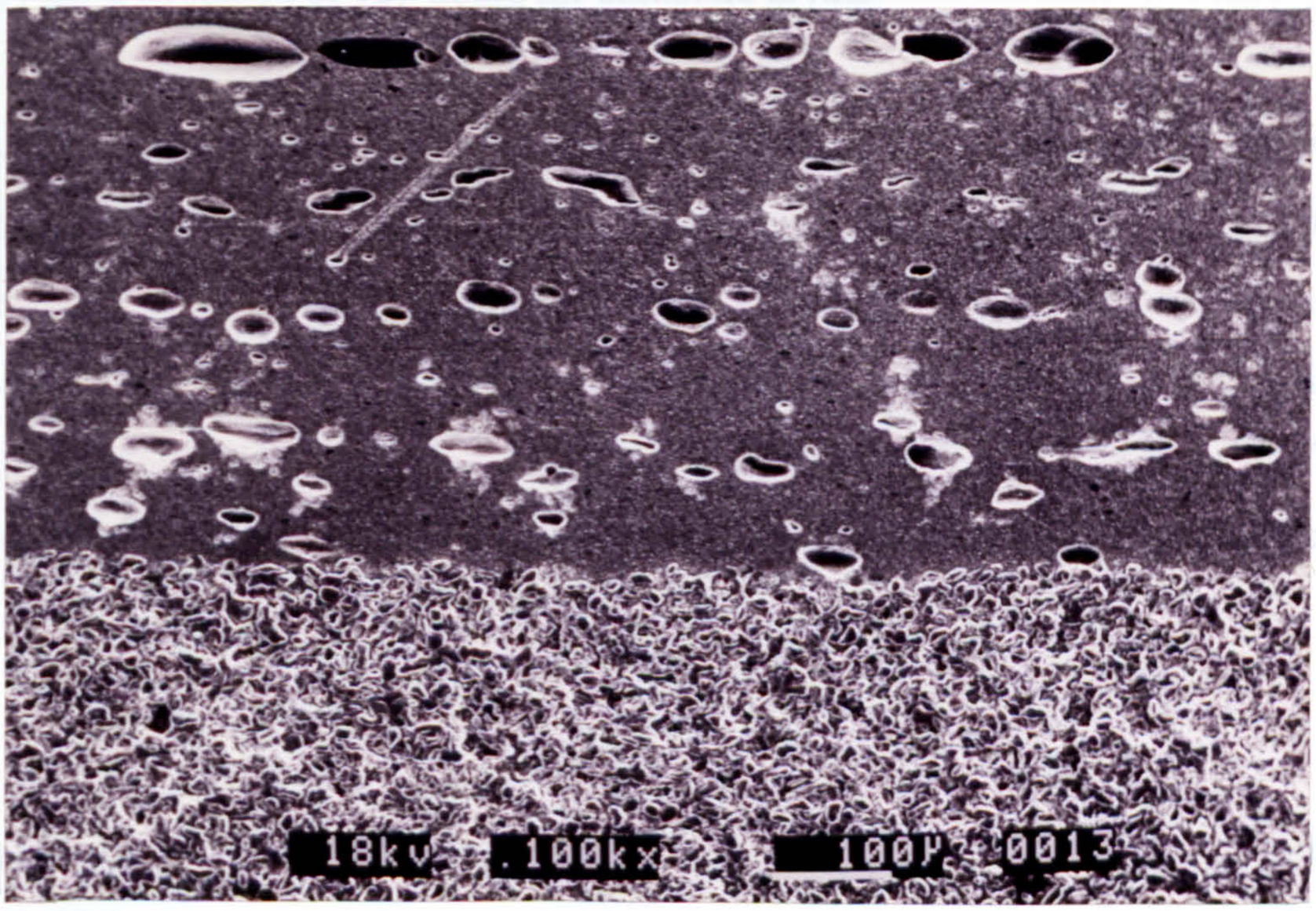

Fig. 8.9 Lamination Bubbles of Tape Casting Stacked in Air

A density measurement based on mean calculated density of all the components in the slip except for the water revealed a possible 25 volume % of trapped air in the tape, although the actual value was likely to be less due to residual moisture content in the tape. Complete drying of the tape at temperature could not be achieved without the danger of removing some other ingredients in the process. The porosity was thought to be largely due to trapped air bubbles within the tape, which were observable under optical microscopes.

Stacking of multiple tape layers (up to 6) and onto the coarse substrate was done by re-wetting the tape surface and applying a uniaxial pressure of 0.3 MPa. Initially, the stacking was done in open air. SEM sections of such a specimen revealed substantial lamination bubbles (Fig. 8.9), which were largely removed by performing the stacking in an evacuated environment. The tapes, stacked in their proper sequence on the substrate, were placed in a PTFE tooling. Air was removed by evacuation in a desiccator. Degassed, deionised water was then allowed in until the entire tooling was submerged. The desiccator was repressurised, and stacking pressure applied via dead weight for a minimum of 120 hours for complete drying.

After thorough drying, the binders and plasticisers in the mixture had to be removed by debinding at elevated temperature. The single stage debinding cycle as suggested by Chartier [255] resulted in hairline crack formation in the stacked, tape-cast layers even before sintering. The problem did not reappear after changing to a different debinding cycle as shown in Fig. 8.10, as a direct result of a thermo-gravimetric analysis (TGA) of a tape sample to determine the burn-off temperatures for its various ingredients (Fig. 8.11).

The excellent processing characteristics of the tape casting slip were fully demonstrated by the artefact shown in Fig. 8.12. Cut from a 0.5 μm alumina tape 0.24 mm in thickness, the petals were simply 'glued' together with water. The finished article was then debound and sintered at 1400 °C for one hour. The black bakelite support measures 30 mm in diameter, to give a sense of scale.

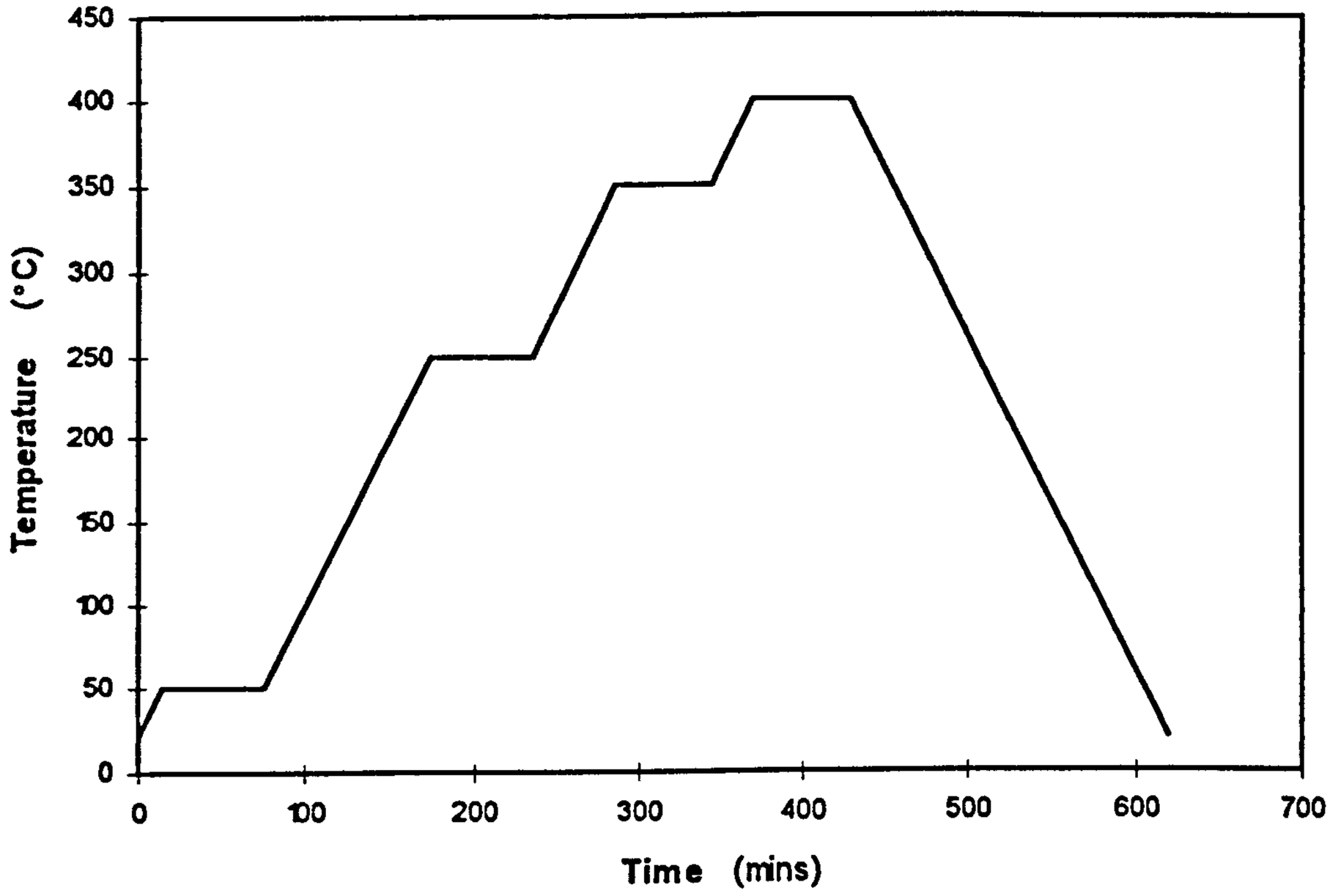

Fig. 8.10 Debinding Cycle for Tape Casting

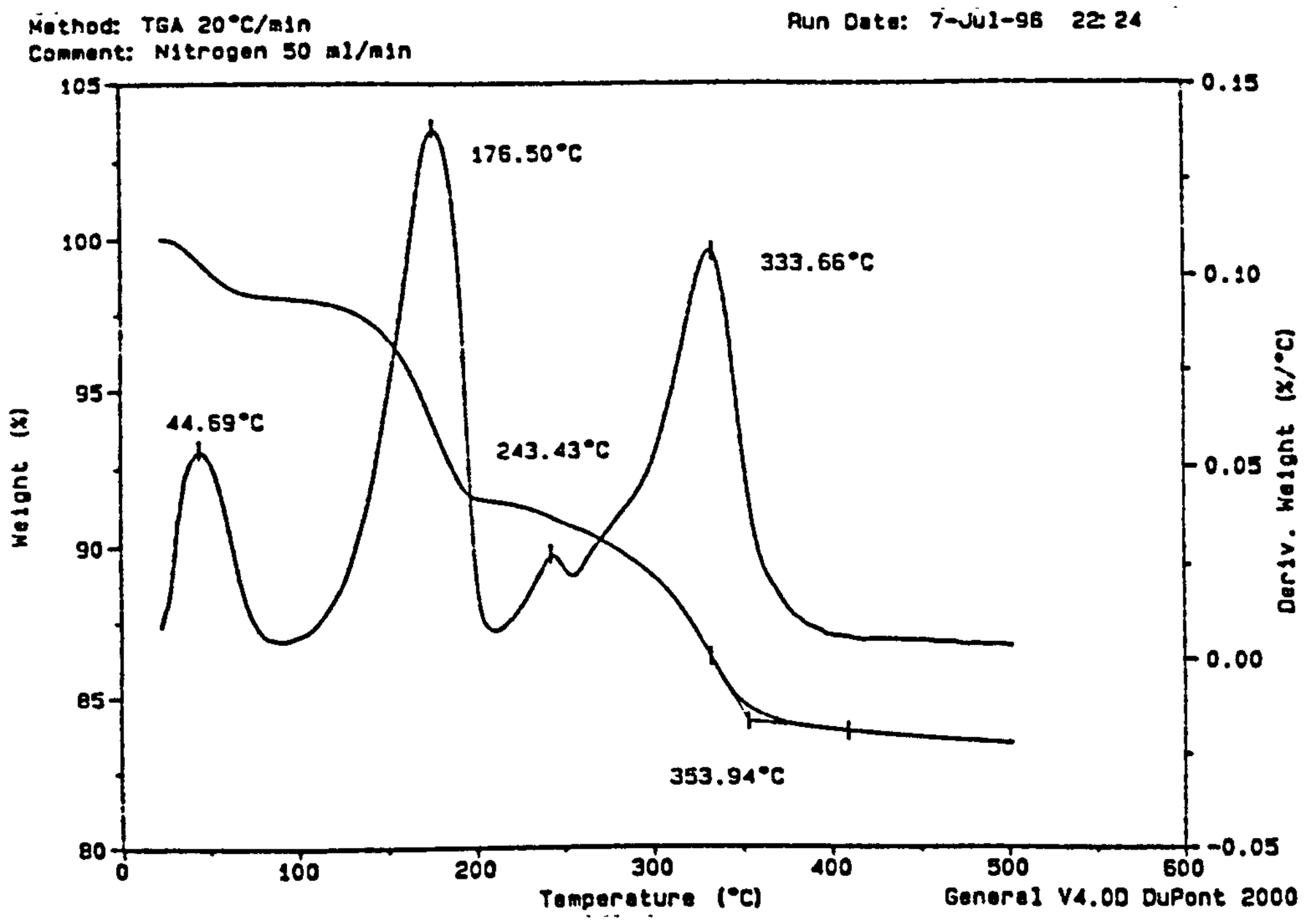

Fig. 8.11 Thermo - Gravimetric Analysis of a Tape Casting Sample

(based on modified Chartier formulation)

Fig. 8.12 Artefact Produced from a 0.5 μm Alumina Tape Casting

HIPing to 1200 °C of a 23 μm HIPed substrate stacked with 6 layers of 0.5 μm alumina tape, each 0.24 mm thick, resulted in dried riverbed type cracking over the entire tape surface, although each fragment was still firmly attached to the coarse substrate. The fragmentation was due to shrinkage in the tape layers as they densified, while the sintering temperature was too low for any dimensional changes to occur in the coarse substrate onto which the tape was anchored.

Hot pressing of further stacked samples at 1200 °C for an hour with an uniaxial load of 2 kN produced much improved results. By applying a uniaxial load across the thickness of the tape during sintering, densification was encouraged to take place in the direction of the applied load, resulting in much reduced shrinkage in the transverse directions. No surface cracks could be observed for stackings with up to 3 tape layers. Addition of further layers resulted in fine, hairline cracks which were predominantly radial, but nevertheless uniformly distributed. Even in such cases, the size of cracks was small compared with those in the sample sintered under isostatic pressure. Increasing the axial load might reduce cracking further, but the substrate would have a

high probability of fracturing due to local deformation of the tooling holding the specimen in the hot press.

8.4 COMBINED SLIP AND TAPE CASTING

Despite its moderate success, the creation of the two-layered structure with tape casting was not considered a logical approach due to the limitation of the tape thickness. The stacking of multilayer tapes made the process very elaborate and susceptible to lamination weaknesses.

Direct deposition of a thin layer of fine powder on the substrate surface by slip casting was also found to be problematic. Without binders as in tape casting, the slip-cast layer was extremely brittle even in the green state. Shrinkage during drying of the slip, though small, was sufficient to cause cracking. Even in cases where the slip survived the drying stage, cracking invariably occurred due to further shrinkage during sintering and the application of uniaxial load during hot pressing.

If the densification of the cast slip could be allowed to occur on its own during sintering, and the densified object subsequently 'attached' to the coarse substrate, cracking of the fine layer could be avoided.

This was attempted by first sintering a 0.5 μm cast, about 2 mm thick, in a muffle furnace at 1200 °C for one hour. The sintered slip was then ground flat on both surfaces, before being stacked in vacuum onto a coarse substrate, with a 0.5 μm tape between the two. The latter was as before 0.24 mm thick. A uniaxial load of 0.3 MPa was applied throughout the drying in open air. The whole 3 layered assembly was then hot-pressed using the same parameters as before. No cracks could be observed on the slip cast layer after hot-pressing.

Despite the very limited number of trials, this was by far the most promising approach. The finished article, shown in Fig. 8.13, survived all the subsequent machining and bearing testing (refer to Chapter 10) without delamination. Fine cracks could still be observed in the tape layer (Fig. 8.14), but the tape layer in this case only served to hold the slip-cast layer onto the substrate, with most of the pressure restricting function performed by the slip alone. Deep penetration of the tape into the pores of the coarse substrate, observable under scanning electron microscope (Fig. 8.15), gave further evidence to the good lamination strength between the two layers.

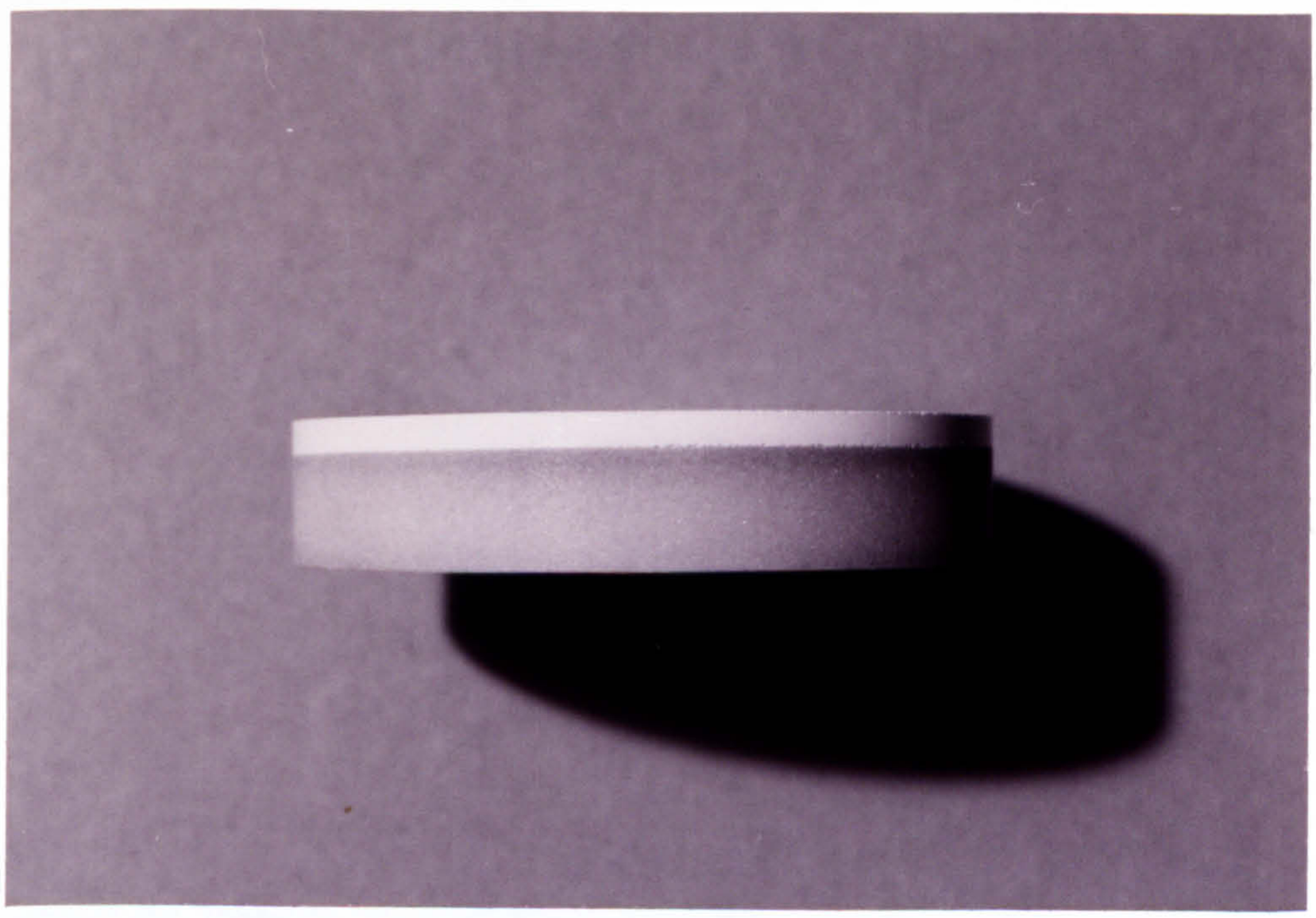

Fig. 8.13 Two-layered Porous Structure -- Combined Slip & Tape Casting

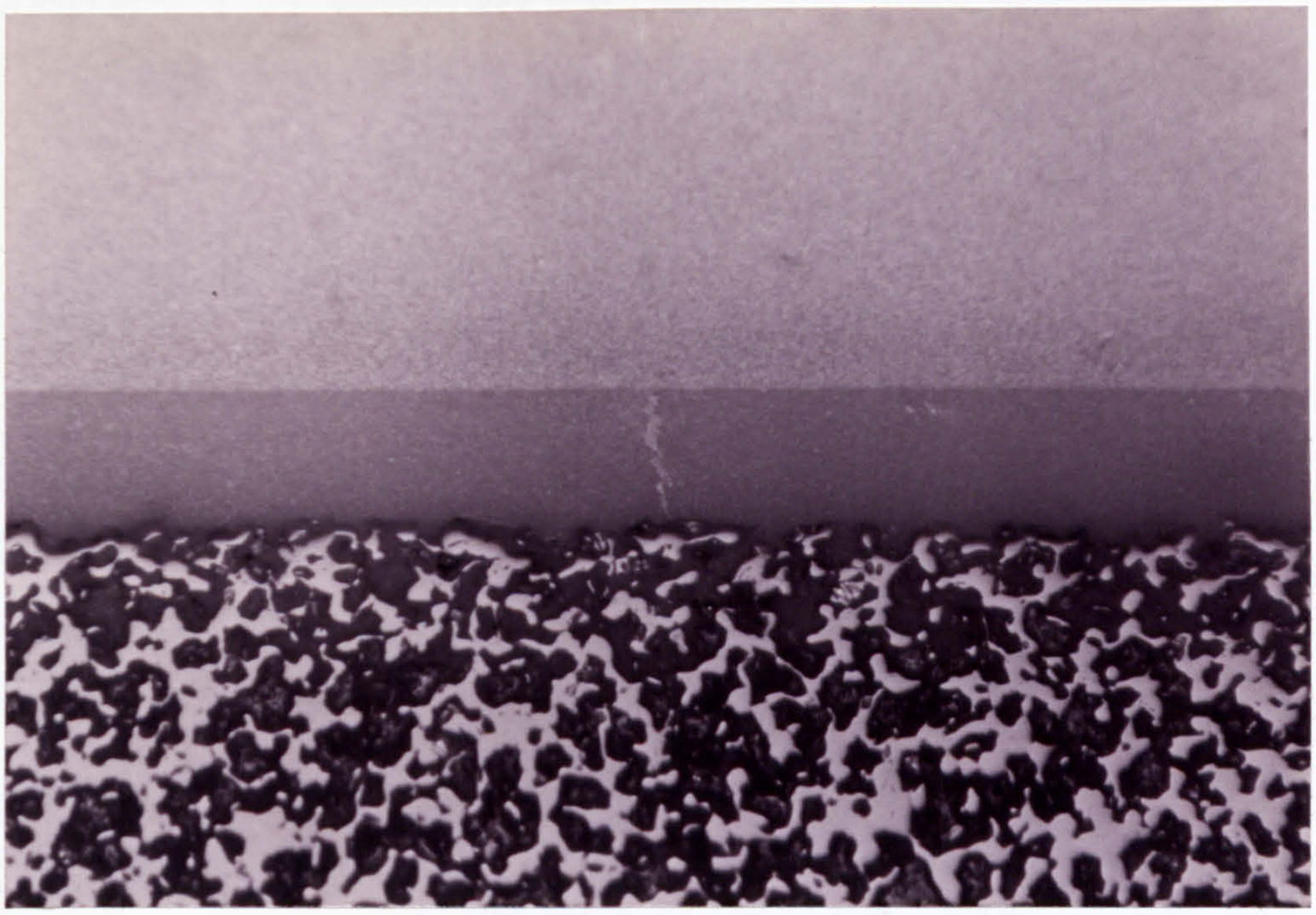

Fig. 8.14 Optical Micrograph Section of the Two-Layered Structure

(Hairline cracks visible in the centre tape-cast layer)

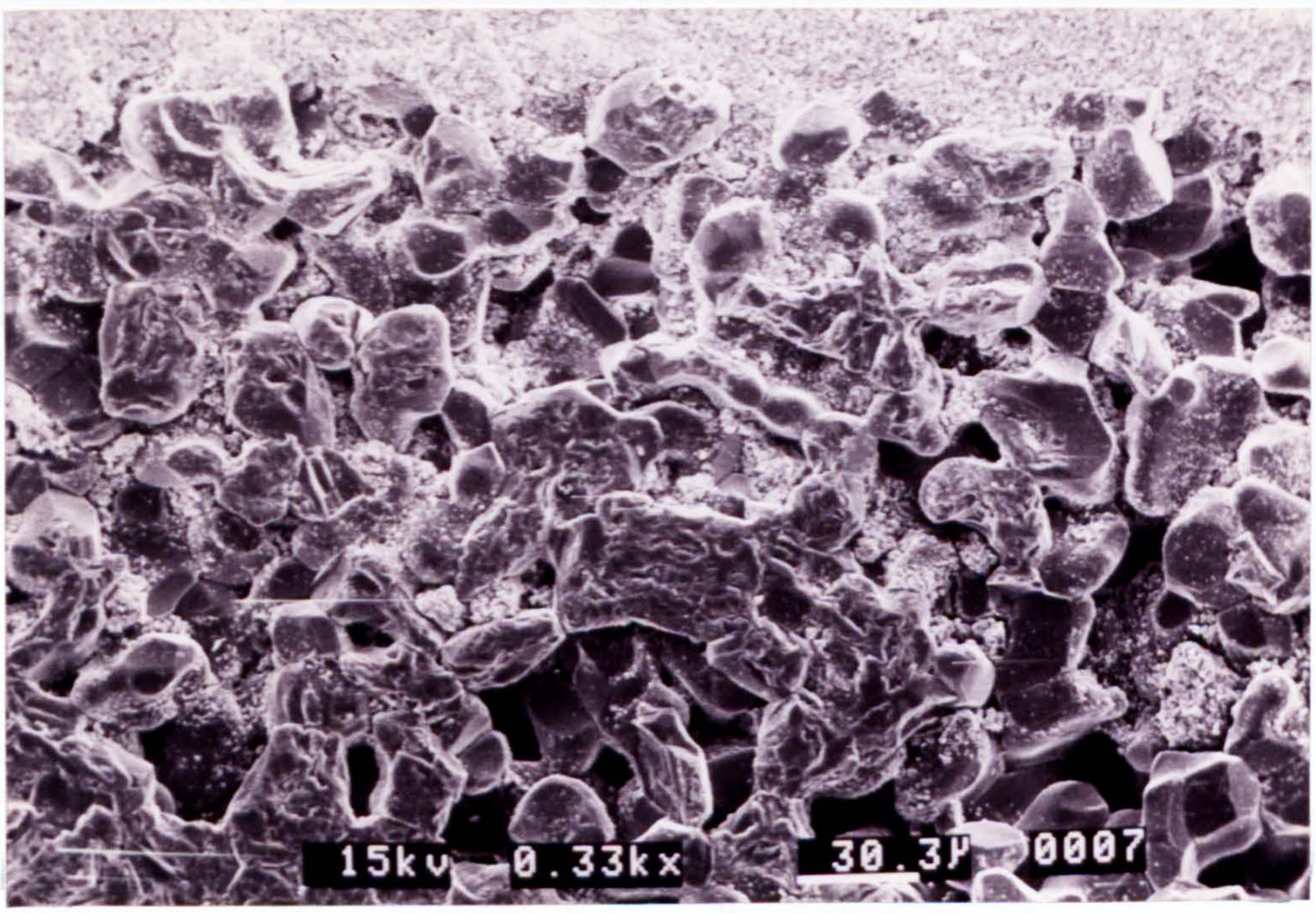

Fig. 8.15 Penetration of Tape-cast Layer into the HIPed Substrate

9. DISCUSSIONS

9.1 PREDICTING PERMEABILITY

Permeability of the porous material is the most important fluid flow parameter for the design of aerostatic bearings, and is often expressed as a function of the particle size and open porosity of the porous material. Their relationship in hot isostatically pressed porous alumina has been discussed in Chapter 6. Permeability is highly sensitive to open porosity (to the power 2 to 6, depending on particle size) while its dependence on particle size is less sensitive (to the power 0.68). Using the information in Table 6.1, and equations 6.3 to 6.6, the required porosity level and particle size to achieve a given permeability value can be determined.

Semi-empirical modelling of permeability as a function of porosity and particle size was also attempted, using the results of the pore-size distribution tests and assuming the pores to be simple capillaries. By expressing mean pore size as a function of porosity and particle size, the Poiseuille's flow through a single pore could be calculated. The total number of pores was then obtained by dividing the void area across any section by the cross-sectional area of the capillary. The permeability could then be expressed as :

$$\Phi_v = \frac{d_{pk}^{\,2}}{32}\left[1-(1-\zeta_o)^{2/3}\right] \qquad (9.1)$$

The derivation of the above equation can be found in Appendix A. The calculated values were then compared with measured data (Fig. 9.1). The mathematical model underestimates the permeability value for most specimens. The ratio of calculated to measured viscous permeability reaches a minimum at an open porosity of around 0.20, but changes steeply at $\zeta_o = 0.12$. The ratio also shows a slight increasing trend as open porosity increases from 0.20. As the pore size measurement in the water expulsion method was based on the smallest throat of a through-pore, it is not

surprising that the calculated values are lower than actual. The pore shape also changes with porosity, becoming more cylindrical as porosity reduces. This may well explain the shape change in the permeability ratio at $\zeta_o = 0.10 \sim 0.15$ in Fig. 9.1. The method of estimating the total number of pores may also be too simplified, but calculations based on average particle spacing produced even poorer results. In any case, equation 9.1 can be used in conjunction with Fig. 9.1 to obtain a first estimate of the viscous permeability coefficient.

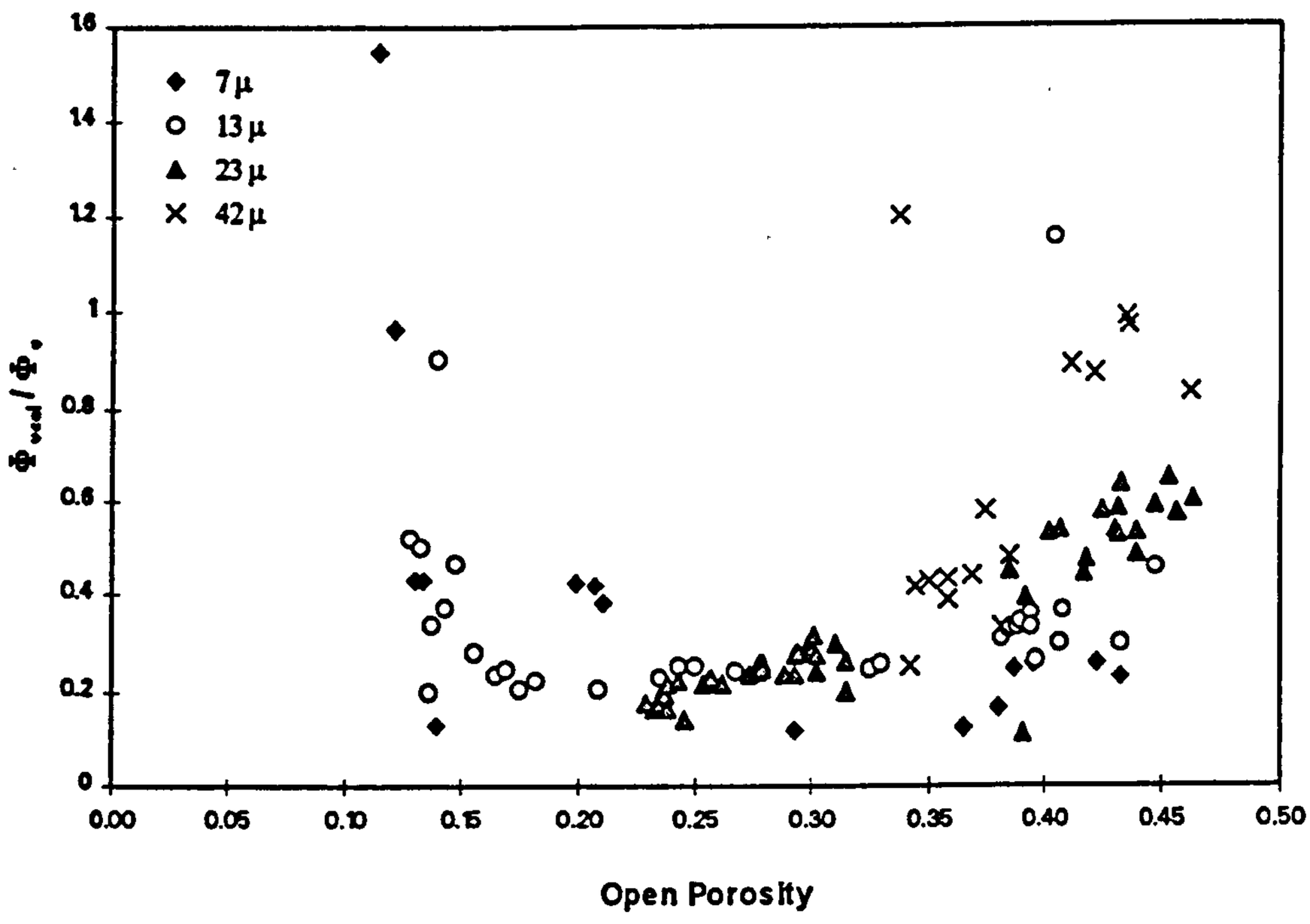

Fig. 9.1 Modelling of Permeability by Poiseuille's Flow through Capillaries

To obtain a specific value of permeability, either the particle size or the level of open porosity could be varied. Ceramic particles come in discrete sizes, and the choice is limited by what is available on the market. Open porosity is thus the main process variable.

Other considerations such as structural requirements might put certain restrictions on the useful range of porosity. Elastic moduli and flexural strength of porous alumina have been expressed as a power law function of {1 - total porosity} in equations 7.3 and 7.7. The empirical constants summarised in Tables 7.1 and 7.2 can therefore be used to determine the required porosity level to attain specific strength and rigidity values. The target values set out in Chapter 3, for example, can be satisfied with a porosity of less than 0.3. It was not evident from experimental results that HIPing improved the strength of the porous material, as suggested by Ishizaki [169, 170].

The desire to achieve uniformity in the pore microstructure and permeability also places additional limitations to the lower limit of porosity level. The pore size distribution, as discussed in Section 6.2, is influenced by the porosity level. In almost all cases, 80% of the pores lie between 0.9 and 1.2 of the median pore size for open porosity values of 0.25 and above, but the distribution widens at an increasing rate as porosity drops below 0.25. This value of 0.25 therefore represents the lower threshold of open porosity, in the interest of uniform permeability.

To obtain in repeatable manner a predetermined level of permeability requires a high consistency in both powder size and porosity level. Ceramic powders are by virtue of their manufacturing process not uniform in both size and shape. The particle size distribution for commercial ceramic powders could therefore not be improved upon significantly.

Final porosity after sintering is, in turn, influenced by both green density and the level of densification (equation 5.13). It has been shown in Section 4.2 that the average green density could be controlled to a consistency of a few percent or less with a variety of established packing methods. Although vibratory packing has produced consistent results for powders larger than 10 μm, the packing density is inferior to other methods such as slip casting. A high value of the packing density implies less bridging of particles, and therefore the likelihood of obtaining more consistent pore size and permeability in the final sintered body. Injection moulding of ceramics

produces similar results to slip casting in terms of packing density, but suffers from debinding problems and a limited particle size range.

Densification is, as discussed in Chapter 5, highly dependent on sintering temperature, and to a lesser extent on sintering time and pressure. The rate of densification is expected to be high at the beginning, but drops off exponentially at the later stage of sintering. This is due to a relaxation in the driving force and the increase in diffusion distances with further neck growth. It is therefore not surprising that the effect of time becomes less significant. The role that the pressure plays in free-capsule HIPing is not well understood. It has been proven effective in preventing the formation of closed pores, but in doing so also appears to hinder densification. Experimental evidence also indicated that the HIPing pressure helps to eliminate inherent closed porosity in large powders. This is of importance structurally, as closed pores do not play any part in the flow restricting function of the material, but affect its structural properties adversely.

The level of porosity after HIPing is therefore largely determined by particle size and HIPing temperature. A degree of fine control can be achieved by varying pressure and HIPing time, although the range of adjustment is limited to no more than ±20% of open porosity. Equation 5.4, together with Figs. 5.7 to 5.9, provides a guideline for estimating the required HIPing conditions for a given particle size and densification.

The suspected non-uniform temperature distribution within the HIPing chamber, and the uncertainties in the HIPing temperature measurement, resulted in poor repeatability of the densification and specimen porosity between samples processed using identical parameters. Experimental evidence also indicated that permeability was not uniform across diameter, due possibly to packing density or sintering temperature variations. With the existing equipment, the permeability of the porous specimen is at best repeatable to some ± 25 %, even using only the uniform temperature, middle section of the furnace.

Densification was not always isotropic, and could take place in preferred directions under the influence of a small external load, such as dead weight of graphite tooling.

Geometrical distortion of the HIPed specimens was high, and was most significant across thickness, requiring generous allowance for machining (minimum 25% on thickness, 5 to 10% on diameter).

9.2 PROCESSING OF TWO-LAYERED STRUCTURES

Two-layered structures in porous alumina have been successfully produced on HIPed substrates, with the fine layer applied either by physical vapour deposition, or by the hot-pressing of a combination of slip and tape casts. The former method suffered from uniformity problems, but could improve with further process optimisation. This method is suitable for batch production, and can be applied freely to open geometries such as flat pads or spherical bearings. Application of the method on the bore of journal bearings might also be possible. The range and degree of control of the permeability of the fine layer are, however, limited. Machining of the deposited layer to achieve air bearing qualities could be the greatest difficulty.

The hot-press process, on the other hand, gives much better range and control over the fluid flow properties of the fine layer. The latter has also been machined successfully to mirror finishes and sub-micrometer flatness. Inter-layer bond strength may need further improvement. The biggest drawback of the method is its complexity and therefore high cost of manufacture. Adapting the technique for journal bearings may also be difficult.

9.3 VELOCITY SLIP AND INERTIA EFFECTS

Results from the slip coefficient measurements have not been conclusive, and were affected adversely by the poor surface finish of the specimens. The measured values lie between 0.003 and 0.06, and appear to increase with open porosity. A logical

relationship with particle size could not be established from the limited data. The slip coefficient is near constant for flow clearances larger than $2.d_w$, but reduces in value drastically as the clearance reduces. In the case of the single-layer bearing, typical clearances for aerostatic bearing applications lie unfortunately well below this threshold value. The Beavers' criterion of velocity slip does not adequately describe the effect of the porous bearing surface on the resistance to fluid flow within the bearing gap.

The significance of the inertia effect in a porous bearing is determined by the permeability coefficients, Φ_v and Φ_i, of the porous material. Flow through the porous pad is predominantly viscous, when the inertia term in the Forchheimer equation (equation 2.4) is much smaller than the viscous one; i.e.,

$$\frac{z_p.\eta.(Q/A_p)}{\Phi_v} \gg \frac{z_p.\rho.(Q/A_p)^2}{\Phi_i}$$

or

$$\frac{\Phi_v}{\Phi_i} \ll \frac{\eta.A_p}{\rho.Q} \qquad (9.2)$$

Assuming a perfect gas,

$$\rho = \frac{p_{ref}}{R.T} \qquad (9.3)$$

Also, from Appendix D,

$$\frac{p_1^2 - p_2^2}{2.p_{ref}} = \frac{z_p.\eta.(Q/A_p)}{\Phi_e} \qquad (9.4)$$

Substituting for (Q / A_p) and ρ,

$$\frac{\Phi_v}{\Phi_i} \ll \frac{2.\eta^2.R.T}{p_1^2 - p_2^2} \cdot \frac{z_p}{\Phi_e} \qquad (9.5)$$

For a given bearing design, however, the term Φ_e / z_p should be constant. This is because a larger thickness would be required for a more permeable material in order to achieve the same degree of pressure restriction. Taking the parameters of the test bearing in Chapter 3 as an example, Φ_e / z_p equals 4.16×10^{-12} for a bearing number of 20 and a design gap of 10 μm.

Knowing the operating conditions of the bearing, the right hand side of equation 9.4 can be determined. The average exit pressure of the porous pad is approximately 0.67 of that of the gauge supply pressure according to Gerke[82] ; i.e.,

$$p_2 - p_a = \frac{2}{3} \cdot (p_1 - p_a) \tag{9.6}$$

Substituting,

$$p_1^2 - p_2^2 = p_1^2 \cdot \left[1 - \frac{1}{9} \cdot \left(4 + 4 \cdot \bar{p}_a + \bar{p}_a^2 \right) \right] \tag{9.7}$$

Using standard properties of air at 20 °C, and assuming a supply pressure of 4 bar,

$$\frac{\Phi_v}{\Phi_i} << 8.1 \times 10^{-5} \tag{9.8}$$

if deviation from Darcy's law due to inertia effects could be neglected.

The relationship of the ratio of Φ_v / Φ_i with open porosity and particle size is shown in Fig. 9.2. As can be seen, the ratio of permeability coefficients for most of the single layer, HIPed specimens lies below the value in equation 9.8, suggesting that Darcy's law could be applied to single-layer bearings without incurring significant errors. The variation of permeability ratio with particle size is difficult to judge, but an increasing trend can be observed as open porosity reduces. The widely spread data for specimens sintered from 13 μm powders could well be attributed to the low green density achieved in the vibration packing for that powder size.

The same is, however, not always true for the two-layered material. The PVD specimens have an average value of permeability ratio of around 2×10^{-5}, and thus can still be regarded as Darcian. The value for the combined slip and tape-cast specimen, on the other hand, is much higher at 6.7×10^{-3}. Inertia effects can no longer be ignored in that case. As the open porosity for the latter specimen was as high as 0.28, the particle size might well be the dominant factor determining this high permeability ratio. Additional data for intermediate powder sizes would be required to establish a clearer idea of any relationship that might exist.

In all cases, the Forchheimer model can be used to describe the inertia flow adequately.

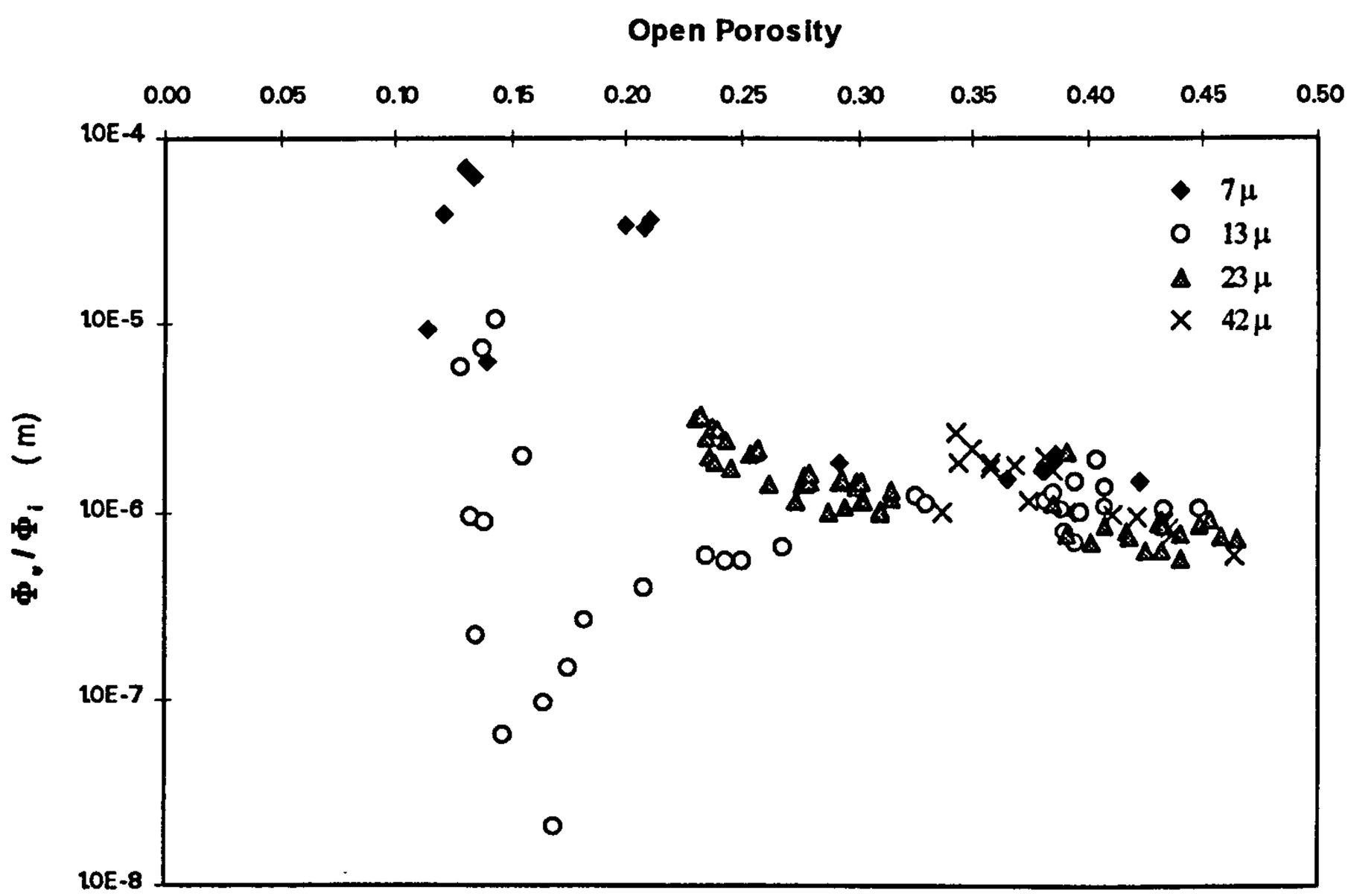

Fig. 9.2 Variation of Permeability Ratio with Particle Size and Porosity

10. TESTING OF BEARING MATERIALS

The suitability of both the single and two-layered porous materials for aerostatic bearing applications could only be evaluated in actual bearing performance tests. Specimens, one single and one two-layered, with suitable structural and fluid flow properties, were chosen and machined into a 40 mm diameter bearing pad for static performance testing.

10.1 DESIGN OF BEARING TEST RIG

To facilitate bearing performance testing, a bearing test rig was purposely designed and constructed.

10.1.1 Mechanical Design

The layout of the rig was typical of that for aerostatic thrust bearing testing, and consisted of a reference surface on which the thrust bearing sat. Material for the reference surface, lapped to a flatness of better than 1 μm over 50 mm, was restricted to 316 stainless steel, as it also served as the target for the inductive bearing displacement sensors. To measure the pressure profile across the bearing surface, a pressure sensor was incorporated inside the reference plate, which had a centre pressure tapping of 0.4 mm. The plate was guided on its sides by two bronze strips, so that it could be moved across the diameter of the thrust pad to record the pressure profile. A micrometer mounted at one end measured the radial position of the pressure tapping.

The static load was applied onto the bearing pneumatically. This was preferred to the use of dead weight as the bearing mass was believed to have a critical influence on the onset of pneumatic instability [88]. By loading the bearing with air pressure, variation in

load could be achieved easily without any change in the total moving mass that the bearing supports. The loading cylinder was mounted on a four-pillared frame that straddled the reference plate, and had a piston attached to a ball-ended load shaft via a load cell which measured the applied load. By using a clearance seal only on the piston, seal friction was eliminated, which might otherwise have had a damping effect and therefore affected the detection of instability. To complete the frictionless system, a double-entry, slot-restricted journal bearing unit was used to guide the load shaft. The design of the slot-restricted bearing was based on the method by Stout [257]. Details of the calculations can be found in Appendix B.

Although the performance tests were static, allowance had been made so that future expansion to include dynamic loading would be possible. Suggestions for the required modifications will be discussed in detail in Chapter 13.

10.1.2 Design of Porous Thrust Bearing

The porous ceramic bearing pad was held in a bearing housing which also provided mounting for the inductive sensors for measuring the change in bearing clearance. In most conventional porous bearing designs, metal loaded epoxy was used to attach the porous pad to the bearing housing at its perimeter. The epoxy also served to seal the porous pad around its edge. Shear deformation of the adhesive layer would, however, have a negative effect on the total stiffness of the bearing, and in some cases had to be calibrated for.

A shoulder location in the current design provided much stiffer axial support between the bearing pad and the housing, with the edge of the porous pad being sealed with silicone sealant. This also allowed the reuse of the same housing for different bearing pads. Width of the shoulder was kept to a minimum, minimising any effect that the local change in diameter might have on fluid flow within the porous pad, while at the same time being sufficient to accommodate the compressive stresses and provide a reasonable

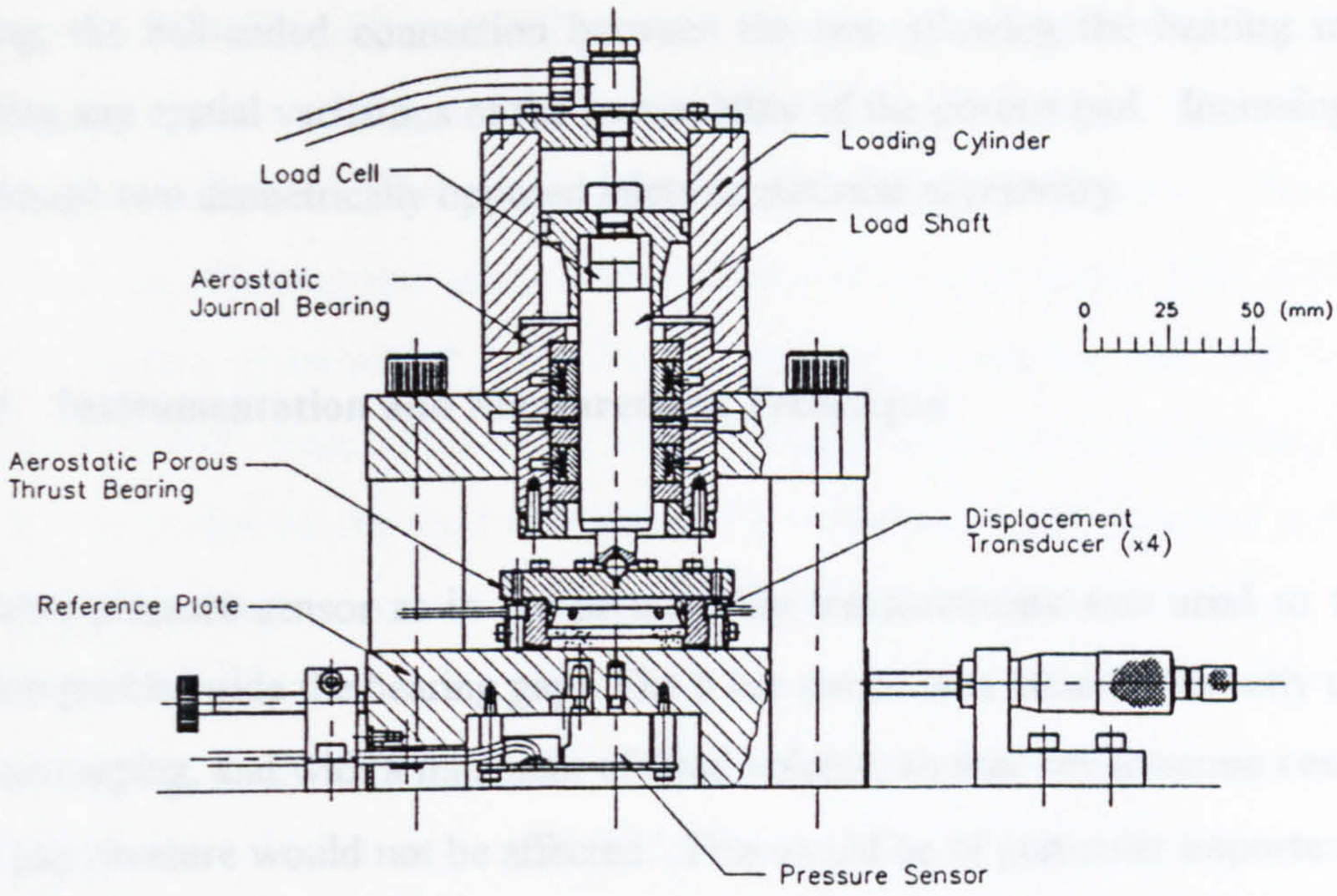

Fig. 10.1 Sectional View of the Bearing Test Rig

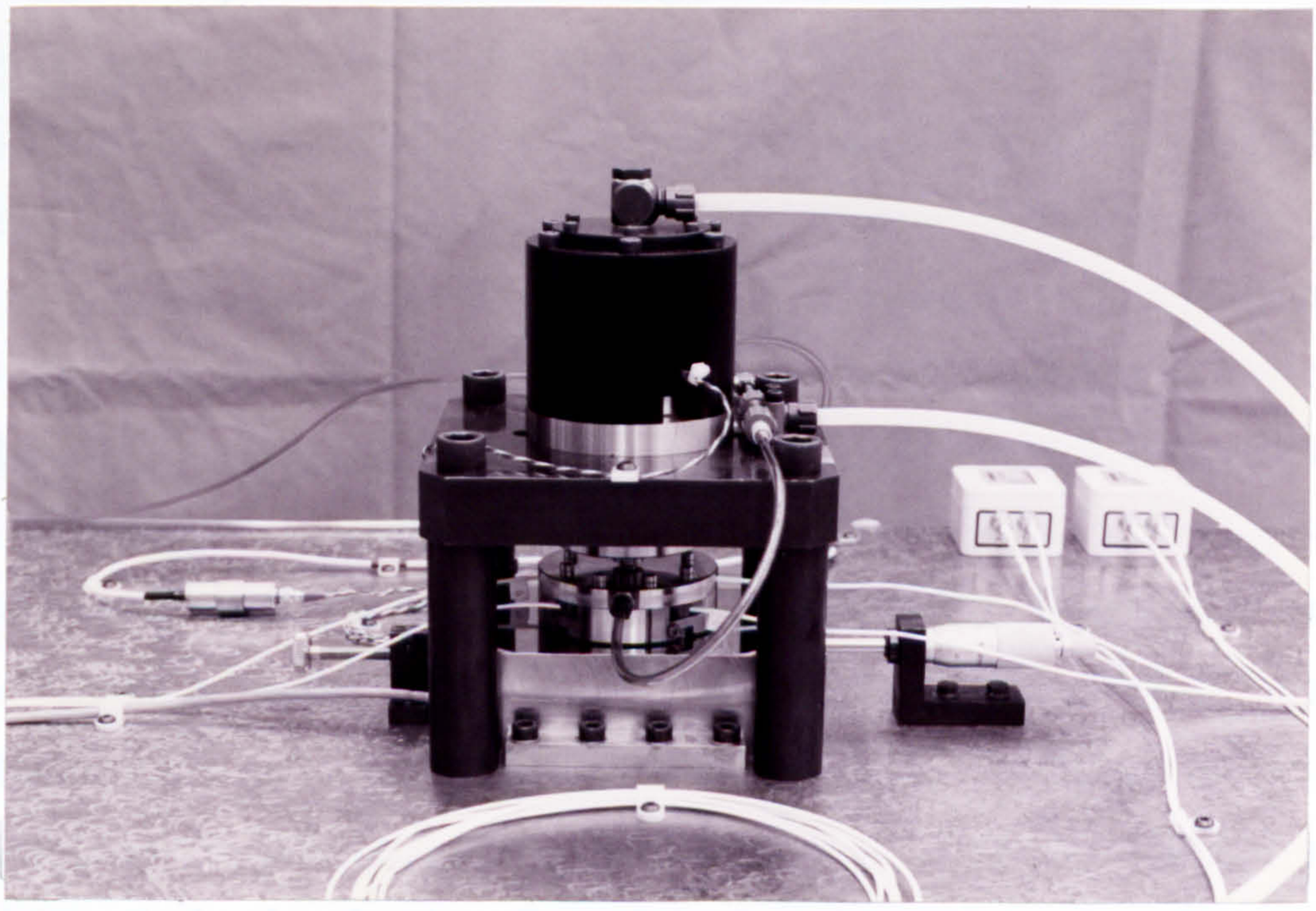

Fig. 10.2 Porous Aerostatic Thrust Bearing Test Rig

contact stiffness. Loading was applied via the load shaft onto the centre of the bearing housing, the ball-ended connection between the two allowing the bearing to swivel, revealing any spatial variations of the permeability of the porous pad. Incoming air was fed through two diametrically opposed inlets to minimise asymmetry.

10.1.3 Instrumentation and Measurement Technique

The same pressure sensor as in the permeability measurements was used to track the pressure profile inside the bearing gap. The 5 bar sensor was mounted directly under the pressure tapping, and with a minimum of dead volume, so that any dynamic components of the gap pressure would not be affected. This would be of particular importance when testing for dynamic performances. The void volume between the sensing element and the pressure tapping point should ideally be zero, but this would require a change of sensor type.

Four inductive displacement sensors, mounted 90° apart, provided measurement of the change in bearing clearance as well as bearing tilt along two orthogonal axes. These sensors (Kaman SMU-9200-15N) had a range of 50 μm, and were calibrated against a 316 stainless steel targeting surface, to a linearity of better than 0.5% span. Actual calibrated values were used in the data acquisition software to convert the signals to linear displacements. Arguably, optical sensors based on back scattering or triangulation principles should provide better thermal stability and noise immunity, and would place fewer restrictions on the choice of material for the targeting surface. The choice was, however, restricted due to conflicting requirements of parallel research work on water hydrostatic journal bearings. Long term drifts were found to be in excess of 2 μm, with an additional noise ripple of 1 μm peak to peak at 13.5 Hz. As the current tests were static, software low-pass filters with a cut-off frequency of 10 Hz were used, in addition to rezeroing the bearing clearance datum for every measurement point. This was done by dumping the load and bearing supply pressure and resetting the measured displacement values.

An Entran ELH-TC16-1KZ load cell of 1 kN range was placed under the loading piston to measure the pneumatically applied load. The datum of the load cell was also reset before every measurement, with the loading air pressure reduced to zero. This was, as in the case of the displacement sensors, to minimise long term sensor drift, measured as some 5 N with a hysteresis of 2 N. Dead weight of the bearing unit, and that of the complete load shaft, were added to the measured value to give the total bearing load. To minimise errors due to the load cell hysteresis, consecutive measurement points were taken by approaching the target displacement value from alternate directions.

Data acquisition was software controlled, but all pressure adjustments were done manually to give a higher degree of flexibility, in case instability should occur. Two different measurements were performed on each bearing sample, the static load - displacement curve with various supply pressures, and the pressure profile measurement across the entire bearing diameter at a fixed bearing supply pressure and a number of fixed bearing clearances.

10.2 MACHINING OF TEST BEARINGS

To attain the required geometry of the bearing pads, the two test samples were first rough machined using the same set-up as in Section 4.4. Depth of cut was at 5 μm for at least the last four cuts. The grinding was performed without coolant to avoid clogging up the pores. All diameters were finished to size, with only a 50 μm allowance on the bearing surface for ultra-precision finishing.

Final machining of the bearing surface was done on the 7-axes, ultra-precision ceramic cup grinder in Cranfield Precision Engineering Ltd. The 120 mm diameter, 3 μm grit diamond wheel used was first dressed in situ with a diamond dressing wheel of 252 μm grit on a Westwind air bearing dressing spindle. Each porous pad was mounted in the

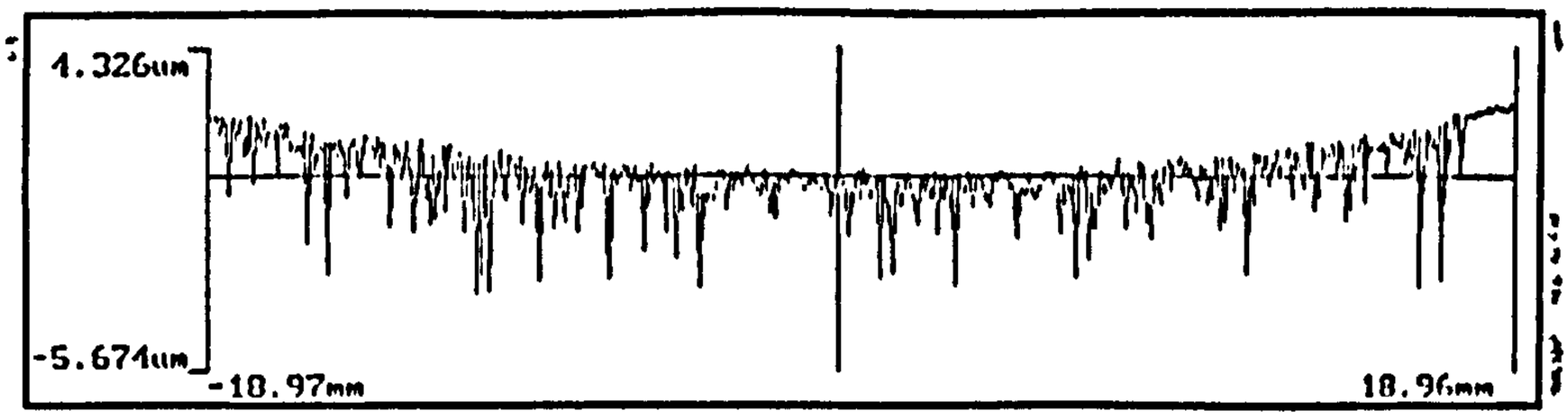

Fig. 10.3 Talysurf Profile of the Single Layer Bearing Surface

Fig. 10.4 Talysurf Profile of the Two-Layered Bearing Surface

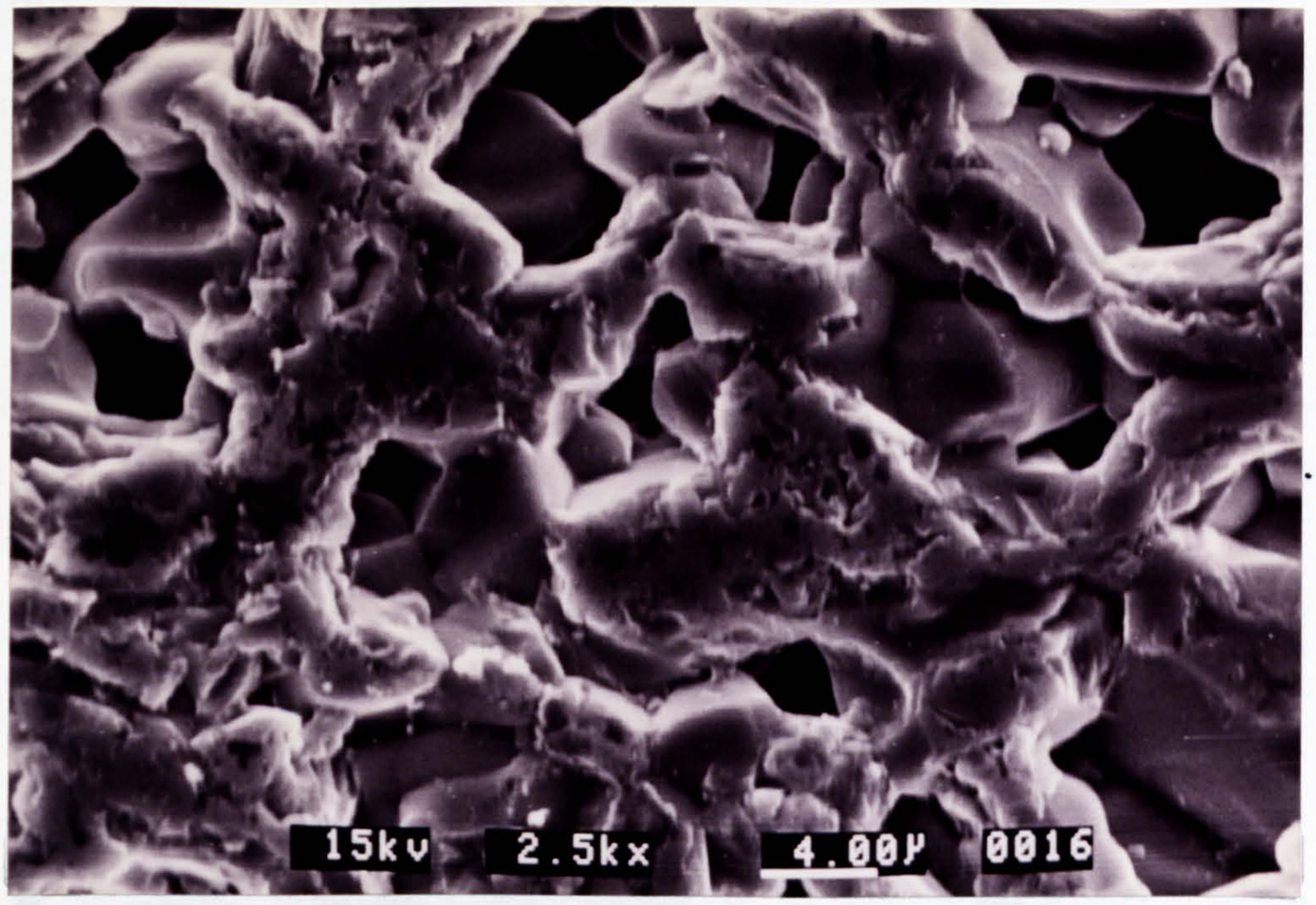

Fig. 10.5 Microstructure of the Machined Single Layer Bearing Surface

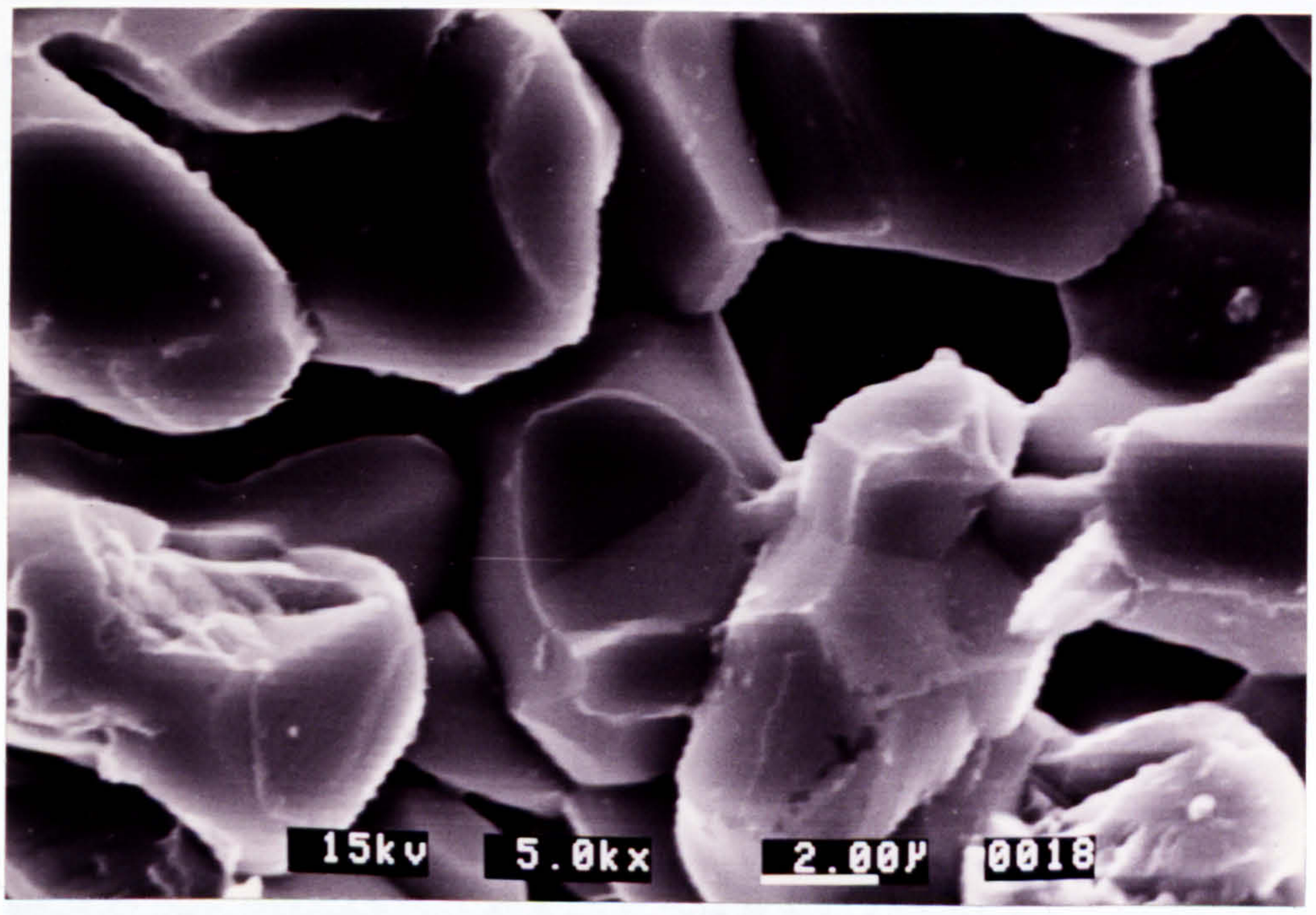

Fig. 10.6 Neck Formation in the Single Layer Bearing Material

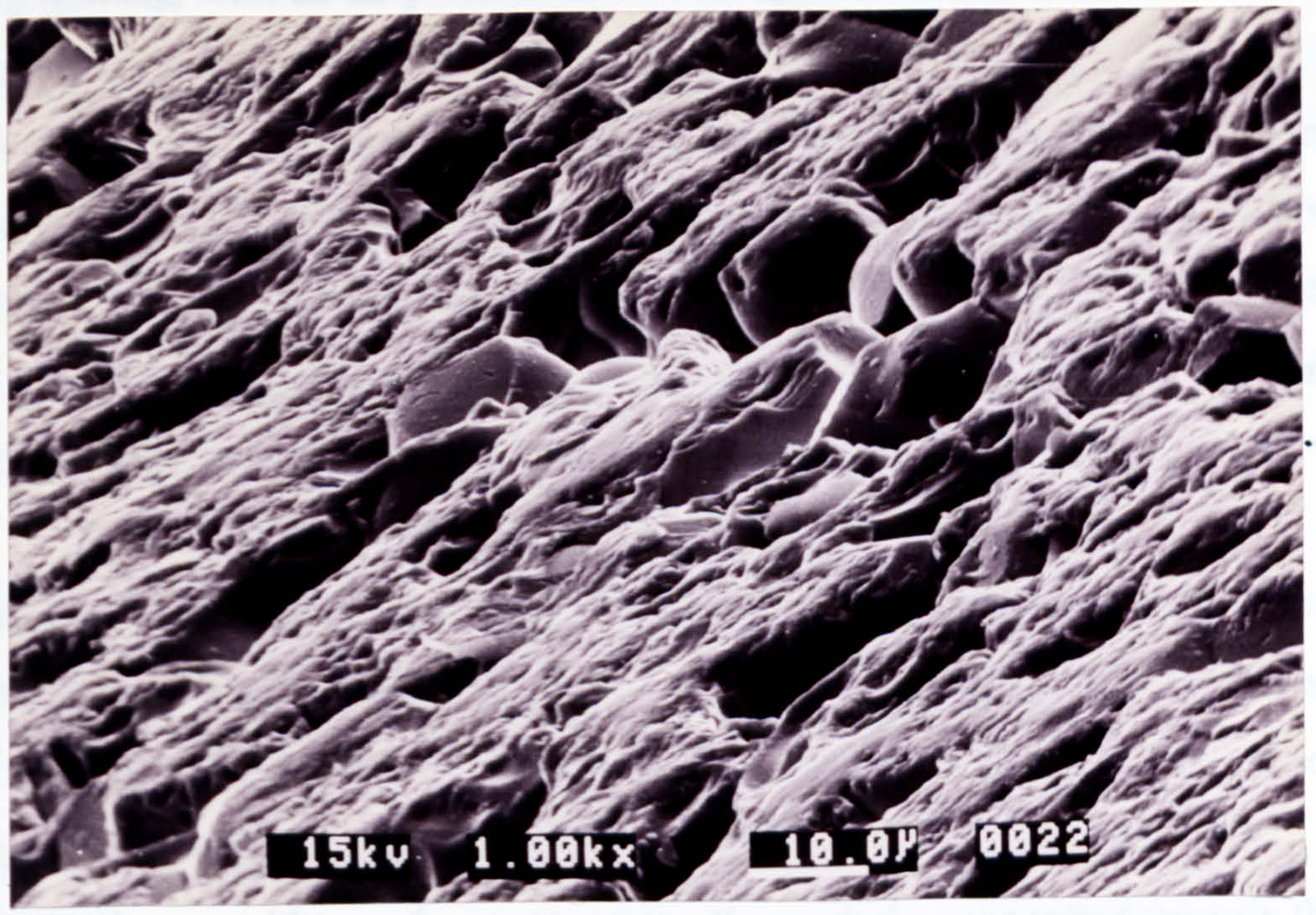

Fig. 10.7 Topology of the Machined Single Layer Bearing Surface

(SEM dynamic angle = 70°)

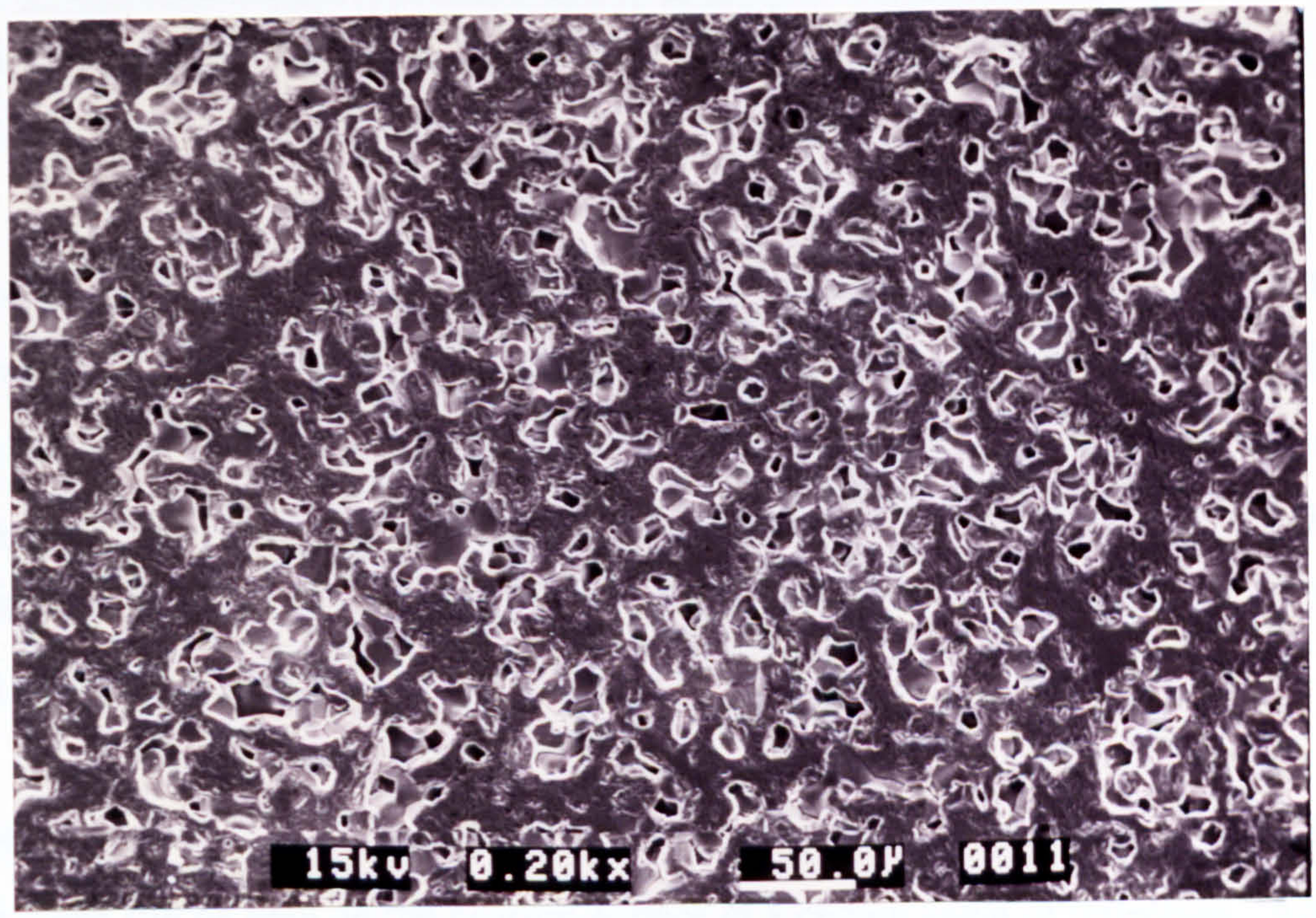

Fig. 10.8 Macroscopic View of the Single Layer Bearing Surface

bearing housing, with an air pressure of 1.5 bar applied to the air inlets. This was so arranged as to compensate partially for elastic deflection of the porous pad under working conditions. The finished bearing surface, though slightly concave in its natural state (Figs. 10.3, 10.4), would resume a flat geometry at the designed nominal bearing clearance. Depth of cut was fixed at 1 μm at a wheel speed of 4000 rpm. Feed rate was set at 1 mm s^{-1}. Coolant had to be applied, so that the grinding debris could be removed effectively. Pore clogging by the coolant was prevented by the pressurising air.

Scanning electron micrographs of the finished bearing surface of the single layer specimen are shown in Figs. 10.5 to 10.8. The specimen was hot isostatically pressed from 7 μm alumina. Successful flattening of the protruding grains above the nominal surface by the precision grinding could clearly be observed (Figs. 10.7, 10.8). There appeared to be no evidence of pore smearing. Komanduri[258] suggested recently that the grinding of brittle materials, even at extremely fine depth of cut, was still likely to be due to microcrack formation and not plastic deformation. Pore warping as in the case of metals is therefore unlikely to occur in porous ceramics. Pictures at high magnification showed that the machined surface did not have the mirror finishes that one normally associates with ultraprecision grinding (Fig. 10.5), but the grinding process was by no means optimised due to restricted access to the machine.

A two-layered bearing pad was also finished using the same machining parameters. This was based on a 23 μm substrate. The fine layer was a hot-pressed, combined slip and tape-cast of 0.5 μm alumina. The bearing pad was ground to a total thickness of 6 mm, 0.5 mm of which being the fine layer. The shoulder of the bearing pad was positioned such that the bearing surface, when fully finished, was less than 0.1 mm proud of the rim of the bearing housing (Fig. 10.9).

Despite the mirror finishes achieved with the ultra-precision grinding, slight grinding marks could still be seen on the bearing surface at a certain angle of reflection. Attempts to pick up such marks in the surface roughness measurement were not successful, suggesting that these marks were either of very fine width (the stylus on the Talysurf had

a 2 μm radius) or very small depth. Very fine alumina debris found attached to the diamond grinding wheel after machining was believed to be the cause. Cleaning the diamond wheel after every cut was not sufficient to eliminate this wheel clogging problem.

As the particle size in the two-layered structure already approached the limit of resolution of the SEM, it was difficult to observe whether the same grain flattening as in the single layer specimen had been achieved. Considering that the diamond grit size was 6 -10 times that of the alumina particles, the likely mode of material removal was thought to be grain pullout. Nevertheless, measured surface roughness values were much better than the single layer specimen (Fig. 10.4).

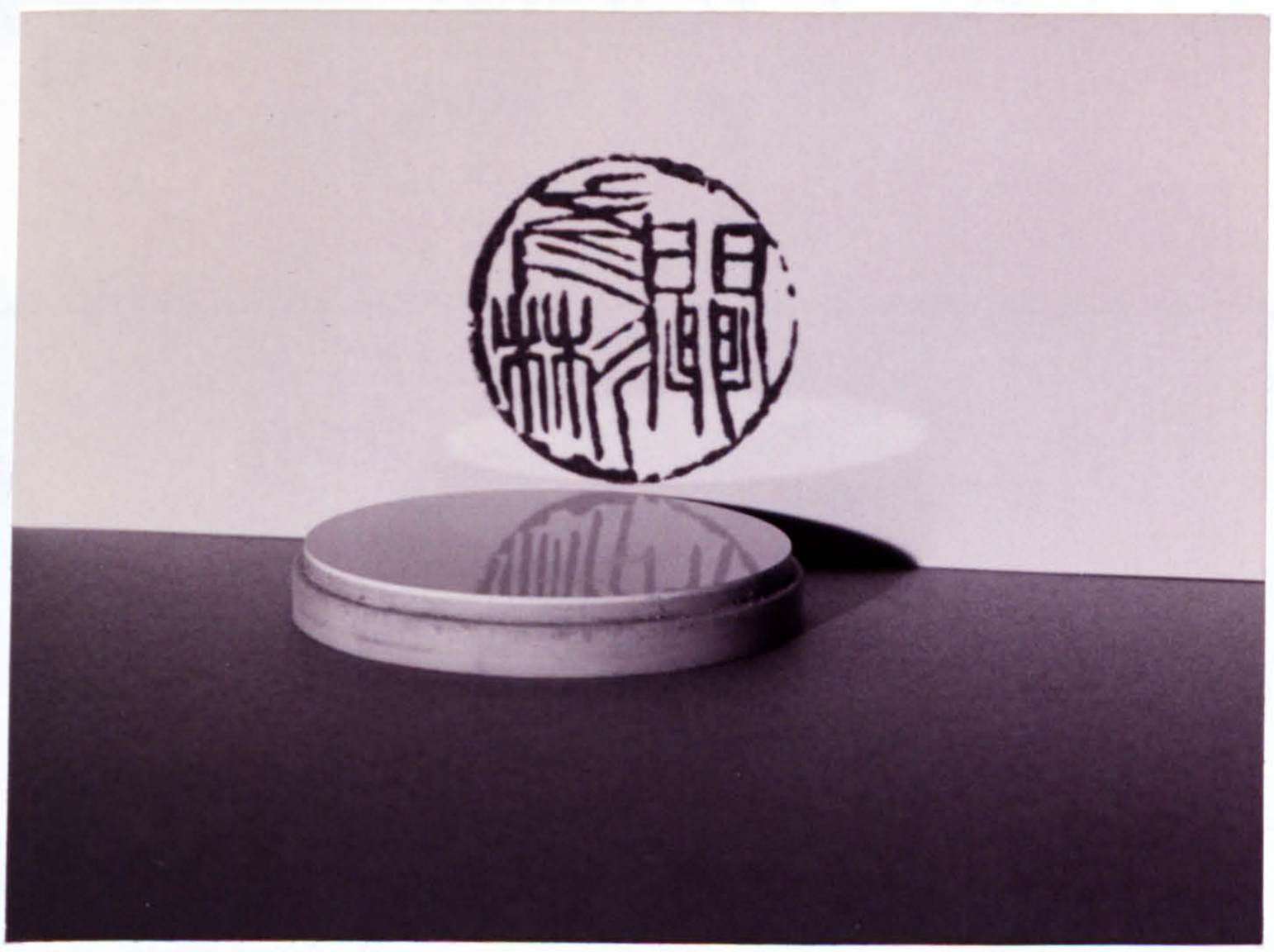

Fig. 10.9 Ground Surface Finish of the Two-Layered Bearing Pad

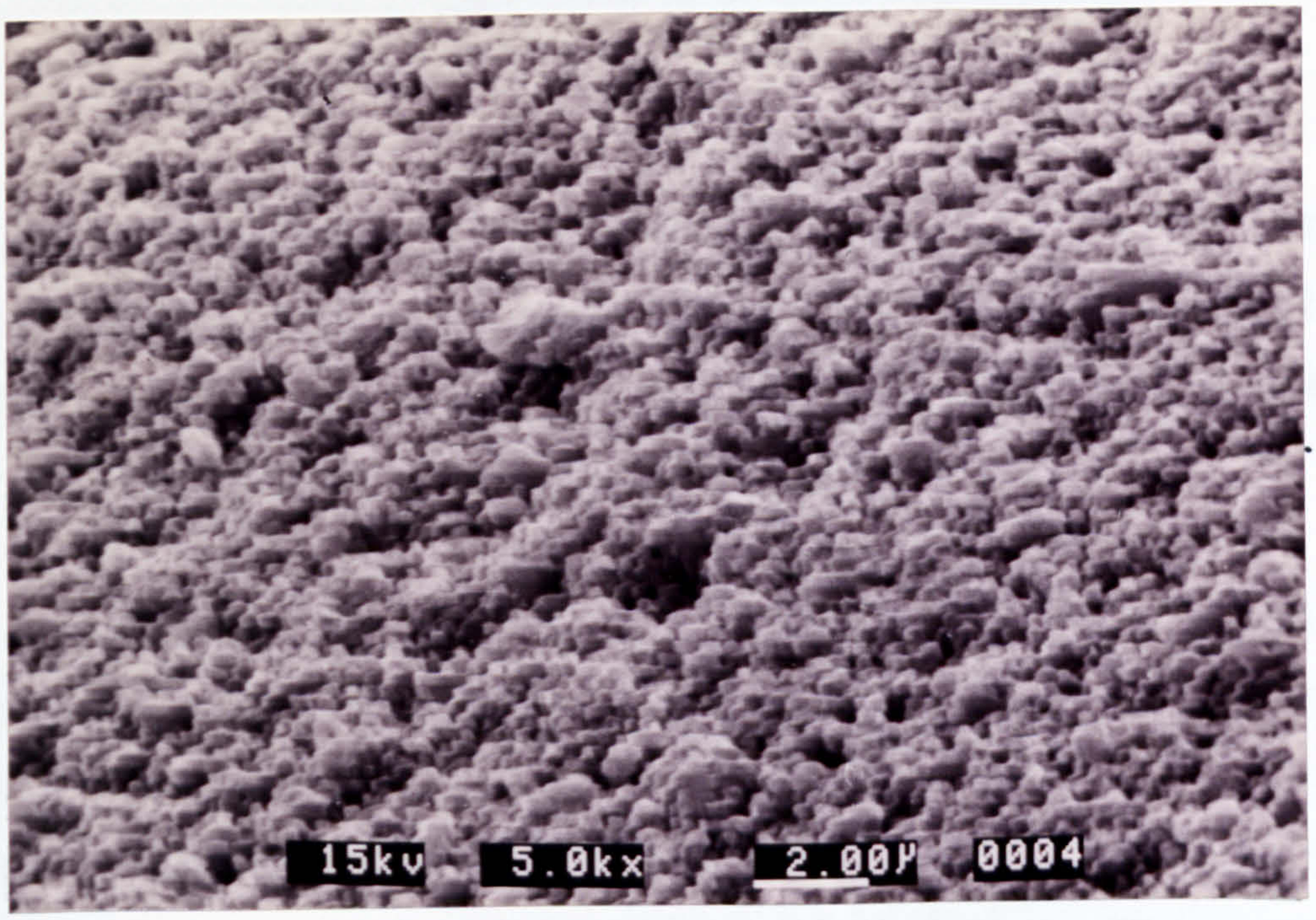

Fig. 10.10 Topology of the Machined Two-Layered Bearing Surface

(SEM dynamic angle = 70°)

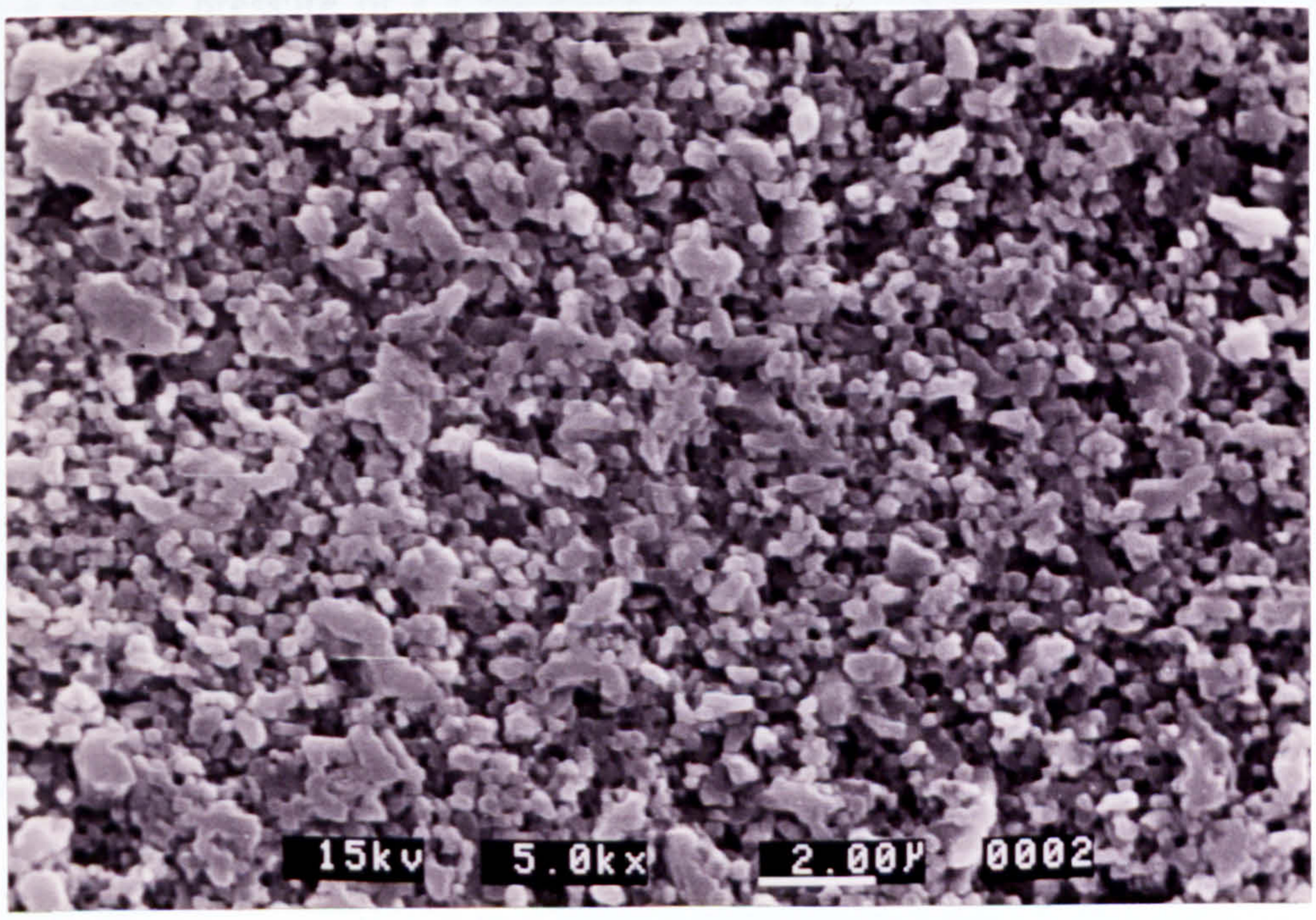

Fig. 10.11 Topology of the Machined Two-Layered Bearing Surface

(Top view)

10.3 TESTING OF THE SINGLE LAYER POROUS BEARING

The single layer specimen was sintered from 7 μm alumina particles by hot isostatic pressing at 1750 °C, 1000 bar for an hour to a porosity of 0.208, which was all open. Viscous permeability was measured as 4.75×10^{-15} m^2, inertia permeability coefficient 1.41×10^{-10} m. Flow through the specimens was essentially Darcian.

After machining and ultrasonic cleaning, the bearing was tested for static load characteristics. Dry filtered air at 5 bar was allowed to pass through the test bearing for a minimum of 15 minutes to remove any adsorpted moisture within the pores. Measurement then commenced at a fixed bearing supply pressure, and the applied load was varied by adjusting the air pressure to the loading cylinder from zero, and increasing to that corresponding to a bearing gap of 1 μm. Bearing clearance and tilt in two orthogonal directions were recorded against applied load.

Above a supply pressure of 1.5 bar (gauge), the single layered test bearing exhibited pneumatic instability over a large range of bearing clearance, especially around the point of maximum stiffness. This region of instability became more extensive as the supply pressure increased. Two regions of stable operations were observable, one close to zero bearing clearance (≤ 5 μm), and one at very low load (≤ 25 N) and large clearances. The onset of stability was not clear cut, and depended considerably on the rate at which the load was altered to a new measurement setting. This was particularly the case for the instability region at large clearances (to the right hand side of the performance curve in Fig 10.12). Hollow legends in Fig 10.12 indicate measurement points with such marginal stability. At a supply pressure of 1.5 bar and below, no instability was observable over the entire range of bearing clearance.

Bearing tilt was slightly larger at large bearing clearances, due to lower tilt stiffnesses at those points, but was generally below 2 μm across 40 mm, approaching the repeatability of the displacement measurements.

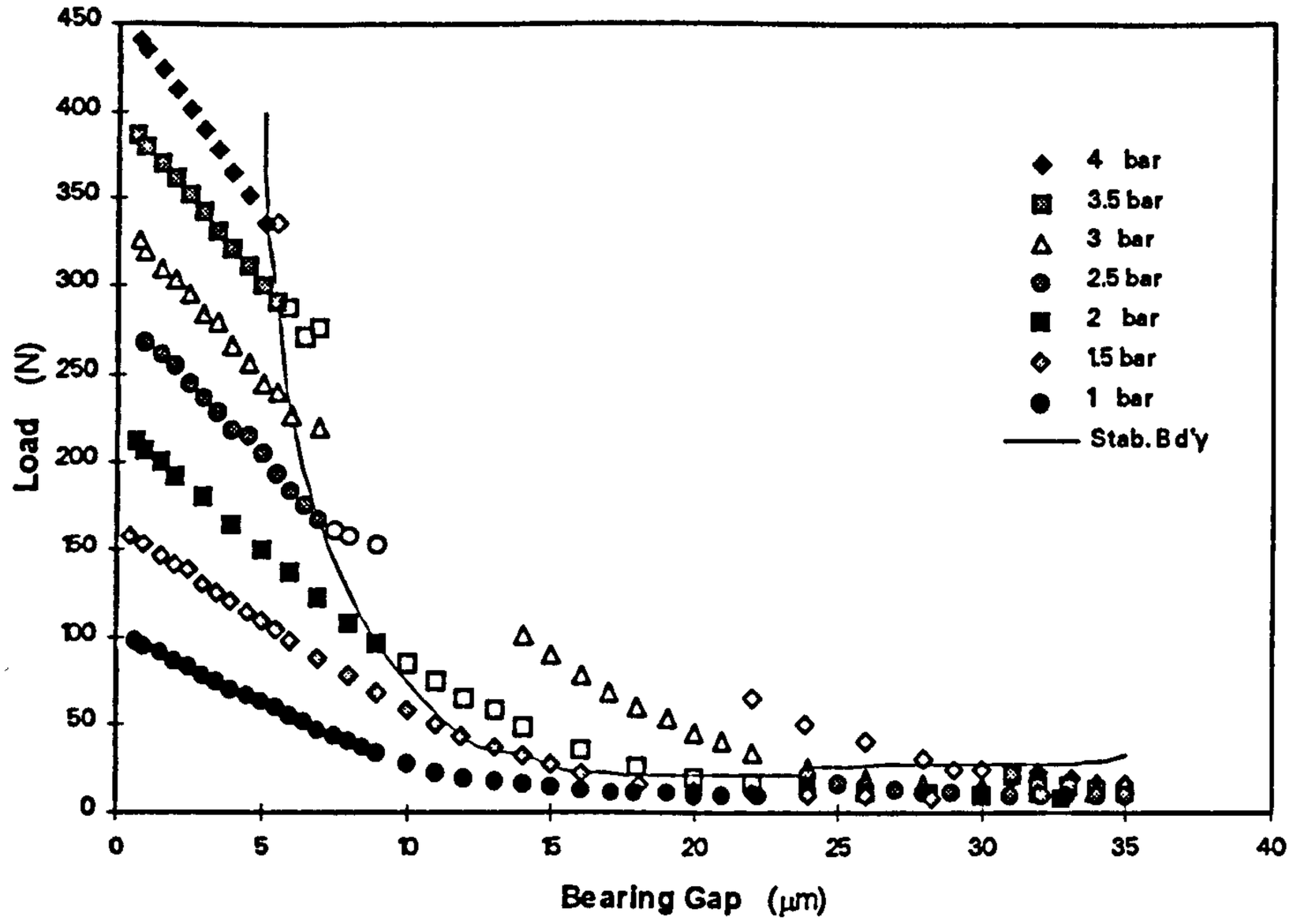

Fig. 10.12 Static Performance of the Single Layer Porous Test Bearing

(Hollow data points had marginal stability)

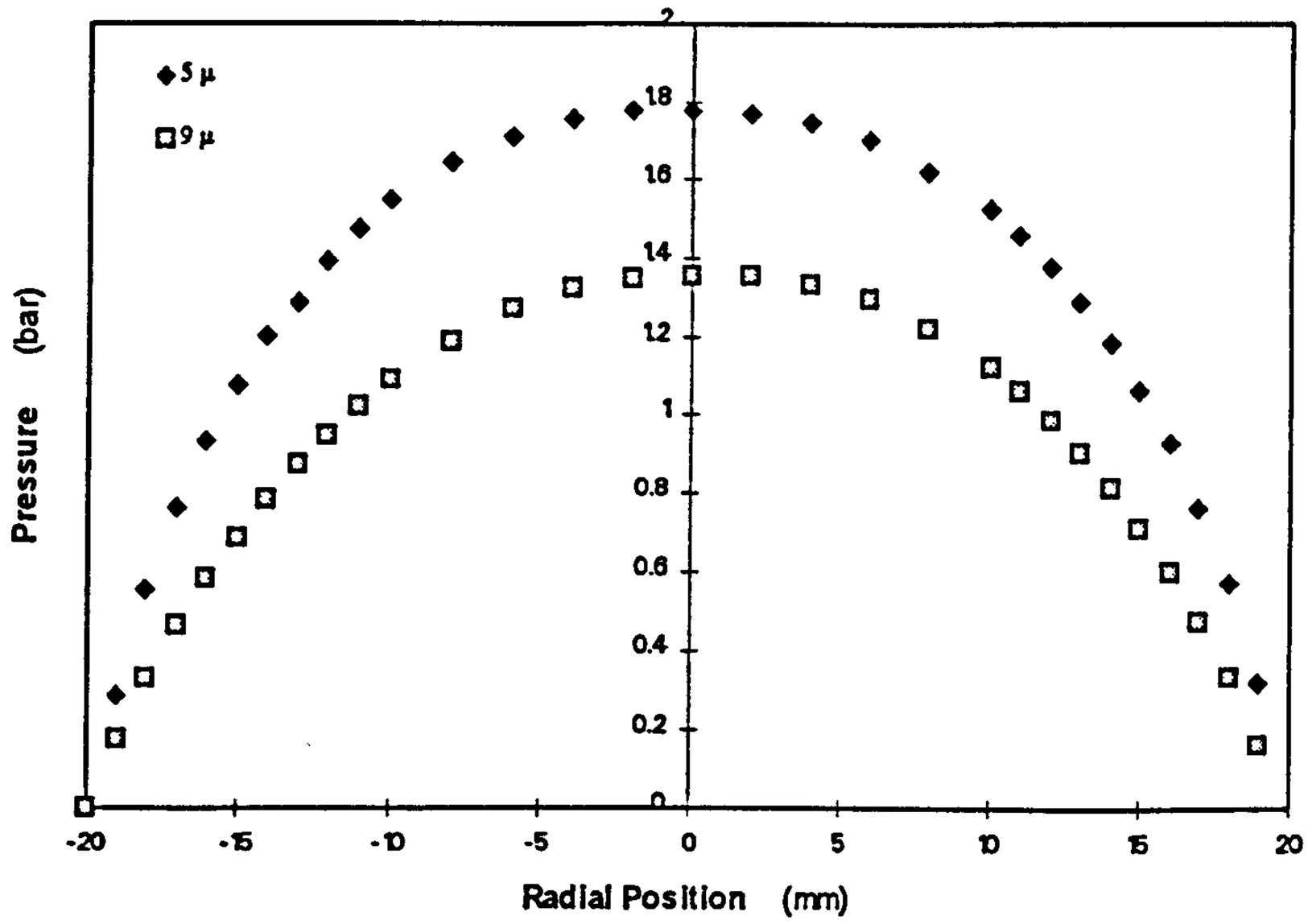

Fig. 10.13 Pressure Profiles of the Single Layer Porous Test Bearing

(Bearing supply pressure = 2 bar, bearing gap = 5 & 9 μm)

The pressure profile across the diameter of the bearing was then measured at a bearing clearance of 5 μm and 9 μm (Fig. 10.13). Supply pressure to the bearing was set at 2 bar above atmospheric, such that the two measurements were still within the stable operating region. Pressure readings were recorded at 1 mm radial intervals for the outer 10 mm, the rest at 2 mm intervals.

The bearing pad had its permeability remeasured following the static tests. Measurement over the central 23 mm gave permeability values of 4.22×10^{-15} m^2 and 4.13×10^{-10} m respectively. Over the entire bearing area, the values were 5.04×10^{-15} m^2 and 2.61×10^{-10} m.

10.4 TESTING OF THE TWO-LAYERED POROUS BEARING

The two-layered porous specimen was based on a 23 μm substrate HIPed at 1900 °C, 500 bar for an hour to a porosity of 0.277. The fine layer was a 1200 °C pre-sintered 0.5 μm slip cast, attached to the substrate by hot pressing at 1200 °C for an hour under an axial load of 2 kN, with a 55 μm thick alumina tape of 0.5 μm particles sandwiched in between. Porosity of the slip-cast layer was 0.285.

The permeability coefficients of the slip and tape-cast layers could only be determined in combination with the substrate. The viscous and inertia permeability coefficients of the substrate were measured as 2.68×10^{-13} m^2 and 1.72×10^{-7} m respectively. Coefficients for the slip-cast layer were determined by measuring the total equivalent permeability coefficients of the combined layers at two different thicknesses, as described in Appendix C. This method has the advantage that it does not require any information on the substrate or intermediate layer that remains unchanged in both measurement settings. The reduction in thickness for the second measurement was therefore entirely by material removal from the slip cast layer only. The calculated viscous permeability coefficient for the slip cast layer was 2.19×10^{-16} m^2, and the inertia permeability coefficient 3.28×10

$^{-14}$ m. Thicknesses of the different layers were measured optically, using a Mitutoyo PJ-300 profile projector. The substrate thickness was measured as 6.99 mm, that of the tape-cast 0.09 mm. The thickness of the slip cast layer was 1.94 mm and 1.44 mm respectively for the two measurements.

The coefficients for the tape-cast layer were determined by measuring the combined values with the coarse substrate, using measured substrate permeability data for direct calculation. To facilitate the measurement, the slip cast layer was removed entirely by grinding. The use of the two-thickness method as mentioned above was not possible as the tape layer was already very thin. The permeability values for the tape-cast layer were found to be 9.85×10^{-16} m^2 and 1.25×10^{-10} m respectively. The much higher values compared with those of the slip-cast layer suggested a lower packing density of particles, and possible existence of hairline cracks due to shrinkage, despite the application of uniaxial pressure during sintering. As the tape layer was thin (0.09 mm) compared to the slip cast (0.44 mm), its higher permeability implied that the pressure restricting function was not more than 5% of that of the slip cast layer.

The 2-layered bearing was tested following similar procedures as before. The bearing was found to be stable over the entire operating range, with bearing supply pressures of up to 5 bar. The static load curves (Fig. 10.14) showed a near constant stiffness between 0 - 7 μm at all values of supply pressure. For bearing clearances below 13 μm, measured bearing tilt remained essentially fixed at 0.013 mrad between sensors 1 and 3, and 0.03 mrad between sensors 2 and 4. Both values reduced sharply towards zero at gaps below 1 μm (Figs. 10.15, 10.16). As will be discussed in the following chapter, these values were only nominal, and might not necessarily represent the real bearing clearance, due to debris picked up by the bearing surface when in contact with the reference plate during the setting-up of the displacement sensors.

Pressure profiles were obtained at a fixed supply pressure of 4 bar, at various bearing clearances (Fig. 10.17).

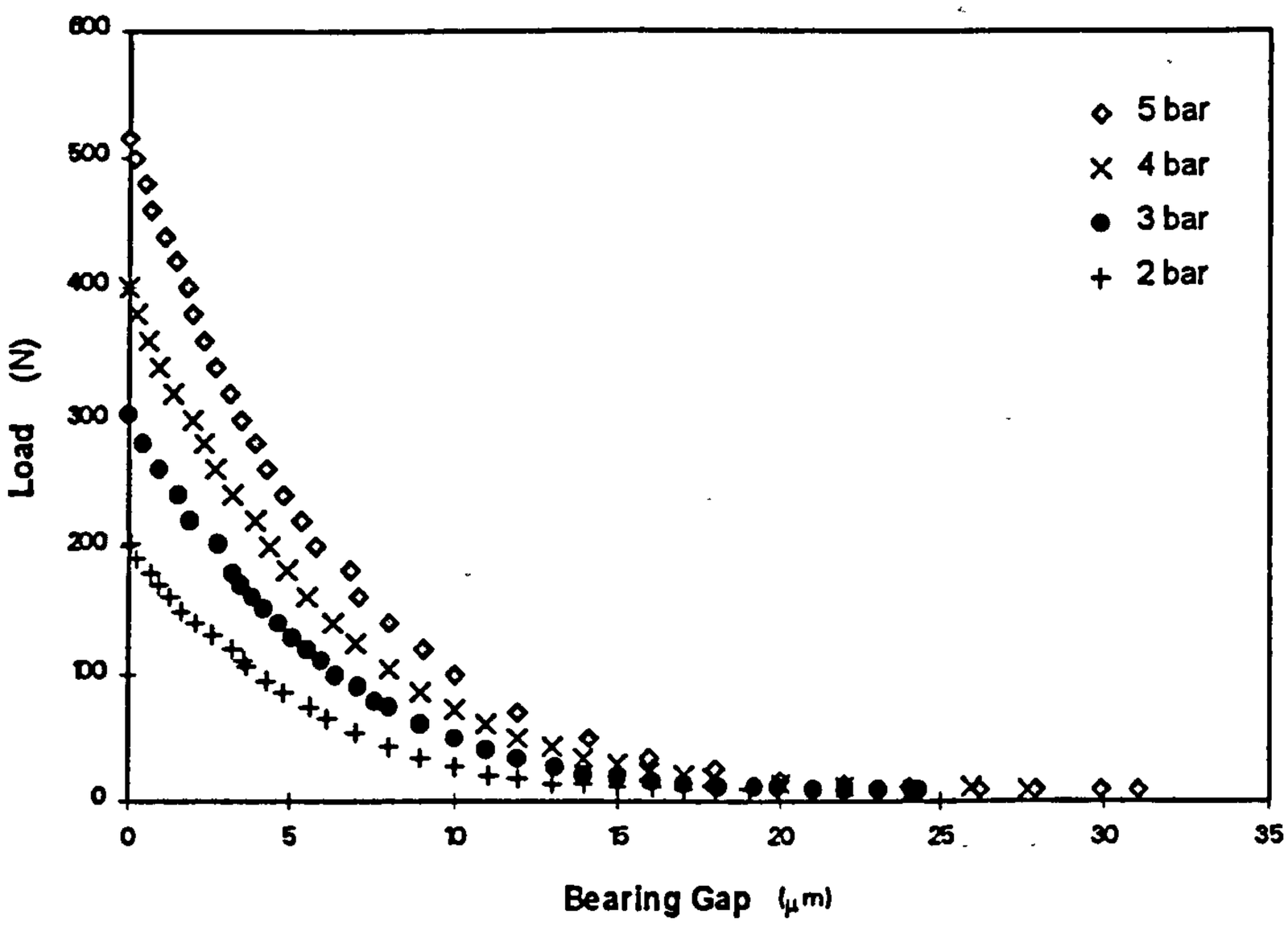

Fig. 10.14 Static Performance of Two Layered Porous Test Bearing

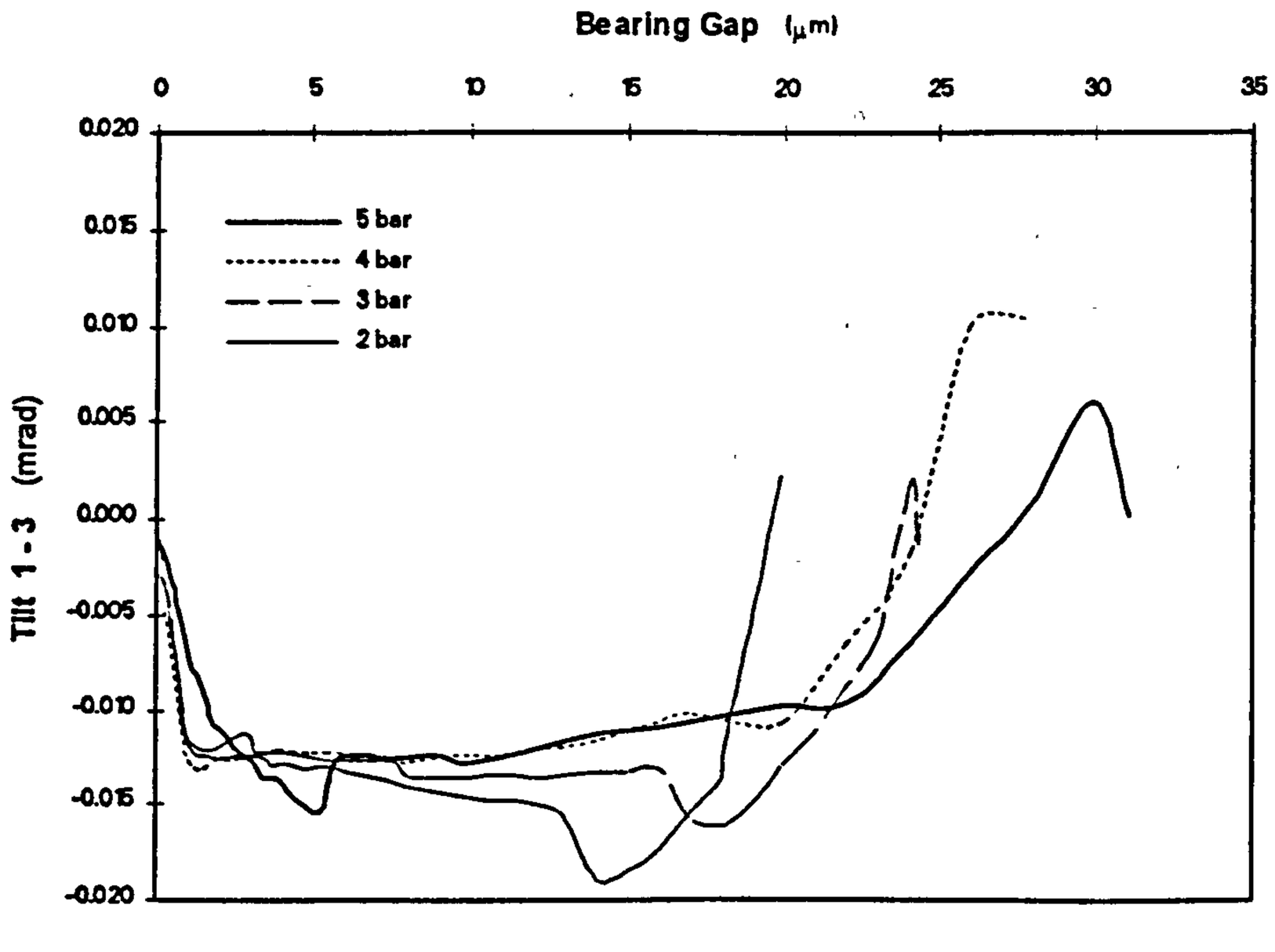

Fig. 10.15 Two Layered Porous Test Bearing -- Bearing Tilt across 1 - 3

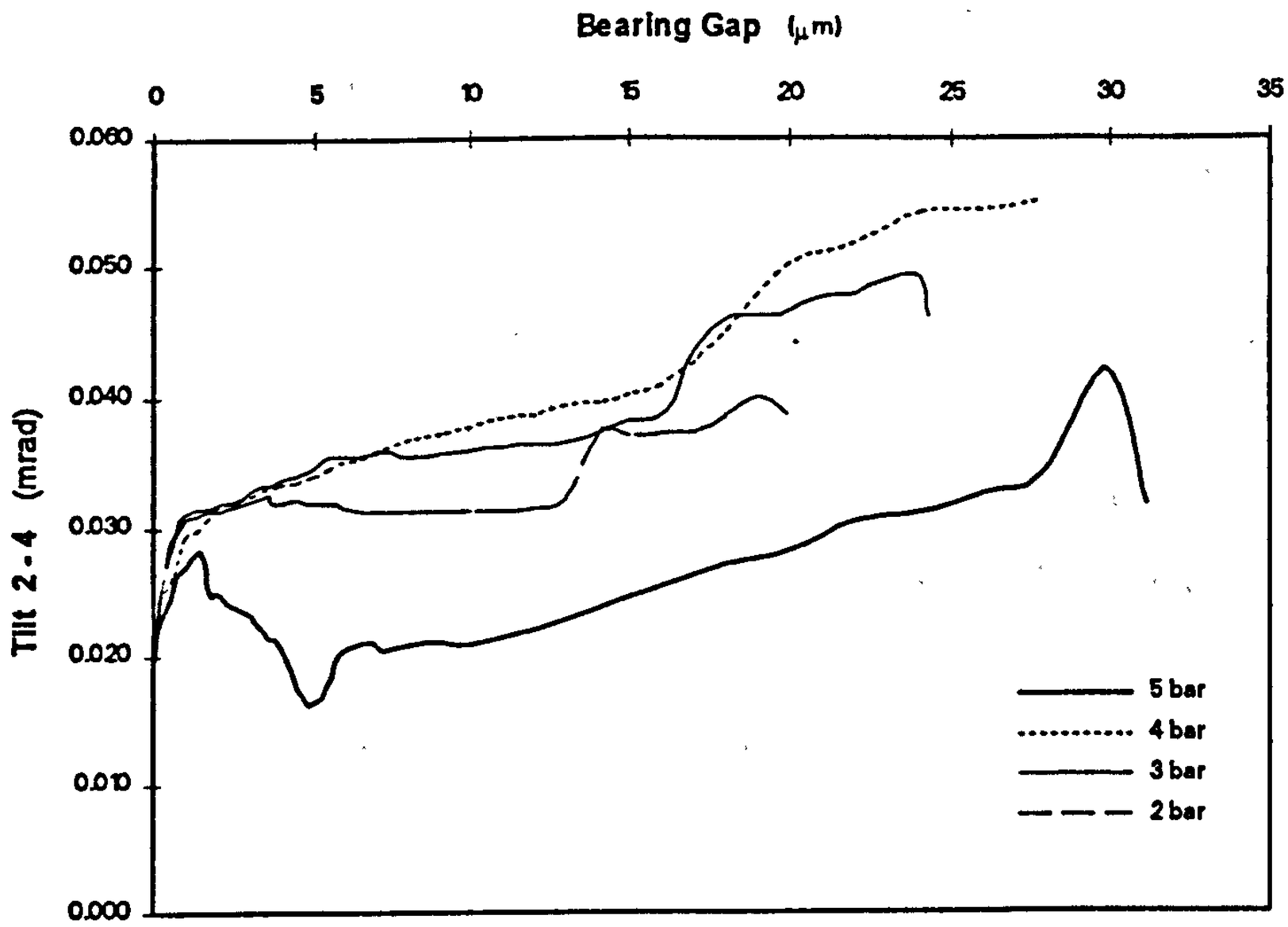

Fig. 10.16 Two Layered Porous Test Bearing -- Bearing Tilt across 2 - 4

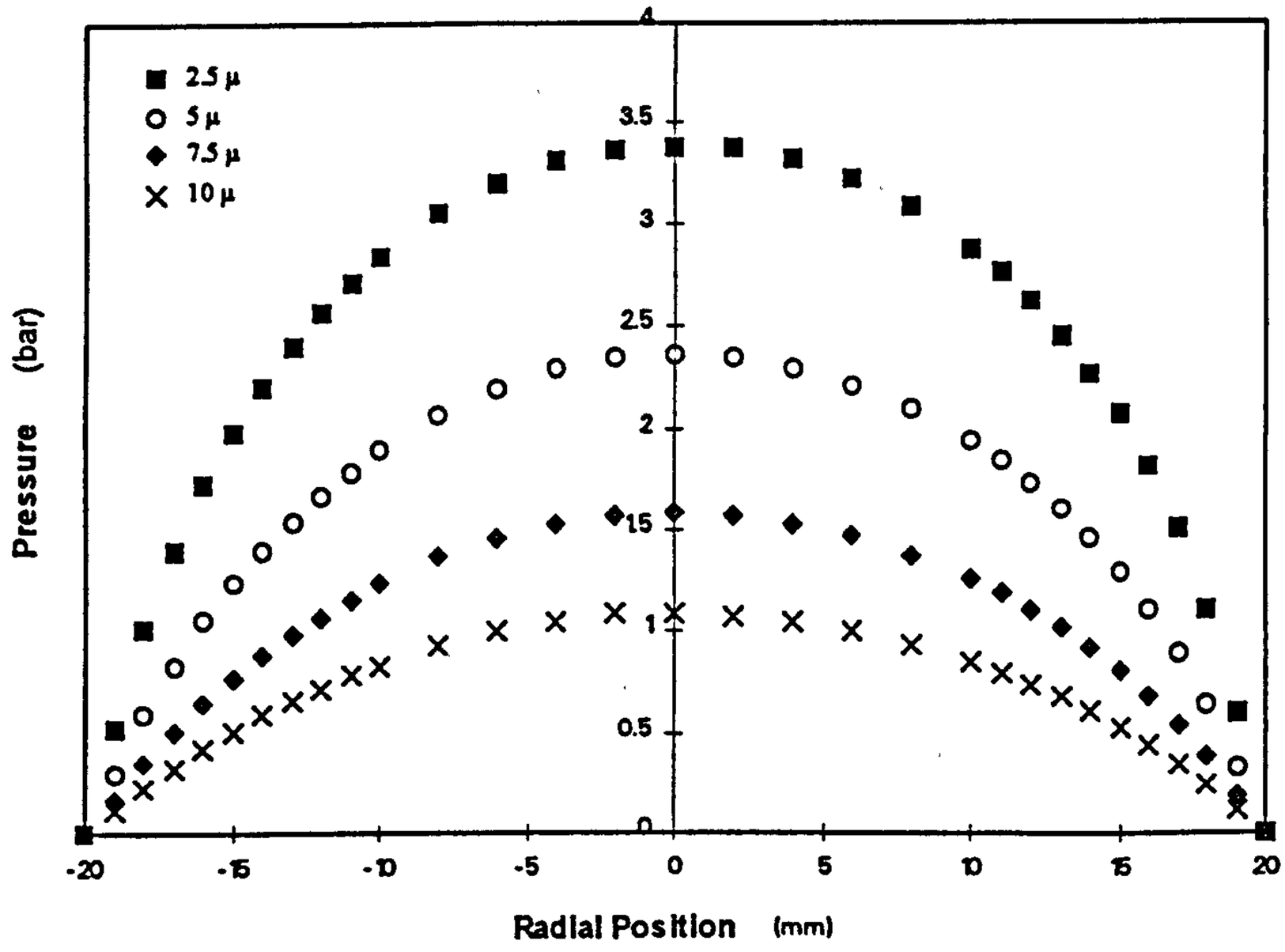

Fig. 10.17 Pressure Profiles of Two Layered Porous Test Bearing

(Bearing clearance = 2.5 μm)

On several occasions when the bearing was tested without a pre-purging with dry air, it was observed that the load carrying capacity measured was some 20% less than that measured with a well-purged bearing. The values returned to normal after dry compressed air was allowed to flow through the porous pad for 15 - 20 minutes. This problem was not noticeable with the single layer test bearing. Alumina is known to have great affinity with water, and fine alumina stored in free air can pick up as much as 5% moisture by weight, which is very difficult to remove. The reduction in load capacity could possibly be explained by a reduction of permeability of the fine pored layer due to adsorption of water vapour when left standing in free air. Continuous purging with dry air helped to remove the adsorbed moisture and return the restricting performance of the fine layer to its normal state. Pores in the single layer bearing were about an order of magnitude larger in size, and would therefore be less affected by the effects of moisture pickup. All results listed here were therefore obtained after a minimum purging period of 30 minutes.

The permeability coefficients of the combined layers were measured again, as a cross reference, on the bearing pad after the performance tests were completed. The value measured over the centre 23 mm of the entire bearing pad were found to be 2.59×10^{-16} m^2 and 3.38×10^{-13} m respectively. The higher values than those for the slip cast layer alone were not surprising, due to the more permeable tape layer being included in the measurement and treated as homogenous with the slip layer. The measurement was also repeated over the entire bearing surface (40 mm diameter). The resulting values of 2.19×10^{-16} m^2 and 2.02×10^{-13} m indicated that the outer annulus might be slightly less permeable, due possible to non-uniform densification. Moisture adsorption also appeared to have a noticeable effect. Measurement over the central region on the same specimen, but without a 30 minute pre-purging with dry air, resulted in slightly different values of 2.43×10^{-16} m^2 and 3.64×10^{-13} m. The lower permeability values so obtained appeared to support the moisture adsorption hypothesis.

11. COMPARISON OF EXPERIMENTAL RESULTS WITH THEORETICAL PREDICTIONS

Of interest to any porous aerostatic bearing designer is the accurate prediction of a bearing's load carrying capacity, from which the static bearing stiffness can also be deduced. Of secondary importance, especially in precision engineering applications, is the gas consumption. Load carrying capacity is obtained theoretically by integration of the pressure profile. Comparison of the latter between measured and calculated values therefore gives a measure of the precision of the bearing theory.

Both load carrying capacity and pressure profile have been measured under various operating conditions for the single and two-layered bearings. No gas consumption data were however available, due to limits on the operating pressure of the flow sensors on hand.

11.1 TWO-LAYERED BEARING

As the single-layer bearing was only stable at low supply pressures, the comparison of the measured static load carrying capacities with published theories was first carried out using data from the two-layered bearing. The latter was stable over the entire range of supply pressures and bearing clearances.

11.1.1 Load Carrying Capacity

Before the bearing characteristics could be compared with theoretical predictions, a correction to the measured bearing clearance was found to be necessary.

Bearing tilt measurements (Fig. 10.15, 10.16) revealed a sudden increase in tilt between 0 and 1 μm as measured. Beyond that point, the inclination remained largely constant except for large clearances, at which the tilt stiffness was very low. Tilt measurements at such clearances were therefore easily influenced by external disturbances such as moments exerted by the stiffness of sensor cables.

The sharp change in tilt at zero gap was thought to be unusual. Further investigation revealed that the bearing surface was not in full contact with the reference plate, due to a small piece of debris embedded in the porous pad near its perimeter. Talysurf measurement confirmed that a piece of debris 42 μm in width was protruding from the surface by 1.4 μm. The measured bearing-clearance values were therefore smaller than actual. All measured clearance values were therefore corrected before any comparison with theories. The debris, metallic in appearance, was possibly picked up during the setting-up of the displacement sensors, when the pad was in contact with the reference plate. Even etching with hydrofluoric acid did not remove it entirely.

Most bearing theories present load capacity as a function of a bearing number, which in turn is a function of the bearing clearance, amongst others. The definition of bearing number in equation 3.4 :

$$\Lambda = \frac{12.\Phi.r_p^{\,2}}{z_p.z_g^{\,3}}$$

was used by Sheinberg [44] and Gargiulo [45]. Sheinberg assumed that the flow through the porous pad was one-dimensional and Darcian, and obtained an analytical solution for the pressure profile :

$$\bar{p}^2 = 1 - \frac{I_0.(\sqrt{\Lambda}.\bar{r})}{I_0.(\sqrt{\Lambda})}.(1 - \bar{p}_a^{\,2}) \qquad (11.1)$$

The dimensionless load capacity $\overline{W}$ was then obtained by integrating pressure with respective to radius :

$$\overline{W} = \frac{2}{1-\bar{p}_a} \cdot \int_0^1 \bar{p}.\bar{r}.d\bar{r} \qquad (11.2)$$

The numerical solution by Gargiulo, on the other hand, was based on two-dimensional flow, with various ratios of permeability in the axial and radial directions. Results for load capacity were published for a bearing pad with a diameter-to-thickness ratio of 5, and at a supply pressure of 2 bar (gauge). No information was available for the pressure profile.

Equation 11.1 also appeared in a number of later reports, but with a modified definition of bearing number to allow for slip flow and compressible flow. Murti [50], for example, applied a correction to Λ to allow for compressibility of the fluid medium:

$$\Lambda_1 = \frac{12.\Phi.r_p^{\,2}}{z_p.z_g^{\,3}} \cdot \frac{1}{1+6.\Phi.z_p / z_g^{\,3}} \qquad (11.3)$$

A further correction for slip flow was also reported by the same author [51] :

$$\Lambda_2 = \frac{12.\Phi.r_p^{\,2}}{z_p.z_g^{\,3}} \cdot \frac{1}{1+3/(1+\alpha_s.\sigma_s)} \qquad (11.4)$$

Equations for the pressure profile and the load capacity were essentially the same as Sheinberg.

Both Jones [53] and McCrea [57] used a slightly different bearing number from equation 11.3 to allow for compressible flow :

$$\Lambda_3 = \frac{12.\Phi.r_p^{\,2}}{z_p.z_g^{\,3}} \cdot \frac{1}{1+6.\Phi / z_g^{\,2}} \qquad (11.5)$$

assuming that the fluid velocity at the bearing surface obeyed Darcy's law. The high increase in flow rate at small clearances in the slip coefficient measurement, however, does not appear to support this assumption.

The simplest way to compare experimental results and various published theories is to calculate the bearing number for each measurement point, based on each definition. The results could then be compared with equation 11.2. Fig. 11.1 shows such a comparison for the two-layered bearing, at a supply pressure of 4 bar. Also included were the results of Gargiulo, although strictly speaking, comparison with the latter is not entirely valid due to the differences in bearing dimensions.

The inertia effect of the fine-pored layer in the two-layered bearing was not negligible. To account for this effect, the bearing number was also recalculated by using the equivalent permeability Φ_e in equations 3.4, 11.3, and others. This equivalent permeability was calculated for each measurement point according to Appendix D, using the mean pressure in the bearing gap as the exit pressure of the porous pad. The changes in load capacity were, however, not significant, as can be seen from Fig. 11.1.

None of the above-mentioned definitions of bearing number provided good agreement between experimental data and theoretical predictions. The key appeared to be the much higher flow rate in the bearing gap due to velocity slip. This is particularly the case for small clearances. As already mentioned in Section 6.3.4, the model of slip flow by Beavers did not adequately predict the increase in flow rate at small clearances. It was therefore not surprising that the correction in equation 11.4 did not improve the agreement of results.

As mentioned in Chapter 2, another means of correcting for slip flow commonly used was the addition of an equivalent clearance to the bearing gap to account for the 'roughness' effect. The feasibility of this correction was first checked by correlating with the slip coefficient measurement data.

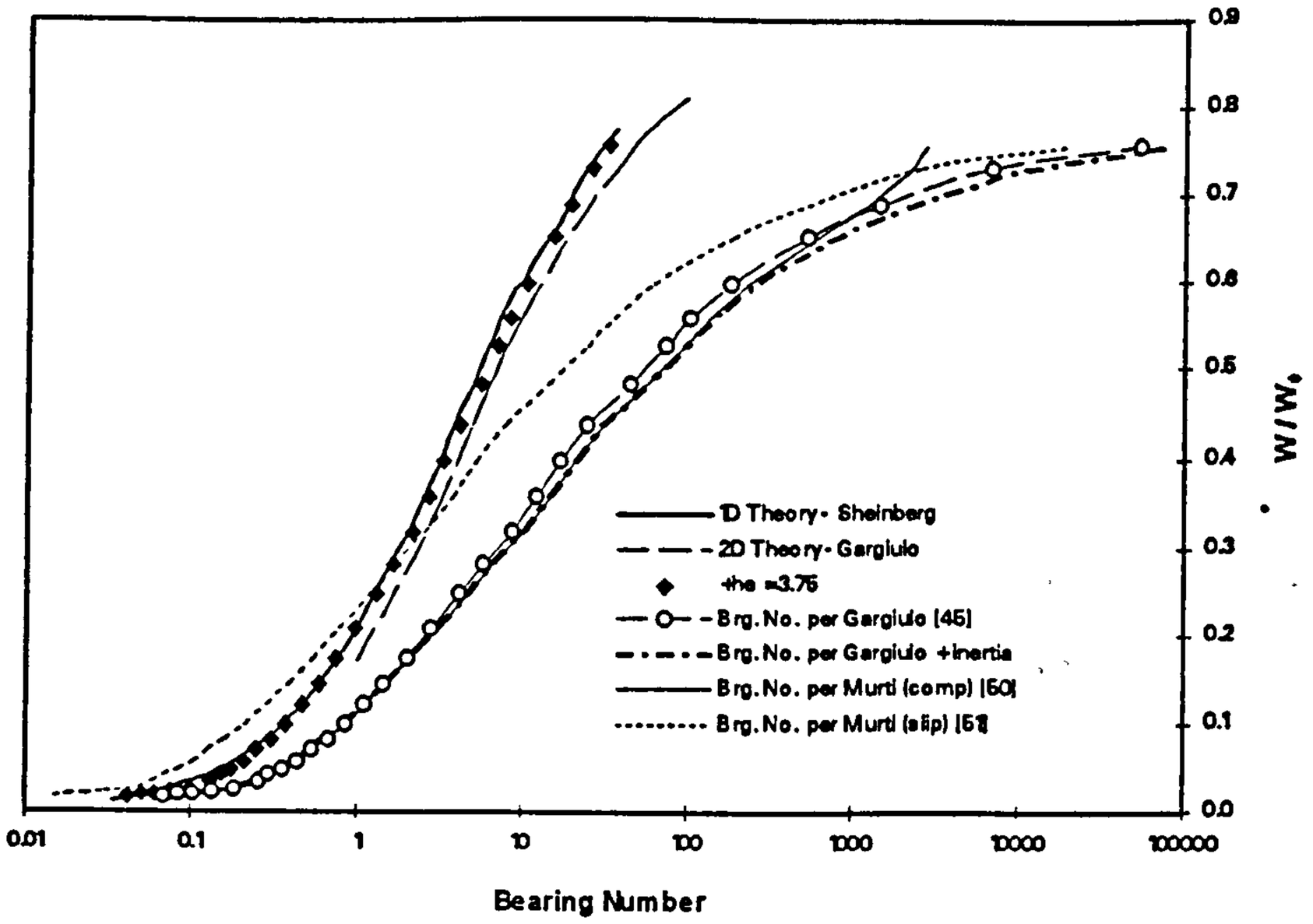

Fig. 11.1 Static Load Characteristics of 2-Layered Porous Thrust Bearing

(Bearing supply pressure = 4 bar)

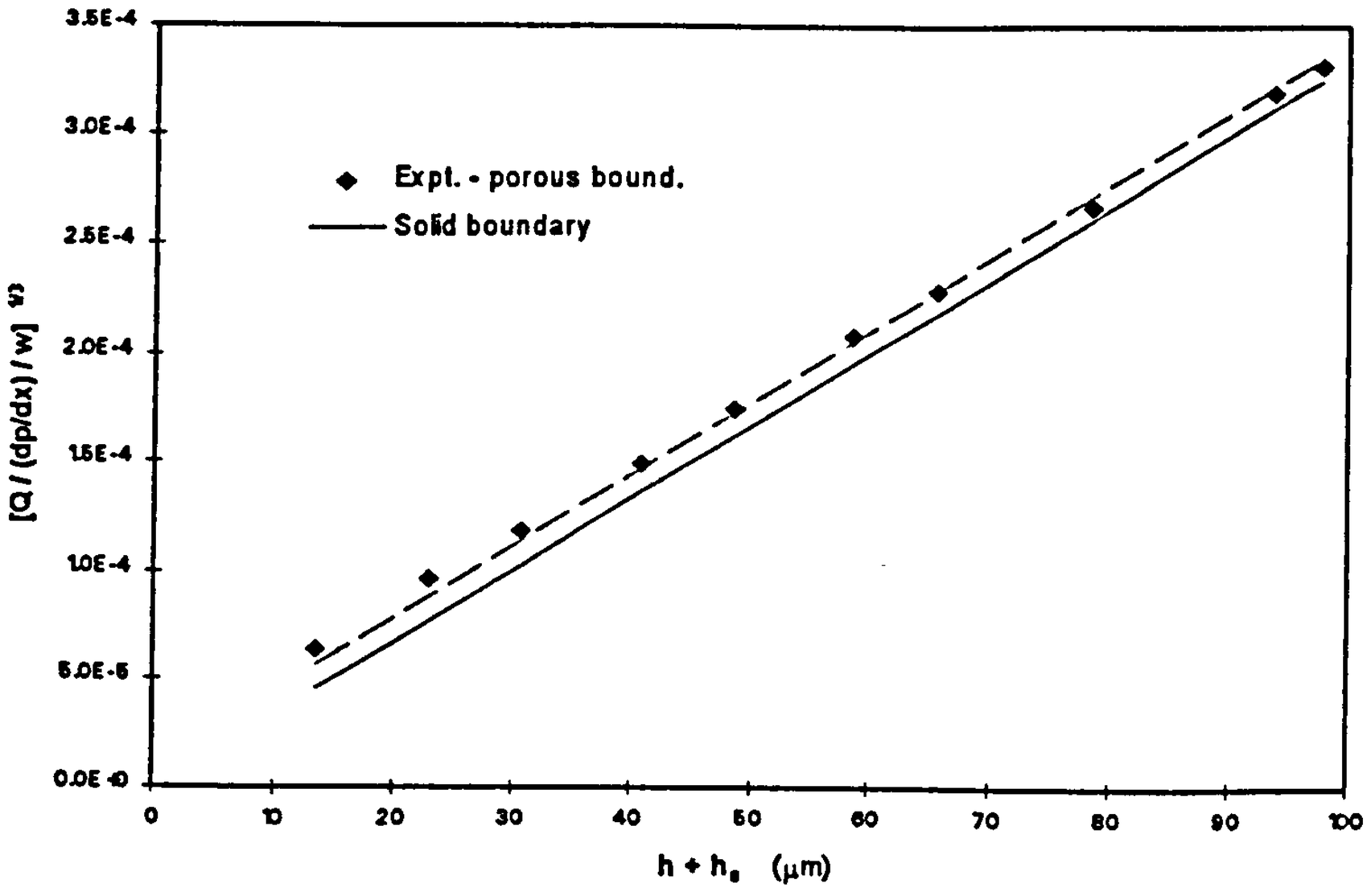

Fig. 11.2 Equivalent Clearance Correction for Velocity Slip

The slip coefficient sample SC1 was similar in structure to the slip-cast layer of the two-layered bearing. The surface was also finished to bearing surface qualities, using the same machining parameters. The slip coefficient measurement should therefore resemble closely the actual conditions in the test bearing.

The correlation technique was similar to that for the calibration of the flow through two solid surfaces (equation 6.25a, Fig. 6.26). The cube root of the flow rate Q_p was plotted against the corrected flow clearance in Fig. 11.2. As can be seen, the measured values lie close to a straight line parallel to the dotted line representing flow between solid surfaces Q_s. This implies that the increase in flow in the presence of the porous surface could be accounted for by an equivalent clearance h_e, given by the negative x-intercept in Fig. 11.2. This amounts to 3.75 μm.

The bearing numbers were therefore recalculated by adding h_e to the measured bearing clearances z_g, using equation 3.4 as the definition of bearing number, and Φ_e as the permeability value. The revised values agreed well with the Sheinberg theory (Figs. 11.1, 11.3).

$$\Lambda_4 = \frac{12.\Phi_e.r_p^{\,2}}{z_p.(z_g + h_e)^3} \qquad (11.6)$$

To provide further verification to this correction for slip flow, a further comparison was made with the load carrying capacity at a supply pressure of 2 bar. Again, the equivalent-clearance correction for slip provided the best agreement with equations 11.1 and 11.2 (Figs. 11.4, 11.5). Also noticeable is the much improved agreement between the theory by Sheinberg and that by Gargiulo, as the latter was evaluated for a 2 bar supply pressure.

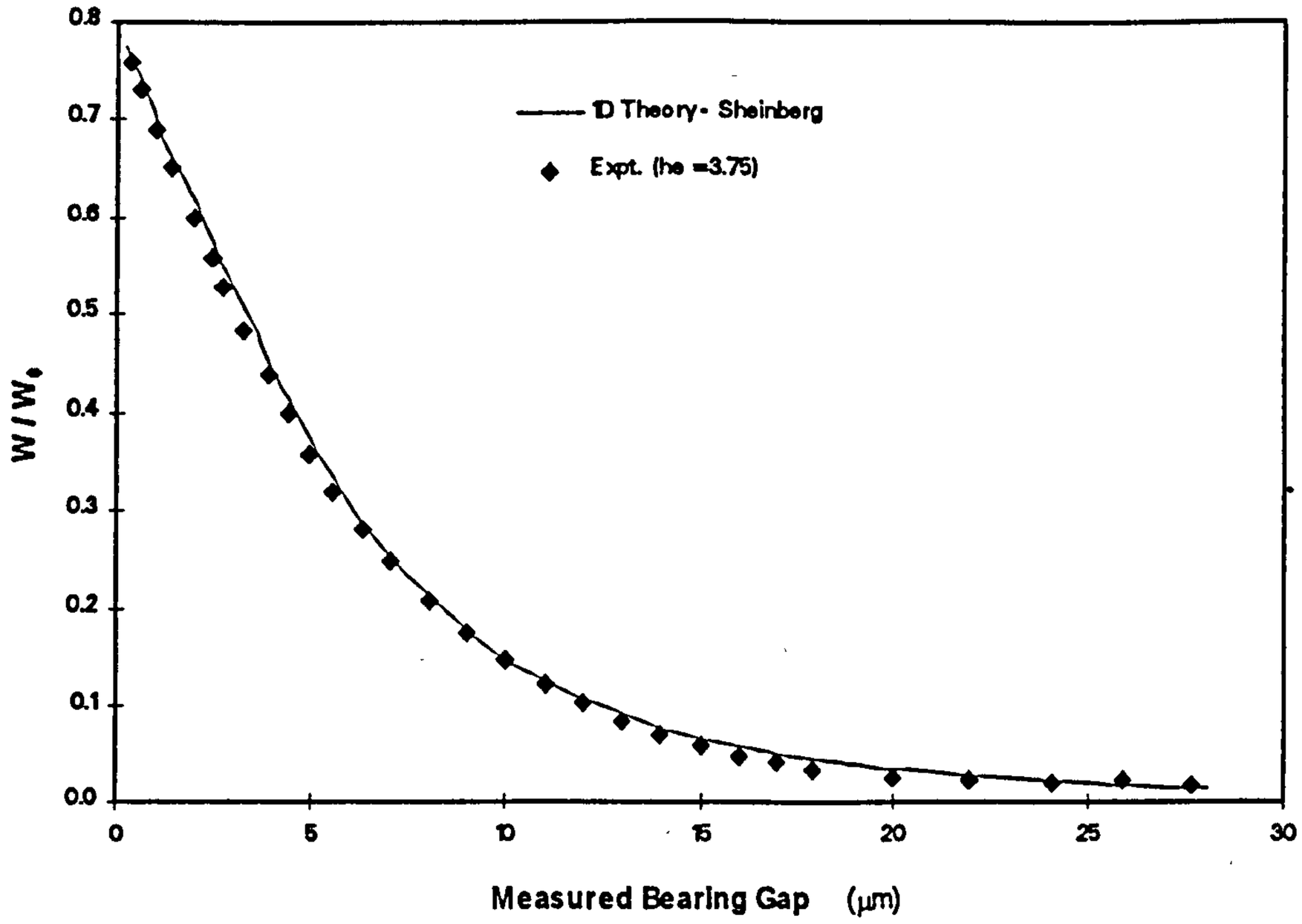

Fig. 11.3 Static Load Capacity of 2-Layered Porous Thrust Bearing

(Bearing supply pressure = 4 bar)

11.1.2 Pressure Profile

The measured pressure profile of the two-layered bearing was compared with the one-dimensional theory by Sheinberg (equation 11.1). Supply pressure to the bearing was 4 bar, with four different values of bearing clearance. The definition of bearing number in equation 11.6 was used in the pressure profile calculations. Also listed for comparison were calculated values based on the viscous permeability coefficient Φ_v.

The results are presented in Fig. 11.6. The use of the equivalent permeability to compensate for inertia effects appeared to improve the accuracy of the theoretical predictions. It could be seen that most measured values lay around the dotted line based on Φ_e. The measured values were higher than theoretical at the centre part of the bearing pad, but lower towards the perimeter. A possible explanation for this could be

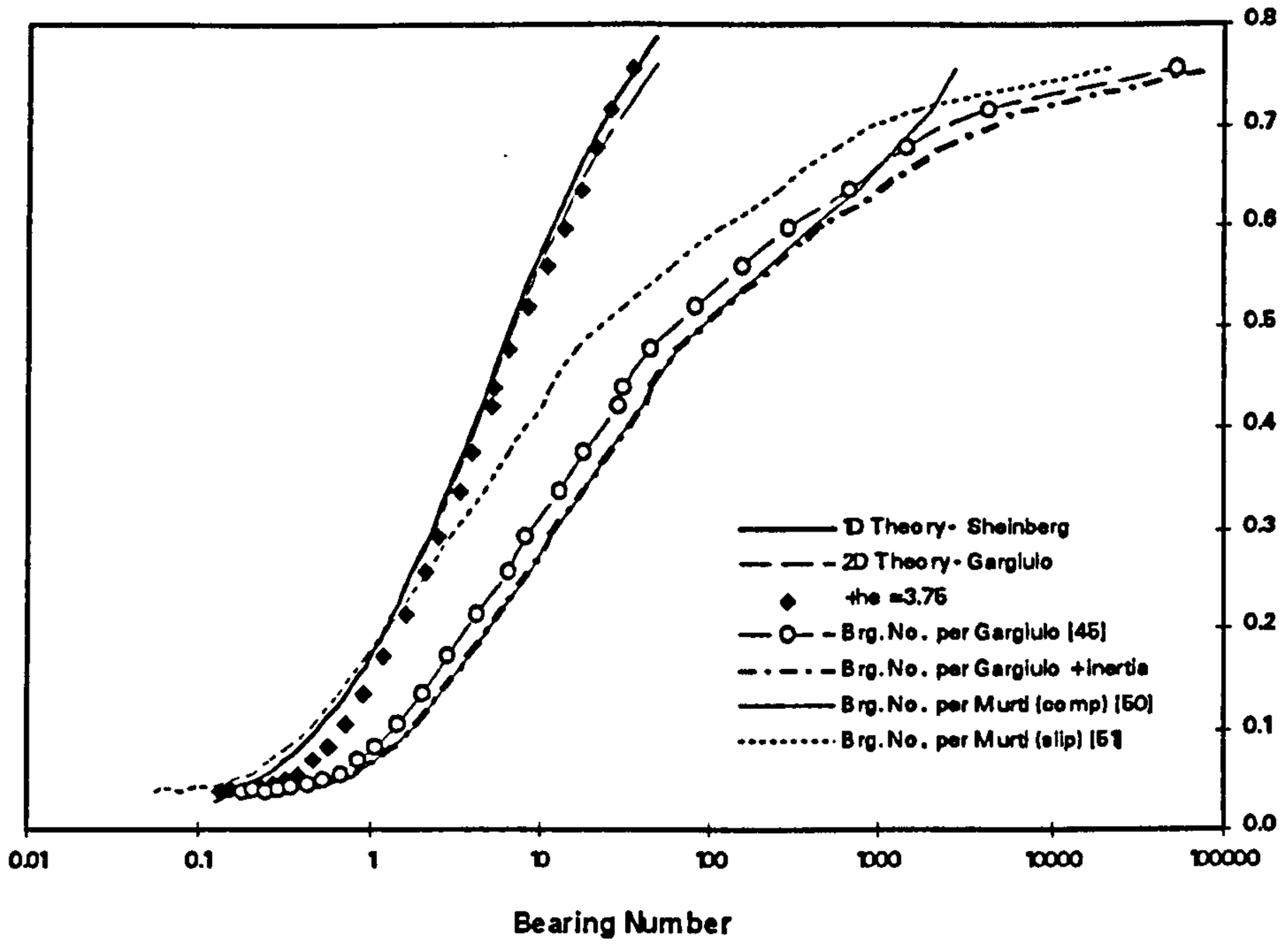

Fig. 11.4 Static Load Characteristics of 2-Layered Porous Thrust Bearing

(Bearing supply pressure = 2 bar)

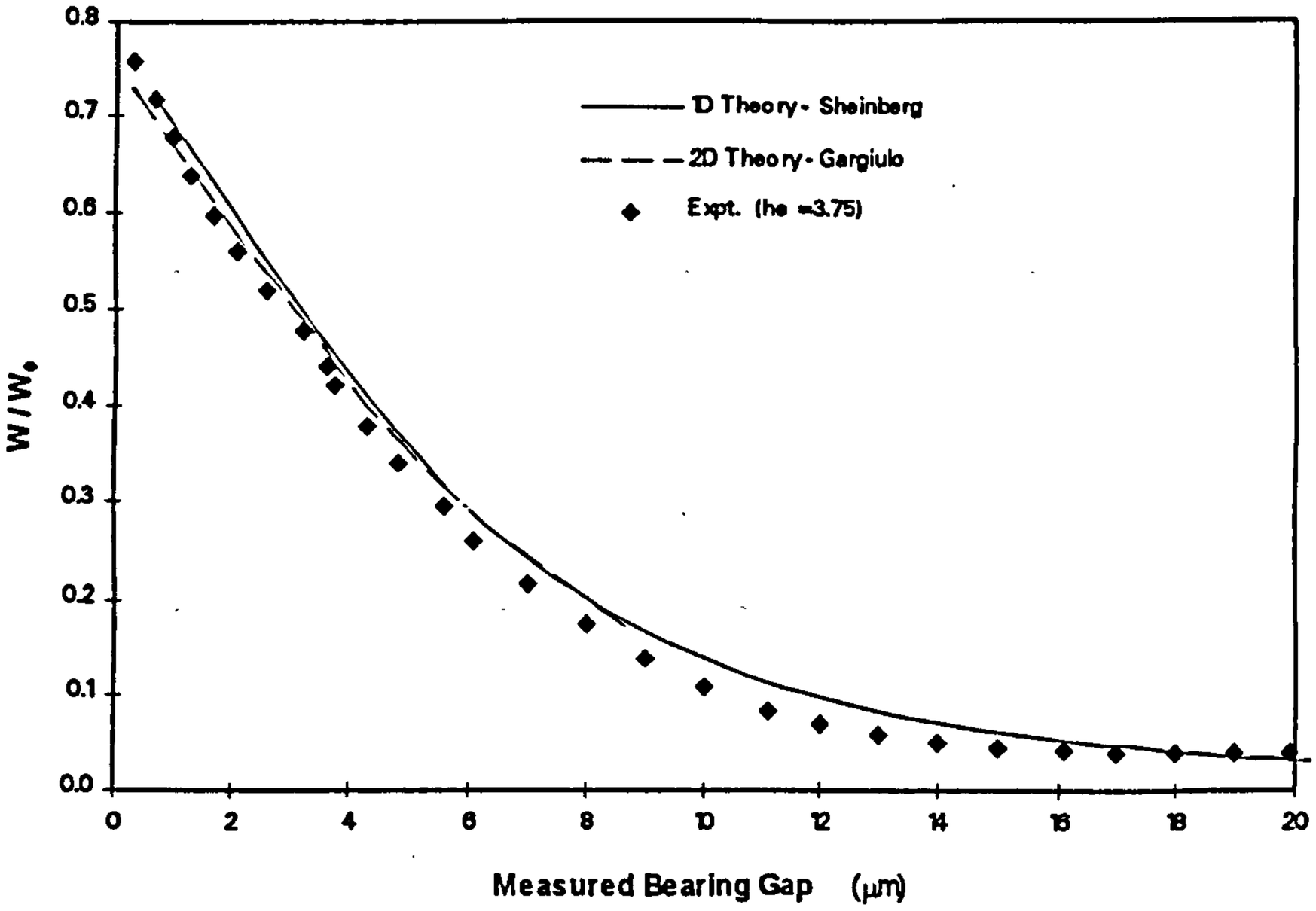

Fig. 11.5 Static Load Capacity of 2-Layered Porous Thrust Bearing

(Bearing supply pressure = 2 bar)

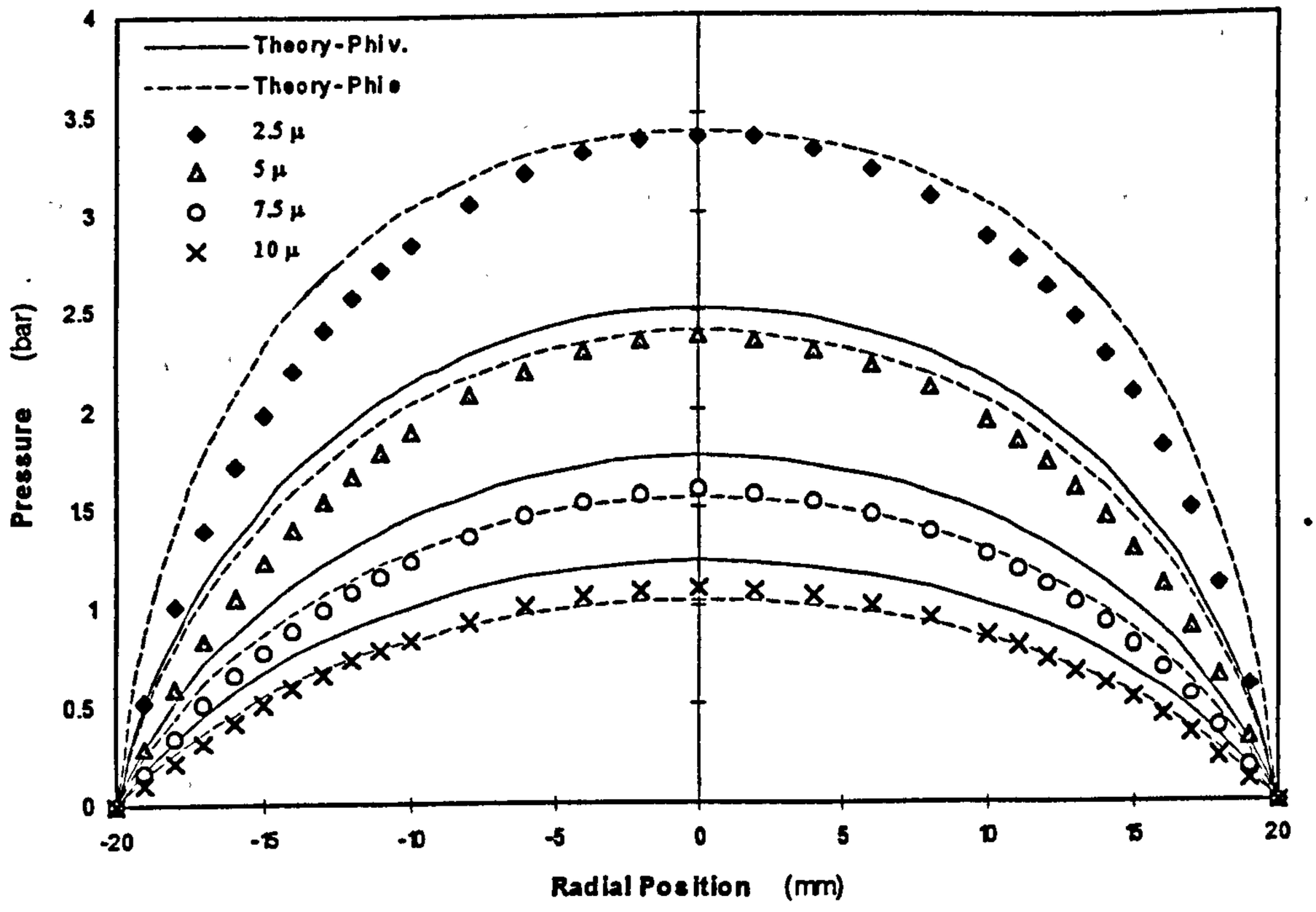

Fig. 11.6 Pressure Profile of 2-Layered Porous Thrust Bearing

(Bearing supply pressure = 4 bar)

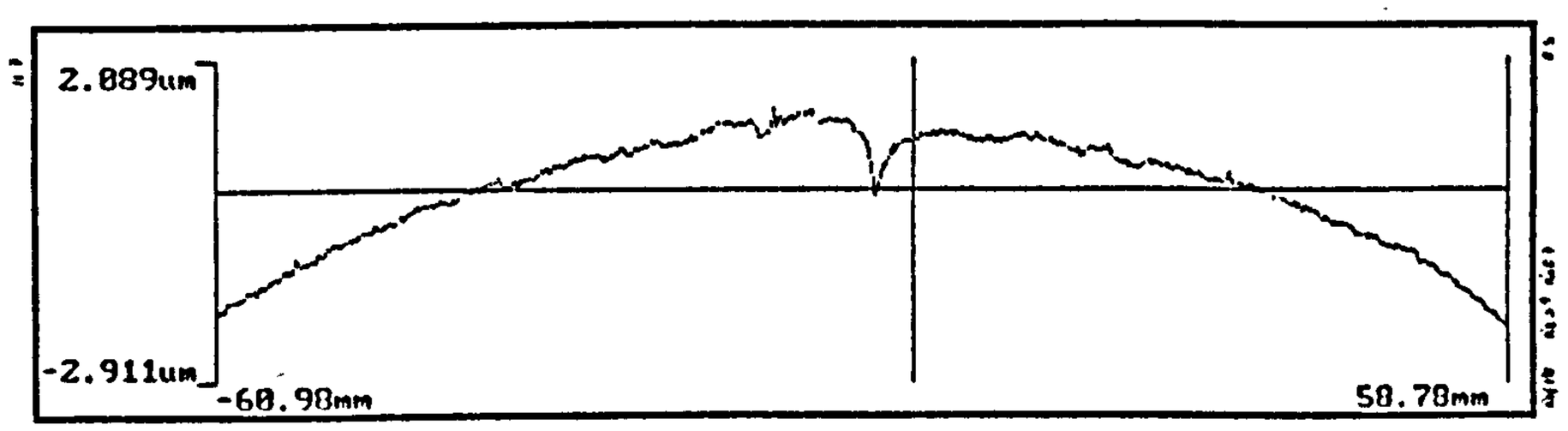

Fig. 11.7 Flatness Measurement of the Test Rig Reference Plate

the non-uniform permeability of the porous material. As already discussed in Chapter 10, the permeability of the two-layered bearing was found to be higher at the centre. The lower permeability around the perimeter of the bearing pad would cause a larger pressure drop there, whereas the reverse would be true for the central portion. The fact that the reference plate was convex in profile (by 0.6 μm over 40 mm) might be another contributing factor (Fig. 11.7). The effect of this deviation from ideal geometry was particularly noticeable at small bearing clearances, reflected by lower measured pressure values than calculated ones.

11.1.3 Bearing Stiffness

Of particular importance in precision engineering applications is the stiffness of the aerostatic bearing. At 4 bar supply pressure, the bearing had a near constant stiffness at bearing clearances below 4 μm. The average stiffness was calculated as 44 N μm^{-1} over that range.

Differentiating equation 11.2 gave a maximum stiffness of 46.3 N μm^{-1} at a bearing number of 17, corresponding to a physical gap of 1.2 μm. This small clearance was largely due to the presence of the slip flow correction h_e of 3.75 μm in equation 11.6, but the latter could be allowed for in future designs.

The bearing number corresponding to maximum stiffness was near the lower end of values quoted by Sheinberg. No explanation was given in the original report on how the bearing number for maximum stiffness was determined. In the present study, the value was obtained by numerical differentiation of load with respect to the bearing clearance (Fig. 11.3). Dimensionless load capacity at maximum stiffness was about 0.67, a value similar to the prediction by Gerke [82].

A much lower value of $\Lambda \approx 5$ was quoted by Murti [50,51]. His definition of dimensionless stiffness

$$K_b = \frac{k_b . z_g . (1/f_1)}{\pi . r_p^{\,2} . (p_o - p_a)} \qquad (11.7)$$

however, contains a z_g term in the numerator. The correction factor f_1 is also a function of the bearing clearance z_g. The value of K would therefore not peak at the same value of z_g as the actual stiffness k, but at a higher value. This, in turn, corresponds to a lower bearing number. The bearing numbers for maximum stiffness quoted by Murti were therefore misleading.

For a bearing supply pressure of 2 bar, maximum stiffness occurred at a bearing number of 17.1. The effect of p_o was therefore negligible.

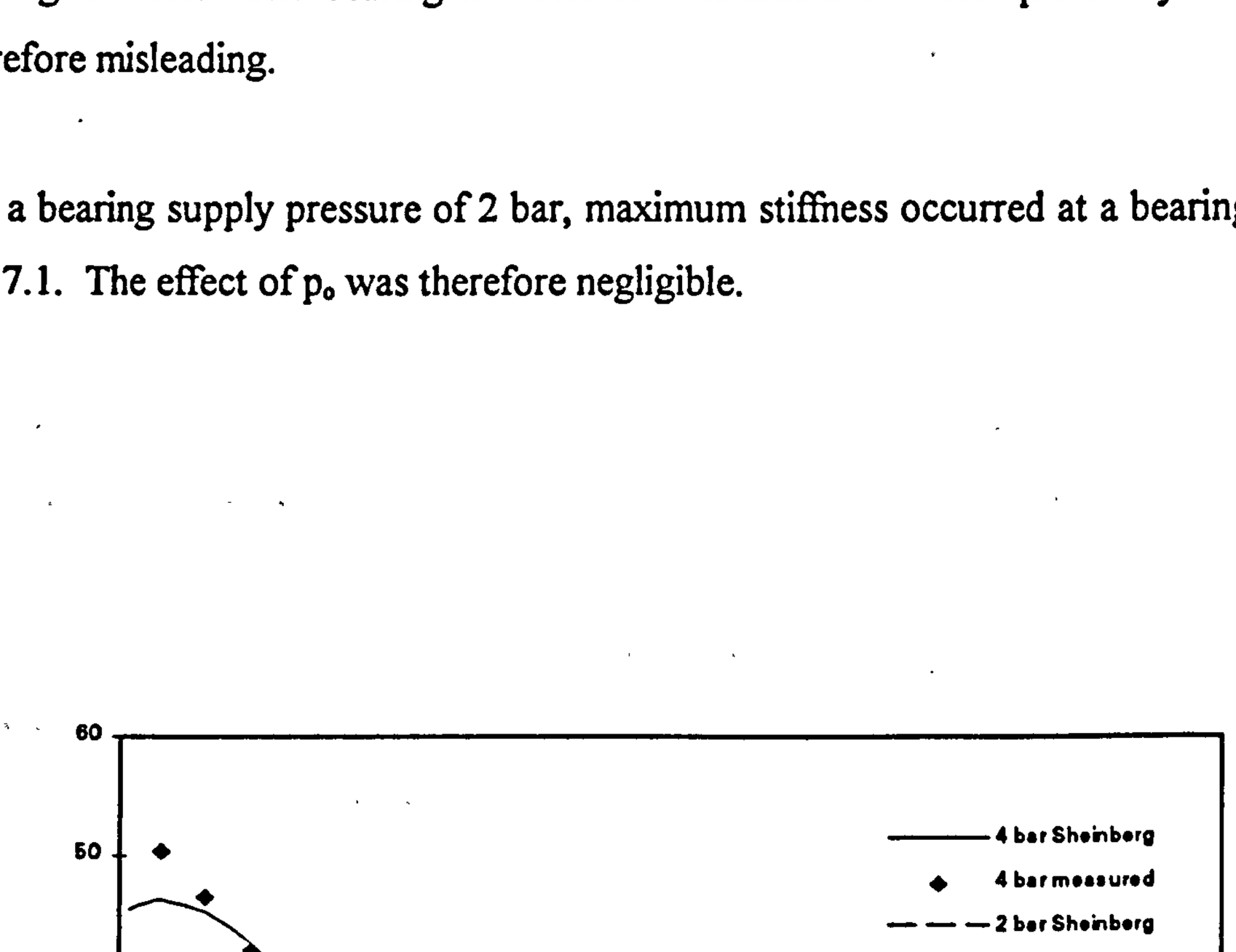

Fig. 11.8 Static Stiffness of 2-Layered Porous Thrust Bearing

11.2 SINGLE-LAYER BEARING

Experimental data for the single-layer bearing were also compared with the theories, in a similar manner to that for the two-layered bearing as already detailed above. As the bearing was unstable for supply pressures above 2 bar, the comparison was made using the latter supply pressure to give direct correlation with the results of Gargiulo. Though the bearing was not entirely stable at this pressure, load data were successfully obtained over the entire operating range by changing the applied load slowly.

11.2.1 Static Load Characteristics

The measured load capacity of the single-layer bearing was compared to the published theories as in Section 11.1.1. The results are summarised in Fig. 11.9.

Inertia effects in the single-layer bearing were not significant. The equivalent permeability coefficient was constant to within 4% over the entire measured range of bearing clearances. The inclusion of inertia effects in the calculation of bearing numbers did not result in any significant differences.

As no slip flow data were available for this particular porous specimen, a slip coefficient value of 0.017 was estimated from other slip coefficient measurements of specimens sintered from 7 μm powders. As before, the inclusion of slip in the mathematical model by Murti [51] did not result in significant improvements.

The lack of slip flow data also implied that the equivalent clearance correction h_e could not be determined from experimental results. An estimated value of 3 μm was nevertheless used, if only to give any idea of how the correlation would change. As in the case of the two-layered bearing, it resulted in much improved agreement between measured and theoretical values.

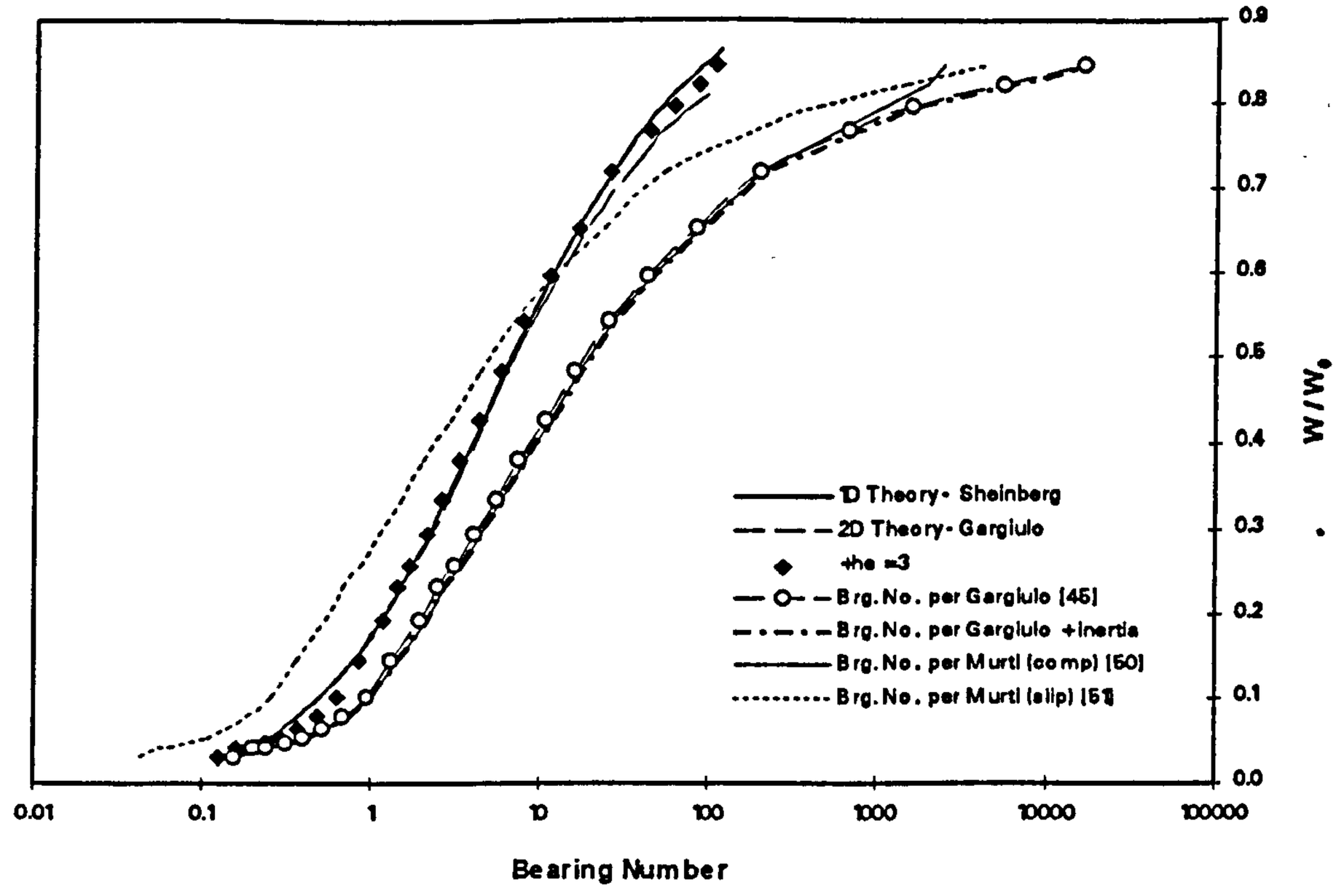

Fig. 11.9 Static Load Characteristics of Single-Layer Porous Thrust Bearing

(Bearing supply pressure = 2 bar)

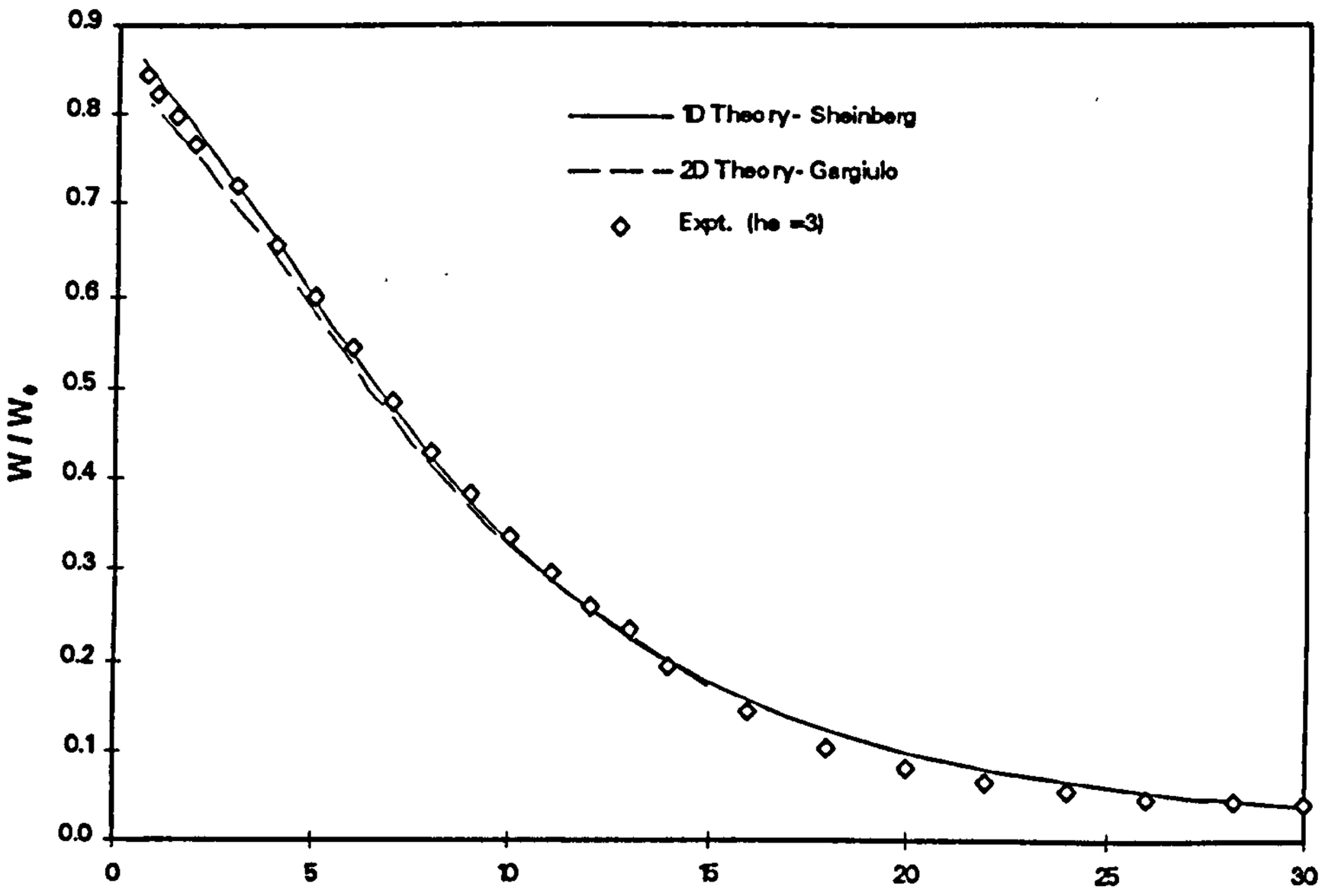

Fig. 11.10 Static Load Capacity of Single-Layer Porous Thrust Bearing

(Bearing supply pressure = 2 bar)

The matching of pressure profile data based on this h_e correction could also be observed in Fig. 11.11. Experimental evidence would be necessary to verify this hypothetical value, when machining facilities become available to machine the slip flow specimen to identical finishes as the bearing surface.

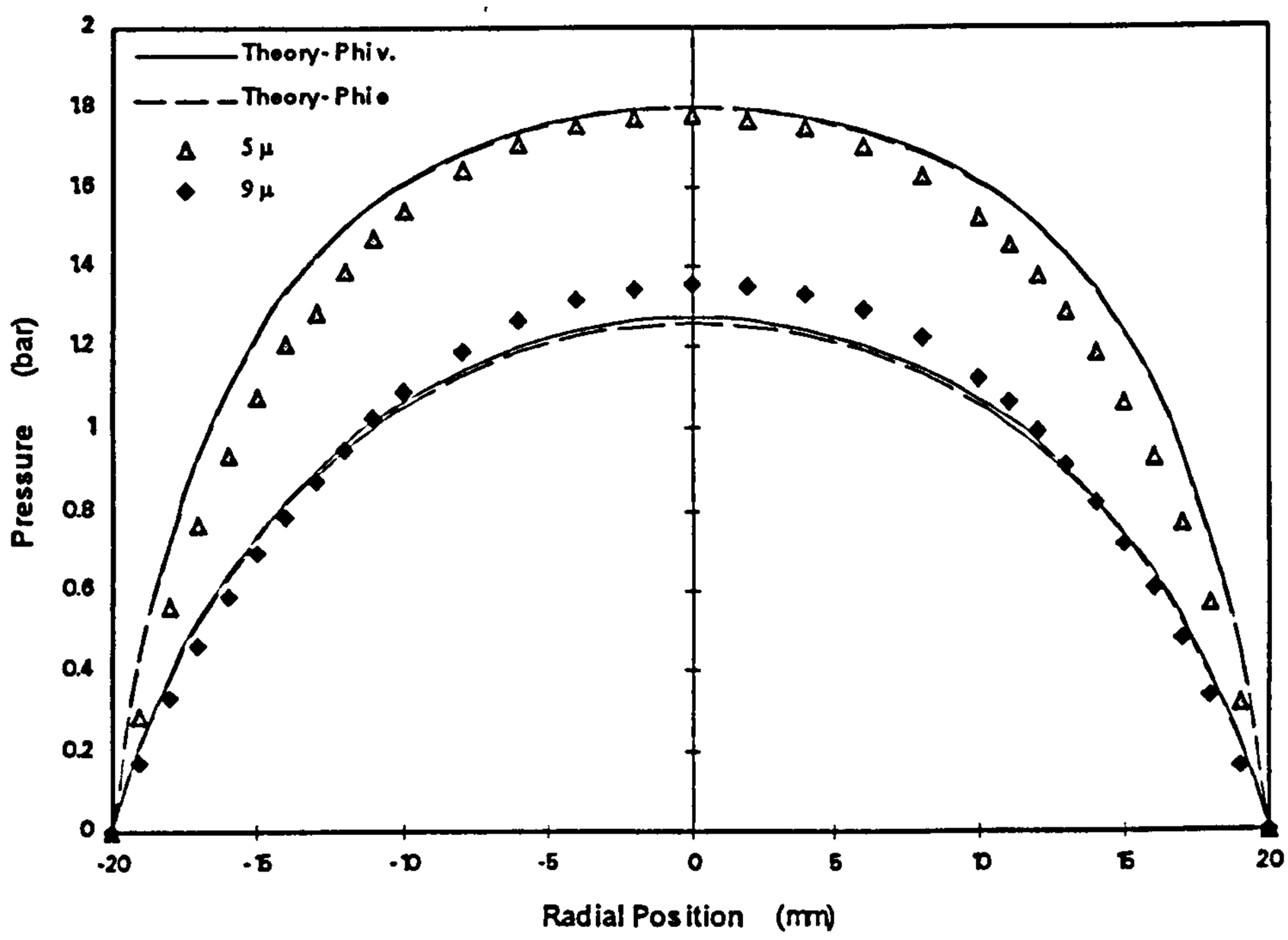

Fig. 11.11 Pressure Profile of Single-Layer Porous Thrust Bearing

(Bearing supply pressure = 2 bar)

11.2.2 Instability

As described in the previous chapter, there were two zones of stable operation for the single-layer porous thrust bearing, one at small and the other at large bearing clearances. These two zones widened as the bearing supply pressure was reduced,

until they merged at a supply pressure of 1.5 bar. Below this pressure, the bearing was stable over the entire range of clearances.

The existence of these two stability zones was similar to the findings by Chang [92]. His mathematical model was based on electrical analogy of fluid mechanics, using resistors and capacitors to represent flow restrictions and dead volumes. These values could only be determined experimentally, and required additional information on phase, amplitude and frequency relationships between the bearing gap, bearing supply line pressure, bearing plenum pressure, and dynamic load. The existing equipment was unfortunately not adequate for the purpose. In addition to equipment limitations, the exact boundary of stable operation would be difficult to define, as the change to instability was not a sudden one.

11.3 DISCUSSIONS

The simple one-dimensional model by Sheinberg has been applied successfully to predict the performance of both the single and two-layered bearings. This was achieved by applying a correction to the bearing number to allow for the effects of velocity slip. The correction took the form of an additional equivalent bearing clearance h_e, which was determined experimentally from slip flow measurements. The Beavers' criterion of slip flow failed to predict the actual increase in flow in the presence of the porous boundary, especially at small clearances commonly encountered in aerostatic bearing applications. The presence of slip effectively reduced the bearing clearance corresponding to maximum stiffness by as much as 3.8 μm, thus increasing the demand for improved geometrical accuracies on the bearing components.

The correction for slip flow was by far the most important. The increase in flow in the presence of the porous surface could be attributed to at least two different mechanisms -- the non-zero boundary velocity at the porous surface, as described in the model by Beavers; and the increase in effective clearance due to the roughness of the surface [259].

The latter is determined only by the surface topography, and is not dependent on the permeability of the material. The large value of h_e in the case of the two-layered specimen, compared with the particle size and the measured roughness values, also suggests a further interaction between fluid in the bearing gap and that within the open pores of the first few particle-layers immediately next to the bearing surface. The uniaxial, slot-like pore structure in the PVD specimens (Section 8.2) might well offer a better solution to problems caused by velocity slip.

The definition of roughness in the presence of through-pores is also problematic. In addition, roughness measurements are largely influenced by the lateral resolution of the measuring probe, contact or otherwise. This is particularly the case when dealing with particles as fine as 0.5 μm. More experimental data at small flow clearances would therefore be required before the mechanics of velocity slip could be fully understood and predicted mathematically.

The effects of other modifications to the bearing number to allow for compressible flow and bearing pad deflection were negligible in comparison.

The two-dimensional analysis by Gargiulo gives slightly improved prediction of load capacity at small clearances. The range of data published was, however, rather limited. The Sheinberg model has the additional benefit that mathematical expressions are available for both the pressure profile and the load capacity, thus allowing optimisation of bearing parameters by analytical, rather than numerical, means. The large diameter-to-thickness ratio in the fine layer of the two-layered bearing also justifies the approximation for one-dimensional flow through the porous pad.

The bearing number corresponding to maximum stiffness was found to be around 17. The effect of supply pressure to this optimum value was not found to be significant. As already discussed in Section 11.1.3, the optimum value of 5 quoted by Murti [50] was thought to be misleading due to the inclusion of a clearance term in his definition of dimensionless stiffness.

The effect of inertia flow through the porous pad depends largely on the material itself. For single-layered bearings, inertia effects could be ignored without compromising the accuracy of the mathematical models. Inertia effects were, on the other hand, not negligible for the two-layered material. A simple correction in the form of an equivalent permeability coefficient (Appendix D) was found to be adequate in improving the correlation between theoretical and measured data.

Even with the successful machining of the bearing material without grain-pullout, the operation of the single-layered bearing was unstable over a large operating range, particularly at high pressures. This is somewhat unexpected, as many successful bearing applications have been reported, based on materials with even larger particle sizes. The surface loading effect, due to pore warping in the machining of the ductile materials, could well be sufficient to reduce the void volume between pores to promote stable bearing operation. This would be an argument against the use of a porous ceramic material for the single layered bearing design. Among the other disadvantages are poor uniformity of pore structure resulting from the large shape variations and wide particle-size distributions of ceramic powders, the abrasive nature of ceramics, and their poor machinability.

No instability could be observed once the two-layered material was used, giving evidence to the importance of minimising void volume at the bearing surface. The adsorption of moisture in the fine pores of the two-layered structure affected load carrying capacity adversely. Continuous pressurisation with clean, dried air is therefore necessary for trouble-free operation.

As mentioned in the previous section, the theoretical prediction of instability is still semi-empirical [92]. The only information that can be directly applied in designing bearings is the stability chart published by Schroter [84], in which a maximum void volume of 0.7 times the gap volume was quoted for a supply pressure of 5 bar. The maximum packing density of monosize spherical particles in a single plane is approximately 0.61. The void volume from the narrowest part of the pores to the top of the particles is then 0.20 times diameter of particle size times area. The void volume would be larger in the case of three dimensional packing, as some of the pores would

be further away from the top surface. If we assumed the void volume to be equivalent to a thickness of half the particle size, the particle size should be a maximum of 1.4 times the design bearing gap, assuming stability up to 5 bar supply pressure.

12. CONCLUSIONS

Free-capsule hot isostatic pressing has been demonstrated as a viable method of producing porous ceramic materials for aerostatic bearing applications. Empirical relationships between processing conditions, porosities, and the fluid flow and structural properties have been established from the experimental data. This allowed the prediction of processing conditions required to achieve a predetermined level of permeability as well as structural properties required by the bearing design. The measurement accuracy and uniformity of temperature within the furnace are identified to be the most important factors affecting consistency and predictability of the permeability of the porous substrate. With the existing equipment, the permeability is at best repeatable to ± 25 %.

The measurement method for open porosity based on ISO 2738 was found to overestimate the closed-porosity content, especially in fine-pored specimens. A mathematical model to describe the phenomenon has been established. Correlation with experimental data indicates that the model predicts precisely the level of inaccuracy in the ISO method. An alternative method of water impregnation has been proposed, resulting in a significant improvement of the accuracy of the open porosity measurement. Extensive measurements based on the new method have demonstrated its effectiveness.

Porous structures with a fine-pored surface layer are believed to enhance bearing stability due to the reduction of surface voids. Two-layered porous structures have been successfully produced with physical vapour deposition of zirconia on HIPed alumina substrates, as well as hot-pressing of alumina slip and tape-cast layers. The surface layer has a lower permeability compared with the substrate, and is responsible for most of the pressure restricting characteristics of the composite material.

The static performance of test bearings based on both the single and two-layered materials has been measured. The single layer bearing suffered from pneumatic instability near the point of maximum stiffness at high bearing supply pressures, while the

operation of the two-layered bearing was stable over the entire range of bearing supply pressures and clearances. The importance of minimising surface void volume has been fully demonstrated.

The experimental results agreed well with both the one-dimensional model by Sheinberg, and the two-dimensional analysis by Gargiulo, but only after corrections for velocity slip and inertia flow were applied. The former is of particular importance, and takes the form of an equivalent clearance h_e. This value was determined from experimental data in the present study. The commonly used Beavers' model of velocity slip failed to predict the increase in flow between the bearing surfaces at small clearance. The effects of inertia flow within the pore structure were not negligible in the two-layered bearing material. This was allowed for by applying the concept of the equivalent permeability. Other published corrections to the Sheinberg's theory to allow for compressible flow and velocity slip had negligible effects in comparison.

13. RECOMMENDATIONS FOR FURTHER WORK

The present investigation has, at best, only laid down the foundation for the future development for porous ceramics, particularly of the two-layered type, for use in aerostatic bearing applications. Much has yet to be done, not only in terms of materials processing, but also in the understanding of fluid flow through small gaps bounded by a porous surface. Further progress, however, would only be possible with the availability of additional resources.

13.1 PARTICLE PACKING

While relatively simple to use, vibratory packing does have its limitations, particularly in terms of the level of green density attainable. Particle size is also limited to 13 μm and above.

The formulations of the slip and tape casting mixture used in the present investigation were by no means optimised. In particular, the amount of dispersant is believed to have a major effect on both the maximum solid content and the viscosity of the mixture. Too much dispersant results in re-flocculation, and hence a lower packing density. Insufficient dispersant allows powder to flocculate, producing a low density and a low uniformity of microstructure in the green body. A simple sedimentation test was performed in an attempt to optimise deflocculant content, but produced results that were difficult to interpret. This was due to the uncertainties in the exact sedimentation level, as powders adhered to the wall of the measuring cylinder. Proper optimisation of the deflocculant content requires the measurement of the zeta potential of the mixture, but the necessary equipment was not available at Cranfield.

Injection moulding of ceramics has been demonstrated as a viable process, especially in the production of complex shapes. Particle size is, however, limited to 10 μm and below due to wear of the barrel and screw, and thickness to not more than 5 mm due to debinding limitations. The process is also economical only in large production runs, which is unlikely to be the case for aerostatic bearings.

In these respects, hot moulding should seriously be considered as an alternative. As pointed out by Lenk[260], the process is an ideal alternative to injection moulding for small batch productions. Green density achievable is similar to that of the latter, but tooling cost is much lower, due to the lower viscosity of the mixture. Successful debinding of up to 30 mm in thickness has already been demonstrated[260]. There also appears to be no limitation on powder size as in the case of injection moulding.

The use of a bimodal mixture, with a fine powder as the second phase, might help to reduce the HIPing temperature, not only in the case of large particles as already demonstrated, but possibly also for smaller particles. A reduction in the primary particle size implies a larger surface area of the former. A higher percentage of secondary (fine) particles is therefore required in a slurry form to ensure complete coverage of the primary-particle surfaces. However, it is unlikely that uniform mixing would be achievable using the current hand mixing method.

13.2 CONTROL OF THE SINTERING PROCESS

One of the most problematic areas of the present investigation is the repeatability of the HIPing process. This is in part due to the statistical nature of ceramic powder processing itself, but also in part due to the accuracy of the HIPing temperature measurements. An uneven temperature distribution within the HIPing furnace has also been shown to be a contributing factor.

Further optimisation of the temperature measurement methods would be difficult, however, as measurement methods currently available for the range involved all have less than ideal accuracies [199]. Using new thermocouples for each sintering run, and placing the specimen only in the central zone of the furnace would probably alleviate both problems to an extent, but are extremely expensive options, especially in a production environment. The use of sintering aids would help to reduce the sintering temperature, and in turn increase the reliability of the temperature readings, but would create other undesirable effects such as much reduced strength and poor microstructure uniformity.

More experimental data, and in particular the use of a dilatometer to measure the sintering rate during the HIPing cycle, would provide further information for a more accurate modelling of the free-capsule HIPing process.

13.3 TWO-LAYERED STRUCTURES

Despite the success of the combined slip and tape casting method in producing the two-layered structure, progress so far has not gone beyond the stage of a feasibility demonstration. The effects of pre-sintering and hot pressing conditions on a range of particle sizes above and below 0.5 μm, among others, require further attention.

13.3.1 Inter-layer Bond Strength

There were occasions in the course of the current investigation in which delamination occurred on two-layered specimens during the final grinding of the bearing surface under air pressure. In all cases to date, this has taken place at the interface between the pre-sintered fine particle layer and the tape. The bonding between the tape and the coarse substrate is thought to be provided mostly by mechanical anchorage of fine powders in the tape layer which penetrated into the pores of the substrate, and is therefore expected

to be of higher strength. Adhesion between the tape and the slip-cast layer is, on the other hand, purely due to sintering. As the slip-cast layer is of the same particle size as the tape, particle arrangement at the interface between the two is unlikely to be orderly. Further improvements to the inter-layer bond strength through optimisation of the bonding / hot pressing process should therefore be investigated.

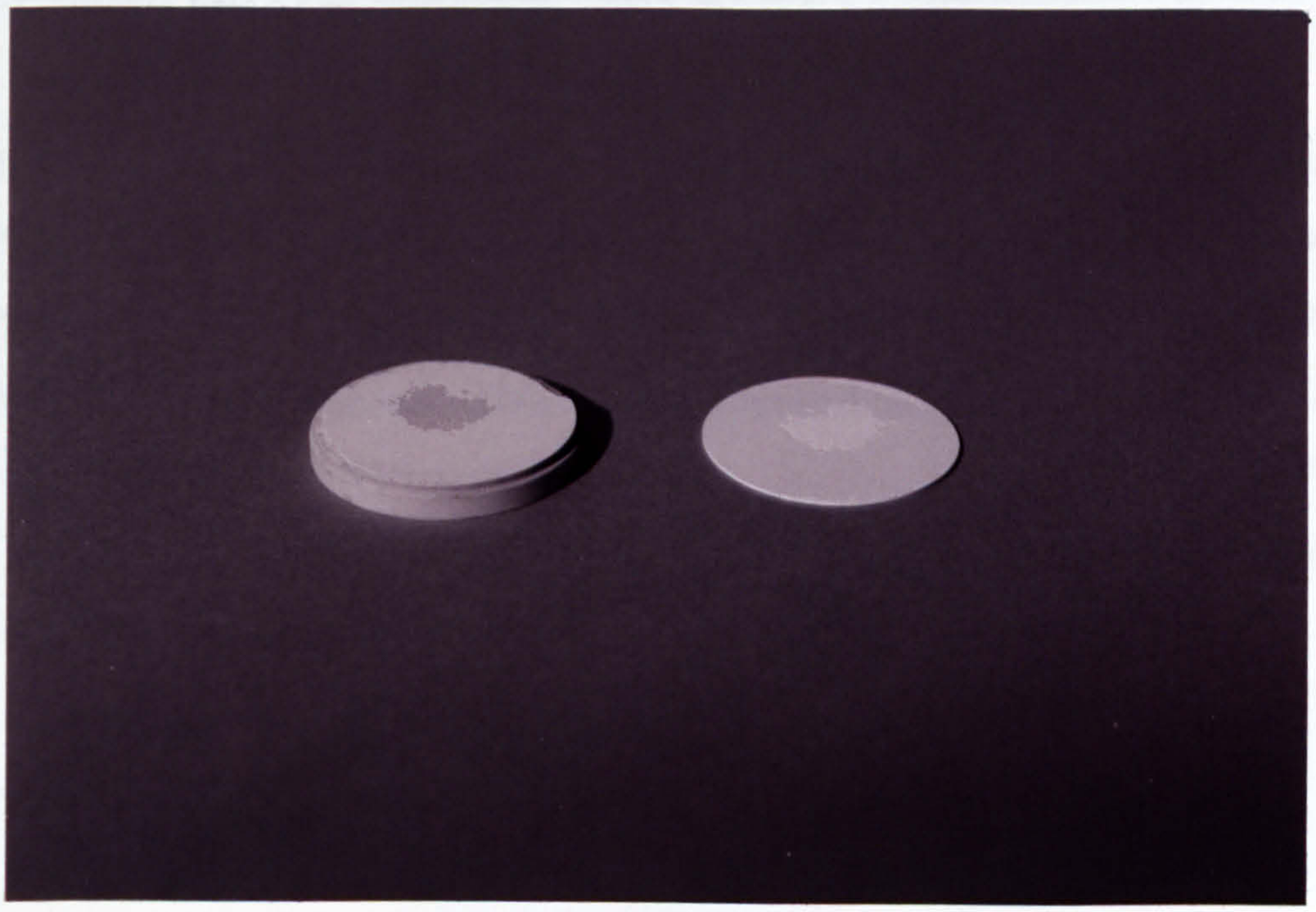

Fig 13.1 Delamination of a Two-Layered Porous Bearing Pad

13.3.2 Physical Vapour Deposition

Physical vapour deposition (PVD) could arguably provide the most favourable characteristics of a two-layered porous structure for aerostatic bearing applications, provided that the process could be controlled to a high degree of consistency, and the problems associated with the machining of the bearing could be overcome.

The pores formed by PVD are essentially one-dimensional fine slits between pillars of zirconia crystals. Not only does this type of pore structure imply reduced gas

consumption due to the absence of radial flow within the porous pad, but more importantly, a drastic reduction in the interaction of fluid flow in the bearing gap with that within the porous structure at the bearing surface. This is because the porosity in the PVD layer is much lower, the path for any possible cross-flow more tortuous, and the surface voids non-existent. The two trial samples produced in the present work, however, did not demonstrate a high degree of consistency and uniformity, unwanted splats of zirconia being one of the main problems.

The machining of PVD specimens has not been looked into, due to restricted access to ultra-precision grinding equipment. Scanning electron microscopy as well as surface roughness measurements have already shown that the as-deposited surface did not have the required finish for aerostatic bearing applications (Chapter 8). Whether machining parameters could be optimised such that the long zirconia 'needles' (of around 20 x 20 μm in section, and some 200 to 500 μm in length) could be finished to sub-micron flatness without breakage or chip-off remains one of the biggest challenges.

13.3.3 Alternative Methods

Other coating methods, e.g. chemical vapour deposition [261] , have been known to produce successful two-layered porous structures for various applications such as filtration. The suitability of these techniques for aerostatic bearing use should also be investigated, when access to the required equipment could be gained.

13.4 BEARING SURFACE PREPARATION

13.4.1 Machining of Bearing Surface

Although reasonable surface qualities have been achieved in both the single and two-layered bearing materials without much grain pullout, the very limited access to ultra-precision grinding equipment has prevented further optimisation of the grinding process. It is believed that further improvements could be made, for example, to reduce sub-surface cracking on the flattened surfaces of individual grains in the single-layer material, thus further reducing the surface void volume. The use of ultra-fine grain diamond wheels, combined with reduced depth of cut, should also bring about similar improvements in the two-layered material [255].

The clogging of the diamond grinding wheel by fine powders in the two-layered material also requires the search for a more effective debris removal method.

13.4.2 Bearing Surface Coating

One of the few undesirable characteristics of the porous ceramic material in aerostatic bearing applications is its abrasive nature. When instability occurred during the bearing performance tests, the bearing vibration was sufficient to cause the rim of the bearing pad to come into contact with the reference plate, resulting in scratches on the lapped stainless steel surface. More detrimental was the build-up of this stainless steel at the rim of the porous bearing surface, causing changes in the datum of the measured bearing clearance.

Use of an equally abrasion resistant material such as granite or fully dense alumina as the guiding surface would alleviate the problem, but the danger of accidental contact of the bearing surfaces and the resulting damage to both surfaces is still very real [262, 263, 264]. Coating of a thin layer of solid lubricant such as PTFE [265] or MoS_2 [266] by an evaporative method should be looked at as a possible remedy.

13.5 SLIP COEFFICIENT MEASUREMENT

The poor surface finish of all but one of the test samples, obtained by using ordinary toolroom grinders and coarse grain diamond wheels, has cast doubts on the validity of the measurement results with reference to actual surface conditions in aerostatic bearing. As pointed out by both Beavers [52] and Larson [116], the slip coefficient is extremely sensitive to both the surface finishing method and the definition of the surface boundary. Unless the test specimens are finished using the same process as the actual bearing surfaces, the results are unlikely to provide direct correlation.

The sharp change in slip coefficient values at small gaps also demands further attention. The current measuring equipment is unable to handle flow channel clearances of 10 μm or below. A redesign of the measuring fixture would be required to allow accurate reduction of the gap to a couple of micrometres. Leakage could be kept to a minimum if a high degree of geometrical accuracy, in particular flatness, could be achieved on key components.

13.6 MEASUREMENT OF DYNAMIC CHARACTERISTICS

The present investigation of porous aerostatic thrust bearings has been limited to their static characteristics only. Techniques for dynamic performance measurements are well established [267]. Allowance has already been made in the present test rig for extensions to include dynamic measurement.

Dynamic excitation could be applied in addition to the static load via a voice coil motor, mounted in cascade, on top of the pneumatic loading cylinder. The load cell would, however, no longer adequately reflect the actual dynamic loading, due to acceleration of both the load shaft and the thrust bearing itself. Instead, the reference plate should be placed on kinematic mounting points provided by three load cells. An additional

accelerometer would provide compensation for any minute vibration of the reference plate resulting from the deflections of the load cells under load. All dynamic loading would then be accounted for. The proximity sensors in the current set-up would continue to provide measurement for the displacement response, though much better hardware signal conditioning should be applied to minimise inherent noise from the sensors.

Investigations on the stability criteria of porous aerostatic thrust bearings would also be facilitated by the installation of further sensors. The latter would provide information on the dynamic phase and amplitude relationships between the plenum pressure, bearing supply pressure, and the dynamic bearing clearance. This, in turn, would allow further correlation with the stability theory proposed by Chang [92] to include the influence of the bearing plenum.

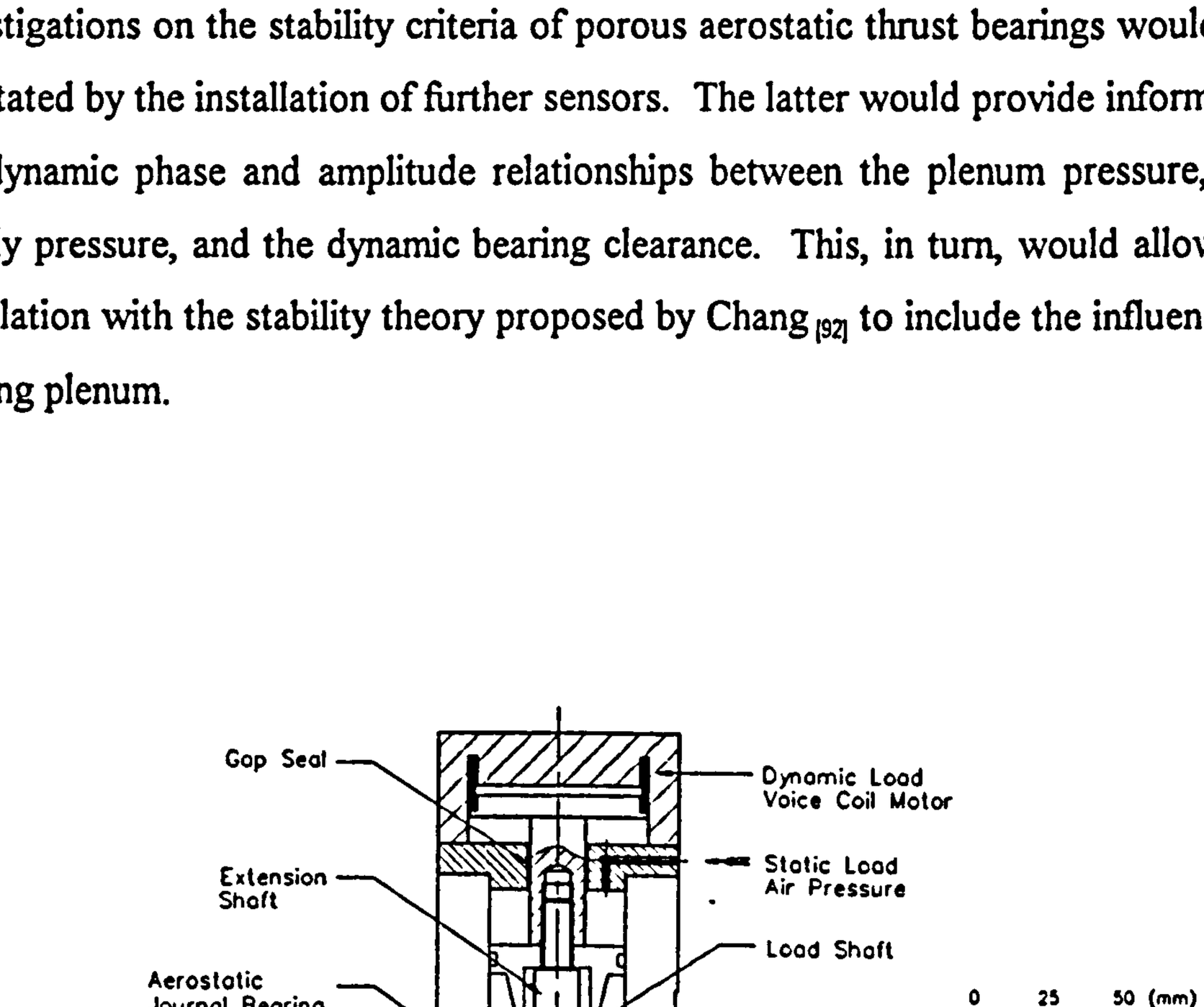

Fig 13.2 Modification of the Bearing Rig for Dynamic Measurements

13.7 FURTHER DEVELOPMENT OF BEARING THEORY

The agreement between experimental data and the simple, one-dimensional theory of Sheinberg was quite satisfactory after applying the correction for slip flow. Any further developments in the theory of porous aerostatic thrust bearings would only be meaningful, when the effects of the velocity slip at the porous bearing surface are fully understood. As already demonstrated in Chapter 11, the use of complicated mathematical models to account for compressible flow and inertia effects does not always result in significant improvements. Simple, analytical expressions to describe the bearing performances are often more valuable to a bearing designer, even at slightly reduced accuracy.

REFERENCES

Chapter 1

1. Taniguchi N. — The state of the art of nanotechnology for processing of ultraprecision and ultrafine products
Precision Engineering, 16(1), 1994, 5-24.

2. Thompson L.F. — Introduction to microlithography
2nd ed. Washington DC: American Chemical Society, 1994.

3. Anon. — Hochpraezisionszerspanen mit geometrisch definierter Schneide: Verbundprojekt im Rahmen des Foerder-programms Fertigungstechnik des Bundesministers fuer Forschung und Technologie / Kernforschungszentrum Karlsruhe.
1st ed. Frankfurt a.M.: Forschungsgemeinschaft Qualitaessicherung e.V., 1994.

4. — PAS 5500/300 deep-ultraviolet (DUV) stepper
Company Brochure, ASM Lithography, Veldhoven, Holland, 1996.

5. Tsuyuzaki H. Shimazu N. Fujinami M. — High speed flat guide ceramic stage for electron beam lithography
Journal of Vacuum Science and Technology, B4(1), 1986, 280-284.

6. Ishihara S. — High precision positioning for submicron lithography
Bulletin of the Japan Society of Precision Engineering, 21(1), 1987, 1-8.

7. Buckley J.D. Galburt D.N. Karatzas C. — Step-and-scan lithography using reduction optics
Journal of vacuum science and technology, B7(6), 1989, 1607-1612.

8. Koga N. Nomura J. *et al.* — High performance synchrotron orbital radiation x-ray stepper
Journal of vacuum science and technology, B8(6), 1990, 1633-1637.

9. Kendall R.
Doran S.
Weissmann E.
A servo guided x-y-theta stage for electron beam lithography
Journal of vacuum science and technology, B9(6), 1991, 3019-3023.

10. Meisser C.
Chip-Kontaktierautomat
Electroniker, 12, 1990, 1-8.

11. Abbott W.G.
Device for utilising fluid under pressure for lubricating relative movable elements
U.S. Patent 1,185,571, 1920.

12. Montgomery A.G.
Sterry F.
A simple air bearing rotor for very high rotational speeds
U.K. A.E.R.E. Report ED/R 1671, 1955.

13. Robinson C.H.
The static strength of pressure fed gas journal bearings
U.K. A.E.R.E. Report ED/R 1672, 1957.

14. Steger P.J.
Air bearing spindle for machine tools - spherical design.
Research and development report Y-1581, Union Carbide Corporation, Nuclear Division, Tennessee, 1965.

15. Wunsch H.L.
Design of air bearings and their application to measuring instrument and machine tools
International Journal of Machine Tool Design Research, 1(3), 1961, 198-212.

16. Gross W.A.
Gas lubricated bearings
Applied Mechanics Reviews, 15(10), 1962, 765-769.

17. Gross W.A.
A review of developments in externally pressurised gas bearing technology since 1959
Journal of Lubrication Technology, Trans ASME, 91, 1969, 161-165.

18. Munday A.J.
A review of externally pressurised gas bearings
Proceeding to Conference on Externally Pressurised Bearings, London, 1971, 65-75.

19. Majumdar B.C.
Externally pressurised gas bearings : A review
Wear, 62(2), 1980, 299-314.

20. Yabe H.
Current research on externally pressurised gas-lubricated bearings
JSME International Journal, 30(267), 1987, 1369-1374.

21. Bartz W.J. — Luftlagerungen - Kontakt & Studium Band 78
Grafenau: Technische Academie Esslingen / Expert Verlag(1), 1982.

22. Constantinescu V. — Gas Lubrication
New York: The American Society of Mechanical Engineers, 1969.

23. Powell J.W. — Design of Aerostatic Bearings
London: Machinery Publishing Co., Ltd., 1970.

24. Stout K.J. — Design of aerostatic Bearings
Lecture notes, short course at the National Bureau of Standards, Washington D.C., 1986.

25. Tabachnikov Y.B. — Experimental investigation of flat, microgrooved, gas-lubricated bearings
Machine & Tooling, 39(11), 1963,25-29.

26. Yabe H. Shiokawa T. Mori H. — A study on angular stiffness and damping properties of externally pressurised gas thrust bearing with surface-restriction compensation.
Bulletin of JSME, 26(222), Dec. 1983, 2251-2257.

27. Yabe H. Aoki S. Mori H. — Fundamental characteristics of an externally pressurised thrust gas bearing with surface-restriction compensation through triangular restricting grooves.
Bulletin of JSME, 28(244), Oct. 1985, 2394-2399.

28. Tawfik M. Stout K.J. — The design of high efficiency flat pad aerostatic bearing using laminar restrictions
Tribology International, 22(4), Aug. 1989, 273-281.

29. Roblee J.M. Mote C.D. Jr. — Design of externally pressurised gas bearing for stiffness & damping
Tribology International, 23(5), Oct. 1990, 333-345.

30. Allais D.C. — The design of externally pressurised gas thrust bearing for maximum stiffness and stability
ASLE Transaction, 5, 1962, 254-260.

31. Unterberger R. — Gaslager mit hoher Tragfähigkeit
Feinwerktechnik, 69(4), 1965, 154-156.

32. Patterson E.B. — The use of porous material in air bearings

Ph.D. Thesis, The Queen's University of Belfast, Department of Mechanical and Manufacturing Engineering, Belfast, 1972.

33. Lohiya S.H.
Pande S.S.
Analysis of tapered land aerostatic thrust bearing operating under nonsteady loads
Mechanism & Machine Theory, 24(6), 1989, 515-521.

34. Wang J.M.
Schellenkens P.H.
Tri-conical gap-shaped externally pressurised gas bearing pads
Tribology Transactions, 37(4), 1994, 850-856.

35. Blondeel E.
Snoeys R.
Devrieze L.
Aerostatic bearings with infinite stiffness
Annals of the CIRP, 25(1), 1976, 291-296.

36. Holster P.L.
Jacobs J.A.H.
Theoretical analysis and experimental verification on the static properties of externally pressurised air bearing pads with load compensation.
Tribology International, 20(5), Oct. 1987, 276-296.

37. Unterberger R.
Die Steifigkeit der Luftlager
Feinwerktechnik, 65(1), 1961, 17-24.

38. Mori H.
Yabe H.
Analysis of externally pressurised circular thrust gas-bearing with multiple supply holes
ASLE Transaction, 7, 1964, 269-276.

39. Stout K.J.
Sweeney F.
Design of aerostatic flat pad bearings using pocketed orifice restrictors
Tribology International, 17(4), Aug. 1984, 191-198.

Chapter 2

40. Stout K.J.
Aerostatic Bearings
in Slocum A.H. Precision Machine Design, 1st ed., Prentice-Hall, 1992.

41. Kanai M.
Ishihara S.
Air bearing lead screw and nut using porous material
Bulletin of JSPE, 56(12), 1990, 2201-2207.

42. Sneck H.J.
A survey of gas-lubricated porous bearings

Journal of Lubrication Technology, Trans. ASME, 90(4), 1968, 804-809.

43. Majumdar B.C.
Gas-lubricated porous bearings: a bibliography
Wear, 36, 1976, 269-273.

44. Sheinberg S.A.
Shuster V.G.
Resistance to vibration of a hydrostatic thrust bearing
Machine & Tooling, 31(11), 1960, 24-29.

45. Gargiulo E.P. Jr.
Gilmour P.W.
A numerical solution for the design of externally pressurised porous gas bearings : Thrust bearings
Journal of Lubrication Technology, Trans. ASME, Oct. 1968, 810-817.

46. Mori H.
Yabe H.
Ono T.
Theory of externally pressurised circular thrust porous gas bearing
Journal of Basic Engineering, Trans ASME, Sept. 1965, 613-621.

47. Mori H.
Yabe H.
Shibayama T.
Theoretical solution as a boundary value problem for externally pressurised porous gas-bearings
Journal of Basic Engineering, Trans. ASME, 87(3), 1965, 622-630.

48. Andrisano A.
Maggiore A.
Theoretical and experimental analysis of externally pressurised porous gas thrust bearings
Tribology International, October 1978, 285-288.

49. Ishizawa S.
Hori E.
The flow of a viscous fluid through a porous wall into a narrow gap
Bulletin of JSME 9(36), 1966, 719-730.

50. Murti P.R.K.
Analysis of externally pressurised gas porous bearings
Journal of Lubrication Technology, Trans. ASME, 96(3), 1974, 354-360.

51. Murti P.R.K.
Effect of velocity slip in an externally pressurised porous thrust bearing working with an incompressible fluid
Journal of Applied Mechanics, Trans ASME, 43(3), 1976, 404-408.

52. Beavers G.S.
Joseph D.D.
Boundary conditions at a naturally permeable wall
Journal of Fluid Mechanics, Trans ASME, 30(1), 1967, 197-207.

53. Jones O.K.
Michalski J.
Lewis G.K.
The steady state performance of an externally pressurised gas lubricated porous thrust bearing with a uniform film
Joint IMechE/IProdE Conference on Externally Pressurised Bearings, Paper C12, 1971, 23-42.

54. Verma R.L.
Effect of velocity slip in an externally pressurised porous circular thrust bearing
Wear, 63, 1980, 239-244.

55. Singh K.C.
Effect of velocity slip on the performance of aerostatic porous thrust bearings with uniform film thickness
Wear, 88(3), 1983, 323-333.

56. Hsing F.C.
The effect of fluid inertia on a porous thrust plate - an analytical solution.
Journal of Lubrication Technology, Trans. ASME, 93(1), 1971, 202-206.

57. McCrea R.J.
Donaldson I.S.
The significant of fluid inertia and slip velocity in the steady-stage analysis of externally pressurised gas lubricated partially porous thrust bearings
Proceedings of the 7th International Gas Bearing Symposium, Paper A-1, 1976, 1-20.

58. Wang C.
Limitations of the Reynolds Equation for porous thrust bearings.
Journal of Lubrication Technology, Trans. ASME, 97(4), 1975, 642-643.

59. Bhatt B.S.
Sacheti N.C.
Comments on the limitation of the Reynolds Equation for porous thrust bearings
Wear, 53, 1979, 377-379.

60. Taylor R.
Lewis G.K.
Steady-state solutions for an aerostatic thrust bearing with an elastic porous pad
Proceedings of the 6th International Gas Bearing Symposium, Paper C5, 1974, 5-74.

61. Polome J.
Gorez R.
The use of ground porous materials in gas lubrication
Wear, 60, 1980, 349-356.

62. Rehsteiner F.H.
Cannon R.H. Jr.
Static properties of hydrostatic thrust gas bearings with curved surfaces
Journal of Lubrication Technology, Trans. ASME, 94(1), 1972, 49-55.

63. Majumdar B.C.
Design of externally pressurised rectangular porous thrust bearings
Wear, 32, 1975, 1-8.

64. Rao N.S.
Analysis of externally pressurised porous gas bearings: rectangular thrust bearings
International Journal of Machine Tool Design and Research, 19, 1979, 87-93.

65. Singh K.C.
Rao R.C.
Static Characteristics of aerostatic porous rectangular thrust bearings
Wear, 77, 1982, 229-236.

66. Koyama T.
Aoyama T.
Inasaki I.
Characteristics of externally pressurised porous ceramics air bearings
Transaction of JSME, 55(511), 1989, 750-758.

67. Aoyama T.
Inasaki I.
Application of porous ceramic materials to externally pressurised air bearings
Proceedings of the 5th International Congress on Tribology, 1, June 1989.

68. Rao N.S.
Analysis of aerostatic porous rectangular thrust bearings with offset loads.
Wear, 59, 1980, 333-344.

69. Singh K.C.
Rao N.S.
Static characteristics of aerostatic porous rectangular thrust bearings with offset load
Journal of Lubrication Technology, Trans. ASME, 105(1), 1983, 143-146.

70. Singh K.C.
Singh K.C.
Rao N.S.
Static characteristics of aerostatic porous rectangular
Steady-state characteristics of aerostatic porous rectangular thrust bearings incorporating the effects of velocity slip, anisotropy and tilt.
Proceedings of IMechE, 197C, 1983, 179-187.

71. Rao N.S.
Effect of slip flow in aerostatic porous rectangular thrust bearings
Wear, 61, 1980, 77-86.

72. Singh K.C.
Rao N.S.
Majumdar B.C.
Effect of velocity slip on the performance of aerostatic porous thrust bearings with uniform film thickness
Wear, 88(3), 1983,323-333.

73. Shih Y.D.
Yang J.Y.
Analysis of narrow rectangular aerostatic porous thrust bearings moving with a uniform transverse velocity

Wear, 141, 1990, 125-136.

74. Liaw S.P.
Lin D.G.
Sliding effect of gas-lubricated porous rectangular thrust bearings
Wear, 141, 1991, 235-248.

75. Wu K.H.
Cusano C.
Analysis of externally pressurised, double-pad, gas porous thrust bearing.
Journal of Lubrication Technology, Trans. ASME, 105(1), 1983, 113-119.

76. Kilmister G.T.F.
The use of porous materials in externally pressurised porous gas bearings
Powder Metallurgy, 12(24),1969, 400-409.

77. Mori H.
Yabe H.
Theoretical investigation of externally pressurised gas-lubricated porous journal bearing with surface loading effect
Journal of Lubrication Technology, Trans. ASME, 95(2), 1973, 195-203.

78. Kawashima I.
Porous ceramic gas bearing 2
Proceeding to the 1988 Autumn Symposium of the Japan Society of Precision Engineering, 1988, 843-844.

79. Okano M.
Studies of externally pressurised porous gas bearings
Researches of the Electrotechnical Laboratory, 952, April 1991, 1-145.

80. Heinzl J.
Aerostatisches Lager
German Patent DE 31 10712 A1, Munich, 1982.

81. Köhler H.
Druckgespeiste Gaslager mit flächig verteilten Mikro-düsen
Dr.-Ing. Thesis, TU München, Lehrstuhl für Fein-gerätebau und Getriebelehre, 1985.

82. Gerke M.
Auslegung von ebenen und zylindrischen aerostatischen Lagern bei stationärem Betrieb
Dr.-Ing. Thesis, TU München, Lehrstuhl für Fein-gerätebau und Getriebelehre, 1991.

83. Hopfner J.
Fertigung von aerostatischen Lagern aus poröser Sinterbronze mit oberflächenverdichteter Drossel-schicht
Dr.-Ing. Thesis, TU München, Lehrstuhl für Fein-gerätebau und Getriebelehre, 1991.

84. Schroter A.
Heinzl J.
Air-bearings with areal disposed Micro-orifices (FVM-bearings)
Proceedings of the 3rd International Conference on Ultraprecision in Manufacturing Engineering, Aachen, 1994.

85. Schultz B.
Muth M.
A new technique to manufacture high-performance air bearings
Proceedings of the 8th International Precision Engineering Seminar, Compiègne, May 1985, 533-536.

86. Taylor R.
Lewis G.K.
The dynamic performance of aerostatic porous thrust bearings with uniform films
Proceedings of the 7th International Gas Bearing Symposium, Paper A-4, 1976, 49-66.

87. Taylor R.
A numerical solution of the dynamic characteristics of an aerostatic, porous thrust bearing having a uniform film subjected to linear axial load variations
Journal of Mechanical Engineering Science, 19(3), 1977, 122-127.

88. Sun D.C.
On the stiffness and damping properties on an externally pressurised, gas-lubricated porous thrust bearing
Proceedings of the 7th International Gas Bearing Symposium, Paper A-5, 1976, 5-67.

89. Andrisano A.
Maggiore A.
Parenti Castelli V.
Experimental analysis of the dynamic behaviour of externally pressurised porous thrust bearings
Proceedings of the 8th International Gas Bearing Symposium, Paper 23, 1981, 311-322.

90. Sun D.C.
Stability analysis of an externally pressurised gas-lubricated thrust bearing
Journal of Lubrication Technology, Trans. ASME, 95(4), 1973, 457-468.

91. Sun D.C.
On the stability of gas-lubricated porous thrust bearings
Journal of Lubrication Technology, Trans. ASME, 96(2), 1975, 332-334.

92. Chang H.S.
Wang Z.S.
Sun D.C.
An experimental investigation of the stability of externally pressurised gas-lubricated porous thrust bearings
Journal of Lubrication Technology, Trans. ASME, 105(4), 1983, 630-637.

93. Majumdar B.C.
Dynamic characteristics of externally pressurised rectangular porous gas thrust bearings
Journal of Lubrication Technology, Trans. ASME, 98(1), 1976, 181-186.

94. Majumdar M.C.
Majumdar B.C.
Study of the pneumatic instability of externally pressurised porous gas thrust bearings with slip velocity
Wear, 124, 1988, 261-277.

95. Robinson C.H.
Sterry F.
The static strength of pressure fed gas journal bearings : porous bearings
U.K. A.E.R.E. Report ED/R 1672, Harwell, 1958.

96. German R.M.
Gas flow physics in porous metals
International Journal of Powder Metallurgy & Powder Technology, 15(1), 1979, 23-30.

97. Forchheimer P.
Wasserbewegung durch Boden
Zeitschrift des VDI, 45(50), 1901, 1781-1788.

98. Taylor R.
Lewis G.K.
Experience relating to the steady performance of aerostatic porous thrust bearings
Proceedings of IMechE, 189(22), 1975, 383-390.

99. Cieslicki K.
Investigations of the effect of inertia on flow of air through porous bearing sleeves
Wear, 172, 1994, 73-78.

100. Greenberg D.B.
Weger E.
An investigation of the viscous and inertia coefficients for the flow of gases through porous sintered metals with high pressure gradients
Chemical Engineering Science, 12, 1960, 8-19.

101. Rasoloarijaona M.
Auriault J.-L.
Nonlinear seepage flow through a rigid porous medium
European Journal of Mechanics, B, 13(2), 1994, 177-195.

102. Annon.
ISO 4022 : 1987
Permeable sintered metal materials - Determination of fluid permeability
BS 5600 Part 3, Section 3.6 : 1988, British Standards Institutions.

103. Robinson A.T.
Permeability of tungsten matrices as a function of density, particle size , and shape
Transaction of the ASM, 57, 1964, 650-657.

104. Cliffel E.M. Jr.
Smith W.E.
Schwope A.D.
Theory and applications of controlled permeability
Modern Developments in Powder Metallurgy, 3, 1966, 114-128.

105. German R.M.
Porosity and particle size effects on the gas flow characteristics of porous metal
Powder Technology, 30, 1981, 81-86.

106. Smith D.W.
Marth T.
An examination of the effects of pore morphology on gas flow through sintered compacts
Modern Developments in Powder Metallurgy, 12, 1980, 835-854.

107. Malik M.
Rodkiewicz C.M.
On slip flow considerations in gas-lubricated porous bearings
Journal of Tribology, Trans ASME, 106(4), 1984, 484-491.

108. Burgdorfer A.
The influence of the molecular mean free path on the performance of hydrodynamic gas lubricated bearings
Journal of Basic Engineering, Trans ASME, 81(1), 1959, 94-100.

109. Wu E.R.
Gas lubricated porous bearings of finite length -- Self-acting journal bearings
Journal of Lubrication Technology, Trans ASME, 101, July 1979, 338-348.

110. Kim D.S.
Cho E.S.
Choi C.K.
An experimental study on fluid flow characteristics of superposed porous and fluid layers
Korean Journal of Chemical Engineering, 11(3), 1994, 190-194.

111. Brinkman H.C.
A calculation of the viscous force exerted by a flowing fluid on a dense swarm of particles
Applied Scientific Research, A1, 1947, 27-34.

112. Saffman P.G.
On the boundary condition of a porous medium
Studies in Applied Mathematics, 50, 1971, 93-101.

113. Taylor G.I.
A model for the boundary condition of a porous material Part I
Journal of Fluid Mechanics, 49(2), 1971, 319-326.

114. Richardson S.
A model for the boundary condition of a porous material Part II

Journal of Fluid Mechanics, 49(2), 1971, 327-336.

115. Beavers G.S.
Sparrow E.M.
Magnuson R.A.
Experiments on coupled parallel flows in a channel and a bounding porous medium
Journal of Basic Engineering, Trans ASME, 92(4), 1970, 843-848.

116. Larson R.E.
Higdon J.J.L.
Microscopic flow near the surface of two-dimensional porous media
Part I - axial flow
Journal of Fluid Mechanics, 166, 1986, 449-472.

117. Larson R.E.
Higdon J.J.L.
Microscopic flow near the surface of two-dimensional porous media
Part II - transverse flow
Journal of Fluid Mechanics, 178, 1987, 119-136.

118. Sahraoui M.
Kaviany M.
Slip and no-slip velocity boundary conditions at interface of porous plain media
International Journal of Heat and Mass Transfer, 35(4), 1992, 927-943.

119. Constantinescu V.
Some considerations regarding the design of bearing fed by air under pressure through a large number of holes or through porous surfaces
Studii si Cercetari Mecan. Apl., 13(1), 1962, 173.

120. Sneck H.J.
Yen K.T.
The externally pressurised, porous wall, gas-lubricated journal bearing III
ASLE Transactions, 10, 1967, 339-347.

121. Sneck H.J.
Yen K.T.
The externally pressurised, porous wall, gas-lubricated journal bearing I
ASLE Transactions, 7, 1964, 288-298.

122. Sneck H.J.
Elwell R.C.
The externally pressurised, porous wall, gas-lubricated journal bearing II
ASLE Transactions, 8, 1965, 339-345.

123. Mori H.
Yabe H.
Yamakage H.
Furukawa J.
Theoretical analysis of externally pressurised porous journal gas bearings
Bulletin of JSME, 11(45), 1968, 527-535.

124. Mori H.
Yabe H.
Yamakage H.
Theoretical analysis of externally pressurised porous journal gas bearings
Bulletin of JSME, 12(54), 1969, 1512-1518.

125. Victor I.H. — Druckluftgespeiste Radiallager aus porösem Werkstoff
Industrieanzeiger 92(80), 1970, 1892-1893.

126. Schmidt J. — Aerostatische Radiallager aus porösem Werkstoff
Zeitung der industriellen Fertigung, 61 ,1971, 616-617.

127. Majumdar B.C. — Analysis of externally pressurised, porous gas journal bearings I
Wear, 33, 1975, 25-35.

128. Majumdar B.C. — Analysis of externally pressurised, porous gas journal bearings II
Wear, 33, 1975, 37-43.

129. Majumdar B.C. — Design of externally pressurised gas-lubricated porous journal bearings
Tribology international, April 1976, 71-74.

130. Gargiulo E.P. — Porous wall gas lubricated journal bearings: theoretical investigation
Journal of Lubrication Technology, Trans. ASME, 101(4), 1979, 458-465.

131. Gargiulo E.P. — Porous wall gas lubricated journal bearings: experimental investigation
Journal of Lubrication Technology, Trans. ASME, 101(4), 1979, 466-473.

132. Castelli V.P. — Experimental and theoretical analysis of the gas-lubricated porous rotating journal bearing
ASLE Transactions, 1979, 22(4), 382-388.

133. Rao N.S. — Design of externally pressured porous gas bearings with journal rotation
Wear, 52, 1979, 1-11.

134. Rao N.S. — Analysis of aerostatic porous journal bearings using the slip velocity boundary conditions
Wear, 76, 1982, 35-47.

135. Mori H.
Yabe H. — A theoretical study of the dynamic characteristics of externally pressurised, porous journal gas-bearings
Proceedings of the 6th International Gas Bearing Symposium, Paper C8, 1974, 103-116.

136. Rao N.S.
Majumdar B.C.
An approximate method for the calculation of dynamic stiffness and damping coefficients of externally pressurised porous gas journal bearings
Wear, 61, 1980, 375-379.

137. Malik M.
Rodkiewicz C.M.
The dynamic behaviour of externally pressurised gas-lubricated unloaded porous journal bearings
Proceedings of IMechE, 198 (C4), 1984, 33-41.

138. Malik M.
Hori Y.
Externally-pressurised gas-lubricated floating-ring porous journal bearings, Part 2: dynamic state analysis
Proceedings of IMechE, 200 (C2), 1986, 101-109.

139. Majumdar M.C.
Majumdar B.C.
Non-linear transient analysis for an externally pressurised porous gas journal bearing
Wear, 132, 1989, 139-150.

140. Pal D.K.
Majumdar B.C.
Analysis of stiffness and damping characteristics of externally pressurised gas-lubricated porous bearings under conical mode of vibration
Wear, 118, 1987, 199-216.

141. Majumdar B.C.
Whirl instability of externally pressurised gas-lubricated porous journal bearings
Wear, 40, 1976, 141-153.

142. Majumdar M.C.
Majumdar B.C.
Theoretical analysis of pneumatic instability of externally pressurised porous gas journal bearings considering velocity slip
Journal of Tribology, Trans. ASME, 110(4), 1988, 730-733.

143. Rao N.S.
Majumdar B.C.
Analysis of pneumatic instability of externally pressurised porous gas journal bearings
Journal of Lubrication Technology, Trans. ASME, 101(1), 1979, 48-53.

144. Steger P.J.
Air-bearing spindle for machine tools - spherical design
Research and development report, NO. Y-1581, Union Carbide Corp., Tennessee, 1967.

145. Gorez R.
A study of the stability of externally pressurised gas bearings with porous wall by Liapunov's direct method
Journal of Lubrication Technology, Trans. ASME, 105(2), 1973, 204-207.

146. Fourka M.
Tian Y.
Bonis M.
Influence of compensation type on air bearings performance: comparison between orifice and porous compensation
Proceedings of the 8th International Precision Engineering Seminar, Compiègne, May 1985, 545-548.

147. Loch E.
Gaszufuhr über Flächen aus porösem Material in aerostatischen Axiallagern
Schmiertechnik, 9(6), 1962, 307-313.

148. Mori H.
Yabe H.
Ono T.
Yamada H.
Research of externally pressurised porous thrust gas bearing
Bulletin of JSME, 7(28), 1964, 821-826.

149. Gorez R.
Szwarcman M.
Hydrostatic slider gas bearings fed through a row of porous discs.
International Journal of Machine Tool Design and Research, 11, 1971, 89-108.

150. Gorez R.
Szwarcman M.
Externally pressurised gas bearings with partially porous wall
Proceedings of the 6th International Gas Bearing Symposium, Paper C7, 1974, 89-102.

151. Donaldson I.S.
Patterson E.B.
The use of porous inserts in plain externally pressurised air thrust bearings at high supply pressures
Proceedings of the 6th International Gas Bearing Symposium, Paper C6, 1974, 6-75.

152.
Standardised Air Thrust Bearings
Company Brochure, Dexter Continental N.V., Zele, Belgium.

153. Wills-Moren W.J.
Private Communication
Cranfield, March 1995.

154. Rasnick W.H.
Porous graphite air-bearing components as applied to machine tools
SME Technical Report MRR 74-02.

155. Furukawa Y.
Morinuki M.
Kitagawa K.
Development of ultra-precision machine tool made of ceramics
Annals of CIRP, 35(1), 1986, 279-282.

156. Ueno S.
Development of an ultra-precision machine tool using a ceramic bed

Trans. JSME, 54(500C), 1987, 1004-1008.

157. Schellschmidt T.
Guyenot V.
Eberhardt R.
Risse S.
Herold V.
Aerostatic linear guide made of high performance ceramics
Proceedings to the 3rd International Conference on Ultraprecision in Manufacturing Engineering, Aachen, 1994, 249-252.

158. Trimm D.L.
Stanislaus A.
The control of pore size in alumina catalyst supports : A review
Applied Catalysis, 21, 1986, 215-238.

159. Yasutomi Y.
Chiba A.
Sobue M.
Development of reaction-bonded electroconductive silicon nitride - titanium nitride and resistive silicon nitride - aluminium oxide composites
Journal of the American Ceramic Society, 74(5), 1991, 950-957.

160. Tantry P.K.
Misra S.N.
Shashi Mohan A.L.
Developmental studies of porous alumina ceramics
Ceramic Transactions, Vol. 31 Porous Materials, American Ceramic Society, 1993, 89-99.

161. Chou K.S.
Liu H.C.
Chang K.L.
Microstructure evolution during fabrication of porous ceramic filter
Ceramic Transactions, Vol. 31 Porous Materials, American Ceramic Society, 1993, 101-110.

162. Sakka S.
Kozuka H.
Adachi T.
Preparation of porous materials by the sol-gel method
Ceramic Transactions, Vol. 31 Porous Materials, American Ceramic Society, 1993, 27-40.

163. Atkinson A.
Gel processing routes to porous ceramics
Ceramic Transactions, Vol. 31 Porous Materials, American Ceramic Society, 1993, 41-49.

164. Ishizaki K.
Takata A.
Okada S.
Mechanically enhanced open porous materials by a HIP process
Journal of the Japan Ceramic Society, 98(6), 1990, 533-540.

165. Nanko M.
Ishizaki K.
Takata A.
Production of high strength and uniform-size micro-pore porous materials by HIP process
Nippon Kikai Gakkai Tsujo Sokai Koenkai Koen Ronbunshu, 70(930-9), 1993, 339-341.

166. Nanko M.
Ishizaki K.
Sintering of porous materials by a capsule free HIP process

Takata A. *Ceramic Transactions, Vol. 31 Porous Materials, American Ceramic Society, 1993, 117-126.*

167. Ishizaki K. Nanko M. A hot isostatic process for fabricating porous materials *Journal of Porous Material, 1(1), 1995, 19-27.*

168. Sheppard L.M. Trends in HIP equipment capabilities *Ceramic Bulletin, 71(3), 1992, 323-327.*

169. Takata A. Ishizaki K. Okada S. Improvement of a porous material's mechanical property by hot isostatic process *Materials Research Society Symposium Proceedings, 207, 1991, 135-140.*

170. Takata A. Ishizaki K. Kondo Y. Shioura T. Influence of hipping pressure on the strength and the porosity of porous copper *Materials Research Society Symposium Proceedings, 251, 1992, 133-138.*

171. Takata A. Ishizaki K. Mechanical properties of hipped porous copper *Ceramic Transactions, Vol. 31 Porous Materials, American Ceramic Society, 1993, 233-242.*

172. Ishizaki K. Kuzjukevics A. Porous alumina by hot isostatic pressing *Materials Research Society Symposium Proceedings, 251, 1992, 121-125.*

173. Kuzjukevics A. Ishizaki K. Production of porous alumina by hot isostatic pressing *Ceramic Transactions, Vol. 31 Porous Materials, American Ceramic Society, 1993, 111-116.*

174. Ishizaki K. Okumoto Y. Takata A. Manufacture of penetrating-pores metals by high gas pressure *Materials Research Society Symposium Proceedings, 251, 1992, 115-120.*

175. Saito N. Ishizaki K. Kuzjukevics A. The production of porous Si_3N_4 ceramics with 100% β phase *Materials Research Society Symposium Proceedings, 251, 1992, 121-125.*

176. Nanko M. Ishizaki K. Fujikawa T. Porous ceramic filters produced by hot isostatic pressing *Journal of the American Ceramic Society, 77(9), 1994, 2437-2442.*

177. Corbett J.
Stephenson D.J.
McKeown P.A.
An investigation for the development of porous ceramic water hydrostatic bearings for ultra high precision applications
EPSRC Research Proposal No. GR/K11710, Oct., 1994.

178. Corbett J.
Stephenson D.J.
The development of 2-layered porous ceramic aerostatic guideway bearings for ultra precision applications
EPSRC Grant Reference GR/K89801, Oct., 1996.

Chapter 3

179. Stout K. J.
Pink E. G.
Design procedure for orifice compensated gas journal bearing based on experimental data
Tribology International, Feb. 1978, 63-75.

180. Stout K. J.
Pink E. G.
Orifice compensated EP gas bearings: the significance of errors of manufacture
Tribology International, June 1980, 105-111.

181. Wagh A.S.
Poeppel R.B.
Singh J.P.
Open pore description of mechanical properties of ceramics
Journal of Material Science, 26, 1991, 3862-3868.

182. Morrell R.
Handbook of properties of technical and engineering ceramics
1st ed. London: HMSO, 1987.

183. Young W.C.
Roark's formulas for stress and strain
6th ed. New York: McGraw-Hill, 1989.

184. Yoshimoto S.
Anno Y.
Nukushina T.
Aerostatic thrust bearing capable of operating in bearing clearance of submicrometer
Transactions of JSPE, 58(12), 1992, 2081-2086.

185. Kingery W.D.
Bowen H.K.
Uhlmann D.R.
Introduction to ceramics
2nd ed. New York: J. Wiley & Son, 1976.

Chapter 4

186. Data sheet 550 - Baco reactive aluminas
Company Brochure, Alcan Chemicals Europe, Gerrards Cross, Bucks.

187. Product specification - white fused alumina
Company Brochure, Universal Abrasives Ltd., Stafford.

188. Duralum special white
Company Brochure, Washington Mills Electro Minerals Corp., North Grafton.

189. German R.M. Particle packing characteristics
1st ed. Metal Powder Industries Federation, 1989.

190. Balmori-Ramirez H. Riguard M. Slip casting of mixed Al_2O_3 - ZrO_2 suspensions
Journal of the Canadian Ceramics Society, 60(3), 1991, 45-50.

191. Ball mills and ancillary equipment
Company Brochure BM-10-82, Pascall Engineering Co., Sussex.

192. Greskovich C. Ceramic fabrication processes
Treatise on Materials Science and Technology, Vol. 9, Ed. Wang F.F.Y., Academic Press, New York, 1976.

193. Kondo Y. Influence of combination of ball diameters and rotation speed on grinding performance of alumina by ball milling
*Journal of the Ceramic Society of Ja*pan, 101(7), 1993, 819-823.

194. Plasters for ceramics
Company brochure, British Gypsum, Industrial Products Division.

195. Lin S.T. German R.M. Interaction between binder and powder in injection moulding of alumina
Journal of Materials Science, 29, 1994, 5207-5212.

196. Hens K.F. Lin S.T. German R.M. Lee D. The effect of binder on the mechanical properties of carbonyl iron products
Journal of the Minerals, Metals and Materials Society, 41(8), 1989, 17-21.

Chapter 5

197. German R.M.
Powder metallurgy science
1st Edition, Princeton: Metal Powder Industries Federation, 1984.

198. Swinkels F.B.
Wilkinson D.S.
Arzt E.
Ashby M.F.
Mechanism of hot-isostatic pressing
Acta Metallurgica, 31(11), 1983, 1829-1840.

199. Gopel W.
Hesse J.
Zemel J.N.
Sensors: a comprehensive survey
Vol. 7 -- mechanical sensors
1st Edition, Weinheim: VCH, 1994.

200. Annon.
ISO 2738 : 1987
Permeable sintered metal materials - Determination of density, oil content and open porosity
BS 5600 Part 3, Section 3.2 : 1988, British Standards Institutions.

201. Coleman S.C.
Beere W.B.
The sintering of open and closed porosity in urania
Philosophical Magazine, Vol.31, 1975, 1403-1413.

202. Ashby M.F.
HIP 487 -- A Program for Constructing Maps for Hot Isostatic Pressing
Cambridge University Engineering Department, Cambridge, Sept., 1987.

Chapter 6

203. Cieslicki K.
Static and dynamic evaluation of permeability of porous bearing sleeves
Wear, 167, 1993, 69-72.

204. Gélinas C.
Angers R.
Improvement of the dynamic water-expulsion method for pore size distribution measurements
Ceramic Bulletin, 65(9), 1986, 1297-1300.

205. Johnson R.G.
Higashi R.E.
A highly sensitive silicon chip microtransducer for air flow and differential pressure sensing applications
Sensor and Actuators, 11, 1987, 63-72.

206. Moser D.
Lenggenhager R.
Wachutka G
Fabrication and modelling of CMOS microbridge gas flow sensors
Sensor and Actuators, 6(B), 1992, 165-169.

207. Van Oudheusden B.
Silicon thermal flow sensor with a 2-dimensional direction sensitivity
Measurement Science & Technology, 1, 1990, 565-575.

208.
Electro - pneumatic regulator, Series IT 2000
SMC Corporation, Tokyo, Catalog no. E609-A, 1993.

209.
Pressure transducers and transmitters
Sensortechnics U.K., Rugby, 1994.

210.
Micro Switch Catalog 15
Honeywell Inc., Illinois, May 1994.

211. Capone A.
et. al.
Permeability distribution in sintered bearings
Tribology International, Dec. 1978, 333-336.

212. Annon.
ISO 4003 : 1977
Permeable sintered metal materials - Determination of bubble test pore size
EN 24003 : 1993, European Committee for Standardisation, Brussels.

213. Meyer K.
Lorenz P.
et. al.
Porous solid and their characterisation
Crystal Research Technology, 29(7), 1994, 903-930.

214. Dullien F.A.
Batra V.
Determination of the structure of porous media
Industrial and Engineering Chemistry, 62(10), 1970, 25-53.

215. Clements J.F.
Vyse J.
A comparison of methods of measuring pore-size distribution in refractories
Transactions of the British Ceramics Society, 67(7), 1968, 285-317.

216. Konsztowicz K.J.
Boutin J.
Study of porosity in corroded refractories
Journal of the American Ceramics Society, 76(5), 1993, 1169-1176.

217. Efremov D.K.
Fenelonov V.B.
Authenticity of pore size distributions obtained by traditional techniques
Pure & Applied Chemistry, 65(10), 1993, 2209-2216.

218. Žagar L.
Ermittlung der Größenverteilung von Poren in feuerfesten Baustoffen - Teil I
Archiv für das Eisenhüttenwesen, 26(9), 1955, 561-562.

219. Žagar L.
Ermittlung der Größenverteilung von Poren in feuerfesten Baustoffen und Glasnutschen - Teil II
Archiv fürs Eisenhüttenwesen, 27(10), 1956, 657- 562.

220. Žagar L.
Über die Textur von feuerfesten Baustoffen
Silicates Industriels, 24, 1959, 306-312.

221. Žagar L.
Porengrößenverteilung nach dem Luft-wasser-Verdrängungsverfahren
Berichte der Deutschen Keramik Gesellschaft, 55(1), 1978, 13-17.

222. Jeschke P.
Texture analysis of basic refractory brick
Journal of the American Ceramics Society, 47(7), 1966, 360-363.

223. Johnston P.R.
The most probable pore-size distribution in fluid filter media I. Evidence of such a distribution from results of extended bubble-point measurements.
Journal of Testing and Evalution, 11(2), 1983, 117-121.

224. Beavers G.S.
Sparrow E.M.
Masha B.A.
Boundary condition at a porous syrface which bounds a fluid flow
AIChE Journal, 20(3), 1974, 596-597.

Chapter 7

225. Davis W.R.
Measurement of the elastic constants of ceramics by resonant frequency methods
Transactions of the British Ceramics Society, 67, 1968, 515-541.

226. Annon.
ASTM C 1198 - 91 : 1991
Standard test method for dynamic Young's modulus, and Poisson's ratio for advanced ceramics by sonic resonance
ASTM Standards Vol. 15.01, American Society for Testing and Materials, Philadelphia.

227. Annon.
JIS R 1602 - 1986
Testing method for elastic modulus of high performance ceramics
Japan Standards Association, Tokyo.

228. Annon.
ASTM C 769 - 80 : 1989
Standard test method for sonic velocity in manufactured carbon and graphite materials for use in obtaining an approximate Young's modulus
ASTM Standards Vol. 15.01, American Society for Testing and Materials, Philadelphia.

229. Wolfenden A. Harmouche M.R. et. al.
Dynamic Young's modulus measurements in metallic materials : results of an interlaboratory testing program
Journal of Testing and Evaluation, January 1989, 2-13.

230. Spriggs R.M.
Expression for effect of porosity on elastic modulus of polycrystalline refractory material, particularly aluminium oxide
Journal of the American Ceramic Society, 44(12), 1961, 628-630.

231. Leissa A.W.
Vibration of plates
NASA Report SP-160, 1969.

232. Weisensel G.N.
Natural frequency information for circular and annular plates
Journal of Sound and Vibration, 133(1), 1989, 129-134.

233. Roberts J.
Elastic modulus of polymers from resonant flexure of clamped disks
Journal of Science and Instrumentation, 41, 1964, 357-360.

234. Azimi S.
Axisymmetric vibration of point-supported circular plates
Journal of Sound and Vibration, 135(2), 1989, 177-195.

235. Azimi S.
Free vibration of circular plates with elastic or rigid interior support
Journal of Sound and Vibration, 120(1), 1988, 37-52.

236. Annon.
Grindosonic : A sound design for non-destructive material testing
Company brochure, J.W. Lemmens-Elektronika N.V., Leuven.

237. Lemmens J.W.
Impulse excitation : A technique for dynamic modulus measurement
Dynamic Measurements in Materials, American Society for Testing and Materials, Philadelphia, 1990.

238. Wolfenden A.
Heritage K.
Clayton F.
Impulse excitation technique for dynamic flexural measurements at moderate temperature
Review of Scientific Instruments, 59(6), 1988, 973-974.

239. Allison R.J.
Boutin J.
Non-destructive determination of Young's modulus and its relationship with compressive strength, porosity and density
Deformation of Sediments and Sedimentary Rocks, Geological Society Special Publication 29, 1987, 63-69.

240. König W.
Föllinger H.
Elasticity modulus of grinding wheels and its impact on their in-process behaviour
Ceramic Forum International, 64(6-7), 1987, 220-224.

241. Mendes C.
The development of an automated vibration technique for measuring the mechanical properties of oxide scale at high temperature
Ph.D. Thesis, Cranfield Institute of Technology, School of Industrial and Manufacturing Science, Cranfield, 1993.

242. Rice R.W.
Relation of tensile strength - porosity effects in ceramics to porosity dependence of Young's modulus and fracture energy, porosity character and grain size
Materials Science and Engineering, A112, 1989, 215-224.

243. Duckworth W.
Discussion of the Ryshkewitch paper
Journal of American Ceramic Society, 36(2), 1953, 68.

244. Spriggs R.M.
Expression for effect of porosity on polycrystalline refractory materials, particularly aluminium oxide
Journal of American Ceramic Society, 44, 1961, 628-629.

245. Phani K.K.
Niyogi S.K.
Elastic-modulus porosity relationship for Si_3N_4
Journal of Material Science Letters, 6), 1987, 511-515.

246. MacKenzie J.K.
Singh J.P.
The elastic constants of a solid containing spherical holes
Proceedings of the Physics Society, 63(B), 1950, 2-11.

247. Godfrey D.J.
Ceramic strength determination with ring loaded disc specimens
British Ceramic Proceedings, 39(2), 1987, 133-140.

248. Favier S.M.
Manufacture and properties of alumina/zirconi ceramics
M.Sc. Thesis, Cranfield Institute of Technology, School of Industrial Science, Cranfield, 1990.

249. Shaw J.H.
Best S.M.
Bonfield W.
Study of the application of viscous plastic processing to hydroxyapatite
Journal of Materials Science Letters, 14(15), 1995, 1055-1057.

250. Wagh A.S.
Poeppel R.B.
Singh J.P.
Dependence of ceramic fracture properties on porosity
Journal of Material Science, 28, 1993, 3589-3593.

251. Annon.
Standard practice for reporting uniaxial strength data and estimating Weibull distribution parameters for advanced ceramics
ASTM Standard C1239 -93, Vol. 15.02, 1993, 371-388.

Chapter 8

252. Maebashi N.
Ceramic membranes and application to the recovery of soy sauce
Ceramic Transactions, Vol. 31 Porous Materials, American Ceramic Society, 1993, 81-87.

253. Plucknett K.
Cáceres C.H.
Wilkinson D.S.
Tape casting of fine alumina/zirconia powders for composite fabrication
Journal of the American Ceramic Society, 77(8), 1994, 2137-2144.

254. Plucknett K.
Cáceres C.H.
Hughes C.
Wilkinson D.S.
Processing of tape casting of fine alumina/zirconia powders
Journal of the American Ceramic Society, 77(8), 1994, 2145-2153.

255. Chartier T.
Bruneau A.
Aqueous tape casting of alumina substrates
Journal of the European Ceramics Society, 12, 1993, 243-247.

256. Hotza D.
Greil P.
Review : aqueous tape casting of ceramics powders
Materials Science & Engineering, A202, 1995, 206-217.

Chapter 10

257. Rowe W.B.
Stout K.J.
Design of externally pressurised gas fed journal bearings employing slot restrictors
Tribology, 6(4), 1973, 140-144.

258. Komanduri R.
On material removal mechanisms in finishing on advanced ceramics and glasses
Annals of CIRP, 45(1), 1996, 509-514.

Chapter 11

259. Mitsuya Y.
Averaged Reynolds equation extended to gas lubrication possessing surface roughness in the slip flow regime
Journal of Tribology, Trans. ASME, 111(3), 1989, 495-503.

Chapter 13

260. Lenk R.
Hot moulding - an interesting forming process
Ceramics Forum International, 72(10), 1995, 636-639.

261. Sherman A.J.
Williams B.E.
Characterisation of porous cellular materials fabricated by chemical vapour deposition
Materials Research Society Symposium, 207, 1991, 141-149.

262. Andersson P.
Blomberg A.
Alumina in unlubricated sliding point, line and plane contacts
Wear, 170, 1993, 191-198.

263. Andersson P.
Holmberg K.
Limitations of the use of ceramics in unlubricated sliding applications due to transfer layer formation
Wear, 175, 1994, 1-8.

264. Hisakado T.
Suda H.
Watanabe H.
The friction and wear mechanisms between ceramics and metals
Wear, 155, 1992, 251-268.

265. Biswas S.K.
Vijayan K.
Friction and wear of PTFE - a review
Wear, 158, 1992, 193-211.

266. Srivastav A.
Kapoor A.
Pathak J.P.
The role of MoS_2 in hard overlay coating of Al_2O_3 in dry sliding
Wear, 155, 1992, 229-236.

267. Plesser P.
Snoeys R.
Dynamic Identification of convergent externally pressurised gas bearing gaps
Journal of Tribology, Trans. ASME, 110(2), 1988, 263-270.

Appendix A Modelling of Permeability by Poiseuille's Flow through Capillaries

Consider the pore structure as a collection of uniformly distributed capillaries of the same diameter, flow through each individual pore is governed by the Poiseuille's equation :

$$Q_{pore} = \frac{p_1^2 - p_2^2}{2.p_{ref}} . \frac{\pi.d_{pk}^4}{128.\eta.z_p} \qquad (a.1)$$

The mean pore size can be expressed as a function of open porosity and particle size, according to equation 6.15 :

$$\frac{d_{pk}}{d_w} = -0.4564 . \ln(1 - \zeta_o)$$

The number of pores over an area A_p is estimated by dividing the void fraction of that area by the area of the capillary. The volumetric void fraction of a porous material is by definition equal to the total porosity. For an isotropic pore structure, the void fraction over an area A_p is therefore :

$$\zeta_a = [1 - (1 - \zeta)^{2/3}] \qquad (a.2)$$

The total number of open pores is then :

$$n_{pore} = \frac{4.A_p.[1-(1-\zeta_o)^{2/3}]}{\pi.d_{pk}^2} \qquad (a.3)$$

If the flow through the porous material obeys Darcy's law, then

$$Q = \frac{\Phi_v . A_p}{z_p . \eta} . \frac{p_1^2 - p_2^2}{2 . p_{ref}} \qquad \text{(a.4)}$$

Multiplying equation a.1 with n_{pore} , the total flow through all the capillaries is :

$$Q = \frac{A_p . d_{pk}^2}{32 . \eta . z_p} . \frac{p_1^2 - p_2^2}{2 . p_{ref}} . [\, 1 - (1 - \zeta_o)^{2/3} \,] \qquad \text{(a.5)}$$

Therefore,

$$\Phi_v = \frac{d_{pk}^2}{32} . [\, 1 - (1 - \zeta_o)^{2/3} \,]$$

$$= 6.51 \times 10^{-3} . d_w^2 . [\, 1 - (1 - \zeta_o)^{2/3} \,] . \{ \ln (1 - \zeta_o)^2 \} \qquad \text{(a.6)}$$

Appendix B Design Calculations for Slot Feed Aerostatic Journal Bearing for Thrust Bearing Rig

Design parameters

bearing supply pressure	p_o	= 5 bar gauge
length to diameter ratio	L_b / d_b	= 1
bearing diameter	d_b	= 22 mm

For a double entry bearing, $L_e / L_b = 0.25$; i.e. the restriction slots are 5.5 mm from each end.

Calculations

Since bearing operates at no nominal radial load and rotation, choose gauge pressure ratio $P_{go} = 0.5$.

$$P_{go} = 0.5$$

$$= \frac{p_e - p_a}{p_o - p_a}$$

$\therefore$ Slot exit gauge pressure

$$p_e - p_a = 2.5 \text{ bar}$$

Slot factor

$$a^* = \frac{p_o^2 - p_e^2}{p_e - p_a^2} \cdot \frac{L_e}{L_b} \cdot \frac{L_b}{d_b}$$

$$= 0.528$$

$$= \frac{2\pi L_{sl} \cdot z_{go}^3}{z_s^3 \cdot w_s \cdot n_s}$$

In order that the slots would fit into around the internal bore of the bearing

$$w_s \cdot n_s \approx 0.75 \pi d_b$$

Take the number of slots $n_s = 12$,

$w_s = 4$ mm

If we set the slot thickness z_s to be equal to the bearing gap z_{go}, then the length of slot

$$L_{sl} = \frac{0.528 \times 4 \times 12}{2\pi}$$

$$= 4.03 \text{ mm}$$

The slot thickness was chosen according to shim materials available, which in this case was 25 μm. The bearing therefore had a diametrical clearance of 50 μm.

At zero eccentricity and for $P_{go} = 0.5$, the dimensionless bearing stiffness

$$K_b = 0.7$$

The actual bearing stiffness

$$k_b = \frac{K_b \times (p_o - p_a) \times L_b d_b}{z_{go}}$$

$$= 6.78 \text{ N } \mu\text{m}^{-1} \quad \text{per bearing}$$

Theory based on :

Rowe W.B.
Stout K.J.

Design of externally pressurised gas fed journal bearings employing slot restrictors
Tribology, 6(4), 1973, 140-144.

Appendix C Determination of the Permeability Coefficients of the Fine Layer of a 2-Layered Bearing Material

Applying the Forchheimer's equation for compressible flow to the coarse substrate gives:

$$\frac{p_1^2 - p_2^2}{2.p_{ref}} = \frac{z_p.\eta.(Q/A_p)}{\Phi_{vc}} + \frac{z_p.\rho.(Q/A_p)^2}{\Phi_{ic}} \quad (c.1)$$

and to the fine layer :

$$\frac{p_2^2 - p_3^2}{2.p_{ref}} = \frac{z_{pf}.\eta.(Q/A_p)}{\Phi_{vf}} + \frac{z_{pf}.\rho.(Q/A_p)^2}{\Phi_{if}} \quad (c.2)$$

with both the area and the flow rate through the two layers being the same.

Adding the two equations,

$$\frac{p_1^2 - p_3^2}{2.p_{ref}} = \eta.(Q/A_p).\left[\frac{z_p}{\Phi_{vc}} + \frac{z_{pf}}{\Phi_{vf}}\right] + \rho.(Q/A_p)^2.\left[\frac{z_p}{\Phi_{ic}} + \frac{z_{pf}}{\Phi_{if}}\right] \quad (c.3)$$

$$= \frac{z_{pf}.\eta.(Q/A_p)}{\Phi_{vt}} + \frac{z_{pf}.\rho.(Q/A_p)^2}{\Phi_{it}} \quad (c.4)$$

where Φ_{vt} and Φ_{it} are coefficients as measured from the 2 layers combined.

Measuring the two combined coefficients again at a reduced fine layer thickness z_{pf1} gives:

$$\frac{p_1^2 - p_3^2}{2.p_{ref}} = \eta.(Q_1/A_p).\left[\frac{z_p}{\Phi_{vc}} + \frac{z_{pf1}}{\Phi_{vf}}\right] + \rho.(Q_1/A_p)^2.\left[\frac{z_p}{\Phi_{ic}} + \frac{z_{pf1}}{\Phi_{if}}\right] \quad (c.5)$$

$$= \frac{z_{pf1}.\eta.(Q_1/A_p)}{\Phi_{vt1}} + \frac{z_{pf1}.\rho.(Q_1/A_p)^2}{\Phi_{it1}} \quad (c.6)$$

Simplifying,

$$\frac{z_{pf}}{\Phi_{vt}} = \frac{z_p}{\Phi_{vc}} + \frac{z_{pf}}{\Phi_{vf}} \qquad (c.7)$$

$$\frac{z_{pf}}{\Phi_{it}} = \frac{z_p}{\Phi_{ic}} + \frac{z_{pf}}{\Phi_{if}} \qquad (c.8)$$

$$\frac{z_{pf1}}{\Phi_{vt1}} = \frac{z_p}{\Phi_{vc}} + \frac{z_{pf1}}{\Phi_{vf}} \qquad (c.9)$$

$$\frac{z_{pf1}}{\Phi_{it1}} = \frac{z_p}{\Phi_{ic}} + \frac{z_{pf1}}{\Phi_{if}} \qquad (c.10)$$

(c.7) - (c.9) gives :

$$\frac{z_{pf} - z_{pf1}}{\Phi_{vf}} = \frac{z_{pf}}{\Phi_{vt}} - \frac{z_{pf1}}{\Phi_{vt1}} \qquad (c.11)$$

and from (c.8) - (c.10) :

$$\frac{z_{pf} - z_{pf1}}{\Phi_{if}} = \frac{z_{pf}}{\Phi_{it}} - \frac{z_{pf1}}{\Phi_{it1}} \qquad (c.11)$$

Knowing the two thicknesses of the fine layer, its permeability coefficients could be determined without relying on any information about the coarse substrate.

Appendix D Determination of the Equivalent Permeability Coefficient from Forchheimer's Equation using Pressure Data only

Forchheimer's equation for compressible flow

$$\frac{p_1^2 - p_2^2}{2.p_{ref}} = \frac{z_p.\eta.(Q/A_p)}{\Phi_v} + \frac{z_p.\rho.(Q/A_p)^2}{\Phi_i}$$

$$= \frac{z_p.\eta.(Q/A_p)}{\Phi_e}$$

$$\therefore \quad \frac{1}{\Phi_e} = \frac{1}{\Phi_v} + \frac{\rho.Q}{\eta.A_p}.\frac{1}{\Phi_i}$$

Substituting for Q/A_p,

$$\frac{Q}{A_p} = \frac{p_1^2 - p_2^2}{2.p_{ref}} \cdot \frac{\Phi_e}{z_p.\eta}$$

$$\frac{1}{\Phi_e} = \frac{1}{\Phi_v} + \frac{\rho}{z_p.\eta^2} \cdot \frac{p_1^2 - p_2^2}{2.p_{ref}} \cdot \frac{\Phi_e}{\Phi_i}$$

$$\frac{1}{\Phi_v} = \frac{1}{\Phi_e} - \frac{\rho}{z_p.\eta^2} \cdot \frac{p_1^2 - p_2^2}{2.p_{ref}} \cdot \frac{\Phi_e}{\Phi_i}$$

$$= \frac{1}{\Phi_e.\Phi_i} \times \left[\Phi_i - \frac{\rho}{z_p.\eta^2} \cdot \frac{p_1^2 - p_2^2}{2.p_{ref}} . \Phi_e^2 \right]$$

$$\frac{\rho}{z_p.\eta^2} \cdot \frac{p_1^2 - p_2^2}{2.p_{ref}} . \Phi_e^2 + \frac{\Phi_i}{\Phi_v} . \Phi_e - \Phi_i = 0$$

or $$\Phi_e = \frac{-\frac{\Phi_i}{\Phi_v} + \left\{ \frac{\Phi_i^2}{\Phi_v^2} + 4.\frac{\rho}{z_p.\eta^2} . \frac{p_1^2 - p_2^2}{2.p_{ref}} . \Phi_i \right\}^{1/2}}{2.\frac{\rho}{z_p.\eta^2} . \frac{p_1^2 - p_2^2}{2.p_{ref}}}$$

Appendix E Sedigraph Measurement Records for Powder Size Distribution

1) 0.5 μm α - Alumina

SEDI
SediGraph 5100 V2.02

SAMPLE DIRECTORY/NUMBER: DATA2 /78 UNIT NUMBER: 1 SAMPLE ID: Alpha Alumina 0.5um
LIQUID TYPE: Water START 11:50:16 05/13/95 SAMPLE DENS: 3.9500 g/cc TEMP: 29.3 deg C

CUMULATIVE MASS PERCENT COARSER VS. DIAMETER

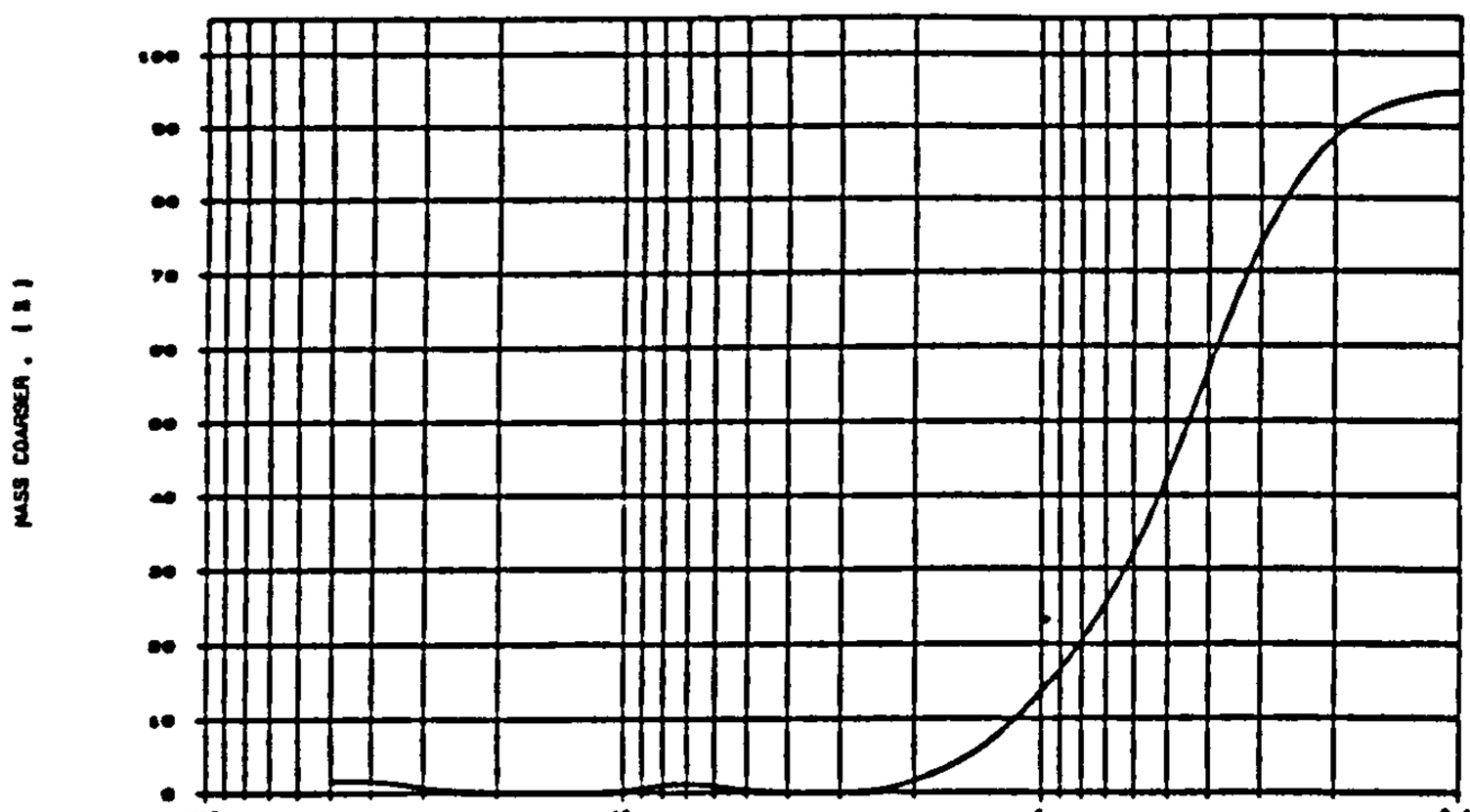

SEDI
SediGraph 5100 V2.02

SAMPLE DIRECTORY/NUMBER: DATA2 /78 UNIT NUMBER: 1 SAMPLE ID: Alpha Alumina 0.5um
LIQUID TYPE: Water START 11:50:16 05/13/95 SAMPLE DENS: 3.9500 g/cc TEMP: 29.3 deg C

MASS POPULATION VS. DIAMETER

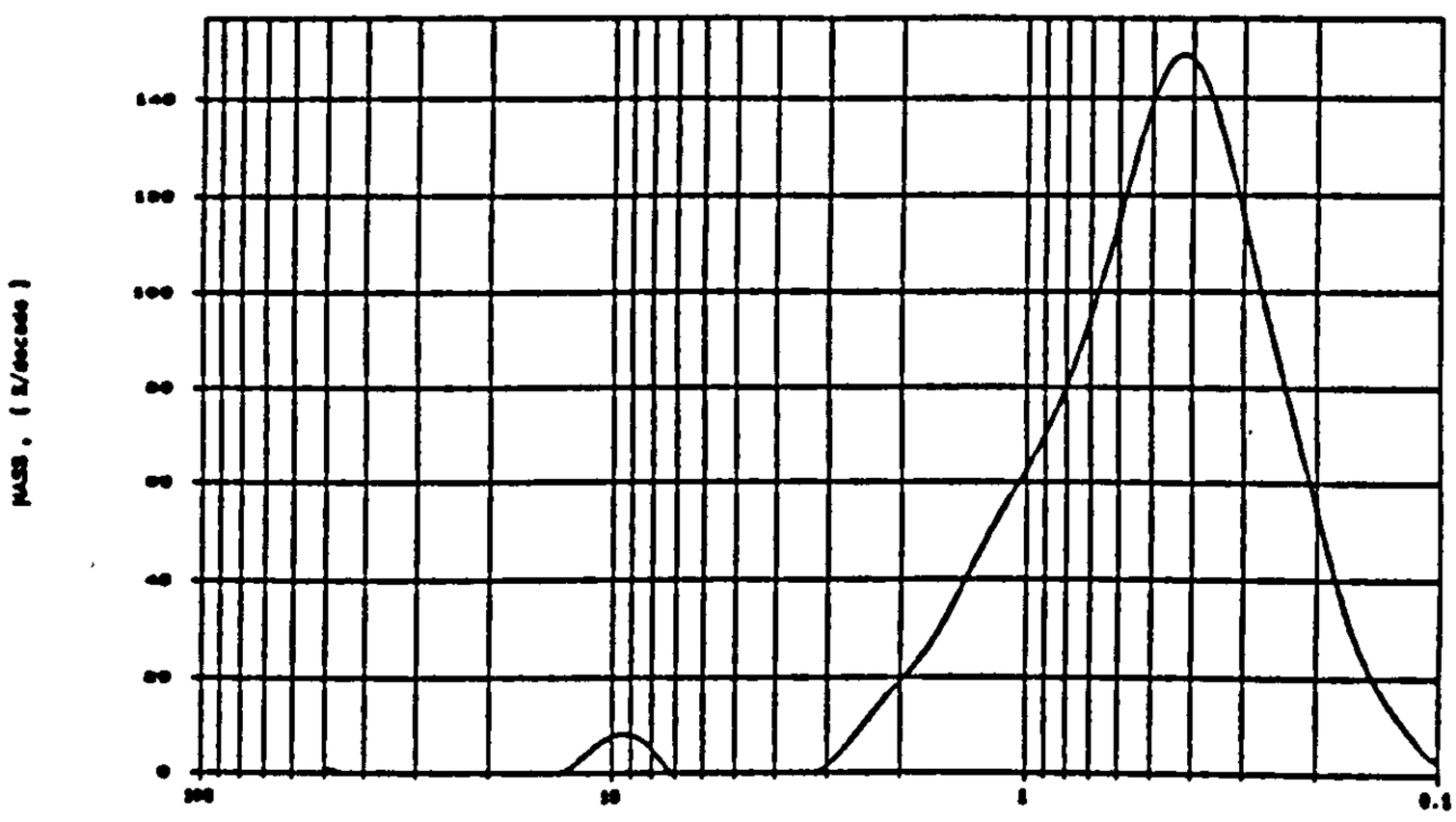

2) 7 μm α - Alumina

SEDI
SediGraph 5100 V2.02

SAMPLE DIRECTORY/NUMBER: DATA2 /77 | UNIT NUMBER: 1 | SAMPLE ID: Alpha Alumina 7 um
LIQUID TYPE: Water | START ID: 4R 38 05/13/98 | SAMPLE DENS: 3.8500 g/cc | TEMP: 28.8 deg C

CUMULATIVE MASS PERCENT COARSER VS. DIAMETER

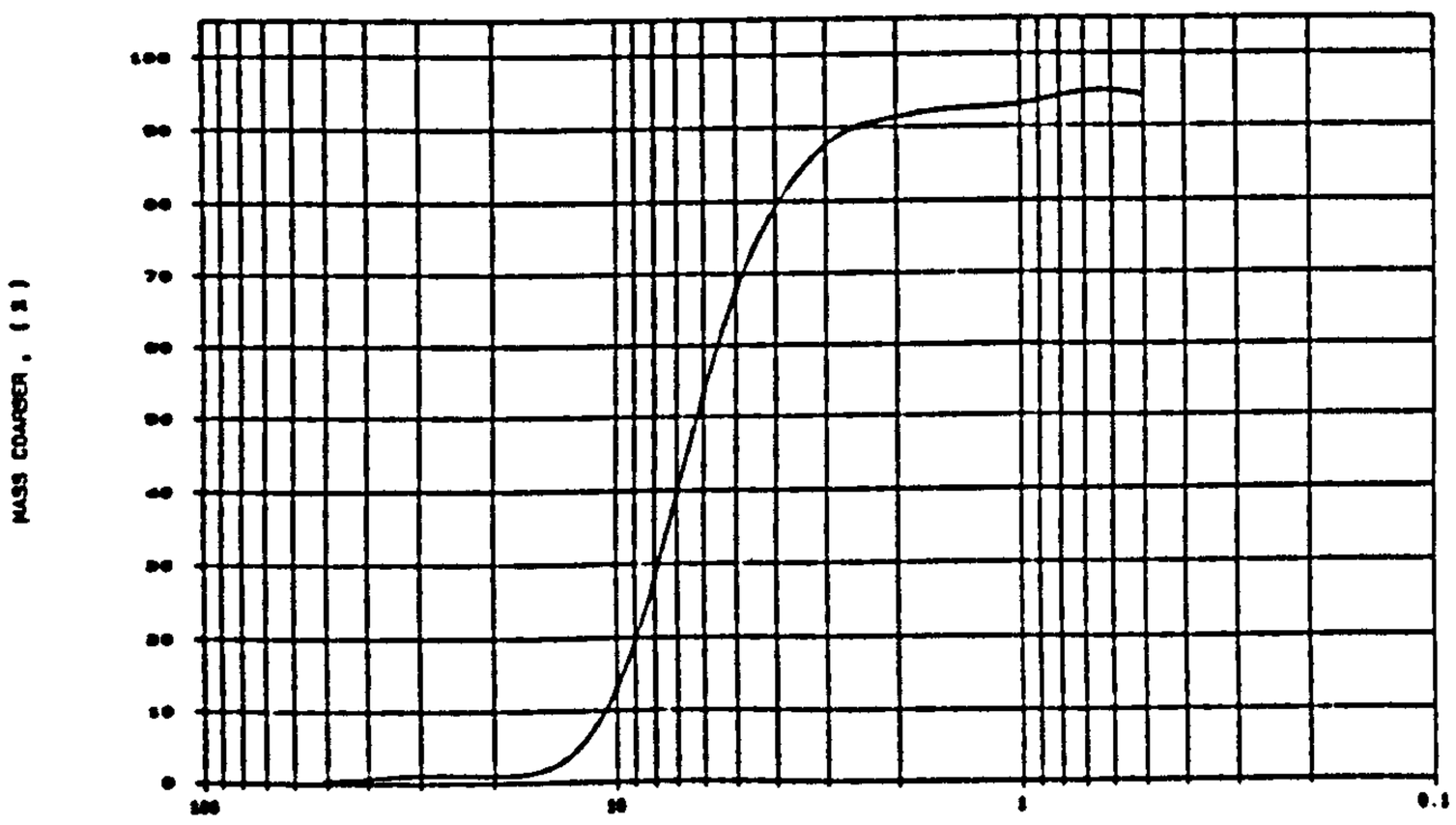

EQUIVALENT SPHERICAL DIAMETER, (μm)

SEDI
SediGraph 5100 V2.02

SAMPLE DIRECTORY/NUMBER: DATA2 /77 | UNIT NUMBER: 1 | SAMPLE ID: Alpha Alumina 7 um
LIQUID TYPE: Water | START ID: 4R 38 05/13/98 | SAMPLE DENS: 3.8500 g/cc | TEMP: 28.8 deg C

MASS POPULATION VS. DIAMETER

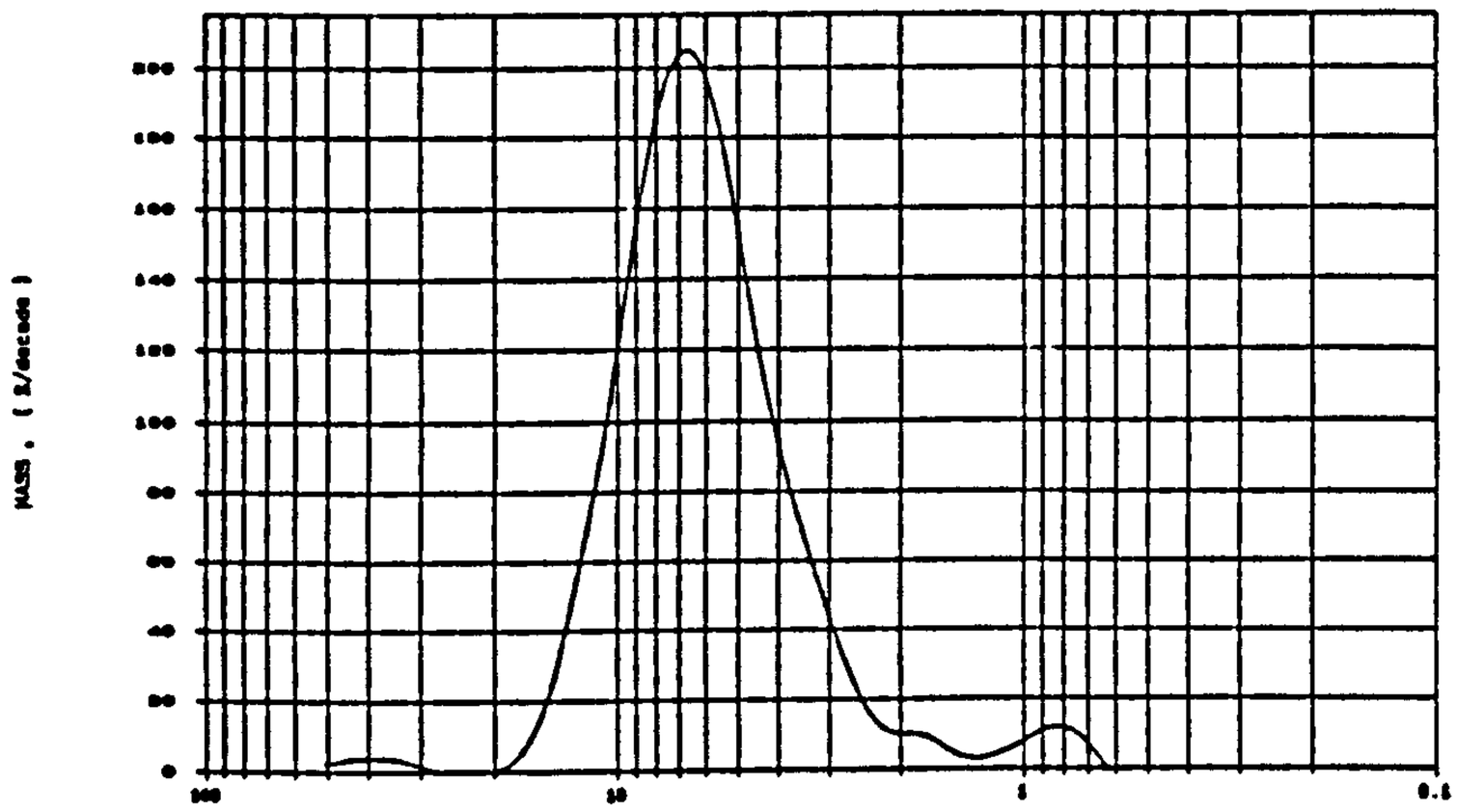

EQUIVALENT SPHERICAL DIAMETER, (μm)

3) 13 µm Fused Alumina

SEDI
SediGraph 5100 V2.02

SAMPLE DIRECTORY/NUMBER: DATA2 /78 | UNIT NUMBER: 1 | SAMPLE ID: Alpha Alumina 13 um
LIQUID TYPE: Water | START 11:30:38 05/13/98 | SAMPLE DENS: 3.7700 g/cc | TEMP: 28.0 deg C

CUMULATIVE MASS PERCENT COARSER VS. DIAMETER

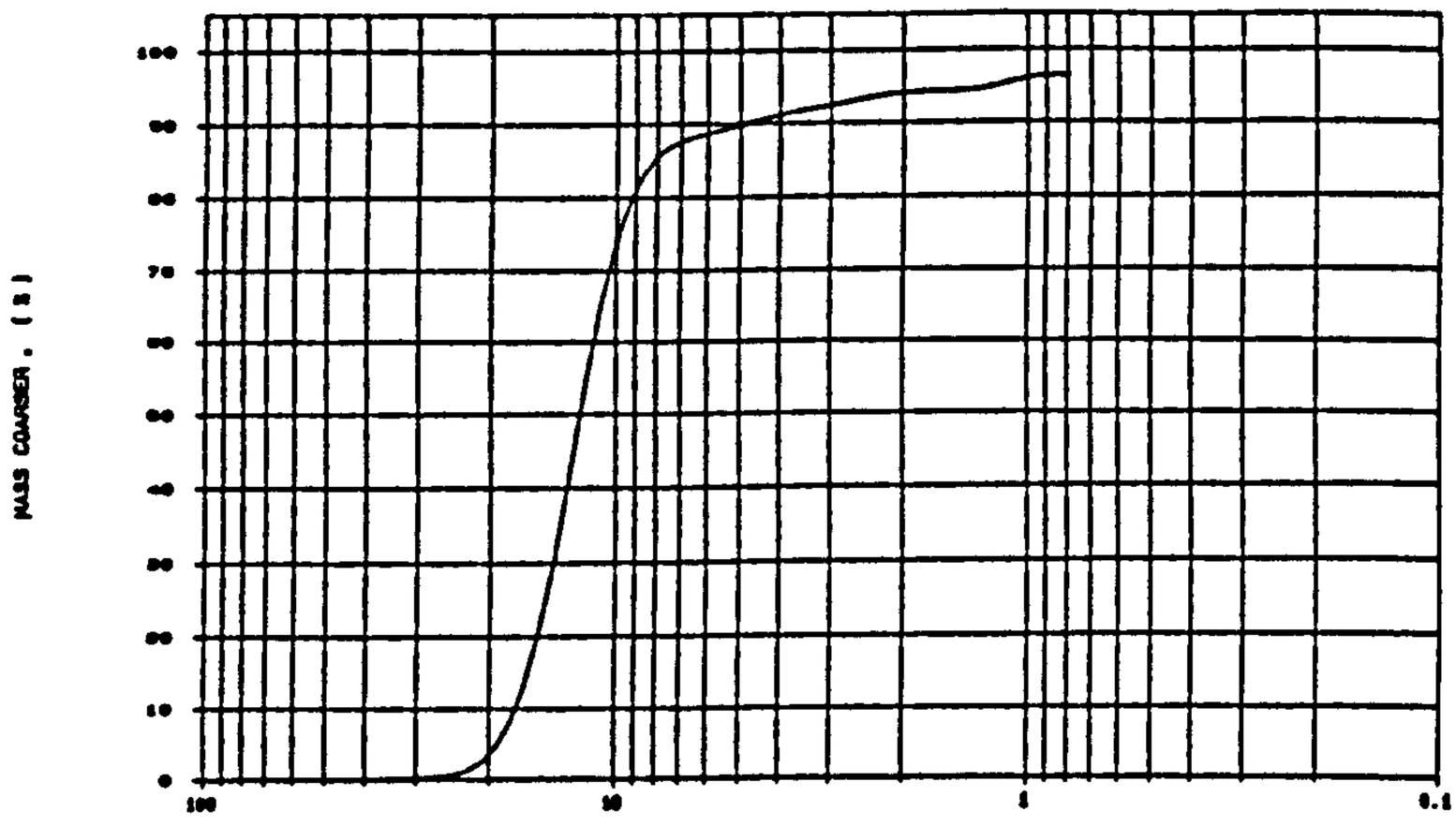

EQUIVALENT SPHERICAL DIAMETER, (µm)

SEDI
SediGraph 5100 V2.02

SAMPLE DIRECTORY/NUMBER: DATA2 /78 | UNIT NUMBER: 1 | SAMPLE ID: Alpha Alumina 13 um
LIQUID TYPE: Water | START 11:30:38 05/13/98 | SAMPLE DENS: 3.7700 g/cc | TEMP: 28.0 deg C

MASS POPULATION VS. DIAMETER

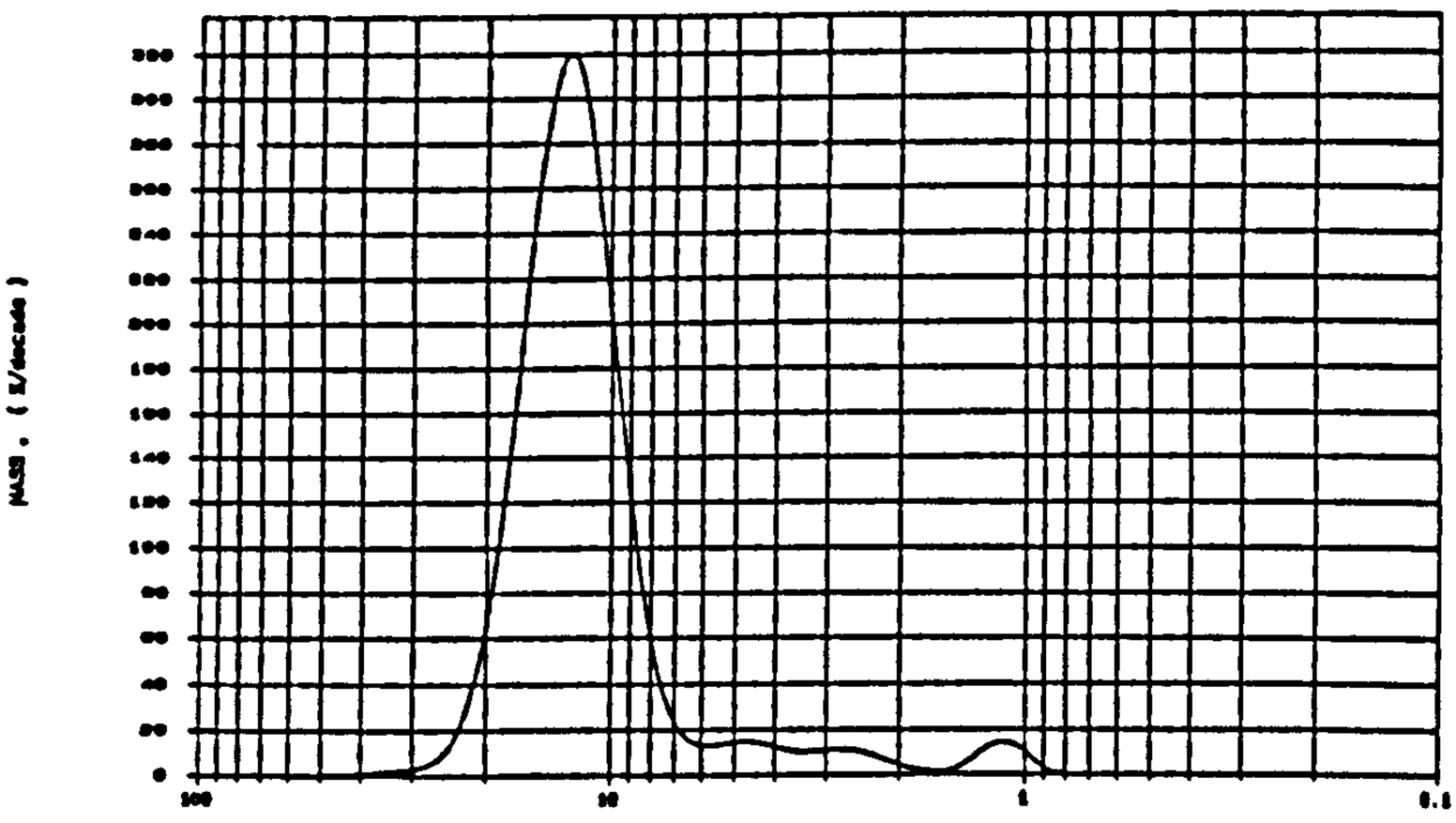

EQUIVALENT SPHERICAL DIAMETER, (µm)

4) 23 µm Fused Alumina

Alumina A
SediGraph 5100 V2.02

SAMPLE DIRECTORY/NUMBER: DATA2 /8
LIQUID TYPE: Water
UNIT NUMBER: 1
START 08:12:30 05/08/98
SAMPLE ID: 23u 0 hr Alumina A
SAMPLE DENS: 3.7700 g/cc
TEMP: 30.7 deg C

CUMULATIVE MASS PERCENT COARSER VS. DIAMETER

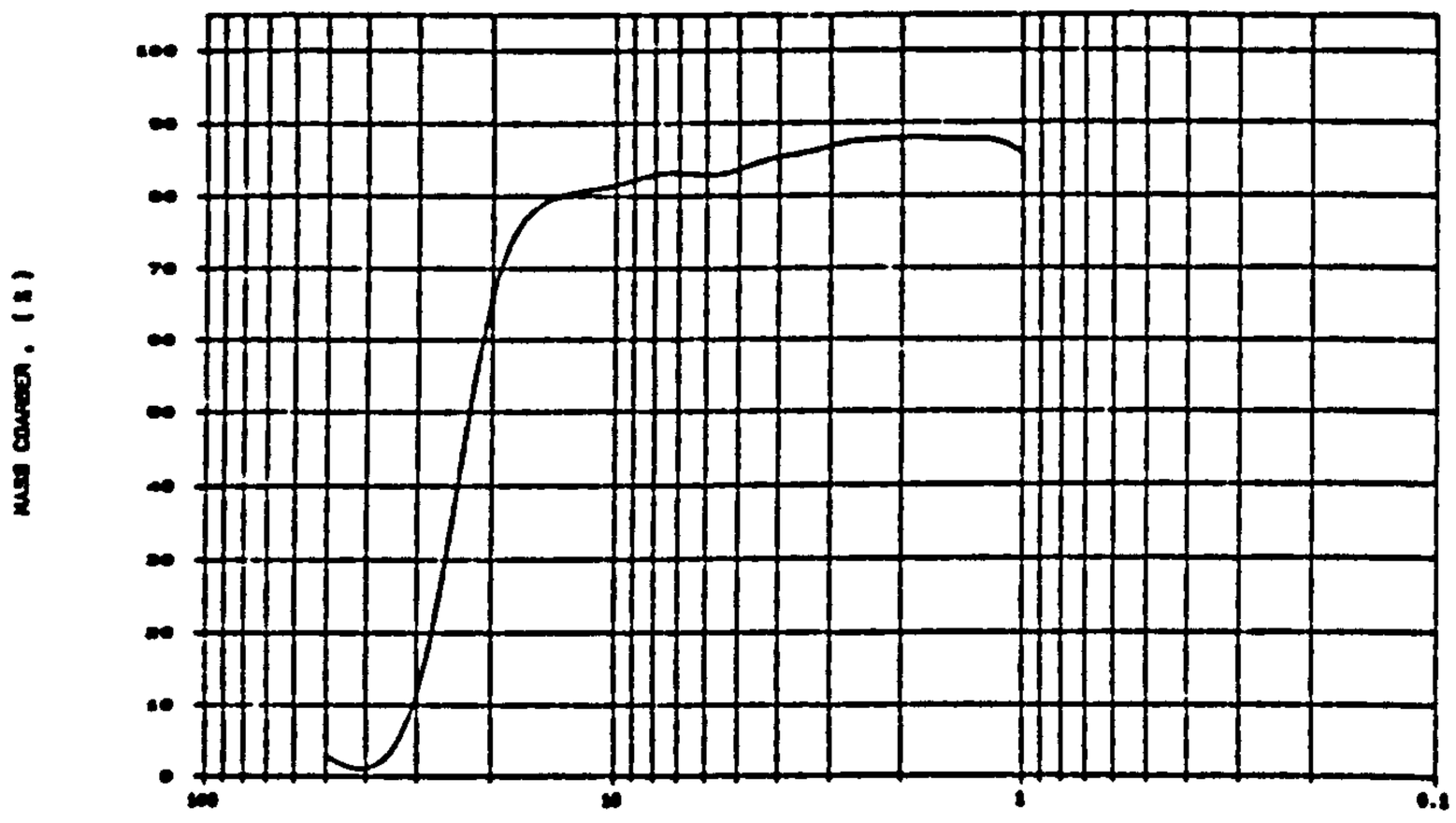

EQUIVALENT SPHERICAL DIAMETER, (µm)

Alumina A
SediGraph 5100 V2.02

SAMPLE DIRECTORY/NUMBER: DATA2 /8
LIQUID TYPE: Water
UNIT NUMBER: 1
START 08:12:30 05/08/98
SAMPLE ID: 23u 0 hr Alumina A
SAMPLE DENS: 3.7700 g/cc
TEMP: 30.7 deg C

MASS POPULATION VS. DIAMETER

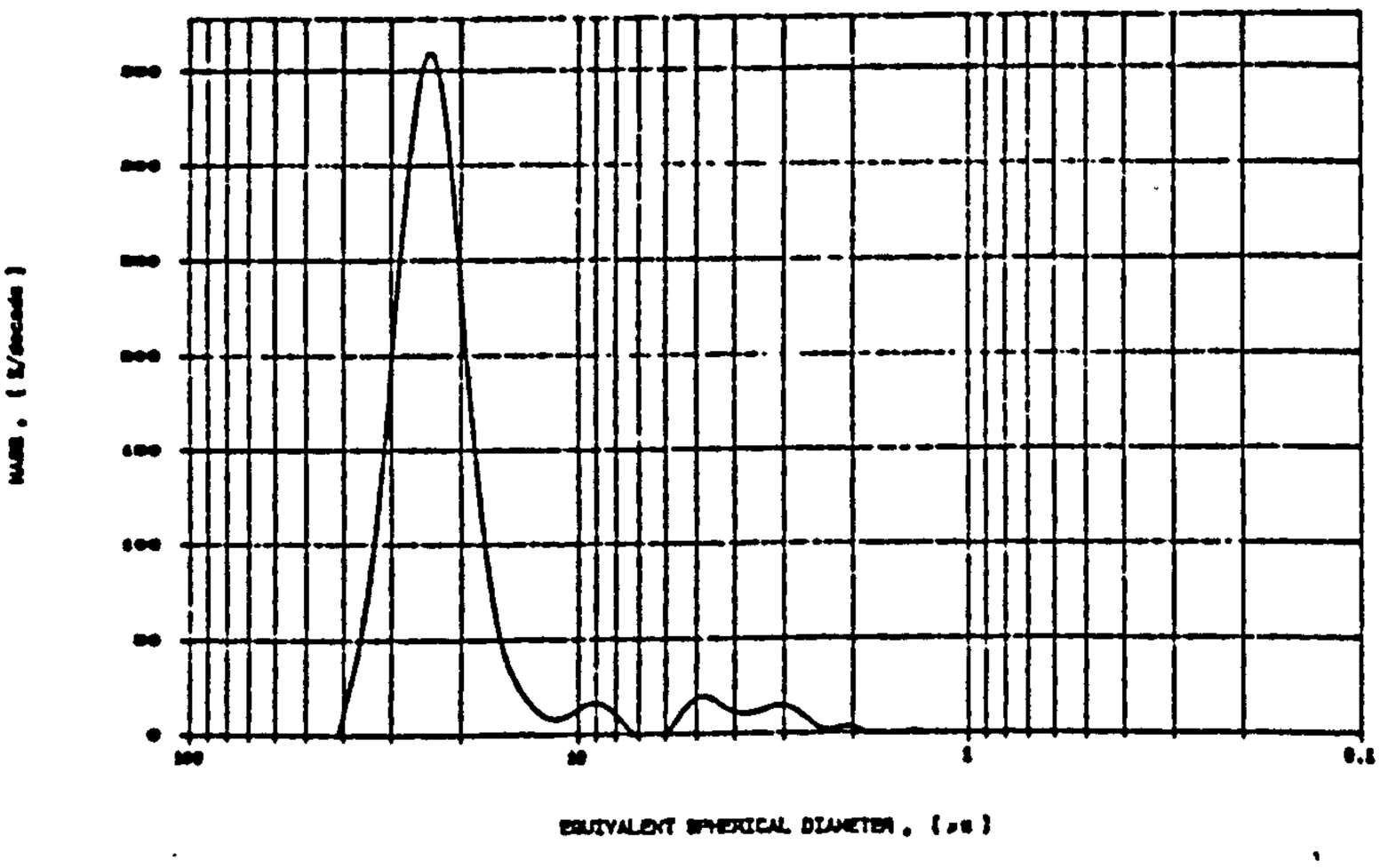

EQUIVALENT SPHERICAL DIAMETER, (µm)

5) 42 µm Fused Alumina

ALUMINA A
SediGraph 5100 V2.02

SAMPLE DIRECTORY/NUMBER: DATA8 /18 | UNIT NUMBER: 1 | SAMPLE ID: ALUMINA A UNIT 5100
LIQUID TYPE: Water | START 12:30:38 05/08/98 | SAMPLE DENS: 3.7700 g/cc | TEMP: 30.0 deg C

CUMULATIVE MASS PERCENT COARSER VS. DIAMETER

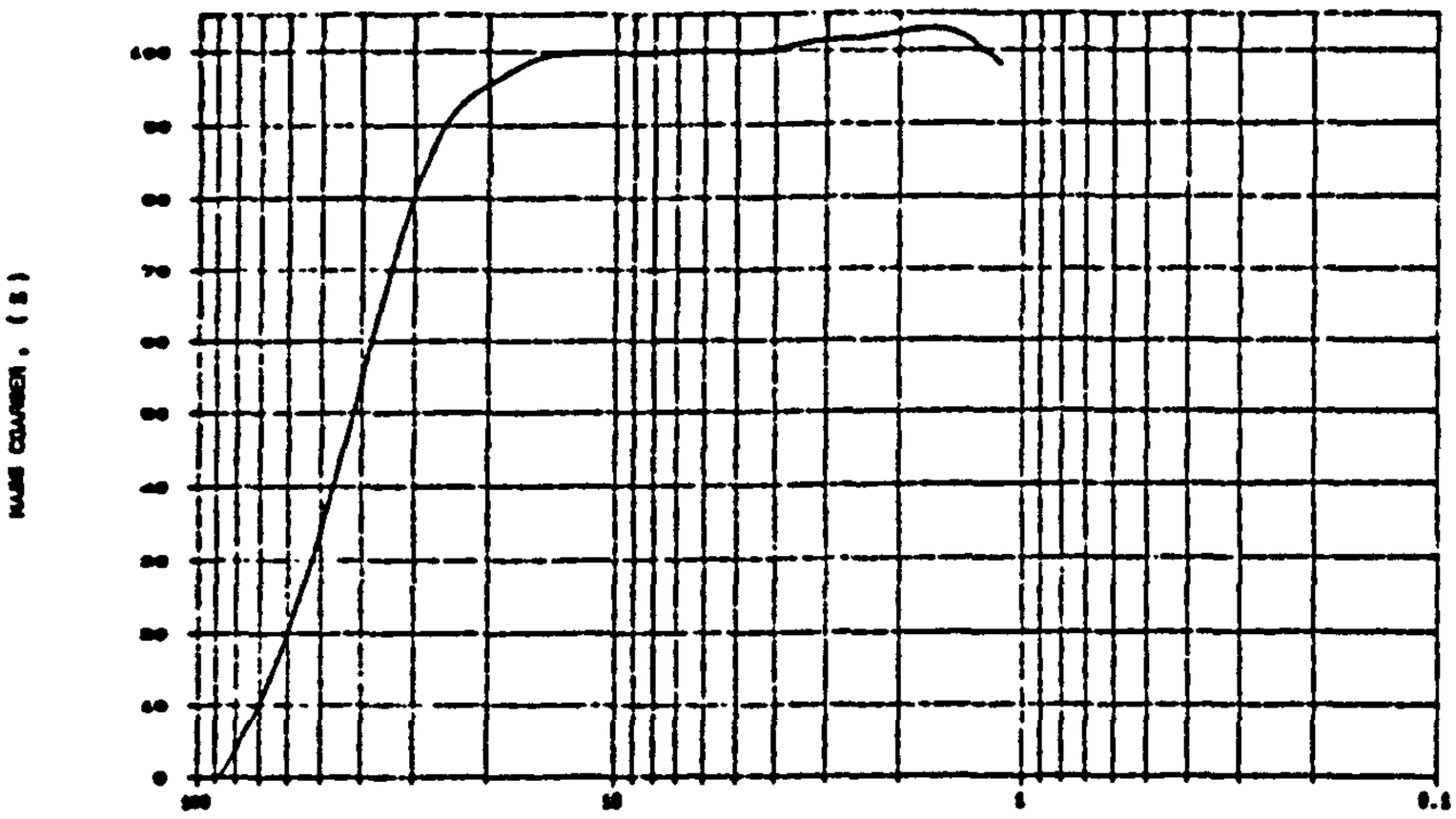

EQUIVALENT SPHERICAL DIAMETER, (µm)

ALUMINA A
SediGraph 5100 V2.02

SAMPLE DIRECTORY/NUMBER: DATA8 /18 | UNIT NUMBER: 1 | SAMPLE ID: ALUMINA A UNIT 5100
LIQUID TYPE: Water | START 12:30:38 05/08/98 | SAMPLE DENS: 3.7700 g/cc | TEMP: 30.0 deg C

MASS POPULATION VS. DIAMETER

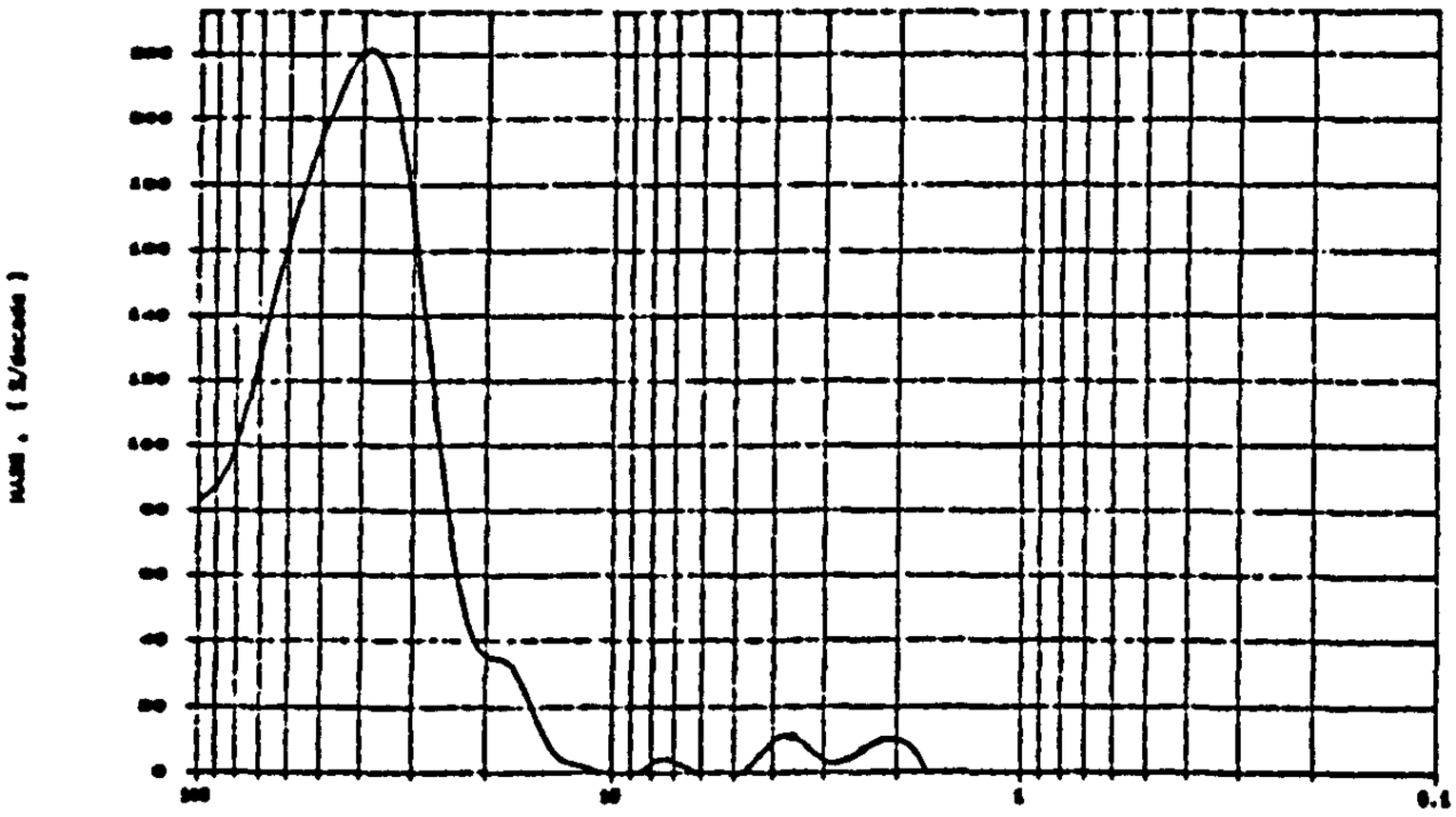

EQUIVALENT SPHERICAL DIAMETER, (µm)

Appendix F Calibration Curves for Pressure and Flow Sensors

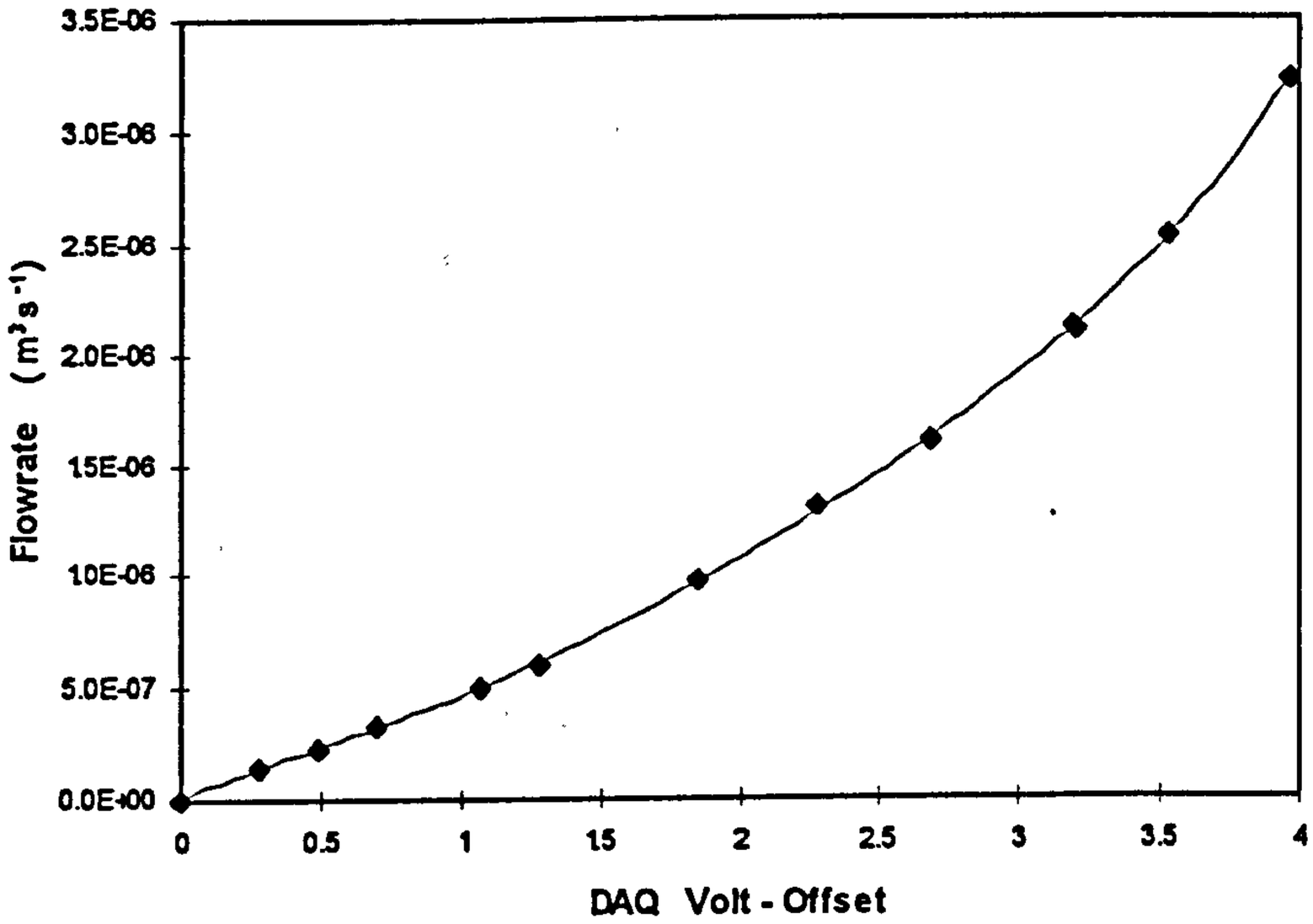

0.2 lit / min Flow Sensor Calibration

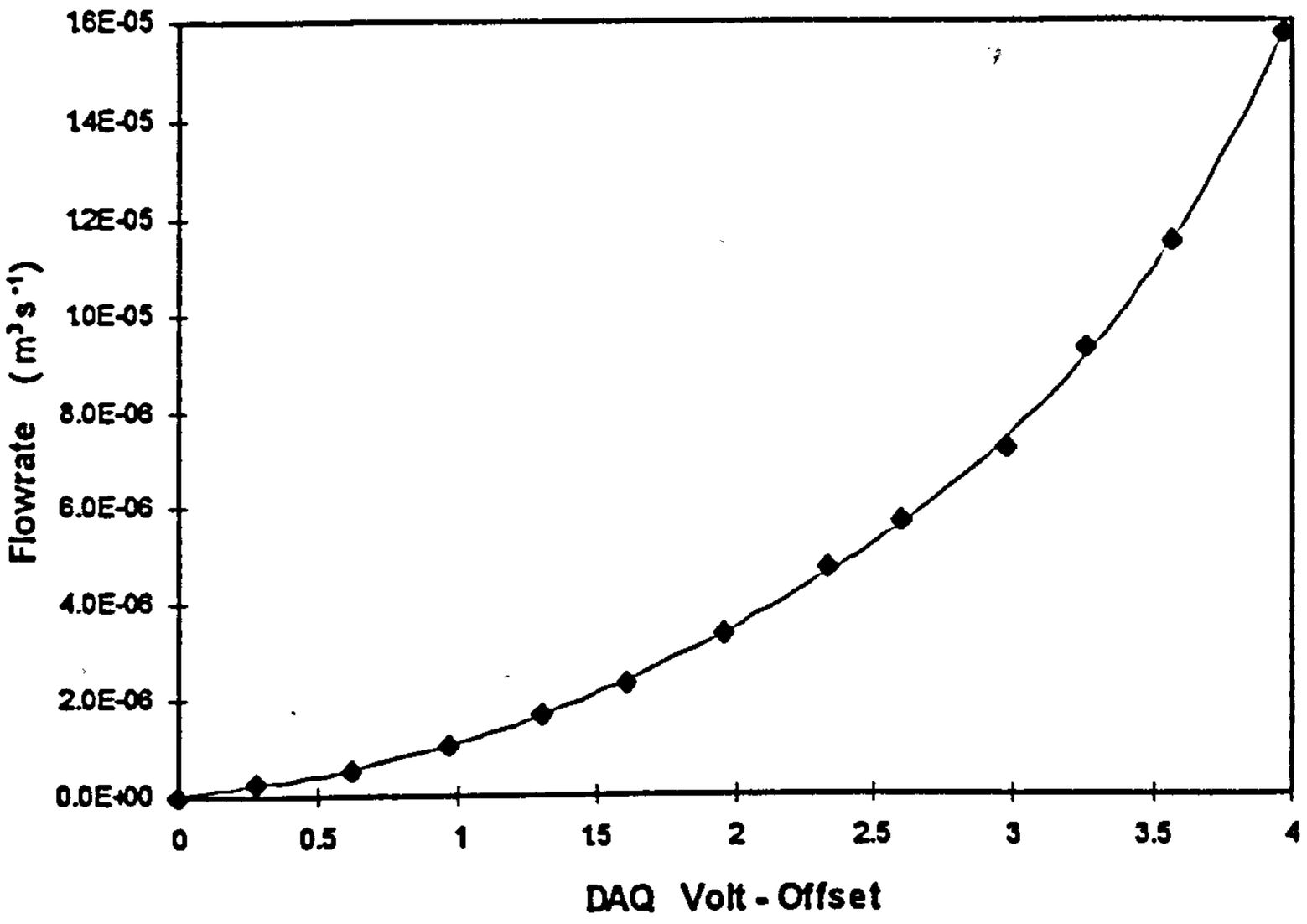

1 lit / min Flow Sensor Calibration

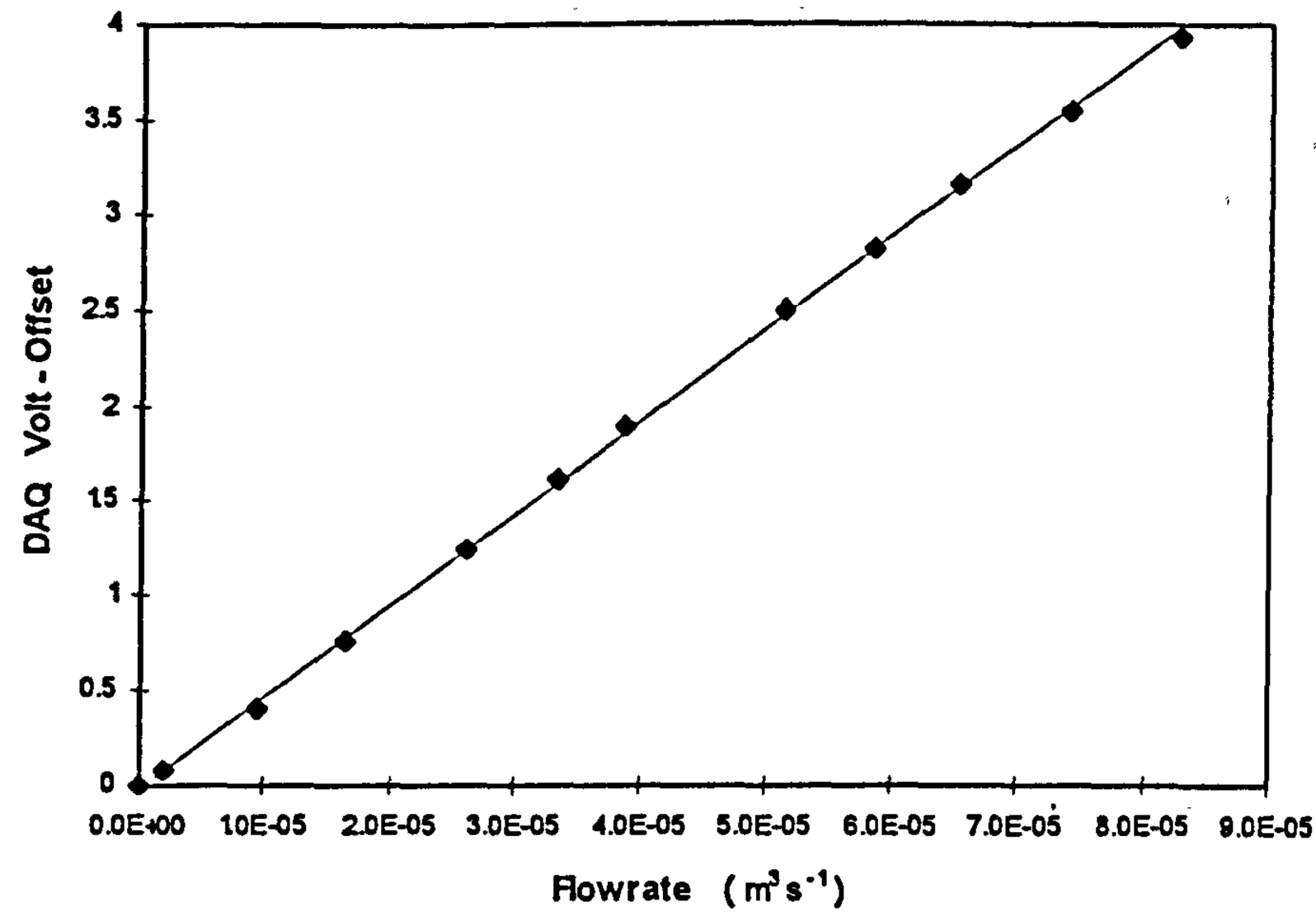

5 lit / min Flow Sensor Calibration

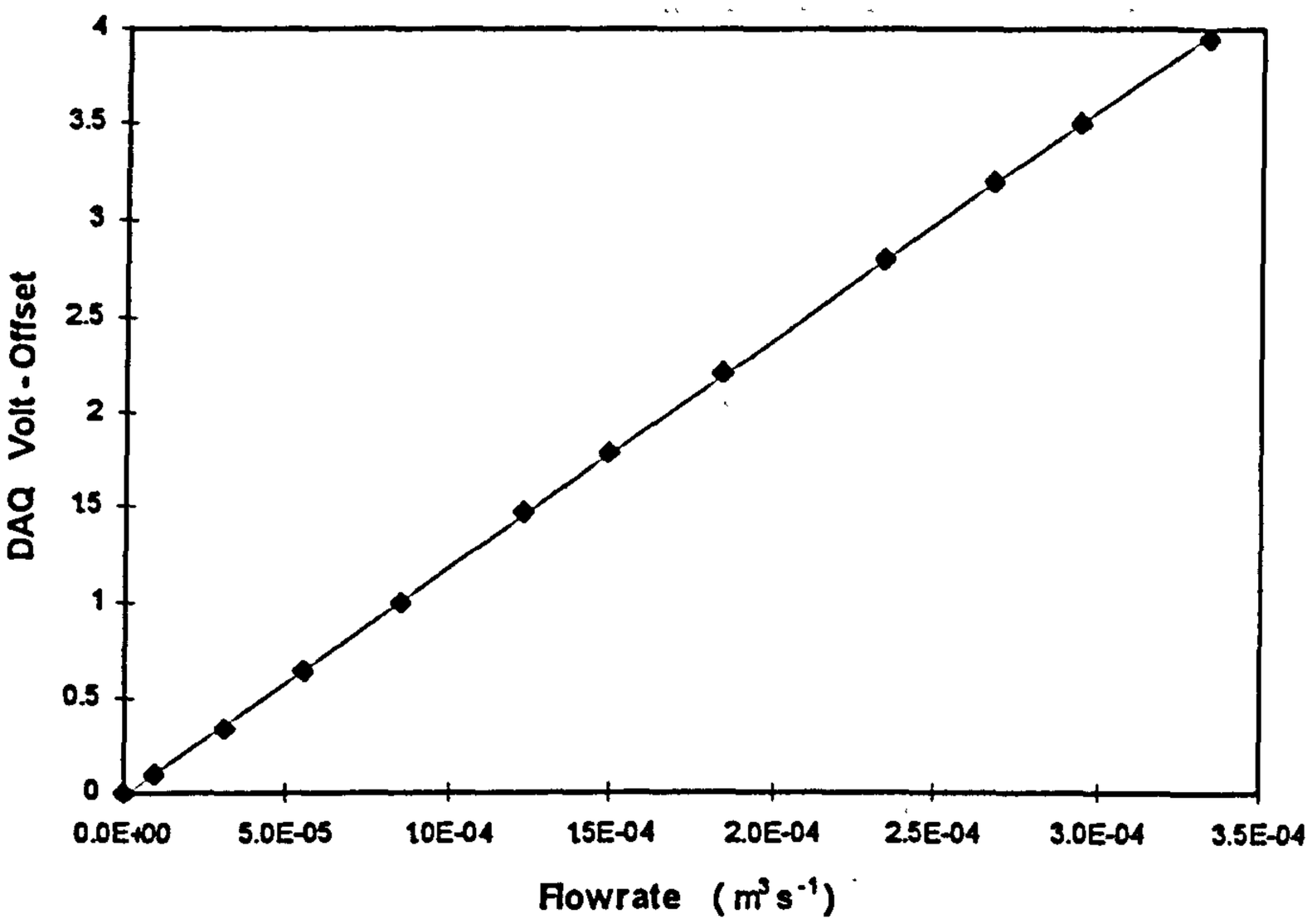

20 lit / min Flow Sensor Calibration

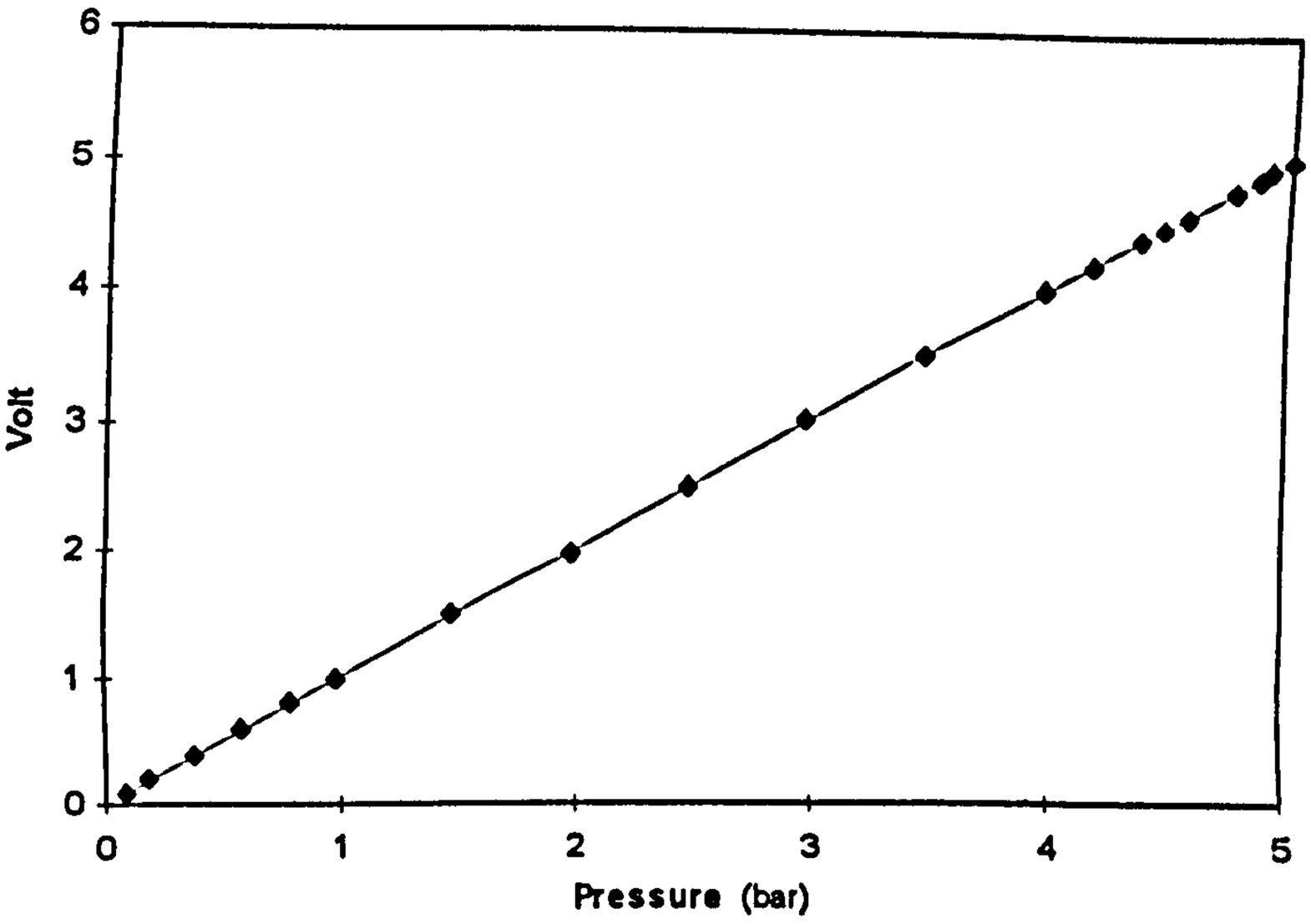

5 bar Pressure Sensor Calibration

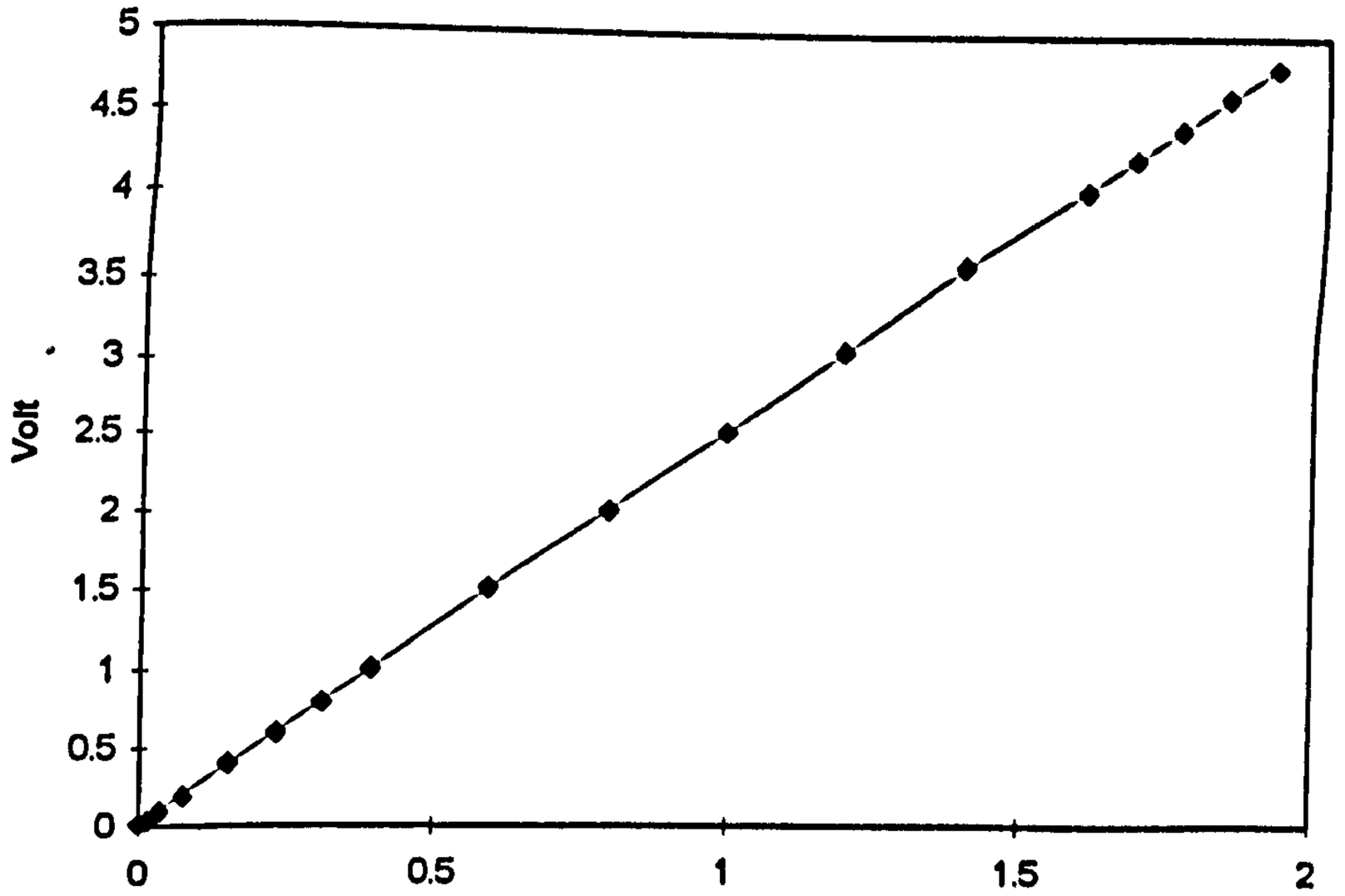

2 bar Pressure Sensor Calibration

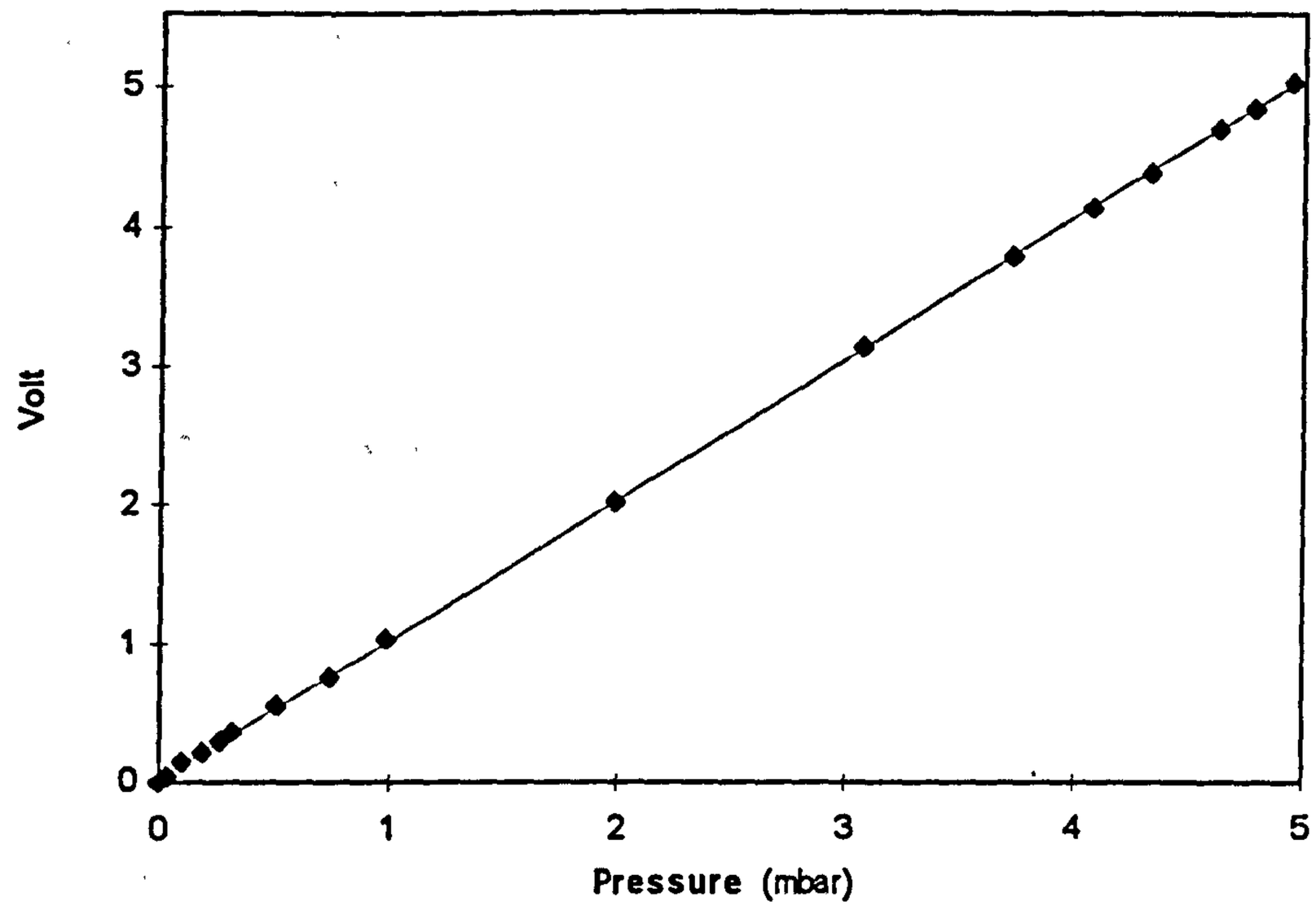

5 mbar Pressure Sensor Calibration

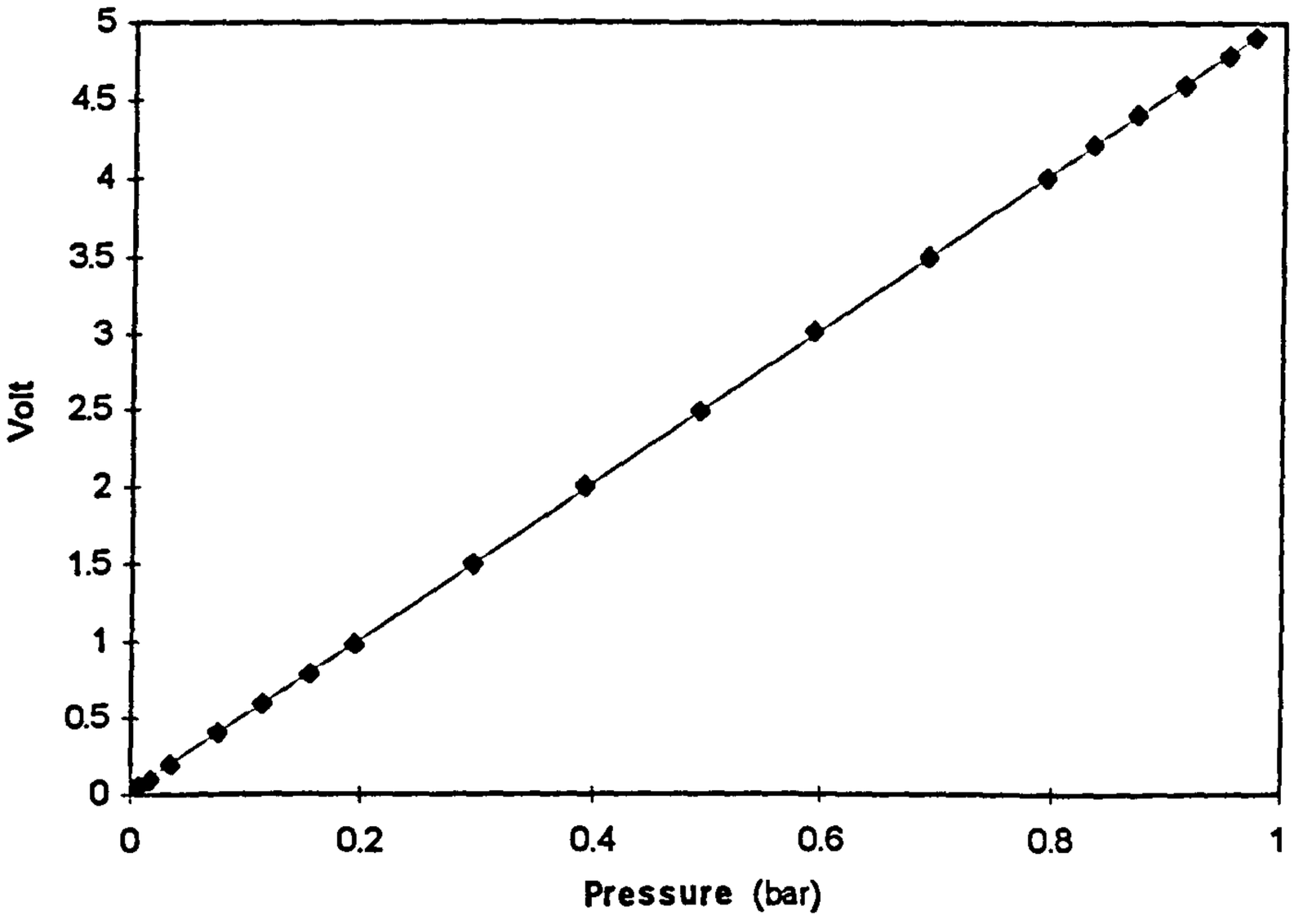

1 bar Pressure Sensor Calibration

Appendix G Labwindows Programs for Permeability Measurement, Dynamic Water Expulsion Test, and Slip Coefficient Measurement

1) Permeability Measurement

```
Labwindows Program for Permeability Measurement
per ISO 4022 : 1987

Version 1.0
Y.B.P.KWAN  20.04.96

ret% = OpenInterrfaceManager%
ph% = LoadPanel% ("permea.uir",PP1)
ret% = DisplayPanel% (ph%)

ret% = AI.Configure% (board%,-1,1,10,1,0)
ret% = AO.Configure% (board%,0,1,0,10,0)
ret% = AO.Configure% (board%,1,1,0,10,0)
ret% = SetInputMode% (ph%,PP1.END,1)
WHILE  end.app% = 0
      CALL Checkkey

      vcurr# = 0.0
      er% = AO.VWrite (board,0,vcurr#)

      ret% = SetInputMode% (ph%,PP1.OK,1)
      ret% = SetInputMode% (ph%,PP1.END,1)
      ret% = SetInputMode% (ph%,PP1.STORE,0)

      CALL ClearIA (chlist%(),channum-1)

      nch% = 1
      npts% = 200
      samplr# = 400.0
      scanr# = 0.0
      scount& = CLNG(nch% * npts%)

      status% = 0
      chlist%(0) = 5

      WHILE status%=0 AND end.app%=0
            er% = SCAN.Op%(board,nch%,chlist%(),gnlist%(),scanbuf%(),scount&,samplr#,
                  scanr#)
            er% = DAQ.VScale%(board,5,gnlist%(5),aigain#(5),aioffset#(5),CLNG(npts%),
                  scanbuf%(),mch5buf#())

            CALL Mean (mch5buf#(),npts%,chmean#(5))
```

```
IF  chmean#(5)<5.5# THEN
        ret% = SetCtrlVal% (ph%,PP1.USERPROMPT,"Supply Pressure Low")
        beep
ENDIF

IF  chmean#(5)>7.0# THEN
        ret% = SetCtrlVal% (ph%,PP1.USERPROMPT,"Supply Pressure High !")
        beep
ENDIF

        IF  chmean#(5)>=5.5# AND chmean#(5)<=7.0# THEN
            ret% = Fmt (temp$,"%s< P^supply = %f[w4p1] Bar",chmean#(5))
            ret% = SetCtrlVal (ph%,PP1.USERPROMPT,temp$)
            CALL Delay (1.5)
            status%=1
        ENDIF

        CALL Checkkey   'for END
WEND
ret% = SetCtrlVal% (ph%,PP1.USERPROMPT," ")

CALL ClearIA (chlist%(),channum-1)

nch% = 1
npts% = 200
samplr# = 400.0
scanr# = 0.0
scount& = CLNG(nch% * npts%)

status% = 0
chlist%(0) = 3

er% = SCAN.Op% (board,nch%,chlist%(),gnlist%(),scanbuf%(),scount&,samplr#,scanr#)
IF er%<>0 THEN
        CALL Error.r("SCAN.Op",er%)
ENDIF

i% = 0
opbin# = 0
WHILE i%<npts%
        opbin# = opbin# + CDBL(scanbuf%(i%))
        i% = i%+1
WEND
opbin# = opbin#/CDBL(npts%)

IF opbin#>1.05*aioffset(3) OR opbin#<0.95*aioffset(3) THEN
        ret% = SetCtrlVal% (ph%,PP1.USERPROMPT,"Ch.3 Zero Dev. > 5%")
        beep
        CALL Delay (3.0)
        ret% = SetInputMode% (ph%,PP1.OK,1)
        ret% = SetCtrlVal% (ph%,PP1.USERPROMPT,"Press OK to update !")
        WHILE   ok.app%=0 AND end.app%=0
                CALL Checkkey
        WEND

ELSE
```

```
        IF end.app%=0 THEN
            ret% = SetCtrlVal% (ph%,PP1.USERPROMPT,"Ch.3 chk'd Press OK")
            beep
        ENDIF
ENDIF

status% = 0
ok.app% = 0

WHILE   status%=0 AND end.app%=0
        CALL Checkkey

        IF ok.app%=1 THEN
            aioffset(3) = opbin#
            status% = 1
            ret% = SetCtrlVal% (ph%,PP1.USERPROMPT," ")
            ok.app% = 0
        ENDIF
WEND
ret% = SetInputMode% (ph%,PP1.OK,0)

ret% = SetCtrlVal (ph%,PP1.USERPROMPT,"Close Ball Valve & Wait !")
CALL Delay (60.0)
ok.app% = 0
CALL ClearIA (chlist%(),channum-1)

nch% = 1
npts% = 200
samplr# = 400.0
scanr# = 0.0
scount& = CLNG(nch% * npts%)

status% = 0
chlist%(0) = 12

er% = SCAN.Op% (board,nch%,chlist%(),gnlist%(),scanbuf%(),scount&,samplr#,scanr#)

i% = 0
opbin# = 0
WHILE i%<npts%
        opbin# = opbin# + CDBL(scanbuf%(i%))
        i% = i%+1
WEND
opbin# = opbin#/CDBL(npts%)

IF opbin#>1.05*aioffset#(12) OR opbin#<0.95*aioffset#(12) THEN
        ret% = SetCtrlVal% (ph%,PP1.USERPROMPT,"Ch.12 Zero Dev. > 5%")
        beep
        CALL Delay (3.0)
        ret% = SetInputMode% (ph%,PP1.OK,1)
        ret% = SetCtrlVal% (ph%,PP1.USERPROMPT,"Press OK to update !")
        WHILE   ok.app%=0 AND end.app%=0
            CALL Checkkey
        WEND

ELSE
```

```
        IF end.app%=0 THEN
            ret% = SetInputMode% (ph%,PP1.OK,1)
            ret% = SetCtrlVal% (ph%,PP1.USERPROMPT,"Open Ball Valve & Press OK")
            beep
            CALL Delay (2.0)
        END IF
END IF

status% = 0
ok.app% = 0

WHILE   status%=0 AND end.app%=0
        CALL Checkkey

        IF ok.app%=1 THEN
            aioffset#(12) = opbin#
            status% = 1
            ret% = SetCtrlVal% (ph%,PP1.USERPROMPT," ")
            ok.app% = 0
        END IF
WEND

status% = 0
ret% = SetInputMode% (ph%,PP1.END,0)
ret% = SetCtrlVal% (ph%,PP1.USERPROMPT,"Enter Min Pressure")
beep
ret% = SetActiveCtrl% (PP1.PMIN)
j% = 0
WHILE j%=0 AND end.app%=0
        IF GetUserEvent% (0,pan%,ctrl%)<>0 THEN
            IF ctrl% = PP1.PMIN THEN
                ret% = GetCtrlVal% (ph%,PP1.PMIN,pmin#)
                j% = 1
            ENDIF
        ENDIF
WEND

vmin# = 2.0 * (pmin#-0.005)

ret% = SetCtrlVal% (ph%,PP1.USERPROMPT,"Enter Max Pressure")
beep
ret% = SetActiveCtrl% (PP1.PMAX)
j% = 0
WHILE j%=0 AND end.app%=0
        IF GetUserEvent% (0,pan%,ctrl%)<>0 THEN
            IF ctrl% = PP1.PMAX THEN
                ret% = GetCtrlVal% (ph%,PP1.PMAX,pmax#)
                j% = 1
            ENDIF
        ENDIF
WEND

vmax# = 2.0 * (pmax#-0.005)

ret% = SetCtrlVal% (ph%,PP1.USERPROMPT,"Enter No of Increments")
beep
```

```
ret% = SetActiveCtrl% (PP1.NMEA)
j% = 0
WHILE j%=0 AND end.app%=0
      IF GetUserEvent% (0,pan%,ctrl%)<>0 THEN
            IF ctrl% = PP1.NMEA THEN
                  ret% = GetCtrlVal% (ph%,PP1.NMEA,n%)
                  j% = 1
            ENDIF
      ENDIF
WEND

vinc# = 2.0 * ((pmax#-pmin#)/CDBL(n%))
ret% = SetInputMode% (ph%,PP1.END,1)

ret% = SetCtrlVal% (ph%,PP1.USERPROMPT,"Load Specimen & Press OK")
beep
status% = 0
ok.app% = 0
ret% = SetInputMode% (ph%,PP1.OK,1)
ret% = SetInputMode% (ph%,PP1.END,1)
WHILE status%=0 AND end.app%=0
      CALL Checkkey
      IF ok.app%=1 THEN
            status% = 1
            ok.app% = 0
      ENDIF
WEND

ret% = SetCtrlVal% (ph%,PP1.USERPROMPT,"Enter Specimen ID")
beep
ret% = SetActiveCtrl% (PP1.ID)
j% = 0
WHILE j%=0 AND end.app%=0
      IF GetUserEvent% (0,pan%,ctrl%)<>0 THEN
            IF ctrl% = PP1.ID THEN
            ret% = GetCtrlVal% (ph%,PP1.ID,specid$)
            j% = 1
            ENDIF
      ENDIF
WEND

ret% = SetInputMode% (ph%,PP1.OK,0)
ret% = SetCtrlVal% (ph%,PP1.USERPROMPT,"Adjusting Pressure Pmin")

IF vmin#<>vcurr# THEN
      vstep# = vmin# - vcurr#
      ramprate1# = vstep#/5.0
      CALL RampAO (vcurr#,vstep#,ramprate1#)
ENDIF

ret% = SetCtrlVal (ph%,PP1.USERPROMPT,"Pressure up to Pmin")
CALL Delay (1.5)

CALL ClearIA (chlist%(),channum-1)

nch% = 4
```

```
npts% = 50
samplr# = 2000.0
scanr# = 100.0
scount& = CLNG(nch% * npts%)

chlist%(0) = 6
chlist%(1) = 13
chlist%(2) = 15
chlist%(3) = 0

er% = SCAN.Op% (board,nch%,chlist%(),gnlist%(),scanbuf%(),scount&,samplr#,
      scanr#)
IF er%<>0 THEN
      CALL Error.r("SCAN.Op",er%)
ENDIF

i% = 0
WHILE i%<npts%
      ch6buf%(i%) = scanbuf%(i%*4)
      ch13buf%(i%) = scanbuf%(i%*4+1)
      ch15buf%(i%) = scanbuf%(i%*4+2)
      ch0buf%(i%) = scanbuf%(i%*4+3)
      i% = i%+1
WEND

er% = DAQ.VScale%(board,6,gnlist%(6),aigain#(6),aioffset#(6),CLNG(npts%),
      ch6buf%(),mch6buf#())
er% = DAQ.VScale%(board,13,gnlist%(13),aigain#(13),aioffset#(13),CLNG(npts%),
      ch13buf%(),mch13buf#())
er% = DAQ.VScale%(board,15,gnlist%(15),aigain#(15),aioffset#(15),CLNG(npts%),
      ch15buf%(),mch15buf#())
er% = DAQ.VScale%(board,0,gnlist%(0),aigain#(0),aioffset#(0),CLNG(npts%),
      ch0buf%(),mch0buf#())

CALL Mean(mch6buf#(),npts%,chmean#(6))
ret% = Fmt (temp$,"%s< Pa = %f[w7p5] Bar",chmean#(6))
ret% = SetCtrlVal (ph%,PP1.USERPROMPT,temp$)
CALL Delay (1.5)

CALL Mean(mch13buf#(),npts%,chmean#(13))
ret% = Fmt (temp$,"%s< T1 = %f[w4p1] degC",chmean#(13))
ret% = SetCtrlVal (ph%,PP1.USERPROMPT,temp$)
CALL Delay (1.5)

CALL Mean(mch15buf#(),npts%,chmean#(15))
ret% = Fmt (temp$,"%s< T2 = %f[w4p1] degC",chmean#(15))
ret% = SetCtrlVal (ph%,PP1.USERPROMPT,temp$)
CALL Delay (1.5)

CALL Mean(mch0buf#(),npts%,chmean#(0))
ret% = Fmt (temp$,"%s< Ta = %f[w4p1] degC",chmean#(0))
ret% = SetCtrlVal (ph%,PP1.USERPROMPT,temp$)
CALL Delay (1.5)

ret% = SetCtrlVal% (ph%,PP1.USERPROMPT,"Press OK to start")
beep
```

```
ok.app% = 0
status% = 0
ret% = SetInputMode% (ph%,PP1.END,1)
ret% = SetInputMode% (ph%,PP1.OK,1)
WHILE status%=0 AND end.app%=0
        CALL Checkkey
        IF ok.app%=1 THEN
              status% = 1
        ENDIF
WEND

CALL ClearIA (chlist%(),channum-1)

nch% = 6
npts% = 500
samplr# = 10000.0
scanr# = 1000.0
scount& = nch% * npts%

chlist%(0) = 1
chlist%(1) = 3
chlist%(2) = 4
chlist%(3) = 12
chlist%(4) = 13
chlist%(5) = 15

store.app% = 0
imeas% = 0
j% = 0
ret% = SetInputMode% (ph%,PP1.OK,0)
ret% = SetInputMode% (ph%,PP1.END,1)

WHILE imeas%<n%+1 AND end.app%=0
        ret% = SetInputMode% (ph%,PP1.STORE,1)
        ret% = SetCtrlVal% (ph%,PP1.USERPROMPT,"Scanning data !")

        WHILE   store.app%=0 AND end.app%=0

              er% = SCAN.Op (board,nch%,chlist%(),gnlist%(),scanbuf%(),scount&,
                    samplr#,scanr#)
              IF er%<>0 THEN
                    CALL Error.r("SCAN.Op",er%)
              ENDIF

              i% = 0
              WHILE i%<npts%
                    ch1buf%(i%) = scanbuf%(i%*6)
                    ch3buf%(i%) = scanbuf%(i%*6+1)
                    ch4buf%(i%) = scanbuf%(i%*6+2)
                    ch12buf%(i%) = scanbuf%(i%*6+3)
                    ch13buf%(i%) = scanbuf%(i%*6+4)
                    ch15buf%(i%) = scanbuf%(i%*6+5)
                    i% = i%+1
              WEND

              er% = DAQ.VScale%(board,1,gnlist%(1),aigain#(1),aioffset#(1),
```

```
        CLNG(npts%),ch1buf%(),mch1buf#())
er% = DAQ.VScale%(board,3,gnlist%(3),aigain#(3),aioffset#(3),
        CLNG(npts%),ch3buf%(),mch3buf#())
er% = DAQ.VScale%(board,4,gnlist%(4),aigain#(4),aioffset#(4),
        CLNG(npts%),ch4buf%(),mch4buf#())
er% = DAQ.VScale%(board,12,gnlist%(12),aigain#(12),aioffset#(12),
        CLNG(npts%),ch12buf%(),mch12buf#())
er% = DAQ.VScale%(board,13,gnlist%(13),aigain#(13),aioffset#(13),
        CLNG(npts%),ch13buf%(),mch13buf#())
er% = DAQ.VScale%(board,15,gnlist%(15),aigain#(15),aioffset#(15),
        CLNG(npts%),ch15buf%(),mch15buf#())

CALL Mean(mch1buf#(),npts%,mean1#)
CALL Mean(mch3buf#(),npts%,mean3#)
CALL Mean(mch4buf#(),npts%,mean4#)
CALL Mean(mch12buf#(),npts%,mean12#)
CALL Mean(mch13buf#(),npts%,mean13#)
CALL Mean(mch15buf#(),npts%,mean15#)

ret% = SetCtrlVal% (ph%,PP1.p12,mean1#)
ret% = SetCtrlVal% (ph%,PP1.P23,mean3#)
ret% = SetCtrlVal% (ph%,PP1.P2,mean4#)
ret% = SetCtrlVal% (ph%,PP1.Q,mean12#)
ret% = SetCtrlVal% (ph%,PP1.T1,mean13#)
ret% = SetCtrlVal% (ph%,PP1.T2,mean15#)

IF ABS(mean3#) > 0.05 THEN
        j% = 0
        k% = 1
        ret% = SetCtrlVal (ph%,PP1.USERPROMPT,"p2-p3 not balnaced !")
        beep

    ELSE
        k% = 0

    ENDIF

    IF j%=0 AND k%=0 AND end.app%=0 THEN
        ret% = SetCtrlVal% (ph%,PP1.USERPROMPT,"Press STORE to store")
        j% = 1
        beep
    ENDIF
    CALL Checkkey
WEND
ret% = SetInputMode% (ph%,PP1.STORE,0)

IF imeas%<>n% THEN
    ret% = SetCtrlVal% (ph%,PP1.USERPROMPT,"Calculating Data !")
ENDIF

CALL Bw.LPF (mch1buf#(),npts%,scanr#,0.1*scanr#,5,mch1buf#())
CALL Bw.LPF (mch3buf#(),npts%,scanr#,0.1*scanr#,5,mch3buf#())
CALL Bw.LPF (mch4buf#(),npts%,scanr#,0.1*scanr#,5,mch4buf#())
CALL Bw.LPF (mch12buf#(),npts%,scanr#,0.1*scanr#,5,mch12buf#())
CALL Bw.LPF (mch13buf#(),npts%,scanr#,0.1*scanr#,5,mch13buf#())
CALL Bw.LPF (mch15buf#(),npts%,scanr#,0.1*scanr#,5,mch15buf#())
```

```
CALL FMean (mch1buf#0,npts%,ch1meas#(imeas%))
CALL FMean (mch3buf#0,npts%,ch3meas#(imeas%))
CALL FMean (mch4buf#0,npts%,ch4meas#(imeas%))
CALL FMean (mch12buf#0,npts%,ch12meas#(imeas%))
CALL FMean (mch13buf#0,npts%,ch13meas#(imeas%))
CALL FMean (mch15buf#0,npts%,ch15meas#(imeas%))

ret% = SetCtrlVal% (ph%,PP1.P12,ch1meas#(imeas%))
ret% = SetCtrlVal% (ph%,PP1.P23,ch3meas#(imeas%))
ret% = SetCtrlVal% (ph%,PP1.P2,ch4meas#(imeas%))
ret% = SetCtrlVal% (ph%,PP1.Q,ch12meas#(imeas%))
ret% = SetCtrlVal% (ph%,PP1.T1,ch13meas#(imeas%))
ret% = SetCtrlVal% (ph%,PP1.T2,ch15meas#(imeas%))

IF imeas%<n% THEN
      ret% = SetCtrlVal% (ph%,PP1.USERPROMPT,"Adjusting Pressure !")
      ramprate# = vinc#/5.0
      CALL RampAO (vcurr#,vinc#,ramprate#)
      ret% = Fmt (temp$,"%s< Next Measurement is No. %i",(imeas%+2))
      ret% = SetCtrlVal% (ph%,PP1.USERPROMPT,temp$)
      CALL Delay (1.5)
ENDIF
imeas% = imeas% + 1
j% = 0
store.app% = 0
CALL Checkkey
WEND
er% = AO.VWrite (board,0,0.0#)
ret% = SetCtrlVal% (ph%,PP1.USERPROMPT,"")
ret% = SetInputMode% (ph%,PP1.STORE,0)
ret% = SetInputMode% (ph%,PP1.END,0)
ret% = SetInputMode% (ph%,PP1.OK,0)

area# = 4.155e-4'Dia = 23mm
pa# = chmean#(6) * 1.0e5
ta# = chmean#(0) + 273.15

ret% = SetCtrlVal% (ph%,PP1.USERPROMPT,"Enter Specimen Thk mm")
beep
ok.app% = 0
ret% = SetInputMode% (ph%,PP1.OK,1)
ret% = SetInputMode% (ph%,PP1.END,1)
WHILE ok.app% = 0
ret% = SetActiveCtrl% (PP1.THK)
j% = 0
WHILE j%=0
      IF GetUserEvent% (0,pan%,ctrl%)<>0 THEN
      IF ctrl% = PP1.THK THEN
      ret% = GetCtrlVal% (ph%,PP1.THK,thk#)
      j% = 1
WEND
k% = 0
WHILE ok.app%=0 AND j%=1 AND end.app%=0
      IF k%=0 THEN
            ret% = SetCtrlVal% (ph%,PP1.USERPROMPT,"Press OK to confirm")
```

```
            ENDIF
            k% = 1
            CALL Checkkey
        WEND
        IF end.app%=1 THEN
            ret% = SetCtrlVal% (ph%,PP1.USERPROMPT,"Re-enter thickness !")
            end.app% = 0
        ENDIF
WEND
thk# = 0.001 * thk#

i% = 0
WHILE  i%<n%+1
        pmean#(i%) = 0.5e5*ch1meas#(i%)+100.*ch4meas#(i%)+pa#
        tmean#(i%) = 0.5*(ch13meas#(i%)+ch15meas#(i%))+273.15
        i% = i%+1
WEND

ret% = SetCtrlVal% (ph%,PP1.USERPROMPT,"Select flow range")
beep
ret% = SetActiveCtrl% (PP1.FLOW)
ok.app% = 0
ret% = SetInputMode% (ph%,PP1.OK,1)
ret% = SetInputMode% (ph%,PP1.END,1)
WHILE ok.app% = 0
        j% = 0
        WHILE j% = 0
        IF GetUserEvent% (0,pan%,ctrl%)<>0 THEN
            IF ctrl% = PP1.FLOW THEN
                ret% = GetCtrlVal% (ph%,PP1.FLOW,flowid%)
                j% = 1
            ENDIF
        ENDIF
WEND

k% = 0
WHILE ok.app%=0 AND j%=1 AND end.app%=0
        IF k%=0 THEN
            ret% = SetCtrlVal% (ph%,PP1.USERPROMPT,"OK to accept,END to
                retype")
        ENDIF
        CALL Checkkey
        k% = 1
WEND
        IF end.app%=1 THEN
            ret% = SetCtrlVal% (ph%,PP1.USERPROMPT,"Reselect flow range")
            end.app% = 0
        ENDIF
WEND
ret% = SetCtrlVal% (ph%,PP1.USERPROMPT,"Calculating Permeability")
ok.app% = 0

IF flowid% = 1 THEN
        i% = 0
        WHILE i%<n%+1
            q#(i%) = 3.0314677e-9
```

```
            q#(i%) = q#(i%)+5.4316808e-7*ch12meas#(i%)
            q#(i%) = q#(i%)-2.6966884e-7*ch12meas#(i%)^2
            q#(i%) = q#(i%)+2.5165936e-7*ch12meas#(i%)^3
            q#(i%) = q#(i%)-7.6805921e-8*ch12meas#(i%)^4
            q#(i%) = q#(i%)+8.788411e-9*ch12meas#(i%)^5
            i% = i%+1
        WEND
END IF

IF flowid% = 2 THEN
        i% = 0
        WHILE i%<n%+1
            q#(i%) = 2.0563519e-8
            q#(i%) = q#(i%)+5.8194241e-7*ch12meas#(i%)
            q#(i%) = q#(i%)+1.4736029e-7*ch12meas#(i%)^2
            q#(i%) = q#(i%)+5.1967192e-7*ch12meas#(i%)^3
            q#(i%) = q#(i%)-2.2000702e-7*ch12meas#(i%)^4
            q#(i%) = q#(i%)+3.3736153e-8*ch12meas#(i%)^5

            i% = i%+1
        WEND
END IF

IF flowid% = 3 THEN
        i% = 0
        WHILE i%<n%+1
            q#(i%) = 20.758e-6*ch12meas#(i%)
            q#(i%) = q#(i%)+2.325e-7

            i% = i%+1
        WEND
END IF

IF flowid% = 4 THEN
        i% = 0
        WHILE i%<n%+1
            q#(i%) = 83.668e-6*ch12meas#(i%)
            q#(i%) = q#(i%)+1.029e-6

            i% = i%+1
        WEND
END IF

i% = 0
WHILE i%<n%+1
        u#(i%) = 1.82e-5*((tmean#(i%)/293.15)^0.76)*(EXP(1e-8*(pmean#(i%)-1e5)))
        q#(i%) = q#(i%)*1.013962e5*tmean#(i%)/pmean#(i%)/273.15
        i% = i%+1
WEND

i% = 0
WHILE i%<n%+1
        rhomean# = 1.184*pmean#(i%)*293.15/1.0e5/tmean#(i%)
        x#(i%) = q#(i%)*rhomean#/u#(i%)/area#
        y#(i%) = 1.0e5*ch1meas#(i%)*area#/thk#/q#(i%)/u#(i%)
        i% = i%+1
```

```
WEND

CALL MaxMin1D (x#(),n%+1,xmax#,ixmax%,xmin#,ixmin%)
CALL MaxMin1D (y#(),n%+1,ymax#,iymax%,ymin#,iymin%)

i% = 0
WHILE i%<n%+1
      xnom#(i%) = x#(i%)/xmax#
      ynom#(i%) = y#(i%)/ymax#
      i% = i%+1
WEND

ret% = DeletePlots% (ph%,PP1.GRAPH)
ret% = SetAxisRange% (ph%,PP1.GRAPH,0,0.0,1.1,0,0.0,1.1)

i% = 0
WHILE i%<n%+1
      ret% = PlotPoint (ph%,PP1.GRAPH,xnom#(i%),ynom#(i%),3,0)
      i% = i%+1
WEND

j% = 0
curveid% = 999
WHILE j%=0
      ret% = SetCtrlVal (ph%,PP1.USERPROMPT," Off n pts for linefit")
      beep
      ret% = SetActiveCtrl% (PP1.NMEA)
      k% = 0
      WHILE k%=0
            IF GetUserEvent% (0,pan%,ctrl%)<>0 THEN
                  IF ctrl% = PP1.NMEA THEN
                        ret% = GetCtrlVal% (ph%,PP1.NMEA,shft%)
                        k% = 1
                  ENDIF
            ENDIF
      WEND

      IF shft%=0 THEN
            CALL LinFit (x#(),y#(),n%+1,yfit#(),slope#,intercept#,mse#)
            j% = 1
      ELSE
            nfit% = n% - shft%
            CALL Shift (x#(),n%+1,-shft%,xnom#())
            CALL Shift (y#(),n%+1,-shft%,ynom#())
            CALL LinFit (xnom#(),ynom#(),n%+1-shft%,yfit#(),slope#,intercept#,mse#)
      ENDIF

      nintercept# = intercept#/ymax#
      nslope# = slope#*xmax#/ymax#
      IF curveid%<>-999 THEN
            ret% = DeleteGraphPlot (ph%,PP1.GRAPH,curveid%,1)
      END IF
      ret% = PlotLine (ph%,PP1.GRAPH,0.0,nintercept#,1.0,nslope#+nintercept#,4)
      IF ret%<0 THEN
            CALL Error.r("PlotLine",er%)
      ELSE
```

```
        curveid% = ret%
END IF

phii# = 1.0 / slope#
ret% = Fmt (temp$,"%s< Phi^i = %f[w11p3e2] m",phii#)
ret% = SetCtrlVal (ph%,PP1.USERPROMPT,temp$)
CALL Delay (5.0)

phiv# = 1.0 / intercept#
ret% = Fmt (temp$,"%s< Phi^v = %f[w11p3e2] m^2",phiv#)
ret% = SetCtrlVal (ph%,PP1.USERPROMPT,temp$)
beep
CALL Delay (5.0)

IF j%=0 THEN
    ret% = SetCtrlVal% (ph%,PP1.USERPROMPT,"OK to accept; END to chg")
    WHILE ok.app%=0 AND end.app%=0
        CALL Checkkey
    WEND
    end.app% = 0

    IF ok.app%=1 THEN
        j% = 1
        ok.app% = 0
    END IF
END IF
WEND

ok.app% = 0
ret% = SetCtrlVal% (ph%,PP1.USERPROMPT,"Press OK to write file")
beep
WHILE ok.app%=0 AND end.app%=0
    CALL Checkkey
WEND

CALL OutputFile

ok.app% = 0
ret% = SetCtrlVal% (ph%,PP1.USERPROMPT,"Another run ?")
ret% = SetInputMode% (ph%,PP1.OK,1)
ret% = SetInputMode% (ph%,PP1.END,1)
ret% = SetInputMode% (ph%,PP1.STORE,0)
WHILE ok.app%=0 AND end.app%=0
    CALL Checkkey
WEND

ret% = AO.VWrite (board,0,0.0)
ret% = CloseInterfaceManager%



SUB RampAO (vcurr#,vs#,ramprates#)

    waverate% = 10
    n1% = waverate% * CINT (vs#/ramprates#)
```

```
beta# = 3.1415926 / 2.0 / CDBL(n1%)

i1%=1
vstart# = vcurr#
WHILE i1%<n1%
        vcurr# = vstart# + vs# * Sin(beta#*CDBL(i1%))
        er% = AO.VWrite (board,0,vcurr#)
        CALL Delay (0.1)
        i1% = i1%+1
WEND
        vcurr# = vstart# + vs#

END SUB


SUB OutputFile

        ret% = GetDir% (dirname$)
        IF FileSelectPopup% (dirname$, "P*.d25", "Select Data File ", 0, 0, 1, filename$) <> 1 THEN
                ret% = SetCtrlVal% (ph%, PP1.USERPROMPT, "File not selected!")
                CALL Delay (2.0)
        END IF

         Write ASCCI

        handle% = OpenFile% (filename$, 2, 0, 1)
        IF handle% <> -1 THEN
                ret% = FmtFile% (handle%, "%s< Specimen ID =   %s " + CHR$(10), specid$)
                ret% = FmtFile% (handle%, "%s< Amb Temperature =   %f[w6p2]  degK" + CHR$(10), ta#)
                ret% = FmtFile% (handle%, "%s< Amb Pressure=   %f[w6p4]  Bar" + CHR$(10) +
CHR$(10),                       pa#*1e-5)
                ret% = FmtFile% (handle%, "%s<  Meas.Pt   Q   p1-p2p2 t1 t2 X Value Y Value  ")
                ret% = FmtFile% (handle%, "%s<  " + CHR$(10) + CHR$(10))
                ret% = FmtFile% (handle%, "%s<  Units  m^3/s  BarmBar   deg.C  deg.C m^-1m^-2   ")
                ret% = FmtFile% (handle%, "%s<  " + CHR$(10) + CHR$(10))
                i2% = 0
                WHILE i2%<n%+1
                        ret% = FmtFile% (handle%, "%s<   %i[w3]   ", i2%+1)
                        ret% = FmtFile% (handle%, "%s< %f[w10p3e2] ", q#(i2%))
                        ret% = FmtFile% (handle%, "%s< %f[w7p4] ", ch1meas#(i2%))
                        ret% = FmtFile% (handle%, "%s< %f[w5p3] ", ch4meas#(i2%))
                        ret% = FmtFile% (handle%, "%s< %f[w5p1] ", ch13meas#(i2%))
                        ret% = FmtFile% (handle%, "%s< %f[w5p1] ", ch15meas#(i2%))
                        ret% = FmtFile% (handle%, "%s< %f[w10p3e2] ", x#(i2%))
                        ret% = FmtFile% (handle%, "%s< %f[w10p3e2] " + CHR$(10), y#(i2%))
                        i2% = i2%+1
                WEND

                ret% = FmtFile% (handle%, "%s<  " + CHR$(10)+ CHR$(10))
                ret% = FmtFile% (handle%, "%s< Discard 1st %i[w3] pts for line-fit" + CHR$(10), shft%)
                ret% = FmtFile% (handle%, "%s< PHIv =   %f[w11p3e3]  m^2" + CHR$(10), phiv#)
                ret% = FmtFile% (handle%, "%s< PHIi =   %f[w11p3e3]  m" + CHR$(10) + CHR$(10),
phii#)
                ret% = FmtFile% (handle%, "%s< Mean sq. error =   %f[w11p3e3]" + CHR$(10) +
CHR$(10),                       mse#)
```

```
            ret% = CloseFile%(handle%)
        ENDIF

END SUB
```

```
SUB Checkkey
        ist% = GetUserEvent% (0, pan%, ctrl%)'check key pressed
        IF ist%=1 THEN
        SELECT CASE ctrl%

            CASE PP1.END
                end.app% = 1

            CASE PP1.OK
                ok.app% = 1

            CASE PP1.STORE
                store.app% = 1

                CASE ELSE
        END SELECT
        ENDIF

END SUB
```

```
SUB ClearIA (array%(),j%)

        i2% = 0
        WHILE i2%<j%
            array% (i2%) = 0
            i2% = i2%+1
        WEND

END SUB
```

```
SUB FMean (array#(),npt%,meanf#)

        j% = 50
        sum# = 0
        WHILE j% < npt%
            sum# = sum# + array#(j%)
            j% = j% + 1
        WEND
        meanf# = sum#/CDBL(npt%-50)

END SUB
```

2) Dynamic Water Expulsion Test

Labwindows Program for Dynamic Water Expulsion Test

5 Bar Version 1.0
Y.B.P.KWAN 24.04.96

```
ret% = OpenInterrfaceManager%
ph% = LoadPanel% ("zagar.uir",PP1)
ret% = DisplayPanel% (ph%)

ret% = AI.Configure% (board%,-1,1,10,1,0)
ret% = AO.Configure% (board%,0,1,0,10,0)
ret% = AO.Configure% (board%,1,1,0,10,0)
ret% = DeletePlots% (ph%,PP1.GRAPH)
ret% = SetAxisRange% (ph%,PP1.GRAPH,0,0.0,1.1,0,0.0,1.1)

ret% = SetInputMode% (ph%,PP1.END,1)

WHILE   end.app% = 0
        CALL Checkkey

        vcurr# = 0.0
        er% = AO.VWrite (board,0,vcurr#)

        ret% = SetInputMode% (ph%,PP1.OK,1)
        ret% = SetInputMode% (ph%,PP1.END,1)
        ret% = SetCtrlVal% (ph%,PP1.USERPROMPT," Scanning ambient conditions")
        beep
        CALL Delay (1.5)

        CALL ClearIA (chlist%(),channum-1)

        nch% = 4
        npts% = 50
        samplr# = 2000.0
        scanr# = 100.0
        scount& = CLNG(nch% * npts%)

        chlist%(0) = 6
        chlist%(1) = 13
        chlist%(2) = 15
        chlist%(3) = 0

        er% = SCAN.Op% (board,nch%,chlist%(),gnlist%(),scanbuf%(),scount&,samplr#,scanr#)

        i% = 0
        WHILE i%<npts%
                ch6buf%(i%) = scanbuf%(i%*4)
                ch13buf%(i%) = scanbuf%(i%*4+1)
                ch15buf%(i%) = scanbuf%(i%*4+2)
                ch0buf%(i%) = scanbuf%(i%*4+3)
```

```
        i% = i%+1
WEND

er% = DAQ.VScale%(board,6,gnlist%(6),aigain#(6),aioffset#(6),CLNG(npts%),
        ch6buf%(),mch6buf#())
er% = DAQ.VScale%(board,13,gnlist%(13),aigain#(13),aioffset#(13),CLNG(npts%),
        ch13buf%(),mch13buf#())
er% = DAQ.VScale%(board,15,gnlist%(15),aigain#(15),aioffset#(15),CLNG(npts%),
        ch15buf%(),mch15buf#())
er% = DAQ.VScale%(board,0,gnlist%(0),aigain#(0),aioffset#(0),CLNG(npts%),
        ch0buf%(),mch0buf#())

CALL Mean(mch6buf#(),npts%,chmean#(6))
ret% = Fmt (temp$,"%s< Pa = %f[w7p5] Bar",chmean#(6))
ret% = SetCtrlVal (ph%,PP1.USERPROMPT,temp$)
CALL Delay (1.5)
CALL Mean(mch13buf#(),npts%,chmean#(13))
ret% = Fmt (temp$,"%s< T1 = %f[w4p1] degC",chmean#(13))
ret% = SetCtrlVal (ph%,PP1.USERPROMPT,temp$)
CALL Delay (1.5)
CALL Mean(mch15buf#(),npts%,chmean#(15))
ret% = Fmt (temp$,"%s< T2 = %f[w4p1] degC",chmean#(15))
ret% = SetCtrlVal (ph%,PP1.USERPROMPT,temp$)
CALL Delay (1.5)
CALL Mean(mch0buf#(),npts%,chmean#(0))
ret% = Fmt (temp$,"%s< Ta = %f[w4p1] degC",chmean#(0))
ret% = SetCtrlVal (ph%,PP1.USERPROMPT,temp$)
CALL Delay (1.5)

gamma# = 0.072+(25.0-chmean#(0))*0.15e-3
ret% = Fmt (temp$,"%s< Gamma = %f[w7p5] N/m",gamma#)
ret% = SetCtrlVal% (ph%,PP1.USERPROMPT,temp$)
CALL Delay (2.5)

dmincal# = 4.0*gamma#*Cos(theta)/4.995e5
dmaxcal# = 4.0*gamma#*Cos(theta)/0.02e5

status% = 0
ret% = SetInputMode% (ph%,PP1.END,0)
ret% = SetCtrlVal% (ph%,PP1.USERPROMPT,"Enter Min Pore Size  um")
beep
ret% = SetActiveCtrl% (PP1.DMIN)
j% = 0
dmin# = 5.0
WHILE j%=0 AND end.app%=0
      IF GetUserEvent% (0,pan%,ctrl%)<>0 THEN
            IF ctrl% = PP1.DMIN THEN
                  ret% = GetCtrlVal% (ph%,PP1.DMIN,dmin#)
                  j% = 1
            END IF
      END IF
WEND

dmin# = dmin# * 1e-6
pmax# = 4.0e-5*gamma#*Cos(theta)/dmin#
vmax# = 2.0 * (pmax#-0.005)
```

```
ret% = SetCtrlVal% (ph%,PP1.USERPROMPT,"Enter Max Pore Size  um")
beep
ret% = SetActiveCtrl% (PP1.DMAX)
j% = 0
dmax# = 80.0
WHILE j%=0 AND end.app%=0
      IF GetUserEvent% (0,pan%,ctrl%)<>0 THEN
            IF ctrl% = PP1.DMAX THEN
                  ret% = GetCtrlVal% (ph%,PP1.DMAX,dmax#)
                  j% = 1
            END IF
      END IF
WEND

dmax# = dmax# * 1e-6
pmin# = 4.0e-5*gamma#*Cos(theta)/dmax#
vmin# = 2.0 * (pmin#-0.005)


ret% = SetCtrlVal% (ph%,PP1.USERPROMPT,"Enter No of Increments")
beep
ret% = SetActiveCtrl% (PP1.NMEA)
j% = 0
WHILE j%=0 AND end.app%=0
      IF GetUserEvent% (0,pan%,ctrl%)<>0 THEN
            IF ctrl% = PP1.NMEA THEN
                  ret% = GetCtrlVal% (ph%,PP1.NMEA,n%)
                  j% = 1
            END IF
      END IF
WEND

vinc# = (vmax#-vmin#)/CDBL(n%)
ret% = SetInputMode% (ph%,PP1.END,1)

ret% = SetCtrlVal% (ph%,PP1.USERPROMPT,"Load Specimen & Press OK")
beep
status% = 0
ok.app% = 0
ret% = SetInputMode% (ph%,PP1.OK,1)
ret% = SetInputMode% (ph%,PP1.END,1)
WHILE status%=0 AND end.app%=0
      CALL Checkkey
      IF ok.app%=1 THEN
            status% = 1
            ok.app% = 0
      END IF
WEND

ret% = SetCtrlVal% (ph%,PP1.USERPROMPT,"Enter Specimen ID")
beep
ret% = SetActiveCtrl% (PP1.ID)
j% = 0
WHILE j%=0 AND end.app%=0
      IF GetUserEvent% (0,pan%,ctrl%)<>0 THEN
```

```
            IF ctrl% = PP1.ID THEN
                ret% = GetCtrlVal% (ph%,PP1.ID,specid&)
                j% = 1
            END IF
        END IF
WEND

ret% = SetCtrlVal% (ph%,PP1.USERPROMPT,"Enter Specimen Thk mm")
beep
ok.app% = 0
ret% = SetInputMode% (ph%,PP1.OK,1)
ret% = SetInputMode% (ph%,PP1.END,1)
ret% = SetActiveCtrl% (PP1.THK)
j% = 0
WHILE j%=0
    IF GetUserEvent% (0,pan%,ctrl%)<>0 THEN
        IF ctrl% = PP1.THK THEN
            ret% = GetCtrlVal% (ph%,PP1.THK,thk#)
            j% = 1
        END IF
    END IF
WEND
thk# = 0.001 * thk#

ret% = SetCtrlVal% (ph%,PP1.USERPROMPT,"Enter measured Phi^v")
beep
ret% = SetActiveCtrl% (PP1.PHIV)
j% = 0
WHILE j%=0 AND end.app%=0
    IF GetUserEvent% (0,pan%,ctrl%)<>0 THEN
        IF ctrl% = PP1.PHIV THEN
            ret% = GetCtrlVal% (ph%,PP1.PHIV,phiv#)
            j% = 1
        END IF
    END IF
WEND


area# = 15.205e-4
pa# = chmean#(6) * 1.0e5
ta# = chmean#(0) + 273.13
pomax# = (((pmax#*1.0e5+pa#)^2)-(pa#^2))/2.0/1.013962e5
u1# = 1.82e-5*((ta#/293.13)^0.76)*(EXP(1.0e-8*(pmax#*1.0e5)/2.0))

qmax# = phiv#*area#*pomax#/u1#/thk#  'm^3/s

ret% = Fmt (temp$,"%s< Max Flow = %f[w7p4] l/min",(qmax#*60.0e3))
ret% = SetCtrlVal (ph%,PP1.USERPROMPT,temp$)
beep
CALL Delay (3.5)

ret% = SetCtrlVal% (ph%,PP1.USERPROMPT,"Select flow range")
beep
ret% = SetActiveCtrl% (PP1.FLOW)
ok.app% = 0
ret% = SetInputMode% (ph%,PP1.OK,1)
```

```
ret% = SetInputMode% (ph%,PP1.END,1)
j% = 0
WHILE j% = 0
      IF GetUserEvent% (0,pan%,ctrl%)<>0 THEN
            IF ctrl% = PP1.FLOW THEN
                  ret% = GetCtrlVal% (ph%,PP1.FLOW,flowid%)
                  j% = 1
            END IF
      END IF
WEND

ret% = SetCtrlVal (ph%,PP1.USERPROMPT,"Close Ball Valve & Wait!")
CALL Delay (60.0)
CALL ClearIA (chlist%(),channum-1)

nch% = 1
npts% = 200
samplr# = 400.0
scanr# = 0.0
scount& = CLNG(nch% * npts%)

status% = 0
chlist%(0) = 12

er% = SCAN.Op% (board,nch%,chlist%(),gnlist%(),scanbuf%(),scount&,samplr#,scanr#)
IF er%<>0 THEN
      CALL Error.r("SCAN.Op",er%)
END IF

i% = 0
ok.app% = 0
opbin# = 0
WHILE i%<npts%
      opbin# = opbin# + CDBL(scanbuf%(i%))
      i% = i%+1
WEND
opbin# = opbin#/CDBL(npts%)

IF opbin#>1.05*aioffset#(12) OR opbin#<0.95*aioffset#(12) THEN
      ret% = SetCtrlVal% (ph%,PP1.USERPROMPT,"Ch.12 Zero Dev. > 5%")
      beep
      CALL Delay (3.0)
      ret% = SetInputMode% (ph%,PP1.OK,1)
      ret% = SetCtrlVal% (ph%,PP1.USERPROMPT,"Press OK to update !")
      WHILE  ok.app%=0 AND end.app%=0
            CALL Checkkey
      WEND
ELSE
      IF end.app%=0 THEN
            ret% = SetCtrlVal% (ph%,PP1.USERPROMPT,"Open Ball V/v, Press OK")
            beep
      END IF
END IF

status% = 0
```

```
ok.app% = 0

WHILE   status%=0 AND end.app%=0
        CALL Checkkey
        IF ok.app%=1 THEN
                aioffset#(12) = opbin#
                status% = 1
                ret% = SetCtrlVal% (ph%,PP1.USERPROMPT," ")
                ok.app% = 0
        END IF
WEND

ret% = SetInputMode% (ph%,PP1.OK,0)
ret% = SetCtrlVal% (ph%,PP1.USERPROMPT,"Adjusting Pressure Pmin")

IF vmin#<>vcurr# THEN
        vstep# = vmin# - vcurr#
        ramprate1# = vstep#/5.0
        CALL RampAO (vcurr#,vstep#,ramprate1#)
END IF

ret% = SetCtrlVal% (ph%,PP1.USERPROMPT,"Starting measurement")
CALL Delay (50.0)
CALL ClearIA (chlist%(),channum-1)

nch% = 5
npts% = 500
samplr# = 10000.0
scanr# = 1000.0
scount& = nch% * npts%

chlist%(0) = 1
chlist%(1) = 4
chlist%(2) = 12
chlist%(3) = 13
chlist%(4) = 15

steady.app% = 0
ok.app% = 0
imeas% = 0
j% = 0
ret% = SetInputMode% (ph%,PP1.OK,1)
ret% = SetInputMode% (ph%,PP1.END,1)

        WHILE imeas%<n%+1 AND end.app%=0
                ret% = SetCtrlVal% (ph%,PP1.USERPROMPT,"Scanning data !")

                WHILE   steady.app%=0 AND end.app%=0

                        er% = SCAN.Op
(board,nch%,chlist%(),gnlist%(),scanbuf%(),scount&,samplr#,scanr#)

                        i% = 0
                        WHILE i%<npts%
                                ch1buf%(i%) = scanbuf%(i%*5)
                                ch4buf%(i%) = scanbuf%(i%*5+1)
```

```
        ch12buf%(i%) = scanbuf%(i%*5+2)
        ch13buf%(i%) = scanbuf%(i%*5+3)
        ch15buf%(i%) = scanbuf%(i%*5+4)
        i% = i%+1
WEND

er% = DAQ.VScale%(board,1,gnlist%(1),aigain#(1),aioffset#(1),
        CLNG(npts%),ch1buf%(),mch1buf#())
er% = DAQ.VScale%(board,4,gnlist%(4),aigain#(4),aioffset#(4),
        CLNG(npts%),ch4buf%(),mch4buf#())
er% = DAQ.VScale%(board,12,gnlist%(12),aigain#(12),aioffset#(12),
        CLNG(npts%),ch12buf%(),mch12buf#())
er% = DAQ.VScale%(board,13,gnlist%(13),aigain#(13),aioffset#(13),
        CLNG(npts%),ch13buf%(),mch13buf#())
er% = DAQ.VScale%(board,15,gnlist%(15),aigain#(15),aioffset#(15),
        CLNG(npts%),ch15buf%(),mch15buf#())

CALL Mean(mch1buf#(),npts%,mean1#)
CALL Mean(mch4buf#(),npts%,mean4#)
CALL Mean(mch12buf#(),npts%,mean12#)
CALL Mean(mch13buf#(),npts%,mean13#)
CALL Mean(mch15buf#(),npts%,mean15#)

ret% = SetCtrlVal% (ph%,PP1.p12,mean1#)
ret% = SetCtrlVal% (ph%,PP1.P2,mean4#)
ret% = SetCtrlVal% (ph%,PP1.Q,mean12#)
ret% = SetCtrlVal% (ph%,PP1.T1,mean13#)
ret% = SetCtrlVal% (ph%,PP1.T2,mean15#)

IF j%<nst THEN
        qst#(j%) = mean12#
ELSE
        i3% = 0
        WHILE i3%<nst-1
                qst#(i3%) = qst#(i3%+1)
                i3% = i3%+1
        WEND
        qst#(nst-1) = mean12#

        CALL StdDev (qst#(),nst,qmean#,sdev#)
        IF sdev#<0.005*qmean# OR sdev#<0.33e-3 THEN
                steady.app% = 1
        END IF
END IF
        j% = j%+1
        CALL Checkkey
WEND

CALL Clear1D (qst#(),nst)
IF imeas%<>n% THEN
        ret% = SetCtrlVal% (ph%,PP1.USERPROMPT,"Calculating Data !")
END IF

CALL Bw.LPF (mch1buf#(),npts%,scanr#,0.1*scanr#,5,mch1buf#())
CALL Bw.LPF (mch4buf#(),npts%,scanr#,0.1*scanr#,5,mch4buf#())
CALL Bw.LPF (mch12buf#(),npts%,scanr#,0.1*scanr#,5,mch12buf#())
```

```
CALL Bw.LPF (mch13buf#(),npts%,scanr#,0.1*scanr#,5,mch13buf#())
CALL Bw.LPF (mch15buf#(),npts%,scanr#,0.1*scanr#,5,mch15buf#())

CALL FMean (mch1buf#(),npts%,ch1meas#(imeas%))
CALL FMean (mch4buf#(),npts%,ch4meas#(imeas%))
CALL FMean (mch12buf#(),npts%,ch12meas#(imeas%))
CALL FMean (mch13buf#(),npts%,ch13meas#(imeas%))
CALL FMean (mch15buf#(),npts%,ch15meas#(imeas%))

ret% = SetCtrlVal% (ph%,PP1.P12,ch1meas#(imeas%))
ret% = SetCtrlVal% (ph%,PP1.P2,ch4meas#(imeas%))
ret% = SetCtrlVal% (ph%,PP1.Q,ch12meas#(imeas%))
ret% = SetCtrlVal% (ph%,PP1.T1,ch13meas#(imeas%))
ret% = SetCtrlVal% (ph%,PP1.T2,ch15meas#(imeas%))

tmean#(imeas%) = 0.5*(ch13meas#(imeas%)+ch15meas#(imeas%))+273.13

IF flowid% = 1 THEN
      q#(imeas%) = 3.0314677e-9
      q#(imeas%) = q#(imeas%)+5.4316808e-7*ch12meas#(imeas%)
      q#(imeas%) = q#(imeas%)-2.6966884e-7*ch12meas#(imeas%)^2
      q#(imeas%) = q#(imeas%)+2.5165936e-7*ch12meas#(imeas%)^3
      q#(imeas%) = q#(imeas%)-7.6805921e-8*ch12meas#(imeas%)^4
      q#(imeas%) = q#(imeas%)+8.788411e-9*ch12meas#(imeas%)^5
END IF

IF flowid% = 2 THEN
      q#(imeas%) = 2.0563519e-8
      q#(imeas%) = q#(imeas%)+5.8194241e-7*ch12meas#(imeas%)
      q#(imeas%) = q#(imeas%)+1.4736029e-7*ch12meas#(imeas%)^2
      q#(imeas%) = q#(imeas%)+5.1967192e-7*ch12meas#(imeas%)^3
      q#(imeas%) = q#(imeas%)-2.2000702e-7*ch12meas#(imeas%)^4
      q#(imeas%) = q#(imeas%)+3.3736153e-8*ch12meas#(imeas%)^5
END IF

IF flowid% = 3 THEN
      q#(imeas%) = 20.758e-6*ch12meas#(imeas%)
      q#(imeas%) = q#(imeas%)+2.325e-7
END IF

IF flowid% = 4 THEN
      q#(imeas%) = 83.668e-6*ch12meas#(imeas%)'Q in cu.m/s  assumed linear
      q#(imeas%) = q#(imeas%)+1.029e-6
END IF

      q#(imeas%) = q#(imeas%)*tmean#(imeas%)/273.13
      u#(imeas%) = 1.82e-5*((tmean#(imeas%)/293.13)^0.76)*(EXP(0.5e-
3*(ch1meas#(imeas%))))

      p2abs# = ch4meas#(imeas%)*100.0 +pa#
      p1abs# = ch1meas#(imeas%)*1.0e5 + p2abs#
      po#(imeas%) = (p1abs#^2 - p2abs#^2)/2.0/1.013962e5
      xnom#(imeas%) = po#(imeas%)/pomax#
      ynom#(imeas%) = q#(imeas%)/qmax#

      ret% = PlotPoint (ph%,PP1.GRAPH,xnom#(imeas%),ynom#(imeas%),3,0)
```

```
IF imeas%<nst THEN
        qsl#(imeas%) = q#(imeas%)/po#(imeas%)
ELSE
        i3% = 0
        WHILE i3%<nst-1
                qsl#(i3%) = qsl#(i3%+1)
                i3% = i3%+1
        WEND
        qsl#(nst-1) = q#(imeas%)/po#(imeas%)
        CALL StdDev (qsl#0,nst,qslmean#,sldev#)
        IF sldev#<0.007*qslmean# THEN
                ret% = SetCtrlVal% (ph%,PP1.USERPROMPT,"All pores cleared !")
                beep
                CALL Delay (2.0)
                ret% = SetCtrlVal% (ph%,PP1.USERPROMPT,"Press OK or END")
                WHILE end.app%=0 AND ok.app%=0
                        CALL Checkkey
                WEND
        END IF
END IF

IF imeas%<n% AND end.app%=0 THEN
        ret% = SetCtrlVal% (ph%,PP1.USERPROMPT,"Adjusting Pressure !")
        ramprate# = vinc#/5
        CALL RampAO (vcurr#,vinc#,ramprate#)
                ret% = Fmt (temp$,"%s< Next Measurement is No. %i",(imeas%+2))
                ret% = SetCtrlVal% (ph%,PP1.USERPROMPT,temp$)
                beep
                CALL Delay (50.0)
        END IF
        imeas% = imeas% + 1
        j% = 0
        steady.app% = 0

WEND
n% = imeas% - 1
end.app% = 0
ret% = SetCtrlVal% (ph%,PP1.USERPROMPT," Measuring Phi^v !")
CALL Delay (1.5)

vdinc# = (vmin#-vcurr#)/5.0
dramprate# = vdinc#/5.0
steady.app% = 0
ok.app% = 0
j% = 0
ret% = SetInputMode% (ph%,PP1.OK,0)
ret% = SetInputMode% (ph%,PP1.END,1)
ret% = PlotPoint (ph%,PP1.GRAPH,xnom#(n%),ynom#(n%),5,14)
ret% = SetCtrlVal% (ph%,PP1.USERPROMPT,"Adjusting Pressure !")
CALL RampAO (vcurr#,vdinc#,dramprate#)

WHILEimeas%<n%+6 AND end.app%=0
        ret% = SetCtrlVal% (ph%,PP1.USERPROMPT,"Scanning data !")
```

```
WHILE   steady.app%=0 AND end.app%=0

        er% = SCAN.Op (board,nch%,chlist%(),gnlist%(),scanbuf%(),scount&,samplr#,scanr#)
        i% = 0
        WHILE i%<npts%
                ch1buf%(i%) = scanbuf%(i%*5)
                ch4buf%(i%) = scanbuf%(i%*5+1)
                ch12buf%(i%) = scanbuf%(i%*5+2)
                ch13buf%(i%) = scanbuf%(i%*5+3)
                ch15buf%(i%) = scanbuf%(i%*5+4)
                i% = i%+1
        WEND

        er% = DAQ.VScale%(board,1,gnlist%(1),aigain#(1),aioffset#(1),CLNG(npts%),
                ch1buf%(),mch1buf#())
        er% = DAQ.VScale%(board,4,gnlist%(4),aigain#(4),aioffset#(4),
                CLNG(npts%),ch4buf%(),mch4buf#())
        er% = DAQ.VScale%(board,12,gnlist%(12),aigain#(12),aioffset#(12),
                CLNG(npts%),ch12buf%(),mch12buf#())
        er% = DAQ.VScale%(board,13,gnlist%(13),aigain#(13),aioffset#(13),
                CLNG(npts%),ch13buf%(),mch13buf#())
        er% = DAQ.VScale%(board,15,gnlist%(15),aigain#(15),aioffset#(15),
                CLNG(npts%),ch15buf%(),mch15buf#())

        CALL Mean(mch1buf#(),npts%,mean1#)
        CALL Mean(mch4buf#(),npts%,mean4#)
        CALL Mean(mch12buf#(),npts%,mean12#)
        CALL Mean(mch13buf#(),npts%,mean13#)
        CALL Mean(mch15buf#(),npts%,mean15#)

        ret% = SetCtrlVal% (ph%,PP1.p12,mean1#)
        ret% = SetCtrlVal% (ph%,PP1.P2,mean4#)
        ret% = SetCtrlVal% (ph%,PP1.Q,mean12#)
        ret% = SetCtrlVal% (ph%,PP1.T1,mean13#)
        ret% = SetCtrlVal% (ph%,PP1.T2,mean15#)

        IF j%<nst THEN
                qst#(j%) = mean12#
        ELSE
                i3% = 0
                WHILE i3%<nst-1
                        qst#(i3%) = qst#(i3%+1)
                        i3% = i3%+1
                WEND
                qst#(nst-1) = mean12#

                CALL StdDev (qst#(),nst,qmean#,sdev#)
                IF sdev#<0.007*qmean# OR sdev#<0.33e-3THEN
                        steady.app% = 1
                END IF
        END IF
        j% = j%+1
        CALL Checkkey
WEND

CALL Clear1D (qst#(),nst)
```

```
IF imeas%<>n%+5 THEN
      ret% = SetCtrlVal% (ph%,PP1.USERPROMPT,"Calculating Data !")
END IF

CALL Bw.LPF (mch1buf#(),npts%,scanr#,0.1*scanr#,5,mch1buf#())
CALL Bw.LPF (mch4buf#(),npts%,scanr#,0.1*scanr#,5,mch4buf#())
CALL Bw.LPF (mch12buf#(),npts%,scanr#,0.1*scanr#,5,mch12buf#())
CALL Bw.LPF (mch13buf#(),npts%,scanr#,0.1*scanr#,5,mch13buf#())
CALL Bw.LPF (mch15buf#(),npts%,scanr#,0.1*scanr#,5,mch15buf#())
CALL FMean (mch1buf#(),npts%,ch1meas#(imeas%))
CALL FMean (mch4buf#(),npts%,ch4meas#(imeas%))
CALL FMean (mch12buf#(),npts%,ch12meas#(imeas%))
CALL FMean (mch13buf#(),npts%,ch13meas#(imeas%))
CALL FMean (mch15buf#(),npts%,ch15meas#(imeas%))

ret% = SetCtrlVal% (ph%,PP1.P12,ch1meas#(imeas%))
ret% = SetCtrlVal% (ph%,PP1.P2,ch4meas#(imeas%))
ret% = SetCtrlVal% (ph%,PP1.Q,ch12meas#(imeas%))
ret% = SetCtrlVal% (ph%,PP1.T1,ch13meas#(imeas%))
ret% = SetCtrlVal% (ph%,PP1.T2,ch15meas#(imeas%))

tmean#(imeas%) = 0.5*(ch13meas#(imeas%)+ch15meas#(imeas%))+273.13

IF flowid% = 1 THEN
      q#(imeas%) = 3.0314677e-9
      q#(imeas%) = q#(imeas%)+5.4316808e-7*ch12meas#(imeas%)
      q#(imeas%) = q#(imeas%)-2.6966884e-7*ch12meas#(imeas%)^2
      q#(imeas%) = q#(imeas%)+2.5165936e-7*ch12meas#(imeas%)^3
      q#(imeas%) = q#(imeas%)-7.6805921e-8*ch12meas#(imeas%)^4
      q#(imeas%) = q#(imeas%)+8.788411e-9*ch12meas#(imeas%)^5
END IF

IF flowid% = 2 THEN 'Flowmeter range 1 litre/min
      q#(imeas%) = 2.0563519e-8
      q#(imeas%) = q#(imeas%)+5.8194241e-7*ch12meas#(imeas%)
      q#(imeas%) = q#(imeas%)+1.4736029e-7*ch12meas#(imeas%)^2
      q#(imeas%) = q#(imeas%)+5.1967192e-7*ch12meas#(imeas%)^3
      q#(imeas%) = q#(imeas%)-2.2000702e-7*ch12meas#(imeas%)^4
      q#(imeas%) = q#(imeas%)+3.3736153e-8*ch12meas#(imeas%)^5
END IF

IF flowid% = 3 THEN
      q#(imeas%) = 20.758e-6*ch12meas#(imeas%)
      q#(imeas%) = q#(imeas%)+2.325e-7
END IF

IF flowid% = 4 THEN
      q#(imeas%) = 83.668e-6*ch12meas#(imeas%)
      q#(imeas%) = q#(imeas%)+1.029e-6
END IF

q#(imeas%) = q#(imeas%)*tmean#(imeas%)/273.13
u#(imeas%) = 1.82e-5*((tmean#(imeas%)/293.13)^0.76)*(EXP(0.5e-3*(ch1meas#(imeas%))))
p2abs# = ch4meas#(imeas%)*100.0 +pa#
p1abs# = ch1meas#(imeas%)*1.0e5 + p2abs#
```

```
po#(imeas%) = (p1abs#^2 - p2abs#^2)/2.0/1.013962e5
xnom#(imeas%) = po#(imeas%)/pomax#
ynom#(imeas%) = q#(imeas%)/qmax#

ret% = PlotPoint (ph%,PP1.GRAPH,xnom#(imeas%),ynom#(imeas%),5,14)

IF imeas%<n%+5 AND end.app%=0 THEN
        ret% = SetCtrlVal% (ph%,PP1.USERPROMPT,"Adjusting Pressure !")
        CALL RampAO (vcurr#,vdinc#,dramprate#)
        ret% = Fmt (temp$,"%s< Next Measurement is No. %i",(imeas%+2))
        ret% = SetCtrlVal% (ph%,PP1.USERPROMPT,temp$)
        CALL Delay (5.0)
    END IF

    imeas% = imeas% + 1
    j% = 0
    steady.app% = 0
WEND

er% = AO.VWrite (board,0,0.0)  'Set AO Ch.0 to 0V
ret% = SetInputMode% (ph%,PP1.END,1)
ret% = SetInputMode% (ph%,PP1.OK,0)

CALL OutputFile

ret% = AO.VWrite (board,0,0.0)
ret% = CloseInterfaceManager%
```

(Subroutines see Permeability Measurement)

3) Slip Coefficient Measurement

Labwindows Program for Slip Coefficient Measurement

Version 3.0
Y.B.P.KWAN 12.07.96

```
ret% = OpenInterrfaceManager%
ph% = LoadPanel% ("slipcoe2.uir",PP1)
ret% = DisplayPanel% (ph%)

ret% = AI.Configure% (board%,-1,1,10,1,0)
ret% = AO.Configure% (board%,0,1,0,10,0)
ret% = AO.Configure% (board%,1,1,0,10,0)

ret% = SetInputMode% (ph%,PP1.END,1)
WHILE   end.app% = 0
      CALL Checkkey'for END key
      vcurr# = 0.0
      er% = AO.VWrite (board,0,vcurr#)  'Set AO Ch.0 to 0V

      ret% = SetCtrlVal% (ph%,PP1.USERPROMPT,"Enter Specimen ID")
      beep
ret% = SetActiveCtrl% (PP1.ID)
j% = 0
WHILE j%=0 AND end.app%=0
      IF GetUserEvent% (0,pan%,ctrl%)<>0 THEN
            IF ctrl% = PP1.ID THEN
                  ret% = GetCtrlVal% (ph%,PP1.ID,specid$)
                  j% = 1
            ENDIF
      ENDIF
WEND

ret% = SetCtrlVal% (ph%,PP1.USERPROMPT,"Enter Phi^v  m^2")
beep
ret% = SetActiveCtrl% (PP1.PHI)
j% = 0
WHILE j%=0 AND end.app%=0
      IF GetUserEvent% (0,pan%,ctrl%)<>0 THEN
            IF ctrl% = PP1.PHI THEN
                  ret% = GetCtrlVal% (ph%,PP1.PHI,phiv#)
                  j% = 1
            ENDIF
      ENDIF
WEND

ret% = SetCtrlVal% (ph%,PP1.USERPROMPT,"Enter Phi^i  m")
beep
ret% = SetActiveCtrl% (PP1.PHII)
j% = 0
```

```
WHILE j%=0 AND end.app%=0
      IF GetUserEvent% (0,pan%,ctrl%)<>0 THEN
            IF ctrl% = PP1.PHII THEN
                  ret% = GetCtrlVal% (ph%,PP1.PHII,phii#)
                  j% = 1
            ENDIF
      ENDIF
WEND

ret% = SetCtrlVal% (ph%,PP1.USERPROMPT,"Select shim")
beep
ret% = SetActiveCtrl% (PP1.SHIM)
ok.app% = 0
ret% = SetInputMode% (ph%,PP1.OK,1)
ret% = SetInputMode% (ph%,PP1.END,1)
WHILE ok.app% = 0
      j% = 0
      WHILE j% = 0
            IF GetUserEvent% (0,pan%,ctrl%)<>0 THEN
                  IF ctrl% = PP1.SHIM THEN
                        ret% = GetCtrlVal% (ph%,PP1.SHIM,shimid%)
                        j% = 1
                  ENDIF
            ENDIF
      WEND

      k% = 0
      WHILE ok.app%=0 AND j%=1 AND end.app%=0
            IF k%=0 THEN
                  ret% = SetCtrlVal% (ph%,PP1.USERPROMPT,"OK to accept,END to retype")
            ENDIF
            CALL Checkkey
            k% = 1
      WEND

      IF end.app%=1 THEN
            ret% = SetCtrlVal% (ph%,PP1.USERPROMPT,"Reselect shim")
            end.app% = 0
      ENDIF
WEND
ok.app% = 0

IF shimid%=1 THEN
      wshim# = 8.032e-3
      gap# = 19.4e-6
      pmax# = 4.9
      presid% = 4
END IF

IF shimid%=2 THEN
      wshim# = 8.035e-3
      gap# = 28.77e-6
      pmax# = 4.9
      presid% = 4
END IF
```

```
IF shimid%=3 THEN
        wshim# = 8.036e-3
        gap# = 36.42e-6
        pmax# = 4.9
        presid% = 4
END IF

IF shimid%=4 THEN
        wshim# = 8.029e-3
        gap# = 46.62e-6
        pmax# = 2.5
        presid% = 3
END IF

IF shimid%=5 THEN
        wshim# = 8.021e-3
        gap# = 54.26e-6
        pmax# = 1.2
        presid% = 2
END IF

IF shimid%=6 THEN
        wshim# = 7.983e-3
        gap# = 64.28e-6
        pmax# = 0.6
        presid% = 2
END IF

IF shimid%=7 THEN
        wshim# = 8.007e-3
        gap# = 71.22e-6
        pmax# = 0.5
        presid% = 2
END IF

IF shimid%=8 THEN
        wshim# = 7.906e-3
        gap# = 84.15e-6
        pmax# = 0.25
        presid% = 2
END IF

IF shimid%=9 THEN
        wshim# = 7.966e-3
        gap# = 99.62e-6
        pmax# = 0.15
        presid% = 2
END IF

IF shimid%=10 THEN
        wshim# = 7.865e-3
        gap# = 103.58e-6
        pmax# = 0.12
        presid% = 2
END IF
```

```
ret% = SetCtrlVal% (ph%,PP1.USERPROMPT,"Select flow range")
ret% = SetActiveCtrl% (PP1.FLOW)
ok.app% = 0
ret% = SetInputMode% (ph%,PP1.OK,1)
ret% = SetInputMode% (ph%,PP1.END,1)
WHILE ok.app% = 0
      j% = 0
      WHILE j% = 0
            IF GetUserEvent% (0,pan%,ctrl%)<>0 THEN
                  IF ctrl% = PP1.FLOW THEN
                        ret% = GetCtrlVal% (ph%,PP1.FLOW,flowid%)
                        j% = 1
                  END IF
            END IF
      WEND

WEND

ret% = SetCtrlVal% (ph%,PP1.USERPROMPT,"Install Flowmeter & Press OK")
beep
status% = 0
ok.app% = 0
ret% = SetInputMode% (ph%,PP1.OK,1)
ret% = SetInputMode% (ph%,PP1.END,1)
WHILE status%=0 AND end.app%=0
      CALL Checkkey
      IF ok.app%=1 THEN
            status% = 1
            ok.app% = 0
      ENDIF
WEND

ret% = SetCtrlVal% (ph%,PP1.USERPROMPT,"Install Pr.Sensor & Press OK")
beep
status% = 0
ok.app% = 0
ret% = SetInputMode% (ph%,PP1.OK,1)
ret% = SetInputMode% (ph%,PP1.END,1)
WHILE status%=0 AND end.app%=0
      CALL Checkkey
      IF ok.app%=1 THEN
            status% = 1
            ok.app% = 0
      ENDIF
WEND

ret% = Fmt (temp$,"%s<Default Pmax = %f[w5p3] Bar",pmax#)
ret% = SetCtrlVal% (ph%,PP1.USERPROMPT,temp$)
CALL Delay (2.0)
ret% = SetCtrlVal% (ph%,PP1.PMAX,pmax#)
ret% = SetCtrlVal% (ph%,PP1.USERPROMPT,"Enter Max Pressure")
beep
ret% = SetActiveCtrl% (PP1.PMAX)
j% = 0
WHILE j%=0 AND end.app%=0
      IF GetUserEvent% (0,pan%,ctrl%)<>0 THEN
```

```
            IF ctrl% = PP1.PMAX THEN
                ret% = GetCtrlVal% (ph%,PP1.PMAX,pmax#)
                j% = 1
            ENDIF
        ENDIF
WEND

ret% = SetCtrlVal% (ph%,PP1.USERPROMPT,"Enter No of Increments")
beep
ret% = SetCtrlVal% (ph%,PP1.NMEA,10)
ret% = SetActiveCtrl% (PP1.NMEA)
j% = 0
WHILE j%=0 AND end.app%=0
        IF GetUserEvent% (0,pan%,ctrl%)<>0 THEN
            IF ctrl% = PP1.NMEA THEN
                ret% = GetCtrlVal% (ph%,PP1.NMEA,n%)
                j% = 1
            ENDIF
        ENDIF
WEND

pmin# = 0.1*pmax#
IF pmin#<0.02 THEN
        pmin# = 0.02
END IF
pinc# = (pmax#-pmin#)/CDBL(n%)
vmin# = 2.0 * (pmin#-0.02) '5Bar <=> 10V
vmax# = 2.0 * (pmax#-0.02) '5Bar <=> 10V
vinc# = 2.0 * ((pmax#-pmin#)/CDBL(n%))

ret% = SetCtrlVal% (ph%,PP1.PMIN,pmin#)
ret% = SetInputMode% (ph%,PP1.END,1)

ret% = SetCtrlVal% (ph%,PP1.USERPROMPT,"Press OK to start")
beep
status% = 0
ok.app% = 0
ret% = SetInputMode% (ph%,PP1.OK,1)
ret% = SetInputMode% (ph%,PP1.END,1)
WHILE status%=0 AND end.app%=0
        CALL Checkkey
        IF ok.app%=1 THEN
            status% = 1
            ok.app% = 0
        ENDIF
WEND

ret% = SetInputMode% (ph%,PP1.OK,0)
ret% = SetCtrlVal% (ph%,PP1.USERPROMPT,"Adjusting Pressure Pmin")

IF vmin#<>vcurr# THEN
        vstep# = vmin# - vcurr#
        ramprate1# = vstep#/5.0
        CALL RampAO (vcurr#,vstep#,ramprate1#)
ENDIF
```

```
ret% = SetCtrlVal (ph%,PP1.USERPROMPT,"Pressure up to Pmin")
CALL Delay (1.5)

CALL ClearIA (chlist%(),channum-1)

nch% = 2
npts% = 50
samplr# = 2000.0
scanr# = 100.0
scount& = CLNG(nch% * npts%)

chlist%(0) = 6
chlist%(1) = 0

er% = SCAN.Op% (board,nch%,chlist%(),gnlist%(),scanbuf%(),scount&,samplr#,scanr#)

i% = 0
WHILE i%<npts%
      ch6buf%(i%) = scanbuf%(i%*2)
      ch0buf%(i%) = scanbuf%(i%*2+1)
      i% = i%+1
WEND

er% = DAQ.VScale%(board,6,gnlist%(6),aigain#(6),aioffset#(6),CLNG(npts%),ch6buf%(),
      mch6buf#())
er% = DAQ.VScale%(board,0,gnlist%(0),aigain#(0),aioffset#(0),CLNG(npts%),ch0buf%(),
      mch0buf#())

CALL Mean(mch6buf#(),npts%,chmean#(6))
ret% = Fmt (temp$,"%s< Pa = %f[w7p5] Bar",chmean#(6))
ret% = SetCtrlVal (ph%,PP1.USERPROMPT,temp$)
CALL Delay (1.5)

CALL Mean(mch0buf#(),npts%,chmean#(0))
ret% = Fmt (temp$,"%s< Ta = %f[w4p1] degC",chmean#(0))
ret% = SetCtrlVal (ph%,PP1.USERPROMPT,temp$)
CALL Delay (1.5)

pa# = chmean#(6) * 1.0e5
ta# = chmean#(0) + 273.15


CALL ClearIA (chlist%(),channum-1)

nch% = 6
npts% = 500
samplr# = 10000.0
scanr# = 1000.0
scount& = nch% * npts%

chlist%(0) = 1
chlist%(1) = 2
chlist%(2) = 3
chlist%(3) = 4
chlist%(4) = 12
chlist%(5) = 0
```

```
store.app% = 0
imeas% = 0
j% = 0
ret% = SetInputMode% (ph%,PP1.OK,0)
ret% = SetInputMode% (ph%,PP1.END,1)
ret% = DeletePlots% (ph%,PP1.GRAPH)
ret% = SetGraphAttribute% (ph%,PP1.GRAPH,0,"Flow vs Pressure Gradient Plot")
ret% = SetGraphAttribute% (ph%,PP1.GRAPH,10,"dP/dx")
ret% = SetGraphAttribute% (ph%,PP1.GRAPH,18,"Qm")
ret% = SetGraphAttribute% (ph%,PP1.GRAPH,15,11)
ret% = SetGraphAttribute% (ph%,PP1.GRAPH,13,0)
ret% = SetGraphAttribute% (ph%,PP1.GRAPH,23,11)
ret% = SetAxisRange% (ph%,PP1.GRAPH,0,0.0,1.1,0,0.0,1.1)

WHILEimeas%<n%+1 AND end.app%=0

    pin# = pmin# + pinc# * CDBL(imeas%)
    ret% = Fmt (temp$,"%s< P^in  = %f[w6p4] Bar",pin#)
    ret% = SetCtrlVal (ph%,PP1.USERPROMPT,temp$)
    ret% = SetInputMode% (ph%,PP1.STORE,1)
    ret% = SetActiveCtrl% (PP1.STORE)

    j%=0
    WHILE   store.app%=0 AND end.app%=0
        er% = SCAN.Op
(board,nch%,chlist%(),gnlist%(),scanbuf%(),scount&,samplr#,scanr#)
    i% = 0
    WHILE i%<npts%
        ch1buf%(i%) = scanbuf%(i%*6)
        ch2buf%(i%) = scanbuf%(i%*6+1)
        ch3buf%(i%) = scanbuf%(i%*6+2)
        ch4buf%(i%) = scanbuf%(i%*6+3)
        ch12buf%(i%) = scanbuf%(i%*6+4)
        ch0buf%(i%) = scanbuf%(i%*6+5)
        i% = i%+1
    WEND
    er% = DAQ.VScale%(board,1,gnlist%(1),aigain#(1),aioffset#(1),CLNG(npts%),
        ch1buf%(),mch1buf#())
    er% = DAQ.VScale%(board,2,gnlist%(2),aigain#(2),aioffset#(2),CLNG(npts%),
        ch2buf%(),mch2buf#())
    er% = DAQ.VScale%(board,3,gnlist%(3),aigain#(3),aioffset#(3),CLNG(npts%),
        ch3buf%(),mch3buf#())
    er% = DAQ.VScale%(board,4,gnlist%(4),aigain#(4),aioffset#(4),CLNG(npts%),
        ch4buf%(),mch4buf#())
    er% = DAQ.VScale%(board,12,gnlist%(12),aigain#(12),aioffset#(12),CLNG(npts%),
        ch12buf%(),mch12buf#())
    er% = DAQ.VScale%(board,0,gnlist%(0),aigain#(0),aioffset#(0),CLNG(npts%),
        ch0buf%(),mch0buf#())

    CALL Mean(mch1buf#(),npts%,mean1#)
    CALL Mean(mch2buf#(),npts%,mean2#)
    CALL Mean(mch3buf#(),npts%,mean3#)
    CALL Mean(mch4buf#(),npts%,mean4#)
    CALL Mean(mch12buf#(),npts%,mean12#)
    CALL Mean(mch0buf#(),npts%,mean0#)
```

```
ret% = SetCtrlVal% (ph%,PP1.P12,mean1#)
ret% = SetCtrlVal% (ph%,PP1.PIN,mean2#)
ret% = SetCtrlVal% (ph%,PP1.P2,mean3#)
ret% = SetCtrlVal% (ph%,PP1.PE,mean4#)
ret% = SetCtrlVal% (ph%,PP1.Q,mean12#)
ret% = SetCtrlVal% (ph%,PP1.TA,mean0#)

p1# = (mean1#+mean3#)*1.0e5+pa#
p2# = mean3#*1.0e5+pa#
pexit# = ((1.0928*p2#^2-0.0928*p1#^2)^0.5-pa#)/1.0e5

ret% = SetCtrlVal% (ph%,PP1.PSET,pexit#)

IF j%=0 AND k%=0 AND end.app%=0 THEN
    ret% = SetCtrlVal% (ph%,PP1.USERPROMPT,"Press STORE to store")
    j% = 1
    beep
ENDIF
CALL Checkkey
WEND
ret% = SetInputMode% (ph%,PP1.STORE,0)

IF imeas%<>n% THEN
    ret% = SetCtrlVal% (ph%,PP1.USERPROMPT,"Calculating Data !")
ENDIF

CALL Bw.LPF (mch1buf#(),npts%,scanr#,0.1*scanr#,5,mch1buf#())
CALL Bw.LPF (mch2buf#(),npts%,scanr#,0.1*scanr#,5,mch2buf#())
CALL Bw.LPF (mch3buf#(),npts%,scanr#,0.1*scanr#,5,mch3buf#())
CALL Bw.LPF (mch4buf#(),npts%,scanr#,0.1*scanr#,5,mch4buf#())
CALL Bw.LPF (mch12buf#(),npts%,scanr#,0.1*scanr#,5,mch12buf#())
CALL Bw.LPF (mch0buf#(),npts%,scanr#,0.1*scanr#,5,mch0buf#())

CALL FMean (mch1buf#(),npts%,ch1meas#(imeas%))
CALL FMean (mch2buf#(),npts%,ch2meas#(imeas%))
CALL FMean (mch3buf#(),npts%,ch3meas#(imeas%))
CALL FMean (mch4buf#(),npts%,ch4meas#(imeas%))
CALL FMean (mch12buf#(),npts%,ch12meas#(imeas%))
CALL FMean (mch0buf#(),npts%,ch0meas#(imeas%))

ret% = SetCtrlVal% (ph%,PP1.P12,ch1meas#(imeas%))
ret% = SetCtrlVal% (ph%,PP1.PIN,ch2meas#(imeas%))
ret% = SetCtrlVal% (ph%,PP1.P2,ch3meas#(imeas%))
ret% = SetCtrlVal% (ph%,PP1.PE,ch4meas#(imeas%))
ret% = SetCtrlVal% (ph%,PP1.Q,ch12meas#(imeas%))
ret% = SetCtrlVal% (ph%,PP1.TA,ch0meas#(imeas%))

pmean#(imeas%) = 0.5e5*ch1meas#(imeas%)+1.0e5*ch3meas#(imeas%)+pa#
tmean#(imeas%) = ch0meas#(imeas%)+273.15

IF flowid% = 1 THEN
    q#(imeas%) = 3.0315e-9
    q#(imeas%) = q#(imeas%)+5.4317e-7*ch12meas#(imeas%)
    q#(imeas%) = q#(imeas%)-2.6967e-7*ch12meas#(imeas%)^2
    q#(imeas%) = q#(imeas%)+2.5166e-7*ch12meas#(imeas%)^3
```

```
        q#(imeas%) = q#(imeas%)-7.6806e-8*ch12meas#(imeas%)^4
        q#(imeas%) = q#(imeas%)+8.7884e-9*ch12meas#(imeas%)^5
END IF

IF flowid% = 2 THEN
        q#(imeas%) = 2.0564e-8
        q#(imeas%) = q#(imeas%)+5.8194e-7*ch12meas#(imeas%)
        q#(imeas%) = q#(imeas%)+1.4736e-7*ch12meas#(imeas%)^2
        q#(imeas%) = q#(imeas%)+5.1967e-7*ch12meas#(imeas%)^3
        q#(imeas%) = q#(imeas%)-2.2001e-7*ch12meas#(imeas%)^4
        q#(imeas%) = q#(imeas%)+3.3736e-8*ch12meas#(imeas%)^5
    END IF

    IF flowid% = 3 THEN
        q#(imeas%) = 20.758e-6*ch12meas#(imeas%)'Q in m^3/s
        q#(imeas%) = q#(imeas%)+2.325e-7
    END IF

    IF flowid% = 4 THEN
        q#(imeas%) = 83.668e-6*ch12meas#(imeas%)'Q in m^3/s  assumed linear
        q#(imeas%) = q#(imeas%)+1.029e-6
    END IF

    u#(imeas%) = 1.82e-5*((tmean#(imeas%)/293.15)^0.76)*(EXP(1e-8*(pmean#(imeas%)-
1e5)))
    q#(imeas%) = q#(imeas%)*1.013962e5*tmean#(imeas%)/pmean#(imeas%)/273.15

    dp#(imeas%) = 1.0e5*ch1meas#(imeas%)/0.03

    rhomean# = 1.184*pmean#(imeas%)*293.15/1.0e5/tmean#(imeas%)
    a# = 2.0*rhomean#*dp#(imeas%)/u#(imeas%)^2
    b# = phii#/phiv#
    phie# = ((b#^2+4.0*a#*phii#)^0.5-b#)/2.0/a#
    sigma#(imeas%) = gap# / phie#^0.5
    re#(imeas%) = 2.0*q#(imeas%)/wshim#/u#(imeas%)
    ret% = SetCtrlVal% (ph%,PP1.RE,re#(imeas%))

    IF imeas%<n% THEN
        ret% = SetCtrlVal% (ph%,PP1.USERPROMPT,"Adjusting Pressure !")
        ramprate# = vinc#/5.0   'Ramp up in 5sec/increment
        CALL RampAO (vcurr#,vinc#,ramprate#)
        ret% = Fmt (temp$,"%s< Next Measurement is No. %i",(imeas%+2))
        ret% = SetCtrlVal% (ph%,PP1.USERPROMPT,temp$)
        CALL Delay (1.5)
        ENDIF
        imeas% = imeas% + 1
        j% = 0
        store.app% = 0
        CALL Checkkey   'for END
WEND

er% = AO.VWrite (board,0,0.0#)
ret% = SetCtrlVal% (ph%,PP1.USERPROMPT,"")
ret% = SetInputMode% (ph%,PP1.STORE,0)
ret% = SetInputMode% (ph%,PP1.OK,1)
```

```
CALL MaxMin1D (dp#(),n%+1,xmax#,ixmax%,xmin#,ixmin%)
CALL MaxMin1D (q#(),n%+1,ymax#,iymax%,ymin#,iymin%)

ret% = DeletePlots% (ph%,PP1.GRAPH)
ret% = SetAxisRange% (ph%,PP1.GRAPH,0,0.0,1.1,0,0.0,1.1)
i% = 0
WHILE i%<n%+1
        qsnom# = dp#(i%)*gap#^3*wshim#/12.0/u#(i%)/ymax#
        xnom#(i%) = dp#(i%)/xmax#
        ynom#(i%) = q#(i%)/ymax#
        ret% = PlotPoint (ph%,PP1.GRAPH,xnom#(i%),ynom#(i%),3,0)
        ret% = PlotPoint (ph%,PP1.GRAPH,xnom#(i%),qsnom#,5,14)
        i% = i%+1
WEND

CALL LinFit (dp#(),q#(),n%+1,qfit#(),slope#,intercept#,mse#)
nintercept# = intercept#/ymax#
nslope# = slope#*xmax#/ymax#
ret% = PlotLine (ph%,PP1.GRAPH,0.0,nintercept#,1.0,nslope#+nintercept#,4)

CALL OutputFile
ok.app% = 0
ret% = SetCtrlVal% (ph%,PP1.USERPROMPT,"Another run ?")
ret% = SetInputMode% (ph%,PP1.OK,1)
ret% = SetInputMode% (ph%,PP1.END,1)
ret% = SetInputMode% (ph%,PP1.STORE,0)
WHILE ok.app%=0 AND end.app%=0
        CALL Checkkey
    WEND
WEND

ret% = AO.VWrite (board,0,0.0)
ret% = CloseInterfaceManager%
```

(Subroutines see permeability measurement)

Appendix H Machine Drawings for Toolings, Permeability Measurement Rig, and Thrust bearing Test Rig

ALL DIMENSIONS IN MILLIMETRES UNLESS OTHERWISE STATED. IF IN DOUBT ASK.

DRAWING NO.	
ISSUE	MODIFICATION

TYPE K THERMOCOUPLE FARNELL 146-867 (4m)

CONNECTORS FARNELL 146-867 (4m)

THERMOCOUPLE INTERFACE CARD

ARCOM SIC-7 TYPE K

PIN 50 PIN 1

50WAY IDC SOCKET FARNELL 311-080

50WAY IDC SOCKET FARNELL 311-080

50WAY IDC HEADER FARNELL 460-339

RS 445-172 (7m)

RS 445-273 (7m)

CH1 CH2 CH3 CH4 CH5 CH6 CH12

+12V 0V -12V

LCD 470R LCD 470R LCD 1.2K

+12V 0V -12V

RED WHITE BLUE BROWN

FROM POWER SUPPLY BOX ED291 B102 1A

TERMINAL BOX A

TERMINAL BOX B

CB100 CABLE ASSEMBLY

CB100 CABLE ASSEMBLY

PIN 1-50 PIN 51-100

NATIONAL INSTRUMRNTS AT-MIO-16DL-9

PERMEABILITY RIG
SENSOR DISTRIBUTION BOX

THIRD ANGLE PROJECTION			SCALE	FINISH
GENERAL TOLERANCE ON DIMENSIONS	JOB No.	No. OF SETS REQ.		
MACHINED				
UNMACHINED				
OTHER DIMENSIONS AS STATED				
WELD WHERE SHOWN THUS — L				
MACHINE WHERE SHOWN THUS ⊿				

SHEET SIZE A1

ITEM	PART No.	DESCRIPTION	No. OFF	MATL.	SPEC.	REMARKS

DRAWN	CHK	DATE
Y.B.P.KWAN		26/6/91

TITLE: PERMEABILITY RIG SENSOR WIRING DIAGRAM

SCHOOL OF INDUSTRIAL & MANUFACTURING SCIENCE
CRANFIELD

DRAWING No. ED291 B101 1A

SHT OF SHEETS

REMOVE ALL SHARP EDGES

DRAWING NO.	
ISSUE	MODIFICATION

ALL DIMENSIONS IN MILLIMETRES UNLESS OTHERWISE STATED. IF IN DOUBT ASK.

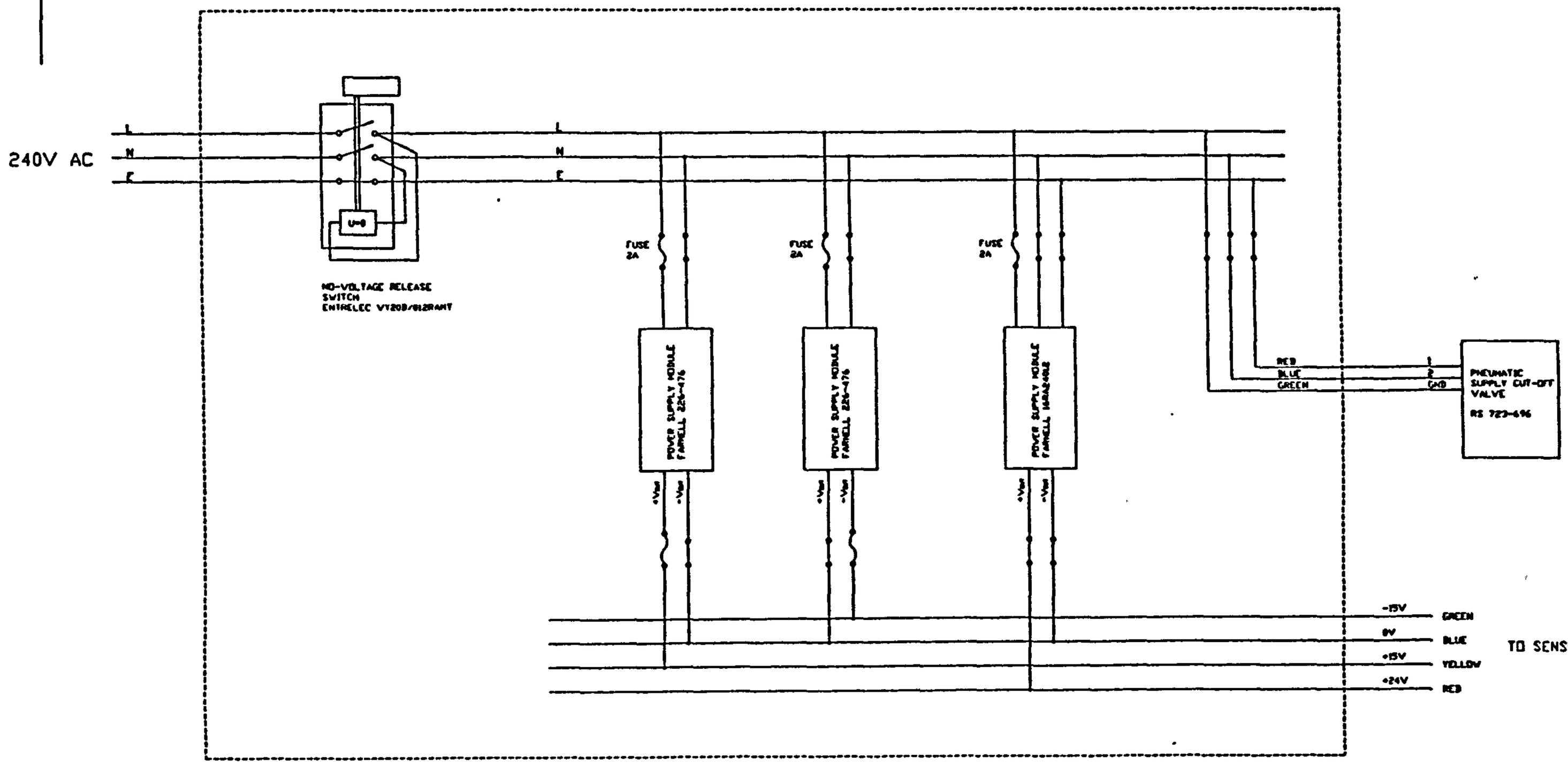

PERMEABILITY RIG POWER SUPPLY BOX

REMOVE ALL SHAPE EDGES

THIRD ANGLE PROJECTION			SHEET SIZE A1
GENERAL TOLERANCE ON DIMENSIONS	JOB No.	No. OF SETS REQ.	SCALE
MACHINED			
UNMACHINED			
OTHER DIMENSIONS AS STATED			FINISH
WELD WHERE SHOWN THUS ⌒ L			
MACHINE WHERE SHOWN THUS ⌭			

ITEM	PART No.	DESCRIPTION	No. OFF	MATL.	SPEC.	REMARKS

DRAWN	CHK	DATE
Y.B.PAVAR		26.05.95

TITLE: PERMEABILITY RIG POWER SUPPLY WIRING DIAGRAM

SCHOOL OF INDUSTRIAL & MANUFACTURING SCIENCE
CRANFIELD

DRAWING No. ED291 B102 1A

SHT. OF SHEETS

DRAWING No.

ISSUE	MODIFICATION

ALL DIMENSIONS IN MILLIMETRES UNLESS OTHERWISE STATED. IF IN DOUBT ASK.

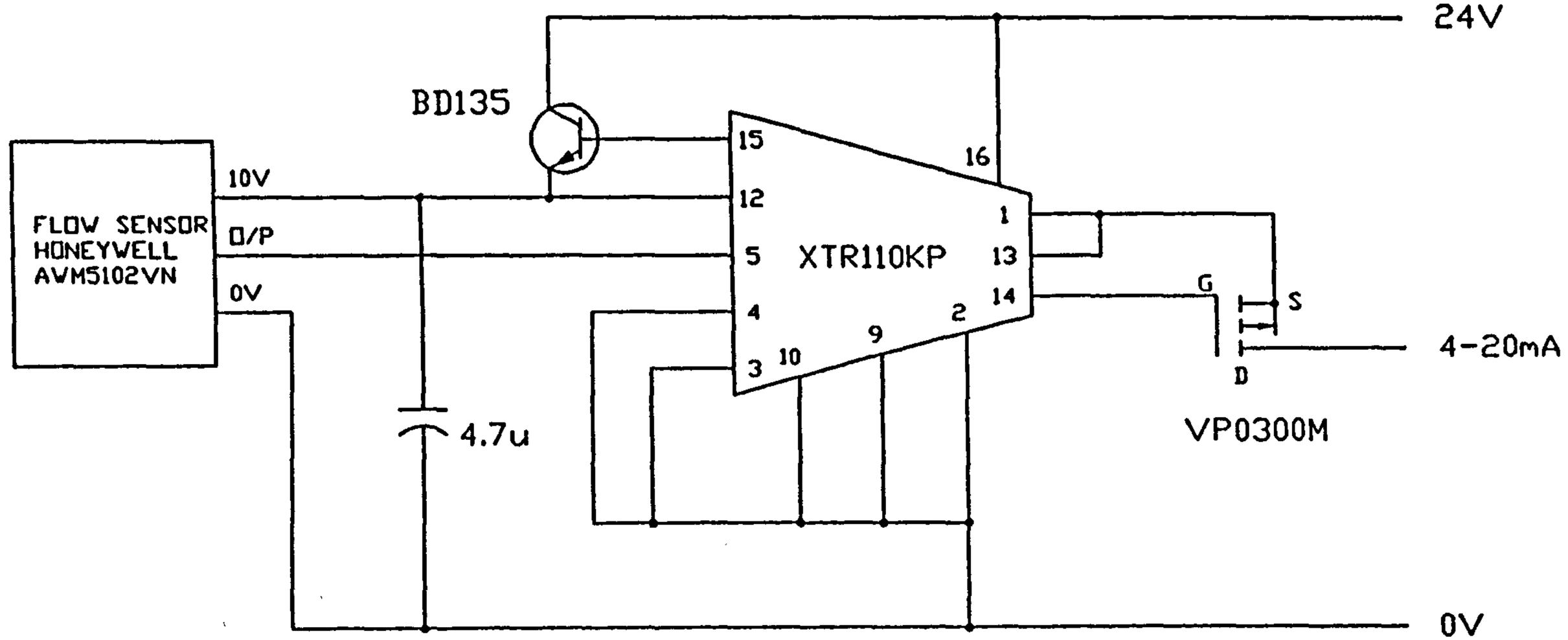

REMOVE ALL SHAPE EDGES

				ITEM	PART No.	DESCRIPTION	No. OFF	MATL.	SPEC.	REMARKS

THIRD ANGLE PROJECTION			SHEET SIZE A4				
GENERAL TOLERANCE ON DIMENSIONS MACHINED UNMACHINED OTHER DIMENSIONS AS STATED WELD WHERE SHOWN THUS ⌒ L MACHINE WHERE SHOWN THUS ⊿	JOB No.	No. OF SETS REQ.	SCALE 1:1	DRAWN	CHK	DATE	TITLE: FLOWMETER DRIVER CIRCUIT DIAGRAM
				Y.B.P.KWAN		23.07.95	
			FINISH	SCHOOL OF INDUSTRIAL & MANUFACTURING SCIENCE CRANFIELD			DRAWING No. ED291 B103 4A SHT. 1 OF 1 SHEETS

DRAWING No.	
ISSUE	MODIFICATION

ALL DIMENSIONS IN MILLIMETRES UNLESS OTHERWISE STATED. IF IN DOUBT ASK.

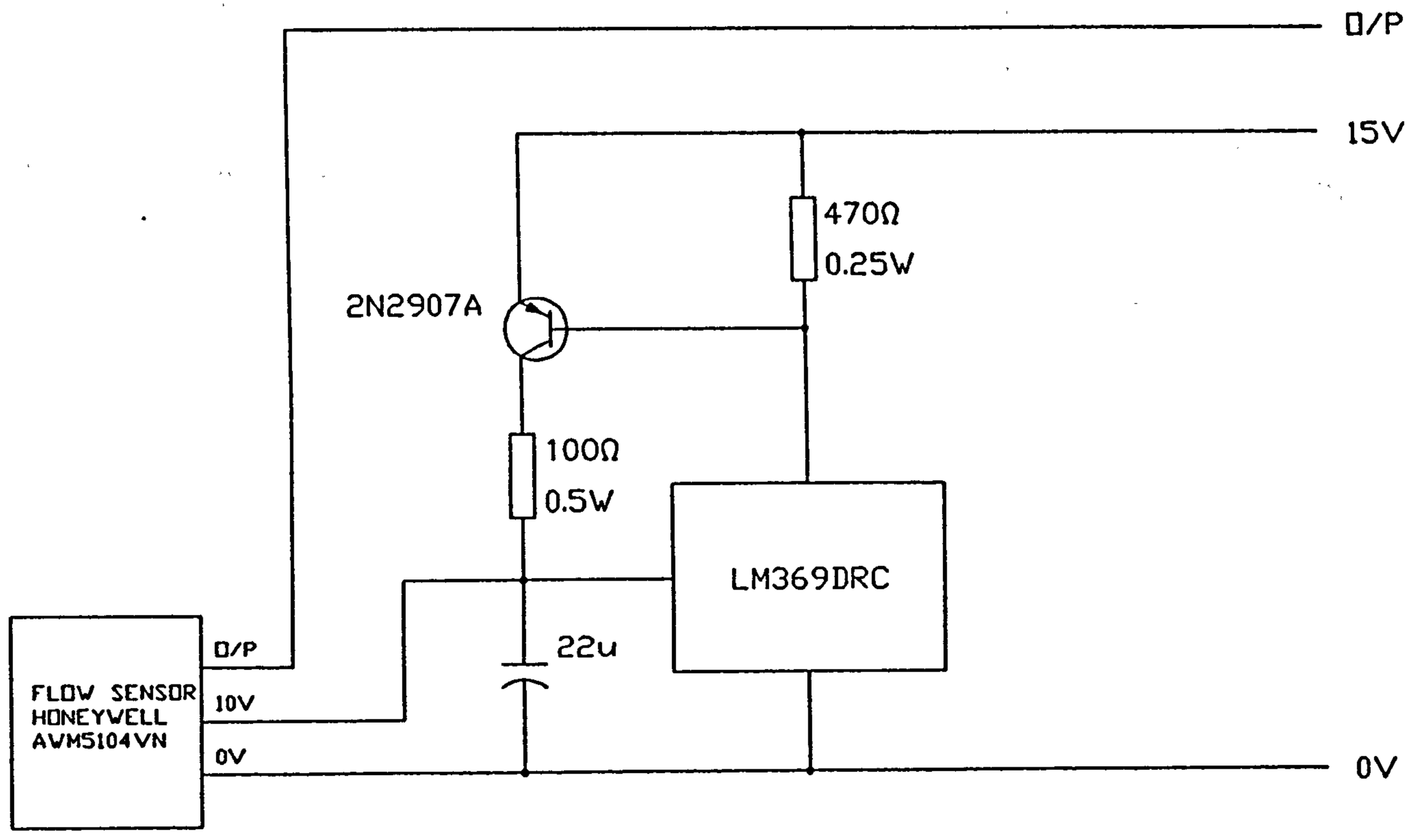

REMOVE ALL SHAPE EDGES

THIRD ANGLE PROJECTION	SHEET SIZE A4	ITEM	PART No.	DESCRIPTION	No. OFF	MATL.	SPEC.	REMARKS
GENERAL TOLERANCE ON DIMENSIONS MACHINED UNMACHINED OTHER DIMENSIONS AS STATED WELD WHERE SHOWN THUS ⌒ L MACHINE WHERE SHOWN THUS ⊿	JOB No. / No. OF SETS REQ.	SCALE 1:1	DRAWN Y.B.P.KWAN	CHK	DATE 28.08.95	TITLE: FLOWMETER DRIVER CIRCUIT DIAGRAM		
		FINISH	SCHOOL OF INDUSTRIAL & MANUFACTURING SCIENCE CRANFIELD			DRAWING No. ED291 B104 4A		
						SHT. 1 OF 1 SHEETS		

ALL DIMENSIONS IN MILLIMETRES UNLESS OTHERWISE STATED. IF IN DOUBT ASK.

ISSUE	MODIFICATION

THRUST BEARING RIG
SENSOR DISTRIBUTION BOX

NATIONAL INSTRUMENTS AT-MIO-16L-9

REMOVE ALL SHARP EDGES

THIRD ANGLE PROJECTION

ITEM	PART No.	DESCRIPTION	No. OFF	MATL.	SPEC.	REMARKS

SIZE A0

SCALE

FINISH

TITLE: THRUST BEARING RIG SENSOR WIRING DIAGRAM

SCHOOL OF INDUSTRIAL & MANUFACTURING SCIENCE
CRANFIELD

DRAWING No. CRPR C00 00

SHT 1 OF 1 SHEET 1

DRAWING No.	
ISSUE	MODIFICATION

ALL DIMENSIONS IN MILLIMETRES UNLESS OTHERWISE STATED. IF IN DOUBT ASK.

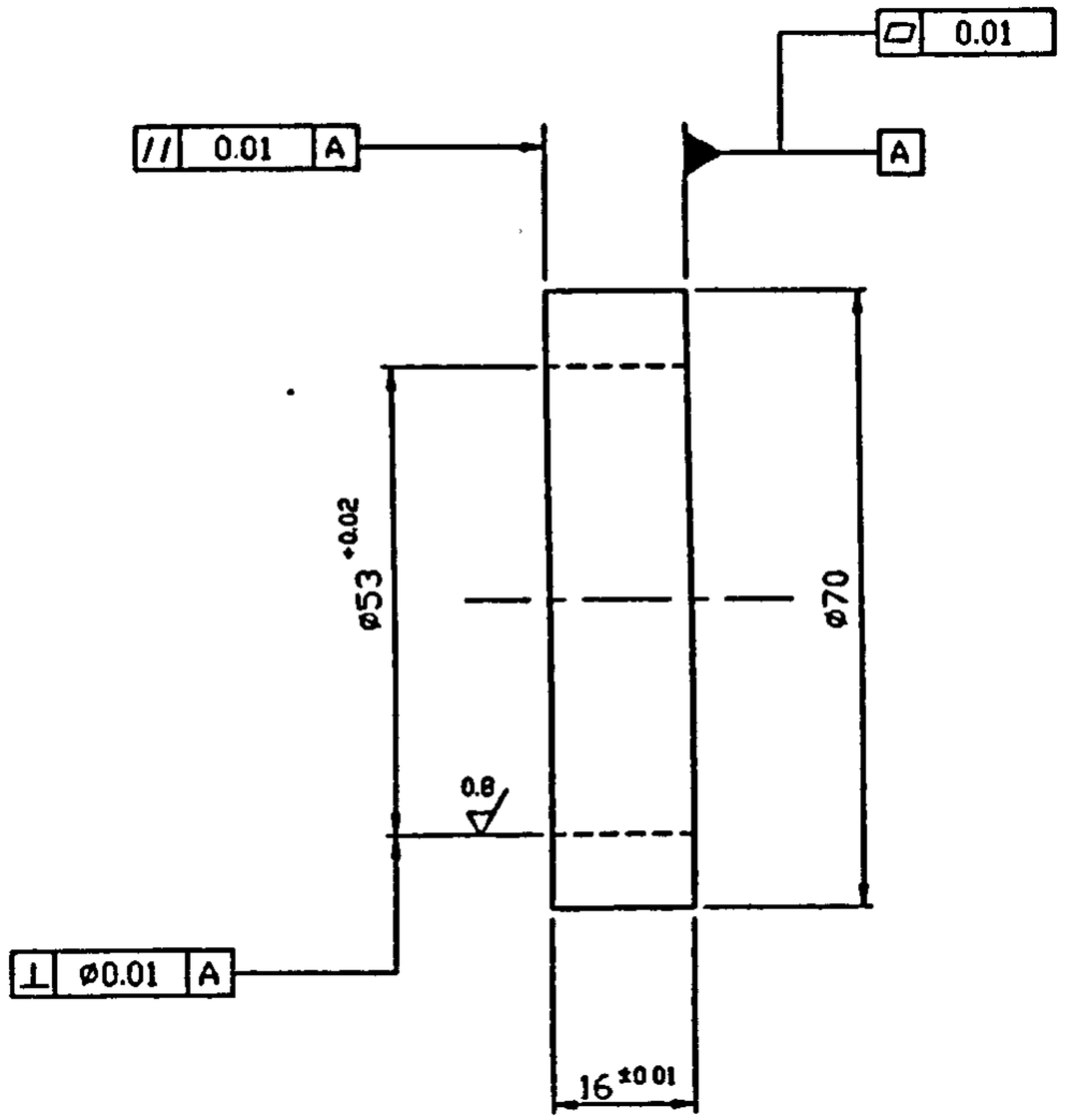

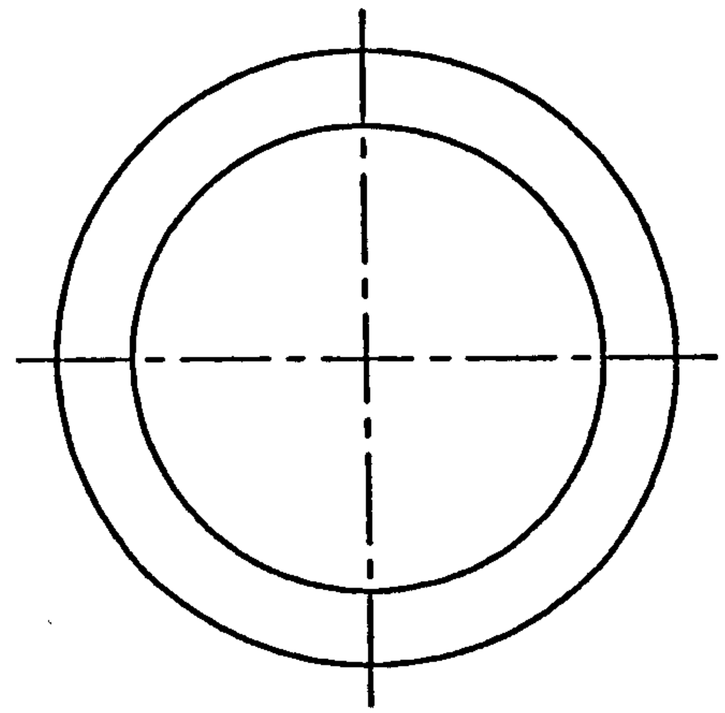

REMOVE ALL SHAPE EDGES

THIRD ANGLE PROJECTION	SHEET SIZE A3	ITEM	PART No.	DESCRIPTION	No. OFF	MATL.	SPEC.	REMARKS
					1	GRAPHITE	IG11	

GENERAL TOLERANCE ON DIMENSIONS MACHINED UNMACHINED OTHER DIMENSIONS AS STATED	JOB No.	No. OF SETS REQ.	SCALE 1:1	DRAWN	CHK	DATE	TITLE: FIXED CAVITY MOULD SLEEVE
				Y.B.P.KWAN		10.11.94	
WELD WHERE SHOWN THUS			FINISH	SCHOOL OF INDUSTRIAL & MANUFACTURING SCIENCE CRANFIELD			DRAWING No. MD291 A101 3A
MACHINE WHERE SHOWN THUS							SHT. 1 OF 1 SHEETS

DRAWING No.	
ISSUE	MODIFICATION

ALL DIMENSIONS IN MILLIMETRES UNLESS OTHERWISE STATED. IF IN DOUBT ASK.

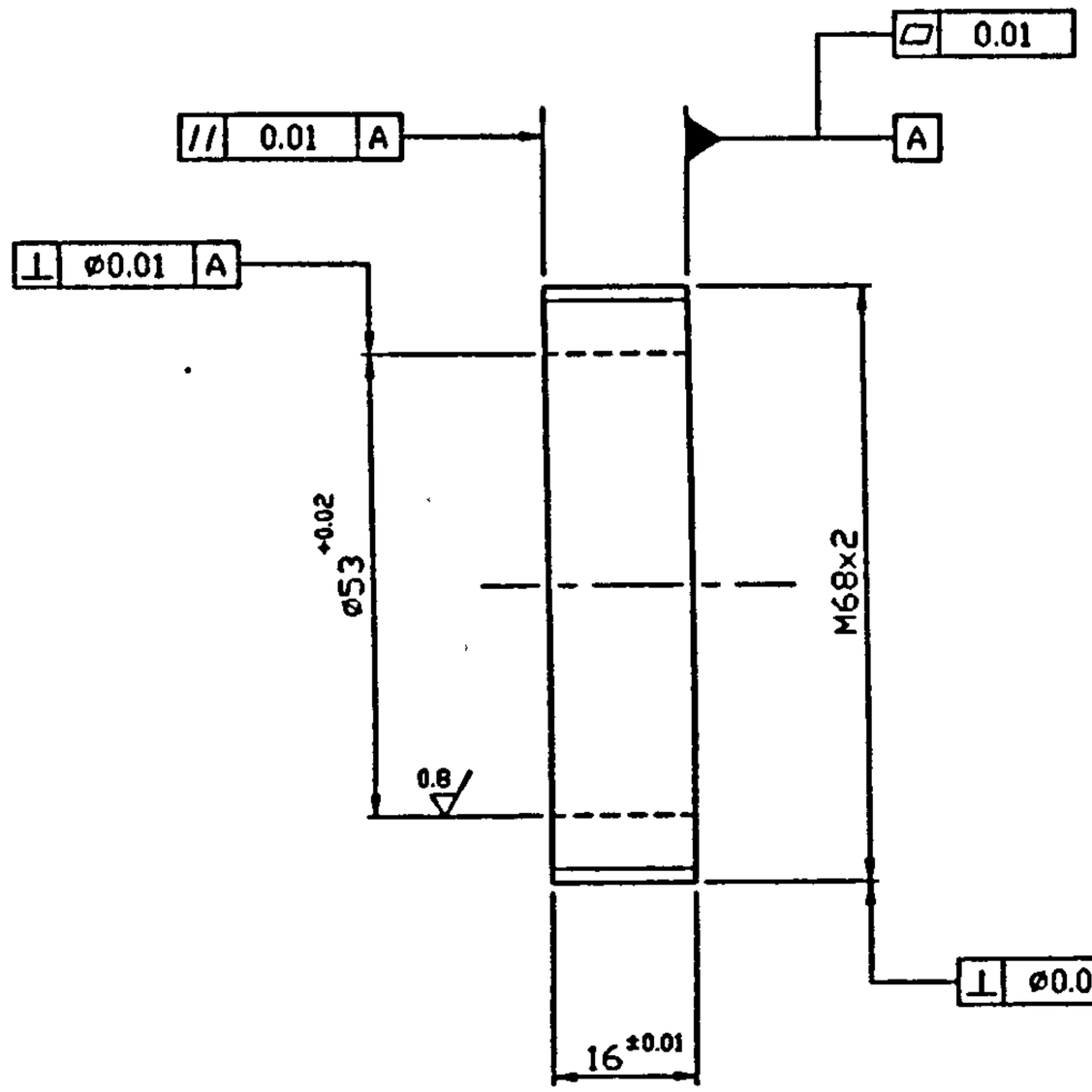

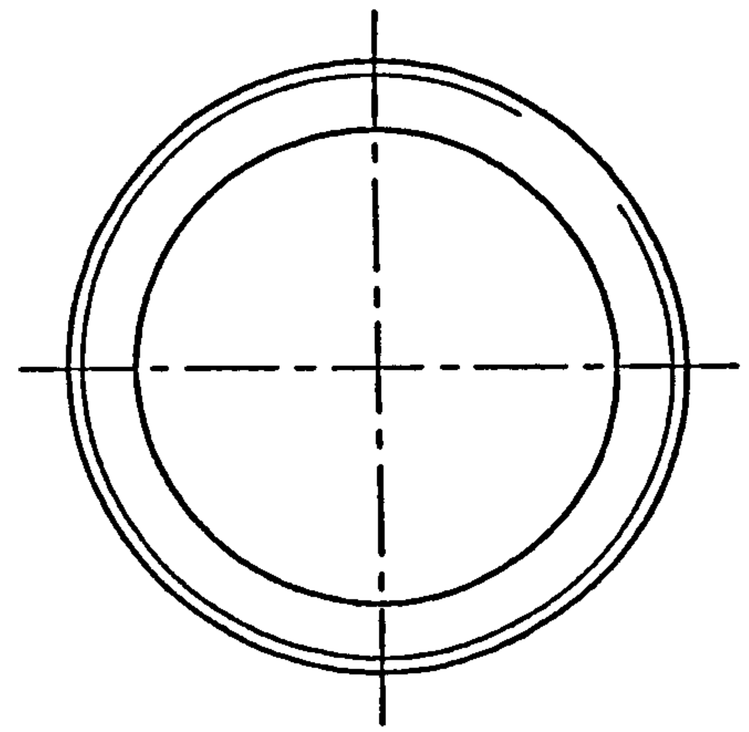

REMOVE ALL SHAPE EDGES

ITEM	PART No.	DESCRIPTION	No. OFF	MATL.	SPEC.	REMARKS
			1	GRAPHITE	IG11	

THIRD ANGLE PROJECTION

SHEET SIZE	DRAWN	CHK	DATE
A3	Y.B.P.KWAN		02.02.95

TITLE: POROUS CAVITY MOULD SLEEVE

GENERAL TOLERANCE ON DIMENSIONS	JOB No.	No. OF SETS REQ.
MACHINED		
UNMACHINED		
OTHER DIMENSIONS AS STATED		
WELD WHERE SHOWN THUS ⌒ L		
MACHINE WHERE SHOWN THUS ✓		

SCALE 1:1

FINISH

SCHOOL OF INDUSTRIAL & MANUFACTURING SCIENCE

CRANFIELD

DRAWING No. MD291 A103 3A

SHT. 1 OF 1 SHEETS

DRAWING No.	
ISSUE	MODIFICATION

ALL DIMENSIONS IN MILLIMETRES UNLESS OTHERWISE STATED. IF IN DOUBT ASK.

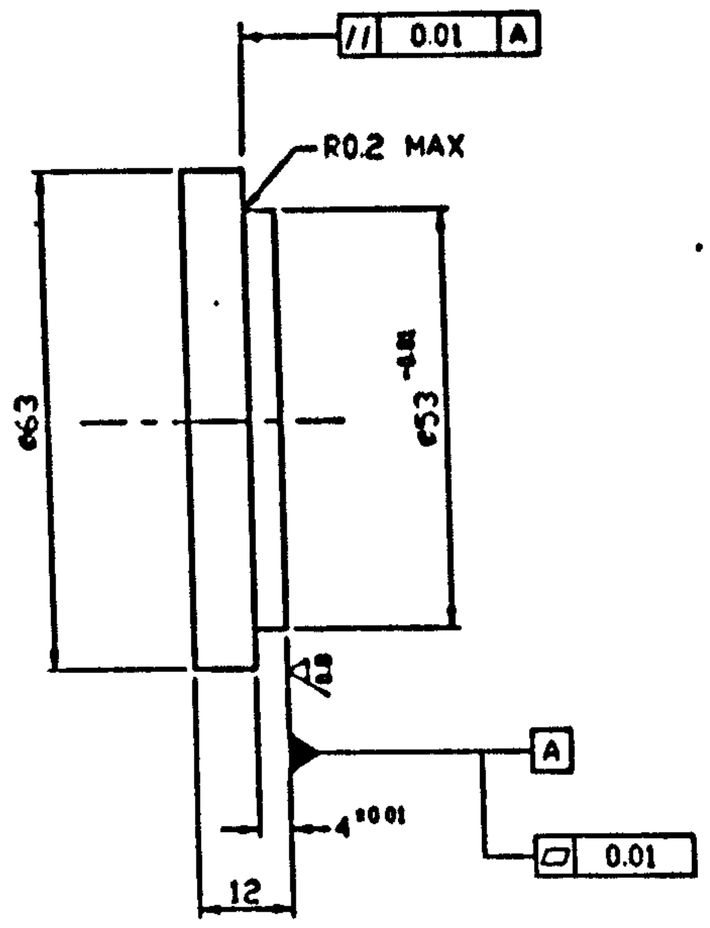

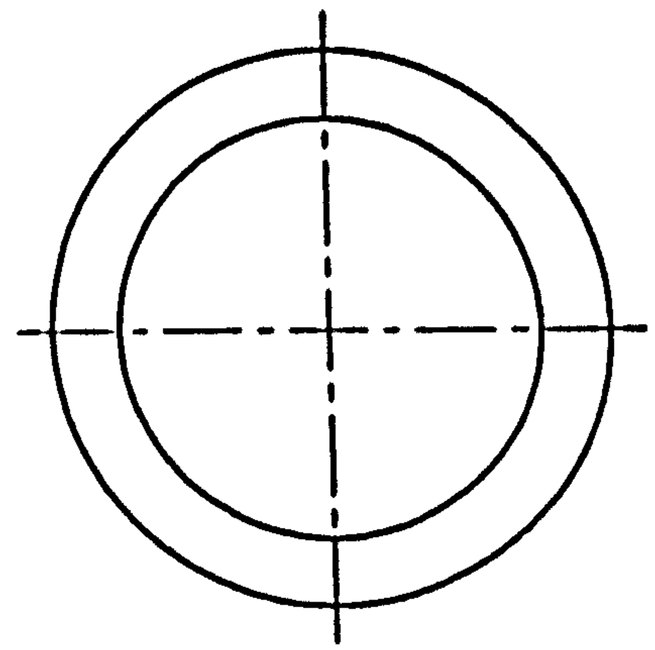

REMOVE ALL SHAPE EDGES

THIRD ANGLE PROJECTION	SHEET SIZE A3	ITEM	PART No.	DESCRIPTION	No. OFF	MATL.	SPEC.	REMARKS
					2	POROUS GRAPHITE	SE30	

GENERAL TOLERANCE ON DIMENSIONS	JOB No.	No. OF SETS REQ.	SCALE 1:1	DRAWN	CHK	DATE	TITLE:
MACHINED				Y.B.P.KWAN		02.02.95	POROUS CAVITY MOULD BASE
UNMACHINED							
OTHER DIMENSIONS AS STATED			FINISH	SCHOOL OF INDUSTRIAL & MANUFACTURING SCIENCE			DRAWING No. MD291 A104 3A
WELD WHERE SHOWN THUS				CRANFIELD			SHT. 1 OF 1 SHEETS
MACHINE WHERE SHOWN THUS							

DRAWING No.	
ISSUE	MODIFICATION

ALL DIMENSIONS IN MILLIMETRES UNLESS OTHERWISE STATED. IF IN DOUBT ASK.

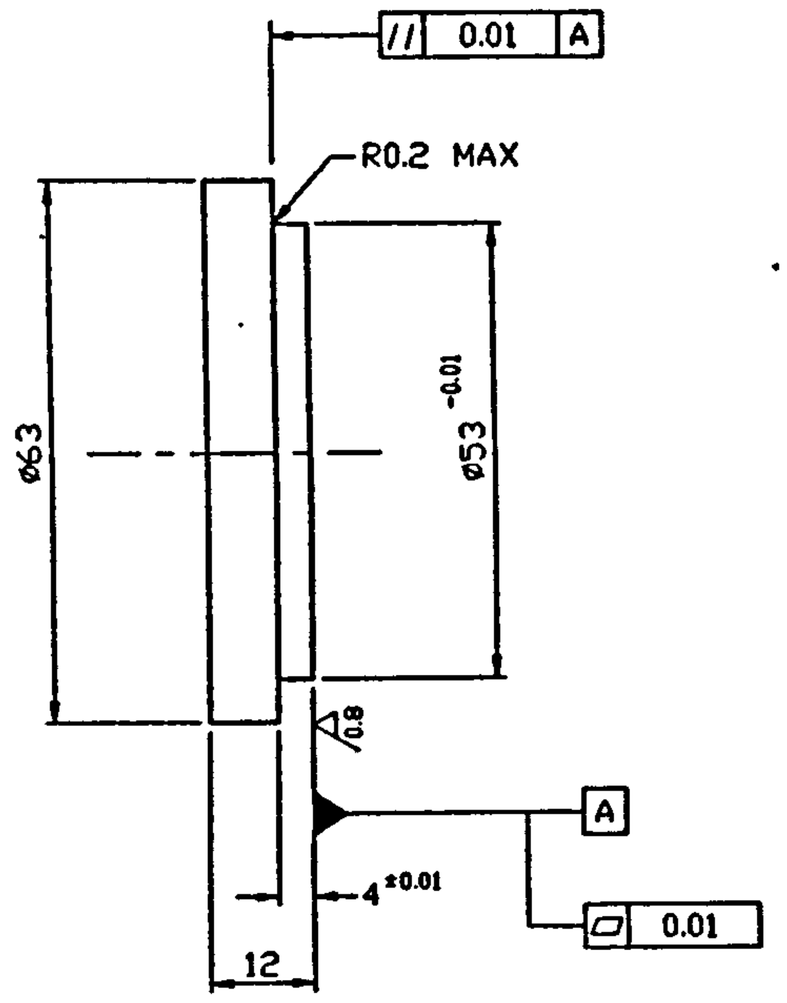

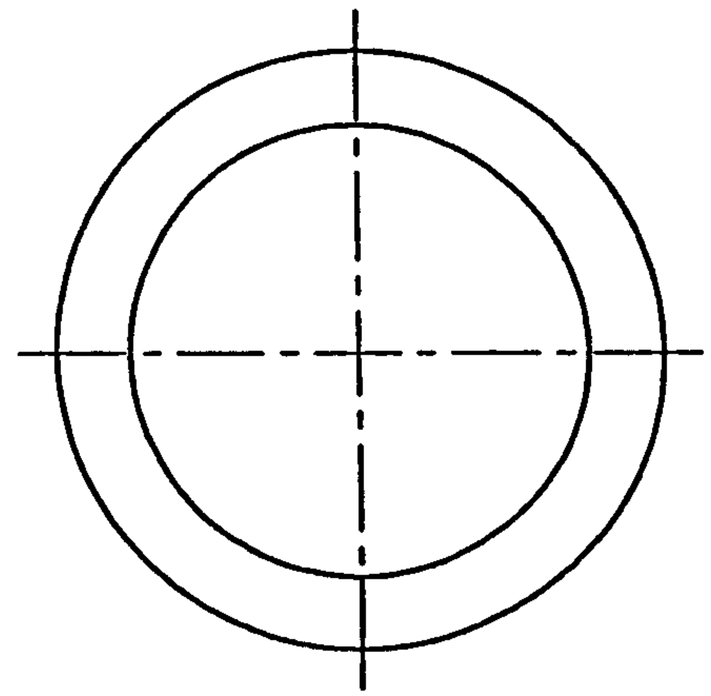

REMOVE ALL SHAPE EDGES

THIRD ANGLE PROJECTION	SHEET SIZE A3	ITEM	PART No.	DESCRIPTION	No. OFF	MATL.	SPEC.	REMARKS
					2	POROUS GRAPHITE	SE30	

GENERAL TOLERANCE ON DIMENSIONS MACHINED UNMACHINED OTHER DIMENSIONS AS STATED	JOB No.	No. OF SETS REQ.	SCALE 1:1	DRAWN	CHK	DATE	TITLE:
				Y.B.P.KWAN		02.02.95	POROUS CAVITY MOULD BASE
WELD WHERE SHOWN THUS			FINISH	SCHOOL OF INDUSTRIAL & MANUFACTURING SCIENCE			DRAWING No. MD291 A104 3A
MACHINE WHERE SHOWN THUS				CRANFIELD			SHT. 1 OF 1 SHEETS

DRAWING No.	
ISSUE	MODIFICATION

ALL DIMENSIONS IN MILLIMETRES UNLESS OTHERWISE STATED. IF IN DOUBT ASK.

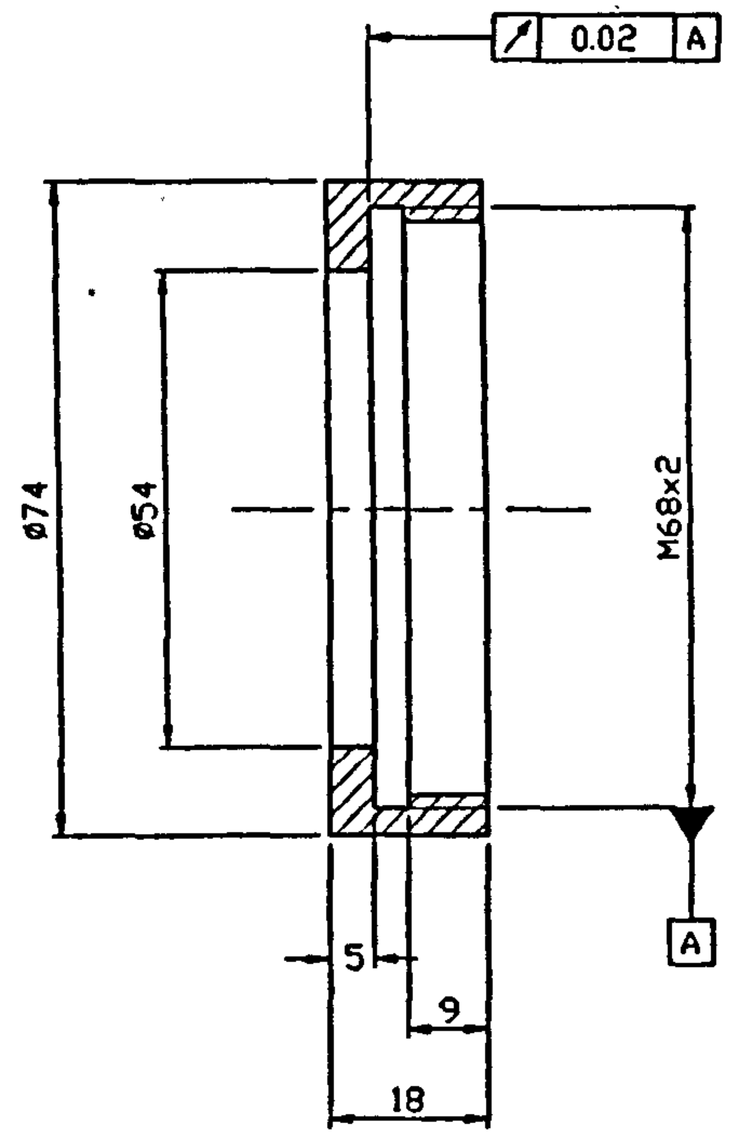

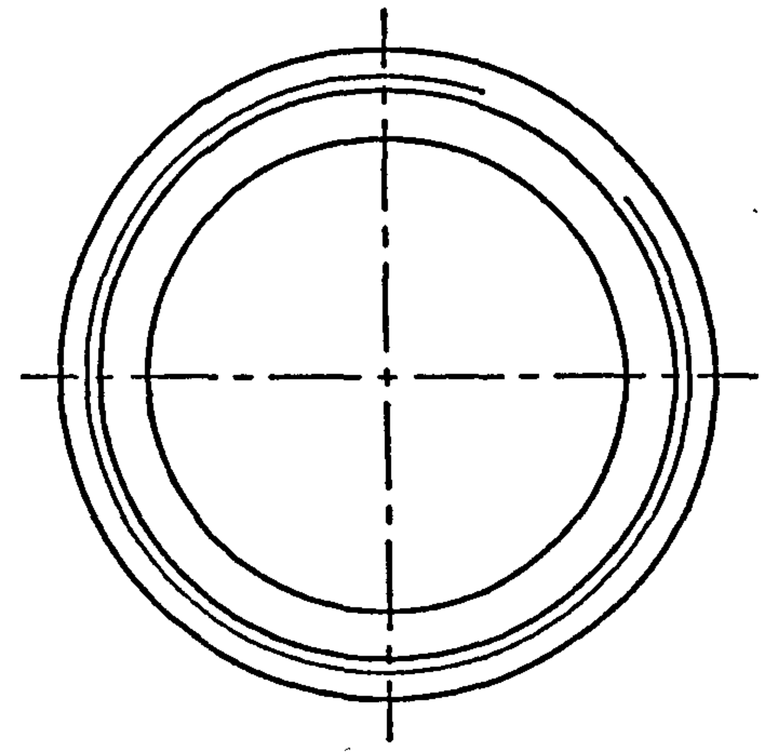

REMOVE ALL SHAPE EDGES

THIRD ANGLE PROJECTION	SHEET SIZE A3	ITEM	PART No.	DESCRIPTION	2 No. OFF	GRAPHITE MATL.	IG11 SPEC.	REMARKS

GENERAL TOLERANCE ON DIMENSIONS MACHINED UNMACHINED OTHER DIMENSIONS AS STATED WELD WHERE SHOWN THUS ⌒ L MACHINE WHERE SHOWN THUS ⊿	JOB No.	No. OF SETS REQ.	SCALE 1:1	FINISH	DRAWN	CHK	DATE	TITLE: POROUS CAVITY MOULD LOCKING RING
					Y.B.P.KWAN		02.02.95	

SCHOOL OF INDUSTRIAL & MANUFACTURING SCIENCE
CRANFIELD

DRAWING No. MD291 A105 3A

SHT. 1 OF 1 SHEETS

DRAWING No.	
ISSUE	MODIFICATION

ALL DIMENSIONS IN MILLIMETRES UNLESS OTHERWISE STATED. IF IN DOUBT ASK.

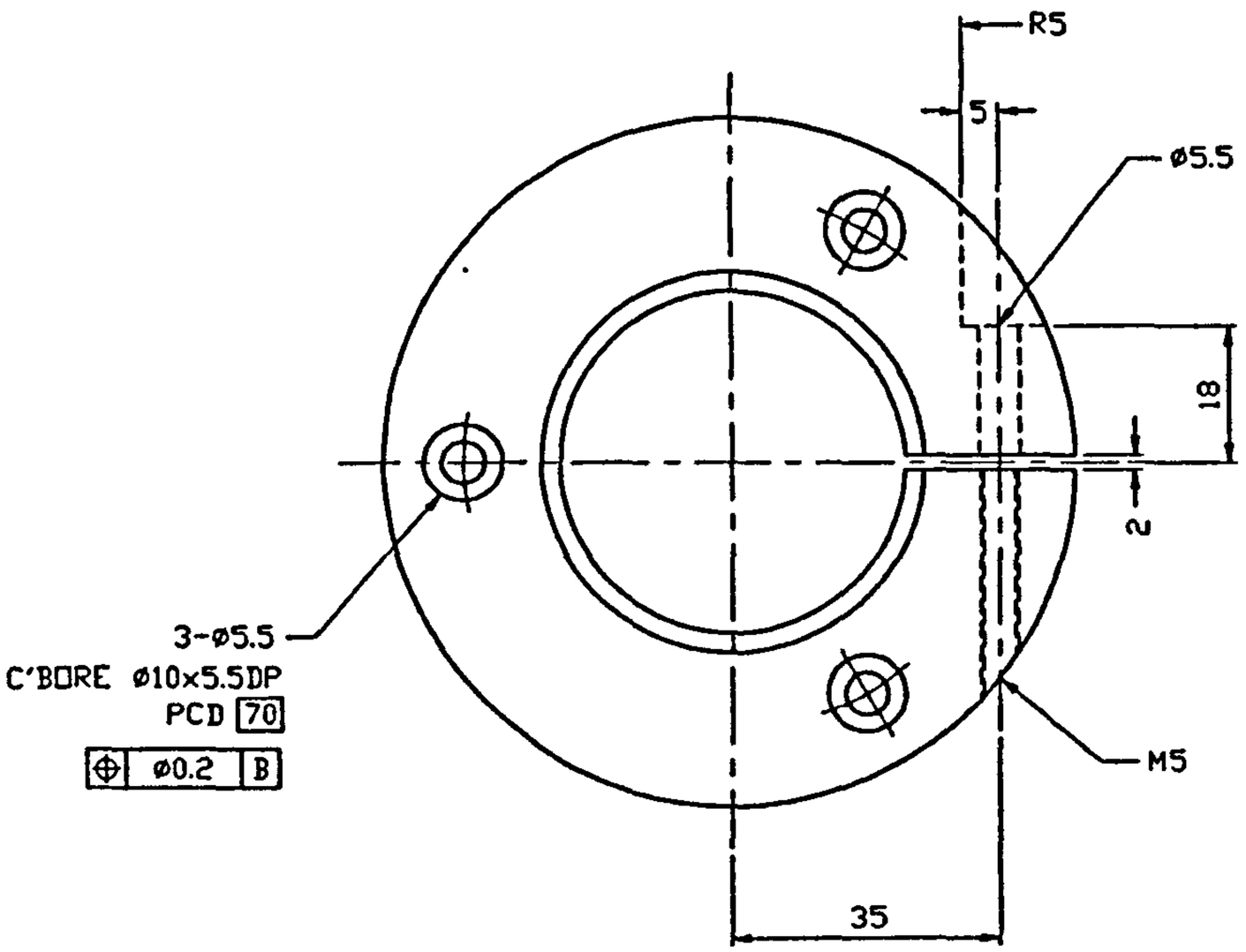

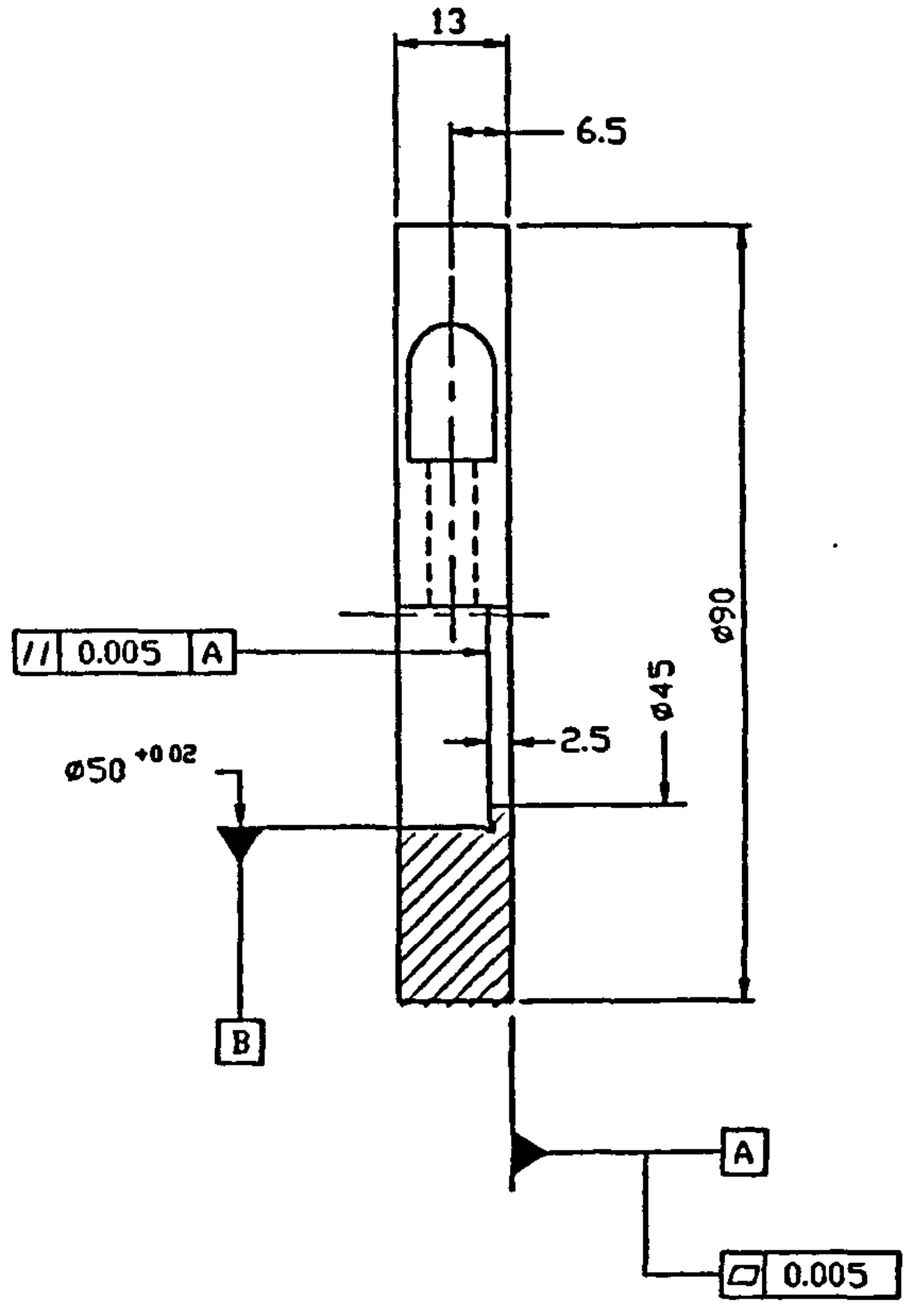

REMOVE ALL SHAPE EDGES

THIRD ANGLE PROJECTION	SHEET SIZE A3	ITEM	PART No.	DESCRIPTION	No. OFF	MATL.	SPEC.	REMARKS
					1	SST	440C	

GENERAL TOLERANCE ON DIMENSIONS	JOB No.	No. OF SETS REQ.	SCALE	DRAWN	CHK	DATE	TITLE:
MACHINED			1:1	Y.B.P.KWAN		02.02.95	SAMPLE HOLDER
UNMACHINED							
OTHER DIMENSIONS AS STATED			FINISH	SCHOOL OF INDUSTRIAL & MANUFACTURING SCIENCE			DRAWING No. MD291 A106 3A
WELD WHERE SHOWN THUS				CRANFIELD			SHT. 1 OF 1 SHEETS
MACHINE WHERE SHOWN THUS							

DRAWING No.	
ISSUE	MODIFICATION

ALL DIMENSIONS IN MILLIMETRES UNLESS OTHERWISE STATED. IF IN DOUBT ASK.

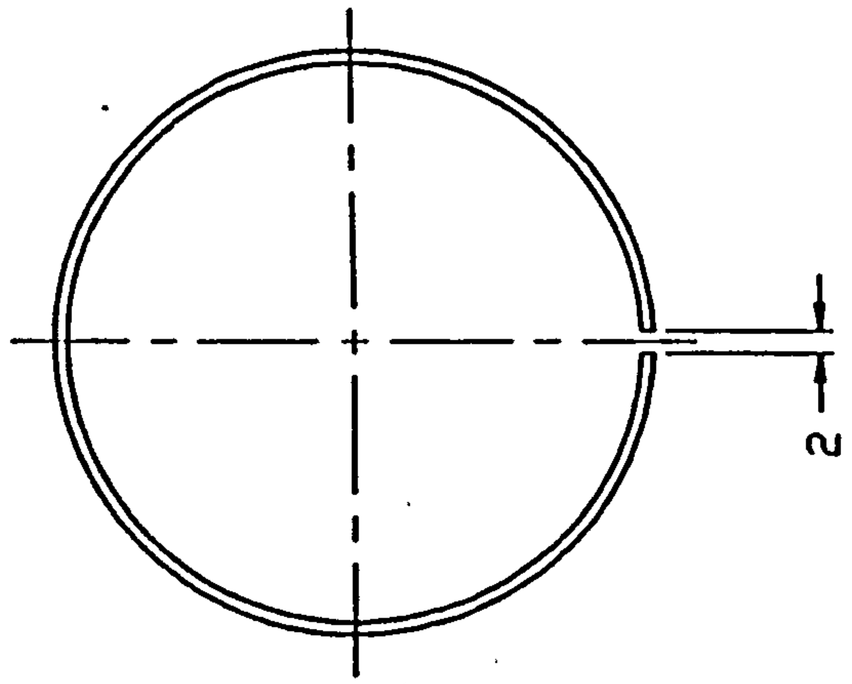

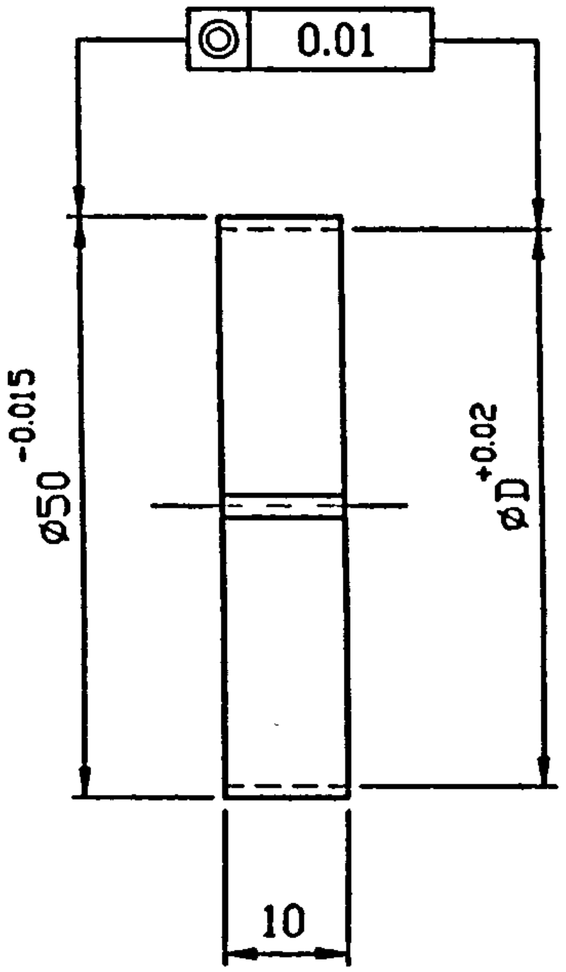

øD=46,47,48,49

REMOVE ALL SHAPE EDGES

THIRD ANGLE PROJECTION			SHEET SIZE A4				1 EACH	BRASS		
				ITEM	PART No.	DESCRIPTION	No. OFF	MATL.	SPEC.	REMARKS
GENERAL TOLERANCE ON DIMENSIONS MACHINED UNMACHINED OTHER DIMENSIONS AS STATED WELD WHERE SHOWN THUS ⌒ L MACHINE WHERE SHOWN THUS ✓	JOB No.	No. OF SETS REQ.	SCALE 1:1	DRAWN	CHK	DATE	TITLE: ADAPTOR SLEEVE			
				Y.B.P.KWAN		02.02.95				
			FINISH	SCHOOL OF INDUSTRIAL & MANUFACTURING SCIENCE CRANFIELD			DRAWING No. MD291 A107 4A			
							SHT. 1 OF 1 SHEETS			

DRAWING No.	
ISSUE	MODIFICATION

ALL DIMENSIONS IN MILLIMETRES UNLESS OTHERWISE STATED. IF IN DOUBT ASK.

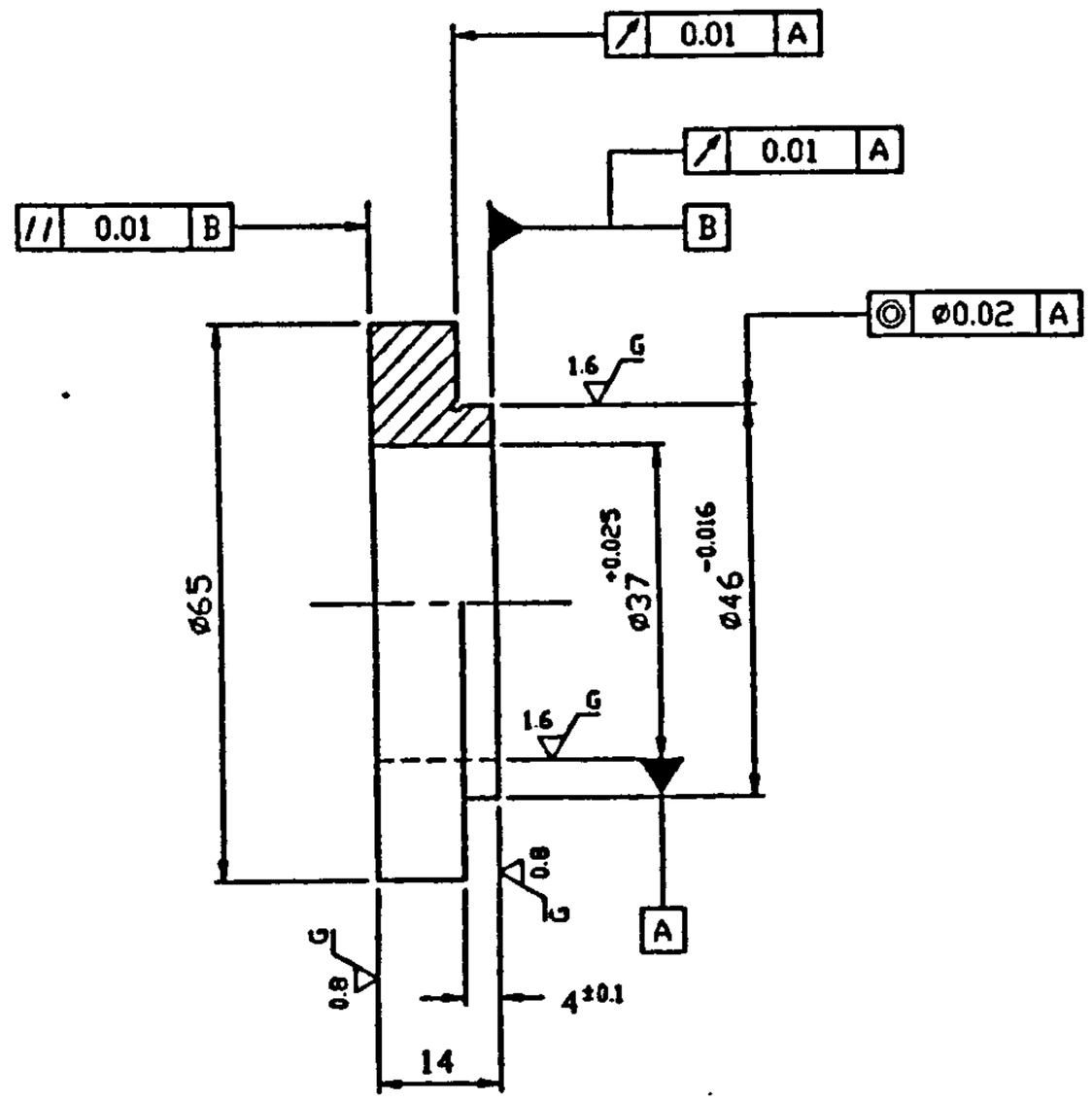

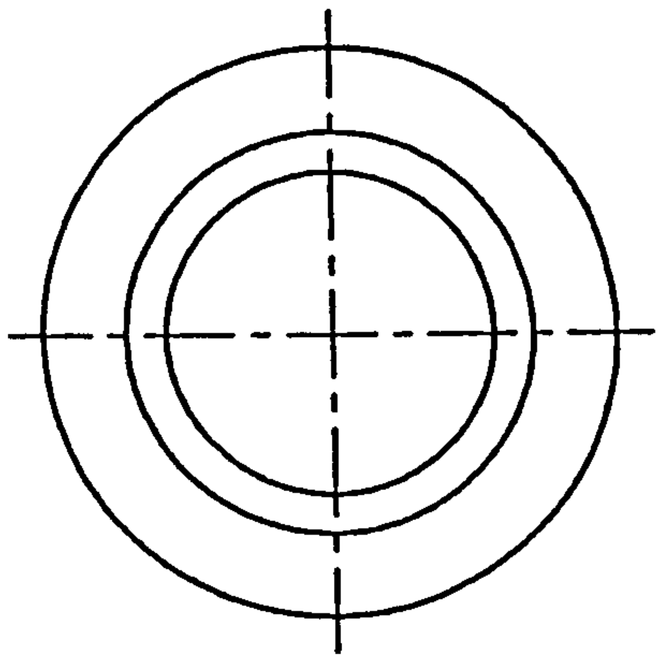

REMOVE ALL SHAPE EDGES

THIRD ANGLE PROJECTION	SHEET SIZE A3	ITEM	PART No.	DESCRIPTION	No. OFF	MATL.	SPEC.	REMARKS
					1	SST	440C	

GENERAL TOLERANCE ON DIMENSIONS MACHINED UNMACHINED OTHER DIMENSIONS AS STATED WELD WHERE SHOWN THUS ⌒ L MACHINE WHERE SHOWN THUS ⊿	JOB No.	No. OF SETS REQ.	SCALE 1:1	FINISH HRc 50-55	DRAWN	CHK	DATE	TITLE: BASE
					Y.B.P.KWAN		14.11.95	

SCHOOL OF INDUSTRIAL & MANUFACTURING SCIENCE
CRANFIELD

DRAWING No. MD291 A201 3A

SHT. 1 OF 1 SHEETS

DRAWING No.	
ISSUE	MODIFICATION

ALL DIMENSIONS IN MILLIMETRES UNLESS OTHERWISE STATED. IF IN DOUBT ASK.

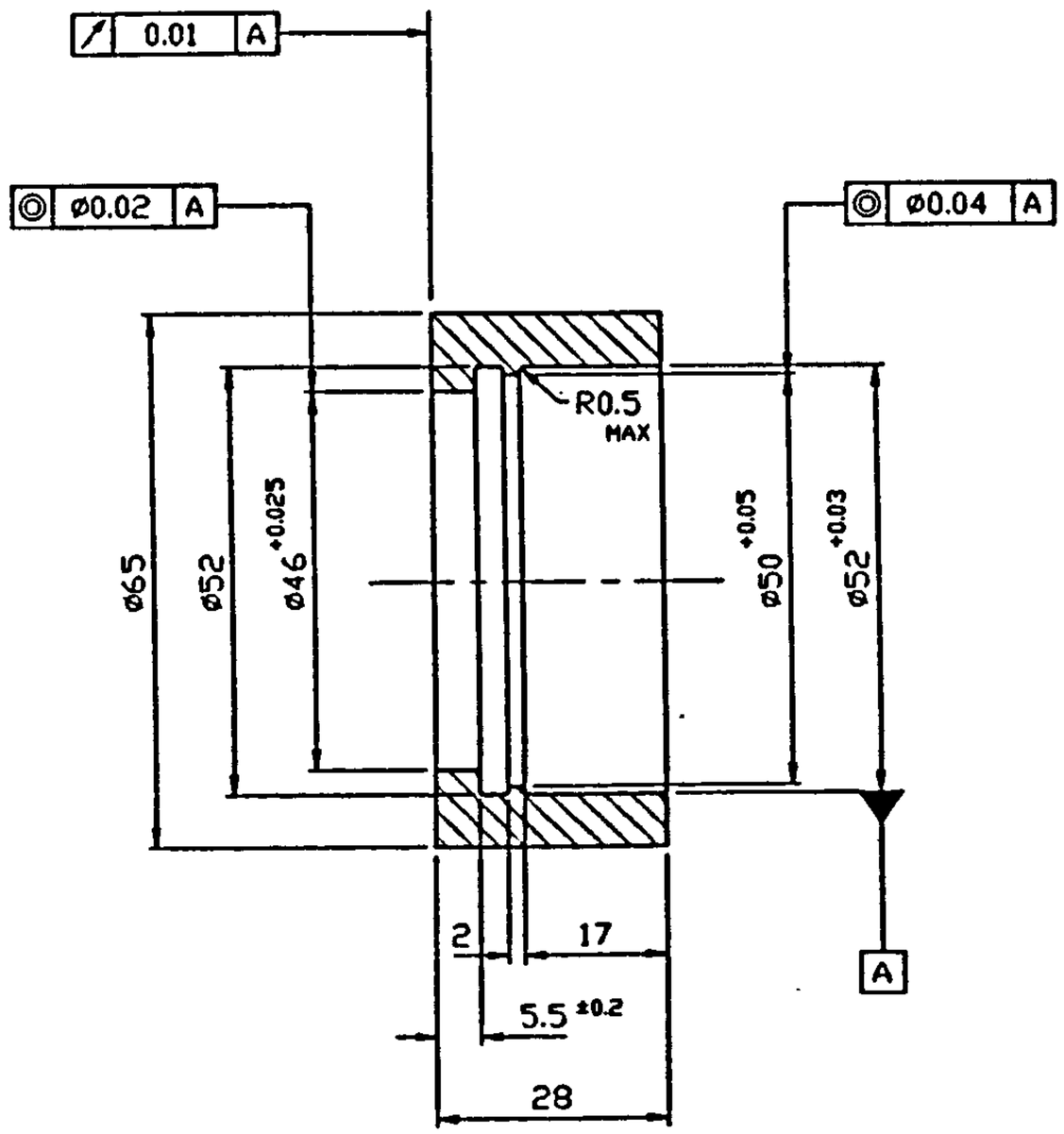

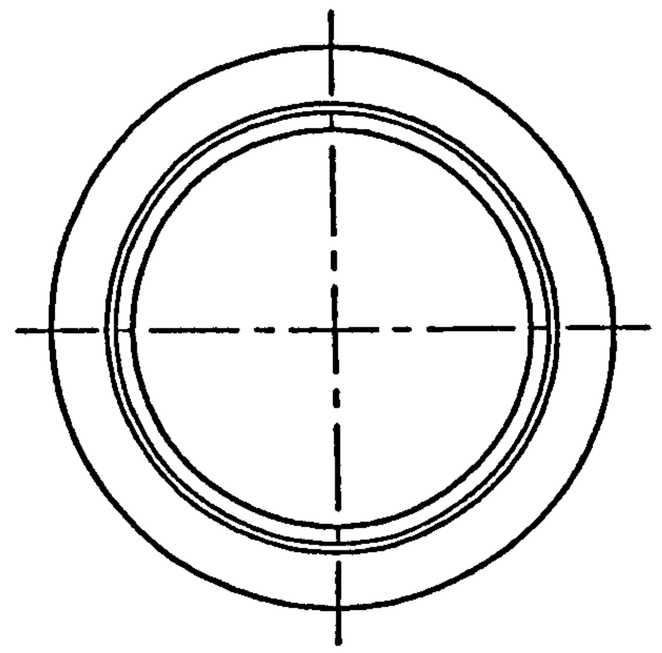

REMOVE ALL SHAPE EDGES

THIRD ANGLE PROJECTION	SHEET SIZE A3	ITEM	PART No.	DESCRIPTION	No. OFF	MATL.	SPEC.	REMARKS
					1	M.S.		

GENERAL TOLERANCE ON DIMENSIONS MACHINED UNMACHINED OTHER DIMENSIONS AS STATED WELD WHERE SHOWN THUS ⌒ L MACHINE WHERE SHOWN THUS ⊿	JOB No.	No. OF SETS REQ.	SCALE 1:1	FINISH CHEMI BLACK	DRAWN	CHK	DATE	TITLE: SLEEVE
					Y.B.P.KWAN		14.11.95	

SCHOOL OF INDUSTRIAL & MANUFACTURING SCIENCE
CRANFIELD

DRAWING No. MD291 A202 3A

SHT. 1 OF 1 SHEETS

DRAWING No.	
ISSUE	MODIFICATION

ALL DIMENSIONS IN MILLIMETRES UNLESS OTHERWISE STATED. IF IN DOUBT ASK.

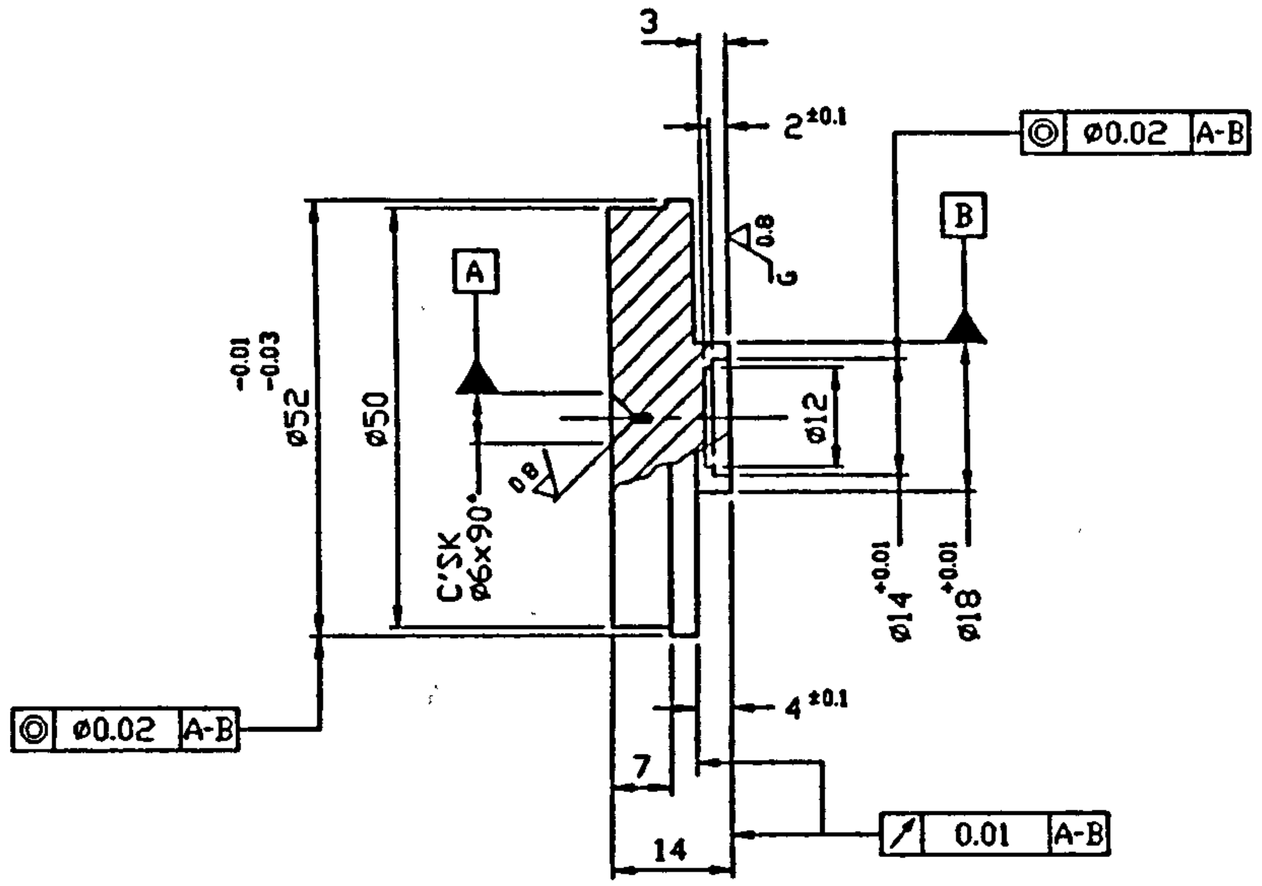

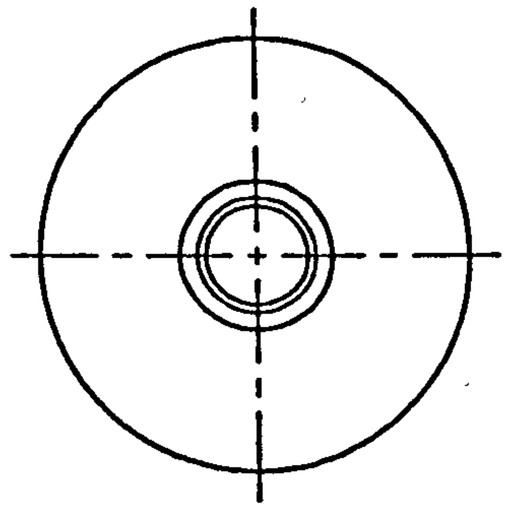

REMOVE ALL SHAPE EDGES

THIRD ANGLE PROJECTION	SHEET SIZE A3					1	SST	440C	
		ITEM	PART No.	DESCRIPTION		No. OFF	MATL.	SPEC.	REMARKS

GENERAL TOLERANCE ON DIMENSIONS	JOB No.	No. OF SETS REQ.	SCALE 1:1	DRAWN	CHK	DATE	TITLE: TOP PLATE
MACHINED				Y.B.P.KWAN		14.11.95	
UNMACHINED							
OTHER DIMENSIONS AS STATED			FINISH HRc 50-55	SCHOOL OF INDUSTRIAL & MANUFACTURING SCIENCE			DRAWING No. MD291 A203 3A
WELD WHERE SHOWN THUS				CRANFIELD			SHT. 1 OF 1 SHEETS
MACHINE WHERE SHOWN THUS							

DRAWING No.	
ISSUE	MODIFICATION

ALL DIMENSIONS IN MILLIMETRES UNLESS OTHERWISE STATED. IF IN DOUBT ASK.

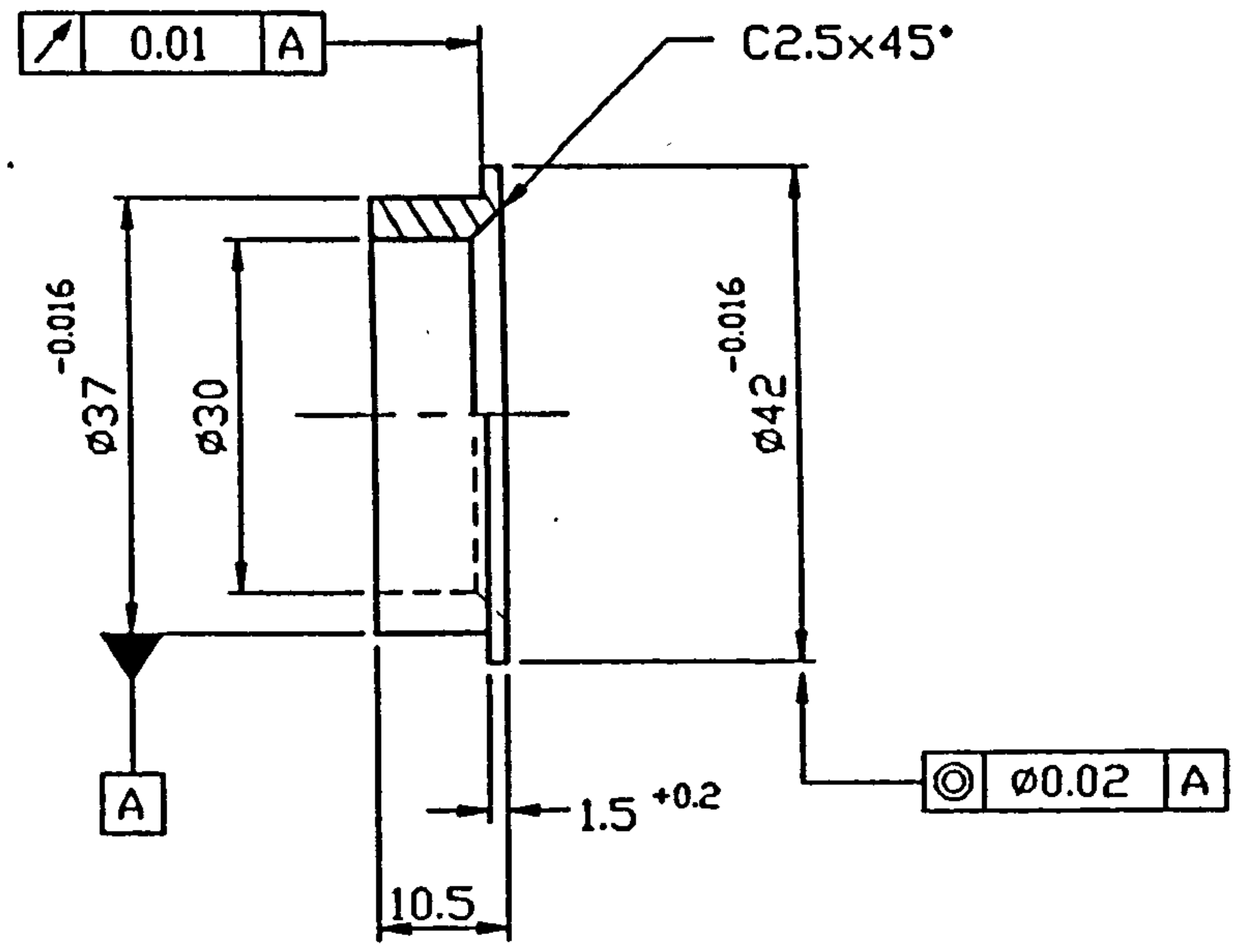

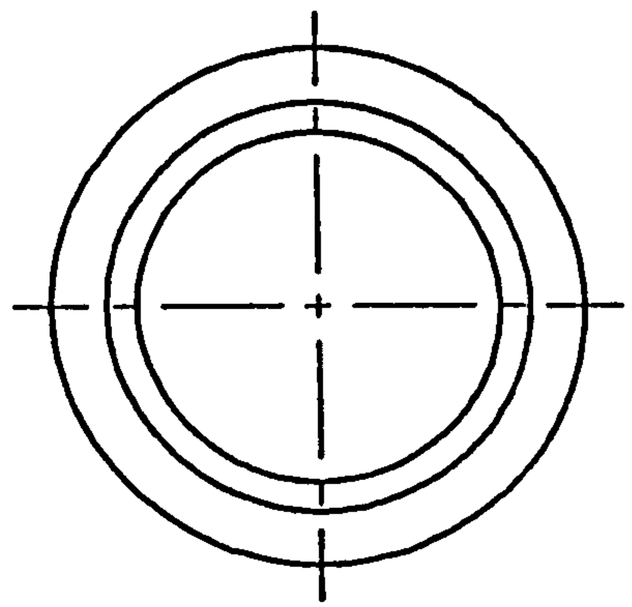

REMOVE ALL SHAPE EDGES

THIRD ANGLE PROJECTION	SHEET SIZE A4	ITEM	PART No.	DESCRIPTION	No. OFF	MATL.	SPEC.	REMARKS
					1	M.S.		

GENERAL TOLERANCE ON DIMENSIONS	JOB No.	No. OF SETS REQ.	SCALE 1:1	DRAWN	CHK	DATE	TITLE: GUIDE RING I
MACHINED				Y.B.P.KWAN		14.11.94	
UNMACHINED							
OTHER DIMENSIONS AS STATED			FINISH CHEMI BLACK	SCHOOL OF INDUSTRIAL & MANUFACTURING SCIENCE			DRAWING No. MD291 A204 4A
WELD WHERE SHOWN THUS ⌒ L				CRANFIELD			SHT. 1 OF 1 SHEETS
MACHINE WHERE SHOWN THUS ✓							

DRAWING No.	
ISSUE	MODIFICATION

ALL DIMENSIONS IN MILLIMETRES UNLESS OTHERWISE STATED. IF IN DOUBT ASK.

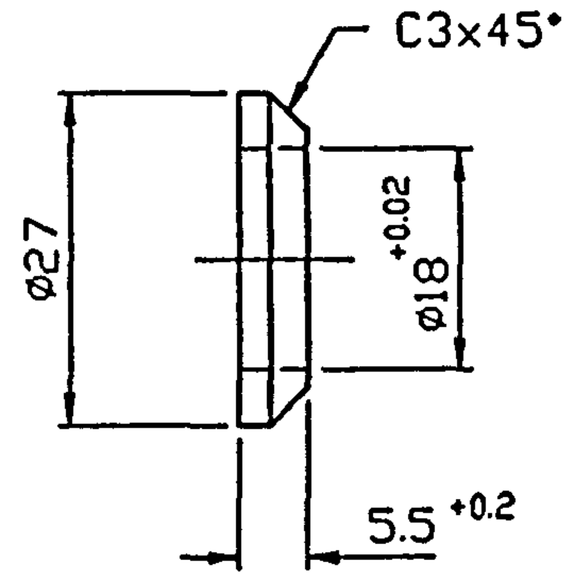

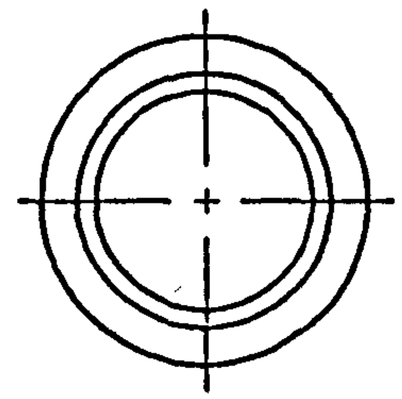

REMOVE ALL SHAPE EDGES

THIRD ANGLE PROJECTION	SHEET SIZE A4	ITEM	PART No.	DESCRIPTION	No. OFF	MATL.	SPEC.	REMARKS
					1	M.S.		

GENERAL TOLERANCE ON DIMENSIONS	JOB No.	No. OF SETS REQ.	SCALE 1:1	DRAWN	CHK	DATE	TITLE: GUIDE RING II
MACHINED				Y.B.P.KWAN		14.11.94	
UNMACHINED							
OTHER DIMENSIONS AS STATED			FINISH CHEMI BLACK	SCHOOL OF INDUSTRIAL & MANUFACTURING SCIENCE			DRAWING No. MD291 A205 4A
WELD WHERE SHOWN THUS ⌒				CRANFIELD			SHT. 1 OF 1 SHEETS
MACHINE WHERE SHOWN THUS ✓							

DRAWING No.	
ISSUE	MODIFICATION

ALL DIMENSIONS IN MILLIMETRES UNLESS OTHERWISE STATED. IF IN DOUBT ASK.

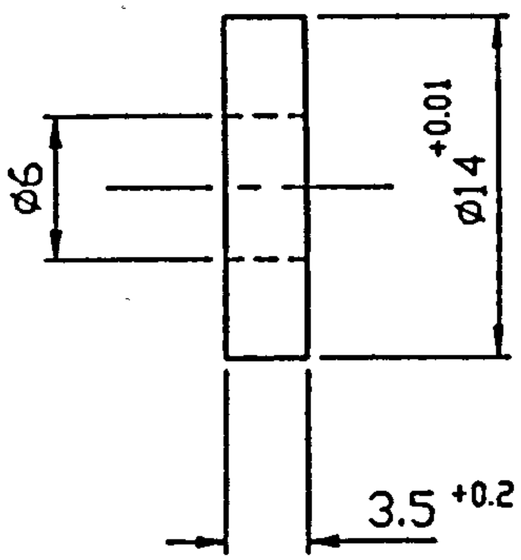

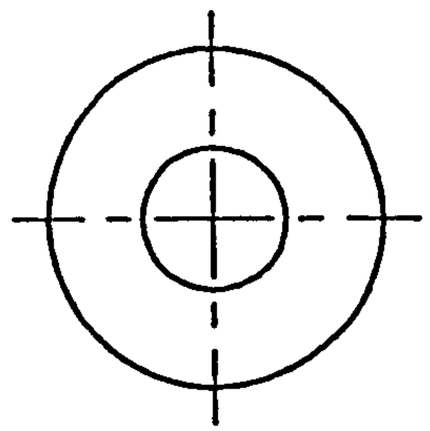

REMOVE ALL SHAPE EDGES

THIRD ANGLE PROJECTION	SHEET SIZE A4	ITEM	PART No.	DESCRIPTION	No. OFF	MATL.	SPEC.	REMARKS
					1	M.S.		

GENERAL TOLERANCE ON DIMENSIONS	JOB No.	No. OF SETS REQ.	SCALE 2:1	DRAWN	CHK	DATE	TITLE: GUIDE RING III
MACHINED				Y.B.P.KWAN		14.11.94	
UNMACHINED							
OTHER DIMENSIONS AS STATED			FINISH CHEMI BLACK	SCHOOL OF INDUSTRIAL & MANUFACTURING SCIENCE			DRAWING No. MD291 A206 4A
WELD WHERE SHOWN THUS ⌒ L				CRANFIELD			SHT. 1 OF 1 SHEETS
MACHINE WHERE SHOWN THUS ✓							

DRAWING No.	
ISSUE	MODIFICATION

ALL DIMENSIONS IN MILLIMETRES UNLESS OTHERWISE STATED. IF IN DOUBT ASK.

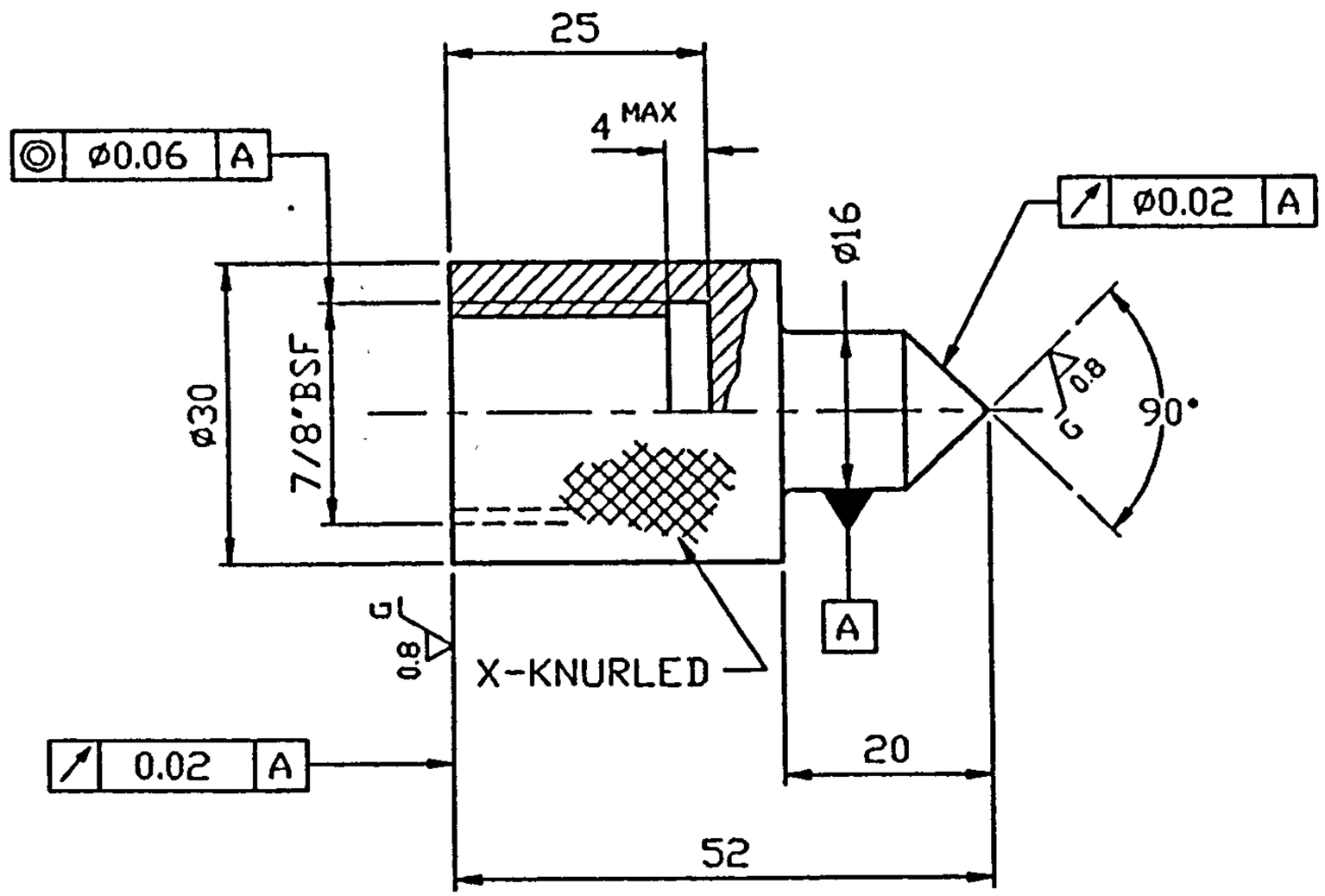

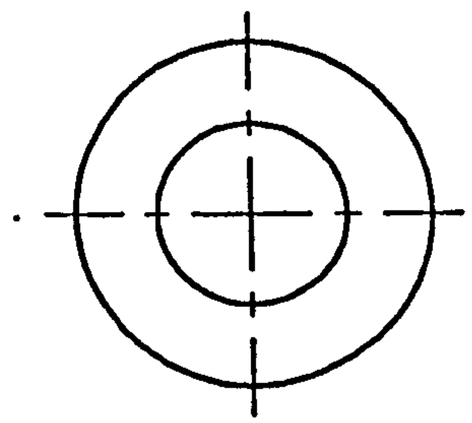

REMOVE ALL SHAPE EDGES

				1	SST	440C	
ITEM	PART No.	DESCRIPTION	No. OFF	MATL.	SPEC.	REMARKS

THIRD ANGLE PROJECTION

GENERAL TOLERANCE ON DIMENSIONS	JOB No.	No. OF SETS REQ.
MACHINED		
UNMACHINED		
OTHER DIMENSIONS AS STATED		
WELD WHERE SHOWN THUS ⌒ L		
MACHINE WHERE SHOWN THUS ⊿		

SHEET SIZE	SCALE	FINISH
A4	1:1	HRc 50-55

DRAWN	CHK	DATE
Y.B.P.KWAN		14.11.94

TITLE: CENTRE

SCHOOL OF INDUSTRIAL & MANUFACTURING SCIENCE
CRANFIELD

DRAWING No. MD291 A207 4A

SHT. 1 OF 1 SHEETS

DRAWING No.	
ISSUE	MODIFICATION

ALL DIMENSIONS IN MILLIMETRES UNLESS OTHERWISE STATED. IF IN DOUBT ASK.

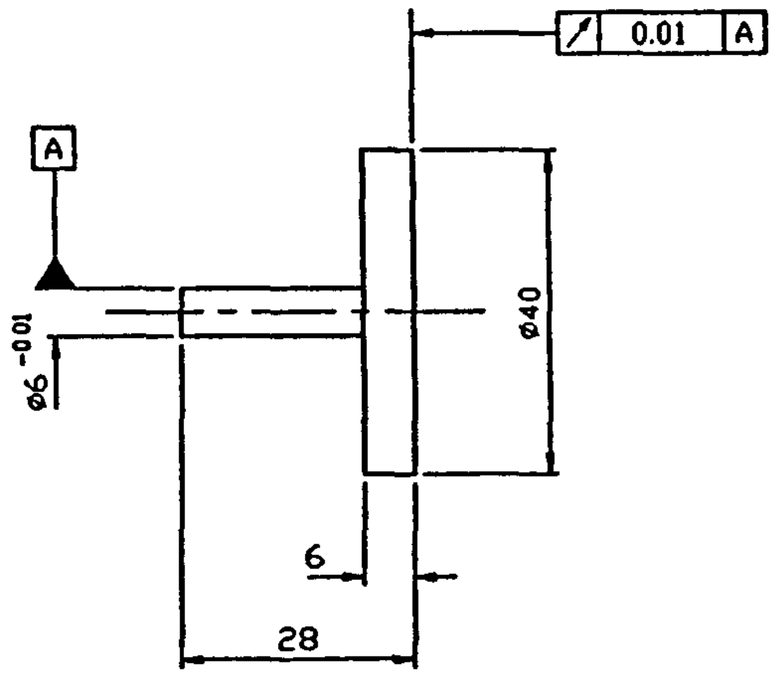

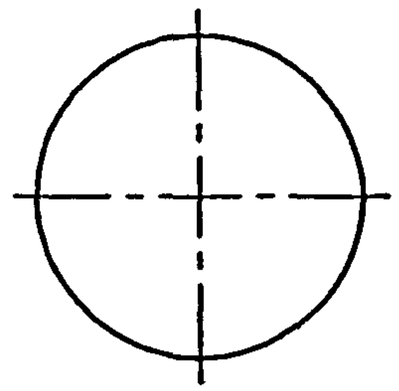

REMOVE ALL SHAPE EDGES

ITEM	PART No.	DESCRIPTION	No. OFF	MATL.	SPEC.	REMARKS
			1	BRASS		

THIRD ANGLE PROJECTION	SHEET SIZE A3	DRAWN	CHK	DATE	TITLE: SPECIMEN HOLDER (HORI)
GENERAL TOLERANCE ON DIMENSIONS MACHINED UNMACHINED OTHER DIMENSIONS AS STATED WELD WHERE SHOWN THUS MACHINE WHERE SHOWN THUS	JOB No. / No. OF SETS REQ.	Y.B.P.KWAN		14.11.94	
	SCALE 1:1				
	FINISH	SCHOOL OF INDUSTRIAL & MANUFACTURING SCIENCE CRANFIELD			DRAWING No. MD291 A301 3A SHT. 1 OF 1 SHEETS

DRAWING No.	
ISSUE	MODIFICATION

ALL DIMENSIONS IN MILLIMETRES UNLESS OTHERWISE STATED. IF IN DOUBT ASK.

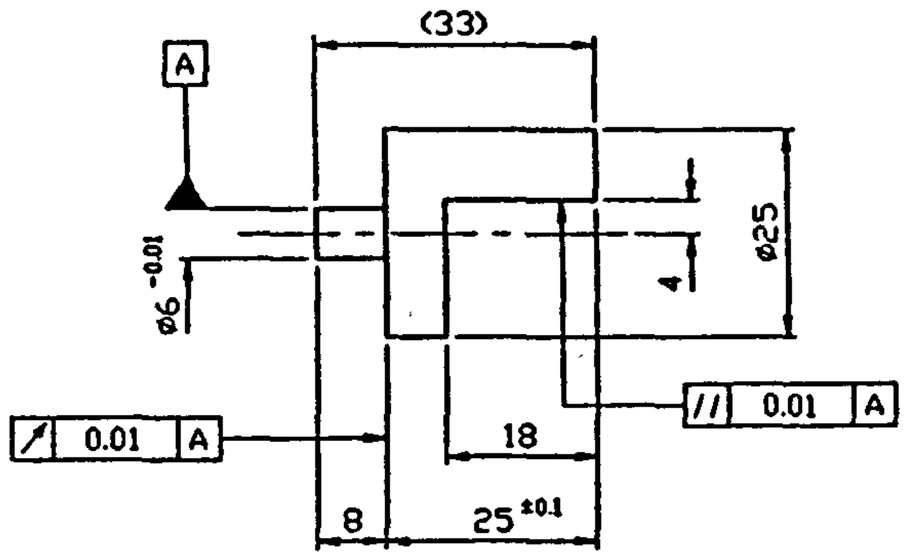

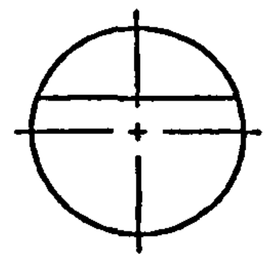

REMOVE ALL SHAPE EDGES

THIRD ANGLE PROJECTION	SHEET SIZE A3	ITEM	PART No.	DESCRIPTION	No. OFF	MATL.	SPEC.	REMARKS
					1	BRASS		

GENERAL TOLERANCE ON DIMENSIONS	JOB No.	No. OF SETS REQ.	SCALE 1:1	DRAWN	CHK	DATE	TITLE: SPECIMEN HOLDER (VERT)
MACHINED				Y.B.P.KWAN		14.11.94	
UNMACHINED							
OTHER DIMENSIONS AS STATED			FINISH	SCHOOL OF INDUSTRIAL & MANUFACTURING SCIENCE			DRAWING No. MD291 A302 3A
WELD WHERE SHOWN THUS				CRANFIELD			SHT. 1 OF 1 SHEETS
MACHINE WHERE SHOWN THUS							

DRAWING No.	
ISSUE	MODIFICATION

ALL DIMENSIONS IN MILLIMETRES UNLESS OTHERWISE STATED. IF IN DOUBT ASK.

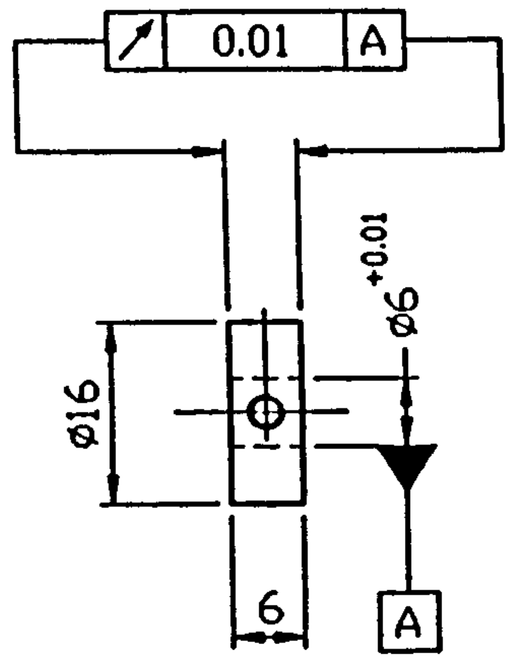

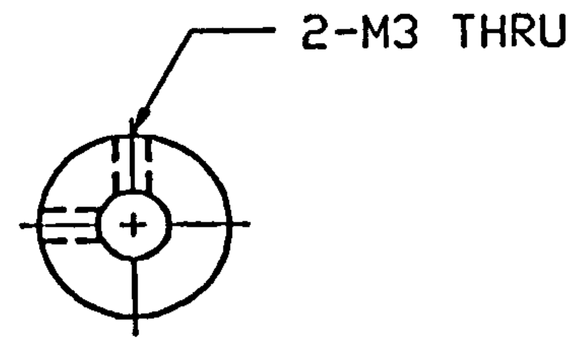

REMOVE ALL SHAPE EDGES

THIRD ANGLE PROJECTION	SHEET SIZE A4	ITEM	PART No.	DESCRIPTION	No. OFF	MATL.	SPEC.	REMARKS
					1	BRASS		

GENERAL TOLERANCE ON DIMENSIONS	JOB No.	No. OF SETS REQ.	SCALE 1:1	DRAWN	CHK	DATE	TITLE: COLLAR
MACHINED				Y.B.P.KWAN		14.11.94	
UNMACHINED							
OTHER DIMENSIONS AS STATED			FINISH	SCHOOL OF INDUSTRIAL & MANUFACTURING SCIENCE			DRAWING No. MD291 A303 4A
WELD WHERE SHOWN THUS				CRANFIELD			SHT. 1 OF 1 SHEETS
MACHINE WHERE SHOWN THUS							

DRAWING No.	
ISSUE	MODIFICATION

ALL DIMENSIONS IN MILLIMETRES UNLESS OTHERWISE STATED. IF IN DOUBT ASK.

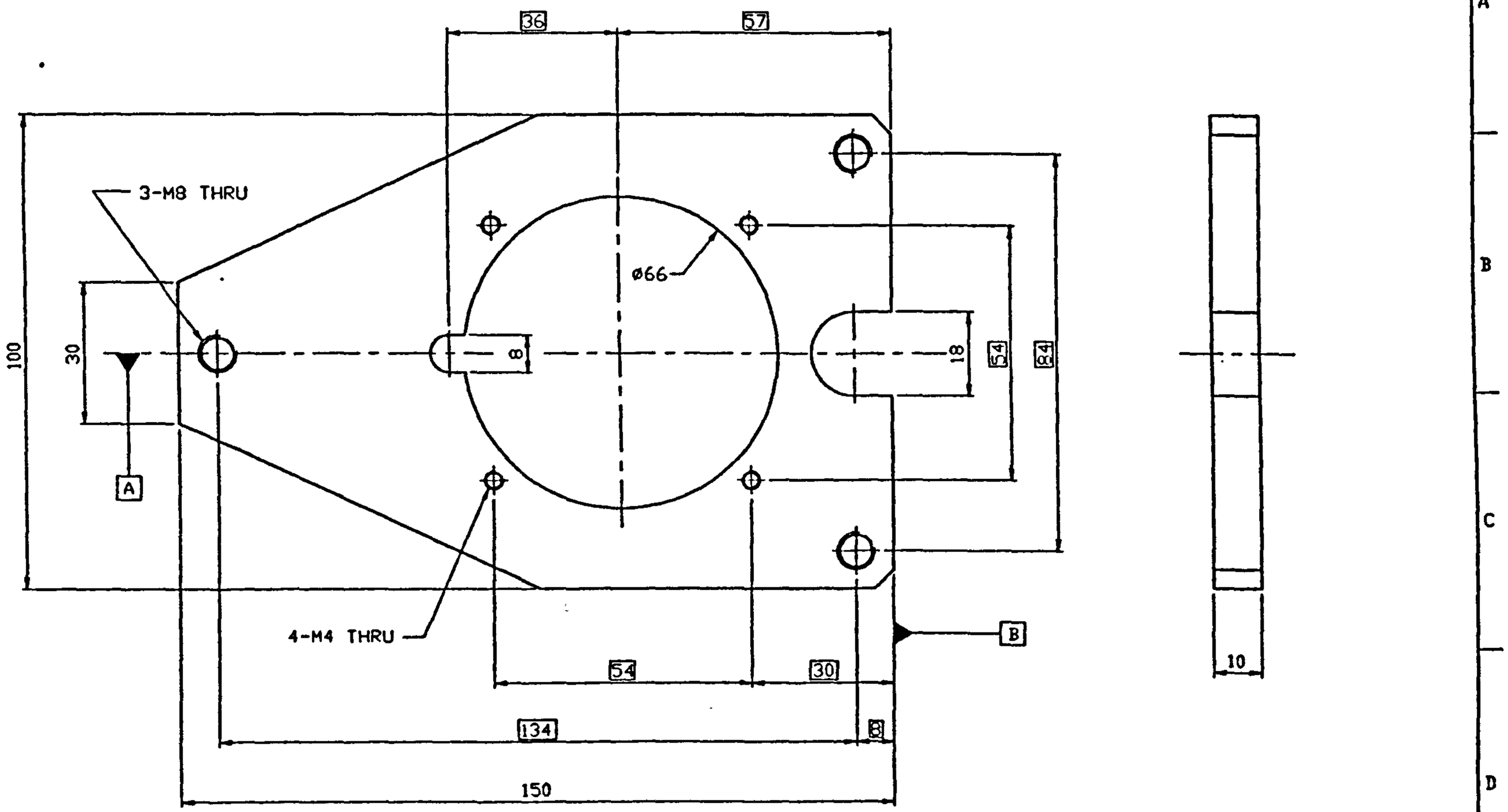

ALL HOLES ⌖ ø0.2 AB

REMOVE ALL SHAPE EDGES

THIRD ANGLE PROJECTION	SHEET SIZE A3	ITEM	PART No.	DESCRIPTION	2 No. OFF	M.S. MATL.	SPEC.	REMARKS
GENERAL TOLERANCE ON DIMENSIONS MACHINED UNMACHINED OTHER DIMENSIONS AS STATED WELD WHERE SHOWN THUS ⌒ L MACHINE WHERE SHOWN THUS ✓	JOB No.	No. OF SETS REQ.	SCALE 1:1	DRAWN Y.B.P.KWAN	CHK	DATE 13.04.95	TITLE: SHAKER MOUNTING PLATE	
			FINISH CHEMI BLACK	SCHOOL OF INDUSTRIAL & MANUFACTURING SCIENCE CRANFIELD			DRAWING No. MD291 A401 3A	
							SHT. 1 OF 1 SHEETS	

DRAWING No.	
ISSUE	MODIFICATION

ALL DIMENSIONS IN MILLIMETRES UNLESS OTHERWISE STATED. IF IN DOUBT ASK.

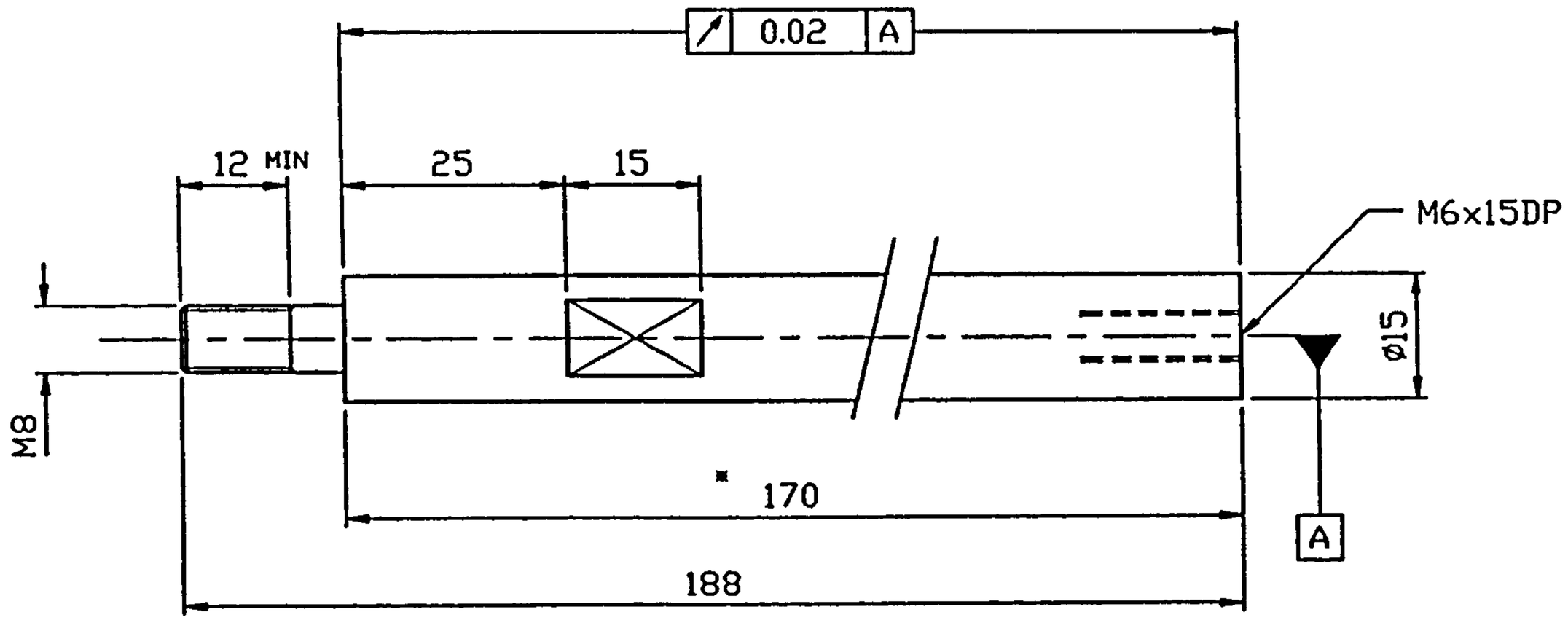

NOTE: HEIGHT DEVIATION BTW. SET OF 3 < 0.03

REMOVE ALL SHAPE EDGES

ITEM	PART No.	DESCRIPTION	No. OFF	MATL.	SPEC.	REMARKS
			3	M.S.		

THIRD ANGLE PROJECTION

SHEET SIZE	DRAWN	CHK	DATE	TITLE:
A4	Y.B.P.KWAN		14.04.95	PILLAR

GENERAL TOLERANCE ON DIMENSIONS	JOB No.	No. OF SETS REQ.	SCALE
MACHINED			1:1
UNMACHINED			
OTHER DIMENSIONS AS STATED			FINISH
WELD WHERE SHOWN THUS ⌒ L			CHEMI BLACK
MACHINE WHERE SHOWN THUS ⊿			

SCHOOL OF INDUSTRIAL & MANUFACTURING SCIENCE
CRANFIELD

DRAWING No. MD291 A402 4A

SHT. 1 OF 1 SHEETS

DRAWING No.	
ISSUE	MODIFICATION

ALL DIMENSIONS IN MILLIMETRES UNLESS OTHERWISE STATED. IF IN DOUBT ASK.

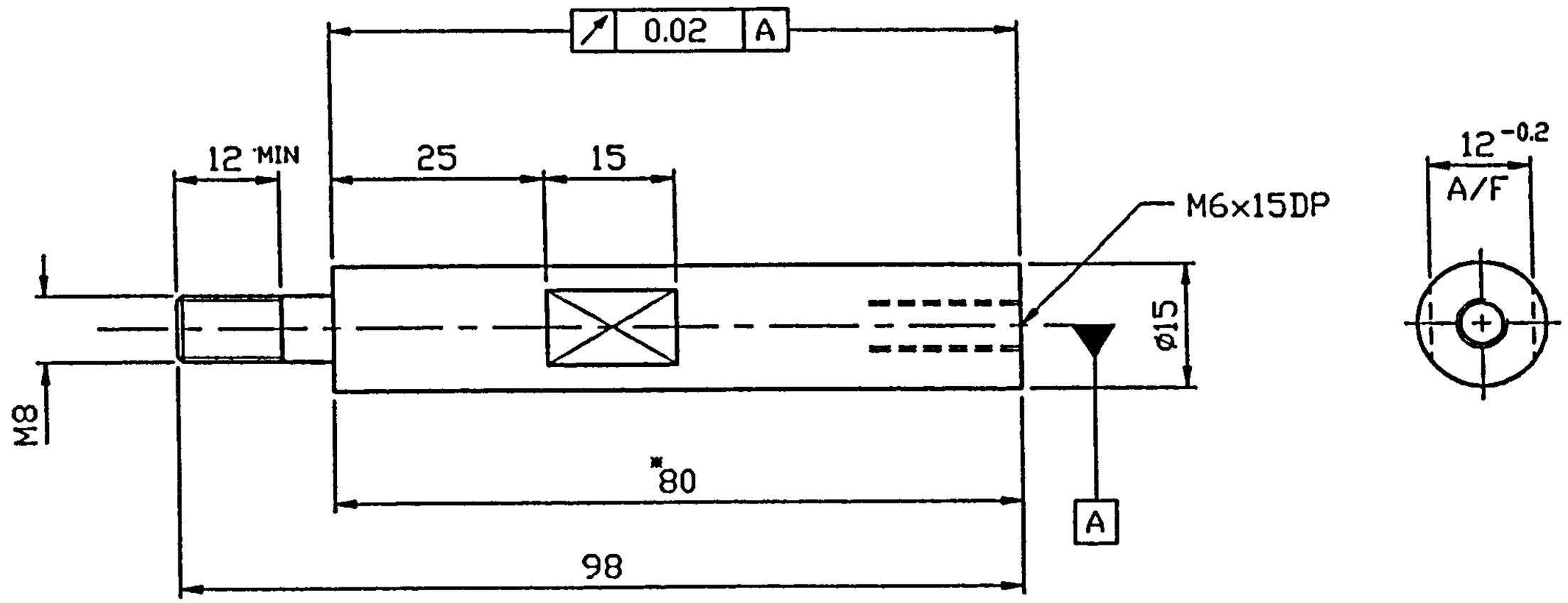

REMOVE ALL SHAPE EDGES

* NOTE: HEIGHT DEVIATION BTW. SET OF 3 < 0.03

ITEM	PART No.	DESCRIPTION	No. OFF	MATL.	SPEC.	REMARKS
			3	M.S.		

THIRD ANGLE PROJECTION

SHEET SIZE A4

GENERAL TOLERANCE ON DIMENSIONS
MACHINED
UNMACHINED
OTHER DIMENSIONS AS STATED
WELD WHERE SHOWN THUS
MACHINE WHERE SHOWN THUS

JOB No.	No. OF SETS REQ.

SCALE 1:1

FINISH CHEMI BLACK

DRAWN	CHK	DATE
Y.B.P.KWAN		14.04.95

TITLE: PILLAR

SCHOOL OF INDUSTRIAL & MANUFACTURING SCIENCE
CRANFIELD

DRAWING No. MD291 A403 4A

SHT. 1 OF 1 SHEETS

DRAWING No.	
ISSUE	MODIFICATION

ALL DIMENSIONS IN MILLIMETRES UNLESS OTHERWISE STATED. IF IN DOUBT ASK.

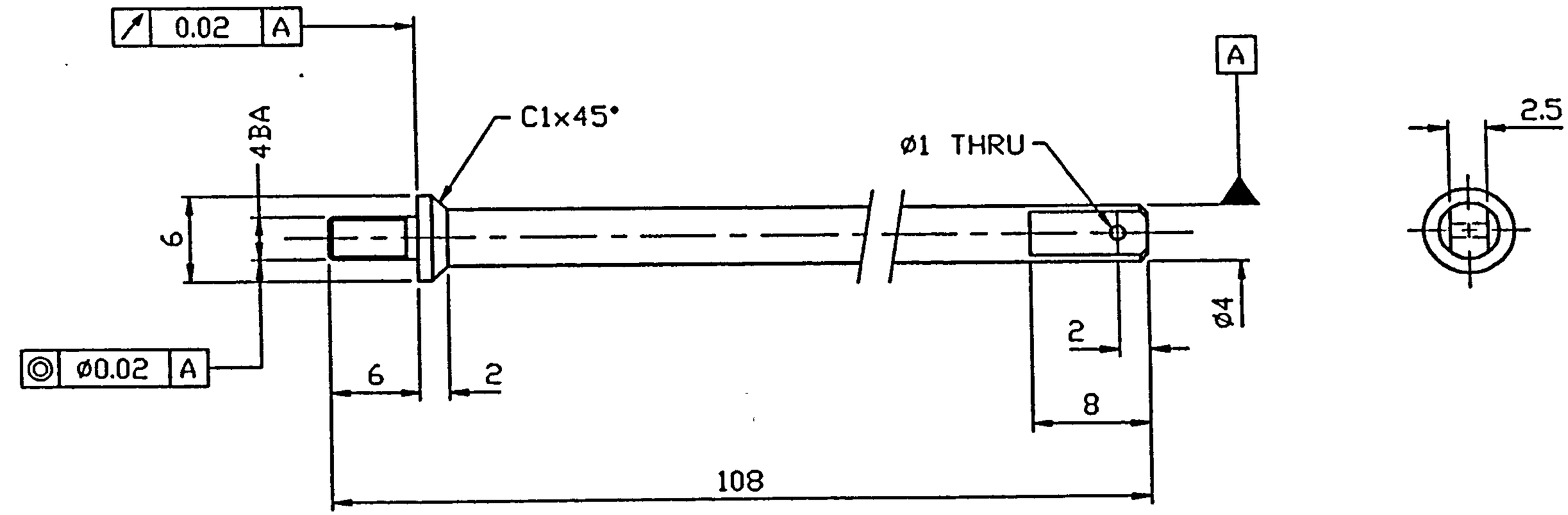

REMOVE ALL SHAPE EDGES

ITEM	PART No.	DESCRIPTION	No. OFF	MATL.	SPEC.	REMARKS
			1	ALUM.	6061-T6	

THIRD ANGLE PROJECTION

SHEET SIZE A4

SCALE 2:1

FINISH BLACK ANOD.

GENERAL TOLERANCE ON DIMENSIONS
MACHINED
UNMACHINED
OTHER DIMENSIONS AS STATED
WELD WHERE SHOWN THUS
MACHINE WHERE SHOWN THUS

JOB No.	No. OF SETS REQ.

DRAWN	CHK	DATE
Y.B.P.KWAN		14.04.95

TITLE: EXTENSION FITTING

SCHOOL OF INDUSTRIAL & MANUFACTURING SCIENCE
CRANFIELD

DRAWING No. MD291 A404 4A

SHT. 1 OF 1 SHEETS

DRAWING No.	
ISSUE	MODIFICATION

ALL DIMENSIONS IN MILLIMETRES UNLESS OTHERWISE STATED. IF IN DOUBT ASK.

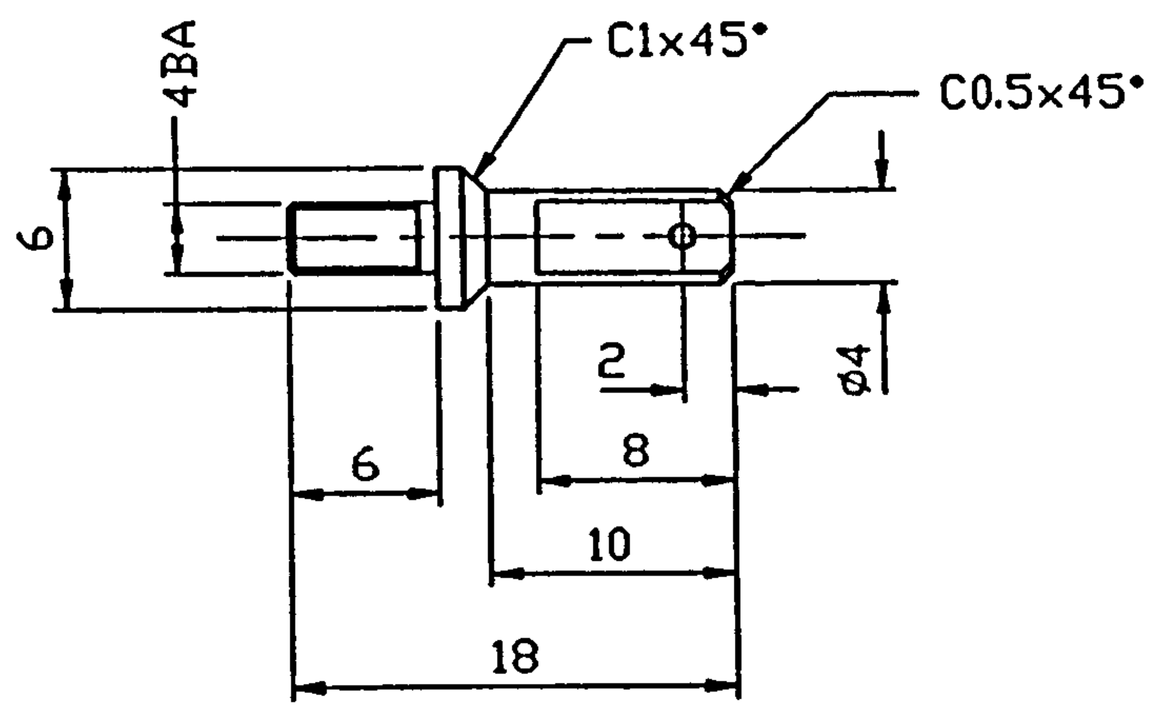

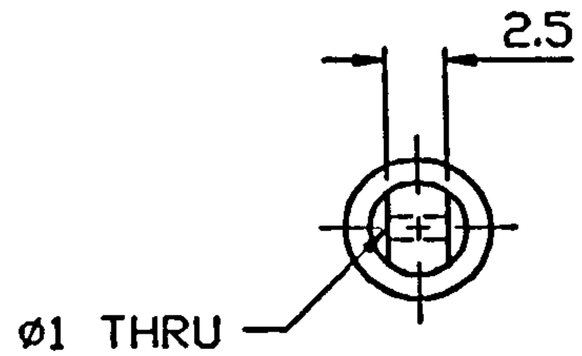

REMOVE ALL SHAPE EDGES

THIRD ANGLE PROJECTION	SHEET SIZE A4	ITEM	PART No.	DESCRIPTION	No. OFF	MATL.	SPEC.	REMARKS
					1	ALUM.	6061-T6	

GENERAL TOLERANCE ON DIMENSIONS	JOB No.	No. OF SETS REQ.	SCALE 2:1	DRAWN	CHK	DATE	TITLE: SHAKER END FITTING
MACHINED				Y.B.P.KVAN		14.04.95	
UNMACHINED							
OTHER DIMENSIONS AS STATED			FINISH BLACK ANOD.	SCHOOL OF INDUSTRIAL & MANUFACTURING SCIENCE CRANFIELD			DRAWING No. MD291 A405 4A
WELD WHERE SHOWN THUS							SHT. 1 OF 1 SHEETS
MACHINE WHERE SHOWN THUS							

DRAWING No.	
ISSUE	MODIFICATION

ALL DIMENSIONS IN MILLIMETRES UNLESS OTHERWISE STATED. IF IN DOUBT ASK.

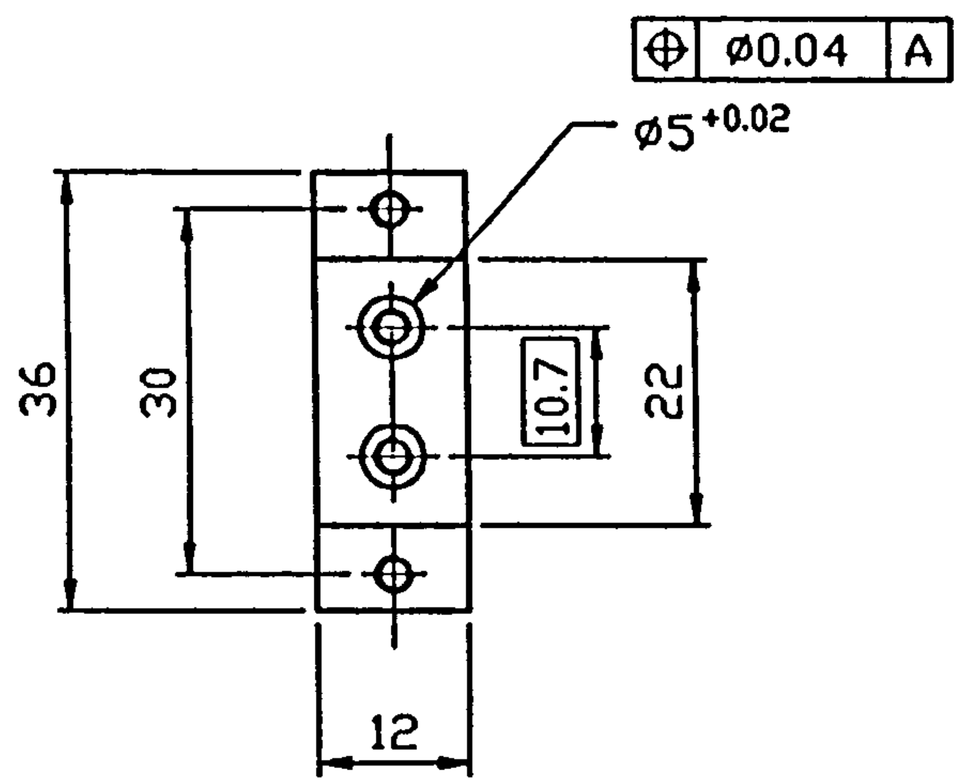

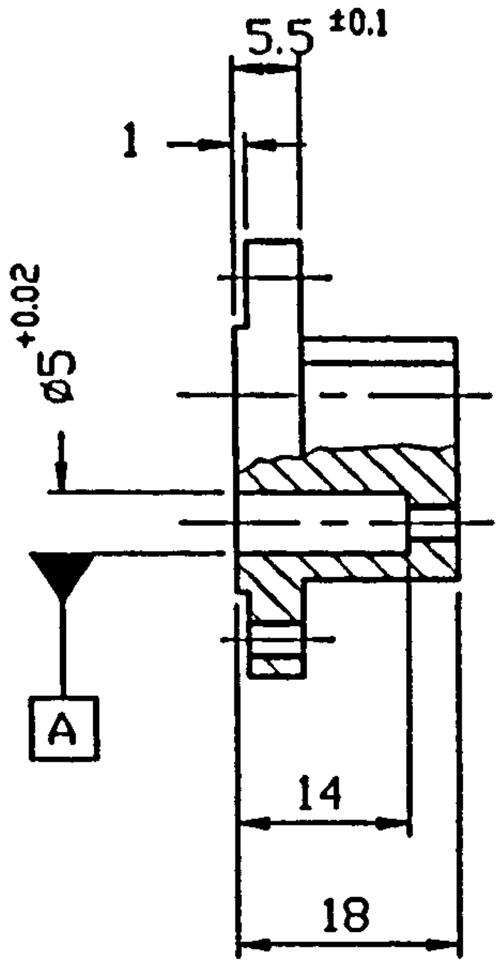

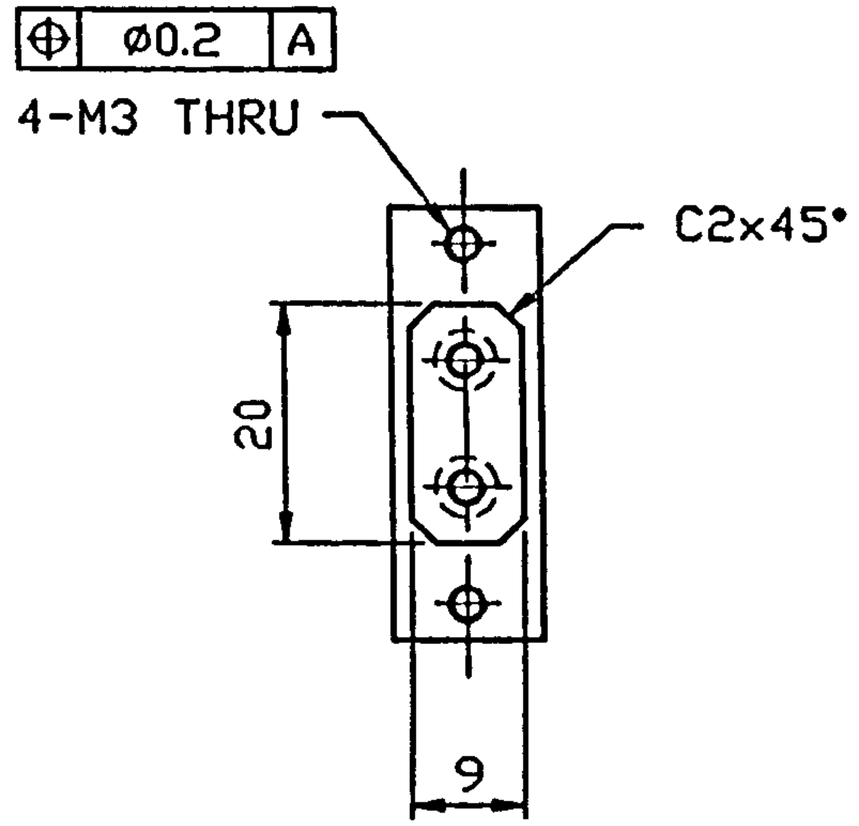

REMOVE ALL SHAPE EDGES

THIRD ANGLE PROJECTION	SHEET SIZE A4	ITEM	PART No.	DESCRIPTION	No. OFF	MATL.	SPEC.	REMARKS
					10	ALUM.	6061-T6	

GENERAL TOLERANCE ON DIMENSIONS	JOB No.	No. OF SETS REQ.	SCALE 1:1	DRAWN	CHK	DATE	TITLE: PRESSURE SENSOR CONNECTOR BLOCK
MACHINED				Y.B.P.KWAN		25.04.95	
UNMACHINED							
OTHER DIMENSIONS AS STATED			FINISH BLACK ANODIZED	SCHOOL OF INDUSTRIAL & MANUFACTURING SCIENCE			DRAWING No. MD291 A501 4A
WELD WHERE SHOWN THUS ⌒ L				CRANFIELD			SHT. 1 OF 1 SHEETS
MACHINE WHERE SHOWN THUS √							

DRAWING No.	
ISSUE	MODIFICATION

ALL DIMENSIONS IN MILLIMETRES UNLESS OTHERWISE STATED. IF IN DOUBT ASK.

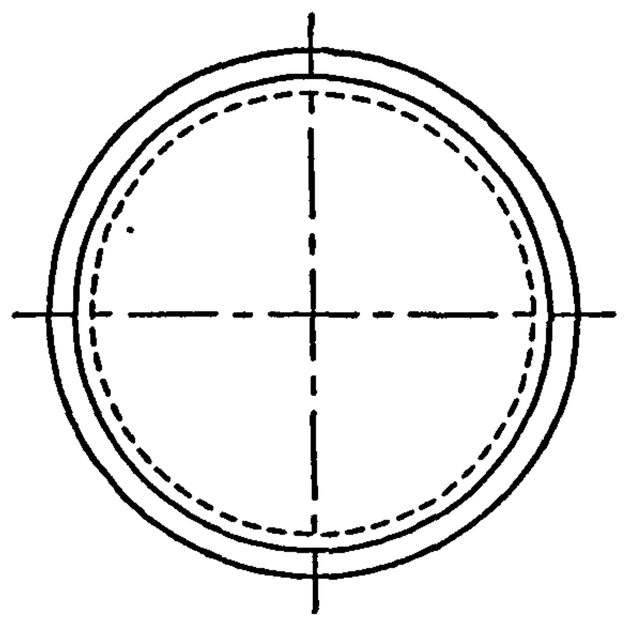

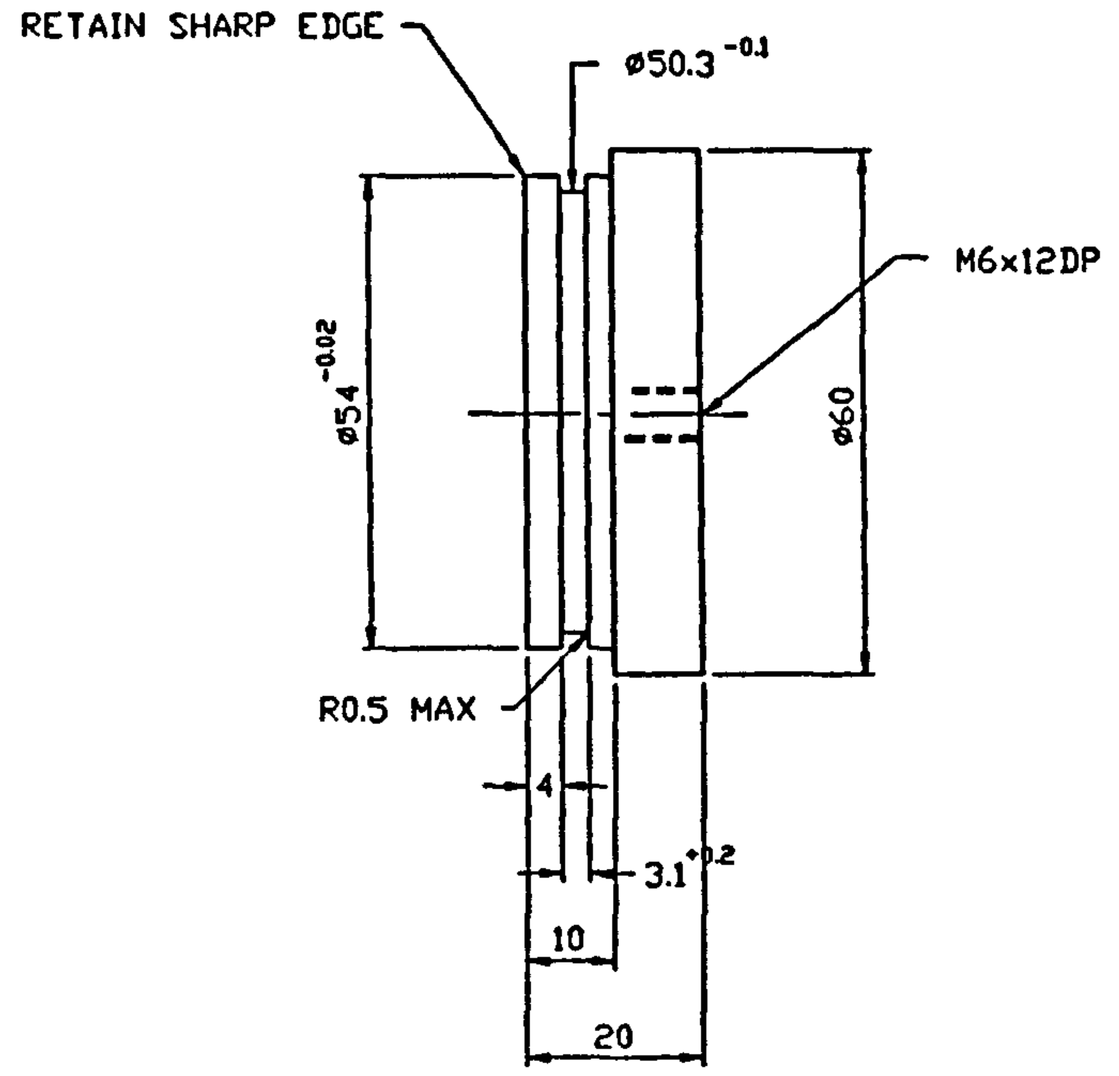

REMOVE ALL SHAPE EDGES

NOTE: * DIA. 54 TO FIT PERSPEX SLEEVE

THIRD ANGLE PROJECTION	SHEET SIZE A3	ITEM	PART No.	DESCRIPTION	No. OFF	MATL.	SPEC.	REMARKS
					1	ALUM.	6061-T6	

GENERAL TOLERANCE ON DIMENSIONS MACHINED UNMACHINED OTHER DIMENSIONS AS STATED WELD WHERE SHOWN THUS MACHINE WHERE SHOWN THUS	JOB No.	No. OF SETS REQ.	SCALE 1:1	DRAWN	CHK	DATE	TITLE: BASE
				Y.B.P.KWAN		20.06.95	

FINISH BLACK ANODIZED	SCHOOL OF INDUSTRIAL & MANUFACTURING SCIENCE CRANFIELD	DRAWING No. MD291 A601 3A
		SHT. 1 OF 1 SHEETS

DRAWING No.	
ISSUE	MODIFICATION

ALL DIMENSIONS IN MILLIMETRES UNLESS OTHERWISE STATED. IF IN DOUBT ASK.

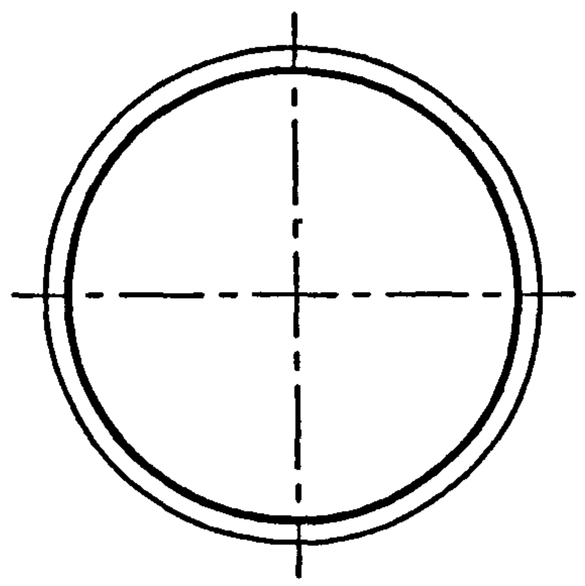

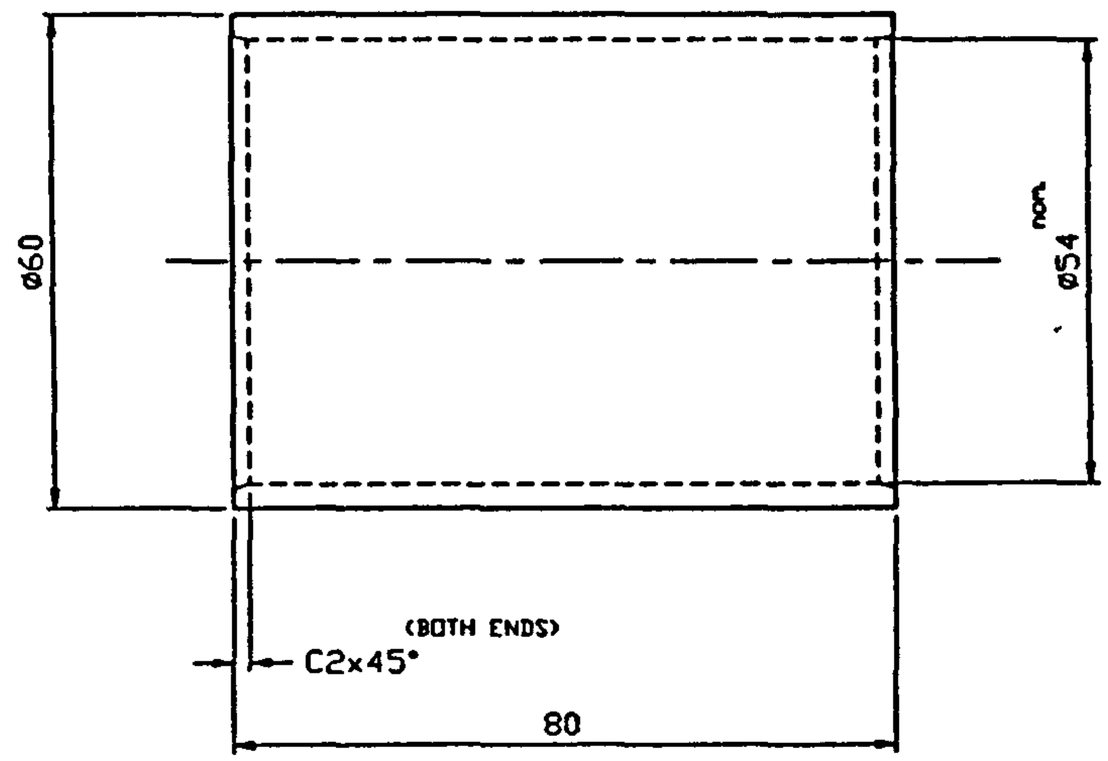

REMOVE ALL SHAPE EDGES

THIRD ANGLE PROJECTION	SHEET SIZE A3	ITEM	PART No.	DESCRIPTION	No. OFF	MATL.	SPEC.	REMARKS
					1	PERSPEX	CAST	

GENERAL TOLERANCE ON DIMENSIONS MACHINED UNMACHINED OTHER DIMENSIONS AS STATED WELD WHERE SHOWN THUS MACHINE WHERE SHOWN THUS	JOB No.	No. OF SETS REQ.	SCALE 1:1	FINISH

DRAWN	CHK	DATE
Y.B.P.KWAN		20.06.95

TITLE: SLEEVE

SCHOOL OF INDUSTRIAL & MANUFACTURING SCIENCE
CRANFIELD

DRAWING No. MD291 A602 3A

SHT. 1 OF 1 SHEETS

DRAWING No.	
ISSUE	MODIFICATION

ALL DIMENSIONS IN MILLIMETRES UNLESS OTHERWISE STATED. IF IN DOUBT ASK.

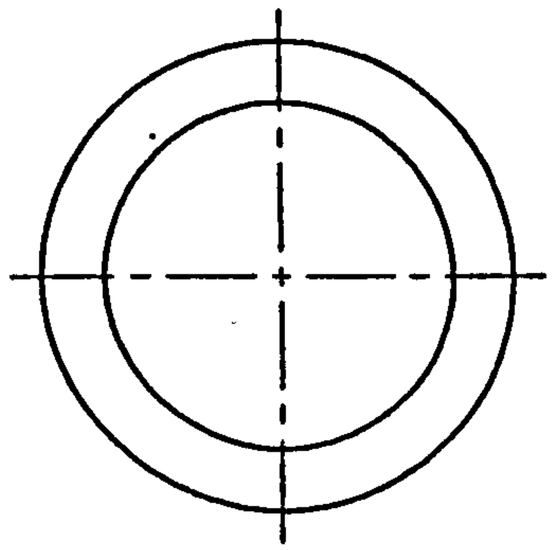

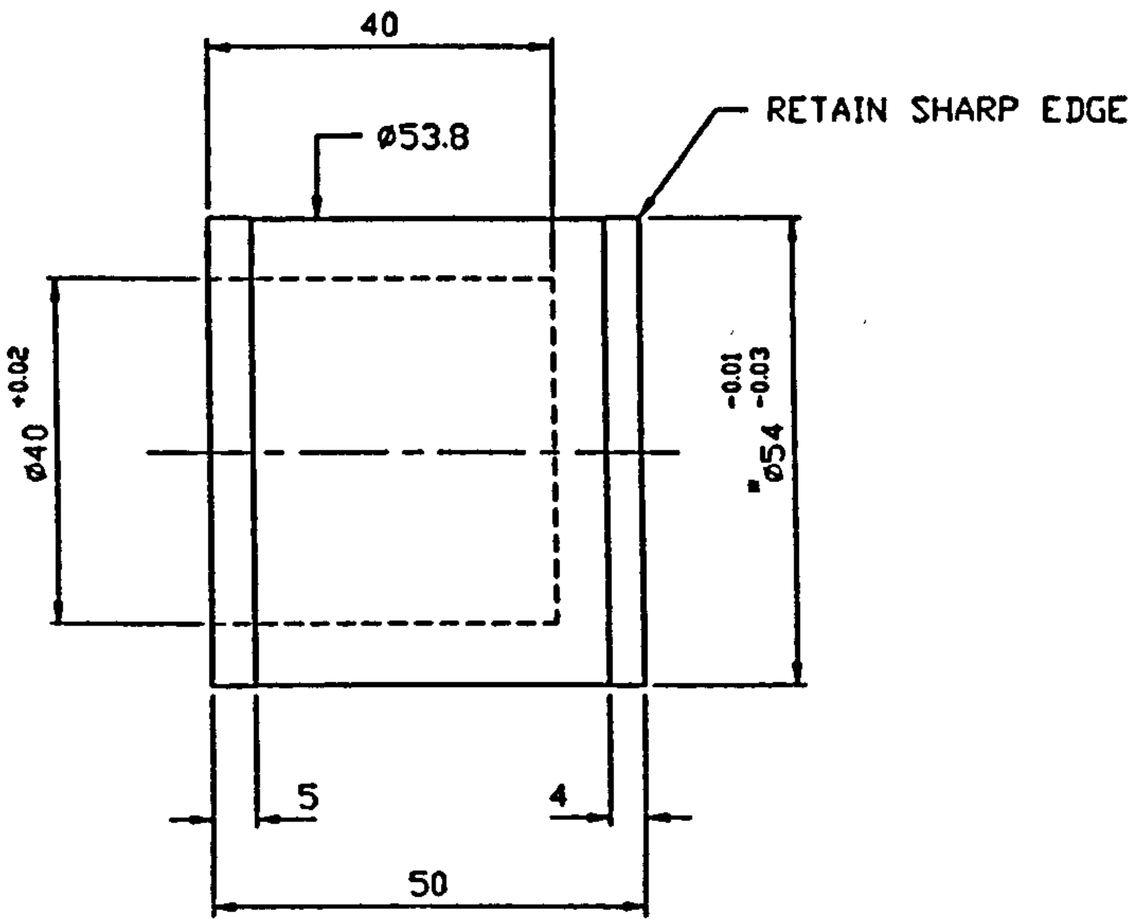

REMOVE ALL SHAPE EDGES

NOTE: *DIA.54 TO FIT PERSPEX SLEEVE

THIRD ANGLE PROJECTION	SHEET SIZE A3	ITEM	PART No.	DESCRIPTION	No. OFF	MATL.	SPEC.	REMARKS
					1	DELRIN		

GENERAL TOLERANCE ON DIMENSIONS	JOB No.	No. OF SETS REQ.	SCALE 1:1	DRAWN	CHK	DATE	TITLE: LOADING PISTON
MACHINED				Y.B.P.KWAN		20.06.95	
UNMACHINED							
OTHER DIMENSIONS AS STATED			FINISH	SCHOOL OF INDUSTRIAL & MANUFACTURING SCIENCE			DRAWING No. MD291 A603 3A
WELD WHERE SHOWN THUS ⌒ L				CRANFIELD			SHT. 1 OF 1 SHEETS
MACHINE WHERE SHOWN THUS ✓							

DRAWING No.	
ISSUE	MODIFICATION

ALL DIMENSIONS IN MILLIMETRES UNLESS OTHERWISE STATED. IF IN DOUBT ASK.

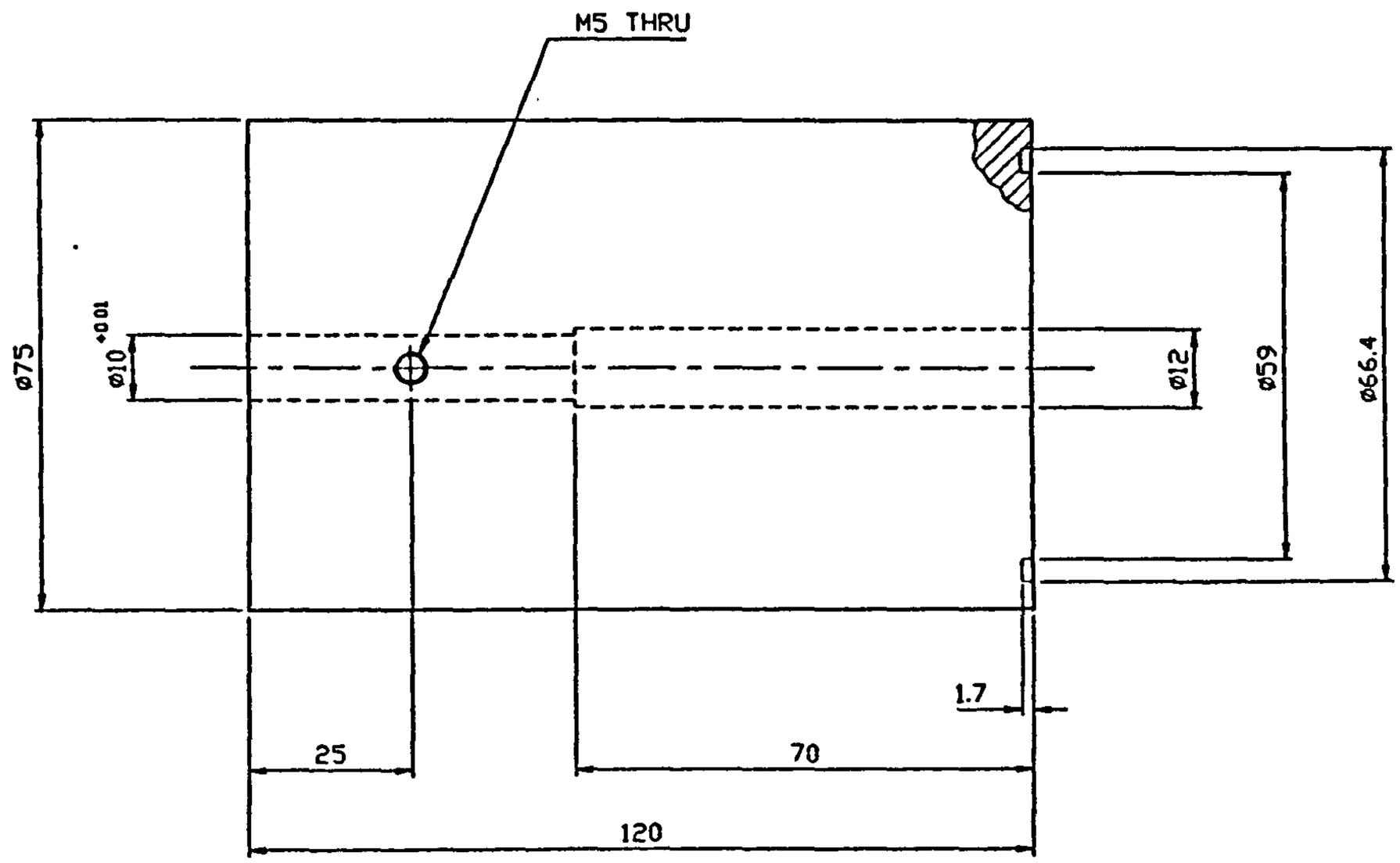

REMOVE ALL SHAPE EDGES

THIRD ANGLE PROJECTION	SHEET SIZE A3	ITEM	PART No.	DESCRIPTION	1 No. OFF	M.S. MATL.	SPEC.	REMARKS
GENERAL TOLERANCE ON DIMENSIONS MACHINED UNMACHINED OTHER DIMENSIONS AS STATED WELD WHERE SHOWN THUS ⌒ L MACHINE WHERE SHOWN THUS ⊿	JOB No. / No. OF SETS REQ.	SCALE 1:1	DRAWN Y.B.P.KWAN	CHK	DATE 24.07.95	TITLE: SENSOR BASE		
		FINISH CHEMI BLACK	SCHOOL OF INDUSTRIAL & MANUFACTURING SCIENCE CRANFIELD			DRAWING No. MD291 A605 3A		SHT. 1 OF 1 SHEETS

DRAWING No.	
ISSUE	MODIFICATION

ALL DIMENSIONS IN MILLIMETRES UNLESS OTHERWISE STATED. IF IN DOUBT ASK.

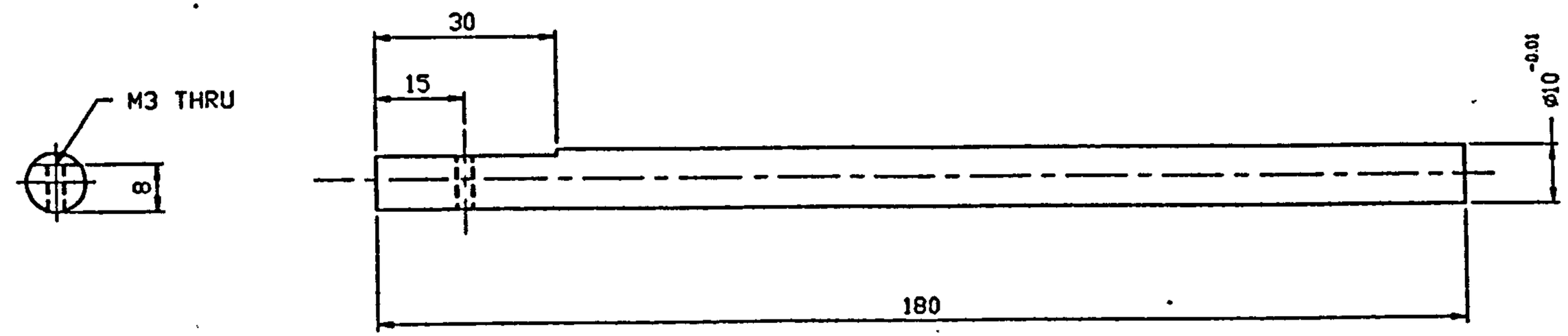

REMOVE ALL SHAPE EDGES

THIRD ANGLE PROJECTION	SHEET SIZE A3	ITEM	PART No.	DESCRIPTION	No. OFF	MATL.	SPEC.	REMARKS
					1	SST	304	

GENERAL TOLERANCE ON DIMENSIONS	JOB No.	No. OF SETS REQ.	SCALE 1:1	DRAWN	CHK	DATE	TITLE: SENSOR MT'G ROD
MACHINED				Y.B.P.KWAN		24.07.95	
UNMACHINED							
OTHER DIMENSIONS AS STATED			FINISH	SCHOOL OF INDUSTRIAL & MANUFACTURING SCIENCE			DRAWING No. MD291 A606 3A
WELD WHERE SHOWN THUS				CRANFIELD			SHT. 1 OF 1 SHEETS
MACHINE WHERE SHOWN THUS							

DRAWING No.	
ISSUE	MODIFICATION

ALL DIMENSIONS IN MILLIMETRES UNLESS OTHERWISE STATED. IF IN DOUBT ASK.

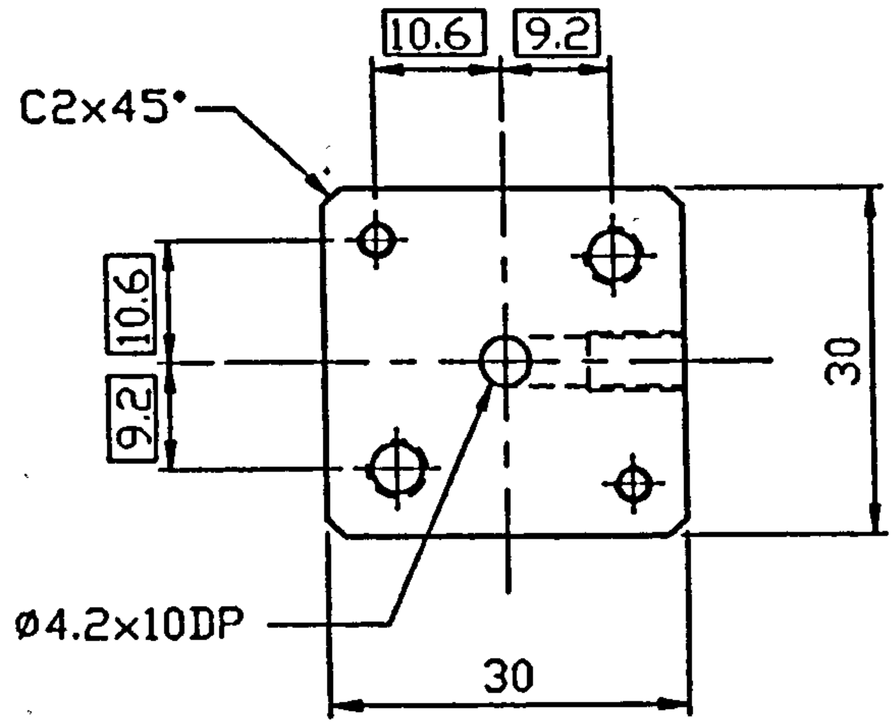

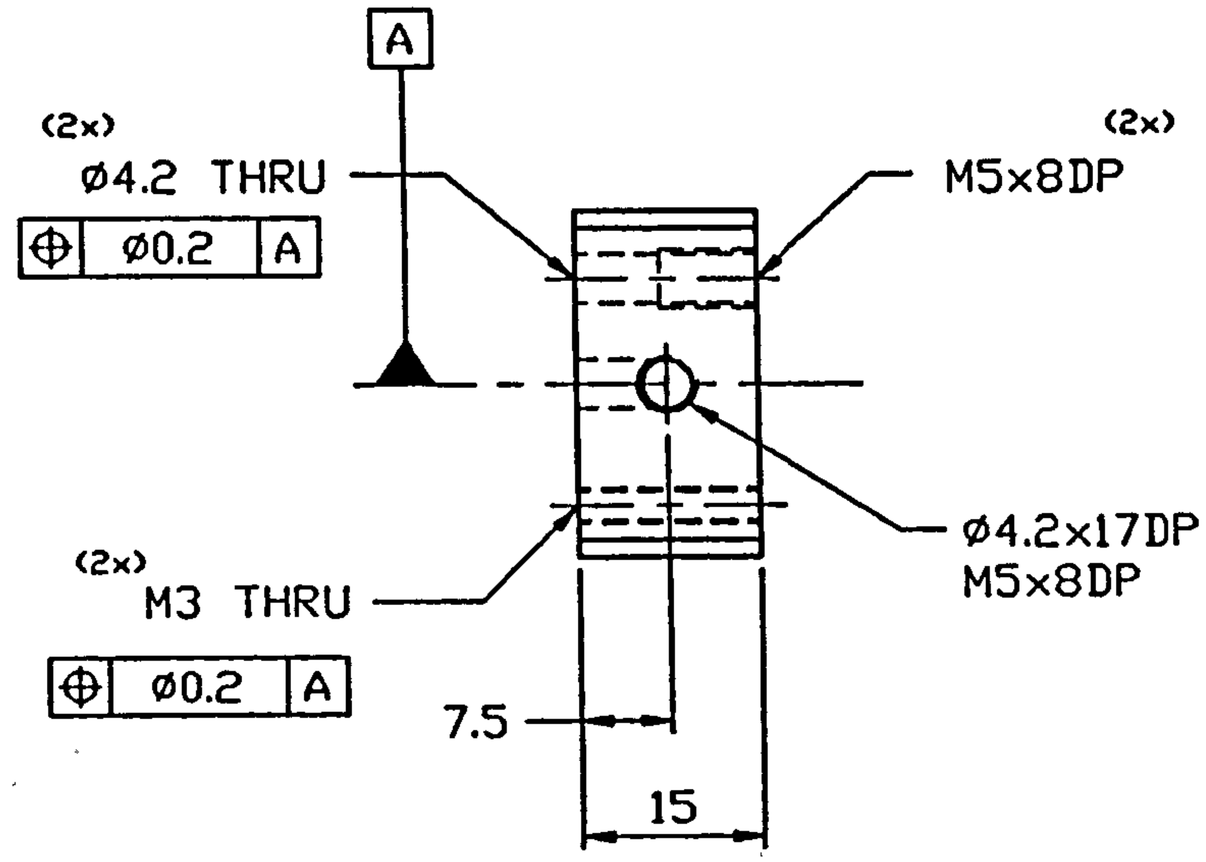

REMOVE ALL SHAPE EDGES

THIRD ANGLE PROJECTION			SHEET SIZE A4				1	ALUM	6061-T6	
				ITEM	PART No.	DESCRIPTION	No. OFF	MATL.	SPEC.	REMARKS
GENERAL TOLERANCE ON DIMENSIONS MACHINED UNMACHINED OTHER DIMENSIONS AS STATED	JOB No.	No. OF SETS REQ.	SCALE 1:1	DRAWN	CHK	DATE	TITLE: MANIFOLD BLOCK			
				Y.B.P.KWAN		10.09.95				
WELD WHERE SHOWN THUS ⌒ L			FINISH BLACK ANODIZED	SCHOOL OF INDUSTRIAL & MANUFACTURING SCIENCE CRANFIELD			DRAWING No. MD291 A607 4A			
MACHINE WHERE SHOWN THUS ✓							SHT. 1 OF 1 SHEETS			

DRAWING No.	
ISSUE	MODIFICATION

ALL DIMENSIONS IN MILLIMETRES UNLESS OTHERWISE STATED. · IF IN DOUBT ASK.

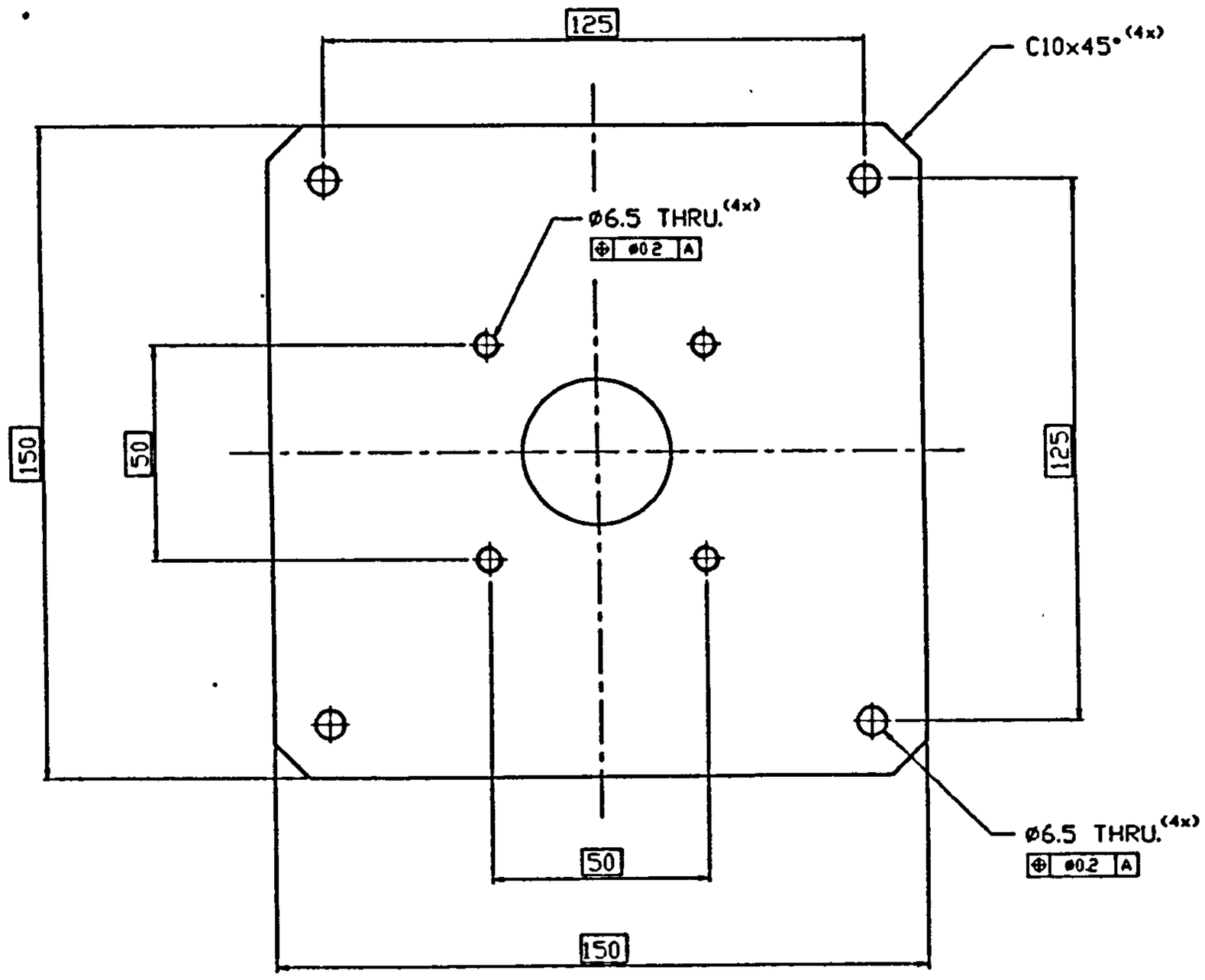

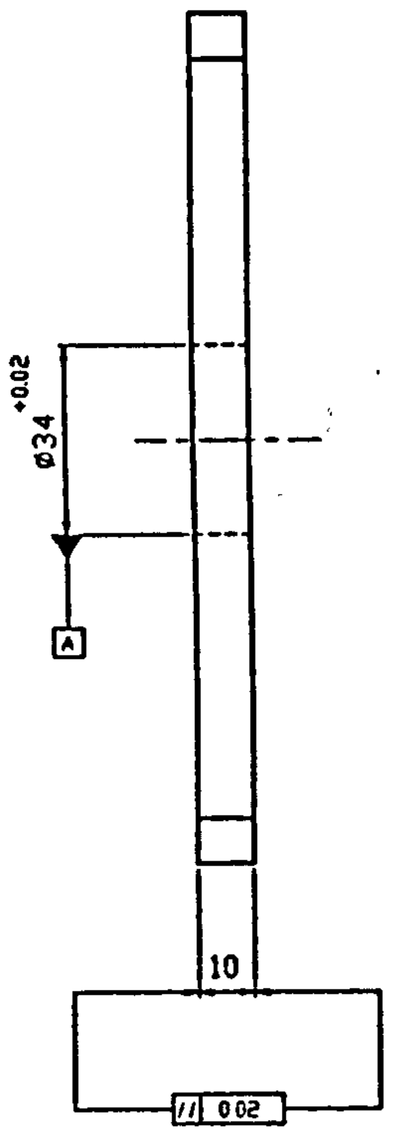

REMOVE ALL SHAPE EDGES

THIRD ANGLE PROJECTION			SHEET SIZE A2
GENERAL TOLERANCE ON DIMENSIONS	JOB No.	No. OF SETS REQ.	SCALE 1:1
MACHINED			
UNMACHINED			
OTHER DIMENSIONS AS STATED			FINISH BLACK ANODIZED
WELD WHERE SHOWN THUS ⌒ L			
MACHINE WHERE SHOWN THUS ✓			

ITEM	PART No.	DESCRIPTION	No. OFF	MATL.	SPEC.	REMARKS
			1	ALUM.	6061-T6	

DRAWN	CHK	DATE
Y.B.P.KWAN		

TITLE: TOP PLATE

SCHOOL OF INDUSTRIAL & MANUFACTURING SCIENCE
CRANFIELD

DRAWING No. MD291 A608 2A

SHT. 1 OF 1 SHEETS

DRAWING No.	
ISSUE	MODIFICATION

ALL DIMENSIONS IN MILLIMETRES UNLESS OTHERWISE STATED. IF IN DOUBT ASK.

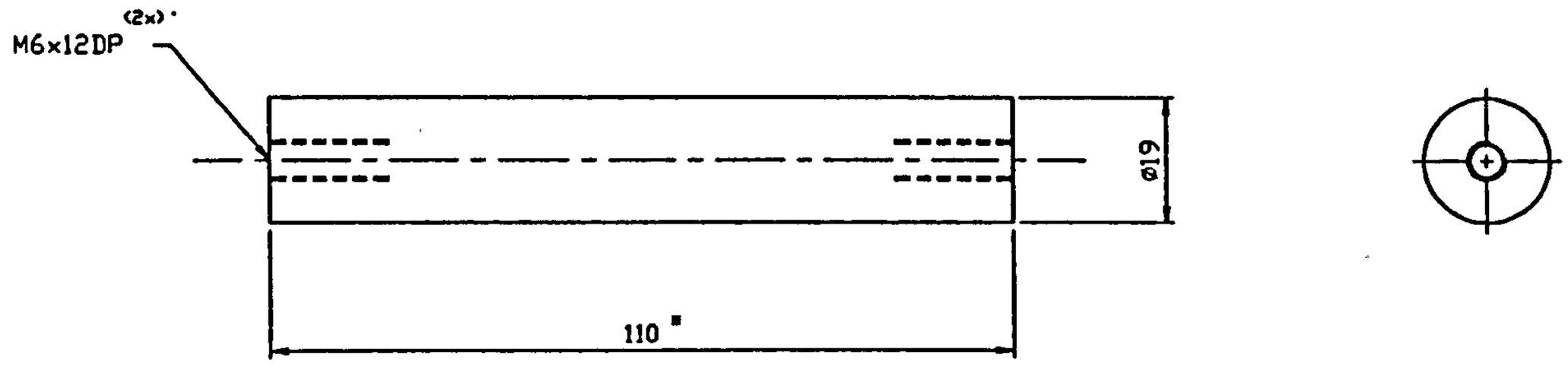

LGTH DEVIATION BTW SET OF 4 <= 0.02

REMOVE ALL SHAPE EDGES

ITEM	PART No.	DESCRIPTION	No. OFF	MATL.	SPEC.	REMARKS
			4	ALUM.	6061-T6	

THIRD ANGLE PROJECTION

SHEET SIZE A3

GENERAL TOLERANCE ON DIMENSIONS	JOB No.	No. OF SETS REQ.
MACHINED		
UNMACHINED		
OTHER DIMENSIONS AS STATED		
WELD WHERE SHOWN THUS ⌒ L		
MACHINE WHERE SHOWN THUS ✓		

SCALE 1:1

FINISH

DRAWN	CHK	DATE
Y.B.P.KWAN		10.09.95

TITLE: PILLAR

SCHOOL OF INDUSTRIAL & MANUFACTURING SCIENCE
CRANFIELD

DRAWING No. MD291 A609 3A

SHT. 1 OF 1 SHEETS

DRAWING No.	
ISSUE	MODIFICATION

ALL DIMENSIONS IN MILLIMETRES UNLESS OTHERWISE STATED. IF IN DOUBT ASK.

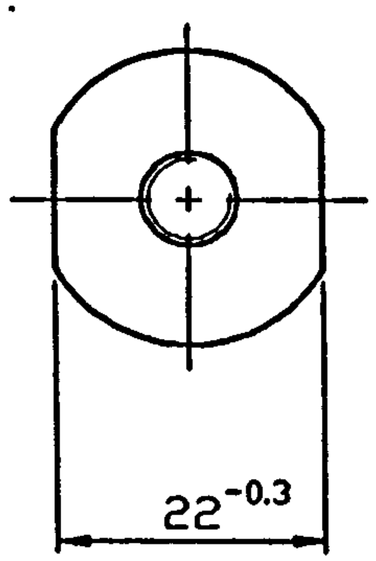

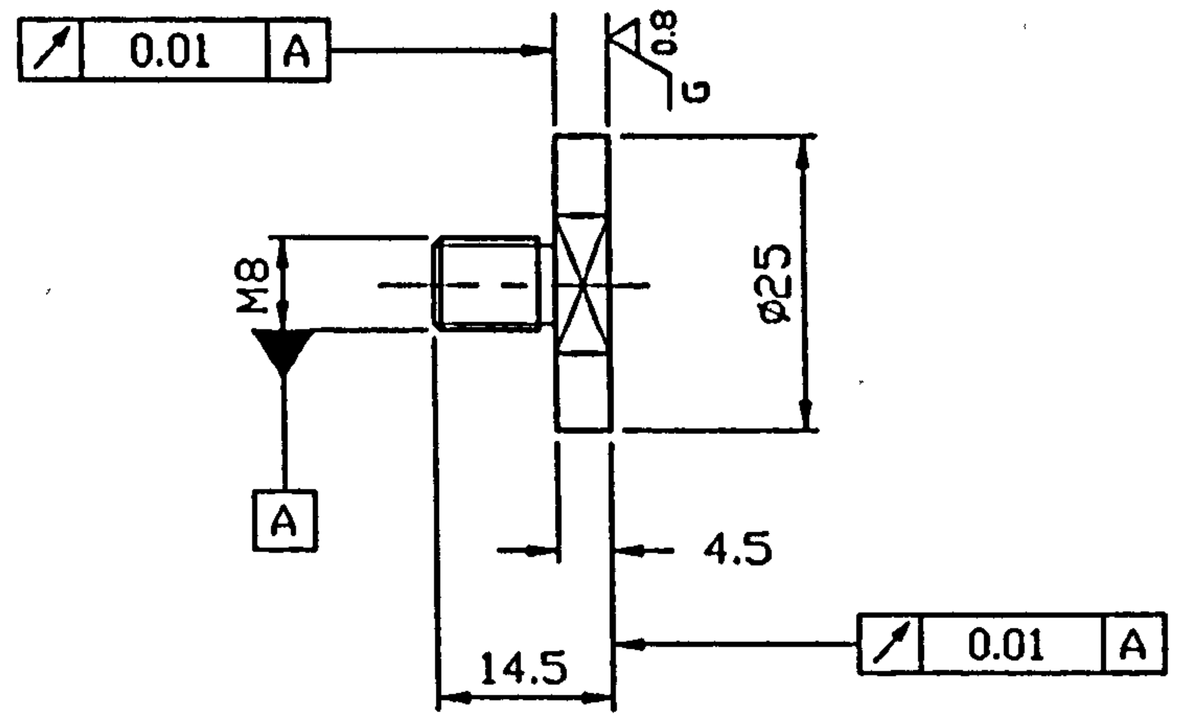

REMOVE ALL SHAPE EDGES

THIRD ANGLE PROJECTION	SHEET SIZE A4	ITEM	PART No.	DESCRIPTION	No. OFF	MATL.	SPEC.	REMARKS
					1	SST	440C	

GENERAL TOLERANCE ON DIMENSIONS	JOB No.	No. OF SETS REQ.	SCALE 1:1	DRAWN	CHK	DATE	TITLE: ROD END FITTING
MACHINED				Y.B.P.KWAN		10.09.95	
UNMACHINED							
OTHER DIMENSIONS AS STATED			FINISH HRc 50-55	SCHOOL OF INDUSTRIAL & MANUFACTURING SCIENCE			DRAWING No. MD291 A610 4A
WELD WHERE SHOWN THUS				CRANFIELD			SHT. 1 OF 1 SHEETS
MACHINE WHERE SHOWN THUS							

DRAWING No.	
ISSUE	MODIFICATION

ALL DIMENSIONS IN MILLIMETRES UNLESS OTHERWISE STATED. IF IN DOUBT ASK.

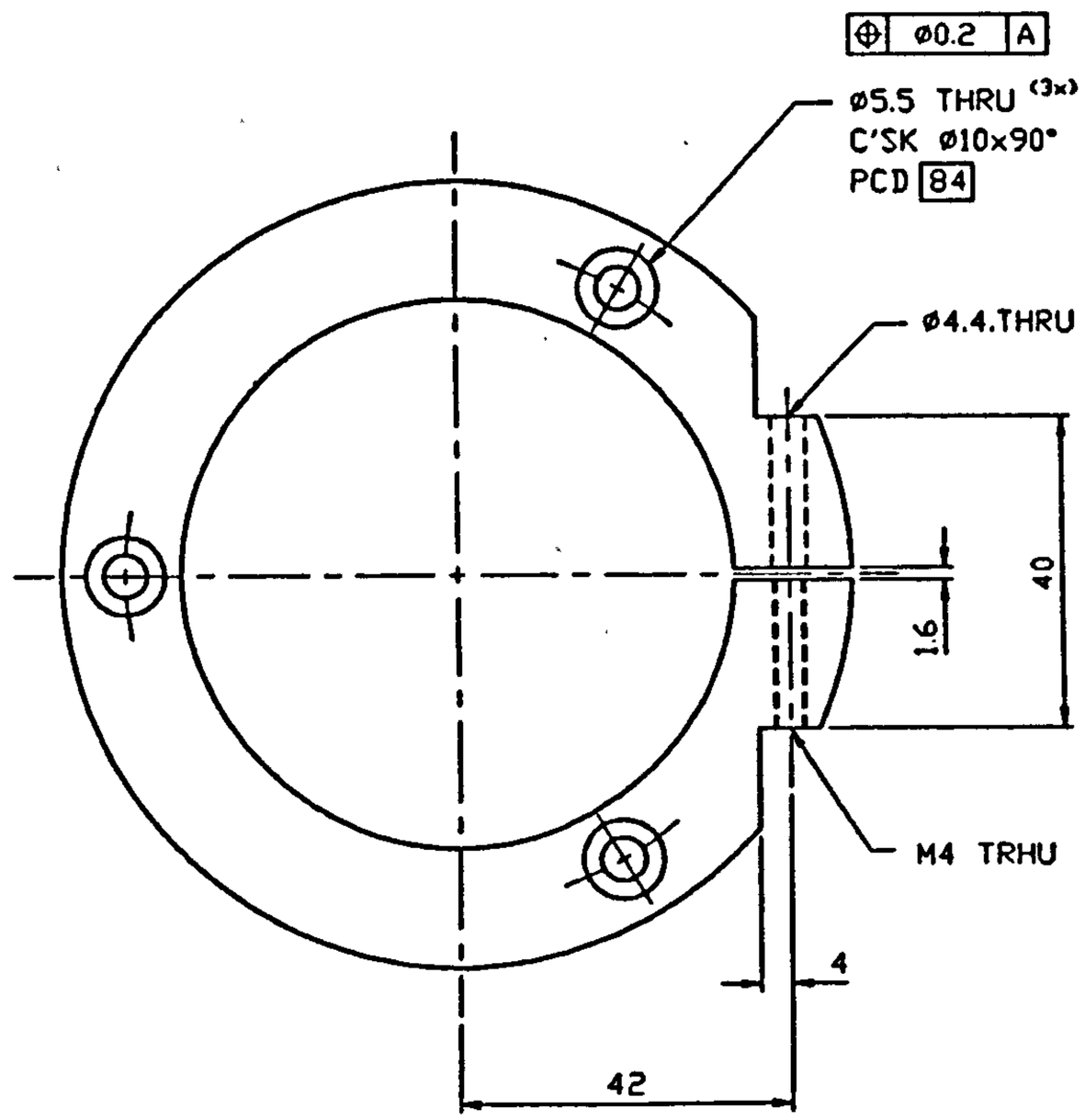

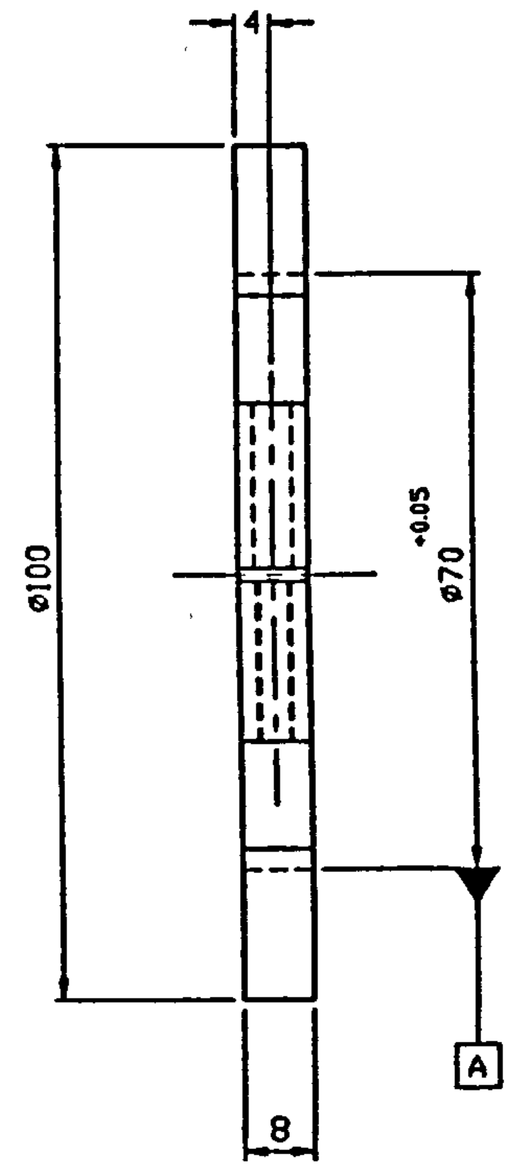

REMOVE ALL SHAPE EDGES

THIRD ANGLE PROJECTION	SHEET SIZE A3	ITEM	PART No.	DESCRIPTION	No. OFF	MATL.	SPEC.	REMARKS
					1	DELRIN		

GENERAL TOLERANCE ON DIMENSIONS	JOB No.	No. OF SETS REQ.	SCALE 1:1	DRAWN	CHK	DATE	TITLE: LOCATING RING
MACHINED				Y.B.P.KWAN		10.09 95	
UNMACHINED							
OTHER DIMENSIONS AS STATED			FINISH	SCHOOL OF INDUSTRIAL & MANUFACTURING SCIENCE			DRAWING No. MD291 A611 3A
WELD WHERE SHOWN THUS ⌒ L				CRANFIELD			SHT. 1 OF 1 SHEETS
MACHINE WHERE SHOWN THUS √							

DRAWING No.	
ISSUE	MODIFICATION

ALL DIMENSIONS IN MILLIMETRES UNLESS OTHERWISE STATED. IF IN DOUBT ASK.

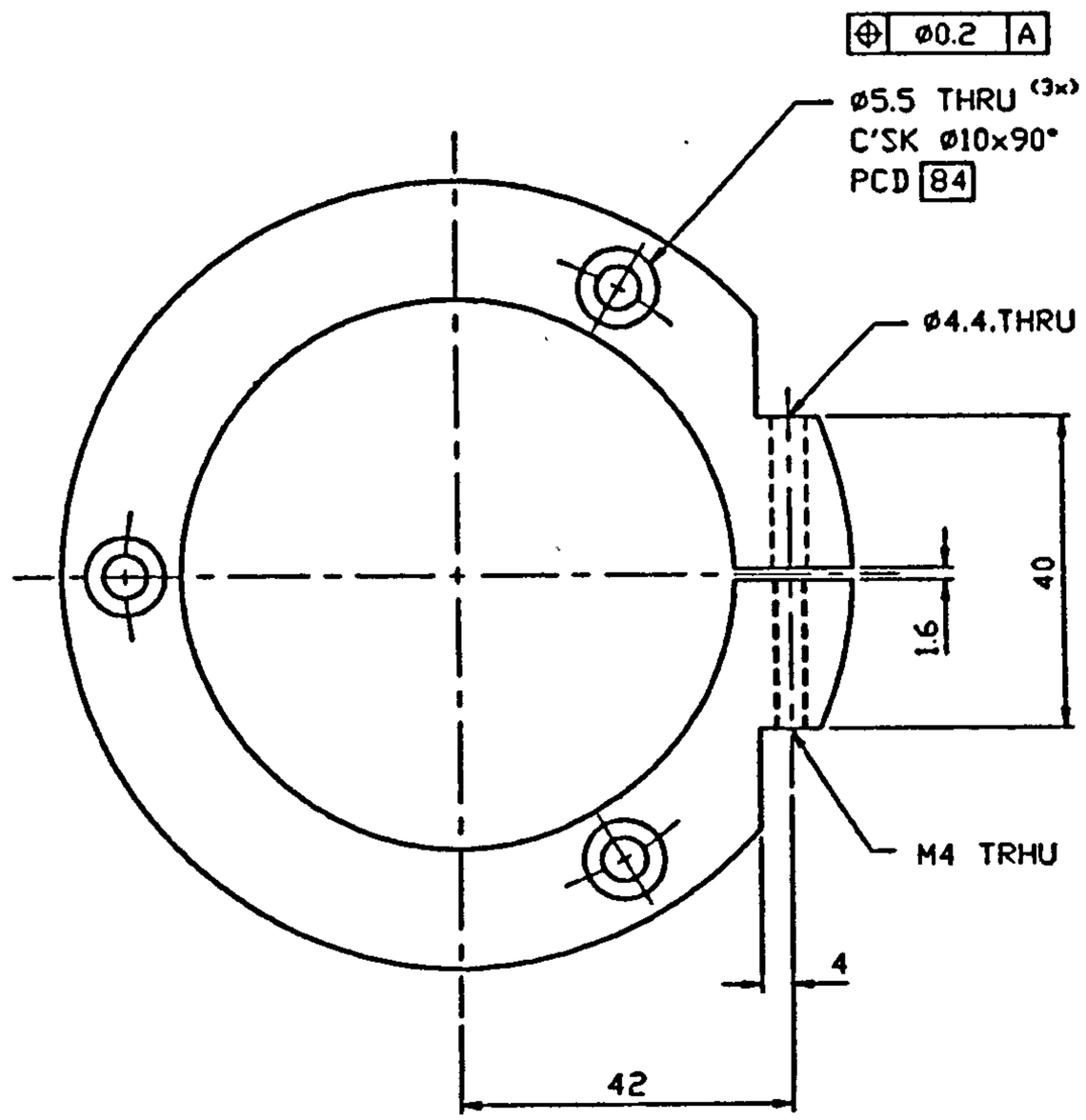

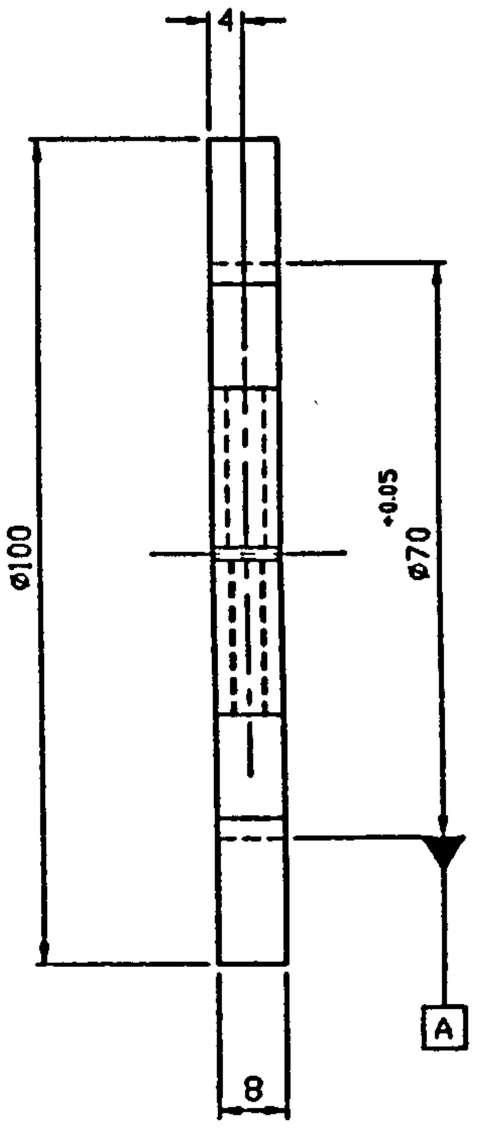

REMOVE ALL SHAPE EDGES

THIRD ANGLE PROJECTION	SHEET SIZE A3	ITEM	PART No.	DESCRIPTION	No. OFF	MATL.	SPEC.	REMARKS
					1	DELRIN		

GENERAL TOLERANCE ON DIMENSIONS	JOB No.	No. OF SETS REQ.	SCALE 1:1	DRAWN	CHK	DATE	TITLE: LOCATING RING
MACHINED				Y.B.P.KWAN		10.09.93	
UNMACHINED							
OTHER DIMENSIONS AS STATED			FINISH	SCHOOL OF INDUSTRIAL & MANUFACTURING SCIENCE			DRAWING No. MD291 A611 3A
WELD WHERE SHOWN THUS				CRANFIELD			SHT. 1 OF 1 SHEETS
MACHINE WHERE SHOWN THUS							

DRAWING No.

ISSUE	MODIFICATION

ALL DIMENSIONS IN MILLIMETRES UNLESS OTHERWISE STATED. IF IN DOUBT ASK.

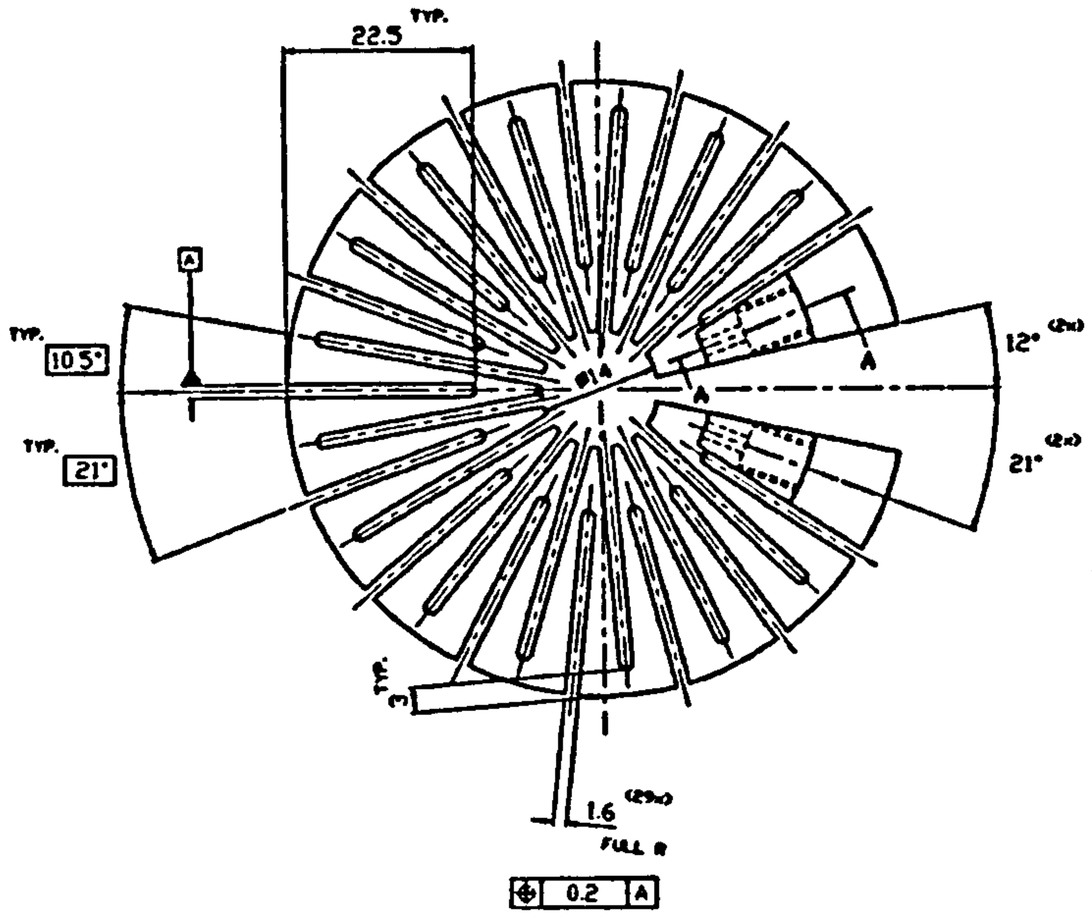

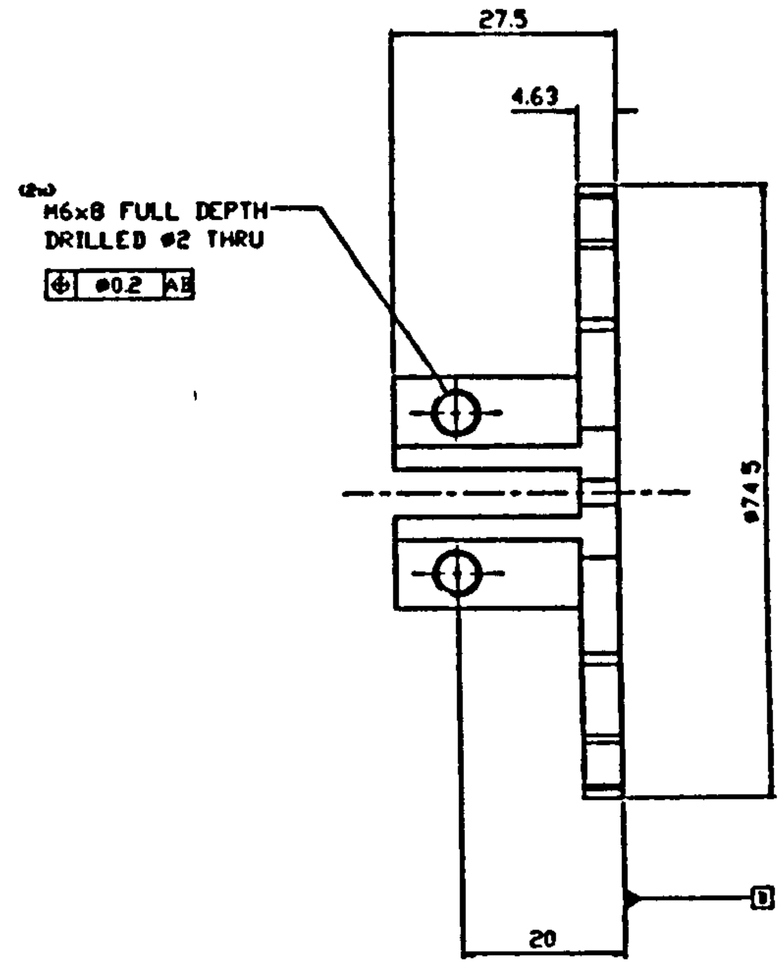

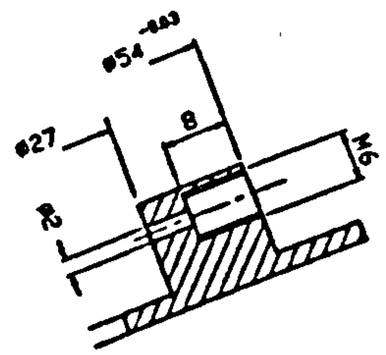

SECTION A-A

REMOVE ALL SHAPE EDGES

THIRD ANGLE PROJECTION			SHEET SIZE A1				1	GRAPHITE	IG-11	
				ITEM	PART No.	DESCRIPTION	No. OFF	MATL.	SPEC.	REMARKS
GENERAL TOLERANCE ON DIMENSIONS MACHINED ±0.2 UNMACHINED OTHER DIMENSIONS AS STATED WELD WHERE SHOWN THUS —L— MACHINE WHERE SHOWN THUS ⊿	JOB No.	No. OF SETS REQ.	SCALE 2:1	DRAWN Y.B.P.KVAN	CHK	DATE 17.11.98	TITLE: BOTTOM HEATING ELEMENT			
			FINISH	SCHOOL OF INDUSTRIAL & MANUFACTURING SCIENCE CRANFIELD			DRAWING No. MD291 A701 2A			
							SHT. 1 OF 1 SHEETS			

DRAWING No.	
ISSUE	MODIFICATION

ALL DIMENSIONS IN MILLIMETRES UNLESS OTHERWISE STATED. IF IN DOUBT ASK.

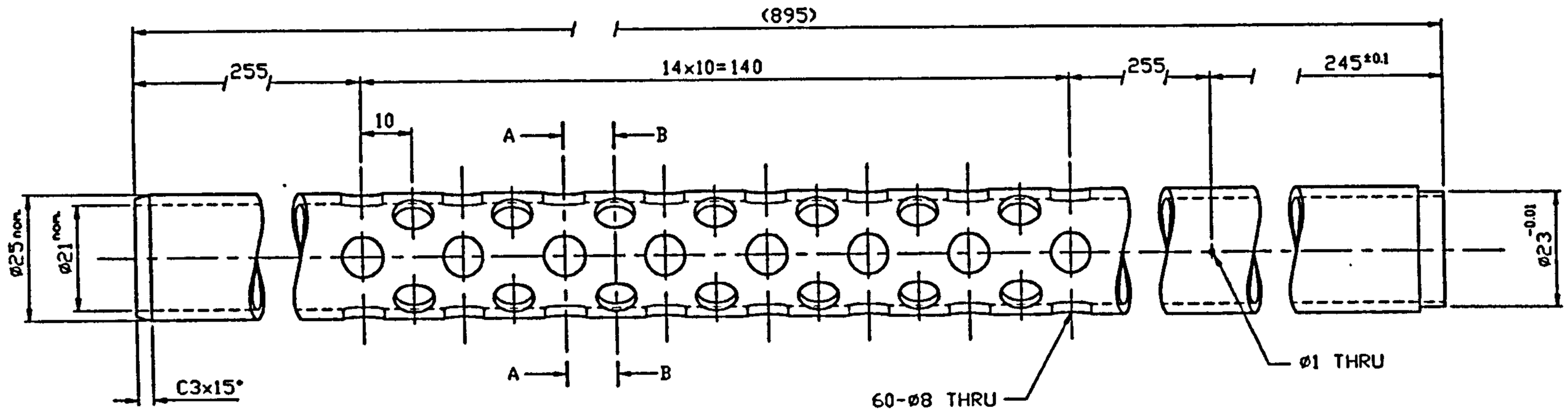

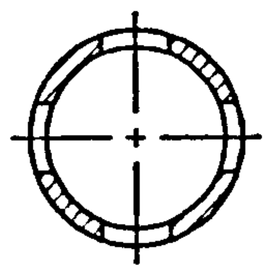

SECTION A-A

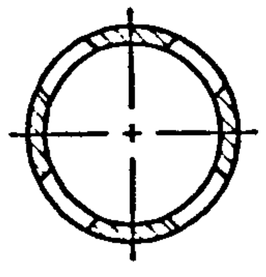

SECTION B-B

NOTE: BOTH INNER & OUTER SURFACES OF TUBE TO REMAIN SCRATCH FREE. TAKE CARE WHEN DEBURRING HOLES.

REMOVE ALL SHAPE EDGES

THIRD ANGLE PROJECTION

SHEET SIZE	ITEM	PART No.	DESCRIPTION	No. OFF	MATL.	SPEC.	REMARKS
A3				1	PERSPEX	CAST	

GENERAL TOLERANCE ON DIMENSIONS	JOB No.	No. OF SETS REQ.
MACHINED		
UNMACHINED		
OTHER DIMENSIONS AS STATED		
WELD WHERE SHOWN THUS ⌒ L		
MACHINE WHERE SHOWN THUS ⊿		

SCALE	DRAWN	CHK	DATE
1:1	Y.B.P.KWAN		25.11.94

FINISH

TITLE: INLET TUBE (INNER)

SCHOOL OF INDUSTRIAL & MANUFACTURING SCIENCE

CRANFIELD

DRAWING No. MD291 B101 3A

SHT. 1 OF 1 SHEETS

DRAWING No.	
ISSUE	MODIFICATION

ALL DIMENSIONS IN MILLIMETRES UNLESS OTHERWISE STATED. IF IN DOUBT ASK.

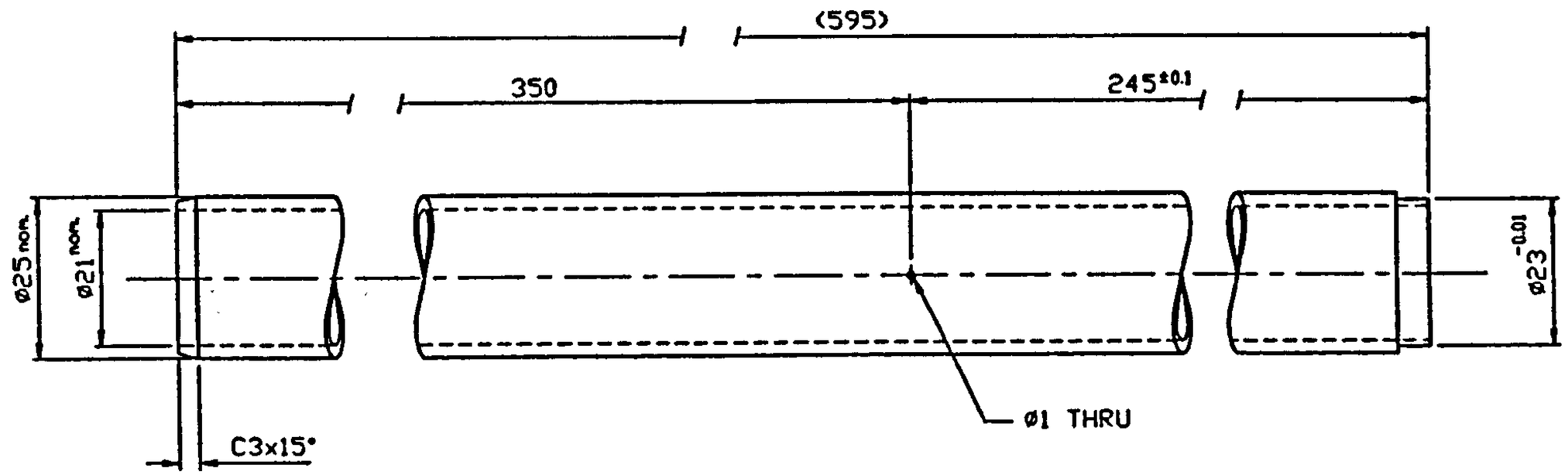

NOTE: BOTH INNER & OUTER SURFACES OF TUBE TO REMAIN SCRATCH FREE.

REMOVE ALL SHAPE EDGES

THIRD ANGLE PROJECTION

SHEET SIZE	ITEM	PART No.	DESCRIPTION	No. OFF	MATL.	SPEC.	REMARKS
A3				1	PERSPEX	CAST	

GENERAL TOLERANCE ON DIMENSIONS	JOB No.	No. OF SETS REQ.	SCALE	DRAWN	CHK	DATE	TITLE:
MACHINED			1:1	Y.B.P.KWAN		25.11.94	OUTLET TUBE (INNER)
UNMACHINED							
OTHER DIMENSIONS AS STATED			FINISH	SCHOOL OF INDUSTRIAL & MANUFACTURING SCIENCE			DRAWING No. MD291 B102 3A
WELD WHERE SHOWN THUS ⌒				CRANFIELD			SHT. 1 OF 1 SHEETS
MACHINE WHERE SHOWN THUS ✓							

DRAWING No.

ISSUE	MODIFICATION

ALL DIMENSIONS IN MILLIMETRES UNLESS OTHERWISE STATED. · IF IN DOUBT ASK.

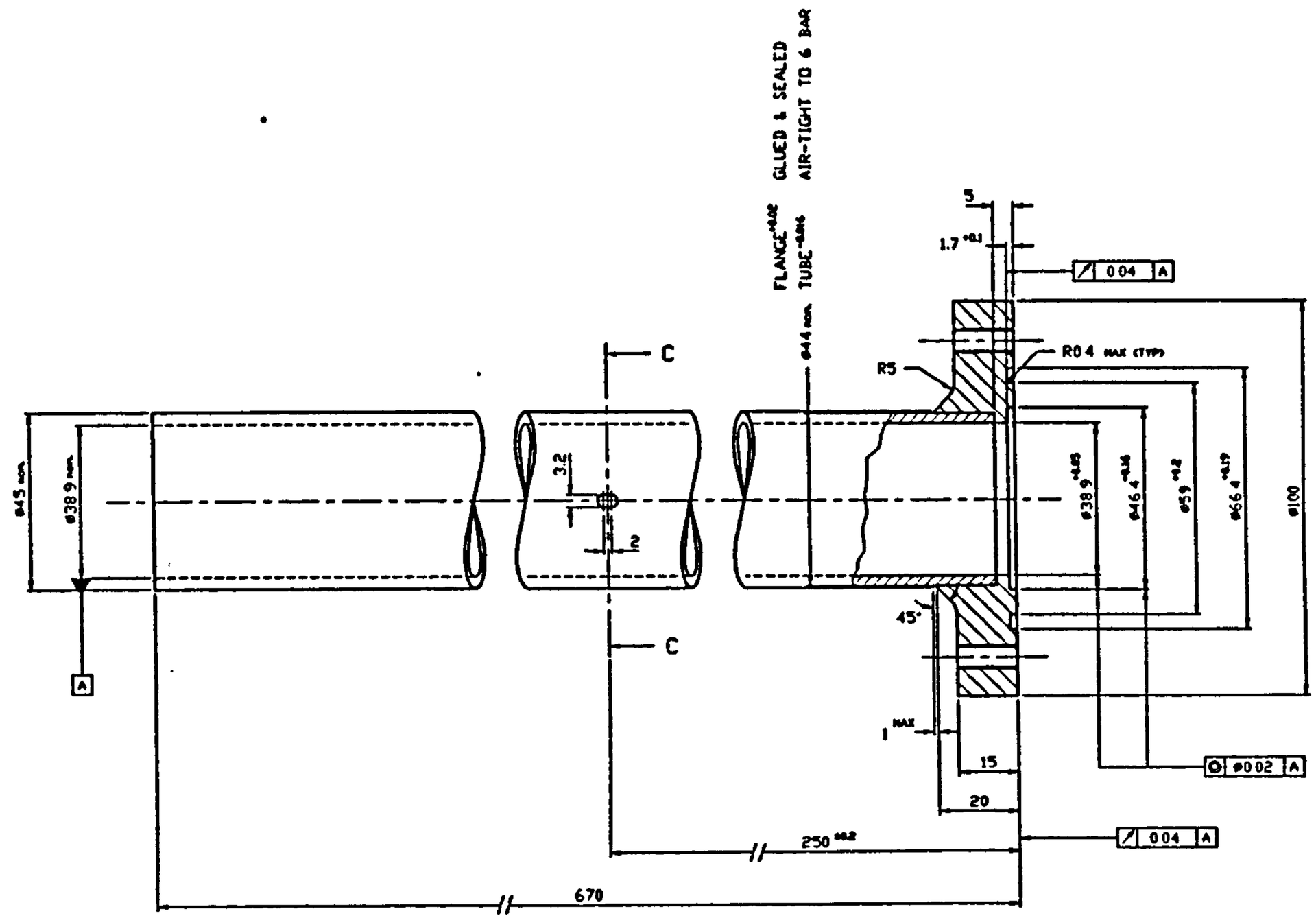

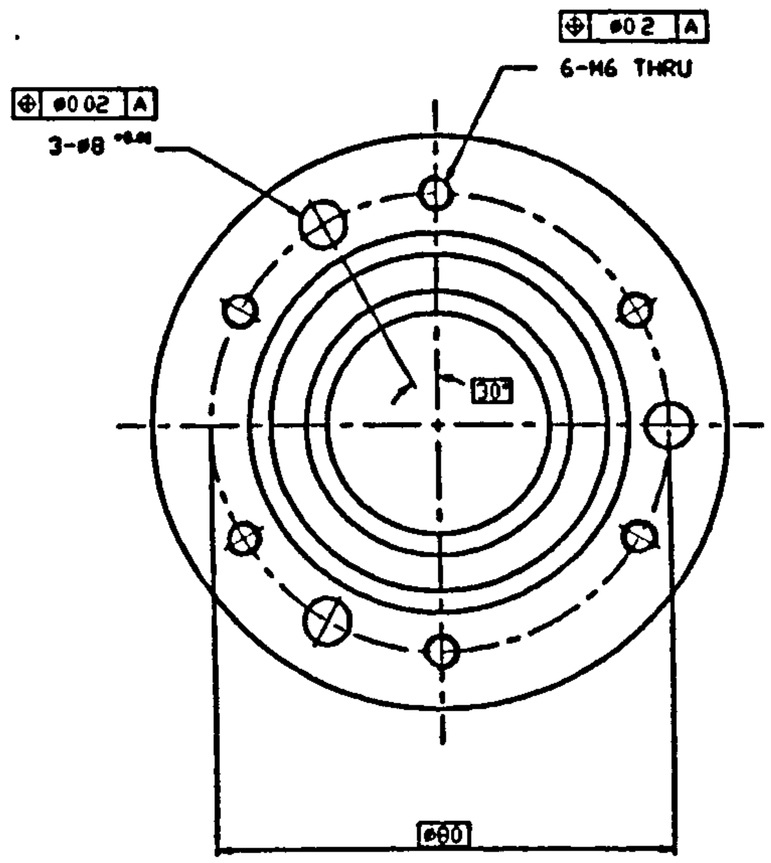

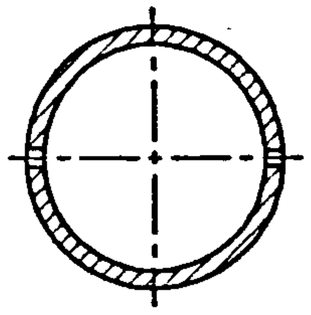

SECTION C-C

REMOVE ALL SHAPE EDGES

THIRD ANGLE PROJECTION			SHEET SIZE A2				1	PERSPEX	CAST	
				ITEM	PART No.	DESCRIPTION	No. OFF	MATL.	SPEC.	REMARKS
GENERAL TOLERANCE ON DIMENSIONS	JOB No.	No. OF SETS REQ.	SCALE 1:1	DRAWN	CHK	DATE	TITLE: INLET TUBE (OUTER)			
MACHINED				Y.B.P.KWAN		28.11.94				
UNMACHINED										
OTHER DIMENSIONS AS STATED			FINISH	SCHOOL OF INDUSTRIAL & MANUFACTURING SCIENCE			DRAWING No. MD291 B103 2A			
WELD WHERE SHOWN THUS ⌐¬				CRANFIELD			SHT. 1 OF 1 SHEETS			
MACHINE WHERE SHOWN THUS ✓										

DRAWING No.	
ISSUE	MODIFICATION

ALL DIMENSIONS IN MILLIMETRES UNLESS OTHERWISE STATED. IF IN DOUBT ASK.

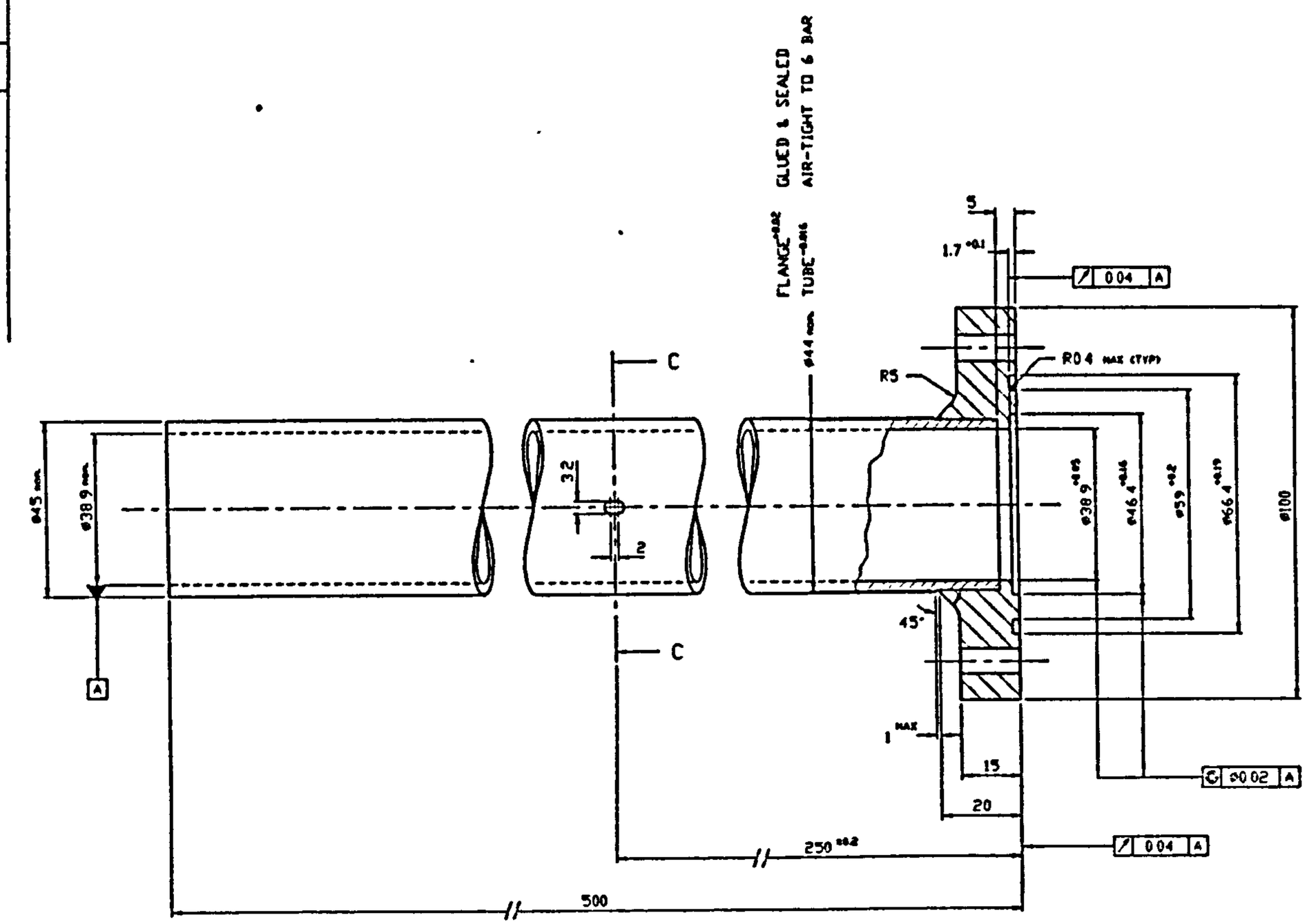

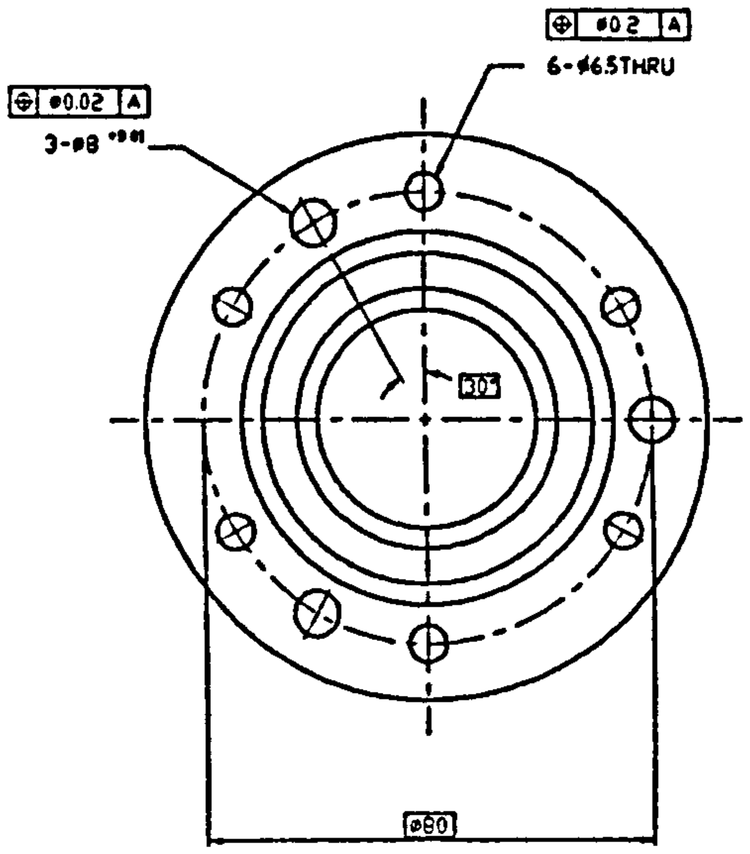

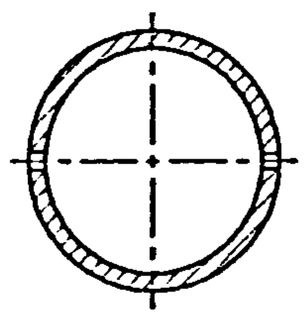

SECTION C-C

REMOVE ALL SHAPE EDGES

THIRD ANGLE PROJECTION			SHEET SIZE A2								
				ITEM	PART No.	DESCRIPTION	No. OFF	MATL.	SPEC.	REMARKS
GENERAL TOLERANCE ON DIMENSIONS	JOB No.	No. OF SETS REQ	SCALE 1:1	DRAWN	CHK	DATE	TITLE: OUTLET TUBE (OUTER)			1	PERSPEX	CAST	
MACHINED				YBPXGAN		28/1/94							
UNMACHINED													
OTHER DIMENSIONS AS STATED			FINISH	SCHOOL OF INDUSTRIAL & MANUFACTURING SCIENCE			DRAWING No. MD291 B104 2A						
WELD WHERE SHOWN THUS ⌐ ⌐				CRANFIELD			SHT. 1 OF 1 SHEETS						
MACHINE WHERE SHOWN THUS ✓													

DRAWING No.	
ISSUE	MODIFICATION

ALL DIMENSIONS IN MILLIMETRES UNLESS OTHERWISE STATED. IF IN DOUBT ASK.

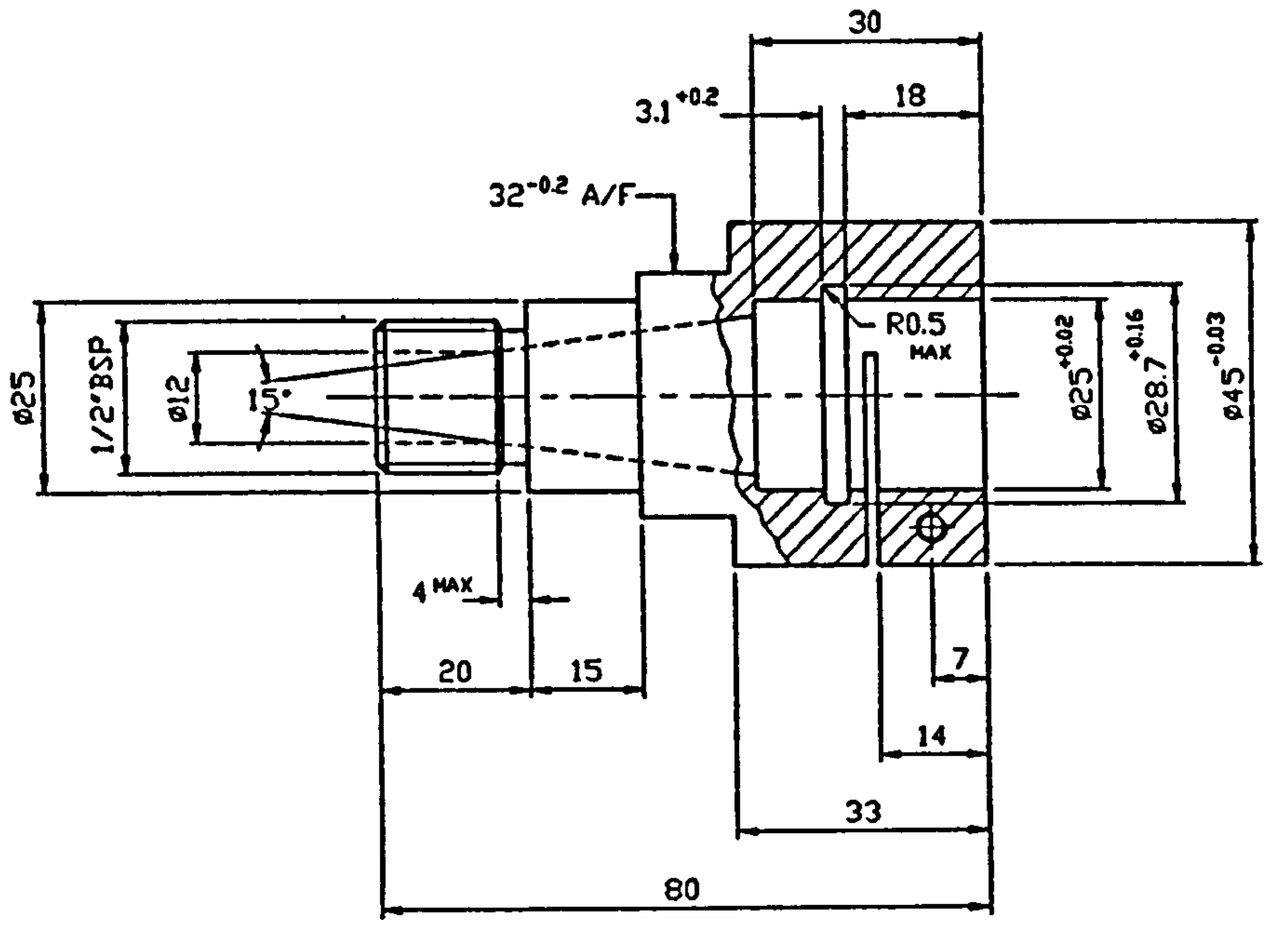

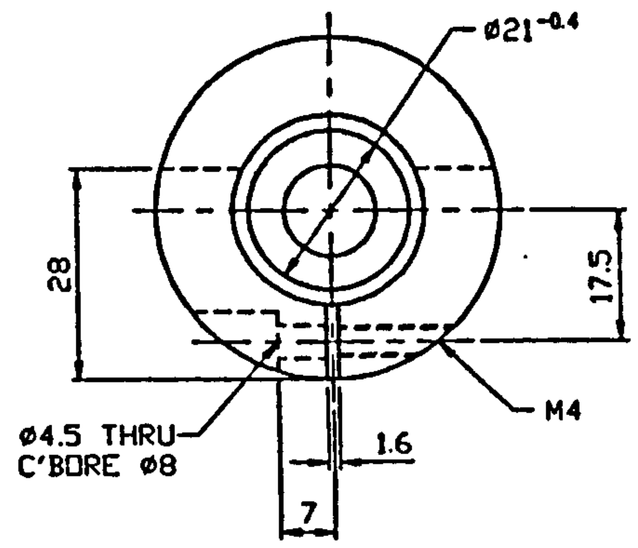

REMOVE ALL SHAPE EDGES

THIRD ANGLE PROJECTION	SHEET SIZE A3	ITEM	PART No.	DESCRIPTION	No. OFF	MATL.	SPEC.	REMARKS
					1	ALUM.	6061-T6	

GENERAL TOLERANCE ON DIMENSIONS	JOB No.	No. OF SETS REQ.	SCALE 1:1	DRAWN	CHK	DATE	TITLE: END FITTING I
MACHINED				Y.B.P.KWAN		25.11.94	
UNMACHINED							
OTHER DIMENSIONS AS STATED			FINISH	SCHOOL OF INDUSTRIAL & MANUFACTURING SCIENCE			DRAWING No. MD291 B105 3A
WELD WHERE SHOWN THUS			BLACK ANODIZED	CRANFIELD			SHT. 1 OF 1 SHEETS
MACHINE WHERE SHOWN THUS							

DRAWING No.	
ISSUE	MODIFICATION

ALL DIMENSIONS IN MILLIMETRES UNLESS OTHERWISE STATED. IF IN DOUBT ASK.

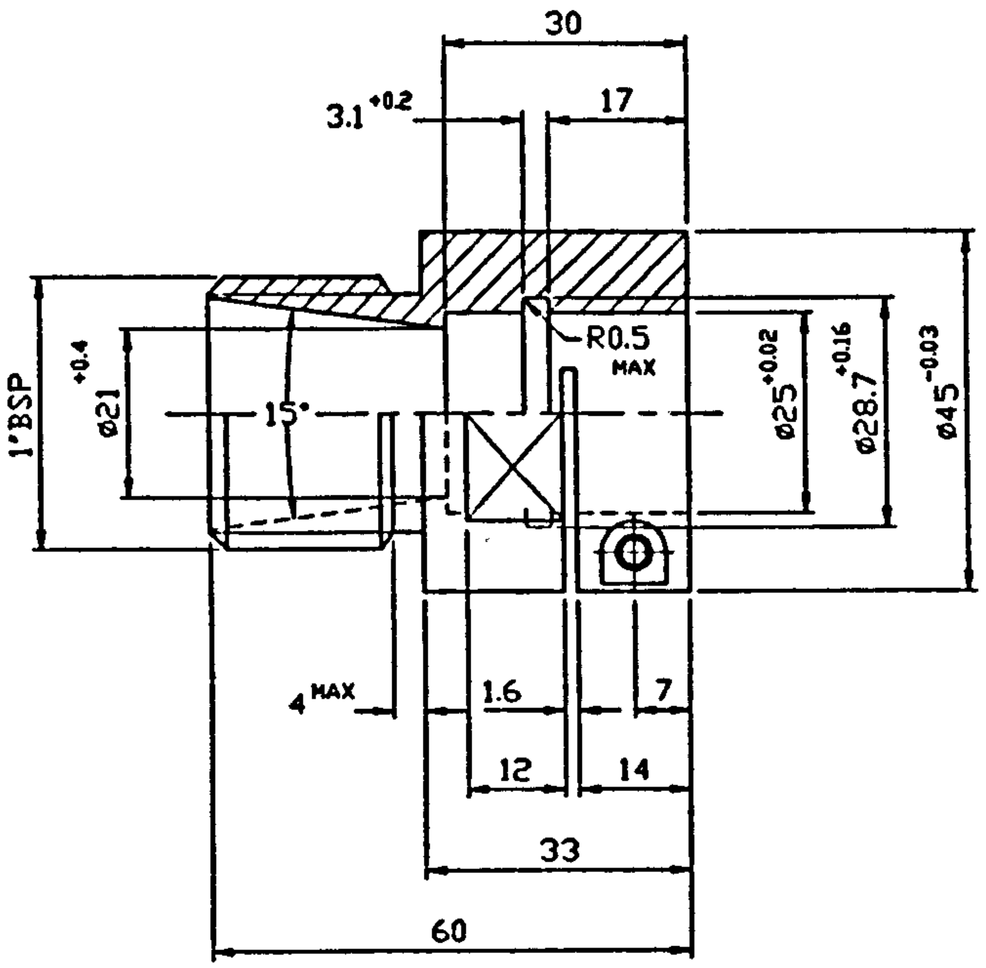

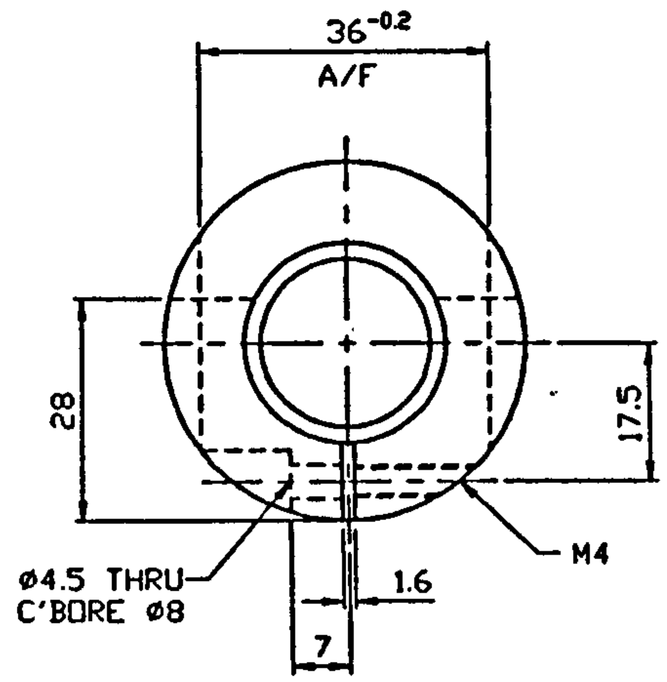

REMOVE ALL SHAPE EDGES

THIRD ANGLE PROJECTION	SHEET SIZE A3	ITEM	PART No.	DESCRIPTION	No. OFF	MATL.	SPEC.	REMARKS
					1	ALUM.	6061-T6	

GENERAL TOLERANCE ON DIMENSIONS	JOB No.	No. OF SETS REQ.	SCALE 1:1	DRAWN	CHK	DATE	TITLE: END FITTING II
MACHINED				Y.B.P.KWAN		25.11.94	
UNMACHINED							
OTHER DIMENSIONS AS STATED			FINISH	SCHOOL OF INDUSTRIAL & MANUFACTURING SCIENCE			DRAWING No. MD291 B106 3A
WELD WHERE SHOWN THUS ⌒ L			BLACK ANODIZED	CRANFIELD			SHT. 1 OF 1 SHEETS
MACHINE WHERE SHOWN THUS ✓							

DRAWING No.	
ISSUE	MODIFICATION

ALL DIMENSIONS IN MILLIMETRES UNLESS OTHERWISE STATED. IF IN DOUBT ASK.

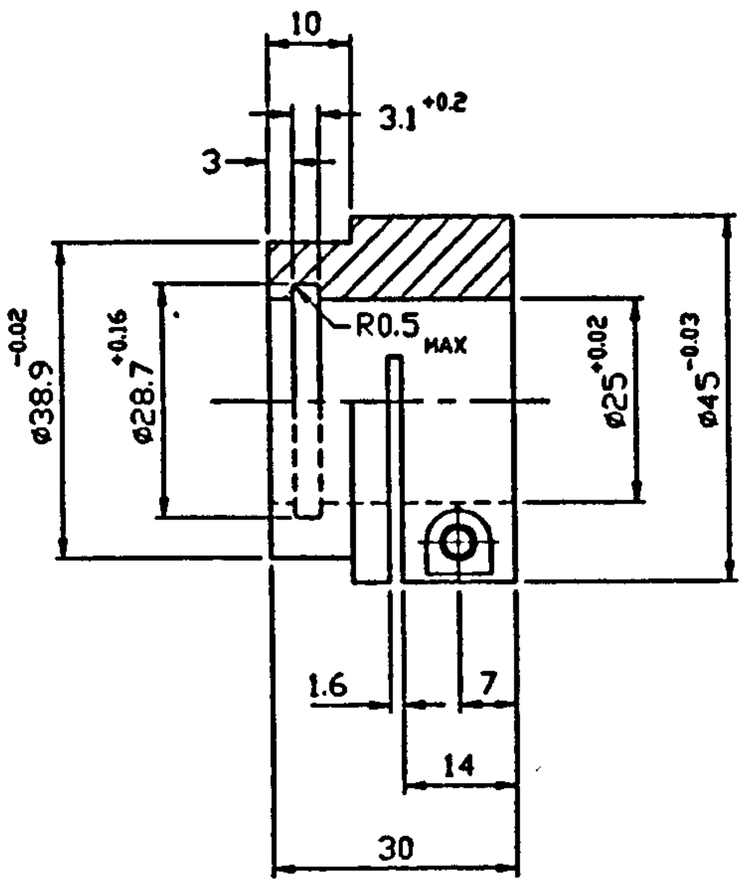

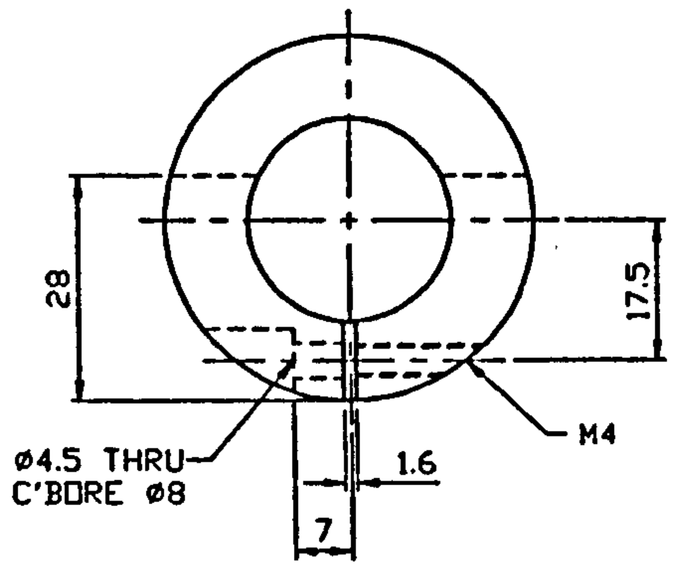

REMOVE ALL SHAPE EDGES

THIRD ANGLE PROJECTION	SHEET SIZE A3	ITEM	PART No.	DESCRIPTION	No. OFF	MATL.	SPEC.	REMARKS
					1	ALUM.	6061-T6	

GENERAL TOLERANCE ON DIMENSIONS	JOB No.	No. OF SETS REQ.	SCALE 1:1	DRAWN	CHK	DATE	TITLE: END FITTING III
MACHINED				Y.B.P.KWAN		27.11.94	
UNMACHINED							
OTHER DIMENSIONS AS STATED			FINISH	SCHOOL OF INDUSTRIAL & MANUFACTURING SCIENCE			DRAWING No. MD291 B107 3A
WELD WHERE SHOWN THUS ⌒			BLACK ANODIZED	CRANFIELD			SHT. 1 OF 1 SHEETS
MACHINE WHERE SHOWN THUS ✓							

DRAWING No.	
ISSUE	MODIFICATION

ALL DIMENSIONS IN MILLIMETRES UNLESS OTHERWISE STATED. · IF IN DOUBT ASK.

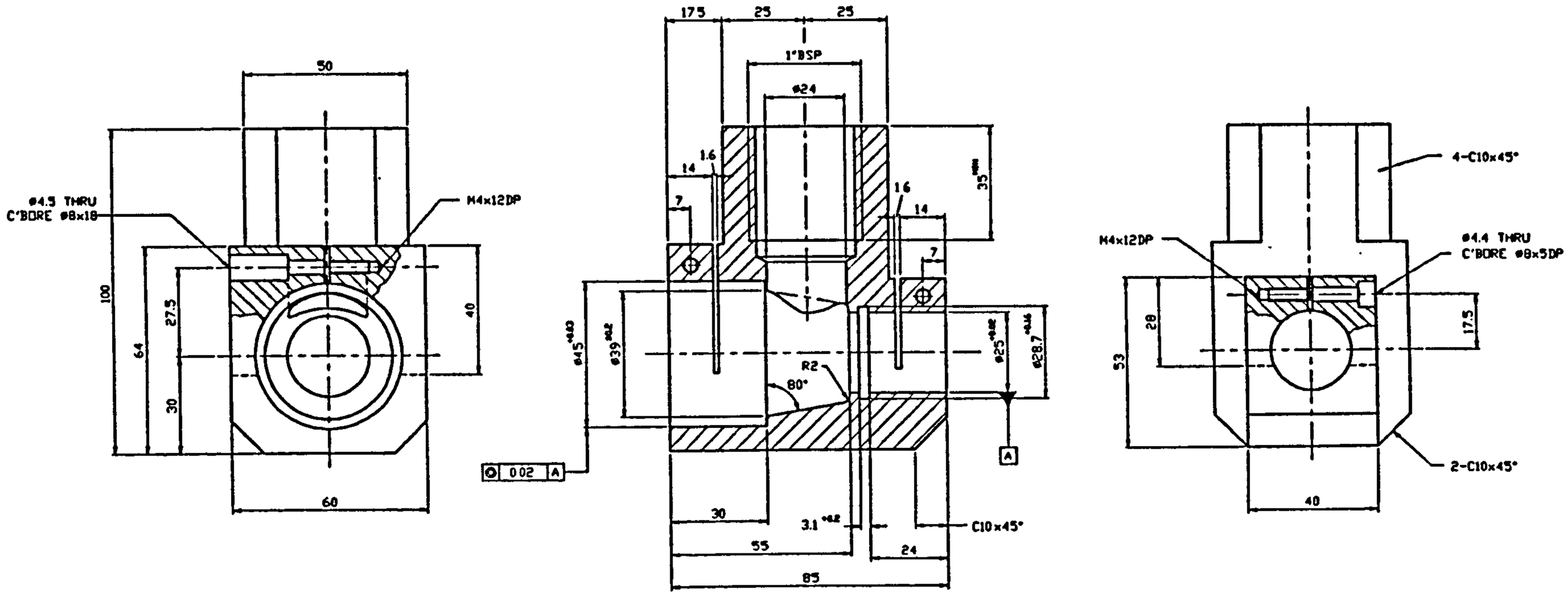

REMOVE ALL SHAPE EDGES

THIRD ANGLE PROJECTION			SHEET SIZE A2
GENERAL TOLERANCE ON DIMENSIONS	JOB No.	No. OF SETS REQ.	SCALE 1:1
MACHINED			
UNMACHINED			
OTHER DIMENSIONS AS STATED			FINISH BLACK ANODIZED
WELD WHERE SHOWN THUS ⌒ L			
MACHINE WHERE SHOWN THUS ✓			

ITEM	PART No.	DESCRIPTION	No. OFF	MATL.	SPEC.	REMARKS
			1	ALUM.	6061-T6	

DRAWN	CHK	DATE
Y.B.P.KVAN		29.11.94

TITLE: END FITTING IV

SCHOOL OF INDUSTRIAL & MANUFACTURING SCIENCE
CRANFIELD

DRAWING No. MD291 B108 2A

SHT. OF SHEETS

DRAWING No.	
ISSUE	MODIFICATION

ALL DIMENSIONS IN MILLIMETRES UNLESS OTHERWISE STATED. IF IN DOUBT ASK.

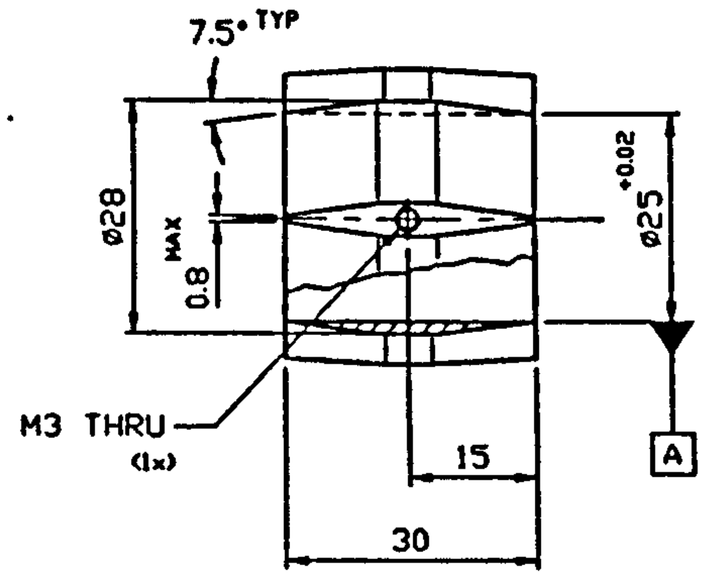

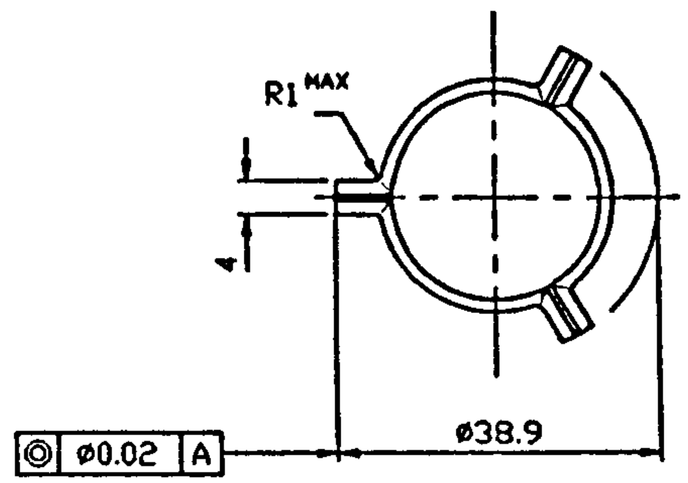

REMOVE ALL SHAPE EDGES

THIRD ANGLE PROJECTION	SHEET SIZE A3	ITEM	PART No.	DESCRIPTION	No. OFF	MATL.	SPEC.	REMARKS
					2	ALUM.	6061-T6	

GENERAL TOLERANCE ON DIMENSIONS MACHINED UNMACHINED OTHER DIMENSIONS AS STATED WELD WHERE SHOWN THUS ⌒ L MACHINE WHERE SHOWN THUS ⊿	JOB No.	No. OF SETS REQ.	SCALE 1:1	DRAWN	CHK	DATE	TITLE: GUIDE VANE
				Y.B.P.KWAN		27.11.94	
			FINISH BLACK ANODIZED	SCHOOL OF INDUSTRIAL & MANUFACTURING SCIENCE CRANFIELD			DRAWING No. MD291 B109 3A
							SHT. 1 OF 1 SHEETS

DRAWING No.	
ISSUE	MODIFICATION

ALL DIMENSIONS IN MILLIMETRES UNLESS OTHERWISE STATED. IF IN DOUBT ASK.

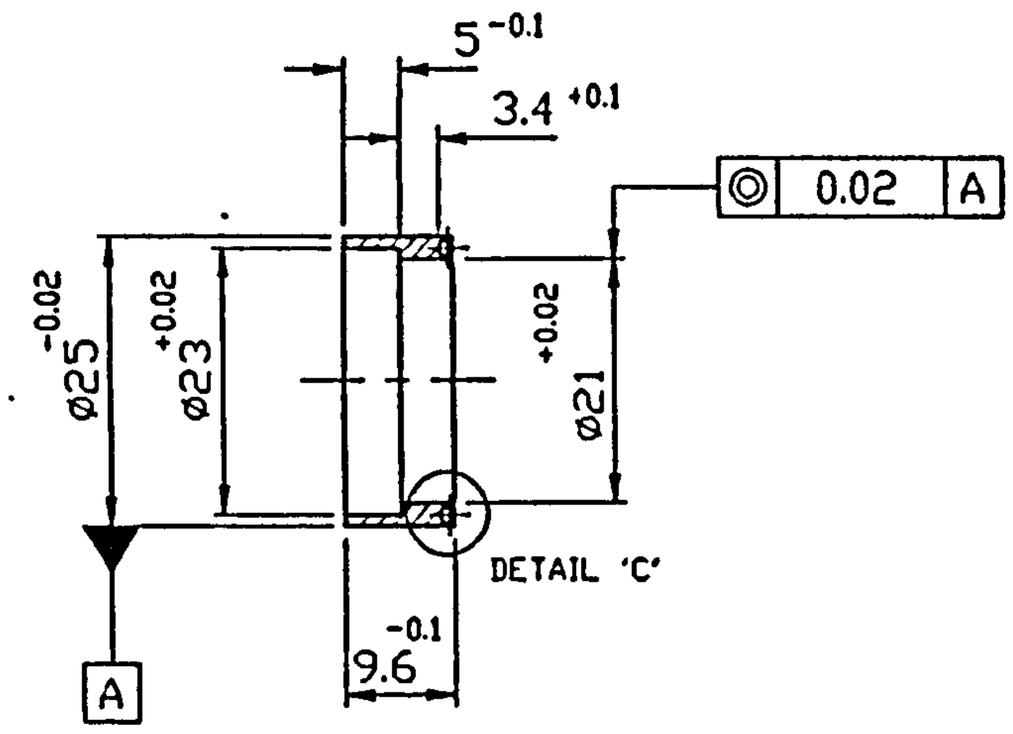

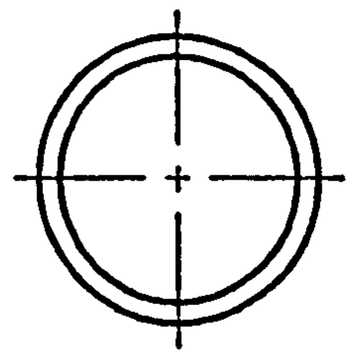

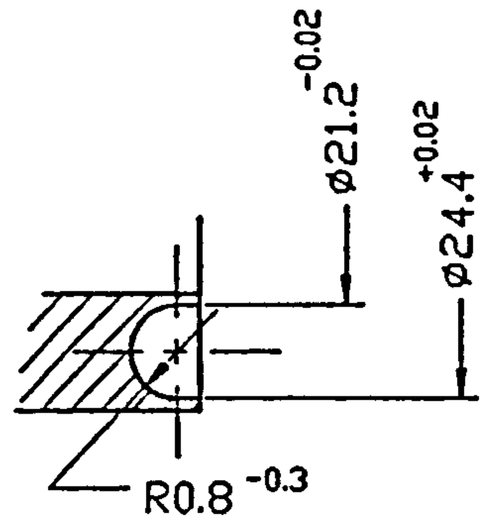

DETAIL 'C'
(5:1)

REMOVE ALL SHAPE EDGES

THIRD ANGLE PROJECTION	SHEET SIZE A4	ITEM	PART No.	DESCRIPTION	No. OFF	MATL.	SPEC.	REMARKS
					2	SST	316	

GENERAL TOLERANCE ON DIMENSIONS	JOB No.	No. OF SETS REQ.	SCALE 1:1	DRAWN	CHK	DATE	TITLE:
MACHINED				Y.B.P.KWAN		28.11.94	O-RING HOLDER
UNMACHINED							
OTHER DIMENSIONS AS STATED			FINISH	SCHOOL OF INDUSTRIAL & MANUFACTURING SCIENCE			DRAWING No. MD291 B110 4A
WELD WHERE SHOWN THUS ⌒				CRANFIELD			SHT. 1 OF 1 SHEETS
MACHINE WHERE SHOWN THUS ✓							

DRAWING No.	
ISSUE	MODIFICATION

ALL DIMENSIONS IN MILLIMETRES UNLESS OTHERWISE STATED. IF IN DOUBT ASK.

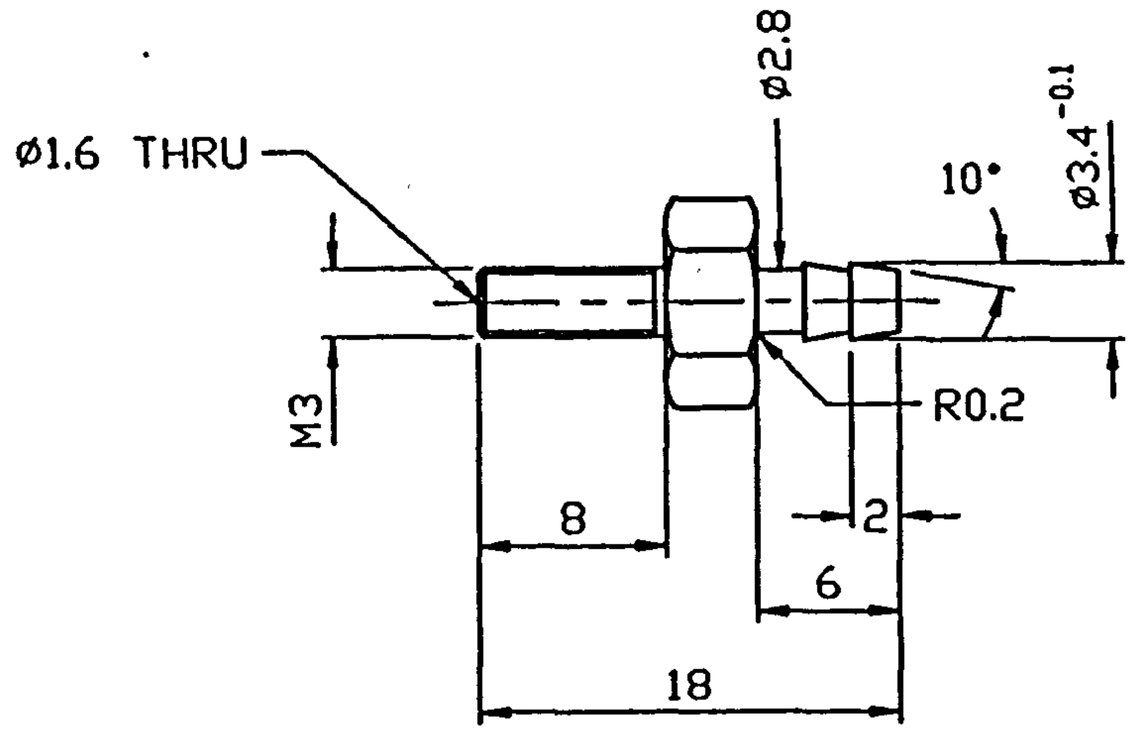

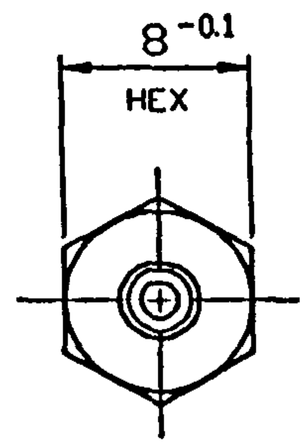

REMOVE ALL SHAPE EDGES

THIRD ANGLE PROJECTION	SHEET SIZE A4	ITEM	PART No.	DESCRIPTION	No. OFF	MATL.	SPEC.	REMARKS
					6	BRASS		

GENERAL TOLERANCE ON DIMENSIONS MACHINED UNMACHINED OTHER DIMENSIONS AS STATED WELD WHERE SHOWN THUS ⌒ L MACHINE WHERE SHOWN THUS ⊿	JOB No.	No. OF SETS REQ.	SCALE 2:1	DRAWN	CHK	DATE	TITLE: BARBED FITTING M3
				Y.B.P.KWAN		28.11.94	
			FINISH	SCHOOL OF INDUSTRIAL & MANUFACTURING SCIENCE CRANFIELD			DRAWING No. MD291 B111 4A SHT. 1 OF 1 SHEETS

DRAWING No.	
ISSUE	MODIFICATION

ALL DIMENSIONS IN MILLIMETRES UNLESS OTHERWISE STATED. IF IN DOUBT ASK.

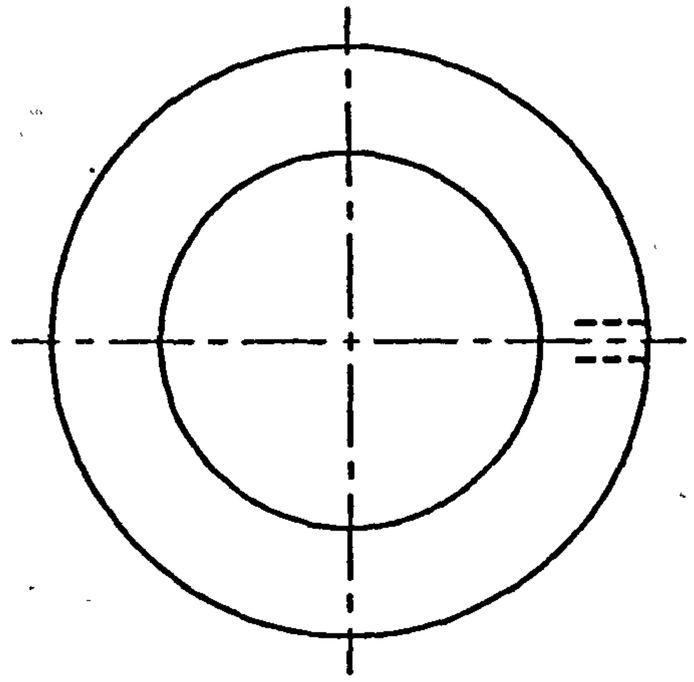

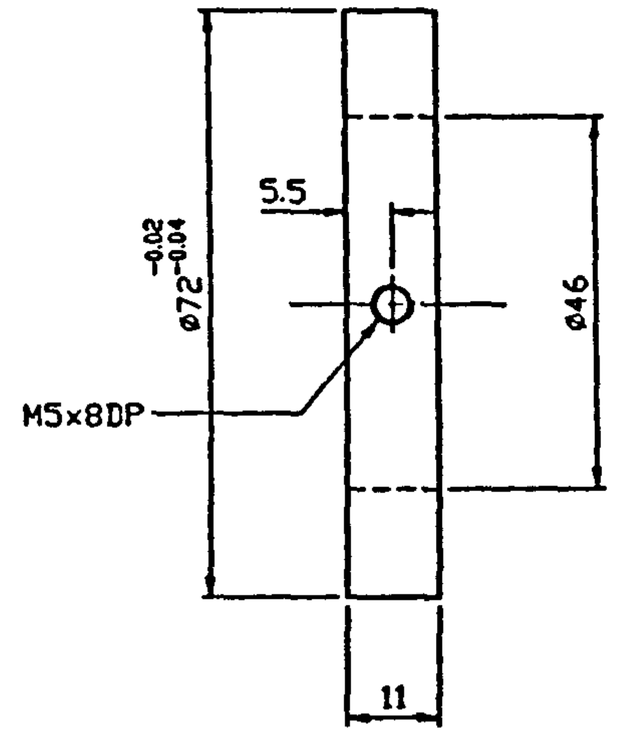

REMOVE ALL SHAPE EDGES

THIRD ANGLE PROJECTION	SHEET SIZE A3				20	ALUM.	6061-T6		
		ITEM	PART No.	DESCRIPTION	No. OFF	MATL.	SPEC.	REMARKS	

GENERAL TOLERANCE ON DIMENSIONS MACHINED UNMACHINED OTHER DIMENSIONS AS STATED WELD WHERE SHOWN THUS ⌒ L MACHINE WHERE SHOWN THUS ⊿	JOB No.	No. OF SETS REQ.	SCALE 1:1	DRAWN Y.B.P.KWAN	CHK	DATE 29.11.94
			FINISH	SCHOOL OF INDUSTRIAL & MANUFACTURING SCIENCE CRANFIELD		

TITLE: SAMPLE HOLDER BLANKS

DRAWING No. MD291 B112 3A

SHT. 1 OF 1 SHEETS

DRAWING No.	
ISSUE	MODIFICATION

ALL DIMENSIONS IN MILLIMETRES UNLESS OTHERWISE STATED. IF IN DOUBT ASK.

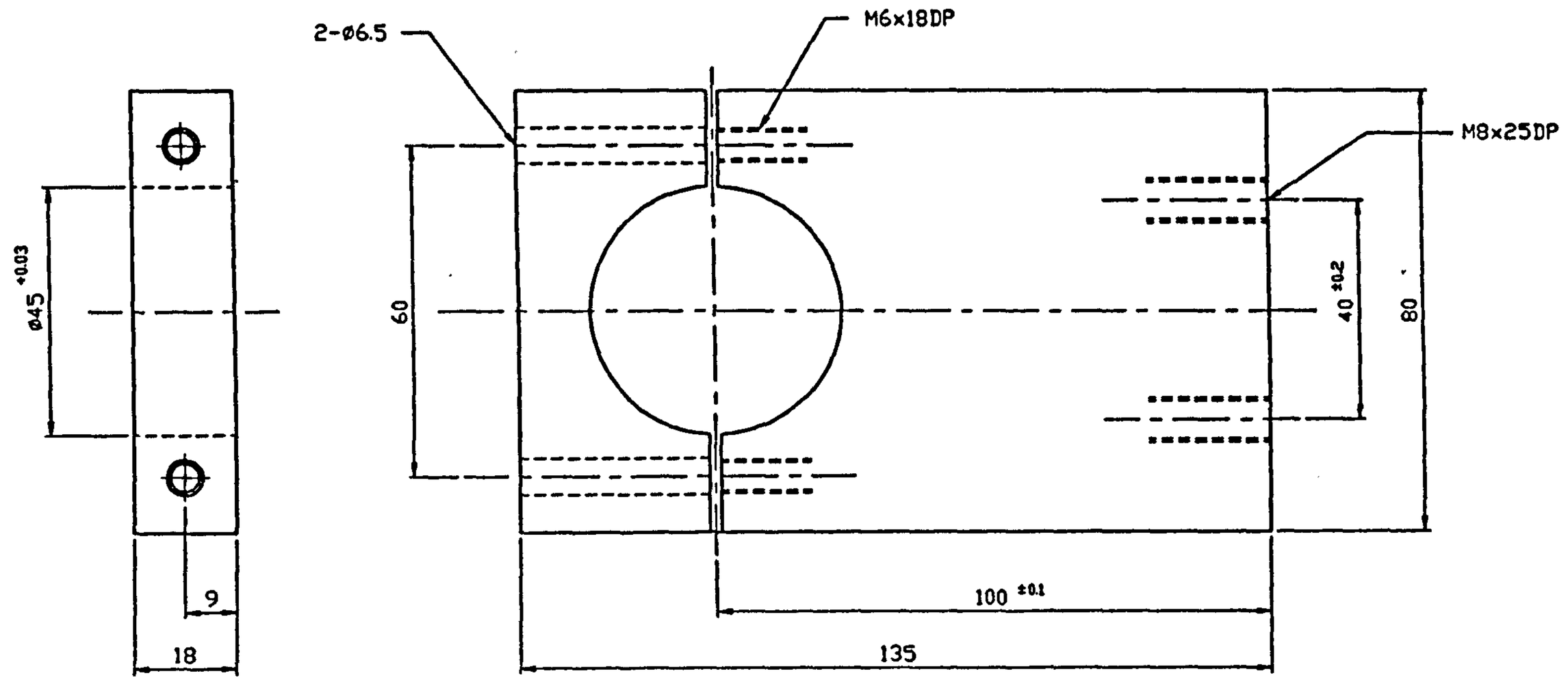

REMOVE ALL SHAPE EDGES

THIRD ANGLE PROJECTION	SHEET SIZE A3	ITEM	PART No.	DESCRIPTION	No. OFF	MATL.	SPEC.	REMARKS
					6	PVC		

GENERAL TOLERANCE ON DIMENSIONS	JOB No.	No. OF SETS REQ.	SCALE 1:1	DRAWN	CHK	DATE	TITLE:
MACHINED				Y.B.P.KWAN		05.12.94	PIPE CLAMP
UNMACHINED							
OTHER DIMENSIONS AS STATED			FINISH	SCHOOL OF INDUSTRIAL & MANUFACTURING SCIENCE			DRAWING No. MD291 B114 3A
WELD WHERE SHOWN THUS				CRANFIELD			SHT. 1 OF 1 SHEETS
MACHINE WHERE SHOWN THUS							

DRAWING No.	
ISSUE	MODIFICATION

ALL DIMENSIONS IN MILLIMETRES UNLESS OTHERWISE STATED. IF IN DOUBT ASK.

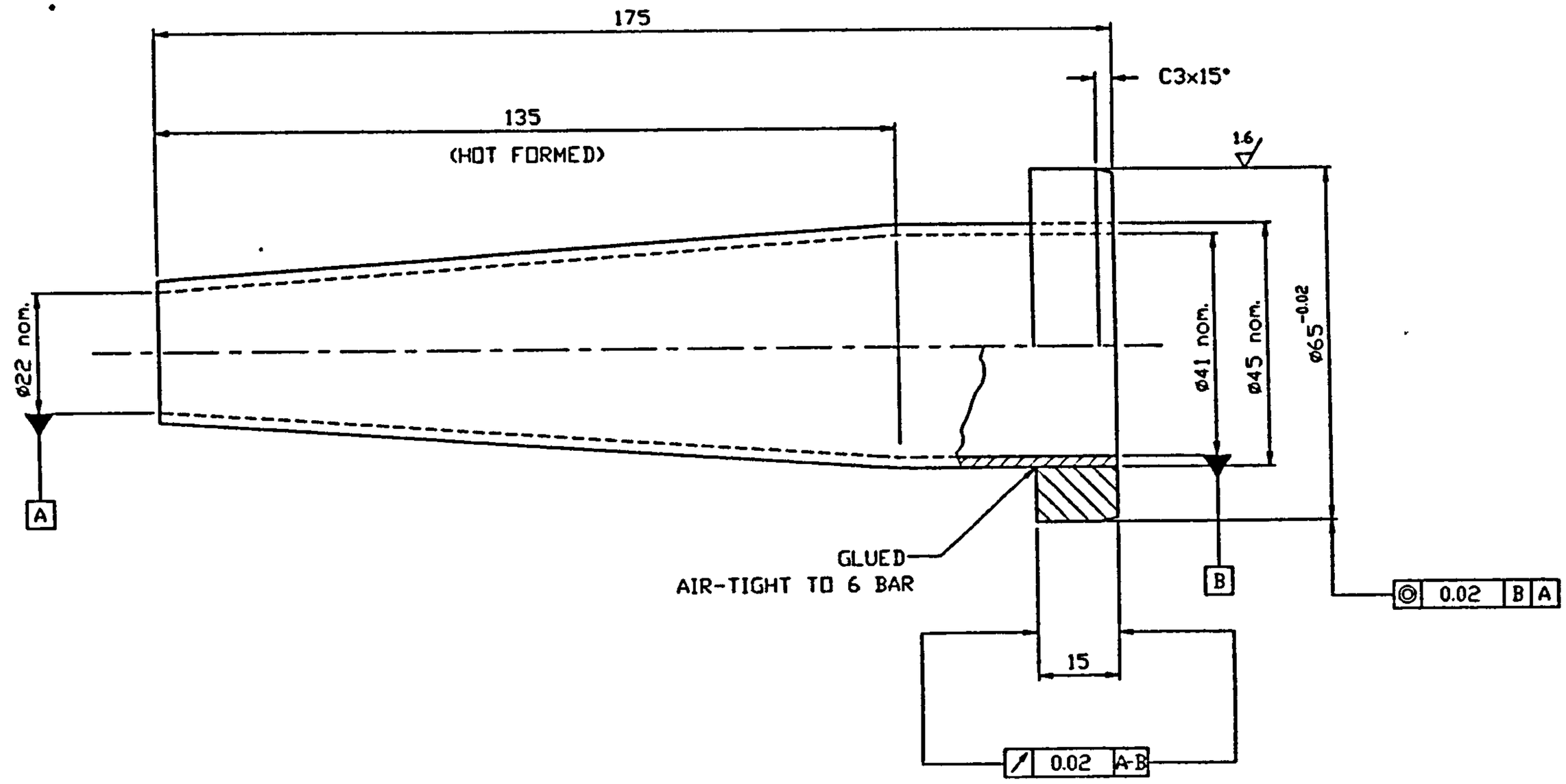

REMOVE ALL SHAPE EDGES

ITEM	PART No.	DESCRIPTION	No. OFF	MATL.	SPEC.	REMARKS
			1	PERSPEX		

THIRD ANGLE PROJECTION

SHEET SIZE A3

GENERAL TOLERANCE ON DIMENSIONS
MACHINED
UNMACHINED
OTHER DIMENSIONS AS STATED
WELD WHERE SHOWN THUS
MACHINE WHERE SHOWN THUS

JOB No.	No. OF SETS REQ.

SCALE 1:1

FINISH

DRAWN	CHK	DATE
Y.B.P.KWAN		05.04.95

TITLE: DRAIN TUBE

SCHOOL OF INDUSTRIAL & MANUFACTURING SCIENCE
CRANFIELD

DRAWING No. MD291 B116 3A

SHT. 1 OF 1 SHEETS

DRAWING No.	
ISSUE	MODIFICATION

ALL DIMENSIONS IN MILLIMETRES UNLESS OTHERWISE STATED. IF IN DOUBT ASK.

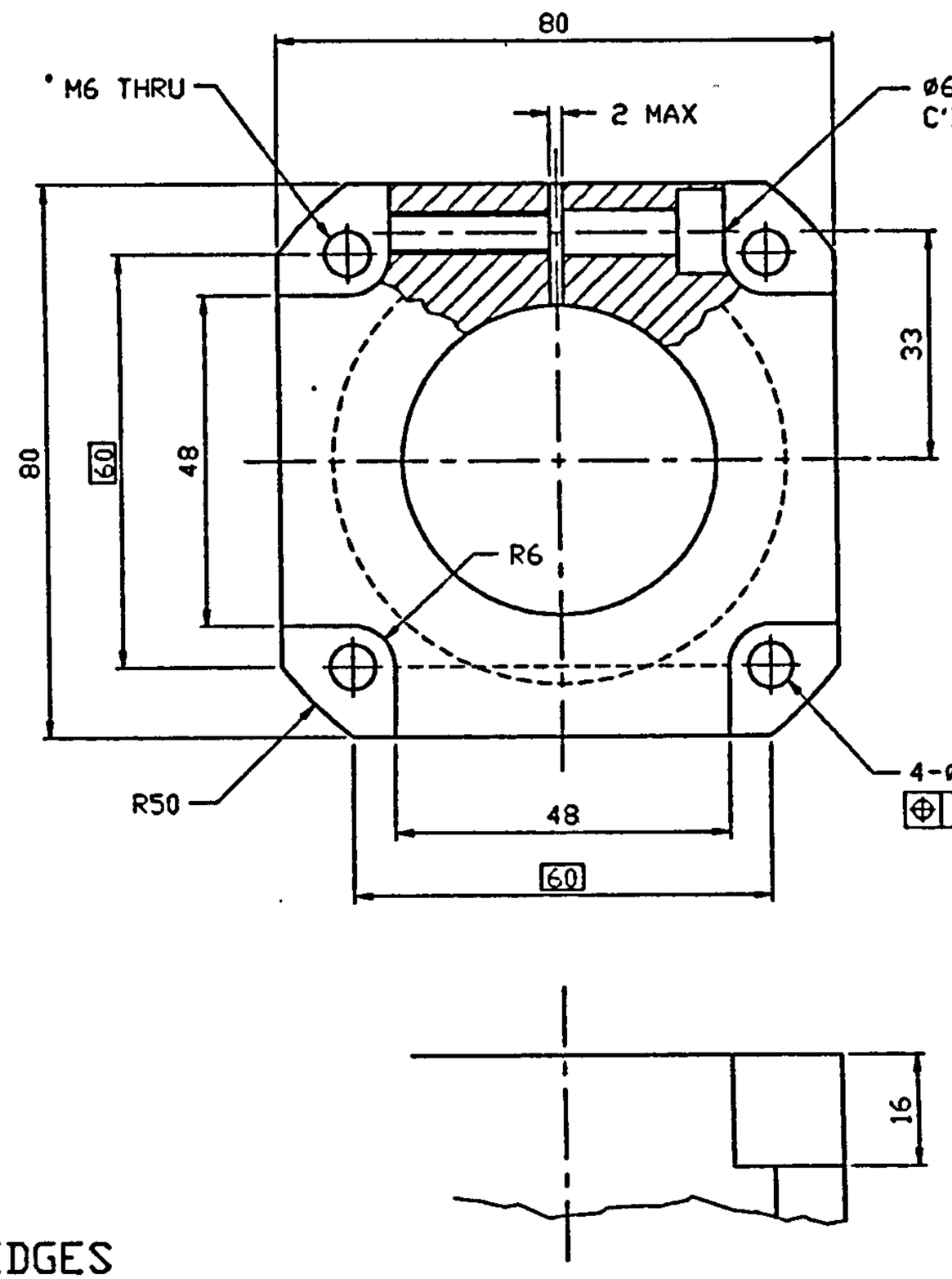

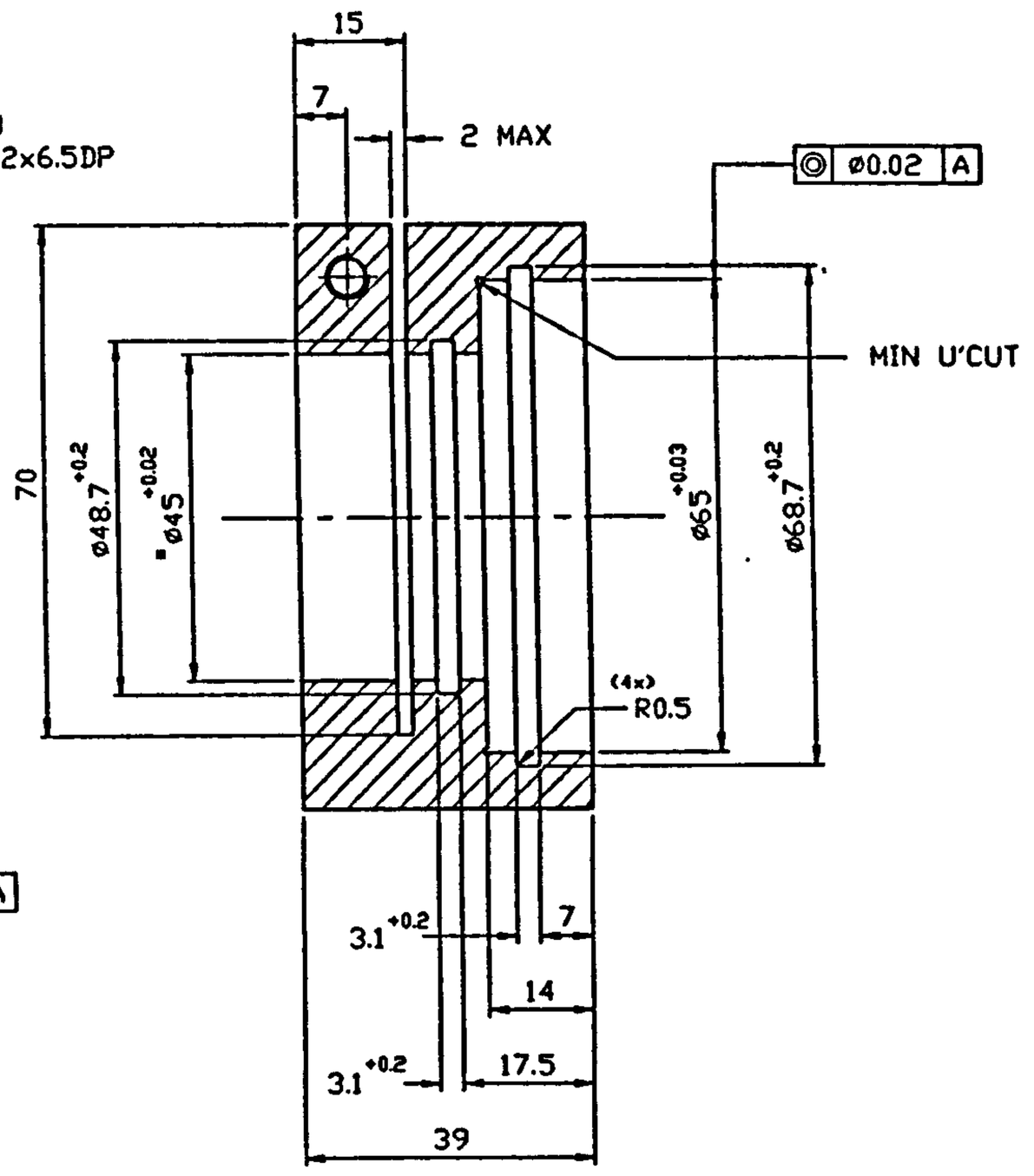

REMOVE ALL SHAPE EDGES

* NOTE: DIA.45 BORE MEASURED OFF Ø45 PERSPEX TUBE

ITEM	PART No.	DESCRIPTION	No. OFF	MATL.	SPEC.	REMARKS
			1	ALUM.	6061-T6	

THIRD ANGLE PROJECTION

SHEET SIZE	DRAWN	CHK	DATE
A3	Y.B.P.KWAN		05 04.95

TITLE: END FITTING (V)

GENERAL TOLERANCE ON DIMENSIONS	JOB No.	No. OF SETS REQ.
MACHINED		
UNMACHINED		
OTHER DIMENSIONS AS STATED		
WELD WHERE SHOWN THUS ⌒ L		
MACHINE WHERE SHOWN THUS ⊿		

SCALE 1:1

FINISH BLACK ANODIZED

SCHOOL OF INDUSTRIAL & MANUFACTURING SCIENCE

CRANFIELD

DRAWING No. MD291 B117 3A

SHT. 1 OF 1 SHEETS

DRAWING No.	
ISSUE	MODIFICATION

ALL DIMENSIONS IN MILLIMETRES UNLESS OTHERWISE STATED. IF IN DOUBT ASK.

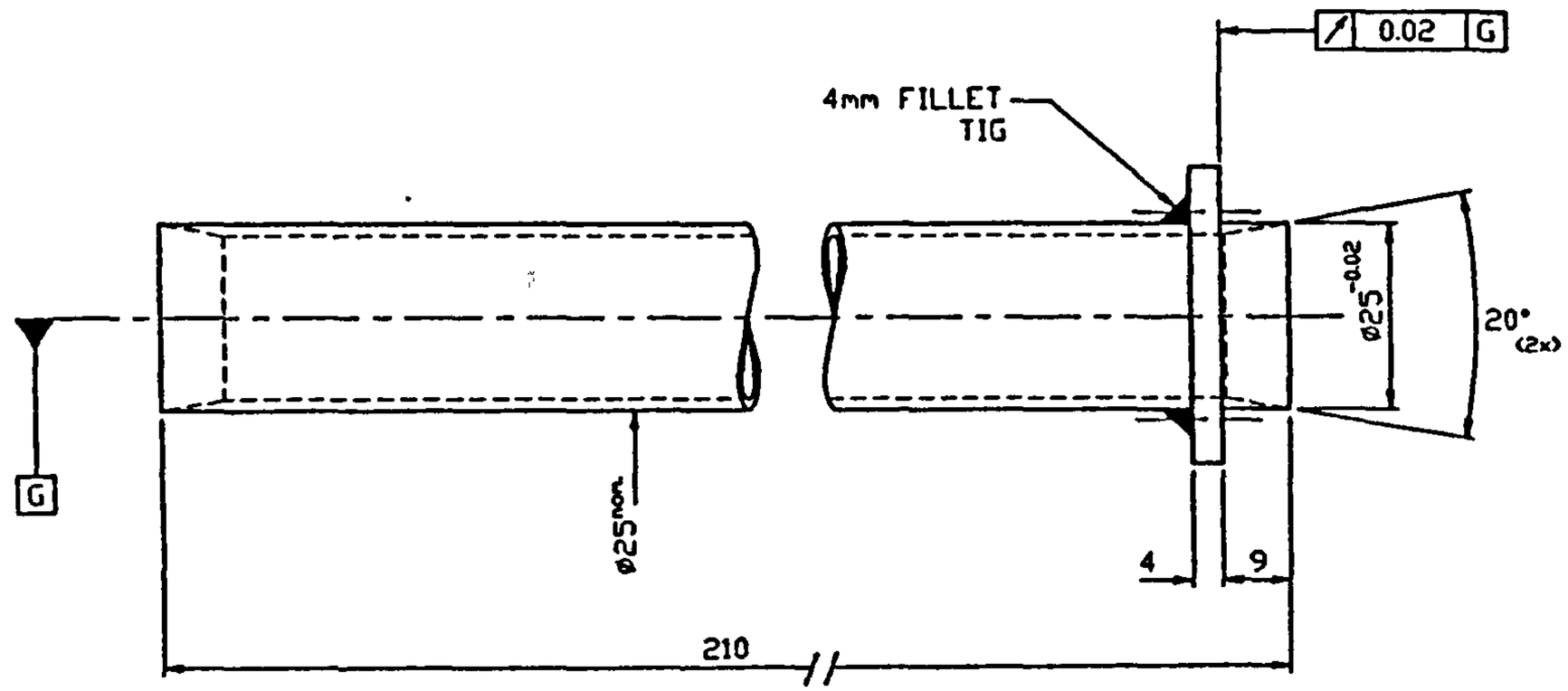

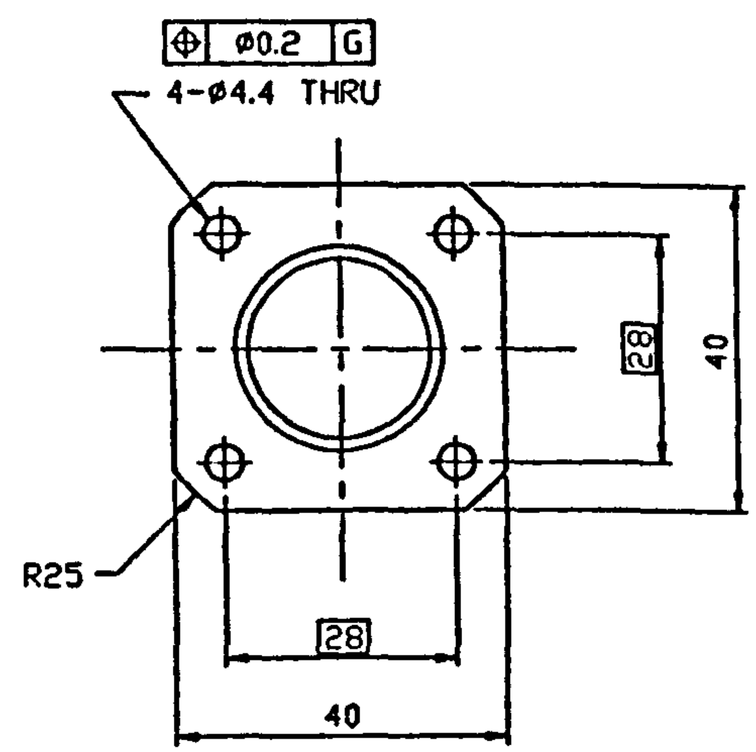

REMOVE ALL SHAPE EDGES

THIRD ANGLE PROJECTION	SHEET SIZE A3	ITEM	PART No.	DESCRIPTION	No. OFF	MATL.	SPEC.	REMARKS
					1	SST	316	

GENERAL TOLERANCE ON DIMENSIONS	JOB No.	No. OF SETS REQ.	SCALE 1:1	DRAWN	CHK	DATE	TITLE: OUTFLOW TUBE
MACHINED				Y.B.P.KWAN		05.04.95	
UNMACHINED							
OTHER DIMENSIONS AS STATED			FINISH	SCHOOL OF INDUSTRIAL & MANUFACTURING SCIENCE			DRAWING No. MD291 B119 3A
WELD WHERE SHOWN THUS ⌒ L				CRANFIELD			SHT. 1 OF 1 SHEETS
MACHINE WHERE SHOWN THUS ✓							

DRAWING No.

ISSUE	MODIFICATION

ALL DIMENSIONS IN MILLIMETRES UNLESS OTHERWISE STATED. IF IN DOUBT ASK.

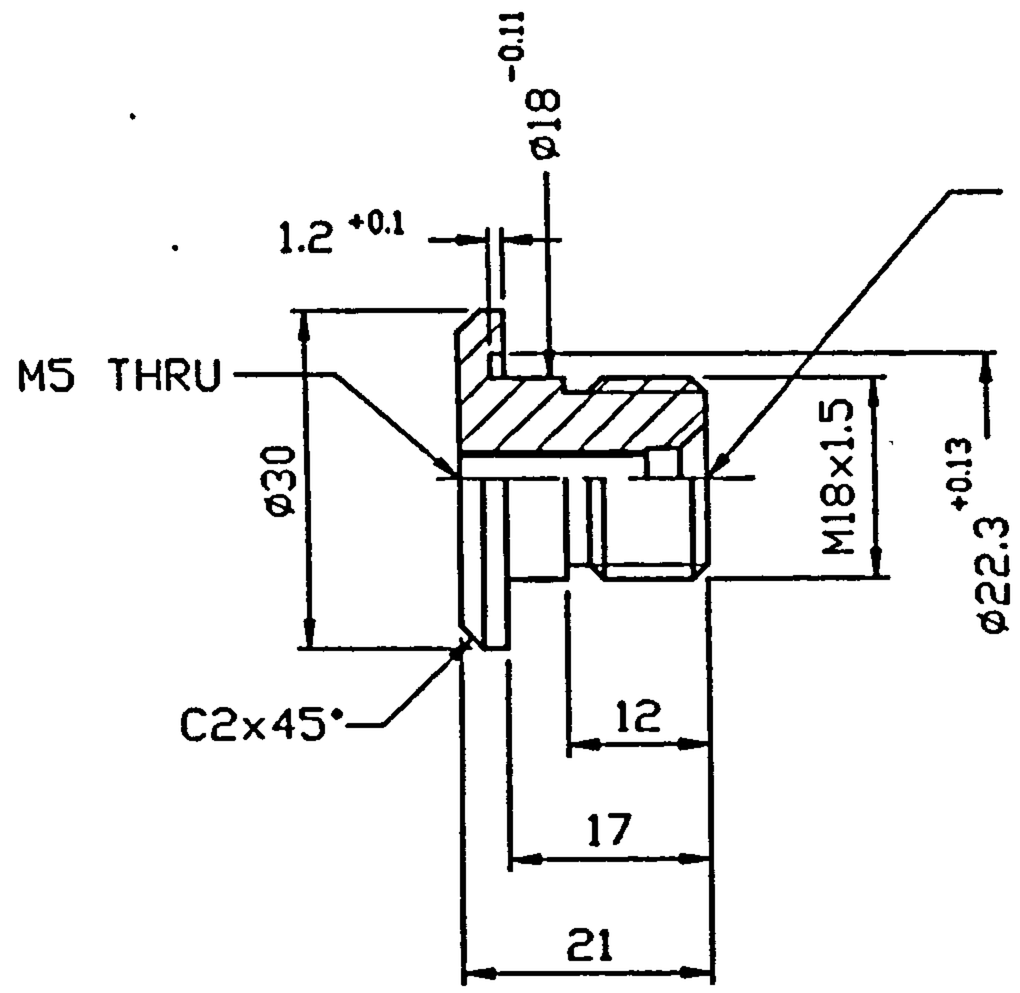

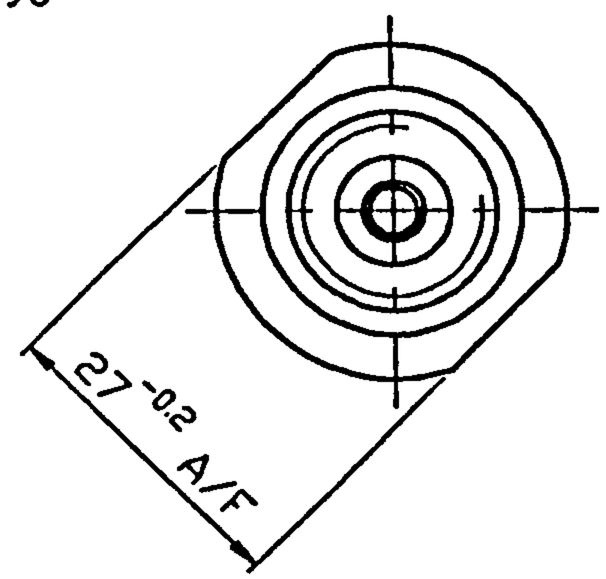

REMOVE ALL SHAPE EDGES

THIRD ANGLE PROJECTION	SHEET SIZE A4				1	SST	304	FITS GACD RM0051-16
		ITEM	PART No.	DESCRIPTION	No. OFF	MATL.	SPEC.	REMARKS
GENERAL TOLERANCE ON DIMENSIONS MACHINED UNMACHINED OTHER DIMENSIONS AS STATED WELD WHERE SHOWN THUS ⌒ L MACHINE WHERE SHOWN THUS ⊿	JOB No.							
	No. OF SETS REQ.							
	SCALE 1:1	DRAWN	CHK	DATE	TITLE: DRAIN FITTING			
		Y.B.P.KWAN		12.04.96				
	FINISH	SCHOOL OF INDUSTRIAL & MANUFACTURING SCIENCE CRANFIELD			DRAWING No. MD291 B120 4A			
					SHT. 1 OF 1 SHEETS			

DRAWING No.	
ISSUE	MODIFICATION

ALL DIMENSIONS IN MILLIMETRES UNLESS OTHERWISE STATED. IF IN DOUBT ASK.

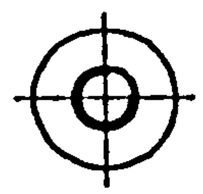

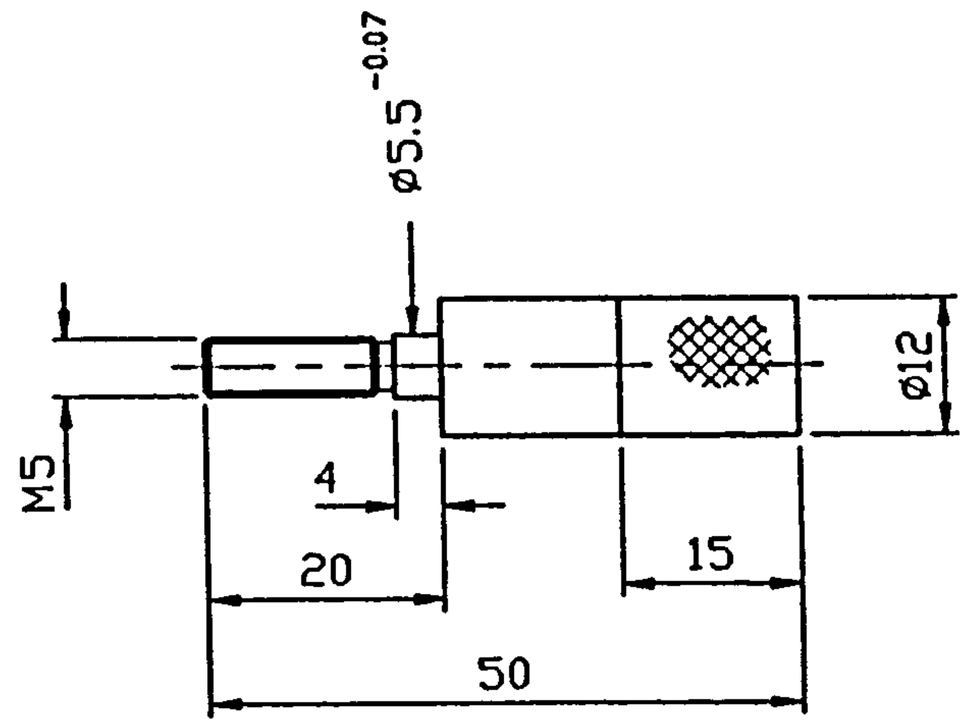

REMOVE ALL SHAPE EDGES

THIRD ANGLE PROJECTION			SHEET SIZE A4							
				ITEM	PART No.	DESCRIPTION	No. OFF	MATL.	SPEC.	REMARKS
							1	SST	304	
GENERAL TOLERANCE ON DIMENSIONS MACHINED UNMACHINED OTHER DIMENSIONS AS STATED WELD WHERE SHOWN THUS ⌒ L MACHINE WHERE SHOWN THUS ⊿	JOB No.	No. OF SETS REQ.	SCALE 1:1	DRAWN	CHK	DATE	TITLE: DRAIN PLUG			
				Y.B.P.KWAN		12.04.95				
			FINISH	SCHOOL OF INDUSTRIAL & MANUFACTURING SCIENCE CRANFIELD			DRAWING No. MD291 B121 4A			
							SHT. 1 OF 1 SHEETS			

DRAWING No.	
ISSUE	MODIFICATION

ALL DIMENSIONS IN MILLIMETRES UNLESS OTHERWISE STATED. IF IN DOUBT ASK.

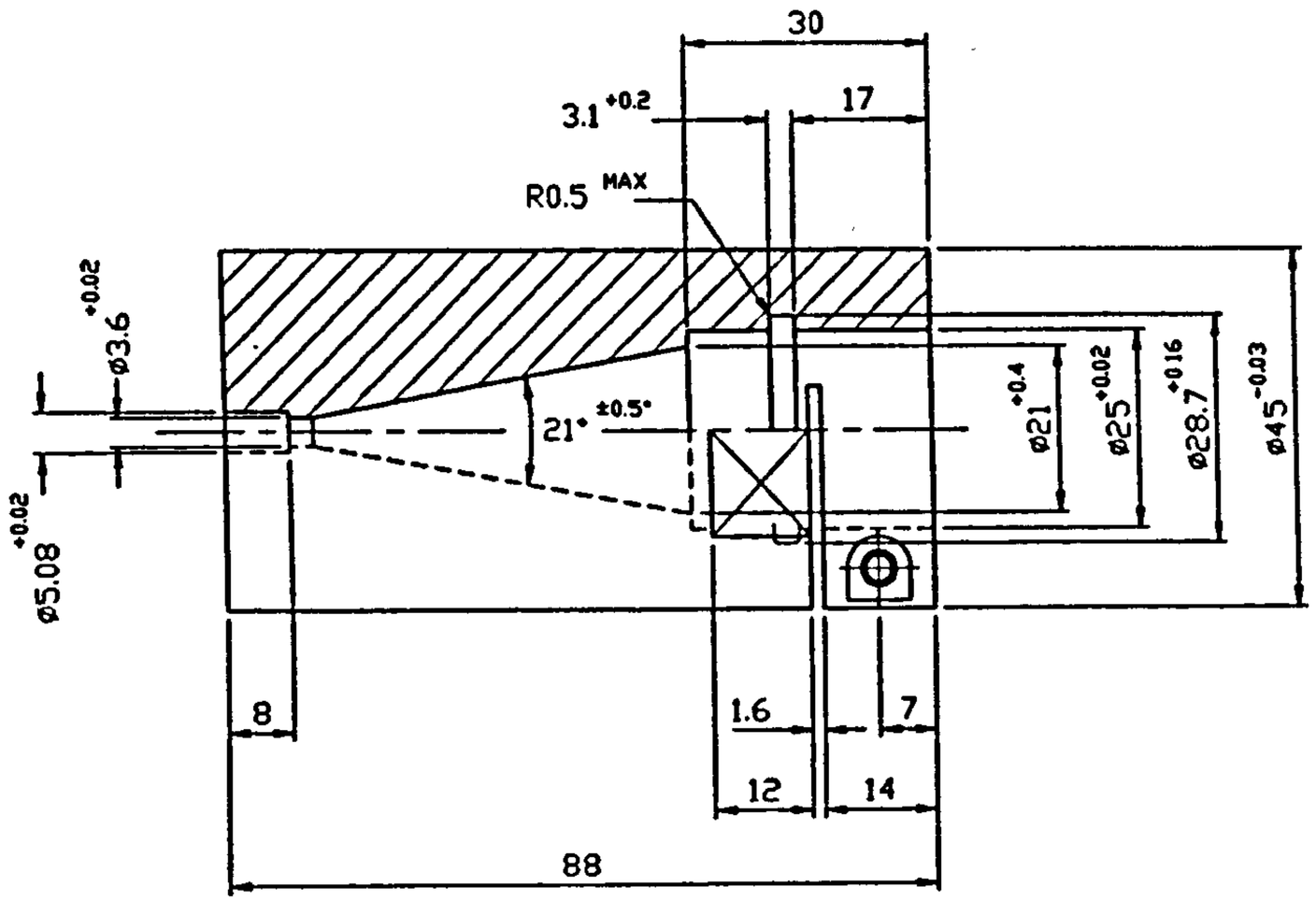

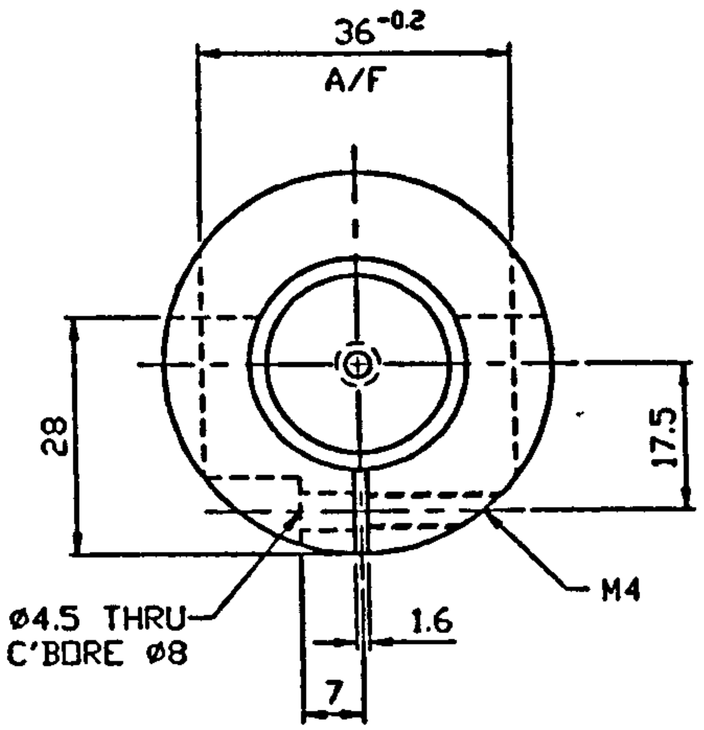

REMOVE ALL SHAPE EDGES

THIRD ANGLE PROJECTION	SHEET SIZE A3	ITEM	PART No.	DESCRIPTION	No. OFF	MATL.	SPEC.	REMARKS
					2	ALUM.	6061-T6	

GENERAL TOLERANCE ON DIMENSIONS	JOB No.	No. OF SETS REQ.	SCALE 1:1	DRAWN	CHK	DATE	TITLE: END FITTING VII
MACHINED				Y.B.P.KWAN		17.07.95	
UNMACHINED							
OTHER DIMENSIONS AS STATED			FINISH	SCHOOL OF INDUSTRIAL & MANUFACTURING SCIENCE			DRAWING No. MD291 B124 3A
WELD WHERE SHOWN THUS			BLACK ANODIZED	CRANFIELD			SHT. 1 OF 1 SHEETS
MACHINE WHERE SHOWN THUS							

DRAWING No.	
ISSUE	MODIFICATION

ALL DIMENSIONS IN MILLIMETRES UNLESS OTHERWISE STATED. IF IN DOUBT ASK.

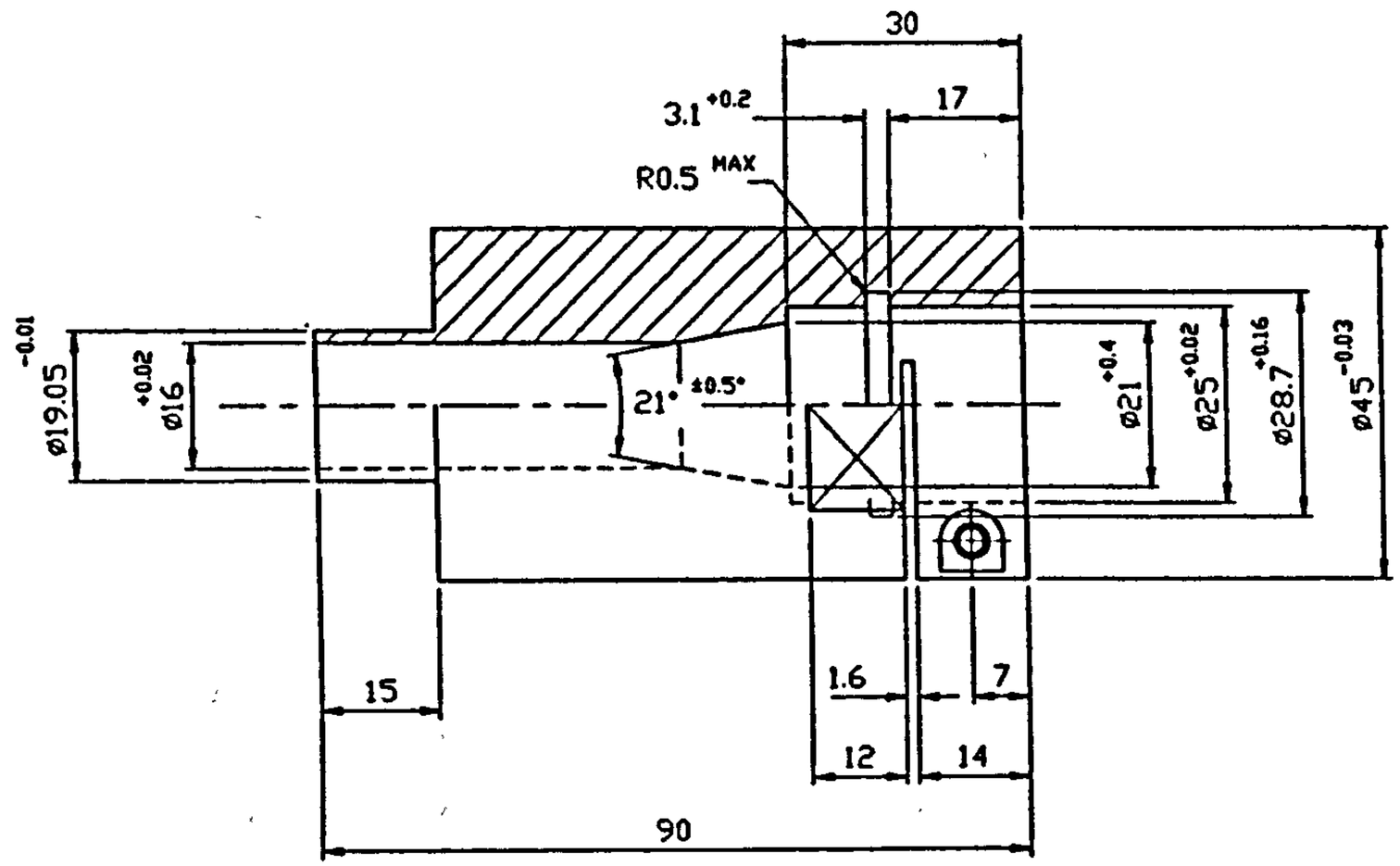

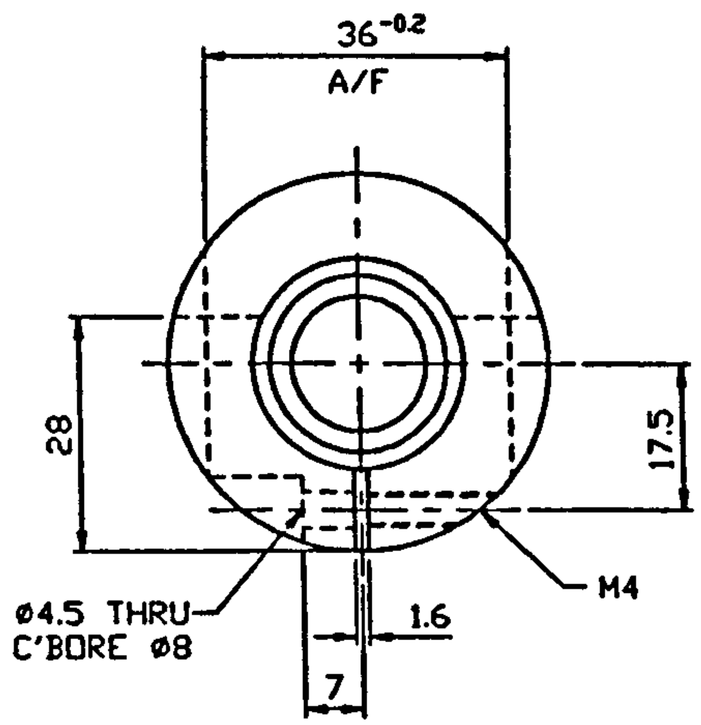

REMOVE ALL SHAPE EDGES

						2	ALUM.	6061-T6		
			ITEM	PART No.	DESCRIPTION	No. OFF	MATL.	SPEC.	REMARKS	

THIRD ANGLE PROJECTION

GENERAL TOLERANCE ON DIMENSIONS	JOB No.	No. OF SETS REQ.
MACHINED		
UNMACHINED		
OTHER DIMENSIONS AS STATED		
WELD WHERE SHOWN THUS ⌒ ⌊		
MACHINE WHERE SHOWN THUS ⊿		

SHEET SIZE	SCALE	FINISH
A3	1:1	BLACK ANODIZED

DRAWN	CHK	DATE
Y.B.P.KWAN		17.07.95

TITLE: END FITTING VIII

SCHOOL OF INDUSTRIAL & MANUFACTURING SCIENCE
CRANFIELD

DRAWING No. MD291 B125 3A

SHT. 1 OF 1 SHEETS

DRAWING No.	
ISSUE	MODIFICATION

ALL DIMENSIONS IN MILLIMETRES UNLESS OTHERWISE STATED. IF IN DOUBT ASK.

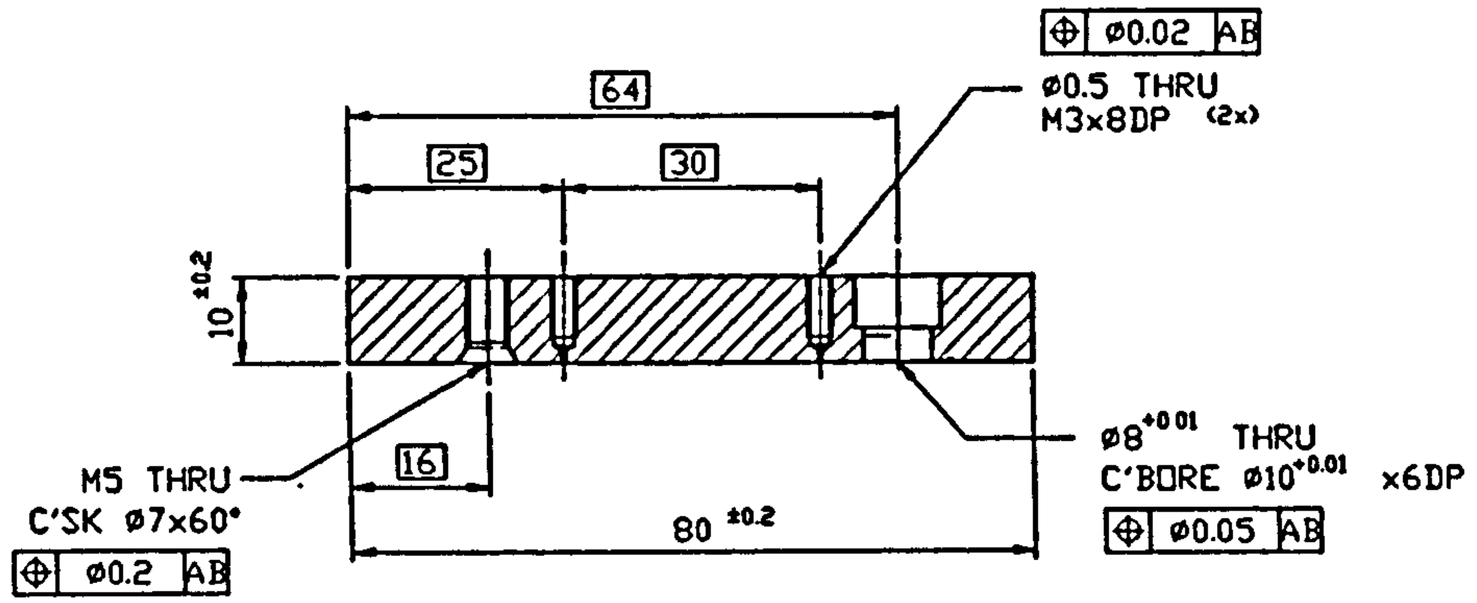

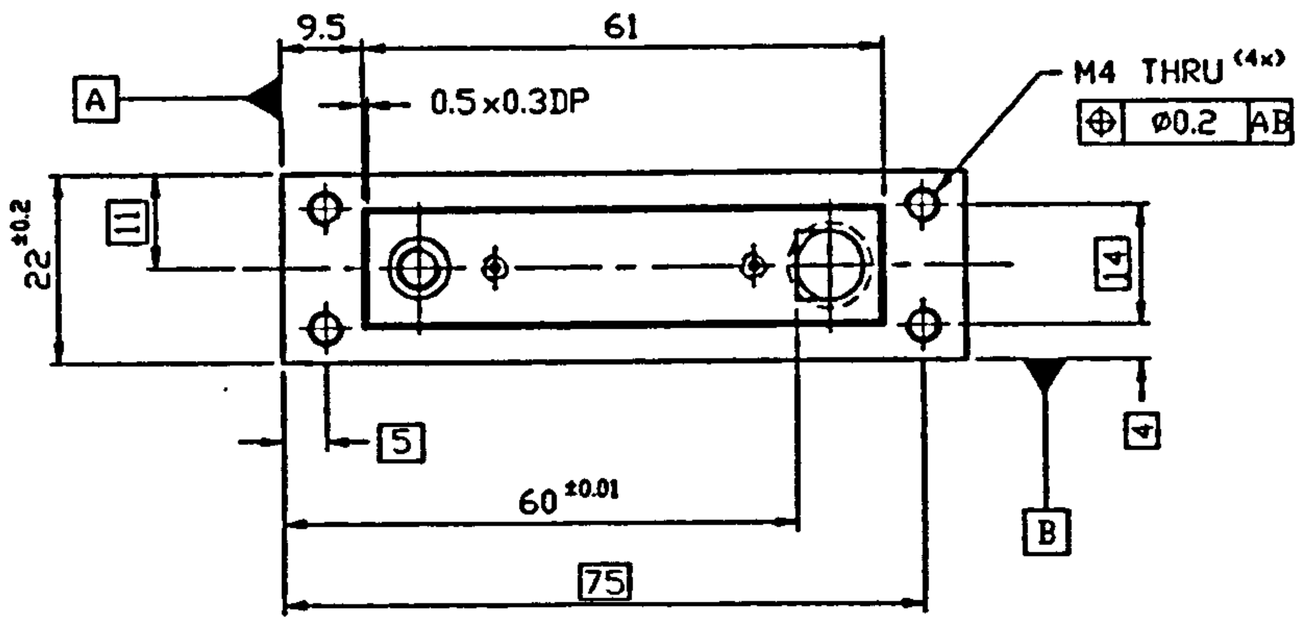

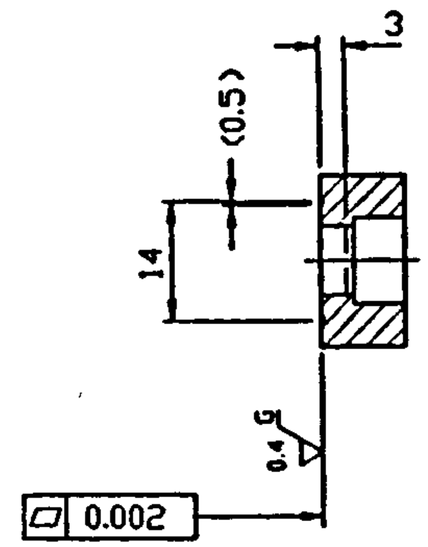

REMOVE ALL SHAPE EDGES

THIRD ANGLE PROJECTION	SHEET SIZE A3				1	SST	440C	
		ITEM	PART No.	DESCRIPTION	No. OFF	MATL.	SPEC.	REMARKS

GENERAL TOLERANCE ON DIMENSIONS MACHINED UNMACHINED OTHER DIMENSIONS AS STATED WELD WHERE SHOWN THUS ⌒ L MACHINE WHERE SHOWN THUS ✓	JOB No.	No. OF SETS REQ.	SCALE 1:1	DRAWN	CHK	DATE	TITLE: TOP PLATE
				Y.B.P.KWAN		01.11.95	
			FINISH	SCHOOL OF INDUSTRIAL & MANUFACTURING SCIENCE CRANFIELD			DRAWING No. MD291 B201 3A SHT. 1 OF 1 SHEETS

DRAWING No.	
ISSUE	MODIFICATION

ALL DIMENSIONS IN MILLIMETRES UNLESS OTHERWISE STATED. IF IN DOUBT ASK.

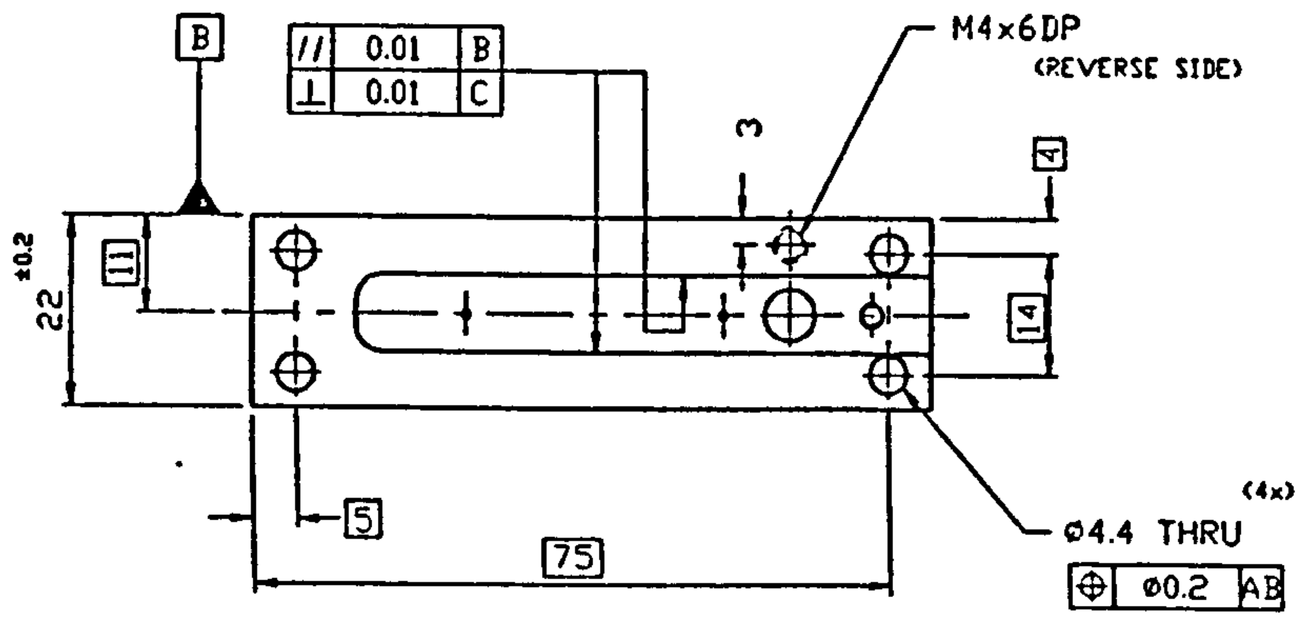

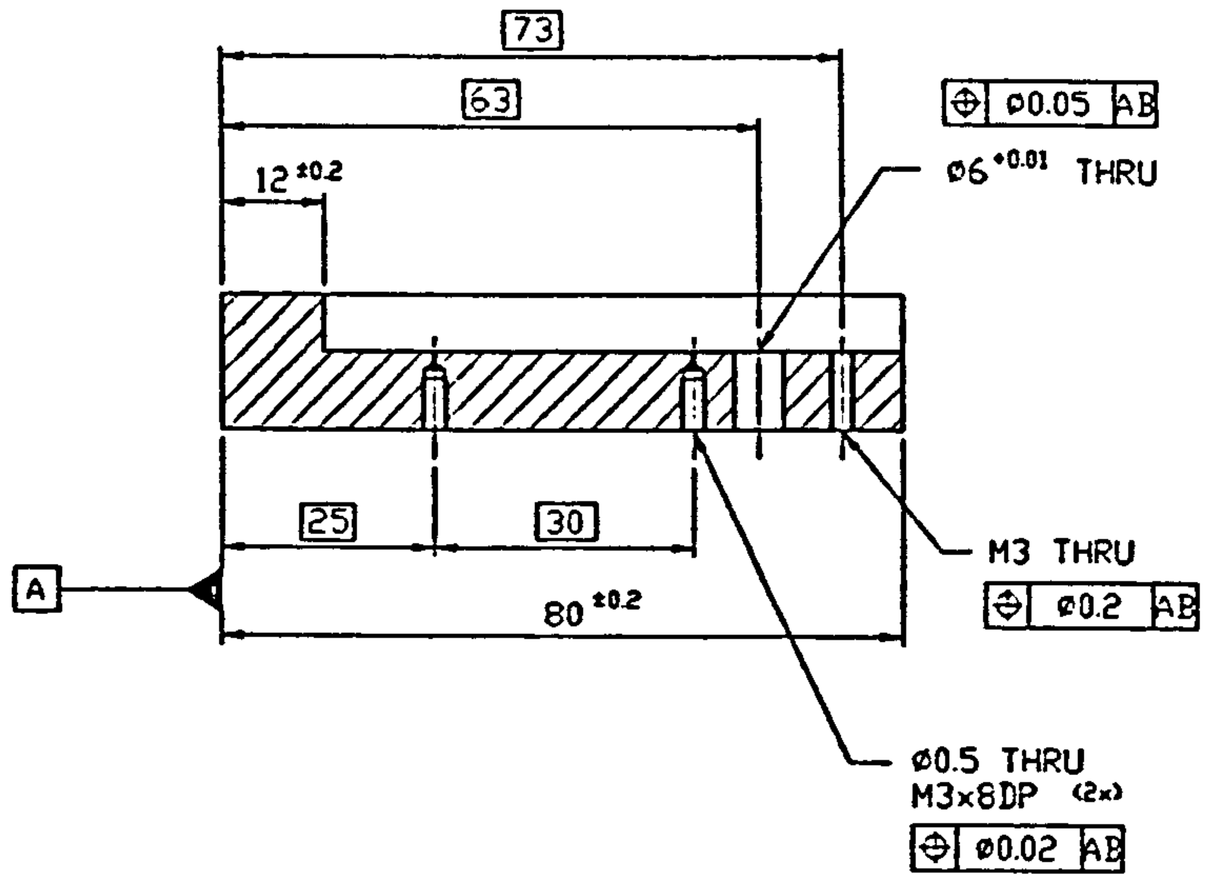

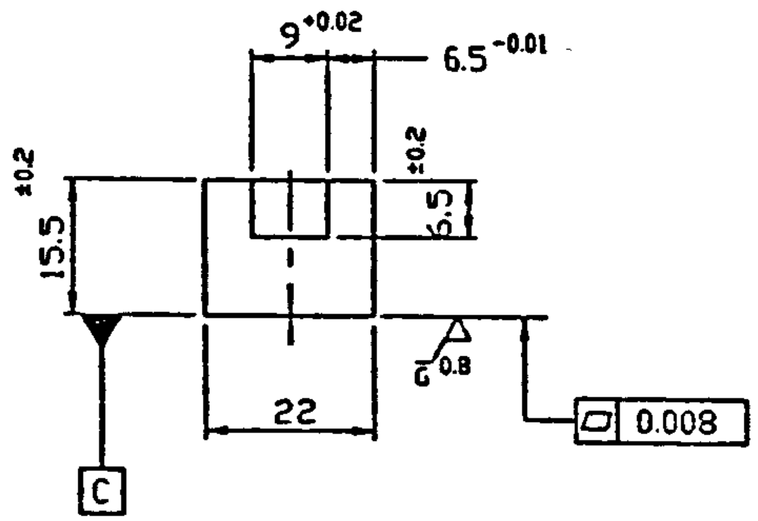

REMOVE ALL SHAPE EDGES

THIRD ANGLE PROJECTION	SHEET SIZE A3	ITEM	PART No.	DESCRIPTION	No. OFF	MATL.	SPEC.	REMARKS
					1	ALUM.	6061-T6	

GENERAL TOLERANCE ON DIMENSIONS	JOB No.	No. OF SETS REQ.	SCALE 1:1	DRAWN	CHK	DATE	TITLE: SPECIMEN CARRIER
MACHINED				Y.B.P.KWAN		01.11.95	
UNMACHINED							
OTHER DIMENSIONS AS STATED			FINISH BLACK ANODIZED	SCHOOL OF INDUSTRIAL & MANUFACTURING SCIENCE CRANFIELD			DRAWING No. MD291 B202 3A
WELD WHERE SHOWN THUS							SHT. 1 OF 1 SHEETS
MACHINE WHERE SHOWN THUS							

DRAWING No.	
ISSUE	MODIFICATION

ALL DIMENSIONS IN MILLIMETRES UNLESS OTHERWISE STATED. IF IN DOUBT ASK.

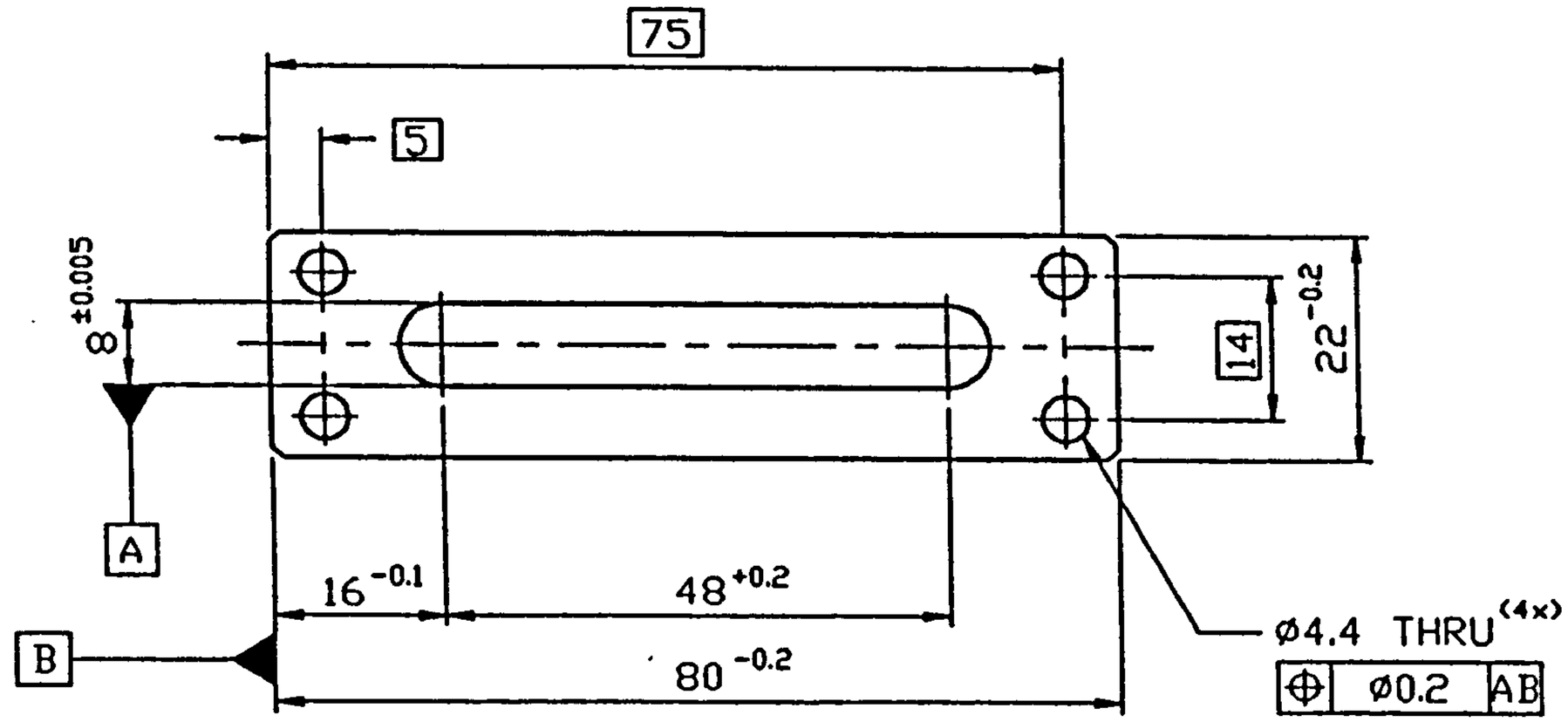

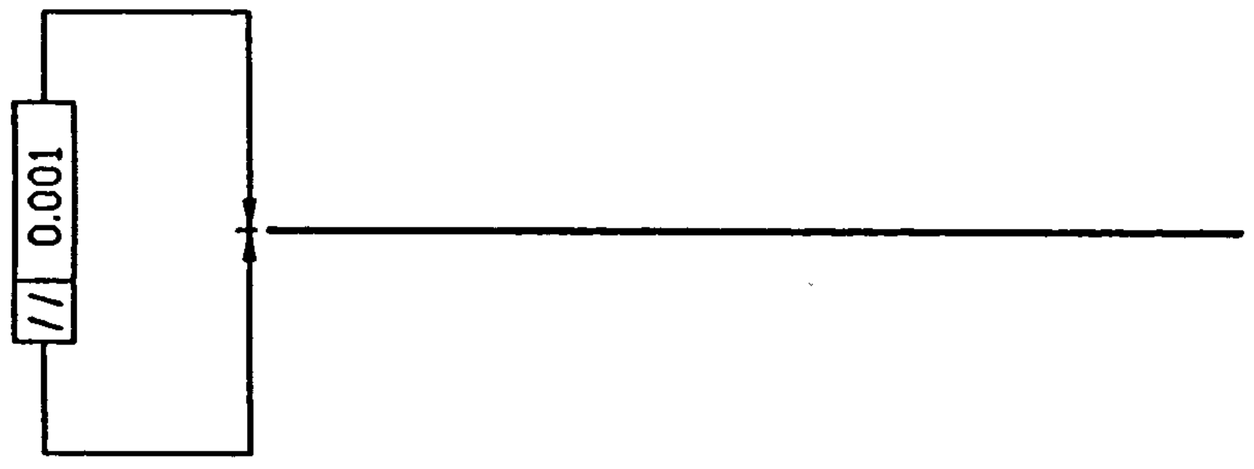

REMOVE ALL SHAPE EDGES

SHIM THICKNESS = 0.01,0.02,0.03,0.04 ±0.003

THIRD ANGLE PROJECTION	SHEET SIZE A4	ITEM	PART No.	DESCRIPTION	No. OFF	MATL.	SPEC.	REMARKS
					1 EACH	SST	304	

GENERAL TOLERANCE ON DIMENSIONS MACHINED UNMACHINED OTHER DIMENSIONS AS STATED	JOB No.	No. OF SETS REQ.	SCALE 1:1	DRAWN	CHK	DATE	TITLE: FLOW CHANNEL SHIM
				Y.B.P.KWAN		01.11.95	
WELD WHERE SHOWN THUS L			FINISH	SCHOOL OF INDUSTRIAL & MANUFACTURING SCIENCE CRANFIELD			DRAWING No. MD291 B203 4A
MACHINE WHERE SHOWN THUS ⊿							SHT. 1 OF 1 SHEETS

DRAWING No.	
ISSUE	MODIFICATION

ALL DIMENSIONS IN MILLIMETRES UNLESS OTHERWISE STATED. IF IN DOUBT ASK.

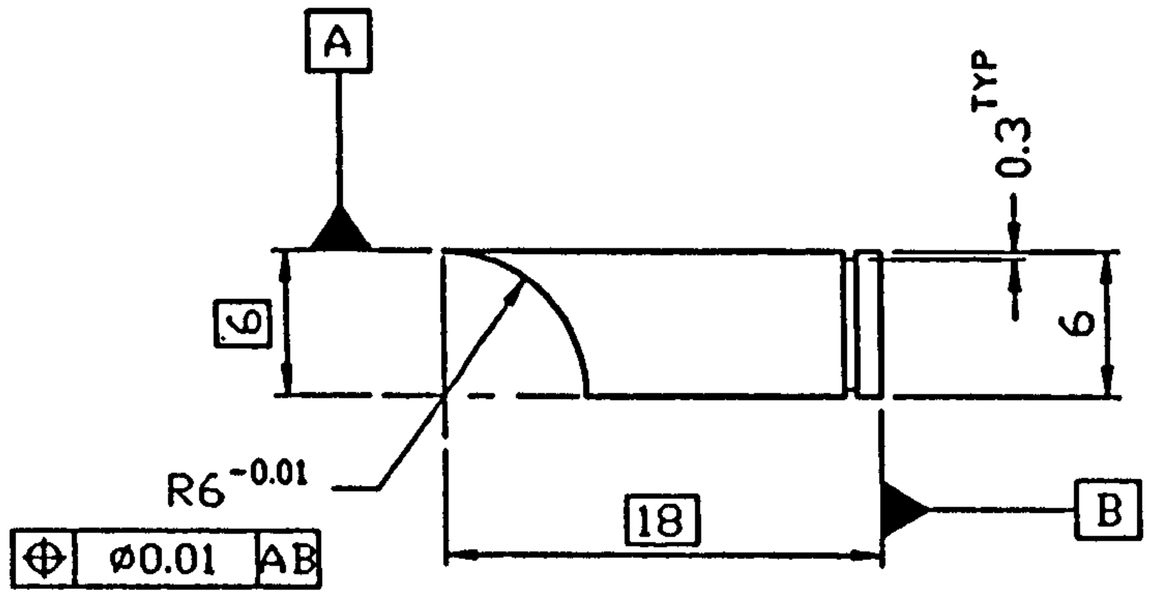

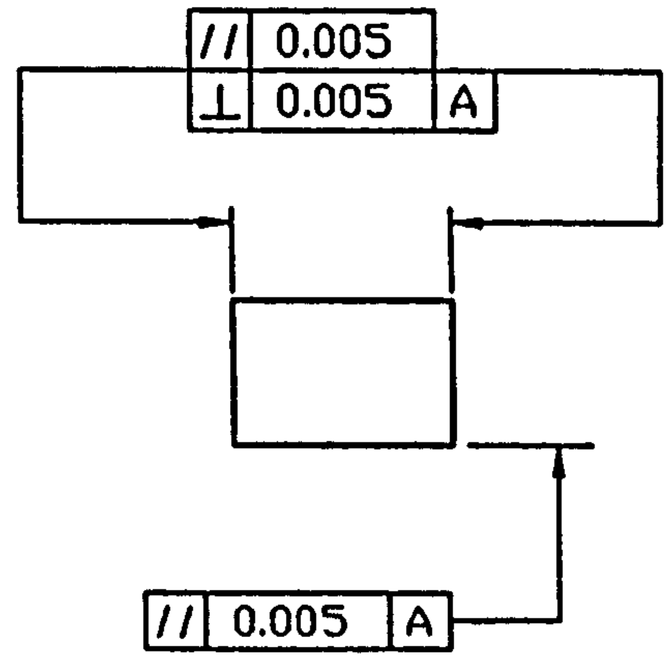

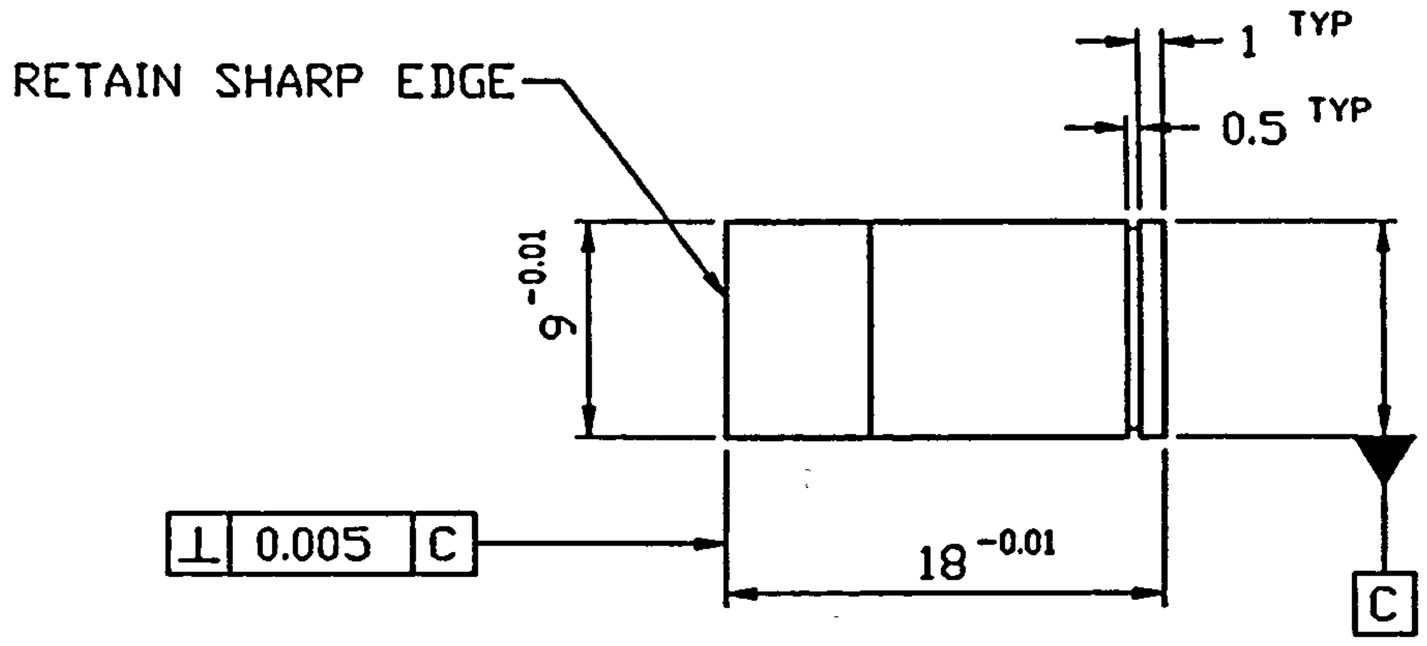

0.8 G ALL OVER

REMOVE ALL SHAPE EDGES

THIRD ANGLE PROJECTION	SHEET SIZE A4	ITEM	PART No.	DESCRIPTION	No. OFF	MATL.	SPEC.	REMARKS
					1	SST	440C	

GENERAL TOLERANCE ON DIMENSIONS	JOB No.	No. OF SETS REQ.	SCALE 2:1	DRAWN	CHK	DATE	TITLE: FLOW DEFLECTOR
MACHINED				Y.B.P.KWAN		01.11.95	
UNMACHINED							
OTHER DIMENSIONS AS STATED			FINISH	SCHOOL OF INDUSTRIAL & MANUFACTURING SCIENCE			DRAWING No. MD291 B204 4A
WELD WHERE SHOWN THUS ⌒ L				CRANFIELD			SHT. 1 OF 1 SHEETS
MACHINE WHERE SHOWN THUS ✓							

DRAWING No.	
ISSUE	MODIFICATION

ALL DIMENSIONS IN MILLIMETRES UNLESS OTHERWISE STATED. IF IN DOUBT ASK.

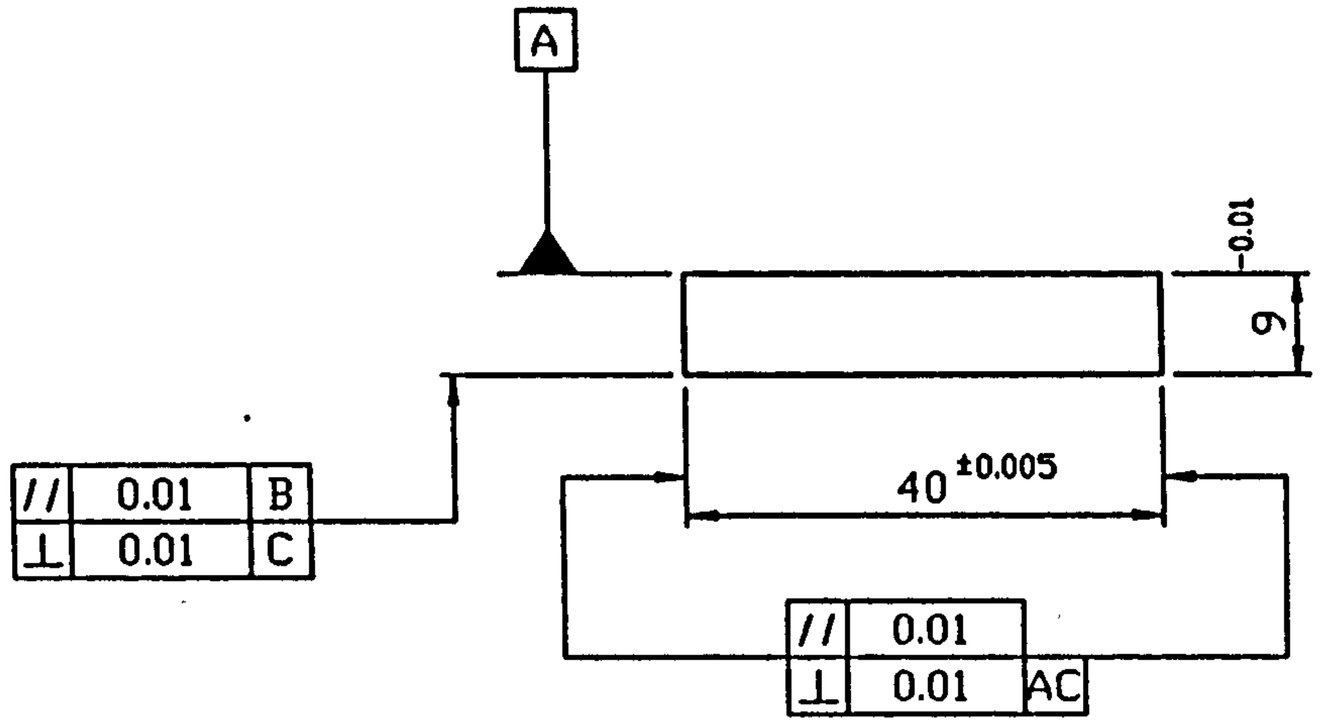

0.8 G ALL OVER

REMOVE ALL SHAPE EDGES

THIRD ANGLE PROJECTION			SHEET SIZE A4								
				ITEM	PART No.	DESCRIPTION	No. OFF	MATL.	SPEC.	REMARKS	
							1	SST	440C		
GENERAL TOLERANCE ON DIMENSIONS MACHINED UNMACHINED OTHER DIMENSIONS AS STATED	JOB No.	No. OF SETS REQ.	SCALE 1:1	DRAWN	CHK	DATE	TITLE: DUMMY SPECIMEN				
				Y.B.P.KWAN		01.11.95					
			FINISH	SCHOOL OF INDUSTRIAL & MANUFACTURING SCIENCE CRANFIELD			DRAWING No. MD291 B205 4A				
VELD WHERE SHOWN THUS ⌒ L							SHT. 1 OF 1 SHEETS				
MACHINE WHERE SHOWN THUS ⊿											

DRAWING No.	
ISSUE	MODIFICATION

ALL DIMENSIONS IN MILLIMETRES UNLESS OTHERWISE STATED. IF IN DOUBT ASK.

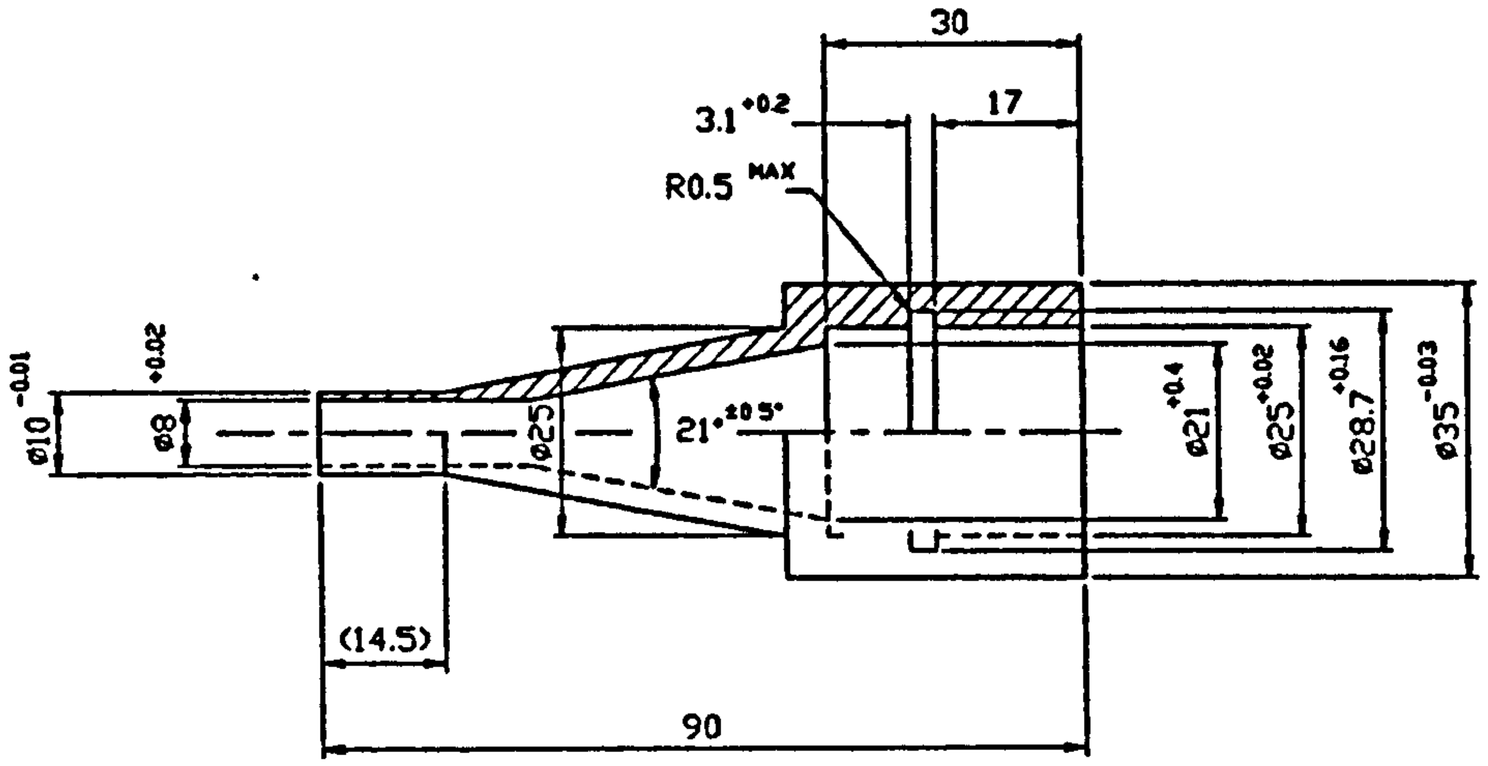

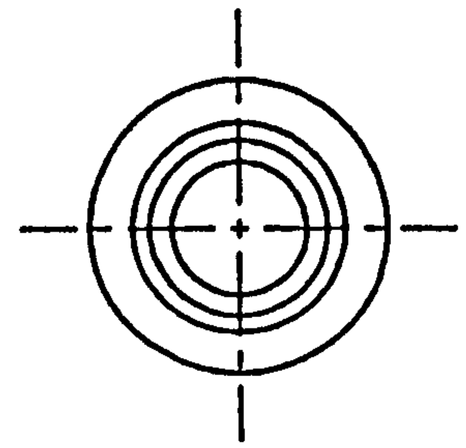

REMOVE ALL SHAPE EDGES

THIRD ANGLE PROJECTION			SHEET SIZE A3				1	ALUM.	6061-T6	
				ITEM	PART No.	DESCRIPTION	No. OFF	MATL.	SPEC.	REMARKS
GENERAL TOLERANCE ON DIMENSIONS	JOB No.	No. OF SETS REQ.	SCALE 1:1	DRAWN	CHK	DATE	TITLE: FLOWSENSOR ADAPTOR			
MACHINED				Y.B.P.KWAN		01.11.95				
UNMACHINED										
OTHER DIMENSIONS AS STATED			FINISH	SCHOOL OF INDUSTRIAL & MANUFACTURING SCIENCE			DRAWING No. MD291 B206 3A			
WELD WHERE SHOWN THUS ⌒			BLACK ANODIZED	CRANFIELD			SHT. 1 OF 1 SHEETS			
MACHINE WHERE SHOWN THUS ✓										

DRAWING No.	
ISSUE	MODIFICATION

ALL DIMENSIONS IN MILLIMETRES UNLESS OTHERWISE STATED. IF IN DOUBT ASK.

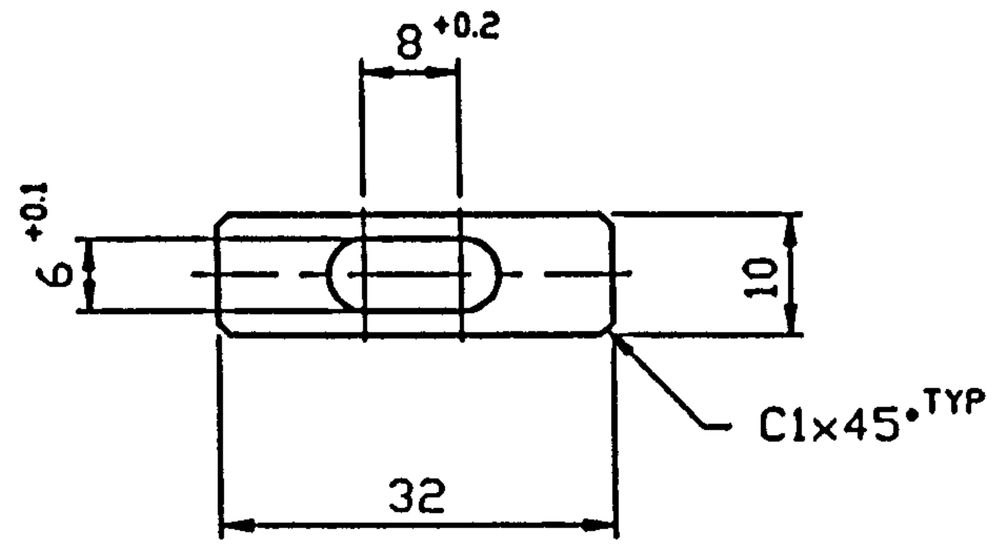

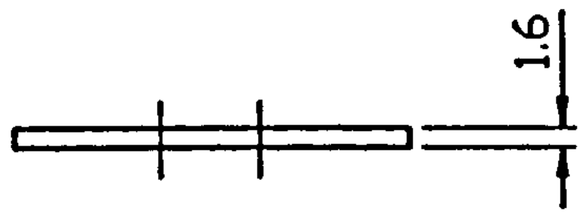

REMOVE ALL SHAPE EDGES

THIRD ANGLE PROJECTION	SHEET SIZE A4					1	ALUM	6061-T6	1.6mm SHEET
		ITEM	PART No.	DESCRIPTION		No. OFF	MATL.	SPEC.	REMARKS

GENERAL TOLERANCE ON DIMENSIONS MACHINED UNMACHINED OTHER DIMENSIONS AS STATED WELD WHERE SHOWN THUS ⌒ L MACHINE WHERE SHOWN THUS ⊿	JOB No.	No. OF SETS REQ.	SCALE 1:1	DRAWN	CHK	DATE	TITLE: SHUTTER PLATE
				Y.B.P.KWAN		02.11.95	
			FINISH	SCHOOL OF INDUSTRIAL & MANUFACTURING SCIENCE CRANFIELD			DRAWING No. MD291 B207 4A SHT. 1 OF 1 SHEETS

DRAWING No.	
ISSUE	MODIFICATION

ALL DIMENSIONS IN MILLIMETRES UNLESS OTHERWISE STATED. IF IN DOUBT ASK.

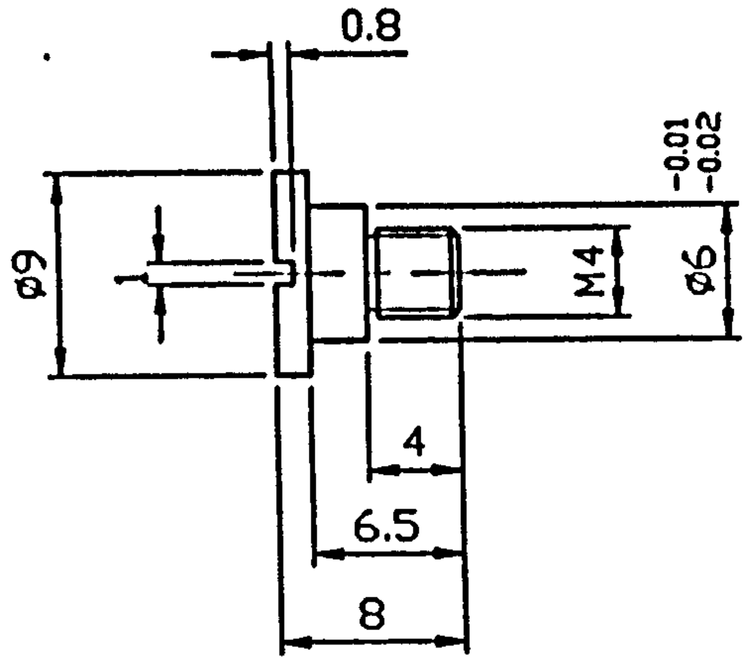

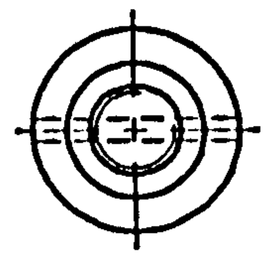

REMOVE ALL SHAPE EDGES

ITEM	PART No.	DESCRIPTION	No. OFF	MATL.	SPEC.	REMARKS
			1	SST	304	

THIRD ANGLE PROJECTION

SHEET SIZE A4

GENERAL TOLERANCE ON DIMENSIONS
MACHINED
UNMACHINED
OTHER DIMENSIONS AS STATED
WELD WHERE SHOWN THUS
MACHINE WHERE SHOWN THUS

JOB No.	No. OF SETS REQ.

SCALE 2:1

FINISH

DRAWN	CHK	DATE
Y.B.P.KWAN		02.11.95

TITLE: SHOULDER SCREW

SCHOOL OF INDUSTRIAL & MANUFACTURING SCIENCE
CRANFIELD

DRAWING No. MD291 B208 4A

SHT. 1 OF 1 SHEETS

DRAWING No.	
ISSUE	MODIFICATION

ALL DIMENSIONS IN MILLIMETRES UNLESS OTHERWISE STATED. IF IN DOUBT ASK.

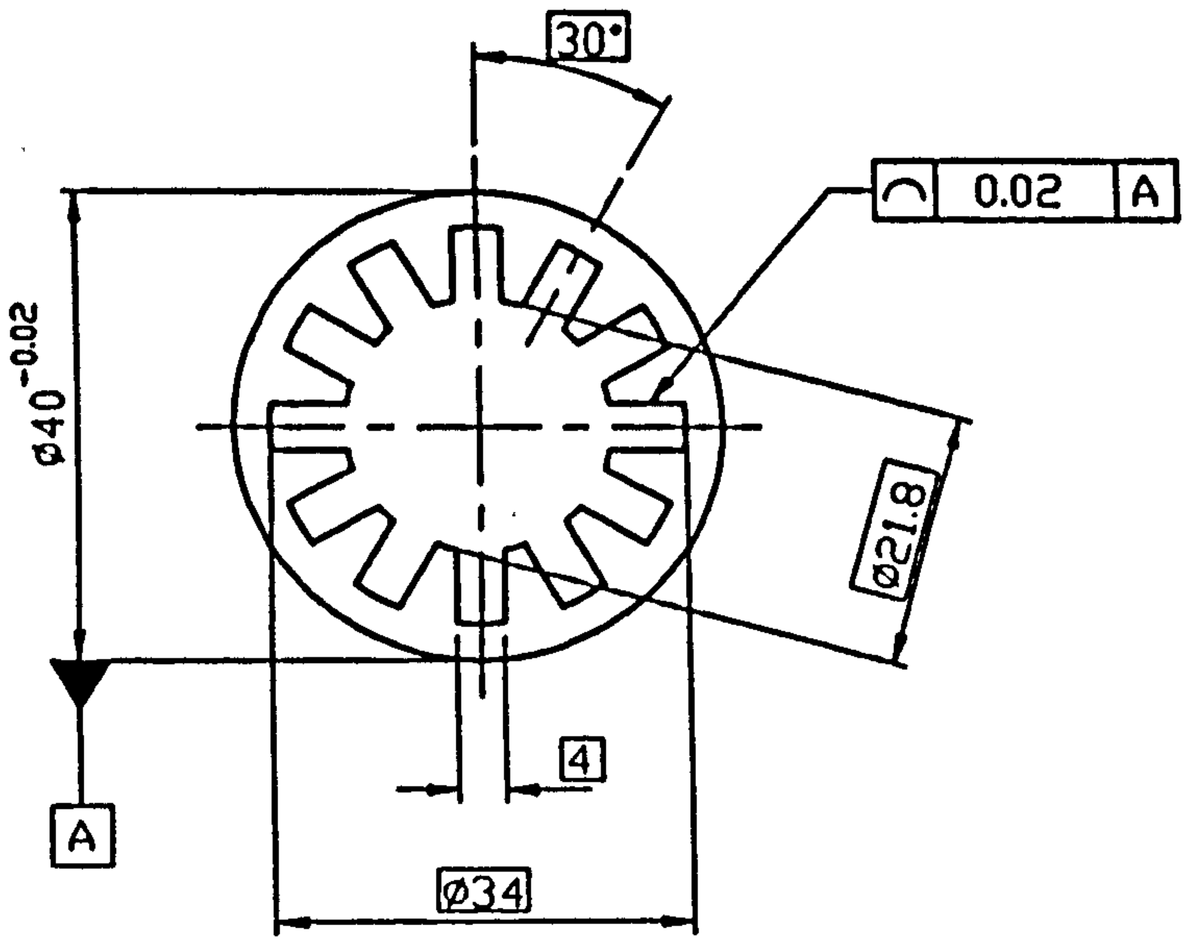

REMOVE ALL SHAPE EDGES

THIRD ANGLE PROJECTION	SHEET SIZE A4	ITEM	PART No.	DESCRIPTION	No. OFF	MATL.	SPEC.	REMARKS
					4	SST	302	12um THK.

GENERAL TOLERANCE ON DIMENSIONS	JOB No.	No. OF SETS REQ.	SCALE 1:1	DRAWN	CHK	DATE	TITLE: ENTRY SLOT DISC
MACHINED				Y.B.P.KWAN		07.04.95	
UNMACHINED							
OTHER DIMENSIONS AS STATED			FINISH PHOTO-CHEM. ETCHED	SCHOOL OF INDUSTRIAL & MANUFACTURING SCIENCE CRANFIELD			DRAWING No. MD291 C101 4A
WELD WHERE SHOWN THUS							SHT. 1 OF 1 SHEETS
MACHINE WHERE SHOWN THUS							

DRAWING No.	
ISSUE	MODIFICATION

ALL DIMENSIONS IN MILLIMETRES UNLESS OTHERWISE STATED. IF IN DOUBT ASK.

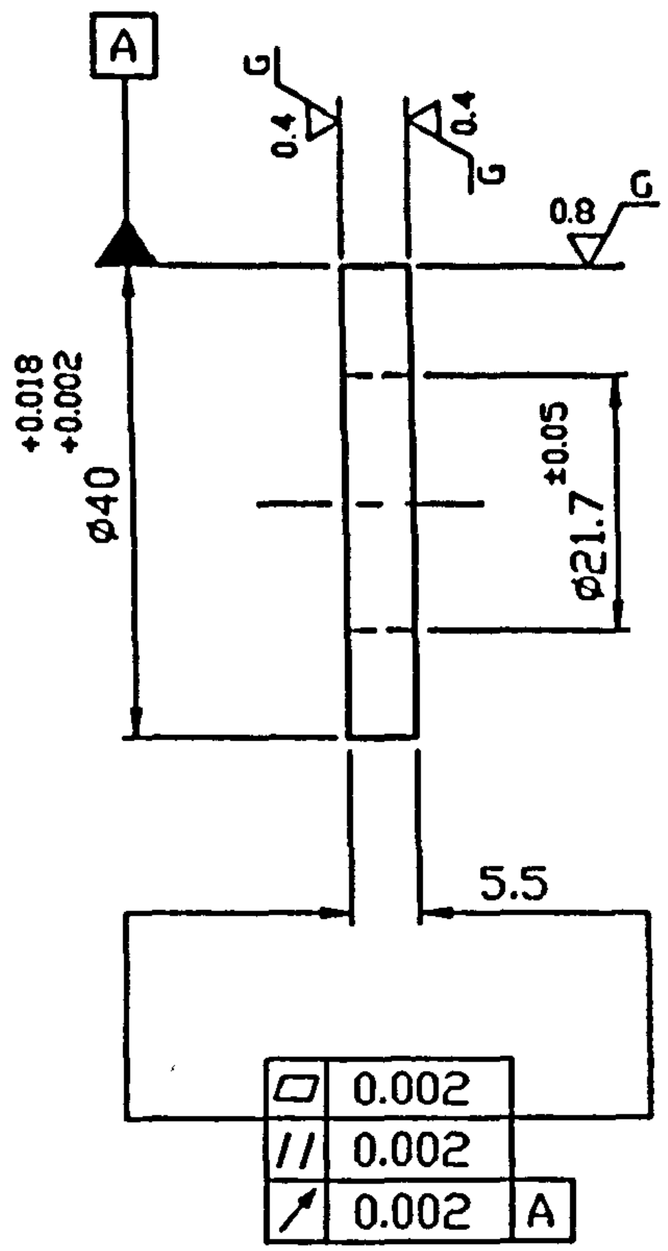

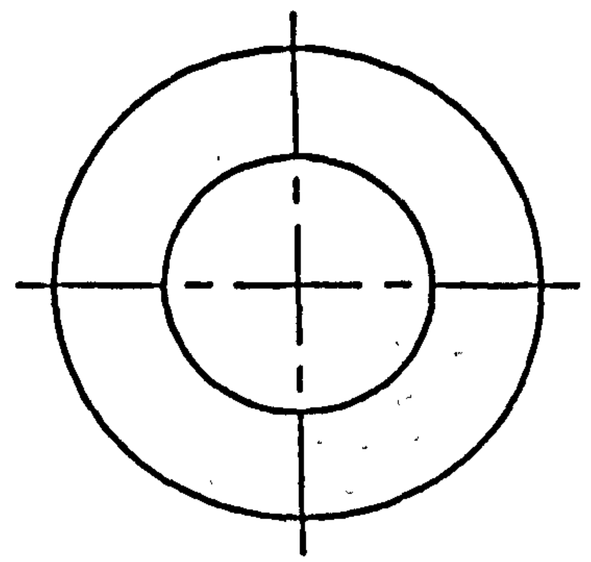

REMOVE ALL SHAPE EDGES

THIRD ANGLE PROJECTION	SHEET SIZE A4				4	SST	440C	
		ITEM	PART No.	DESCRIPTION	No. OFF	MATL.	SPEC.	REMARKS

GENERAL TOLERANCE ON DIMENSIONS MACHINED UNMACHINED OTHER DIMENSIONS AS STATED WELD WHERE SHOWN THUS ⌒ L MACHINE WHERE SHOWN THUS ⊿	JOB No.	No. OF SETS REQ.	SCALE 1:1	DRAWN	CHK	DATE	TITLE: OUTER RING
				Y.B.P.KWAN		07.04.95	
			FINISH	SCHOOL OF INDUSTRIAL & MANUFACTURING SCIENCE CRANFIELD			DRAWING No. MD291 C102 4A SHT. 1 OF 1 SHEETS

DRAWING No.	
ISSUE	MODIFICATION

ALL DIMENSIONS IN MILLIMETRES UNLESS OTHERWISE STATED. IF IN DOUBT ASK.

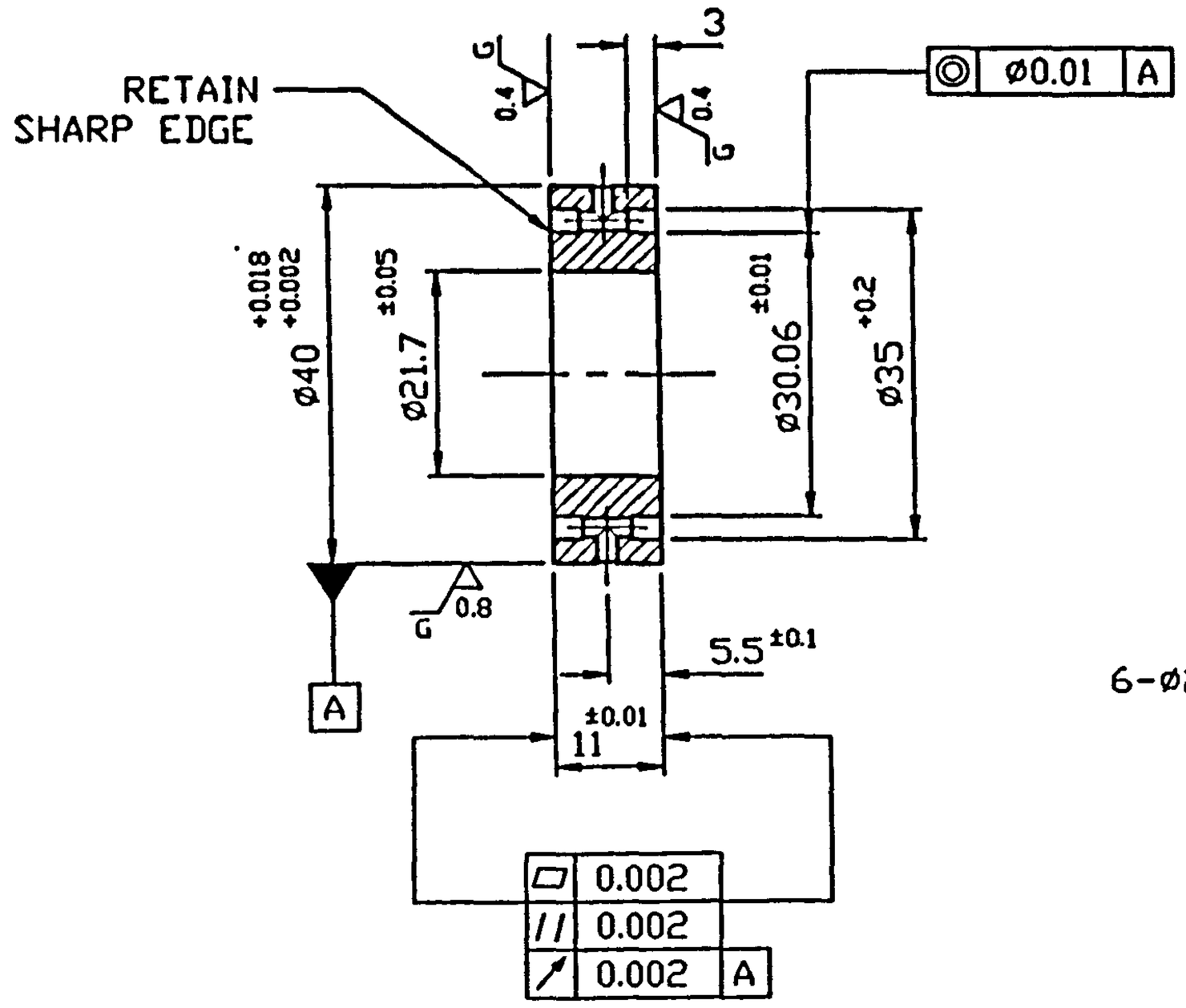

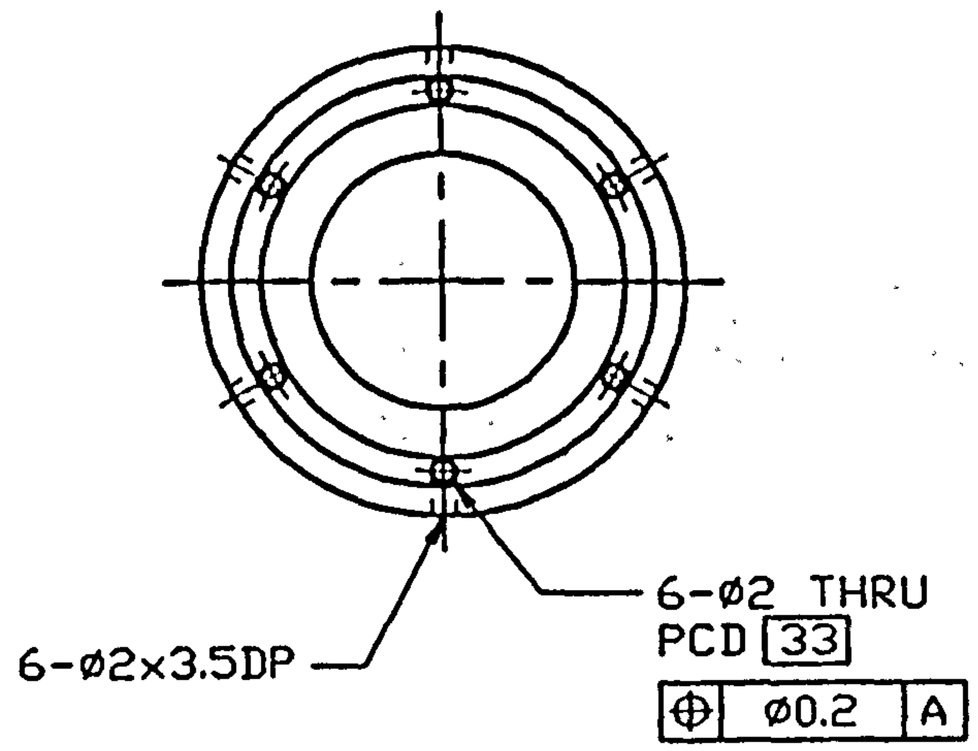

REMOVE ALL SHAPE EDGES

THIRD ANGLE PROJECTION	SHEET SIZE A4	ITEM	PART No.	DESCRIPTION	No. OFF	MATL.	SPEC.	REMARKS
					2	SST	440C	

GENERAL TOLERANCE ON DIMENSIONS	JOB No.	No. OF SETS REQ.	SCALE 1:1	DRAWN	CHK	DATE	TITLE: FEED RING
MACHINED				Y.B.P.KWAN		07.04.95	
UNMACHINED							
OTHER DIMENSIONS AS STATED			FINISH	SCHOOL OF INDUSTRIAL & MANUFACTURING SCIENCE			DRAWING No. MD291 C103 4A
WELD WHERE SHOWN THUS				CRANFIELD			SHT. 1 OF 1 SHEETS
MACHINE WHERE SHOWN THUS							

DRAWING No.	
ISSUE	MODIFICATION

ALL DIMENSIONS IN MILLIMETRES UNLESS OTHERWISE STATED. IF IN DOUBT ASK.

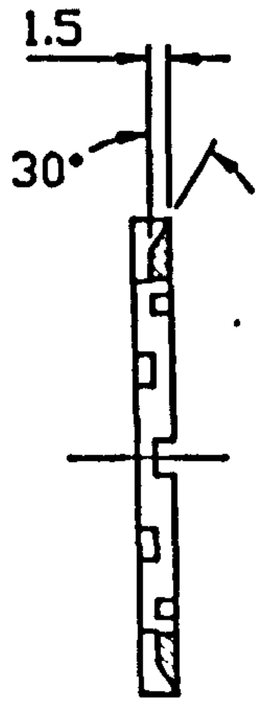

SECTION A-A

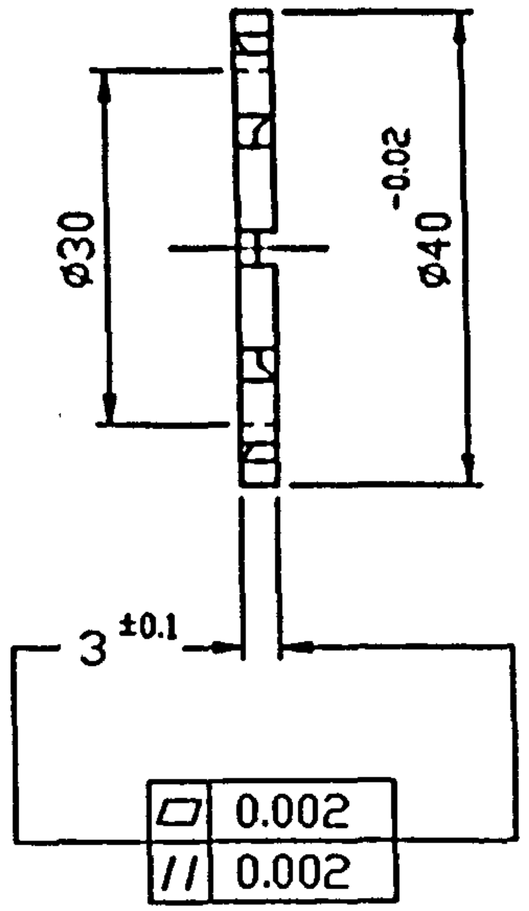

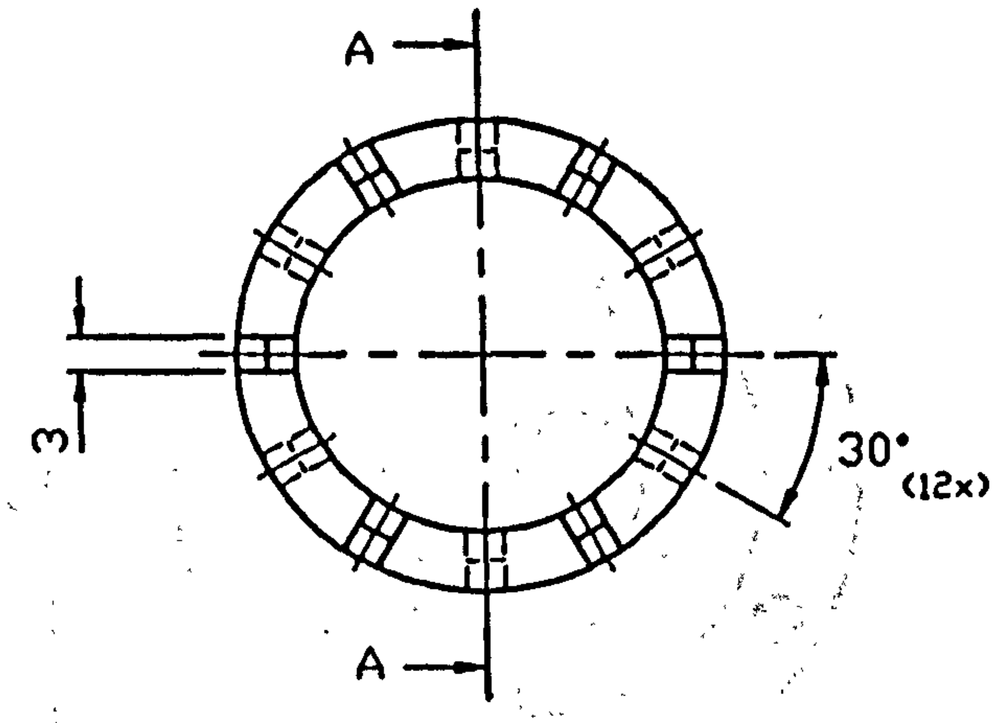

REMOVE ALL SHAPE EDGES

ITEM	PART No.	DESCRIPTION	No. OFF	MATL.	SPEC.	REMARKS
			1	SST	440C	

THIRD ANGLE PROJECTION

SHEET SIZE A4

GENERAL TOLERANCE ON DIMENSIONS	JOB No.	No. OF SETS REQ.
MACHINED		
UNMACHINED		
OTHER DIMENSIONS AS STATED		
WELD WHERE SHOWN THUS ⌒ L		
MACHINE WHERE SHOWN THUS ✓		

SCALE 1:1

FINISH

DRAWN	CHK	DATE
Y.B.P.KWAN		10.04.95

TITLE: SPACER RING

SCHOOL OF INDUSTRIAL & MANUFACTURING SCIENCE

CRANFIELD

DRAWING No. MD291 C104 4A

SHT. 1 OF 1 SHEETS

DRAWING No.	
ISSUE	MODIFICATION

ALL DIMENSIONS IN MILLIMETRES UNLESS OTHERWISE STATED. IF IN DOUBT ASK.

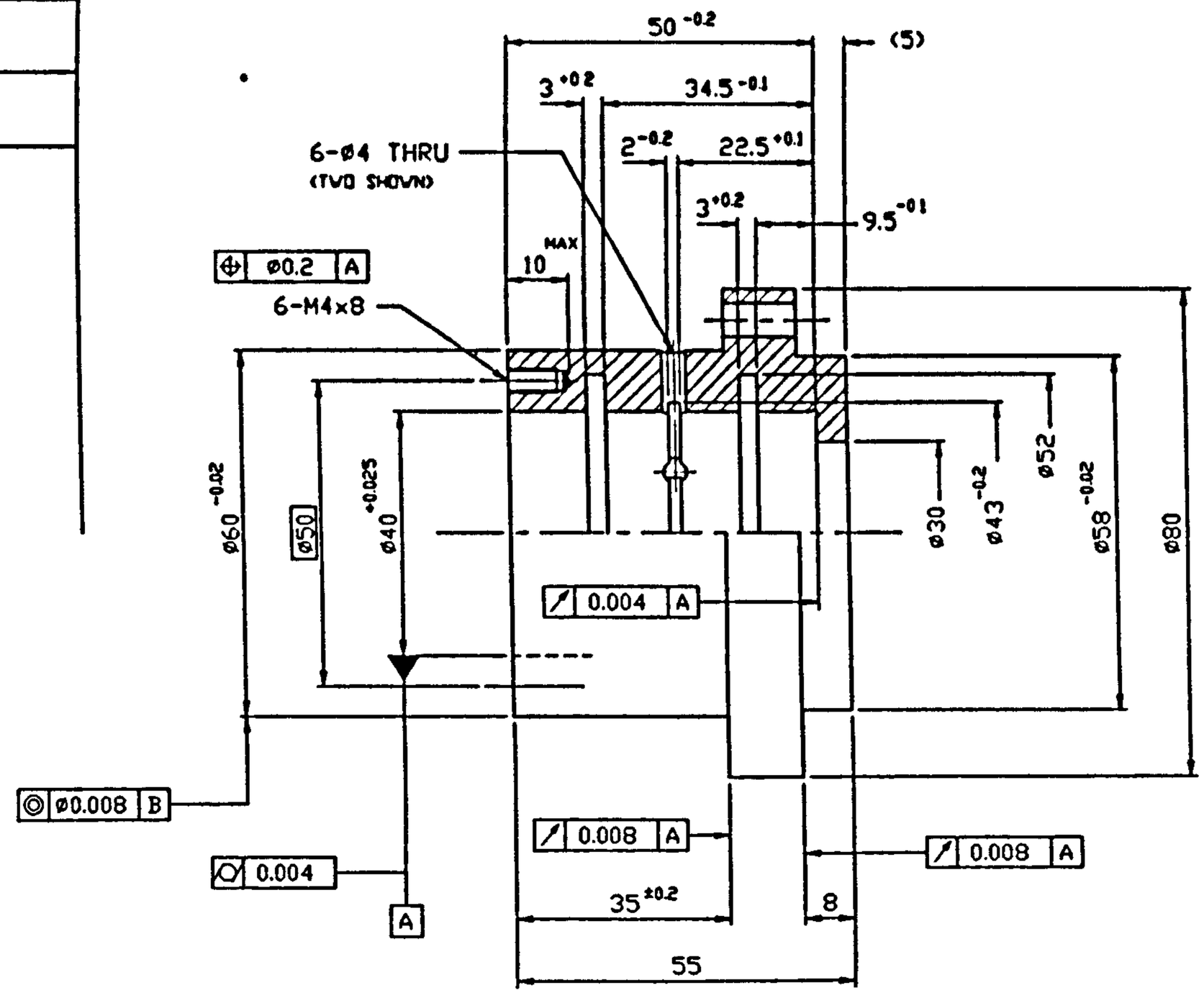

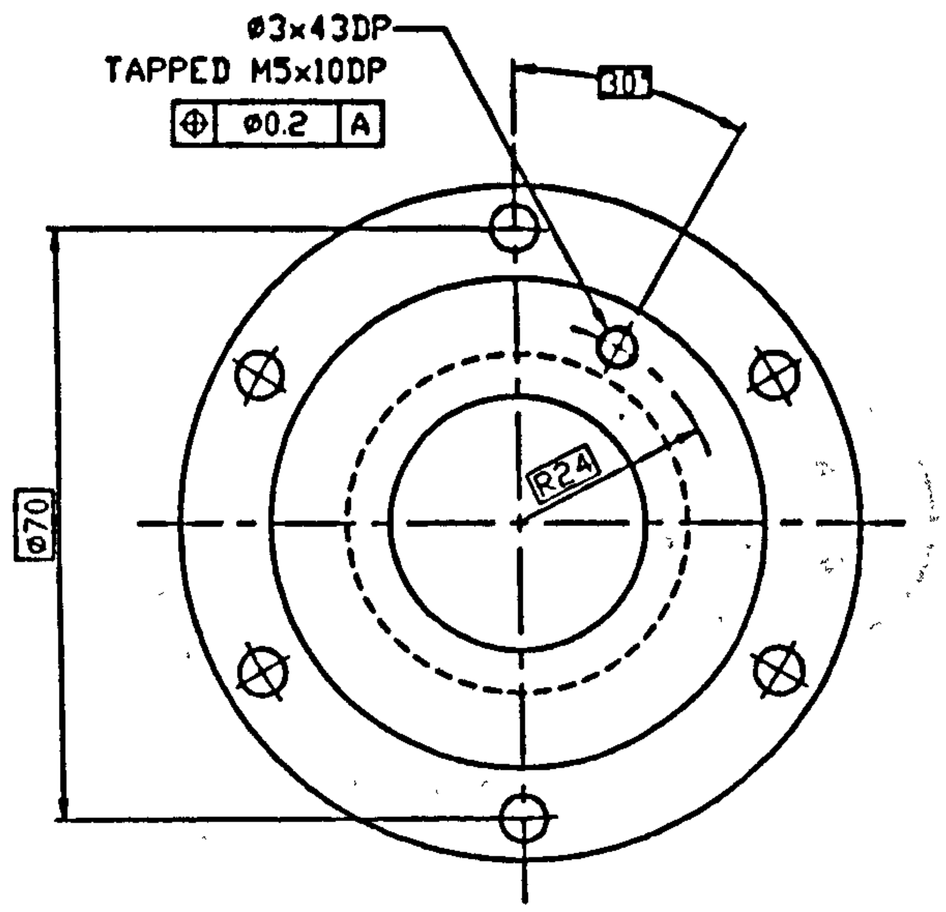

REMOVE ALL SHAPE EDGES

THIRD ANGLE PROJECTION	SHEET SIZE A3	ITEM	PART No.	DESCRIPTION	No. OFF	MATL.	SPEC.	REMARKS
					1	SST	440C	

GENERAL TOLERANCE ON DIMENSIONS	JOB No.	No. OF SETS REQ.	SCALE 1:1	DRAWN	CHK	DATE	TITLE: BEARING HOUSING
MACHINED				Y.B.P.KWAN		10.04.95	
UNMACHINED							
OTHER DIMENSIONS AS STATED			FINISH	SCHOOL OF INDUSTRIAL & MANUFACTURING SCIENCE			DRAWING No. MD291 C105 3A
WELD WHERE SHOWN THUS L				CRANFIELD			SHT. 1 OF 1 SHEETS
MACHINE WHERE SHOWN THUS ✓							

DRAWING No.	
ISSUE	MODIFICATION

ALL DIMENSIONS IN MILLIMETRES UNLESS OTHERWISE STATED. IF IN DOUBT ASK.

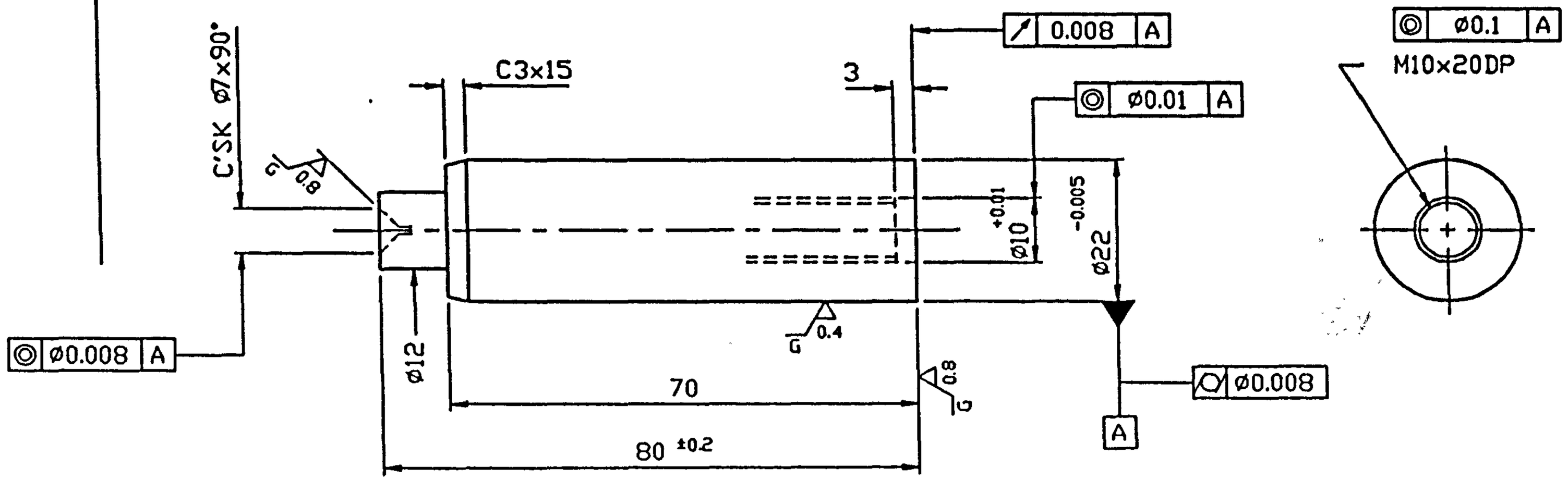

REMOVE ALL SHAPE EDGES

THIRD ANGLE PROJECTION	SHEET SIZE A4	ITEM	PART No.	DESCRIPTION	No. OFF	MATL.	SPEC.	REMARKS
					1	C.S.	230M07	Lloyd-Coley DC22×160

GENERAL TOLERANCE ON DIMENSIONS	JOB No.	No. OF SETS REQ.	SCALE 1:1	DRAWN	CHK	DATE	TITLE: LOAD SHAFT
MACHINED				Y.B.P.KWAN		10.04.95	
UNMACHINED							
OTHER DIMENSIONS AS STATED			FINISH HRc 60-62	SCHOOL OF INDUSTRIAL & MANUFACTURING SCIENCE			DRAWING No. MD291 C106 4A
WELD WHERE SHOWN THUS ⌒ L				CRANFIELD			SHT. 1 OF 1 SHEETS
MACHINE WHERE SHOWN THUS ✓							

DRAWING No.	
ISSUE	MODIFICATION

ALL DIMENSIONS IN MILLIMETRES UNLESS OTHERWISE STATED. IF IN DOUBT ASK.

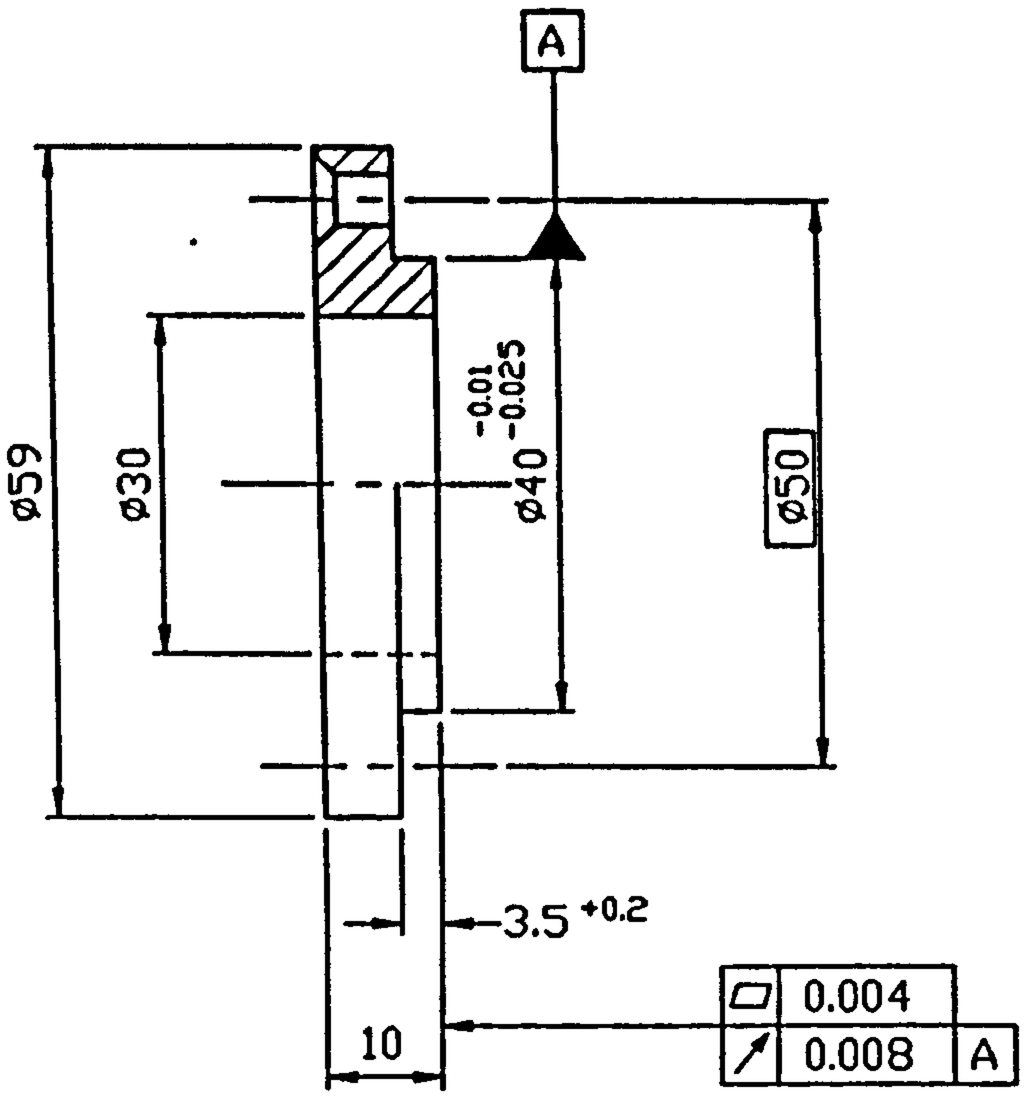

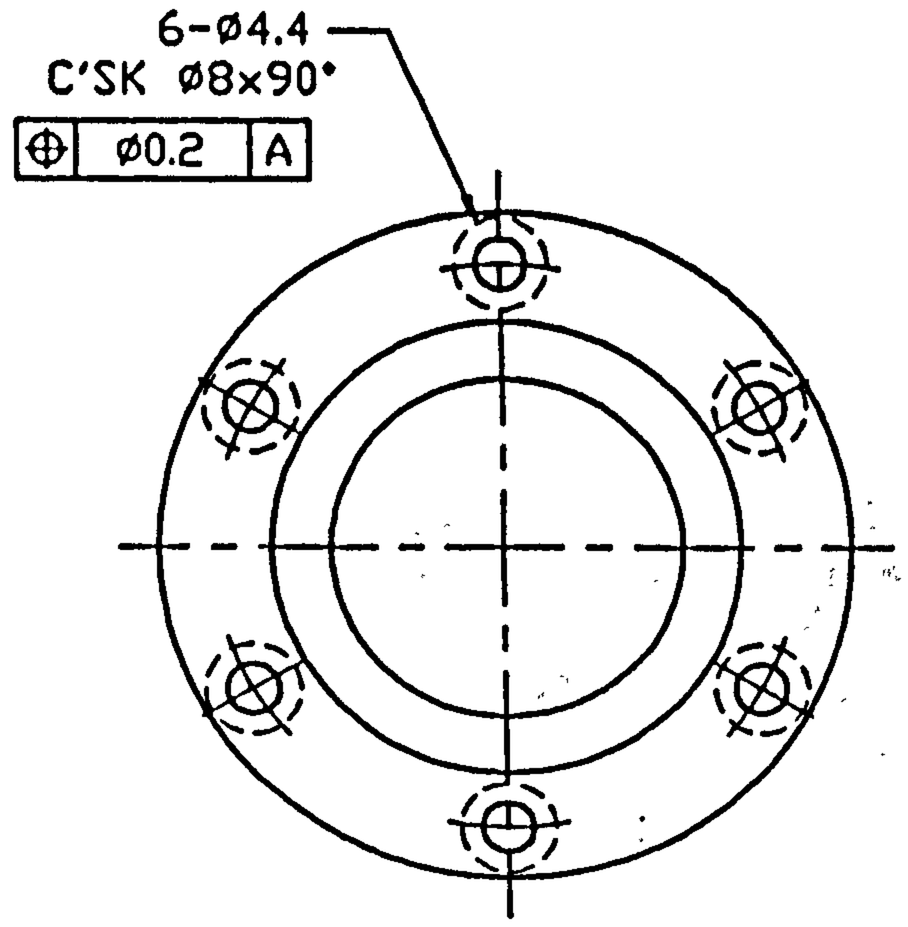

REMOVE ALL SHAPE EDGES

THIRD ANGLE PROJECTION	SHEET SIZE A4	ITEM	PART No.	DESCRIPTION	No. OFF	MATL.	SPEC.	REMARKS
					1	SST	304	

GENERAL TOLERANCE ON DIMENSIONS	JOB No.	No. OF SETS REQ.	SCALE 1:1	DRAWN	CHK	DATE	TITLE: BEARING CAP
MACHINED				Y.B.P.KVAN		10.04.95	
UNMACHINED							
OTHER DIMENSIONS AS STATED			FINISH	SCHOOL OF INDUSTRIAL & MANUFACTURING SCIENCE			DRAWING No. MD291 C107 4A
WELD WHERE SHOWN THUS ⌒ L				CRANFIELD			SHT. 1 OF 1 SHEETS
MACHINE WHERE SHOWN THUS ✓							

DRAWING No.	
ISSUE	MODIFICATION

ALL DIMENSIONS IN MILLIMETRES UNLESS OTHERWISE STATED. IF IN DOUBT ASK.

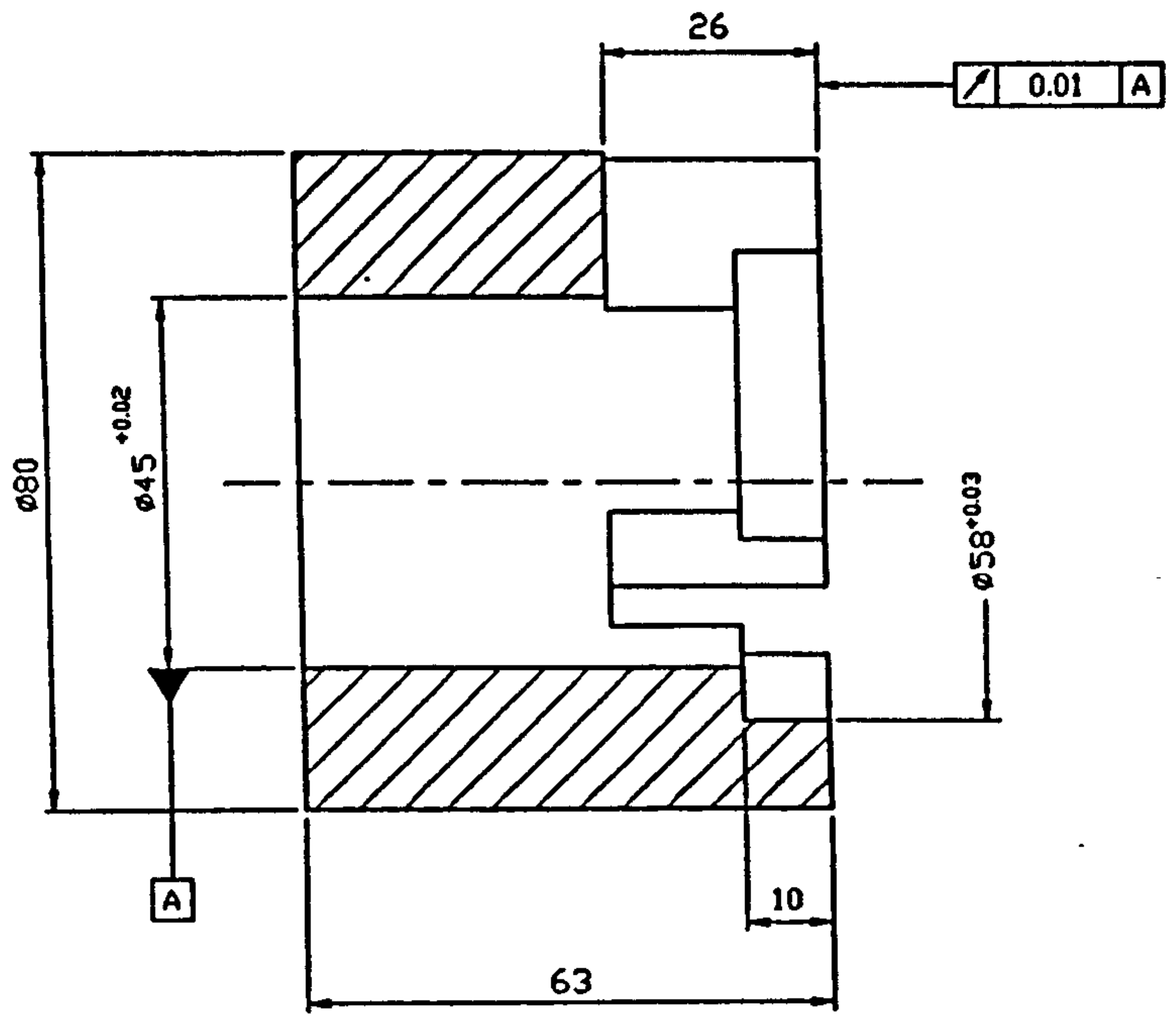

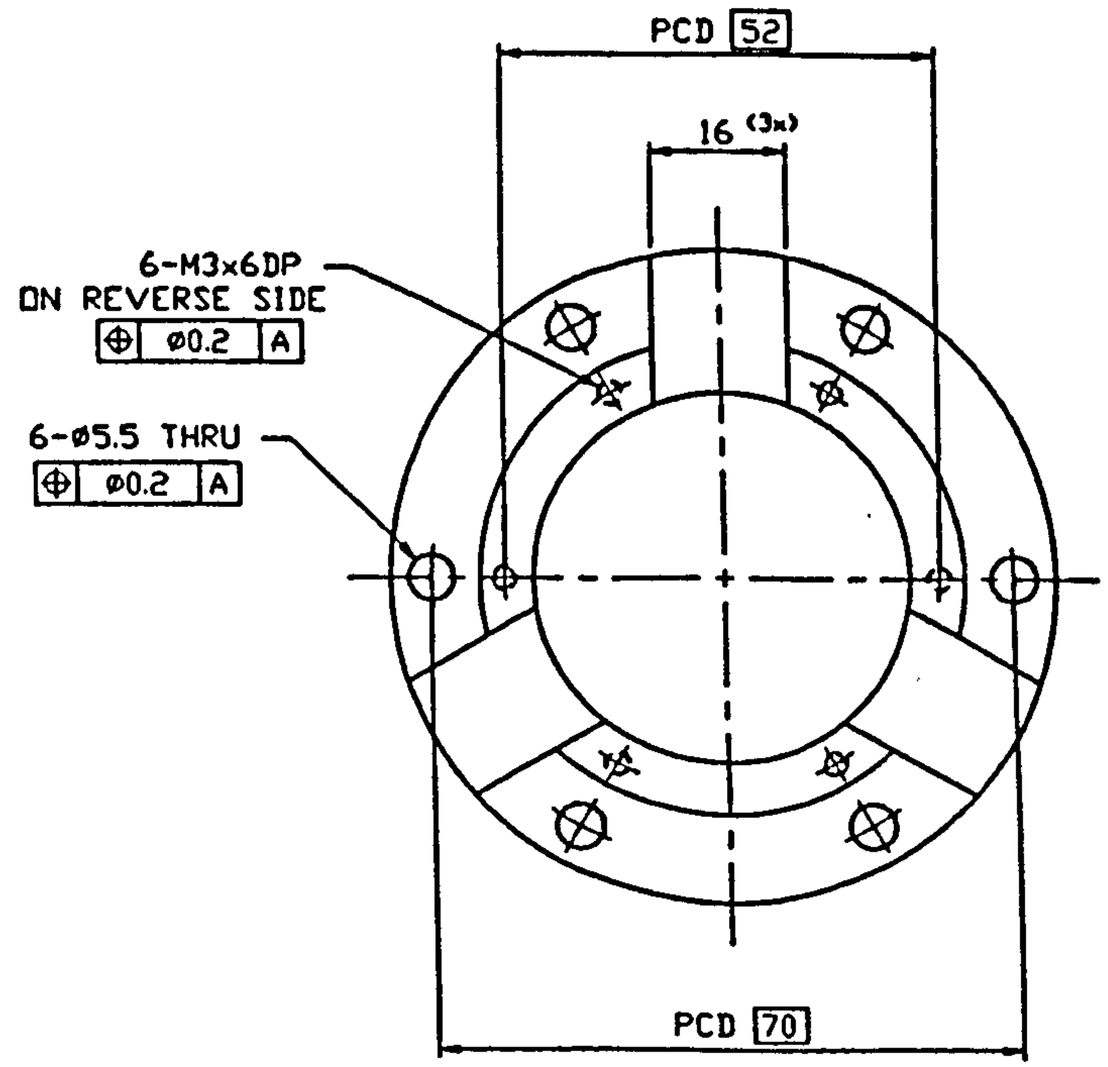

REMOVE ALL SHAPE EDGES

THIRD ANGLE PROJECTION			SHEET SIZE A3				1	ALUM.	6061-T6	
				ITEM	PART No.	DESCRIPTION	No. OFF	MATL.	SPEC.	REMARKS
GENERAL TOLERANCE ON DIMENSIONS MACHINED UNMACHINED OTHER DIMENSIONS AS STATED	JOB No.	No. OF SETS REQ.	SCALE 1:1	DRAWN	CHK	DATE	TITLE: CYLINDER SLEEVE			
				Y.B.P.KWAN		14.04.95				
WELD WHERE SHOWN THUS ⌒ L			FINISH BLACK ANODIZED	SCHOOL OF INDUSTRIAL & MANUFACTURING SCIENCE CRANFIELD			DRAWING No. MD291 C108 3A			
MACHINE WHERE SHOWN THUS √							SHT. 1 OF 1 SHEETS			

DRAWING No.	
ISSUE	MODIFICATION

ALL DIMENSIONS IN MILLIMETRES UNLESS OTHERWISE STATED. IF IN DOUBT ASK.

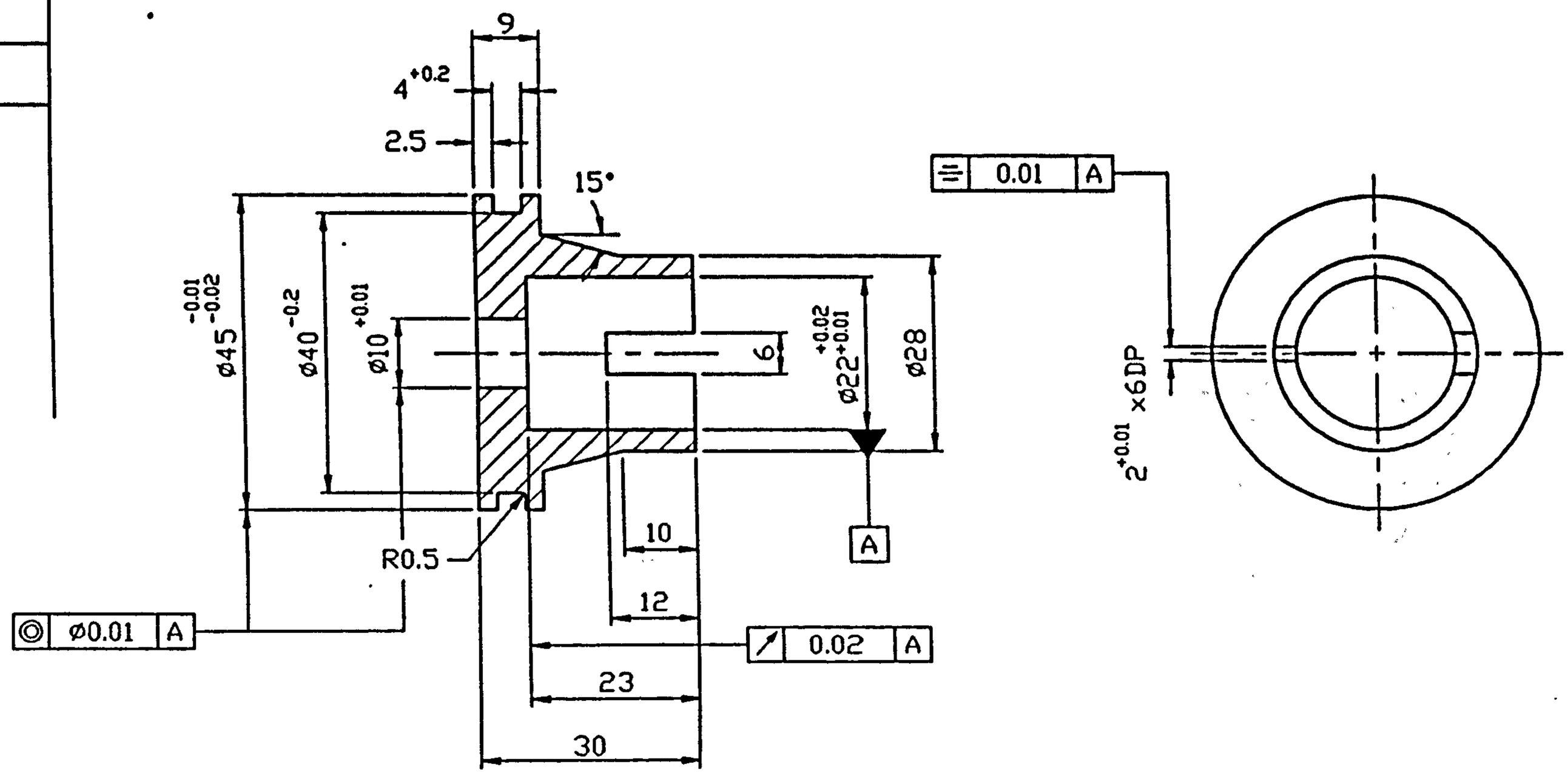

REMOVE ALL SHAPE EDGES

THIRD ANGLE PROJECTION	SHEET SIZE A4				1	ALUM.	6061-T6	FITS GACO RM0395-03
		ITEM	PART No.	DESCRIPTION	No. OFF	MATL.	SPEC.	REMARKS

GENERAL TOLERANCE ON DIMENSIONS MACHINED UNMACHINED OTHER DIMENSIONS AS STATED WELD WHERE SHOWN THUS ⌒ L MACHINE WHERE SHOWN THUS ⊿	JOB No.	No. OF SETS REQ.	SCALE 1:1	DRAWN Y.B.P.KWAN	CHK	DATE 14.04.95
			FINISH			

TITLE: PISTON

SCHOOL OF INDUSTRIAL & MANUFACTURING SCIENCE
CRANFIELD

DRAWING No. MD291 C109 4A

SHT. 1 OF 1 SHEETS

DRAWING No.	
ISSUE	MODIFICATION

ALL DIMENSIONS IN MILLIMETRES UNLESS OTHERWISE STATED. IF IN DOUBT ASK.

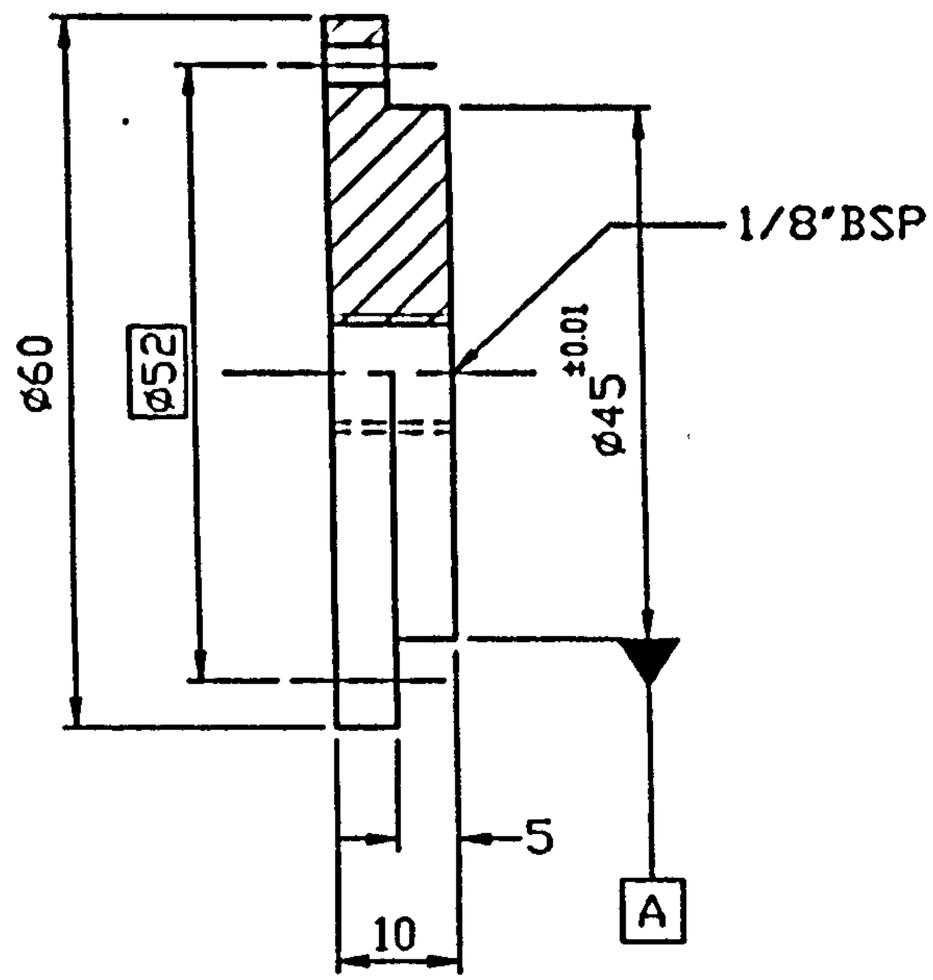

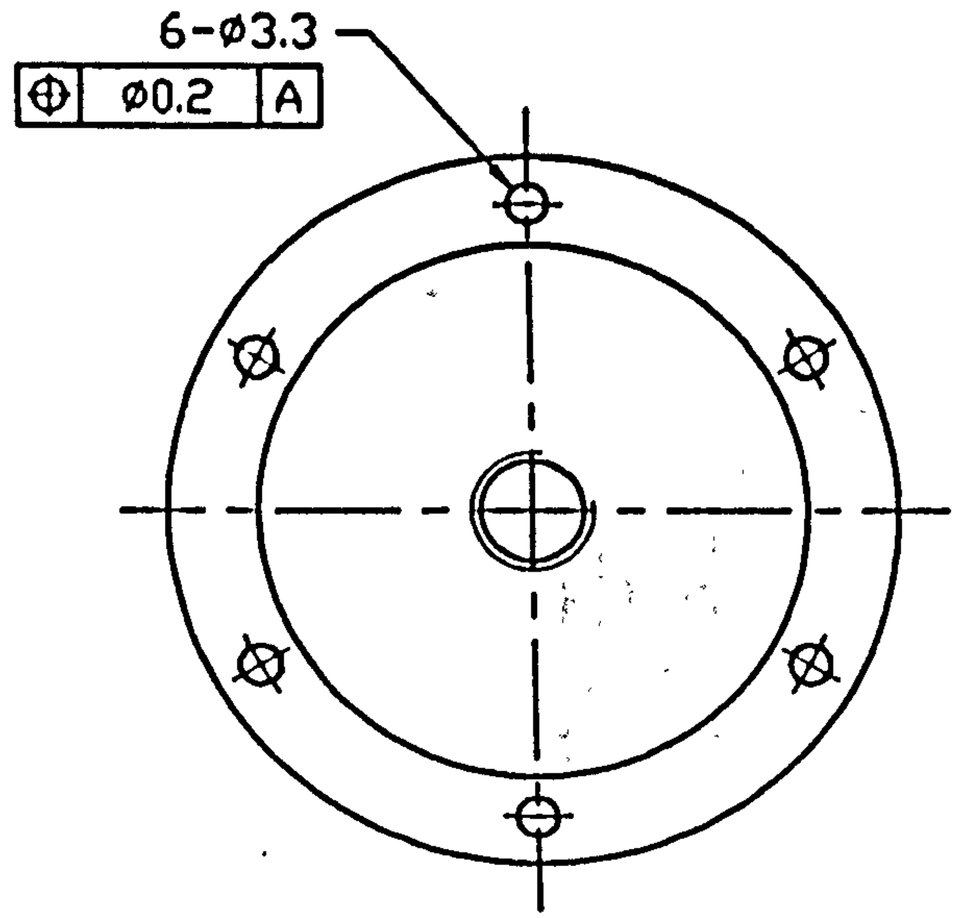

REMOVE ALL SHAPE EDGES

THIRD ANGLE PROJECTION	SHEET SIZE A4	ITEM	PART No.	DESCRIPTION	No. OFF	MATL.	SPEC.	REMARKS
					1	ALUM.	6061-T6	

GENERAL TOLERANCE ON DIMENSIONS	JOB No.	No. OF SETS REQ.	SCALE	DRAWN	CHK	DATE	TITLE:
MACHINED			1:1	Y.B.P.KWAN		15.04.95	CYLINDER CAP
UNMACHINED							
OTHER DIMENSIONS AS STATED			FINISH	SCHOOL OF INDUSTRIAL & MANUFACTURING SCIENCE			DRAWING No.
WELD WHERE SHOWN THUS			BLACK ANODIZED	CRANFIELD			MD291 C110 4A
MACHINE WHERE SHOWN THUS							SHT. 1 OF 1 SHEETS

DRAWING No.	
ISSUE	MODIFICATION

ALL DIMENSIONS IN MILLIMETRES UNLESS OTHERWISE STATED. IF IN DOUBT ASK.

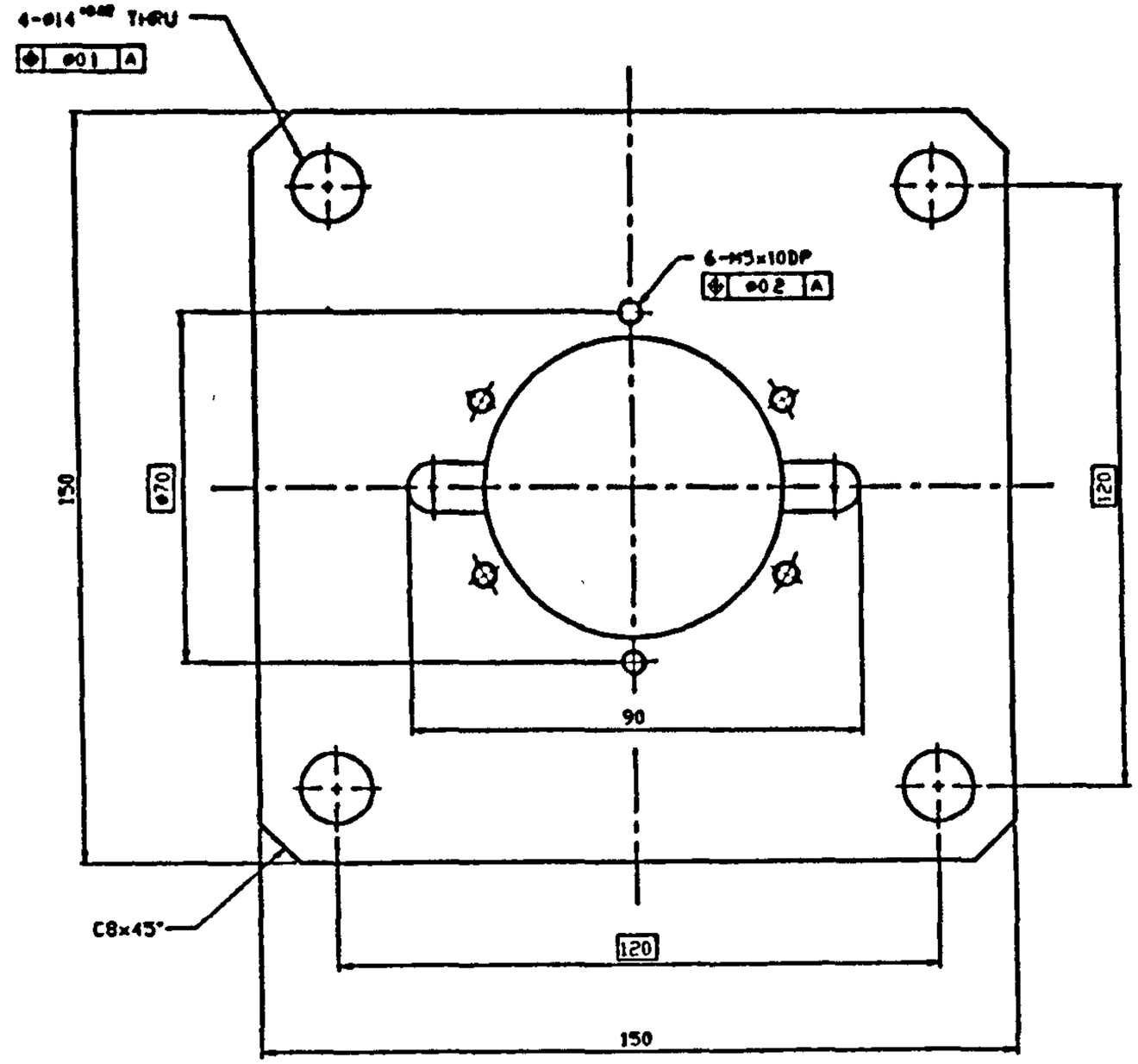

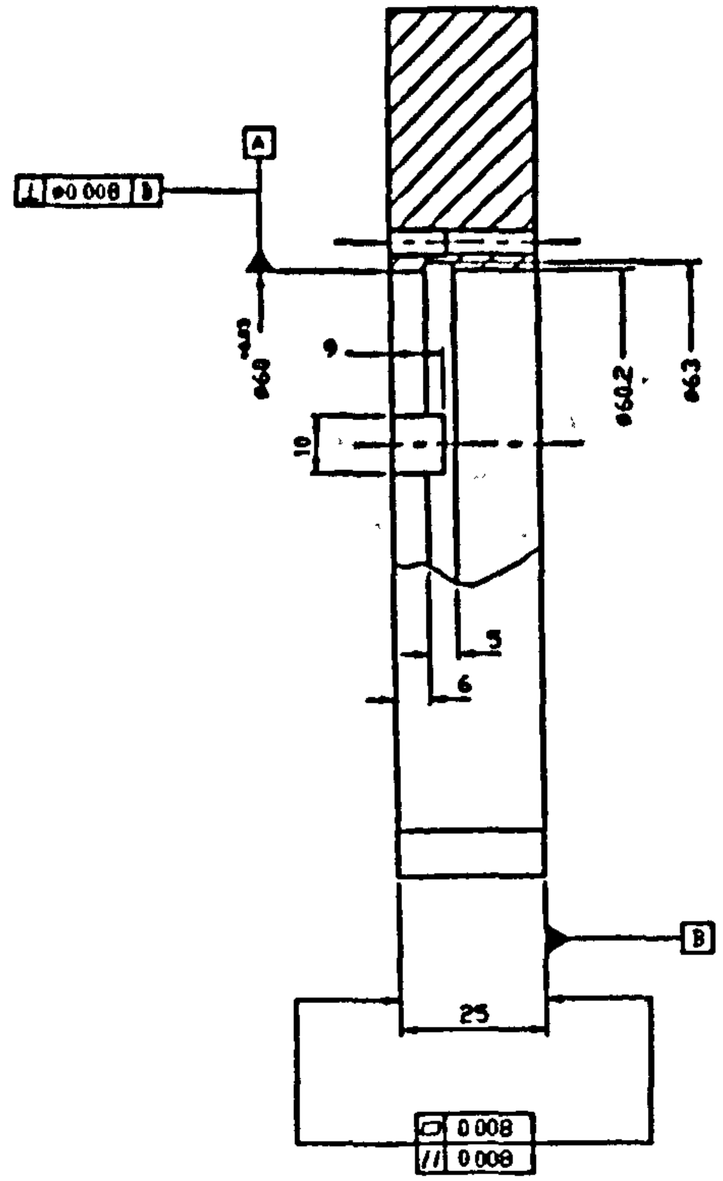

REMOVE ALL SHAPE EDGES

THIRD ANGLE PROJECTION			SHEET SIZE A2				1	M.S.		STRESS RELIEF AFT ROUGH G
				ITEM	PART No.	DESCRIPTION	No. OFF	MATL.	SPEC.	REMARKS
GENERAL TOLERANCE ON DIMENSIONS	JOB No.	No. OF SETS REQ.	SCALE 1:1	DRAWN	CHK	DATE	TITLE: TOP PLATE			
MACHINED				Y.B.P.KWAN		15.04.95				
UNMACHINED										
OTHER DIMENSIONS AS STATED			FINISH CHEMI BLACK	SCHOOL OF INDUSTRIAL & MANUFACTURING SCIENCE CRANFIELD			DRAWING No. MD291 C111 2A			
WELD WHERE SHOWN THUS ⌐ ⌐							SHT. 1 OF 1 SHEETS			
MACHINE WHERE SHOWN THUS ✓										

DRAWING No.	
ISSUE	MODIFICATION

ALL DIMENSIONS IN MILLIMETRES UNLESS OTHERWISE STATED. IF IN DOUBT ASK.

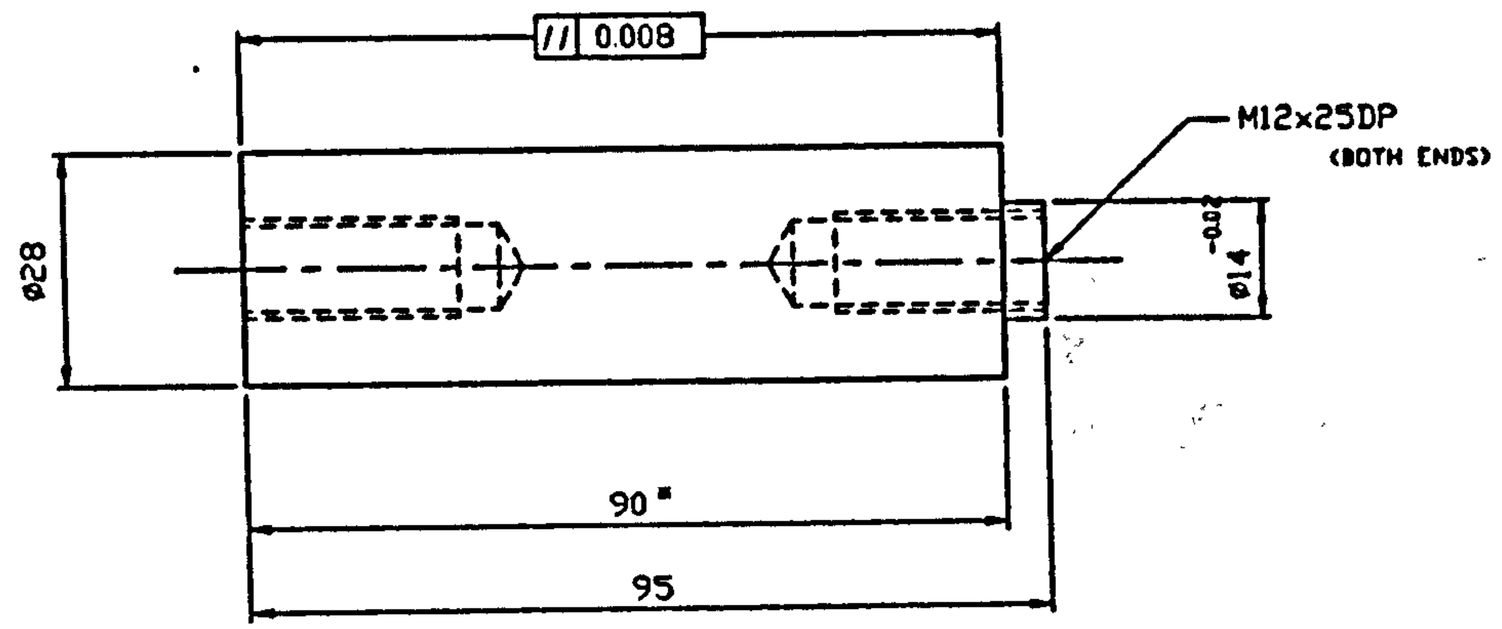

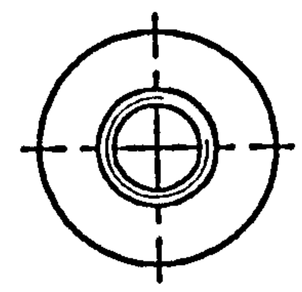

*NOTE: HEIGHT DEVIATION BTW. SET OF 4 < 0.008

REMOVE ALL SHAPE EDGES

THIRD ANGLE PROJECTION	SHEET SIZE A3	ITEM	PART No.	DESCRIPTION	No. OFF	MATL.	SPEC.	REMARKS
					4	M.S.		

GENERAL TOLERANCE ON DIMENSIONS	JOB No.	No. OF SETS REQ.	SCALE 1:1	DRAWN	CHK	DATE	TITLE: PILLAR
MACHINED				Y.B.P.KWAN		15.04.95	
UNMACHINED							
OTHER DIMENSIONS AS STATED			FINISH CHEMI BLACK	SCHOOL OF INDUSTRIAL & MANUFACTURING SCIENCE CRANFIELD			DRAWING No. MD291 C112 3A
WELD WHERE SHOWN THUS ⌒							SHT. 1 OF 1 SHEETS
MACHINE WHERE SHOWN THUS ✓							

DRAWING No.	
ISSUE	MODIFICATION

ALL DIMENSIONS IN MILLIMETRES UNLESS OTHERWISE STATED. IF IN DOUBT ASK.

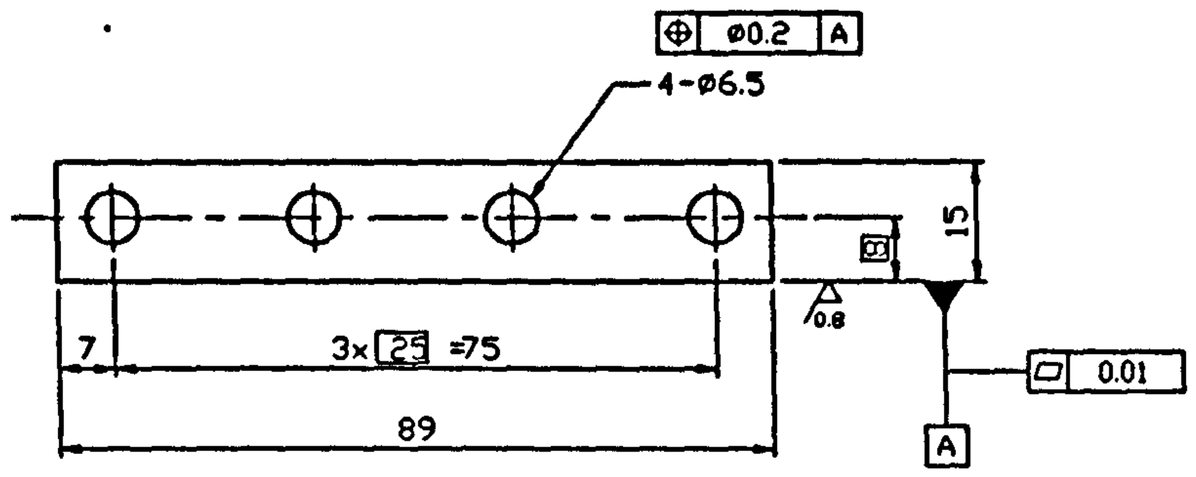

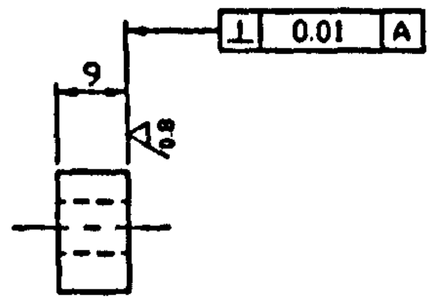

REMOVE ALL SHAPE EDGES

THIRD ANGLE PROJECTION	SHEET SIZE A3	ITEM	PART No.	DESCRIPTION	No. OFF	MATL.	SPEC.	REMARKS
					2	BRASS		

GENERAL TOLERANCE ON DIMENSIONS	JOB No.	No. OF SETS REQ.	SCALE 1:1	DRAWN	CHK	DATE	TITLE: SIDE RAIL
MACHINED				Y.B.P.KWAN		15.04.95	
UNMACHINED							
OTHER DIMENSIONS AS STATED			FINISH	SCHOOL OF INDUSTRIAL & MANUFACTURING SCIENCE			DRAWING No. MD291 C113 3A
WELD WHERE SHOWN THUS ⌒ L				CRANFIELD			SHT. 1 OF 1 SHEETS
MACHINE WHERE SHOWN THUS ✓							

DRAWING No.	
ISSUE	MODIFICATION

ALL DIMENSIONS IN MILLIMETRES UNLESS OTHERWISE STATED. IF IN DOUBT ASK.

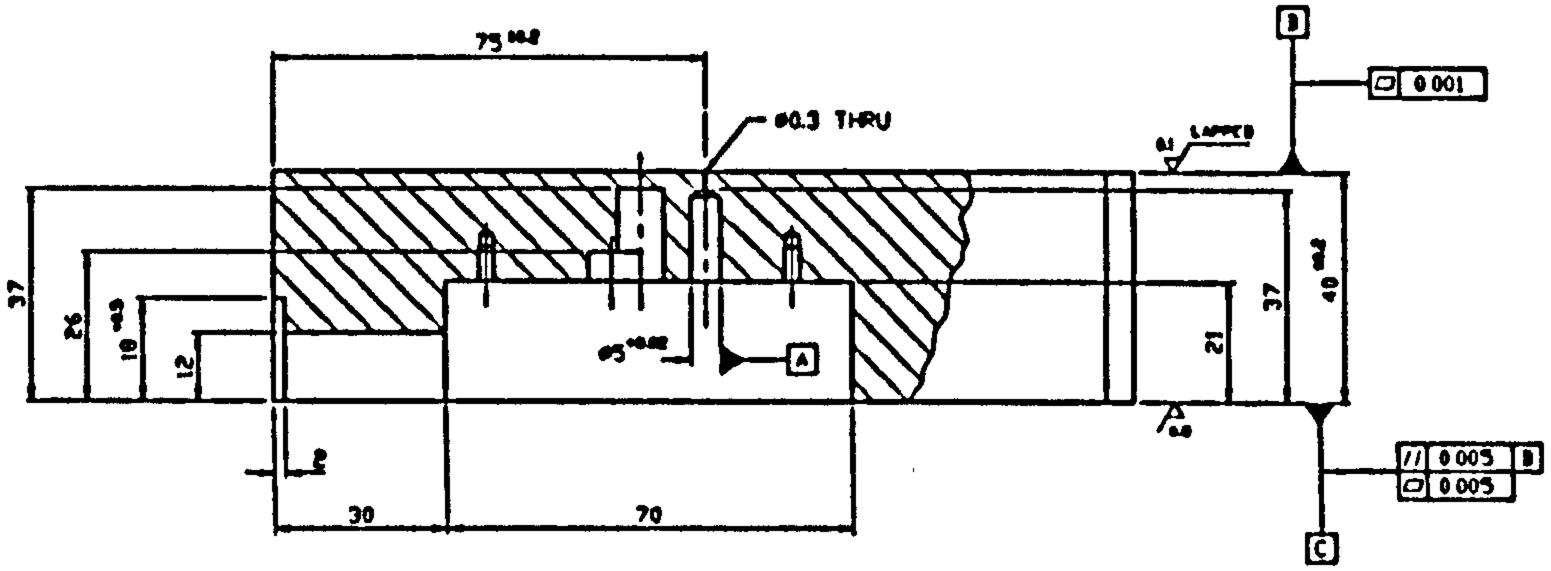

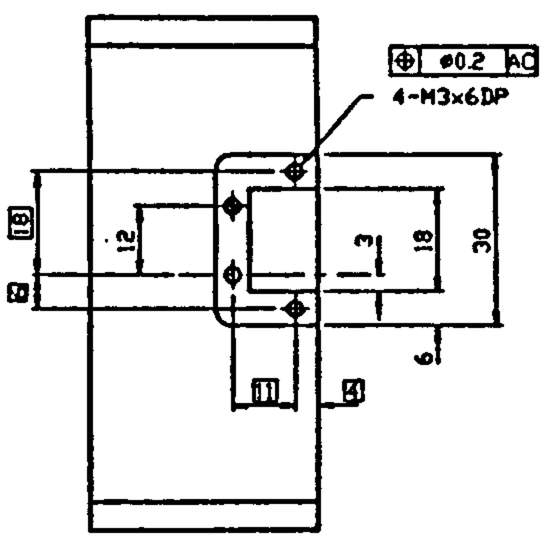

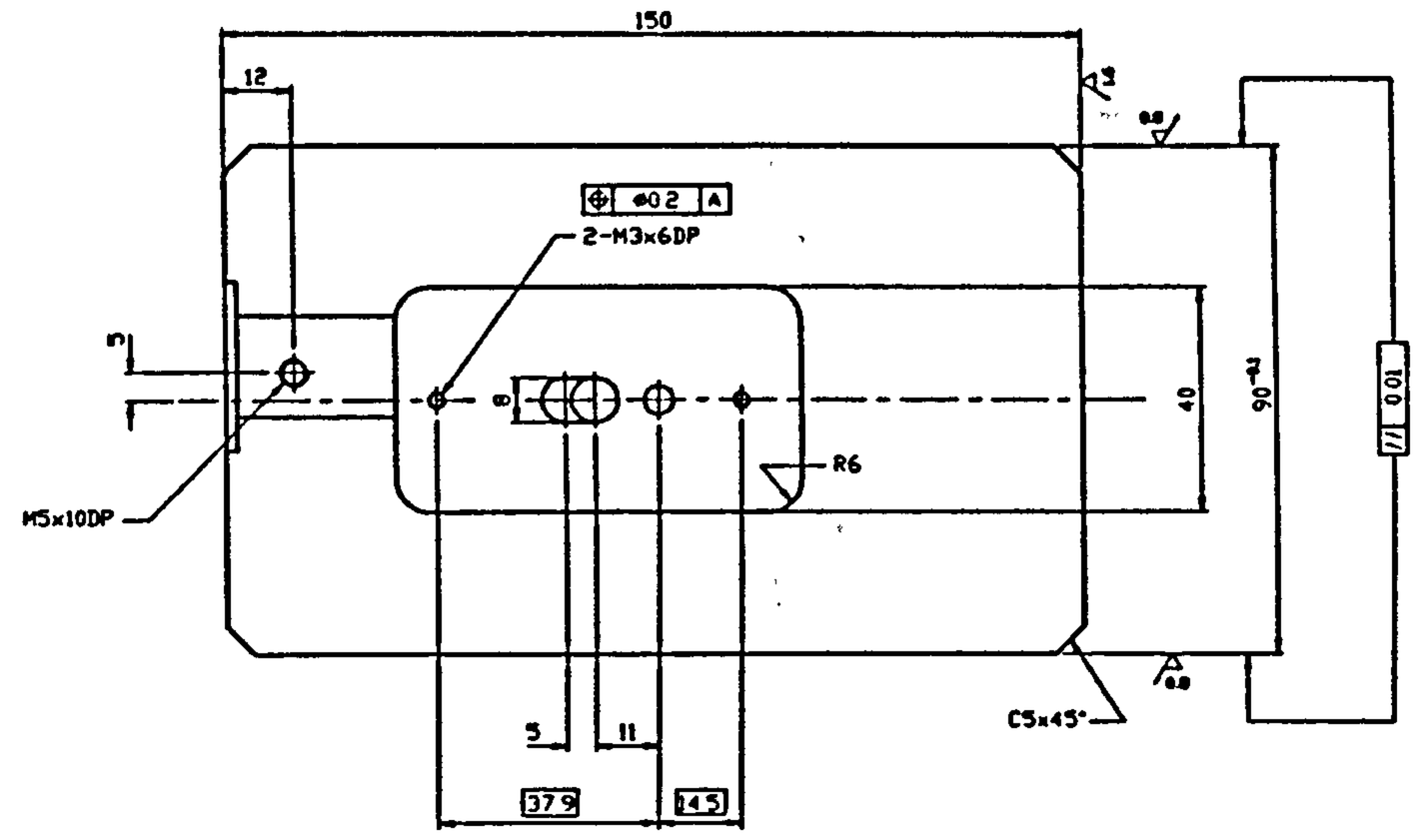

REMOVE ALL SHAPE EDGES

THIRD ANGLE PROJECTION			SHEET SIZE A2	ITEM	PART No.	DESCRIPTION	No. OFF	MATL.	SPEC.	REMARKS
							1	SST	316	
GENERAL TOLERANCE ON DIMENSIONS	JOB No.	No. OF SETS REQ.	SCALE 1:1	DRAWN	CHK	DATE	TITLE: REFERENCE PLATE			
MACHINED				Y.B.P.K.VAN		16.04.95				
UNMACHINED										
OTHER DIMENSIONS AS STATED			FINISH	SCHOOL OF INDUSTRIAL & MANUFACTURING SCIENCE			DRAWING No. MD291 C115 2A			
WELD WHERE SHOWN THUS — L				CRANFIELD			SHT. 1 OF 1 SHEETS			
MACHINE WHERE SHOWN THUS ✓										

DRAWING No.	
ISSUE	MODIFICATION

ALL DIMENSIONS IN MILLIMETRES UNLESS OTHERWISE STATED. IF IN DOUBT ASK.

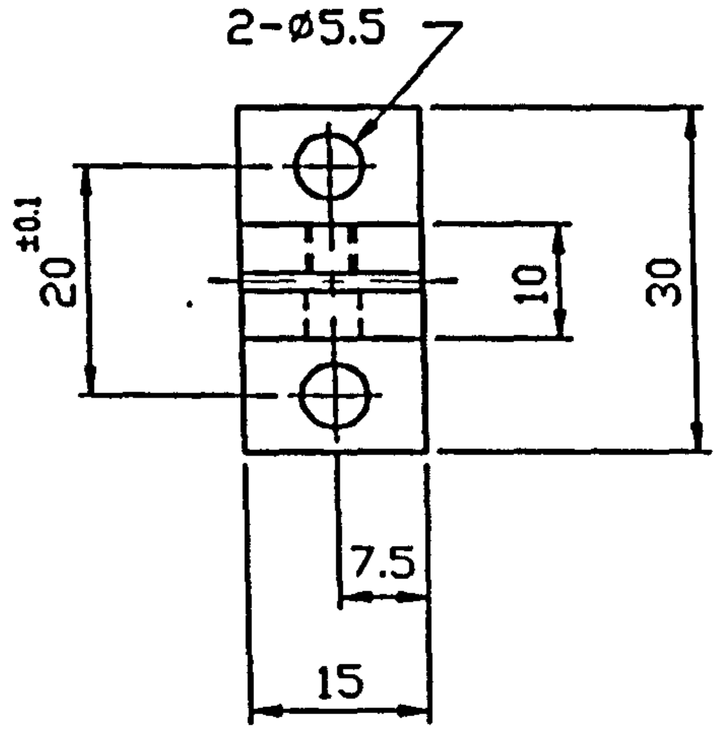

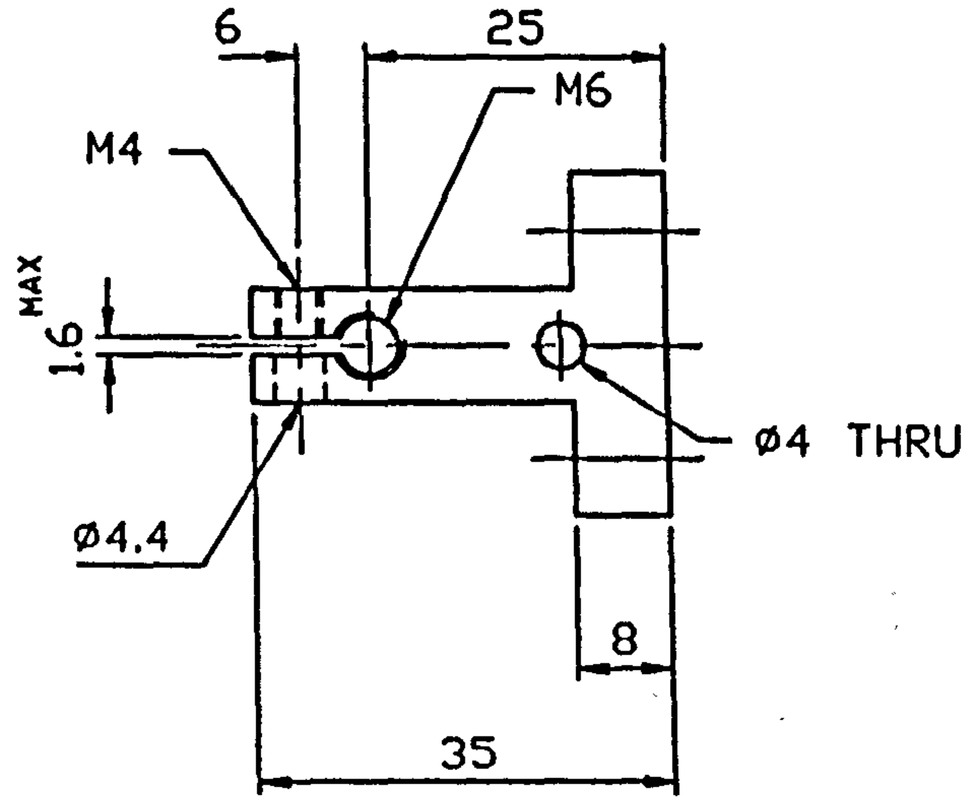

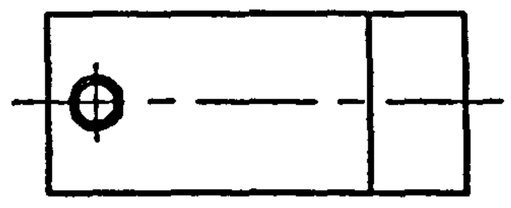

REMOVE ALL SHAPE EDGES

THIRD ANGLE PROJECTION			SHEET SIZE A4	ITEM	PART No.	DESCRIPTION	No. OFF	MATL.	SPEC.	REMARKS
							1	M.S.		
GENERAL TOLERANCE ON DIMENSIONS MACHINED UNMACHINED OTHER DIMENSIONS AS STATED WELD WHERE SHOWN THUS ⌒ L MACHINE WHERE SHOWN THUS ⊿	JOB No.	No. OF SETS REQ.	SCALE 1:1	DRAWN	CHK	DATE	TITLE: ADJUSTING SCREW MOUNT			
				Y.B.P.KVAN		18.04.95				
			FINISH CHEMI BLACK	SCHOOL OF INDUSTRIAL & MANUFACTURING SCIENCE CRANFIELD			DRAWING No. MD291 C116 4A			
							SHT. 1 OF 1 SHEETS			

DRAWING No.	
ISSUE	MODIFICATION

ALL DIMENSIONS IN MILLIMETRES UNLESS OTHERWISE STATED. IF IN DOUBT ASK.

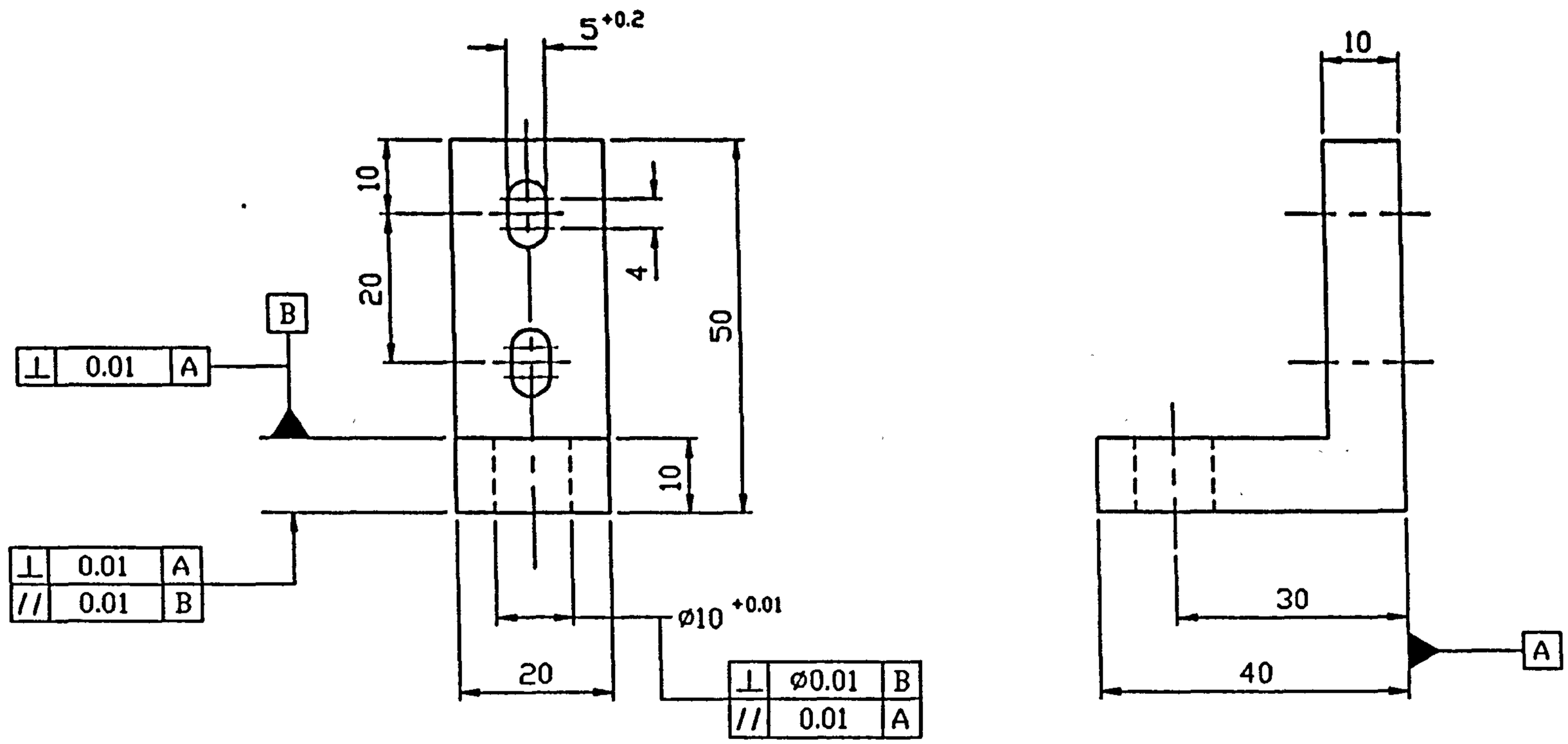

REMOVE ALL SHAPE EDGES

THIRD ANGLE PROJECTION	SHEET SIZE A4	ITEM	PART No.	DESCRIPTION	No. OFF	MATL.	SPEC.	REMARKS
					1	M.S.		

GENERAL TOLERANCE ON DIMENSIONS MACHINED UNMACHINED OTHER DIMENSIONS AS STATED	JOB No.	No. OF SETS REQ.	SCALE 1:1	DRAWN	CHK	DATE	TITLE: MICROMETER MOUNT
				Y.B.P.KWAN		18.04.95	
WELD WHERE SHOWN THUS ⌒			FINISH CHEMI BLACK	SCHOOL OF INDUSTRIAL & MANUFACTURING SCIENCE			DRAWING No. MD291 C117 4A
MACHINE WHERE SHOWN THUS ✓				CRANFIELD			SHT. 1 OF 1 SHEETS

DRAWING No.	
ISSUE	MODIFICATION

ALL DIMENSIONS IN MILLIMETRES UNLESS OTHERWISE STATED. IF IN DOUBT ASK.

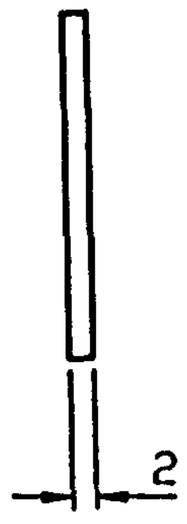

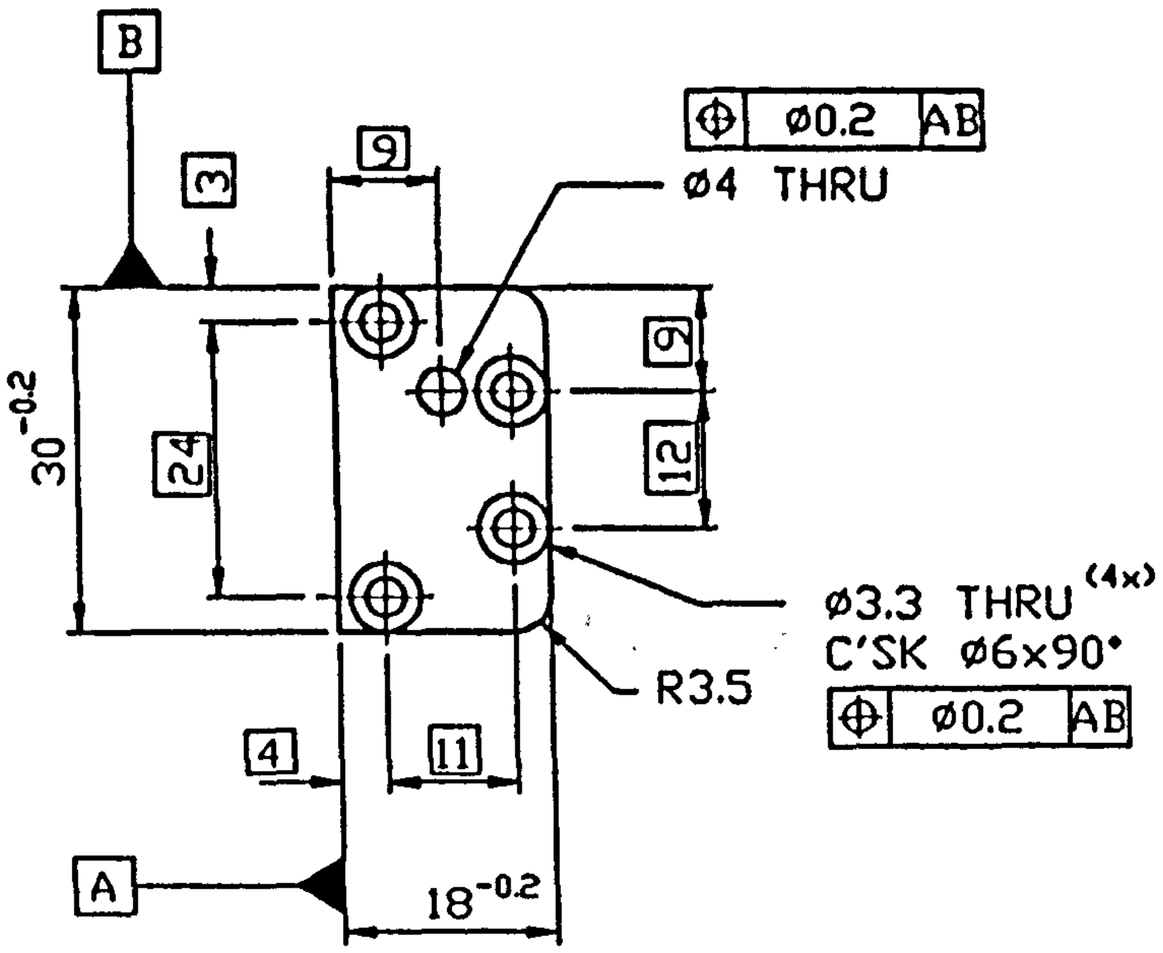

REMOVE ALL SHAPE EDGES

THIRD ANGLE PROJECTION			SHEET SIZE A4				1	ALUM	2mm Sht	
				ITEM	PART No.	DESCRIPTION	No. OFF	MATL.	SPEC.	REMARKS
GENERAL TOLERANCE ON DIMENSIONS MACHINED UNMACHINED OTHER DIMENSIONS AS STATED WELD WHERE SHOWN THUS ⌒ L MACHINE WHERE SHOWN THUS ✓	JOB No.	No. OF SETS REQ.	SCALE 1:1	DRAWN Y.B.P.KVAN	CHK	DATE 27.06.93	TITLE: CABLE COVER			
			FINISH BLACK ANODISED	SCHOOL OF INDUSTRIAL & MANUFACTURING SCIENCE CRANFIELD			DRAWING No. MD291 C118 4A			
							SHT. 1 OF 1 SHEETS			

DRAWING No.	
ISSUE	MODIFICATION

ALL DIMENSIONS IN MILLIMETRES UNLESS OTHERWISE STATED. IF IN DOUBT ASK.

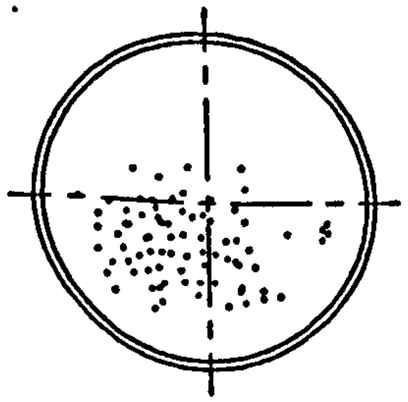

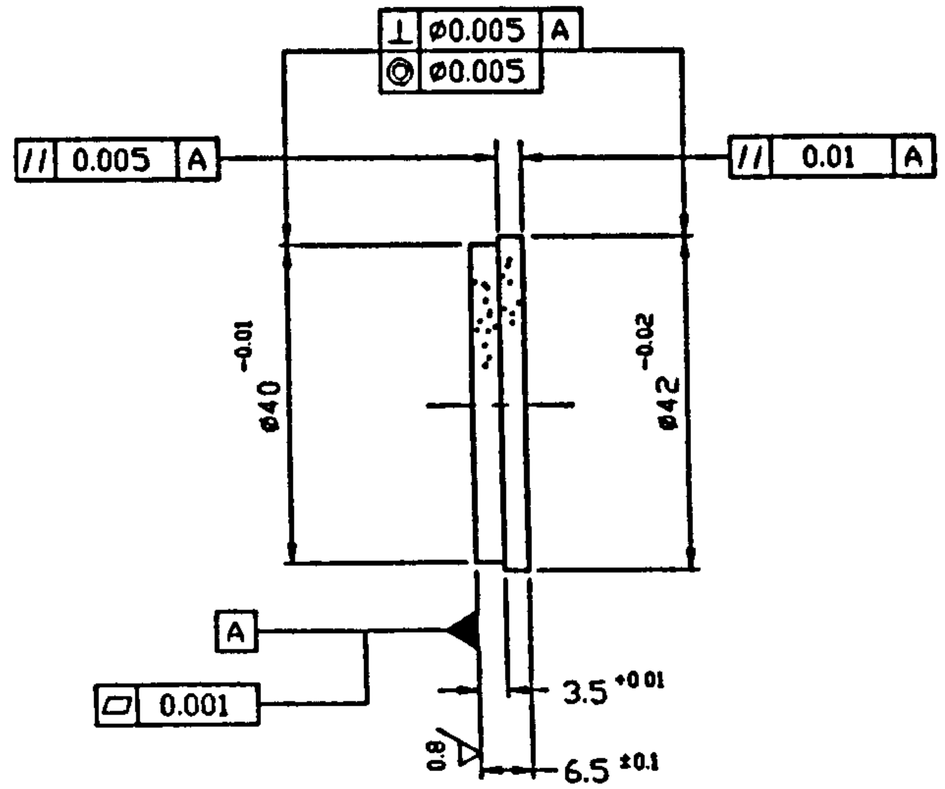

REMOVE ALL SHAPE EDGES

THIRD ANGLE PROJECTION	SHEET SIZE A3	ITEM	PART No.	DESCRIPTION	No. OFF	MATL.	SPEC.	REMARKS
					1	ALUMINA	POROUS	

GENERAL TOLERANCE ON DIMENSIONS	JOB No.	No. OF SETS REQ.	SCALE 1:1	DRAWN	CHK	DATE	TITLE: POROUS PAD
MACHINED				Y.B.P.KWAN		2006.95	
UNMACHINED							
OTHER DIMENSIONS AS STATED			FINISH	SCHOOL OF INDUSTRIAL & MANUFACTURING SCIENCE			DRAWING No. MD291 C121 3A
WELD WHERE SHOWN THUS ⌒ L				CRANFIELD			SHT. 1 OF 1 SHEETS
MACHINE WHERE SHOWN THUS ⊿							

DRAWING No.	
ISSUE	MODIFICATION

ALL DIMENSIONS IN MILLIMETRES UNLESS OTHERWISE STATED. IF IN DOUBT ASK.

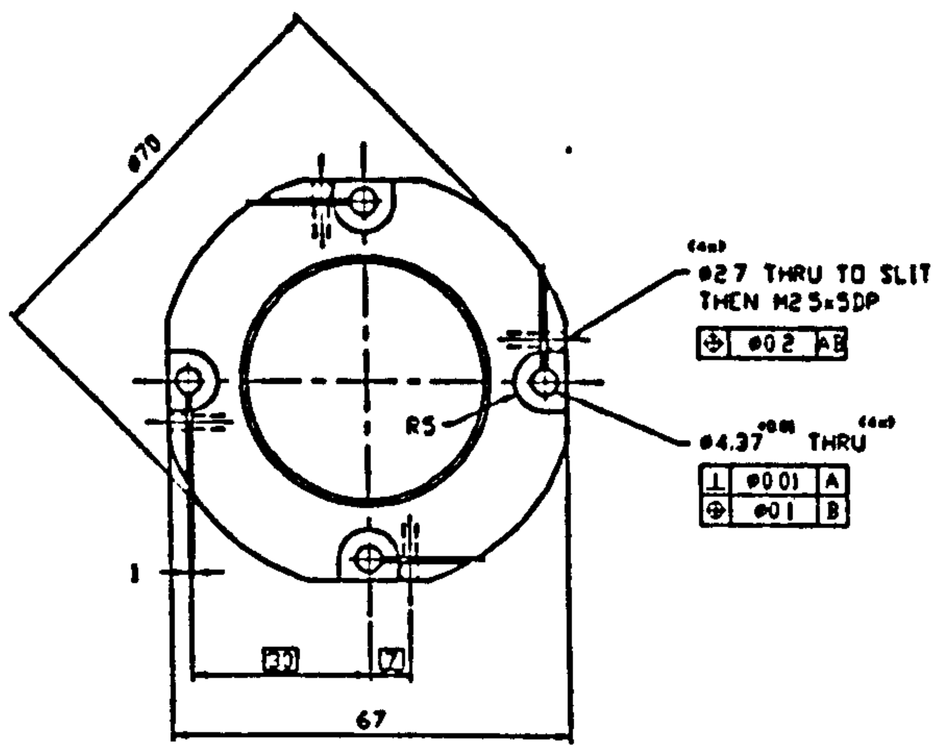

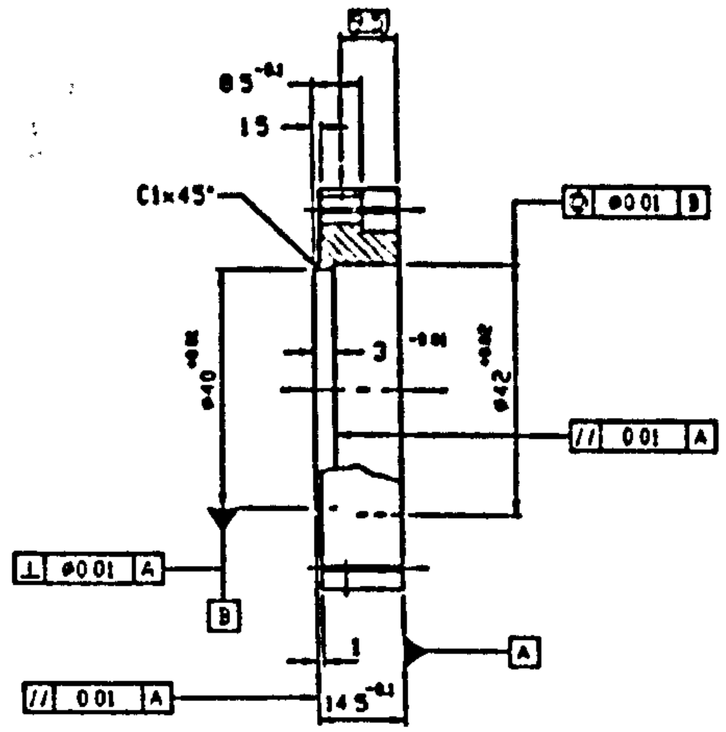

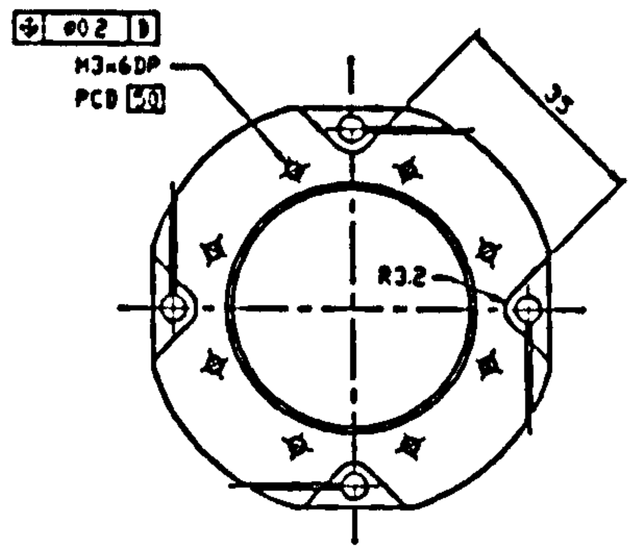

REMOVE ALL SHAPE EDGES

THIRD ANGLE PROJECTION			SHEET SIZE A2	ITEM	PART No.	DESCRIPTION	No. OFF	MATL.	SPEC.	REMARKS
GENERAL TOLERANCE ON DIMENSIONS	JOB No.	No. OF SETS REQ.	SCALE 1:1				1	SST	440C	
MACHINED				DRAWN	CHK	DATE	TITLE: BEARING HOUSING			
UNMACHINED				V.B.P.K.VAN		16/6/95				
OTHER DIMENSIONS AS STATED			FINISH	SCHOOL OF INDUSTRIAL & MANUFACTURING SCIENCE CRANFIELD			DRAWING No. MD291 C122 2A			
WELD WHERE SHOWN THUS — L —							SHT. 1 OF 1 SHEETS			
MACHINE WHERE SHOWN THUS ✓										

DRAWING No.	
ISSUE	MODIFICATION

ALL DIMENSIONS IN MILLIMETRES UNLESS OTHERWISE STATED. IF IN DOUBT ASK.

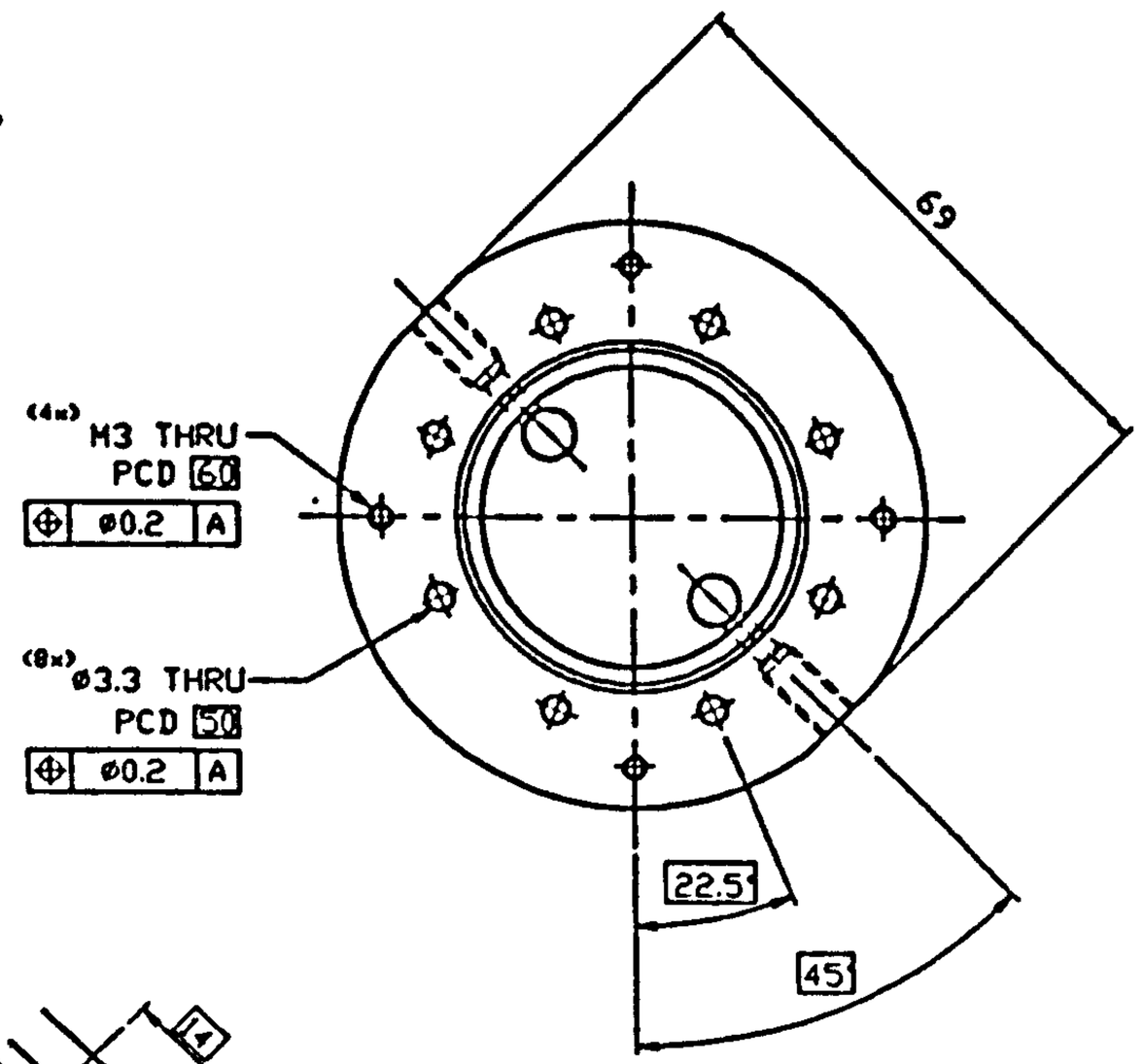

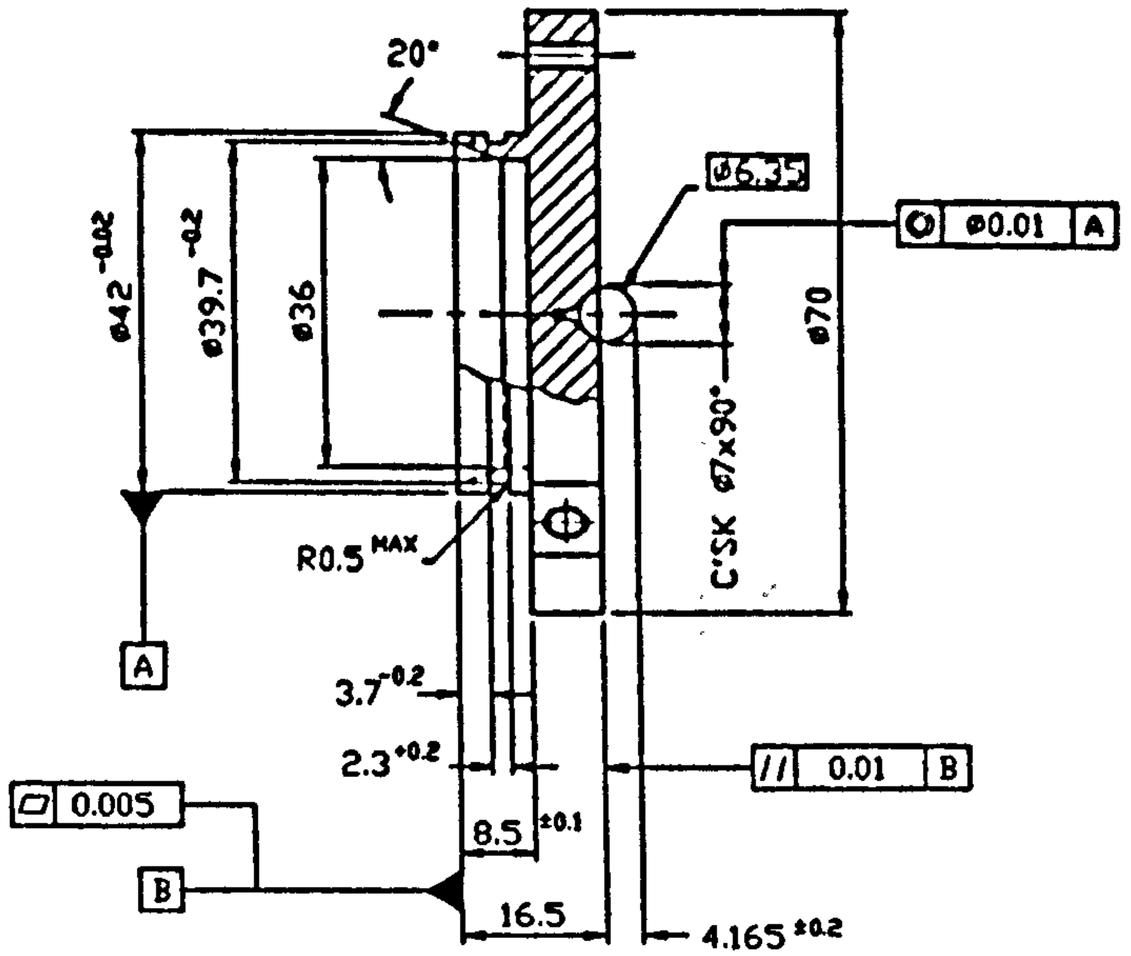

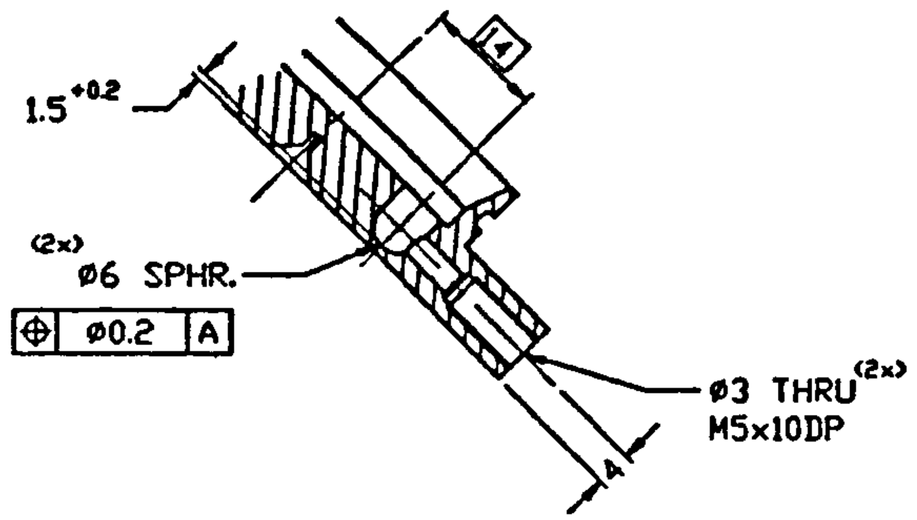

REMOVE ALL SHAPE EDGES

THIRD ANGLE PROJECTION	SHEET SIZE A3	ITEM	PART No.	DESCRIPTION	No. OFF	MATL.	SPEC.	REMARKS
					1	SST	440C	

GENERAL TOLERANCE ON DIMENSIONS	JOB No.	No. OF SETS REQ.	SCALE 1:1	DRAWN	CHK	DATE	TITLE: BEARING COVER
MACHINED				Y.B.P.KWAN		20.06.95	
UNMACHINED							
OTHER DIMENSIONS AS STATED			FINISH	SCHOOL OF INDUSTRIAL & MANUFACTURING SCIENCE			DRAWING No. MD291 C123 3A
WELD WHERE SHOWN THUS ⌒ L				CRANFIELD			SHT. 1 OF 1 SHEETS
MACHINE WHERE SHOWN THUS ⊿							

DRAWING No.	
ISSUE	MODIFICATION

ALL DIMENSIONS IN MILLIMETRES UNLESS OTHERWISE STATED. IF IN DOUBT ASK.

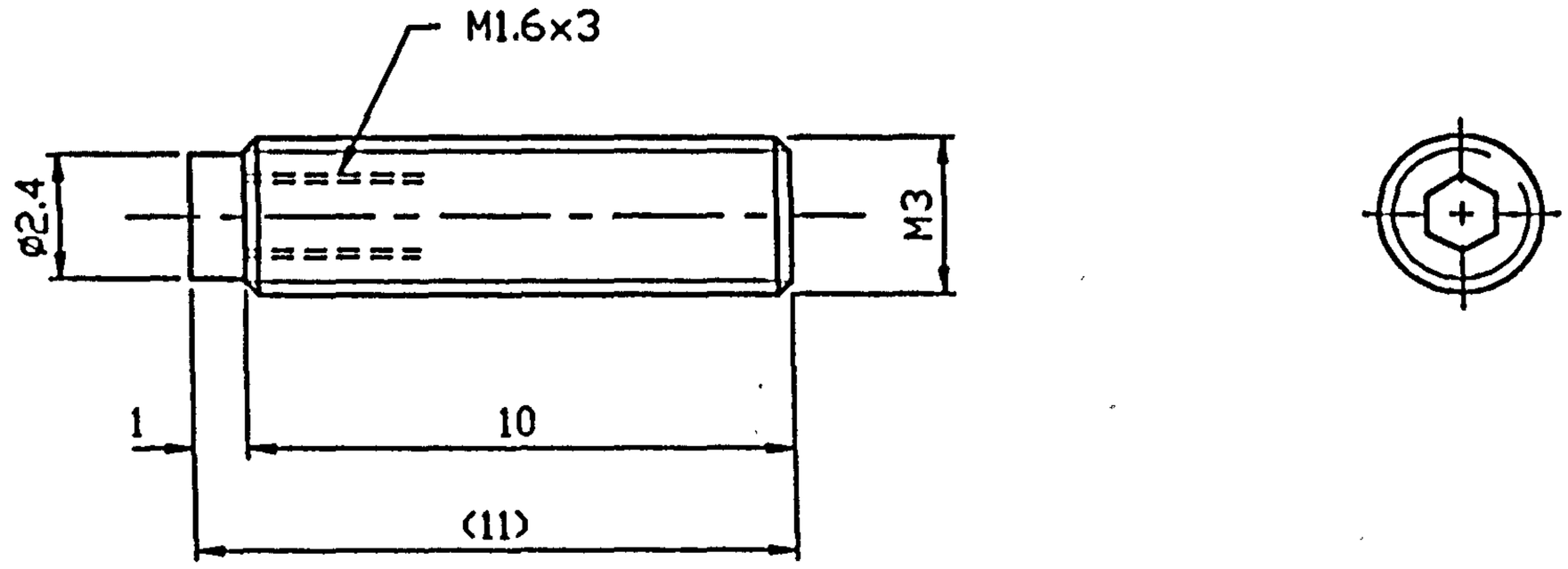

REMOVE ALL SHAPE EDGES

THIRD ANGLE PROJECTION	SHEET SIZE A4	ITEM	PART No.	DESCRIPTION	No. OFF	MATL.	SPEC.	REMARKS
					4	HTS	8.8	NYLON TIPPED

GENERAL TOLERANCE ON DIMENSIONS MACHINED UNMACHINED OTHER DIMENSIONS AS STATED WELD WHERE SHOWN THUS ⌒ L MACHINE WHERE SHOWN THUS ✓	JOB No.	No. OF SETS REQ.	SCALE 5:1	FINISH	DRAWN	CHK	DATE	TITLE: PLASTIC TIPPED SET SCREW
					Y.B.P.KWAN		03.07.95	

SCHOOL OF INDUSTRIAL & MANUFACTURING SCIENCE
CRANFIELD

DRAWING No. MD291 C124 4A

SHT. 1 OF 1 SHEETS

DRAWING NO.	
ISSUE	MODIFICATION

ALL DIMENSIONS IN MILLIMETRES UNLESS OTHERWISE STATED. · IF IN DOUBT ASK.

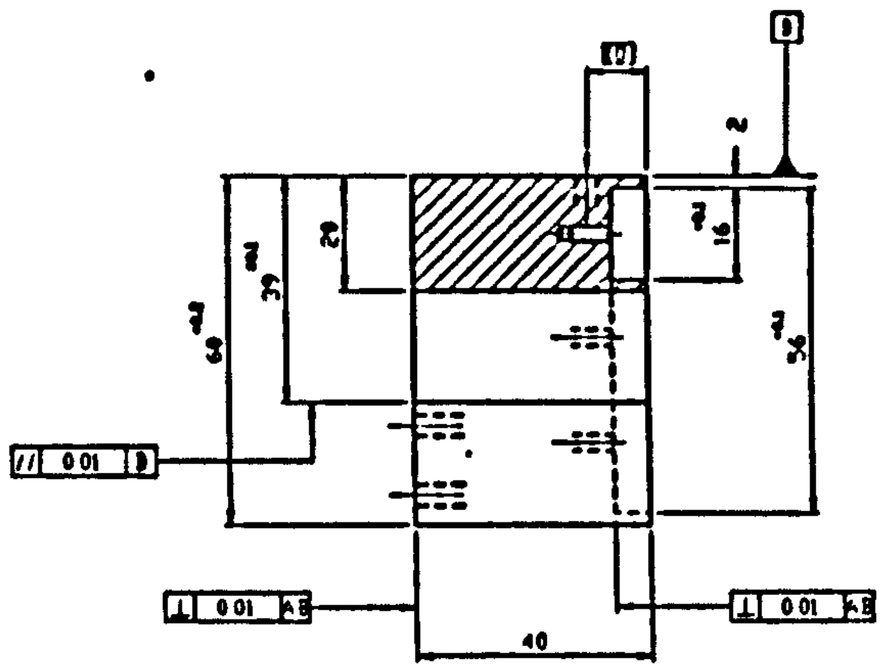

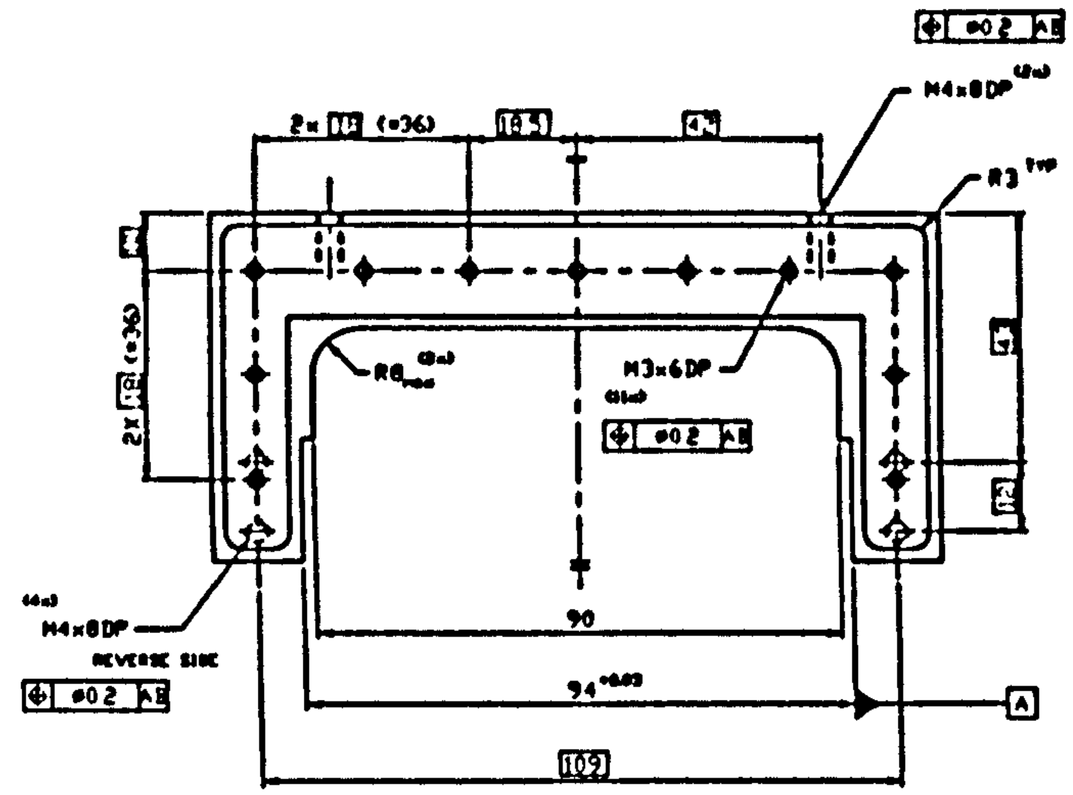

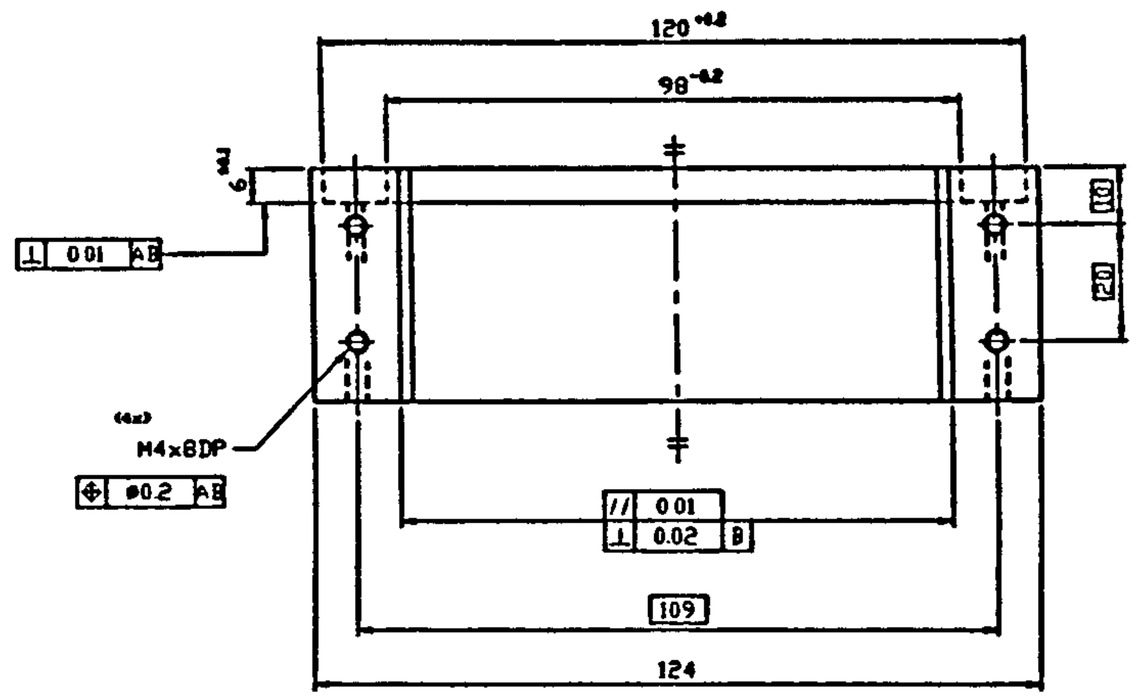

REMOVE ALL SHAPE EDGES

THIRD ANGLE PROJECTION			SHEET SIZE A2
GENERAL TOLERANCE ON DIMENSIONS	JOB No.	No. OF SETS REQ.	SCALE 1:1
MACHINED			
UNMACHINED			
OTHER DIMENSIONS AS STATED			FINISH BLACK ANODIZED
WELD WHERE SHOWN THUS ⌐			
MACHINE WHERE SHOWN THUS ✓			

ITEM	PART No.	DESCRIPTION	No. OFF	MATL.	SPEC.	REMARKS
			1	ALUM.	6061-T6	

DRAWN	CHK	DATE
Y.B.P.KWAN		07.10.95

TITLE: SLURRY RESERVOIR

SCHOOL OF INDUSTRIAL & MANUFACTURING SCIENCE
CRANFIELD

DRAWING No. MD291 D101 2A

SHT. 1 OF 1 SHEETS

DRAWING No.	
ISSUE	MODIFICATION

ALL DIMENSIONS IN MILLIMETRES UNLESS OTHERWISE STATED. IF IN DOUBT ASK.

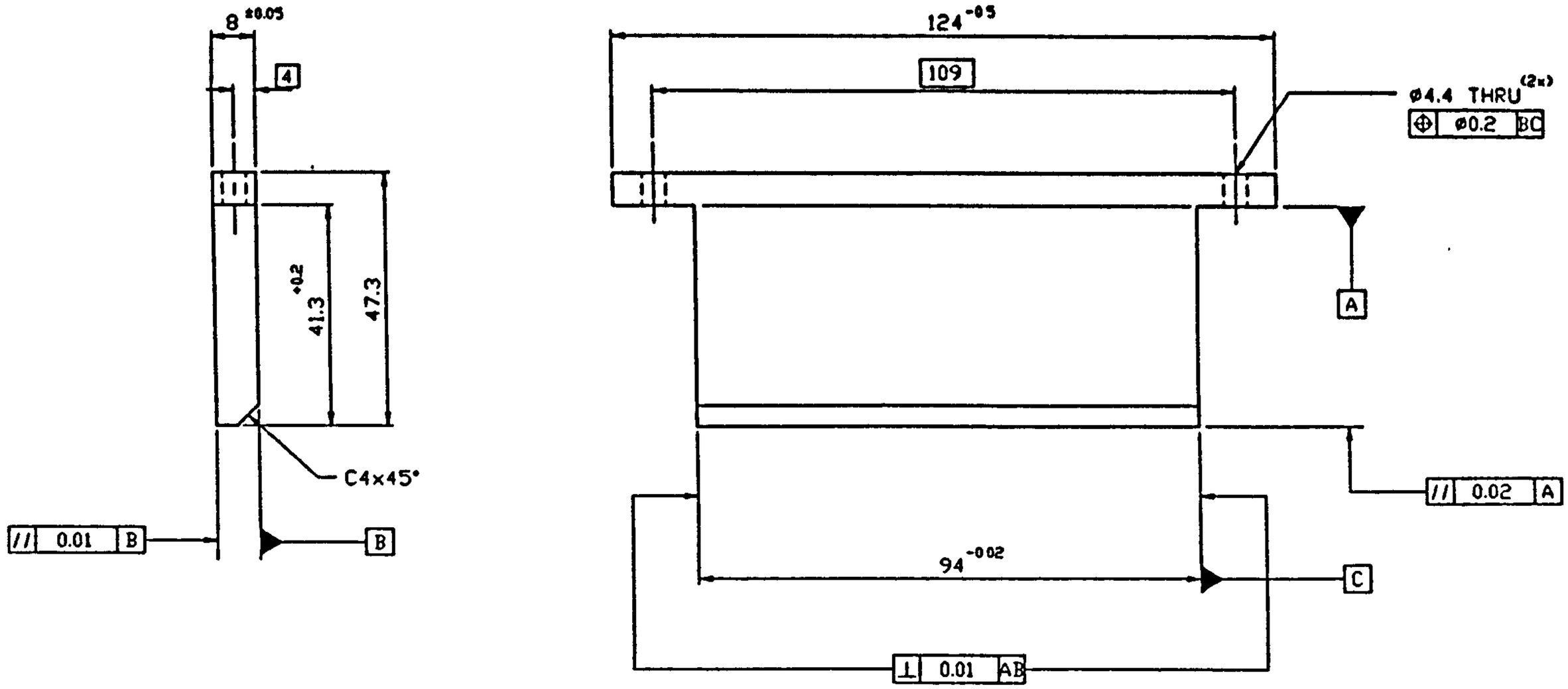

REMOVE ALL SHAPE EDGES

THIRD ANGLE PROJECTION	SHEET SIZE A3					2	GAGE PL	8mm	
		ITEM	PART No.	DESCRIPTION		No. OFF	MATL.	SPEC.	REMARKS
GENERAL TOLERANCE ON DIMENSIONS MACHINED UNMACHINED OTHER DIMENSIONS AS STATED WELD WHERE SHOWN THUS ⌒ L MACHINE WHERE SHOWN THUS ⊿	JOB No.	No. OF SETS REQ.	SCALE 1:1	DRAWN	CHK	DATE	TITLE: BLADE		
				Y.B.P.KWAN		07.10.95			
			FINISH CHEMI BLACK	SCHOOL OF INDUSTRIAL & MANUFACTURING SCIENCE CRANFIELD			DRAWING No. MD291 D102 3A		
							SHT. 1 OF 1 SHEETS		

DRAWING No.	
ISSUE	MODIFICATION

ALL DIMENSIONS IN MILLIMETRES UNLESS OTHERWISE STATED. IF IN DOUBT ASK.

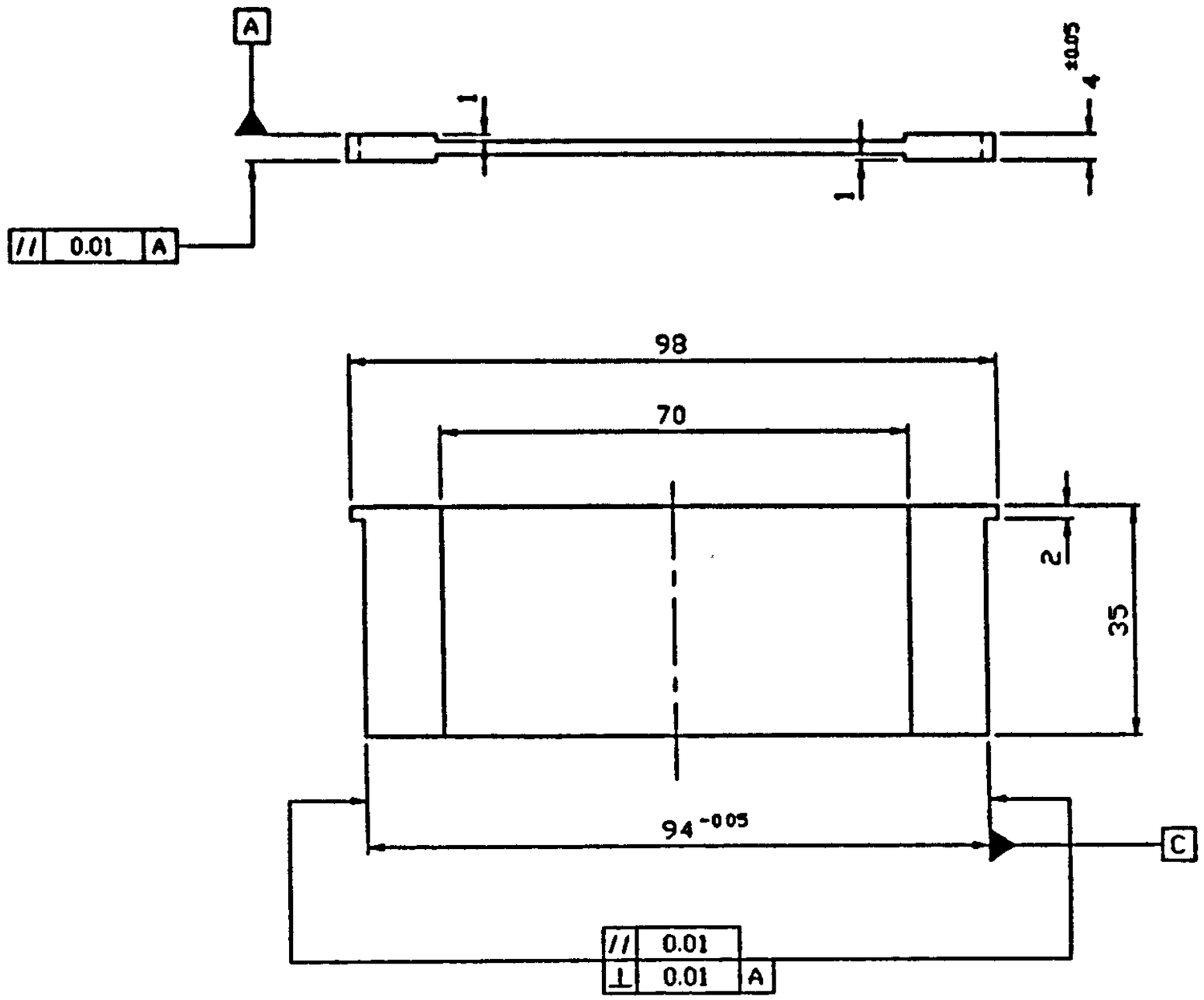

REMOVE ALL SHAPE EDGES

THIRD ANGLE PROJECTION	SHEET SIZE A3	ITEM	PART No.	DESCRIPTION	No. OFF	MATL.	SPEC.	REMARKS
					1	GAGE PL	4mm	

GENERAL TOLERANCE ON DIMENSIONS	JOB No.	No. OF SETS REQ.	SCALE 1:1	DRAWN	CHK	DATE	TITLE: STACKER PLATE
MACHINED				Y.B.P.KWAN		07.10.95	
UNMACHINED							
OTHER DIMENSIONS AS STATED			FINISH CHEMI BLACK	SCHOOL OF INDUSTRIAL & MANUFACTURING SCIENCE CRANFIELD			DRAWING No. MD291 D103 3A
WELD WHERE SHOWN THUS L							SHT. 1 OF 1 SHEETS
MACHINE WHERE SHOWN THUS ✓							

DRAWING No.	
ISSUE	MODIFICATION

ALL DIMENSIONS IN MILLIMETRES UNLESS OTHERWISE STATED. IF IN DOUBT ASK.

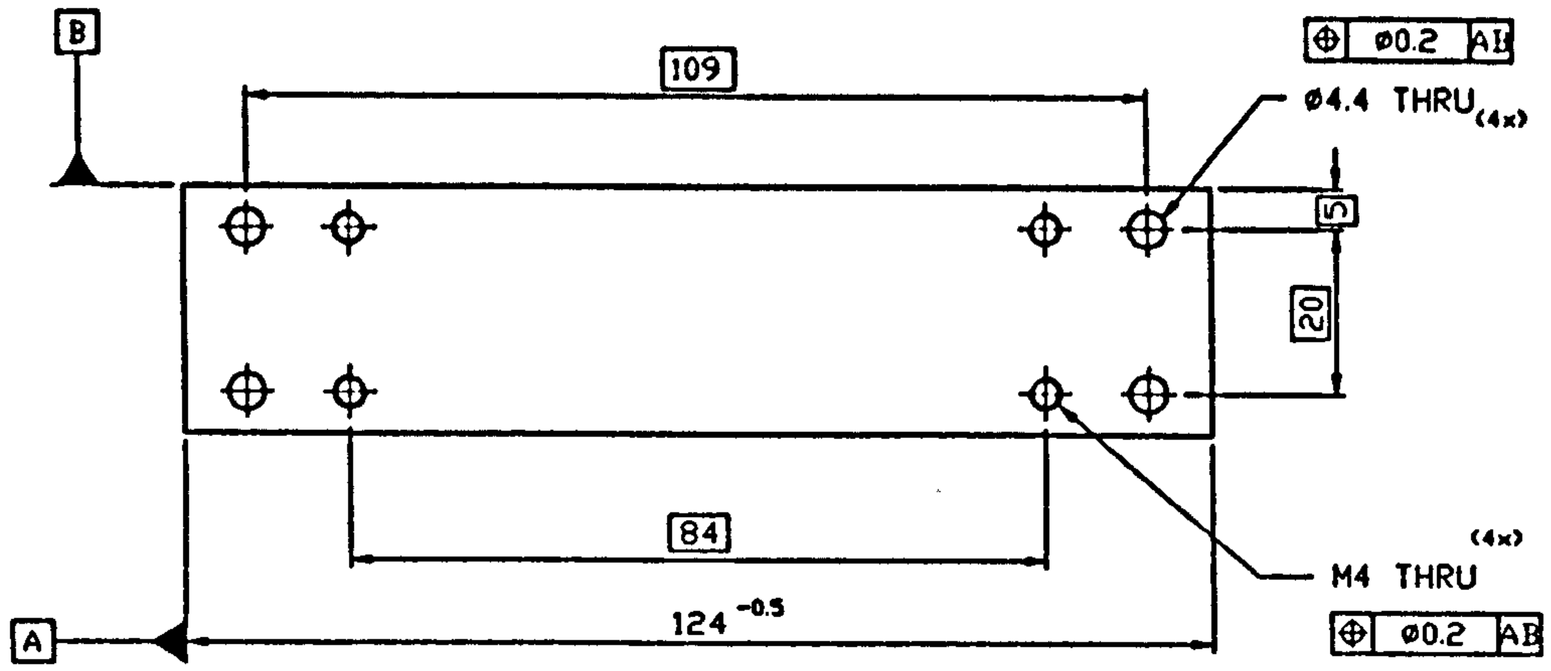

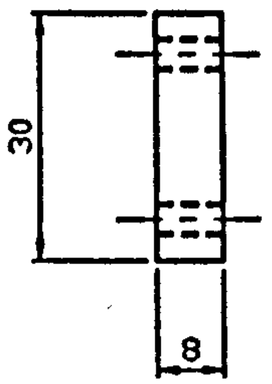

REMOVE ALL SHAPE EDGES

ITEM	PART No.	DESCRIPTION	No. OFF	MATL.	SPEC.	REMARKS
			1	ALUM.	6061-T6	

THIRD ANGLE PROJECTION

SHEET SIZE A3

GENERAL TOLERANCE ON DIMENSIONS
MACHINED
UNMACHINED
OTHER DIMENSIONS AS STATED
WELD WHERE SHOWN THUS
MACHINE WHERE SHOWN THUS

JOB No.	No. OF SETS REQ.

SCALE 1:1

FINISH BLACK ANODISED

DRAWN	CHK	DATE
Y.B.P.KWAN		07.10.95

TITLE: END PLATE

SCHOOL OF INDUSTRIAL & MANUFACTURING SCIENCE
CRANFIELD

DRAWING No. MD291 D104 3A

SHT. 1 OF 1 SHEETS

DRAWING No.	
ISSUE	MODIFICATION

ALL DIMENSIONS IN MILLIMETRES UNLESS OTHERWISE STATED. IF IN DOUBT ASK.

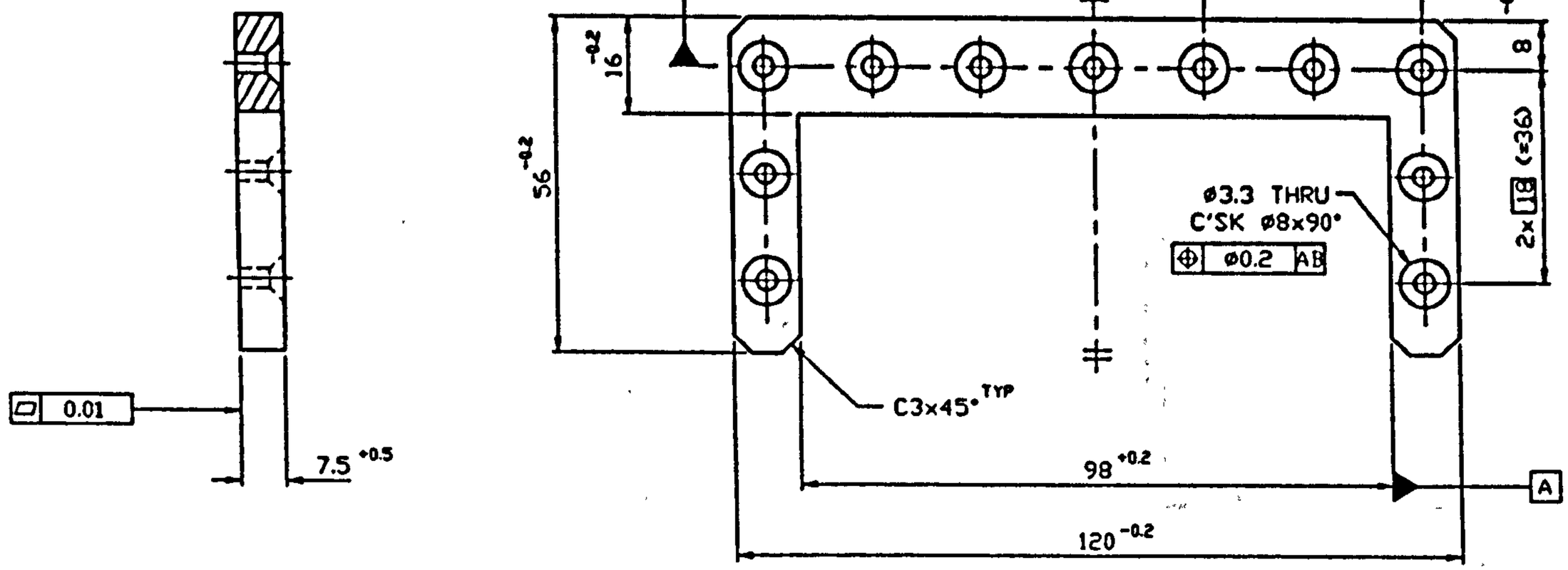

REMOVE ALL SHAPE EDGES

THIRD ANGLE PROJECTION			SHEET SIZE A3				1	PTFE		
				ITEM	PART No.	DESCRIPTION	No. OFF	MATL.	SPEC.	REMARKS
GENERAL TOLERANCE ON DIMENSIONS MACHINED UNMACHINED OTHER DIMENSIONS AS STATED WELD WHERE SHOWN THUS ⌒ L MACHINE WHERE SHOWN THUS ✓	JOB No.	No. OF SETS REQ.	SCALE 1:1	DRAWN	CHK	DATE	TITLE: SKID PAD			
				Y.B.P.KWAN		07.10.95				
			FINISH	SCHOOL OF INDUSTRIAL & MANUFACTURING SCIENCE CRANFIELD			DRAWING No. MD291 D105 3A			
							SHT. 1 OF 1 SHEETS			

DRAWING No.	
ISSUE	MODIFICATION

ALL DIMENSIONS IN MILLIMETRES UNLESS OTHERWISE STATED. IF IN DOUBT ASK.

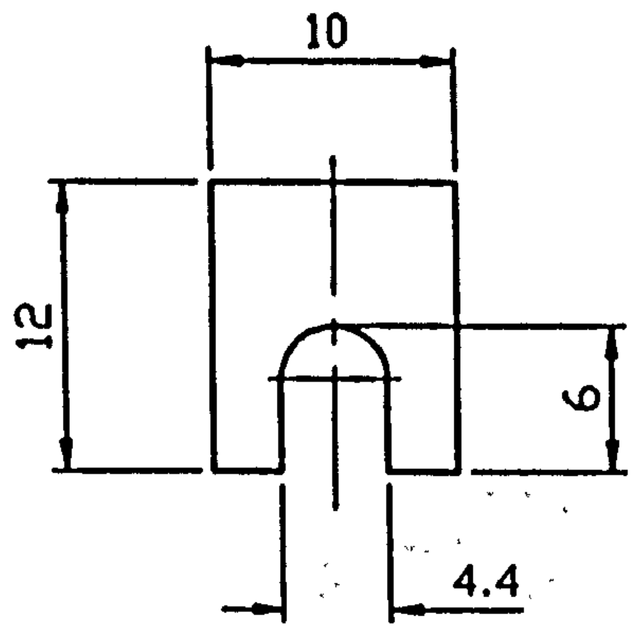

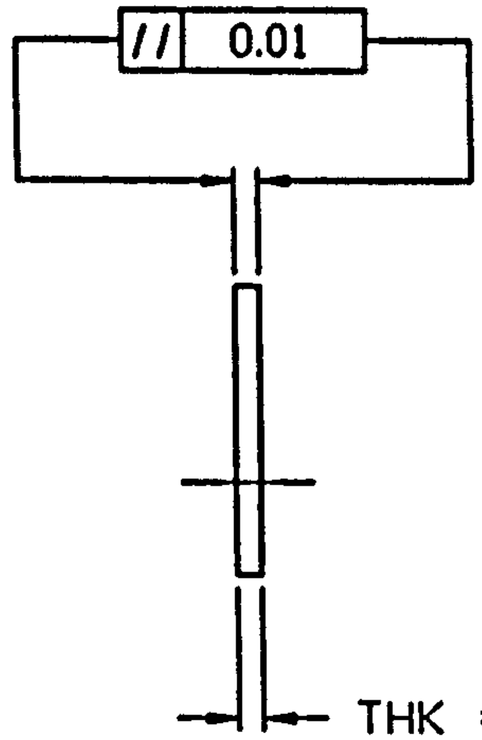

THK = 0.1,0.2,0.5,1,1.5,2 ±0.01

DEVIATION BTW PAIR <= 0.01

REMOVE ALL SHAPE EDGES

THIRD ANGLE PROJECTION	SHEET SIZE A4	ITEM	PART No.	DESCRIPTION	No. OFF	MATL.	SPEC.	REMARKS
					2 EACH	SST	304	

GENERAL TOLERANCE ON DIMENSIONS	JOB No.	No. OF SETS REQ.	SCALE 2:1	DRAWN	CHK	DATE	TITLE: PACKER
MACHINED				Y.B.P.KVAN		07.10.95	
UNMACHINED							
OTHER DIMENSIONS AS STATED			FINISH	SCHOOL OF INDUSTRIAL & MANUFACTURING SCIENCE			DRAWING No. MD291 D106 4A
VELD WHERE SHOWN THUS ⌒				CRANFIELD			SHT. 1 OF 1 SHEETS
MACHINE WHERE SHOWN THUS √							

THIRD ANGLE PROJECTION

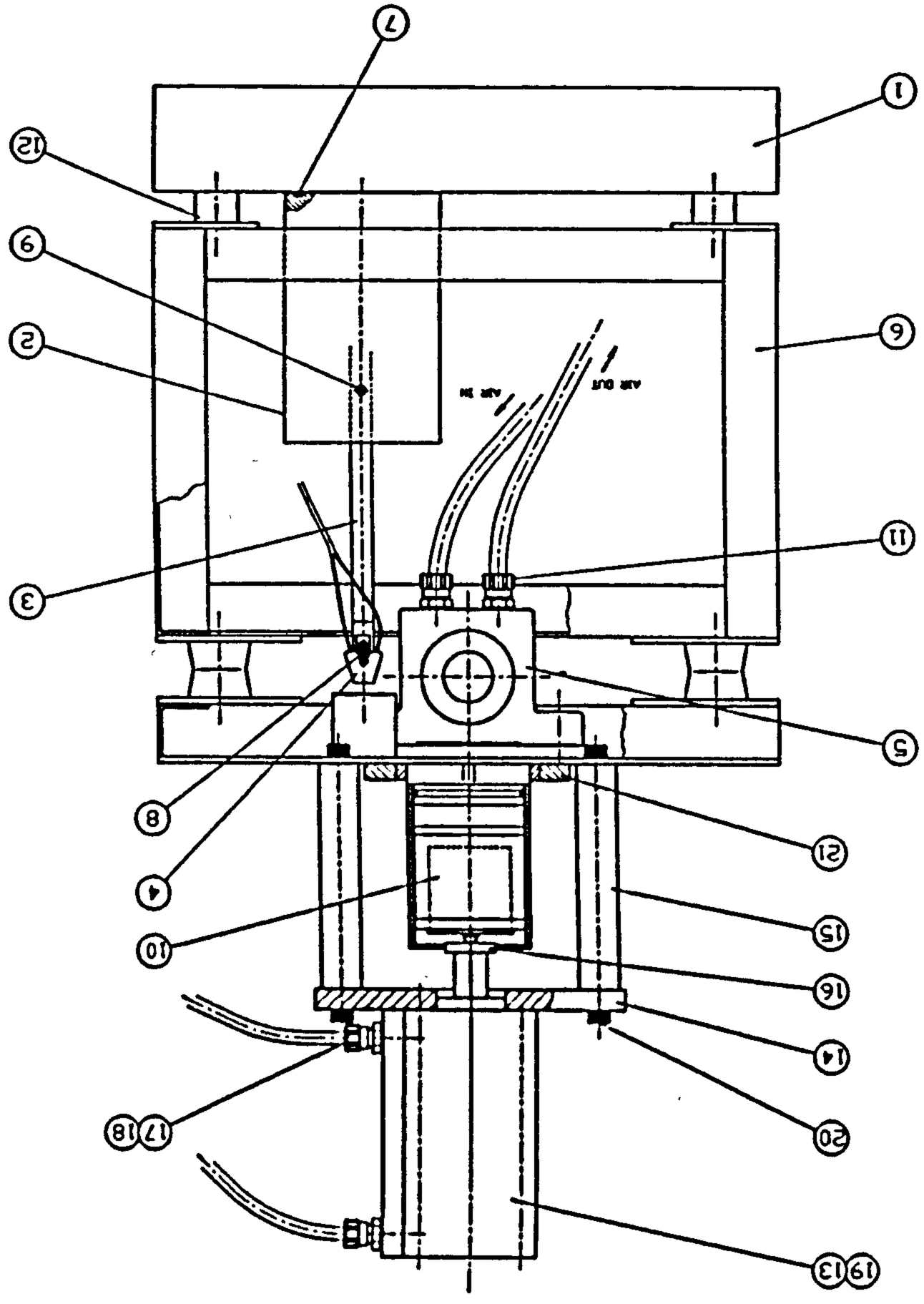

ALL DIMENSIONS IN MILLIMETRES UNLESS OTHERWISE STATED. IF IN DOUBT ASK.

ALL DIMENSIONS IN MILLIMETRES UNLESS OTHERWISE STATED IF IN DOUBT ASK

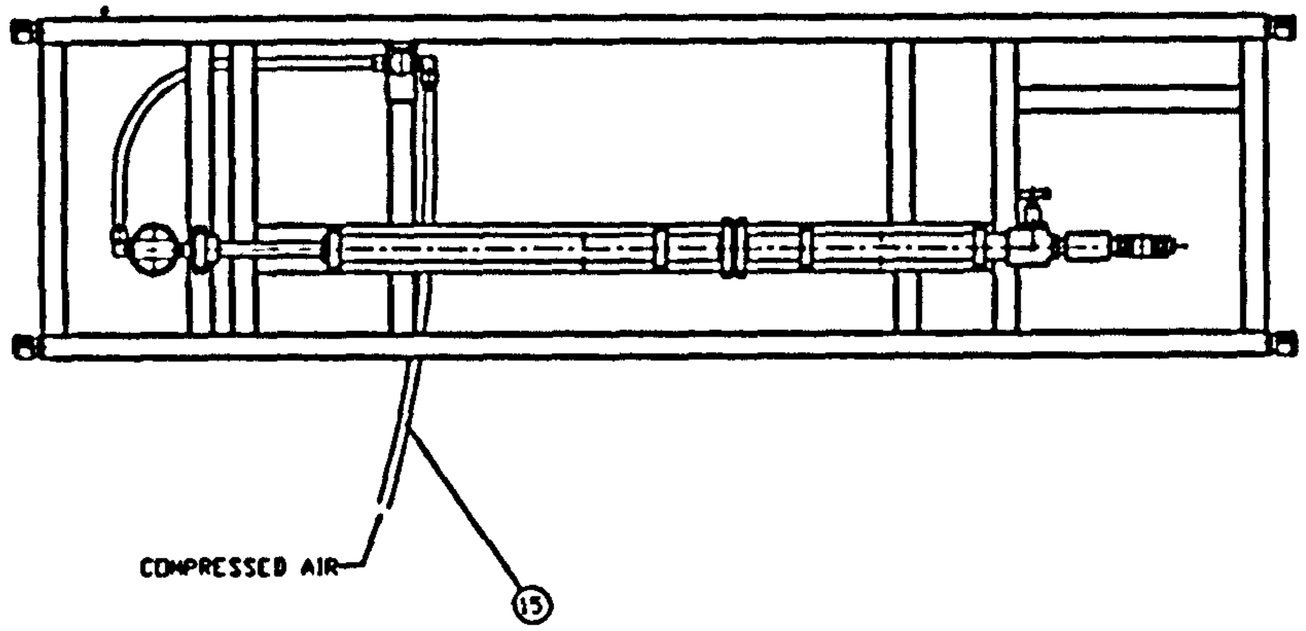

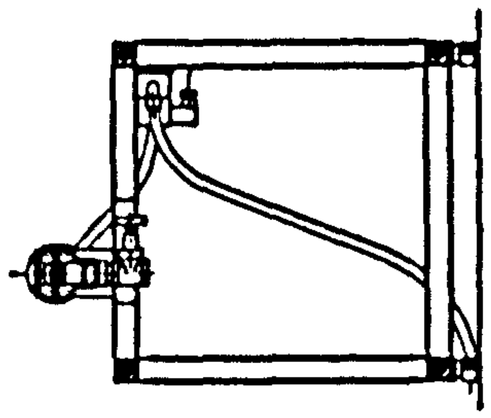

NOTE :
ELECTRICAL DETAILS SEE DRG EXP/01 ISSUE
PNEUMATICS DETAILS SEE DRG HP/01 ISSUE

15						
14						
13						
12						
11						
10						
9						
8						
7						
6						
5						
4						
3						
2						
1						
NO.						

THIRD ANGLE PROJECTION

SHEET SIZE A0

SCALE 1:5

TITLE PERMEABILITY MEASUREMENT RIG

CRANFIELD

ABOVE ALL SHAPE EDGES

ALL DIMENSIONS IN MILLIMETRES UNLESS OTHERWISE STATED. IF IN DOUBT ASK.

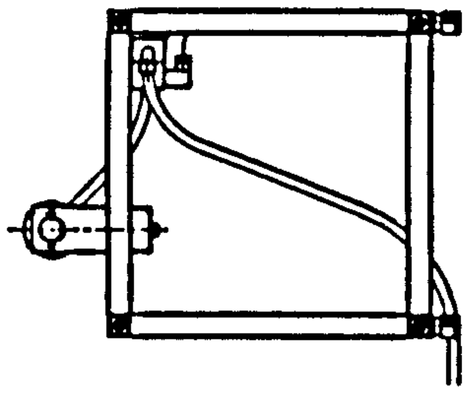

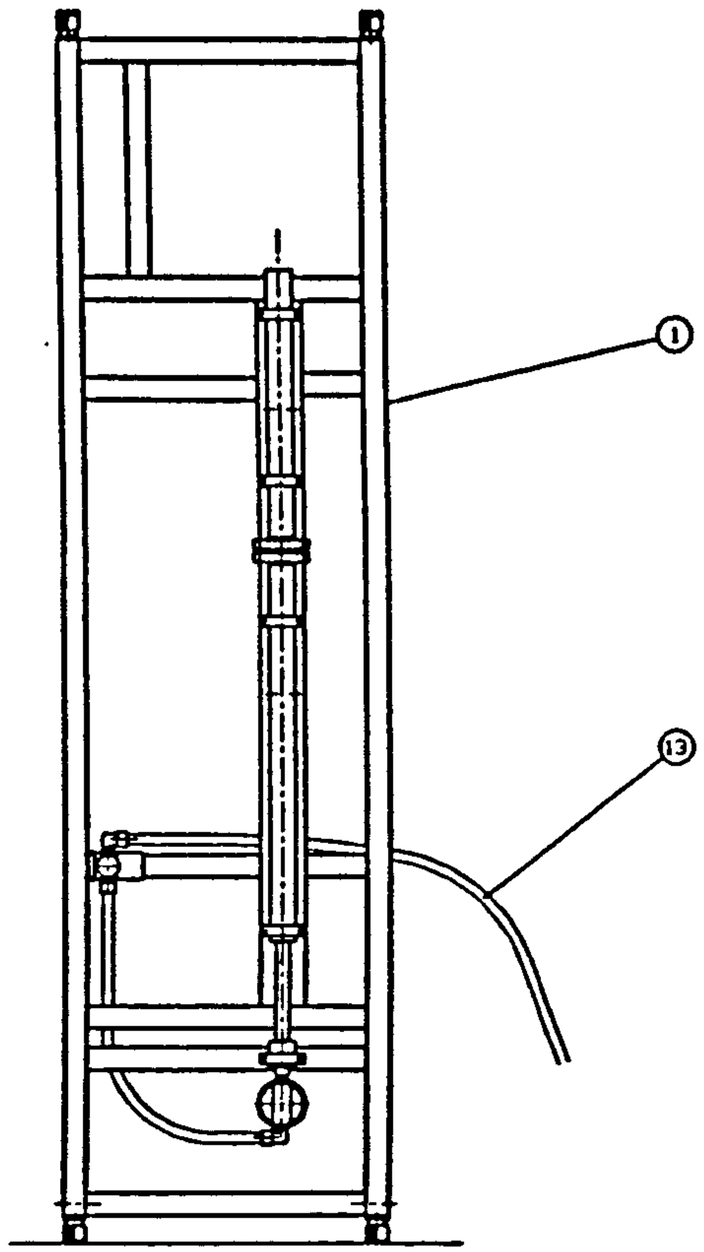

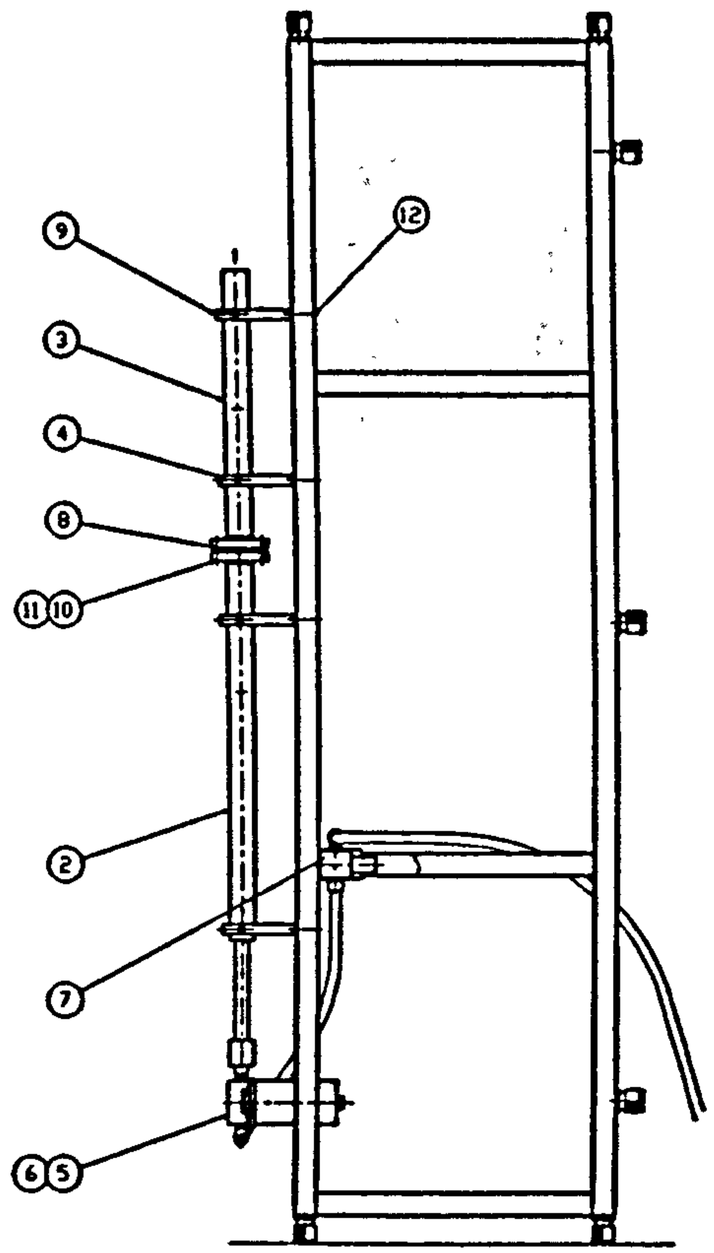

NOTE :
ELECTRICAL DETAILS SEE DWG
PNEUMATICS DETAILS SEE DWG

ITEM	PART NO	DESCRIPTION	QTY	MATERIAL	FINISH	REMARKS
13						
12						
11						
10						
9						
8						
7						
6						
5						
4						
3						
2						
1						

THIRD ANGLE PROJECTION

SIZE A0

SCALE 1:5

TITLE: BUBBLE TEST RIG

SCHOOL OF MECHANICAL & MANUFACTURING ENGINEERING
CRANFIELD

DRAWING NO.

SHEET 1 OF 1 SHEETS

BREAK ALL SHARP EDGES

ALL DIMENSIONS IN MILLIMETRES UNLESS OTHERWISE STATED IF IN DOUBT ASK

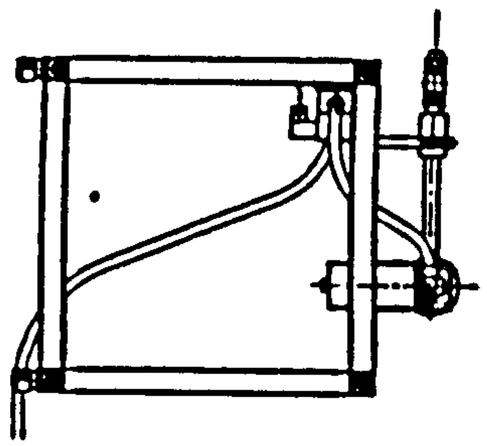

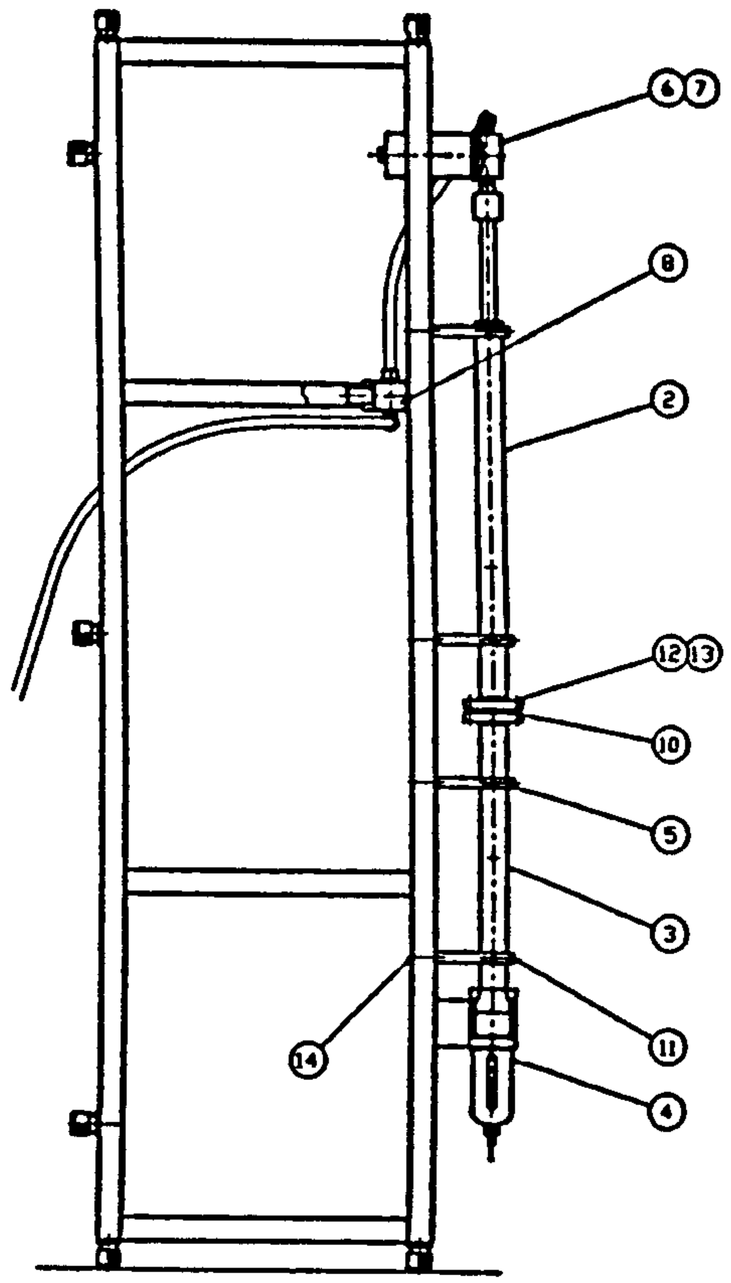

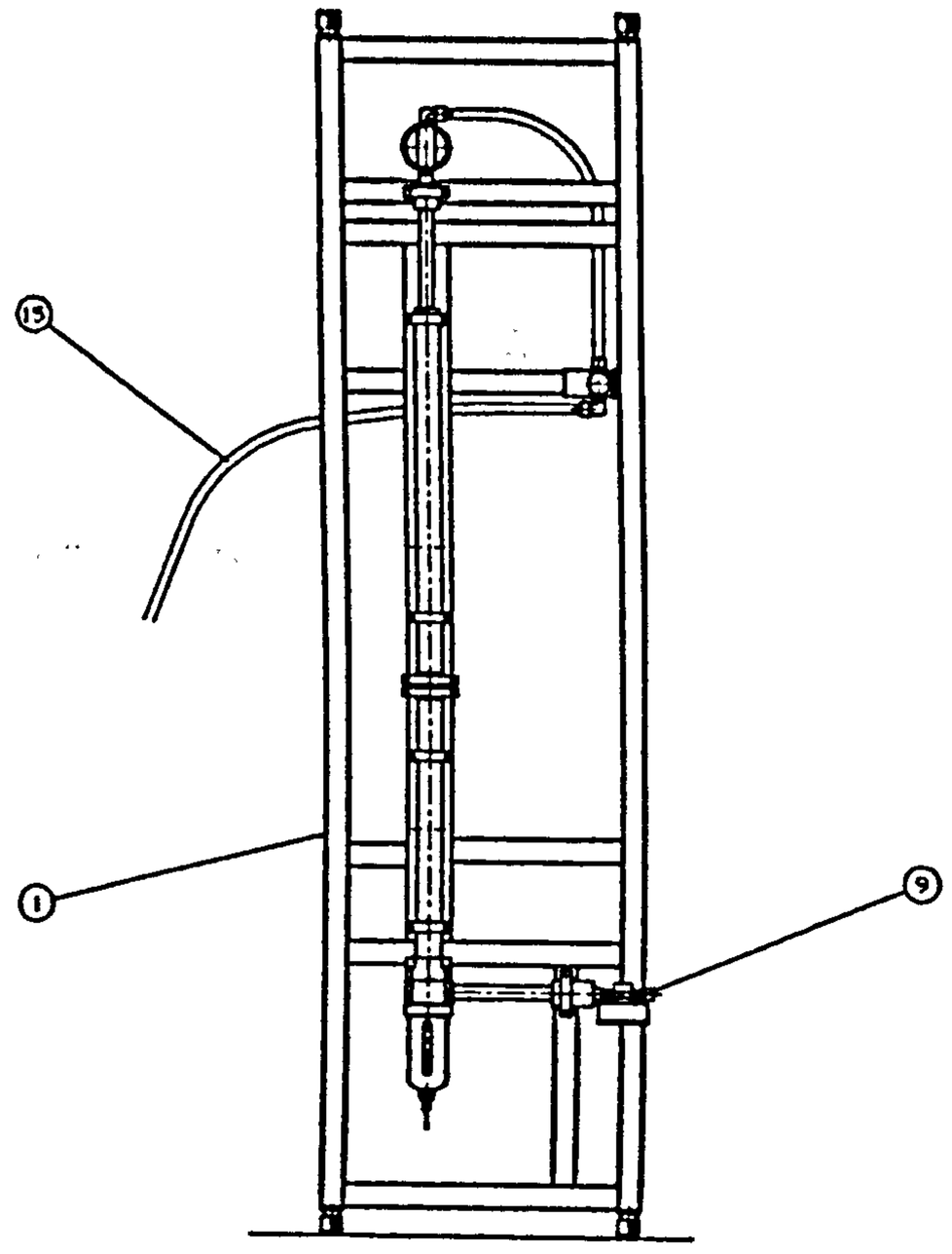

NOTE :
ELECTRICAL DETAILS SEE DWG
PNEUMATICS DETAILS SEE DWG

15		UPVC 90 PVC HOSE	2m	DIA PVC		
14	6MM NUT	STAINLESS FASTENING SET	10	SS		STEEL
13		WASHER SHEET METAL	1	STEEL	6.5	WITH WASHER 6 X 18 DIA
12		SHEET CAP HEAD BOLT	4	STEEL	6.5	WITH FLAT WASHER
11		SHEET CAP HEAD BOLT	10	STEEL	6.5	WITH FLAT WASHER
10		SPACERS WITH HOLES	1	ALUMINIUM		HOLES TO FIT WITH BOLTS
9		PNEUMATIC PLATFORM	1			MOUNTING
8	10MM DIA	PNEUMATIC CYLINDER	1			SMC PNEUMATICS
7	8MM DIA	AIR FILTER REGULATOR	1	PLASTIC		FILE
6	8MM DIA	SOLENOID AIR FILTER VALVE	1			FILE
5	10MM DIA	PIVOT SHAFT	1	PVC		
4	10MM DIA	SPRING RETURN CYLINDER	1			
3	10MM DIA	BALLAST TUBE ASSEMBLY	1			
2	10MM DIA	INLET TUBE ASSEMBLY	1			
1	10MM DIA	FRAME ASSEMBLY	1			
ITEM	10MM DIA	DESCRIPTION	QTY REQ'D	MATL	SPEC	REMARKS

THIRD ANGLE PROJECTION

SHEET SIZE	A0	
SCALE	1:5	
FINISH		

TITLE: WATER REPULSION TEST RIG

SCHOOL OF INDUSTRIAL & MANUFACTURING SCIENCE
CRANFIELD

REMOVE ALL SHARP EDGES

ALL DIMENSIONS IN MILLIMETRES UNLESS OTHERWISE STATED. IF IN DOUBT ASK.

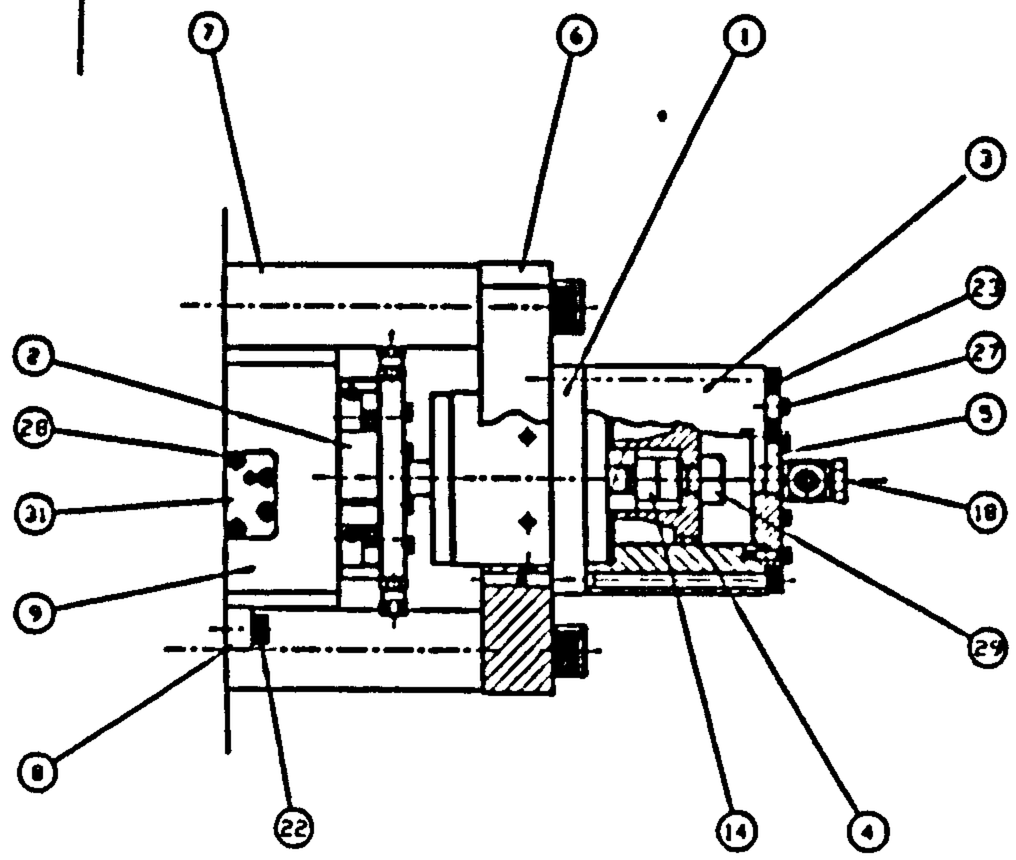

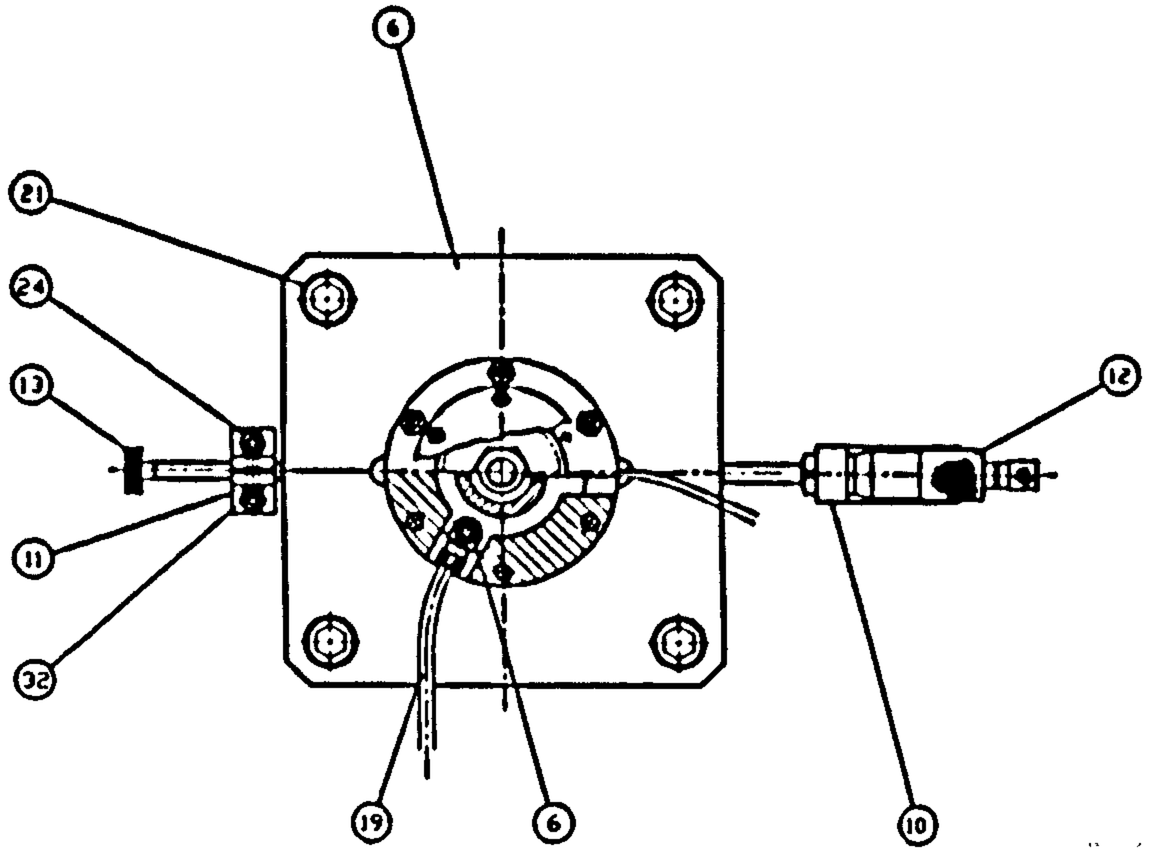

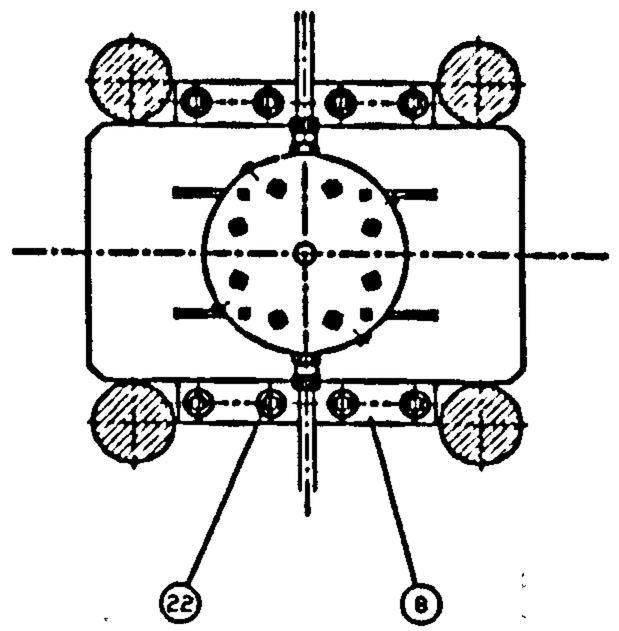

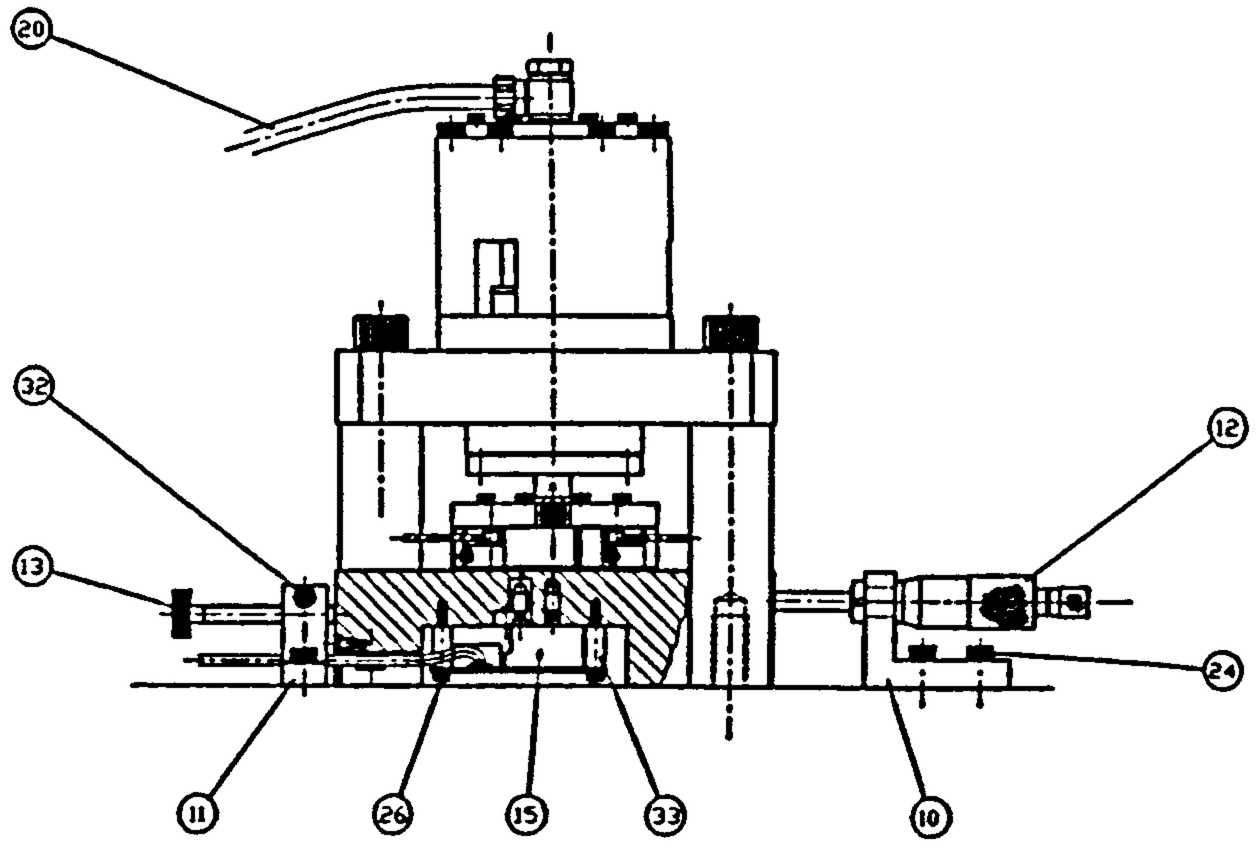

36		STANDOFF HEXAGONAL	3	BRASS		FARNELL 544-264
35		SCREW CAP HEXAGONAL	1	STEEL	A2	
34	METRIC CHECK	CHECK	1	BRASS		
33		PHILIP LYY	1	NYLON		FARNELL 624-697
32		HEX NUT M6	1	STEEL	A2	
31		SCREW CSK HEXAGONAL	4	STEEL	A2	
30		SCREW CAP HEXAGONAL	4	STEEL	A2	
29		SCREW CAP HEXAGONAL	2	STEEL	A2	
28		SCREW CAP HEXAGONAL	1	STEEL	A2	
27		SCREW CAP HEXAGONAL	4	STEEL	A2	
26		SCREW CAP HEXAGONAL	4	STEEL	A2	
25		SCREW CAP HEXAGONAL	3	STEEL	A2	
24		SCREW CAP HEXAGONAL	3	STEEL	A2	
23		PNEUMATIC HOSE LEAD	2m	PU		FESTO PUN
22		PNEUMATIC HOSE LEAD	2m	PU		FESTO PUN
21		PNEUMATIC FITTING	1	BRASS		FESTO LCH-1/8-PK6
20		PNEUMATIC FITTING	1	BRASS		FESTO LCH-1/8-PK4
19		O-RING SEALING	2	RUBBER	AS568-A	
18	METRIC CHECK	PRESSURE SENSOR 0-5 BAR	1			SENSORTECHNICS
17		LOAD CELL 4m T/C	1			OMEGA LCA-TC4-100
16		ADJUSTING SCREW	1	SST	M4	M4
15		25mm MICROMETER	1			STARRETT 263-025
14	METRIC CHECK	ADJUSTING SCREW HEAD	1	BRASS	M20x1.5G	
13	METRIC CHECK	MICROMETER HOUSE	1	BRASS	M20x1.5G	
12	METRIC CHECK	REFERENCE PLANE	1	SST	M4	
11	METRIC CHECK	END RAIL	4	BRASS		
10	METRIC CHECK	PILLAR	4	AL		
9	METRIC CHECK	TOP PLANE	1	AL		
8	METRIC CHECK	CYLINDER CAP	1	BRASS	M30x1.5G	
7	METRIC CHECK	PISTON	1	BRASS	M30x1.5G	
6	METRIC CHECK	CYLINDER SLEEVE	1	BRASS	M30x1.5G	
5	METRIC CHECK	FEMALE THRUST BEARING	1			
4	METRIC CHECK	SLAP RACE OF BEARING	1			
Item	Part No.	DESCRIPTION	No. OFF	MAT'L	SPEC.	REMARKS

THIRD ANGLE PROJECTION

SHEET SIZE A0

SCALE 1:1

TITLE: AEROSTATIC THRUST BEARING RIG

DRAWN | CHK'D | DATE | APPD | DATE

SCHOOL OF INDUSTRIAL & MANUFACTURING SCIENCE

CRANFIELD

DRAWING No. METRIC CHART No.

REMOVE ALL SHARP EDGES

DRAWING No.

ISSUE	MODIFICATION

ALL DIMENSIONS IN MILLIMETRES UNLESS OTHERWISE STATED. IF IN DOUBT ASK.

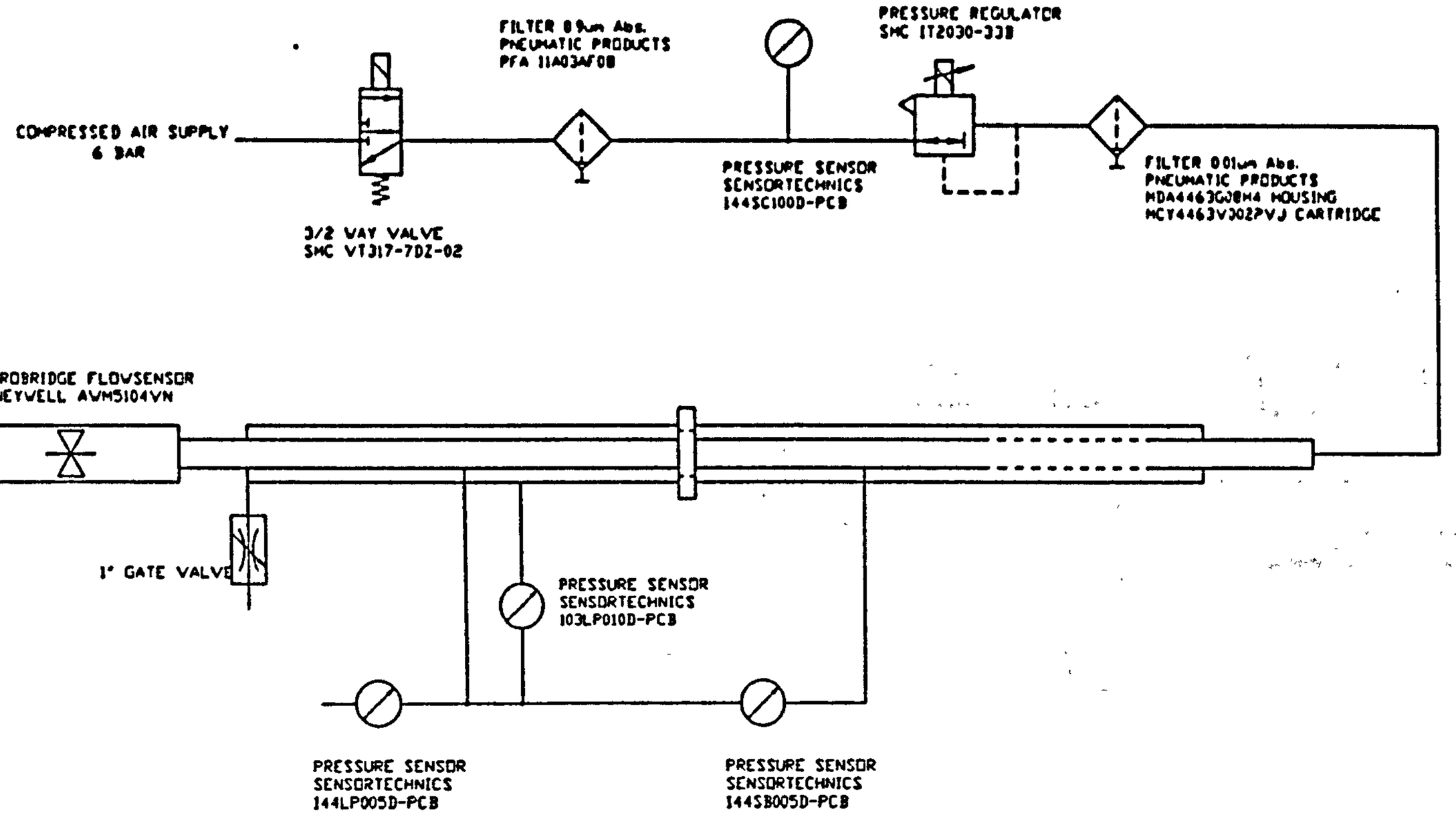

REMOVE ALL SHAPE EDGES

ITEM	PART No.	DESCRIPTION	No. OFF	MATL.	SPEC.	REMARKS

THIRD ANGLE PROJECTION

SHEET SIZE A3

GENERAL TOLERANCE ON DIMENSIONS	JOB No.	No. OF SETS REQ.
MACHINED		
UNMACHINED		
OTHER DIMENSIONS AS STATED		
WELD WHERE SHOWN THUS ⌒		
MACHINE WHERE SHOWN THUS ✓		

SCALE 1:1

FINISH

DRAWN	CHK	DATE
Y.B.P.KWAN		27.06.95

TITLE: PERMEABILITY RIG PNUEMATIC CIRCUIT DIAGRAM

SCHOOL OF INDUSTRIAL & MANUFACTURING SCIENCE

CRANFIELD

DRAWING No. MP291 B101 3A

SHT. 1 OF 1 SHEETS

DRAWING No.	
ISSUE	MODIFICATION

ALL DIMENSIONS IN MILLIMETRES UNLESS OTHERWISE STATED. IF IN DOUBT ASK.

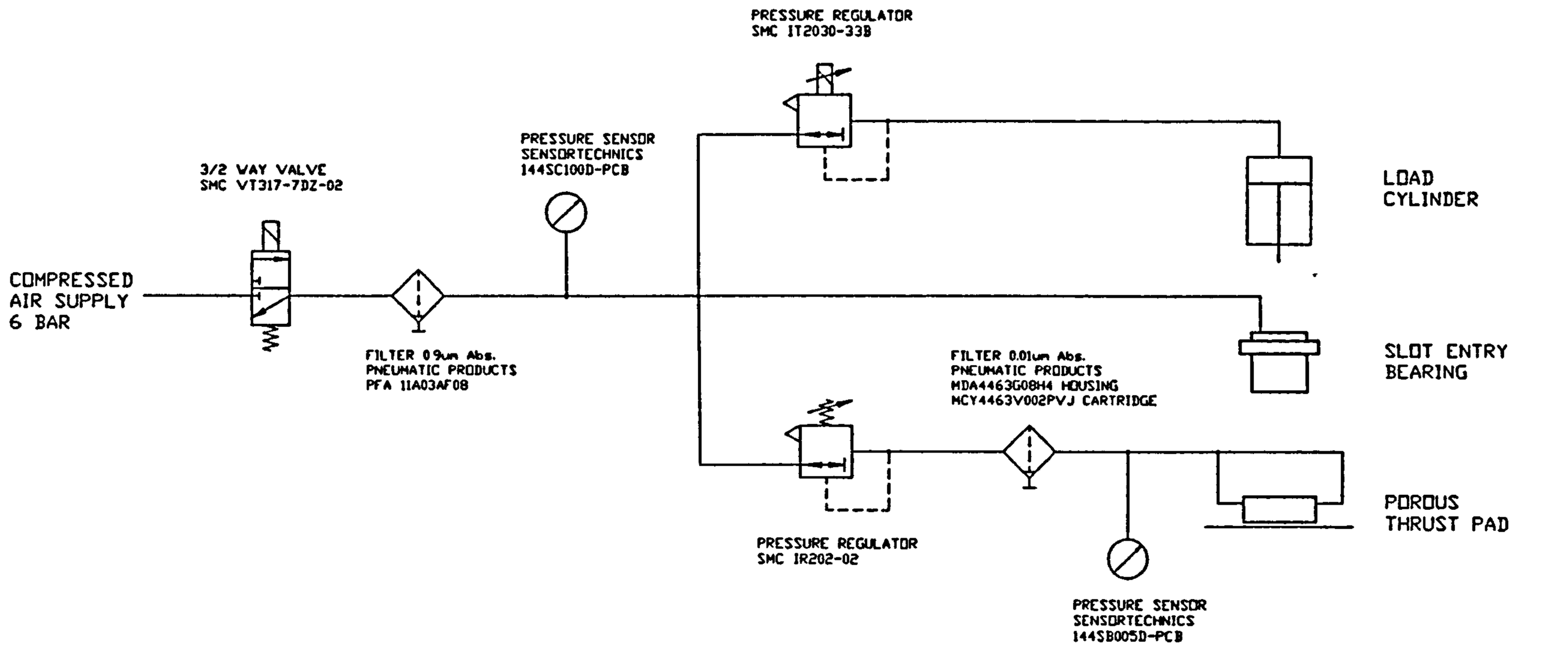

REMOVE ALL SHAPE EDGES

THIRD ANGLE PROJECTION			SHEET SIZE A3	ITEM	PART No.	DESCRIPTION	No. OFF	MATL.	SPEC.	REMARKS
GENERAL TOLERANCE ON DIMENSIONS	JOB No.	No. OF SETS REQ.	SCALE 1:1	DRAWN	CHK	DATE	TITLE: AEROSTATIC THRUST BEARING RIG PNEUMATIC CIRCUIT DIAGRAM			
MACHINED				Y.B.P.KWAN		27.06.95				
UNMACHINED										
OTHER DIMENSIONS AS STATED			FINISH	SCHOOL OF INDUSTRIAL & MANUFACTURING SCIENCE			DRAWING No. MP291 C101 3A			
WELD WHERE SHOWN THUS				CRANFIELD			SHT. 1 OF 1 SHEETS			
MACHINE WHERE SHOWN THUS										

DRAWING No.

ISSUE	MODIFICATION

ALL DIMENSIONS IN MILLIMETRES UNLESS OTHERWISE STATED. · IF IN DOUBT ASK.

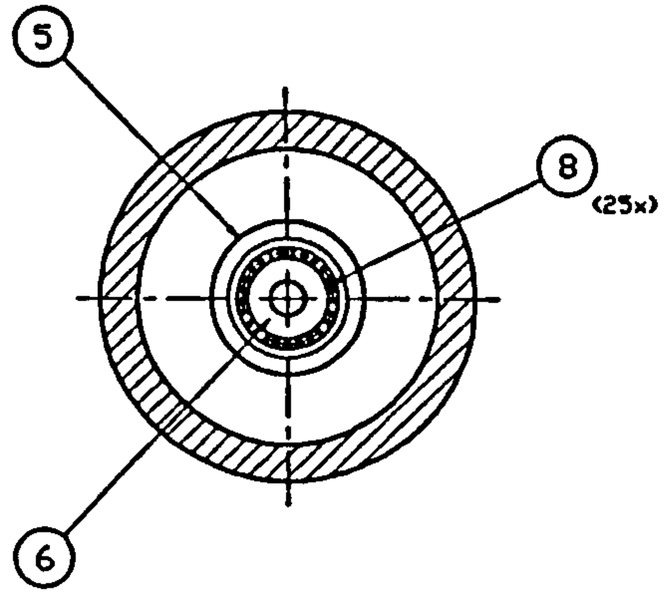

SECTION A-A

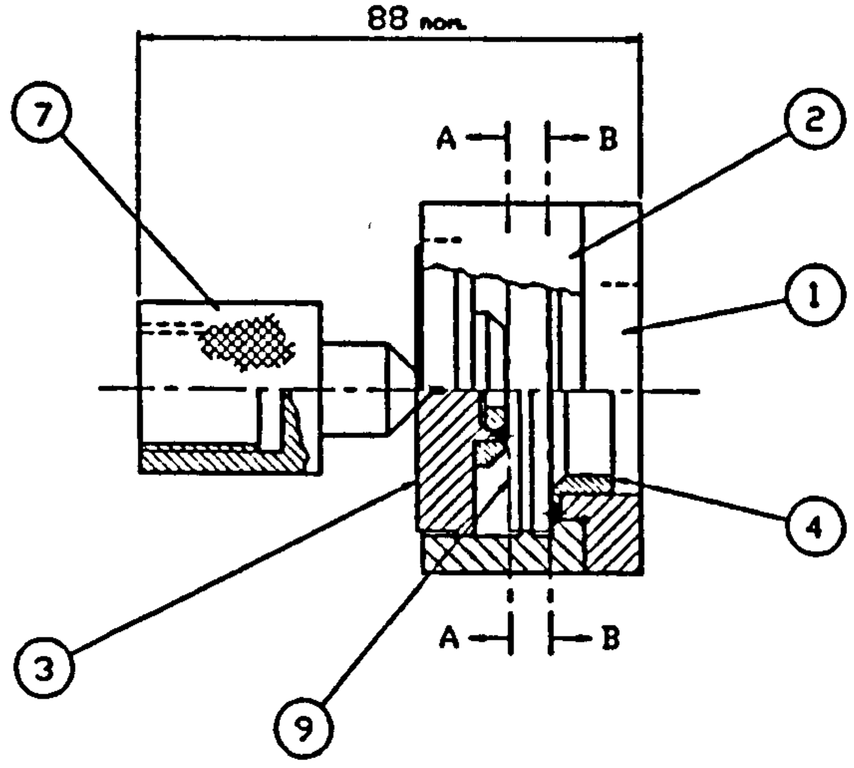

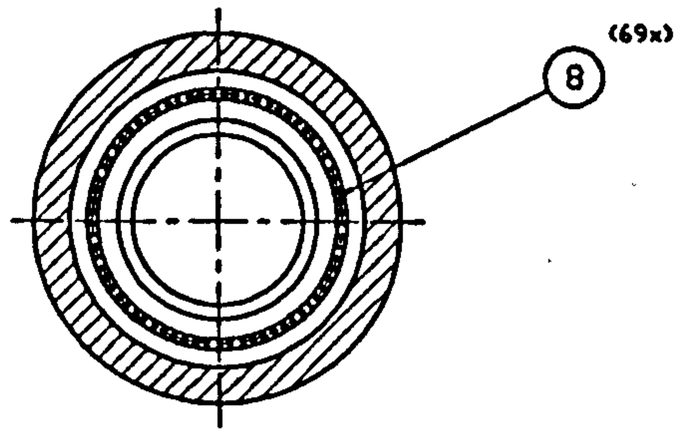

SECTION B-B

ITEM	PART No.	DESCRIPTION	No. OFF	MATL.	SPEC.	REMARKS
9		SPECIMEN	1	ALUMINA		POROUS
8		BEARING BALLS #2	94	SST	440C	HRc 60-62
7	MD291 A207	CENTRE	1	SST	440C	HRc 55-60
6	MD291 A206	GUIDE RING III	1	M.S.		
5	MD291 A205	GUIDE RING II	1	M.S.		
4	MD291 A204	GUIDE RING I	1	M.S.		
3	MD291 A203	TOP PLATE	1	SST	440C	HRc 55-60
2	MD291 A202	SLEEVE	1	M.S.		
1	MD291 A201	BASE	1	SST	440C	HRc 55-60

THIRD ANGLE PROJECTION

SHEET SIZE A2

GENERAL TOLERANCE ON DIMENSIONS
MACHINED
UNMACHINED
OTHER DIMENSIONS AS STATED
WELD WHERE SHOWN THUS ⌒ L
MACHINE WHERE SHOWN THUS ✓

JOB No.	No. OF SETS REQ.

SCALE 1:1

FINISH

DRAWN	CHK	DATE
Y.B.P.KWAN		20.05.95

TITLE: FRACTURE TEST RING ASSEMBLY

SCHOOL OF INDUSTRIAL & MANUFACTURING SCIENCE
CRANFIELD

DRAWING No. MU291 A200 2A

SHT. OF SHEETS

REMOVE ALL SHAPE EDGES

ISSUE	MODIFICATION

ALL DIMENSIONS IN MILLIMETRES UNLESS OTHERWISE STATED. IF IN DOUBT ASK.

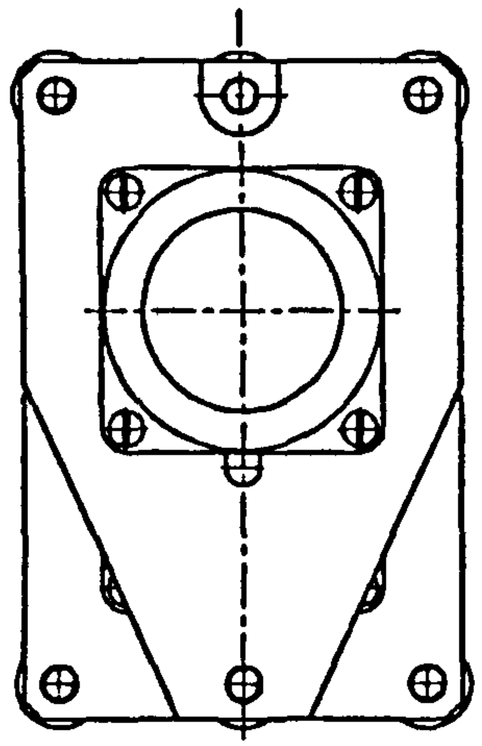

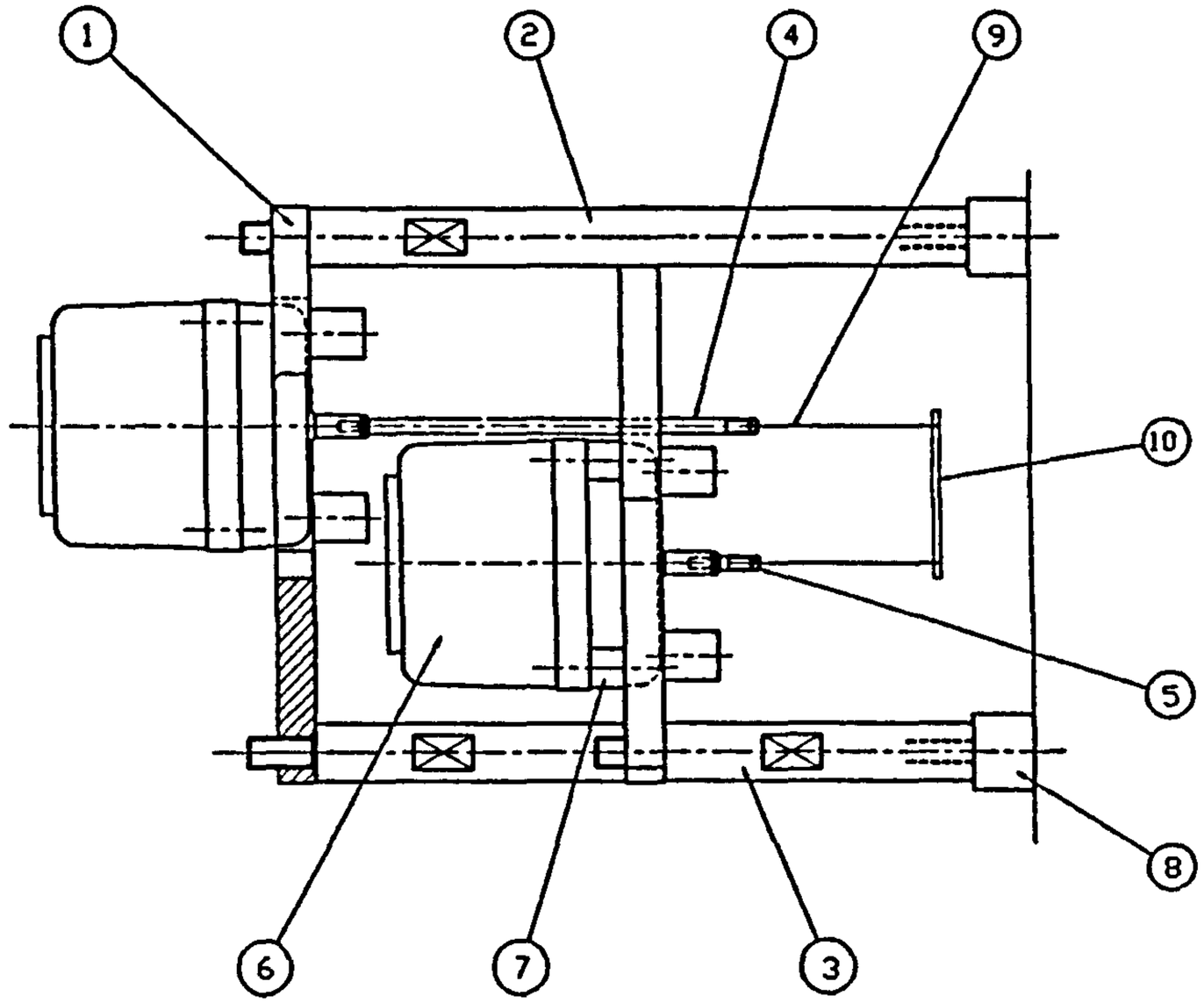

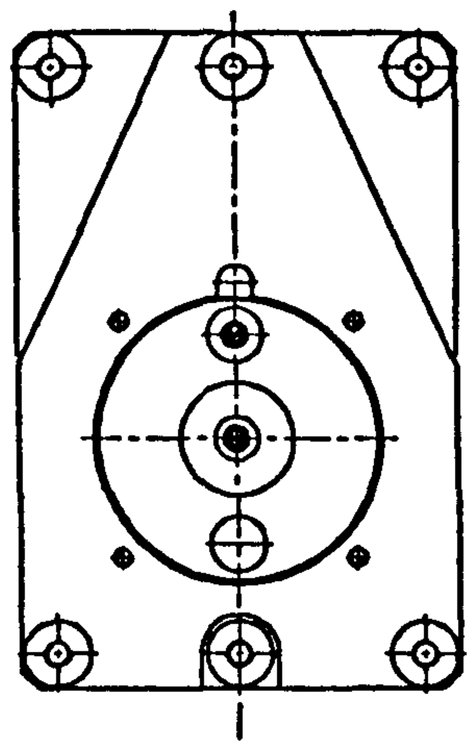

ITEM 8 NOT SHOWN

ITEM	PART No.	DESCRIPTION	No. OFF	MATL.	SPEC.	REMARKS
10		SPECIMEN	1	ALUMINA		POROUS
9		SUSPENSION THREAD	2	NYLON		REMARKS
8		RUBBER FEET	6	RUBBER		FREUNDENBERG 2018868
7		RUBBER MOUNT	8	RUBBER		FREUNDENBERG 3218E36
6		SHAKER	2			LTV LING ALTEC 398 DIA
5	MU291 A405	SHAKER END FITTING	1	ALUM.	6061-T6	
4	MU291 A404	EXTENSION FITTING	1	ALUM.	6061-T6	
3	MU291 A403	PILLAR	3	M.S.		L=80
2	MU291 A402	PILLAR	3	M.S.		L=170
1	MU291 A401	SHAKER MOUNTING PLATE	2	ALUM.	6061-T6	REMARKS

THIRD ANGLE PROJECTION

SHEET SIZE: A1

GENERAL TOLERANCE ON DIMENSIONS
MACHINED
UNMACHINED
OTHER DIMENSIONS AS STATED
WELD WHERE SHOWN THUS ___ L
MACHINE WHERE SHOWN THUS ⊿

JOB No.

No. OF SETS REQ.

SCALE: 1:1

FINISH

DRAWN	CHK	DATE
Y.B.P.KVAN		(MARCH 91)

TITLE: E MODULUS FREQUENCY TEST RIG

SCHOOL OF INDUSTRIAL & MANUFACTURING SCIENCE
CRANFIELD

DRAWING No. MU291 A400 1A

SHT. 1 OF 1 SHEETS

REMOVE ALL SHARP EDGES

DRAWING No.

ISSUE	MODIFICATION

ALL DIMENSIONS IN MILLIMETRES UNLESS OTHERWISE STATED. IF IN DOUBT ASK.

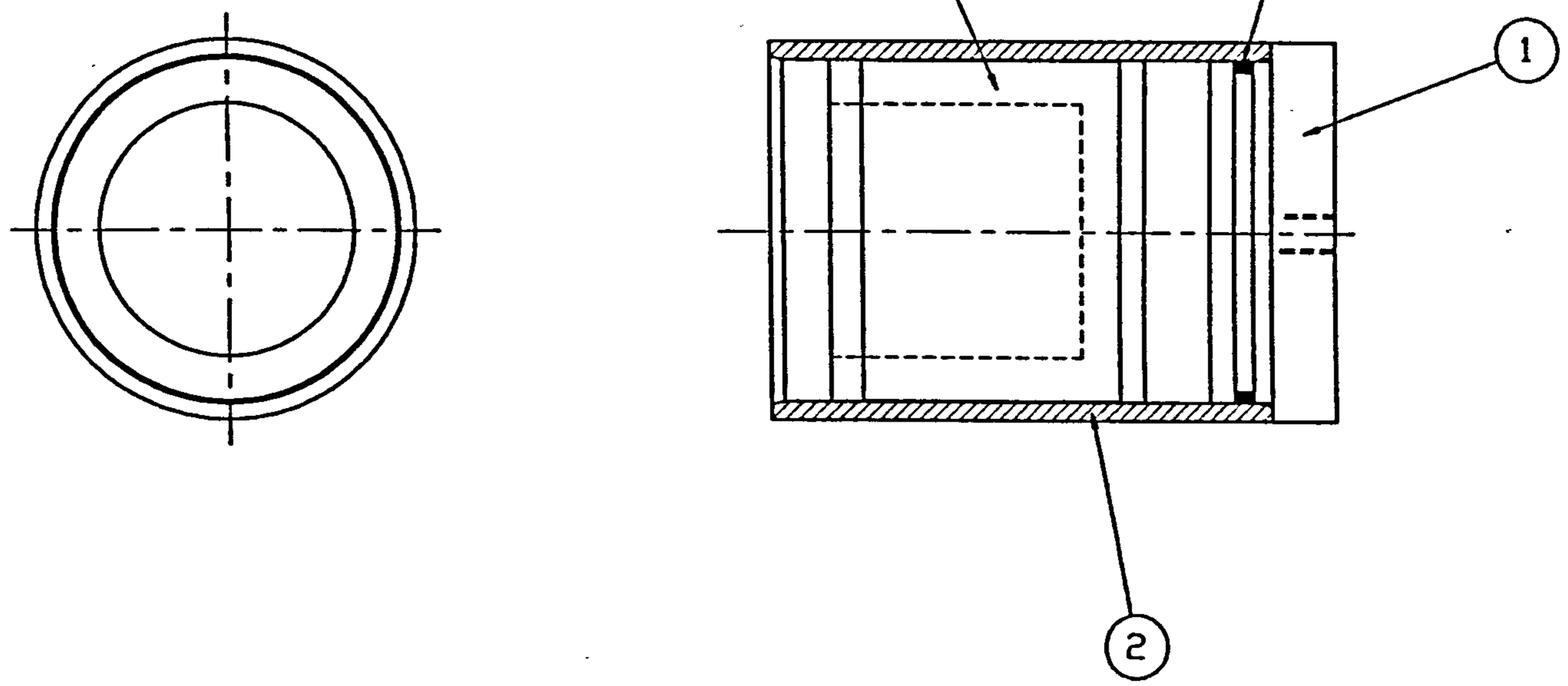

REMOVE ALL SHAPE EDGES

ITEM	PART No.	DESCRIPTION	No. OFF	MATL.	SPEC.	REMARKS
4		O-RING GACO RM0496-24	1	RUBBER	NITRILE	
3	MD291 A603	LOAD PISTON	1	GRAPHITE		
2	MD291 A602	SLEEVE	1	PERSPEX	CAST	
1	MD291 A601	BASE	1	ALUM	6061-T6	

THIRD ANGLE PROJECTION

SHEET SIZE A3

GENERAL TOLERANCE ON DIMENSIONS
MACHINED
UNMACHINED
OTHER DIMENSIONS AS STATED
WELD WHERE SHOWN THUS
MACHINE WHERE SHOWN THUS

JOB No.	No. OF SETS REQ.

SCALE 1:1

FINISH

DRAWN	CHK	DATE
Y.B.P.KWAN		20.06.95

TITLE: POWDER PACKING TEST MOULD

SCHOOL OF INDUSTRIAL & MANUFACTURING SCIENCE
CRANFIELD

DRAWING No. MU291 A601 3A

SHT. 1 OF 1 SHEETS

ISSUE	MODIFICATION

ALL DIMENSIONS IN MILLIMETRES UNLESS OTHERWISE STATED. IF IN DOUBT ASK.

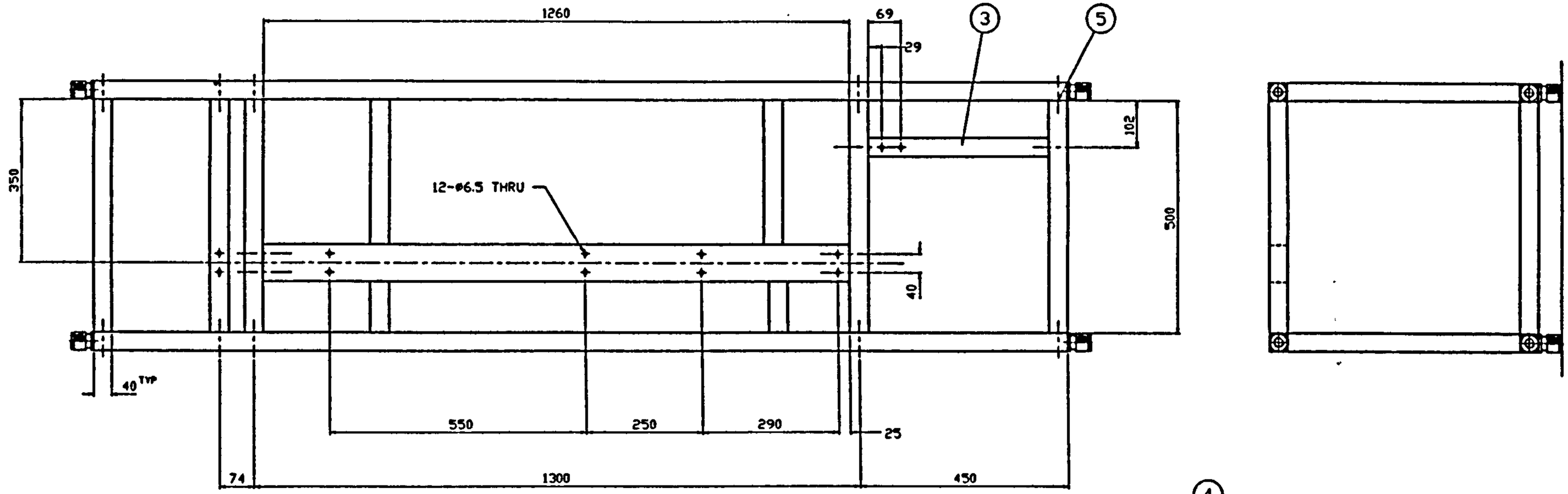

ITEM	PART No.	DESCRIPTION	No. OFF	MATL	SPEC.	REMARKS
6	8.8.826.18	T-SLOT NUT M8	8	ST		
5	8.8.826.87	STANDARD FASTENING SET	52	ST		M8x20 BUTTON HD
4	8.8.196.64	ADJUSTABLE FOOT PA	14	PA		
3	8.8.826.33	ITEM PROFILE 40x40 L	1	ALUM.		L = 298
2	8.8.826.33	ITEM PROFILE 40x40 L	17	ALUM.		L = 500
1	8.8.826.33	ITEM PROFILE 40x40 L	4	ALUM.		L = 2100

THIRD ANGLE PROJECTION

SHEET SIZE A1

GENERAL TOLERANCE ON DIMENSIONS
MACHINED
UNMACHINED
OTHER DIMENSIONS AS STATED
WELD WHERE SHOWN THUS — L
MACHINE WHERE SHOWN THUS ⊿

JOB No. | No. OF SETS REQ.

SCALE 1:5

FINISH CLEAR ANODIZED

DRAWN	CHK	DATE
V.B.P.K.V.A.N		05.11.94

TITLE: FRAME

SCHOOL OF INDUSTRIAL & MANUFACTURING SCIENCE
CRANFIELD

DRAWING No. MU291 B118 1A

SHT. OF SHEETS

REMOVE ALL SHAPE EDGES

REMOVE ALL SHARP EDGES

THIRD ANGLE PROJECTION

ITEM	PART NO.	DESCRIPTION	QTY.	MATL.	SPEC.	REMARKS
1	400016.SHD	INLET TUBE ASSEMBLY	1	A106	A106-16	BLACK ANODIZED
2	400016.SHD	INLET TUBE ADAPTER	1	4130/4140	C451	
3	400016.SHD	INLET TUBE ADAPTER	1	4130/4140	C451	
4	400016.SHD	END FITTING 1	1	A106	A106-16	BLACK ANODIZED
5	400016.SHD	END FITTING II	1	A106	A106-16	BLACK ANODIZED
6	400016.SHD	GUIDE VANE	1	A106	A106-16	BLACK ANODIZED
7	400016.SHD	O-RING #2,837	1	021	70A	
8	400016.SHD	WELDED FITTING #8	1	0M25		
9		SOCKET CAP HEAD SCREW	2	0M2	8A	
10		O-RING GASKET 400016-01	2	0M2021	4130/4140	
11		O-RING GASKET 400016-02	1	0M2021	4130/4140	
12		O-RING GASKET 400016-03	1	0M2021	4130/4140	
13		O-RING GASKET 400016-04	1	0M2021	4130/4140	
14		SEALING WASHER	1	0M2021	4130/4140	

REMOVE BURRS & SHARP EDGES			
MACHINED			
WELD MAGIC SMOOTH FINISH ...			
MACHINE SMOOTH FINISH ...			

ALL DIMENSIONS IN MILLIMETRES UNLESS OTHERWISE STATED IF IN DOUBT ASK

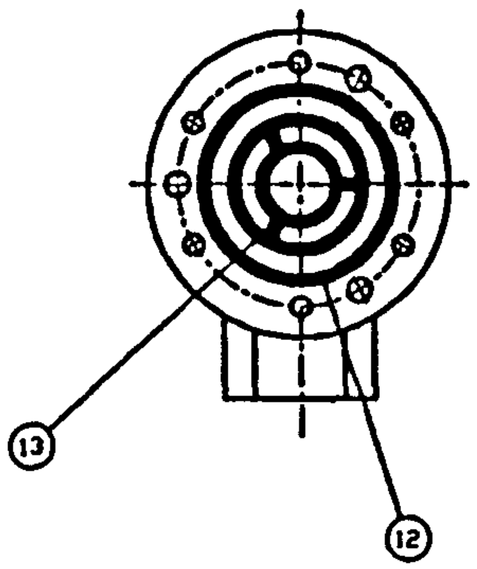

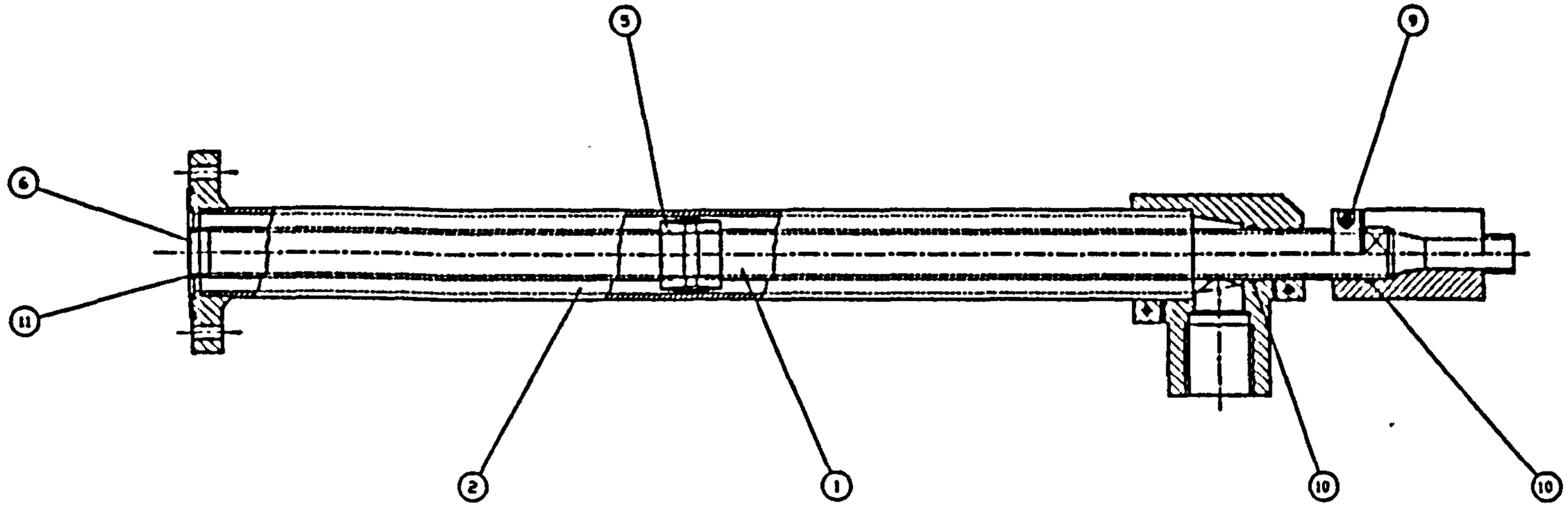

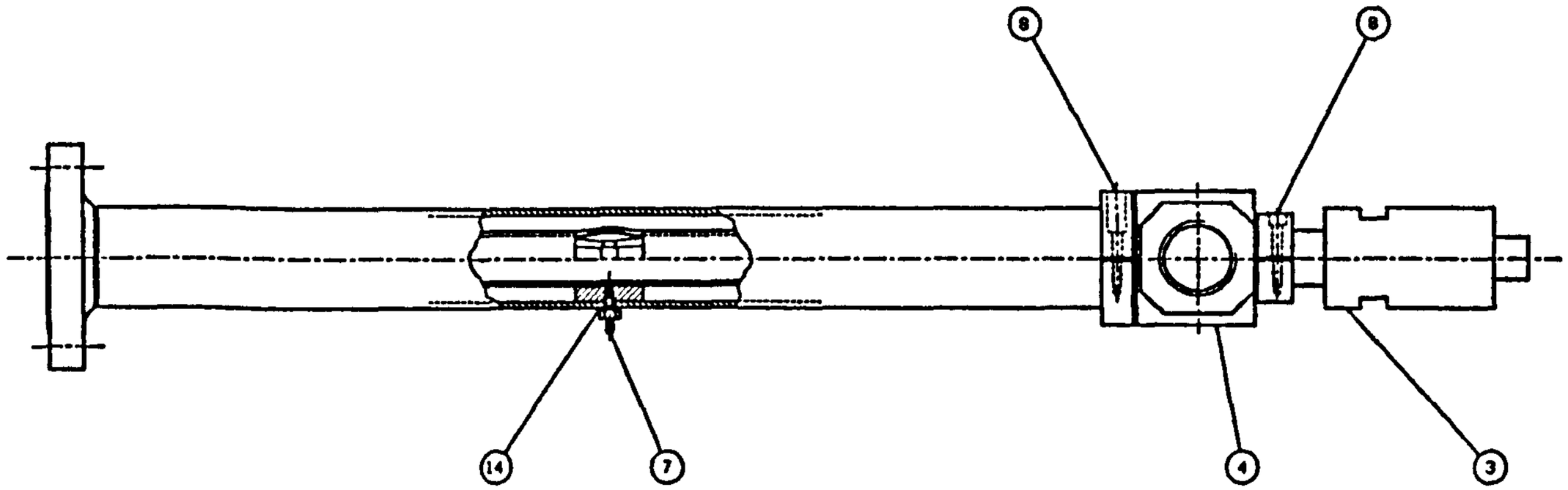

ITEM	PART NO.	DESCRIPTION	No. OFF	MATERIAL	SPEC.	REMARKS
14		SEALING WASHER	1	RUBBER	VITON A	
13		O-RING GACO 0040A-04	1	RUBBER	VITON A	
12		O-RING GACO 0040A-04	1	RUBBER	VITON A	
11		O-RING GACO 0040A-10	1	RUBBER	VITON A	
10		O-RING GACO 0040A-04	2	RUBBER	VITON A	
9		SOCKET CAP HEAD M4x40	1	MILD STEEL	BLACK	
8		SOCKET CAP HEAD M4x25	2	MILD STEEL	BLACK	
7	PARTS DWG	SWAGE FITTING 4D	1	BRASS		
6	PARTS DWG	O-RING 40.0D	1	MILD STEEL	ZINC	
5	PARTS DWG	BASE VANE	1	ALUMINIUM	6082-T6	BLACK ANODISED
4	PARTS DWG	END FITTING IV	1	ALUMINIUM	6082-T6	BLACK ANODISED
3	PARTS DWG	END FITTING VIII	1	ALUMINIUM	6082-T6	BLACK ANODISED
2	PARTS DWG	OUTLET TUBE (OUTER)	1	POLYAMIDE	CAST	
1	PARTS DWG	OUTLET TUBE (INNER)	1	POLYAMIDE	CAST	

THIRD ANGLE PROJECTION

SHEET SIZE A0

SCALE 1:1

FINISH

TITLE: OUTLET TUBE ASSEMBLY

SCHOOL OF INDUSTRIAL & MANUFACTURING SCIENCE
CRANFIELD

DRAWING No. PARTS DWG 00

SHEET 1 OF 1 SHEETS

REMOVE ALL SHARP EDGES

ISSUE	MODIFICATION

ALL DIMENSIONS IN MILLIMETRES UNLESS OTHERWISE STATED. IF IN DOUBT ASK.

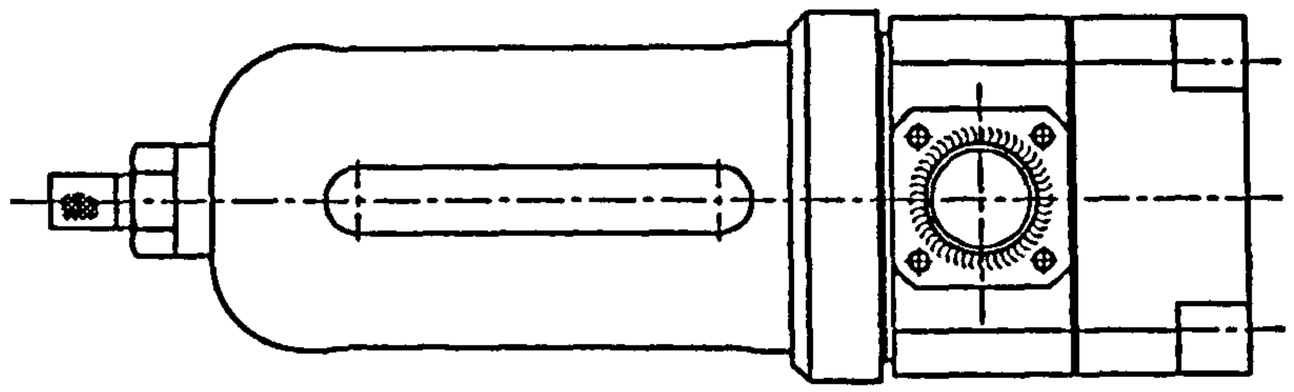

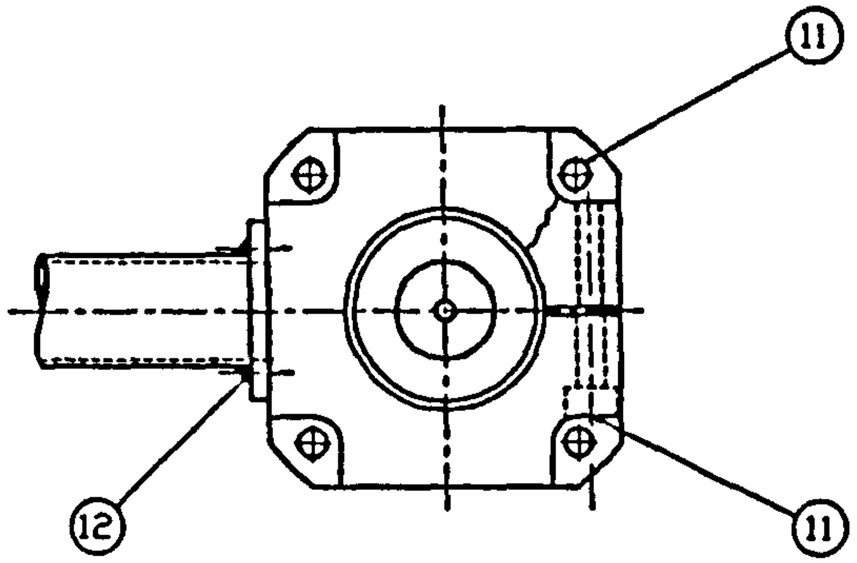

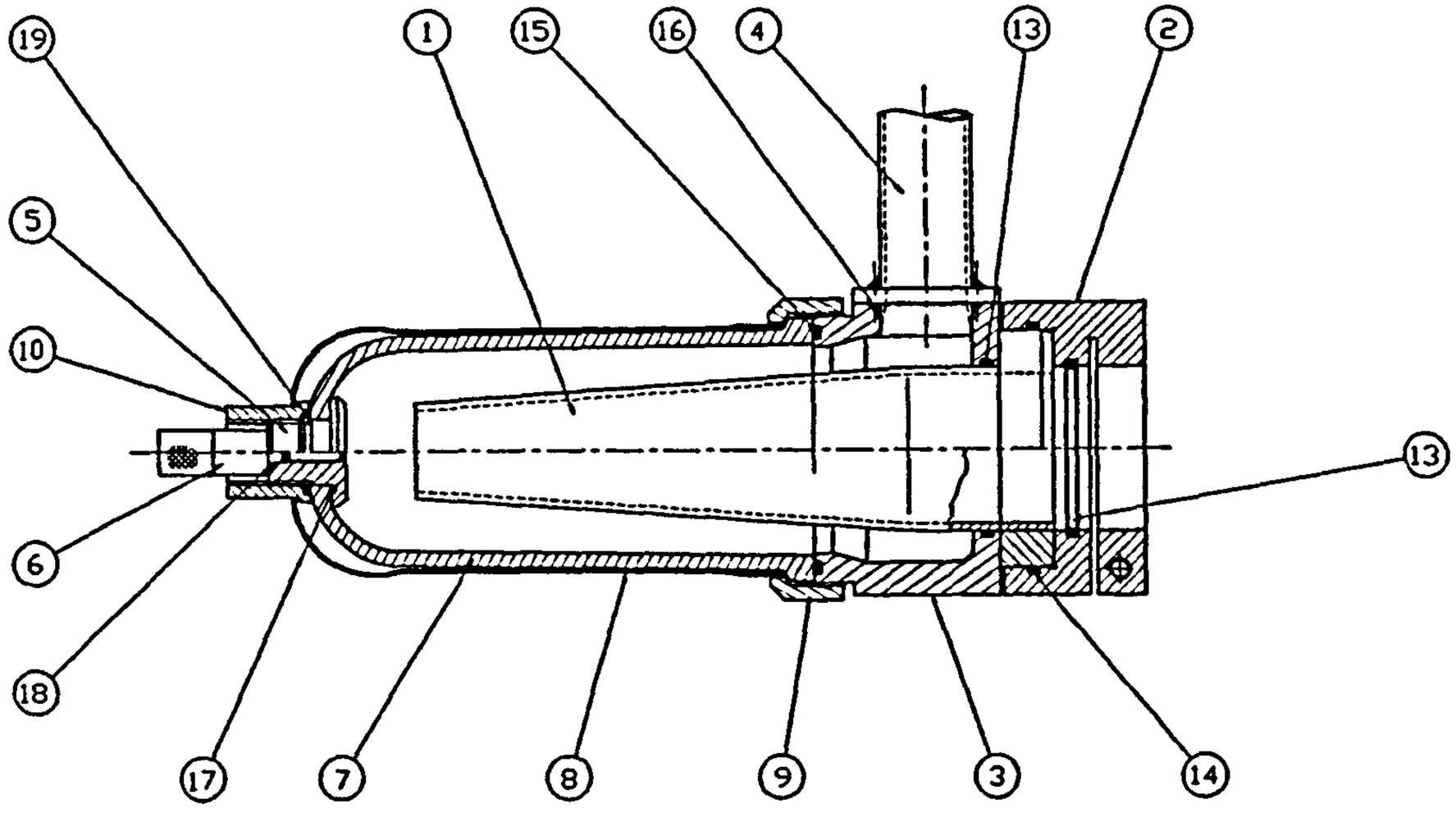

ITEM	PART No.	DESCRIPTION	No. OFF	MATL.	SPEC.	REMARKS
19		O-RING GACO RH0186-24	1	RUBBER	NITRILE	FR SMC AB402 AUTODRAIN
18		O-RING GACO RH0051-16	1	RUBBER	NITRILE	
17		O-RING GACO RH0191-16	1	RUBBER	NITRILE	FR SMC AB402 AUTODRAIN
16		O-RING GACO RH0246-24	1	RUBBER	NITRILE	
15		O-RING GACO RH0395-38	1	RUBBER	NITRILE	FR SMC AB402 AUTODRAIN
14		O-RING GACO RH0646-24	1	RUBBER	NITRILE	
13		O-RING GACO RH0446-24	2	RUBBER	NITRILE	
12		CAP HEAD SCREW M4x12	4	MTS	8.8	
11		CAP HEAD SCREW M6x35	5	MTS	8.8	
10		BRAIN NUT	1	ST		FR SMC AB402 AUTODRAIN
9		LOCKING RING	1	ALUM.		FR SMC AB402 AUTODRAIN
8		METAL COVER	1	ALUM.		FR SMC AB402 AUTODRAIN
7		BRAIN CUP	1	PERSPEX		FR SMC AB402 AUTODRAIN
6	MD291 B121	BRAIN PLUG	1	SST	304	
5	MD291 B120	BRAIN FITTING	1	SST	304	
4	MD291 B119	OUTFLOW TUBE	1	SST	316	SEAMLESS
3	MD291 B118	END FITTING V1	1	ALUM.	6061-T6	BLACK ANODISED
2	MD291 B117	END FITTING V	1	ALUM.	6061-T6	BLACK ANODISED
1	MD291 B116	BRAIN TUBE	1	PERSPEX	CAST	HOT DRAWN TO TAPER

THIRD ANGLE PROJECTION

SHEET SIZE A1

GENERAL TOLERANCE ON DIMENSIONS
MACHINED
UNMACHINED
OTHER DIMENSIONS AS STATED
WELD WHERE SHOWN THUS ⌒
MACHINE WHERE SHOWN THUS ⌓

JOB No.

No. OF SETS REQ.

SCALE 1:1

FINISH

DRAWN	CHK	DATE
Y.B.P.KVAN		23.05.90

TITLE: DRAIN TRAP SUB-ASSEMBLY

SCHOOL OF INDUSTRIAL & MANUFACTURING SCIENCE
CRANFIELD

DRAWING No. MD291 B104 1A

SHT. OF SHEETS

REMOVE ALL SHAPE EDGES

DRAWING No.

ISSUE	MODIFICATION

ALL DIMENSIONS IN MILLIMETRES UNLESS OTHERWISE STATED. IF IN DOUBT ASK.

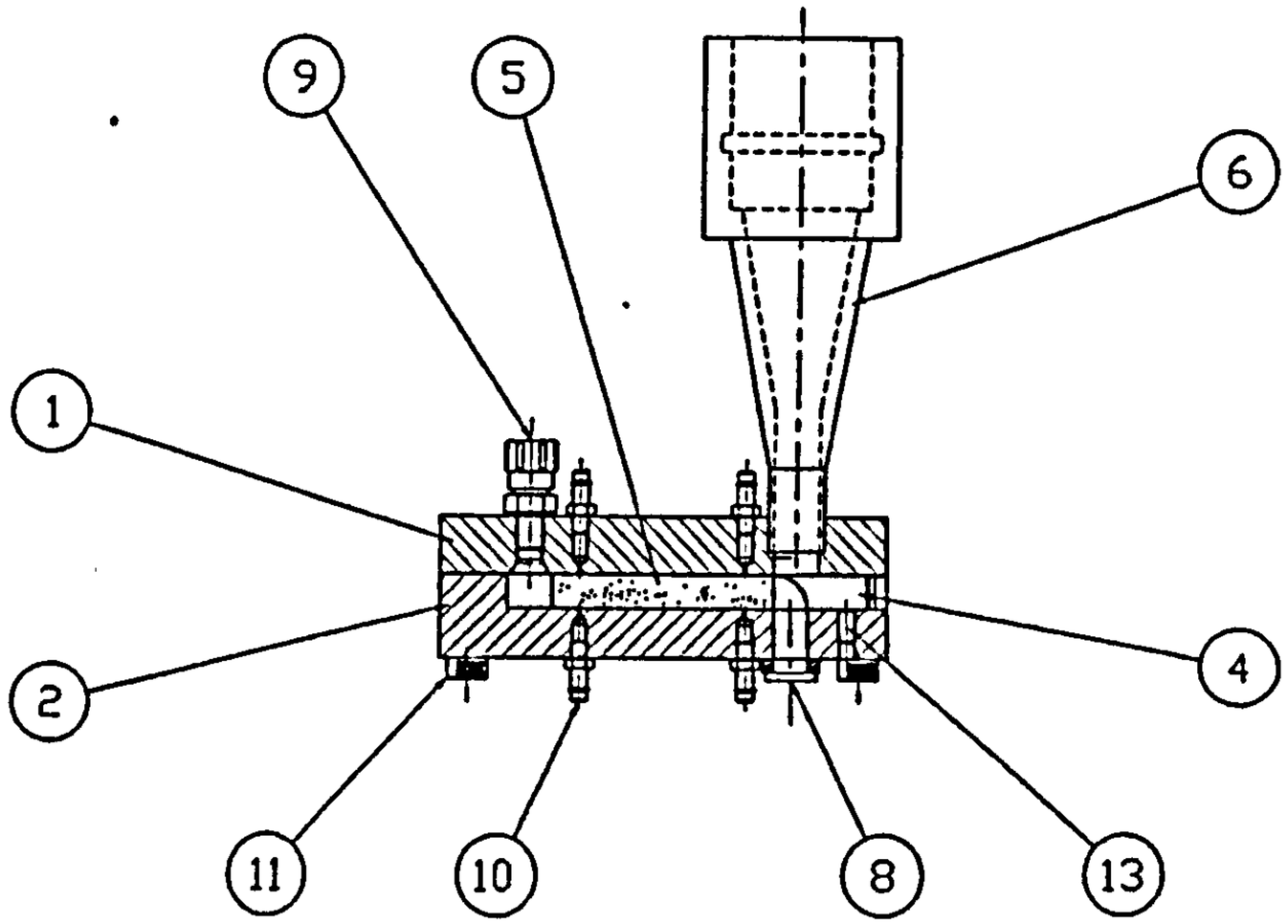

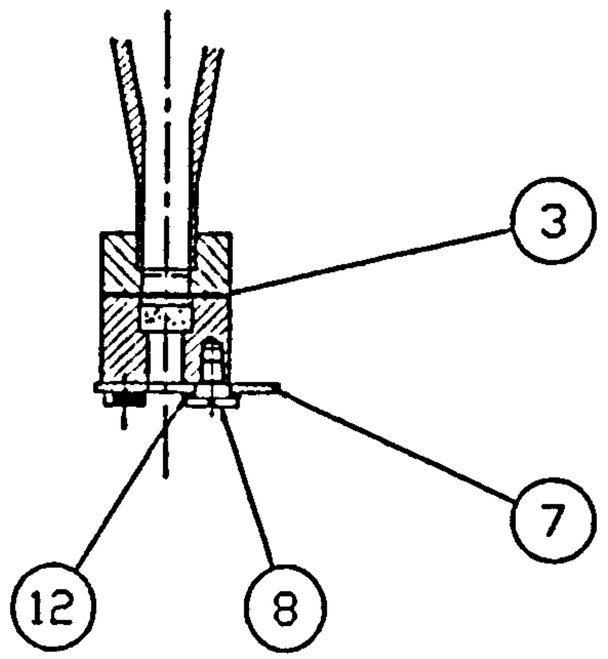

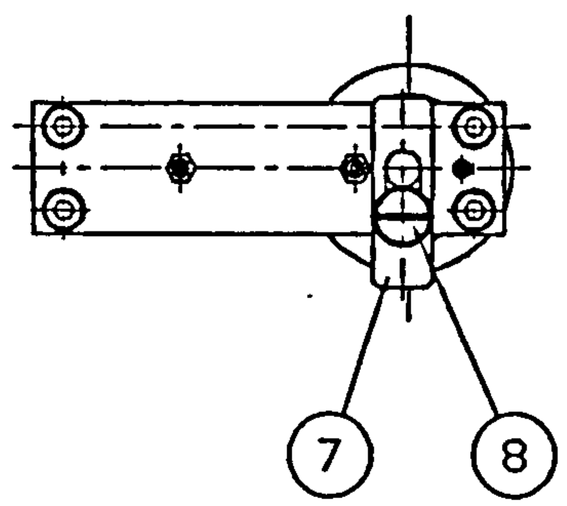

ITEM	PART No.	DESCRIPTION	No. OFF	MATL.	SPEC.	REMARKS
13		SCREW SET M3x6	1	MTS	8.8	
12		WASHER ID 6 x OD 10	1	RUBBER	NITRILE	
11		SCREW CAP HD. M4x25	4	MTS	8.8	
10	CN-M3-PK3	BARBED FITTING	4			FESTO
9	CK-M5-PK4	PNEUMATIC FITTING	1			FESTO
8	MD291 B208	SHOULDER SCREW	1	SST	304	
7	MD291 B207	SHUTTER PLATE	1	ALUM.	6061-T6	
6	MD291 B206	FLOWSENSOR ADAPTOR	1	ALUM.	6061-T6	
5	MD291 B205	SPECIMEN	1	ALUMINA	POROUS	
4	MD291 B204	FLOW DEFLECTOR	1	SST	440C	
3	MD291 B203	FLOW CHANNEL SHIM	1	SST	304	
2	MD291 B202	SPECIMEN CARRIER	1	ALUM.	6061-T6	
1	MD291 B201	TOP PLATE	1	SST	440C	

THIRD ANGLE PROJECTION

SHEET SIZE A2

GENERAL TOLERANCE ON DIMENSIONS
MACHINED
UNMACHINED
OTHER DIMENSIONS AS STATED
WELD WHERE SHOWN THUS ⌒ L
MACHINE WHERE SHOWN THUS ✓

JOB No.	No. OF SETS REQ.

SCALE 1:1

FINISH

DRAWN	CHK	DATE
Y.B.P.KVAN		01.11.95

TITLE:
SLIP COEFFICIENT MEASUREMENT FIXTURE

SCHOOL OF INDUSTRIAL & MANUFACTURING SCIENCE
CRANFIELD

DRAWING No.
MU291 B200 2A

SHT. 1 OF 1 SHEETS

REMOVE ALL SHAPE EDGES

DRAWING No.	
ISSUE	MODIFICATION

ALL DIMENSIONS IN MILLIMETRES UNLESS OTHERWISE STATED. . IF IN DOUBT ASK.

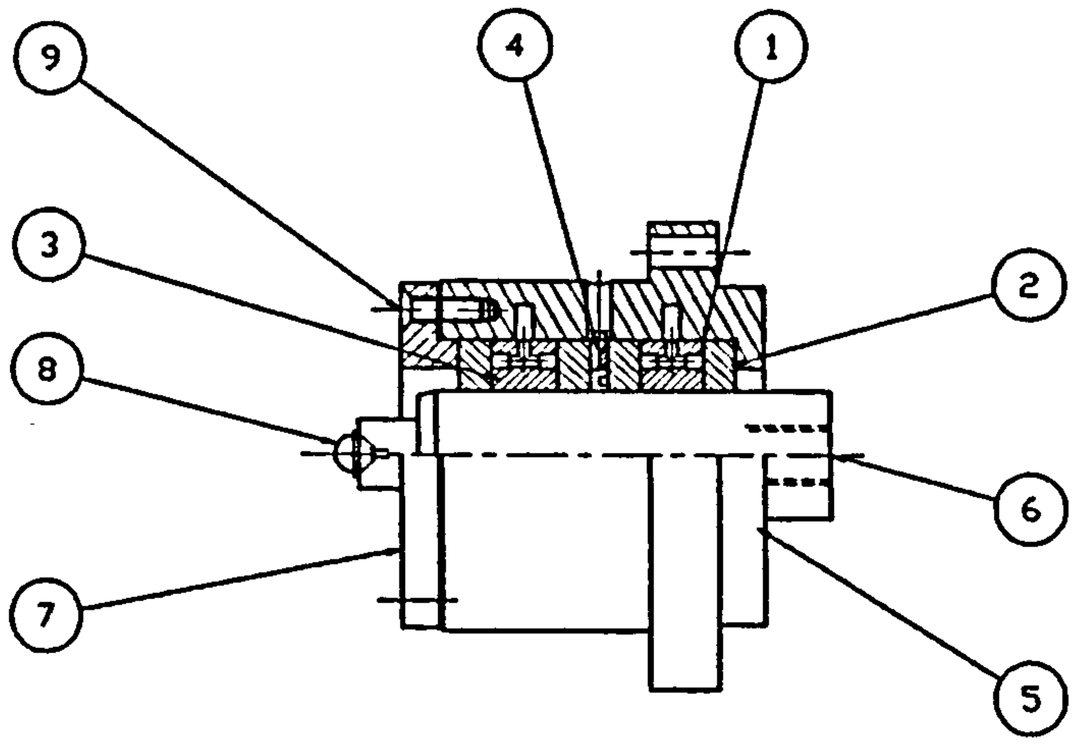

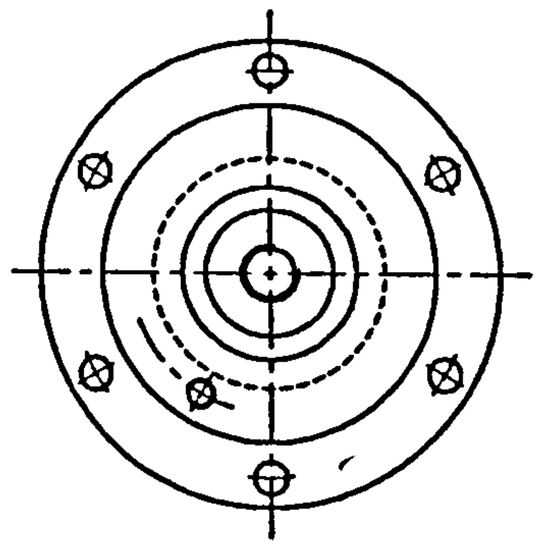

ITEM	PART No.	DESCRIPTION	No. OFF	MATL.	SPEC.	REMARKS
9		SCREW SOC.HD. C'SK M4x14	6	HTS	8.8	
8		BEARING BALL DIA. 1/4"	1	SST	440C	
7	MD291 C107	BEARING CAP	1	SST	304	
6	MD291 C106	LOAD SHAFT	1	C.S.	230M07	
5	MD291 C105	BEARING HOUSING	1	SST	440C	
4	MD291 C104	SPACER RING	1	SST	440C	
3	MD291 C103	FEED RING	2	SST	440C	
2	MD291 C102	OUTER RING	4	SST	440C	
1	MD291 C101	ENTRY SLOT DISC	4	SST	304	12um THK.

THIRD ANGLE PROJECTION

SHEET SIZE A2

GENERAL TOLERANCE ON DIMENSIONS
MACHINED
UNMACHINED
OTHER DIMENSIONS AS STATED
WELD WHERE SHOWN THUS ⌒ ⌐
MACHINE WHERE SHOWN THUS ✓

JOB No.	No. OF SETS REQ.

SCALE 1:1

FINISH

DRAWN	CHK	DATE
Y.B.P.KVAN		16.06.95

TITLE: SLOT ENTRY AIR BEARING

SCHOOL OF INDUSTRIAL & MANUFACTURING SCIENCE
CRANFIELD

DRAWING No. MU291 C101 2A

SHT. 1 OF 1 SHEETS

REMOVE ALL SHAPE EDGES

ISSUE	MODIFICATION

ALL DIMENSIONS IN MILLIMETRES UNLESS OTHERWISE STATED. . IF IN DOUBT ASK.

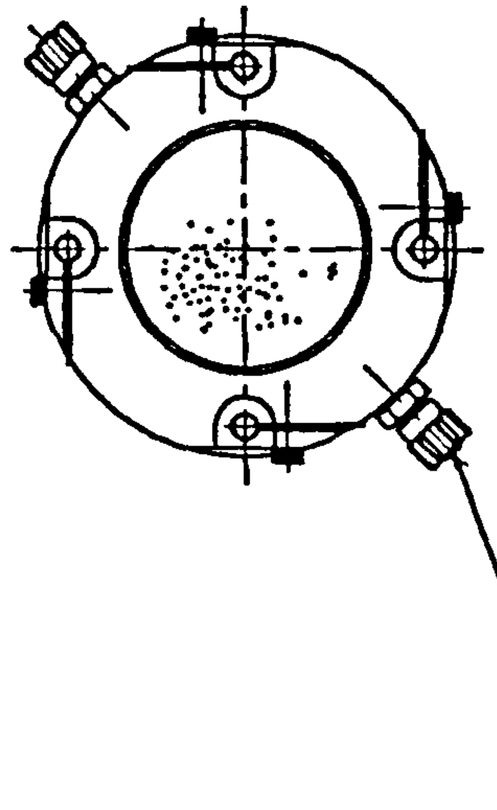

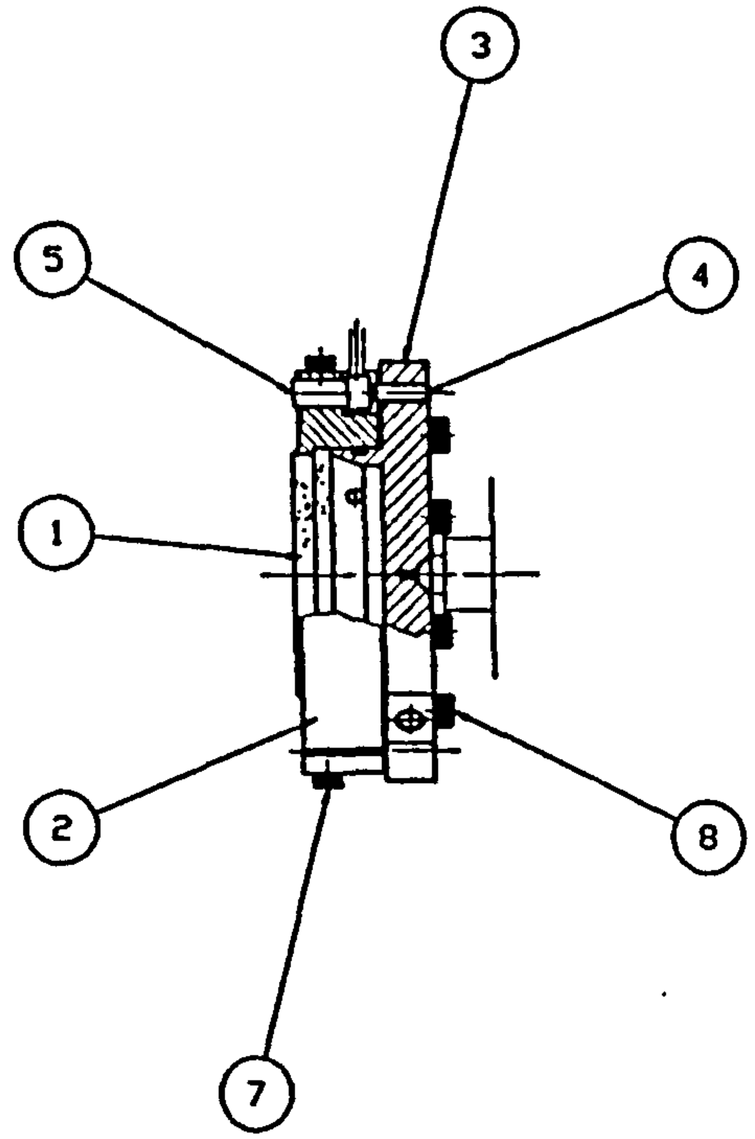

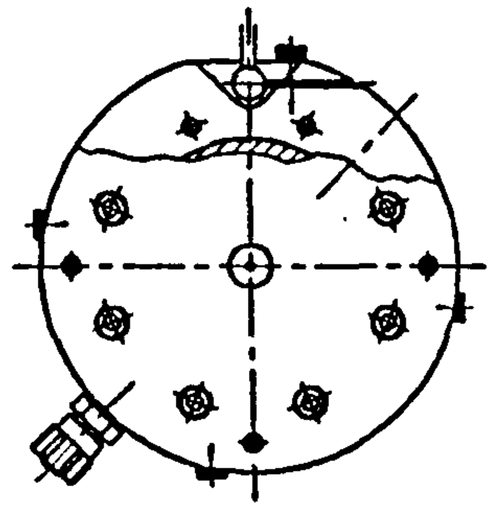

ITEM	PART No.	DESCRIPTION	No. OFF	MATL.	SPEC.	REMARKS
8		SCREW CAP HD. M3x15	8	HTS	8.8	
7		SCREW CAP HD. M2.5x8	4	HTS	8.8	
6		AIR HOSE FITTING	2			FESTO CK-M5-PK3
5		INDUCTIVE SENSOR	4			KAMAN SM9200 15N-004B
4	MD291 C124	SCREW SET M3x10	4	HTS	8.8	PLASTIC TIPPED
3	MD291 C123	BEARING COVER	1	SST	440C	
2	MD291 C122	BEARING HOUSING	1	SST	440C	
1	MD291 C121	POROUS PAD	1	ALUMINA		

THIRD ANGLE PROJECTION

SHEET SIZE A2

GENERAL TOLERANCE ON DIMENSIONS
MACHINED
UNMACHINED
OTHER DIMENSIONS AS STATED
WELD WHERE SHOWN THUS ⌒ L
MACHINE WHERE SHOWN THUS ✓

JOB No.	No. OF SETS REQ.

SCALE 1:1

FINISH

DRAWN	CHK	DATE
Y.B.P.KWAN		16.06.95

TITLE: AEROSTATIC POROUS THRUST BEARING

SCHOOL OF INDUSTRIAL & MANUFACTURING SCIENCE
CRANFIELD

DRAWING No. MU291 C102 2A

SHT. 1 OF 1 SHEETS

REMOVE ALL SHAPE EDGES

DRAWING No.	
ISSUE	MODIFICATION

ALL DIMENSIONS IN MILLIMETRES UNLESS OTHERWISE STATED. · IF IN DOUBT ASK.

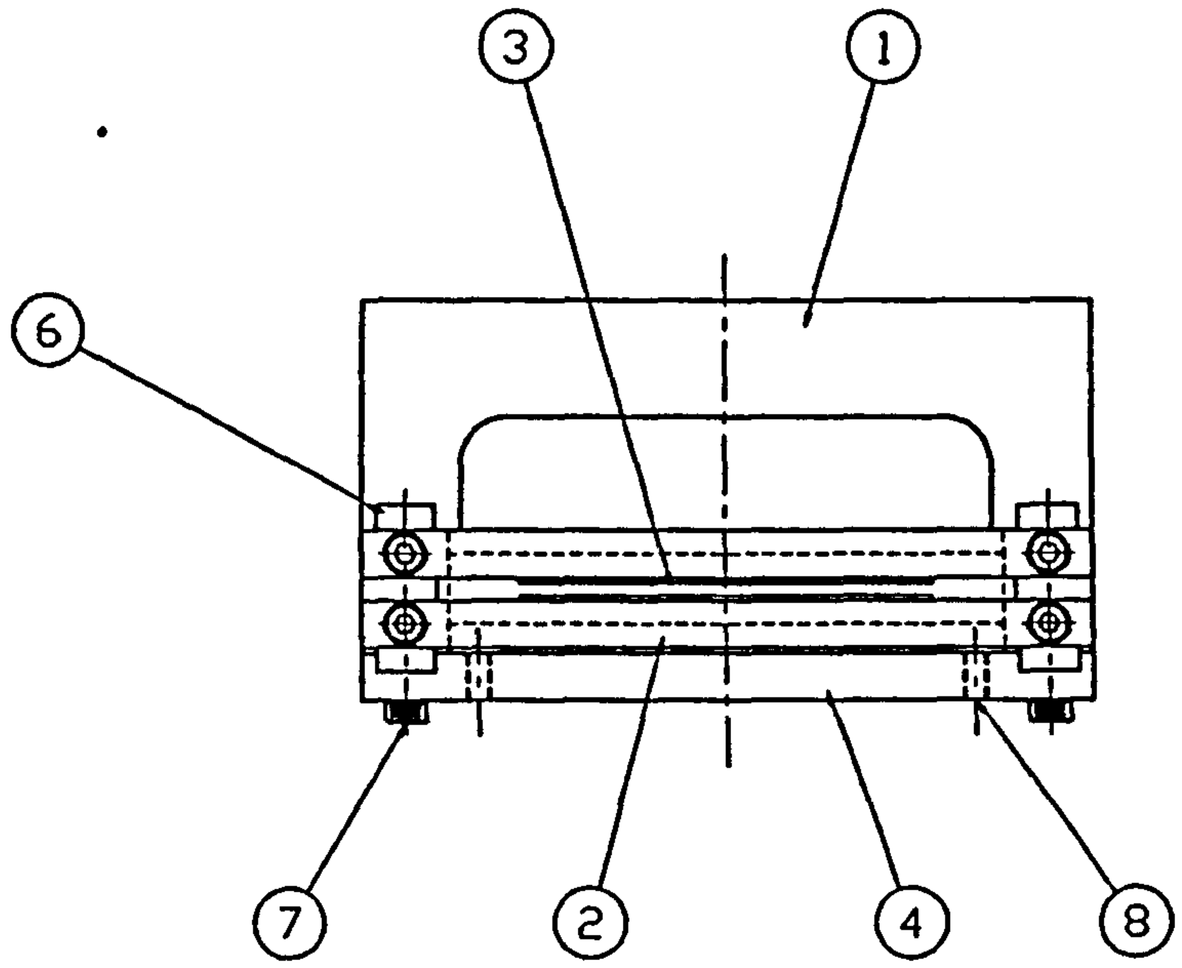

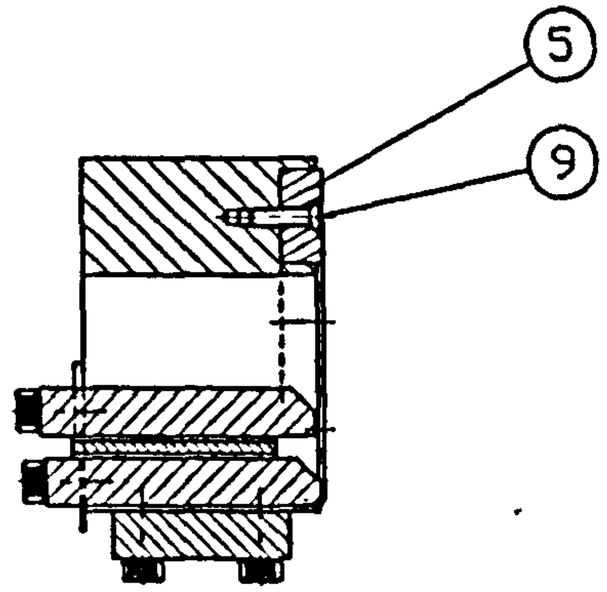

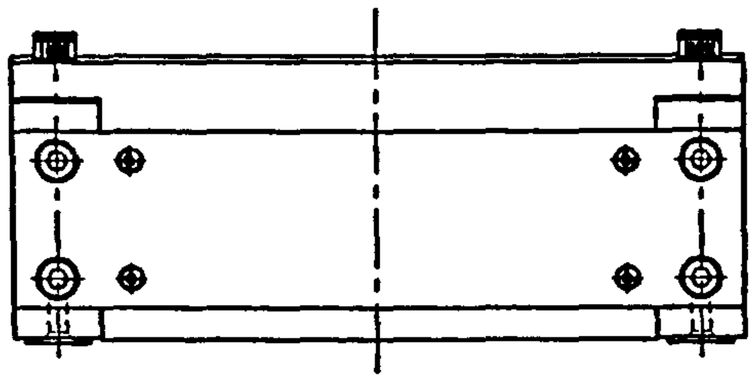

ITEM	PART No.	DESCRIPTION	No. OFF	MATL.	SPEC.	REMARKS
9		SCREW C'SK M3x12	11	HTS	8.8	
8		SCREW SET M4x8	4	HTS	8 8	
7		SCREW CAP HD M4x14	8	HTS	8.8	
6	M291 D106	PACKER	4	SST	304	2 PRS TO SUIT CAST
5	M291 D105	SKID PAD	1	PTFE		
4	M291 D104	END PLATE	1	ALUM.	6061-T6	
3	M291 D101	STACKER PLATE	1	ST		4mm GAUGE PLATE
2	M291 D102	BLADE	2	ST		8mm GAUGE PLATE
1	M291 D101	SLURRY RESERVOIR	1	ALUM.	6061-T6	REMARKS

THIRD ANGLE PROJECTION

SHEET SIZE A2

GENERAL TOLERANCE ON DIMENSIONS	JOB No.	No. OF SETS REQ	SCALE
MACHINED			1:1
UNMACHINED			
OTHER DIMENSIONS AS STATED			FINISH
WELD WHERE SHOWN THUS ⎓ ⌊			
MACHINE WHERE SHOWN THUS ✓			

DRAWN	CHK	DATE
Y.B.P.KVAN		08.10.95

TITLE: TAPE CASTING CARRIAGE ASSEMBLY

SCHOOL OF INDUSTRIAL & MANUFACTURING SCIENCE
CRANFIELD

DRAWING No. MU291 D101 2A

SHT. 1 OF 1 SHEETS

REMOVE ALL SHAPE EDGES